NOTICE: When government or other drawings, specifications or other data are used for any purpose other than in connection with a definitely related government procurement operation, the U. S. Government thereby incurs no responsibility, nor any obligation whatsoever; and the fact that the Government may have formulated, furnished, or in any way supplied the said drawings, specifications, or other data is not to be regarded by implication or otherwise as in any manner licensing the holder or any other person or corporation, or conveying any rights or permission to manufacture, use or sell any patented invention that may in any way be related thereto.

VOLUME I.

Abstracts of the

Twelfth Annual

SYMPOSIUM

USAF ANTENNA RESEARCH

and

DEVELOPMENT PROGRAM

Sponsored by AERONAUTICAL SYSTEMS DIV.

WRIGHT PATTERSON AIR FORCE BASE, OHIO.

In Cooperation With The

UNIVERSITY of ILLINOIS.

October 16., 17., 18., 19., 1962.

Robert ~~Allerton Park,~~ Monticello, Illinois.

UNCLASSIFIED

BIBLIOGRAPHY

1. Boutrel, L., The Antenna, John Wiley and Sons, 1960.

2. [illegible]C. C., "Radiation Patterns for Aperture Antennas with Non-Linear Distributions," IRE Convention Record, Part II, 1953.

3. [illegible], D., "Phase Centers of Microwave Antennas," IRE Transactions, [illegible] October 1956.

4. [illegible]ander, S. and Cheng, B. K., "Phase Center of Helical Beam Antennas," IRE National Convention Record, 1958.

5. Silver, S., Microwave Antenna Theory and Design, McGraw-Hill Book Company, New York, 1949.

6. Stratton, J. A., Electromagnetic Theory, McGraw-Hill Book Company, New York, 1941.

UNCLASSIFIED

VOLUME I

Abstracts of the

TWELFTH ANNUAL SYMPOSIUM

ON

THE USAF ANTENNA RESEARCH AND DEVELOPMENT PROGRAM

SPONSORED BY

AERONAUTICAL SYSTEMS DIVISION

WRIGHT PATTERSON AIR FORCE BASE, OHIO

ROBERT ALLERTON PARK
(University of Illinois)
Monticello, Illinois

16, 17, 18, 19 October 1962

UNCLASSIFIED

NOTICES

When Government drawings, specifications, or other data are used for any purpose other than in connection with a definitely related government procurement operation, the United States Government thereby incurs no responsibility nor any obligation whatsoever; and the fact that the Government may have formulated, furnished, or in any way supplied the said drawings, specifications, or other data is not to be regarded by implication or otherwise as in any manner licensing the holder or any other person or corporation, or conveying any rights or permission to manufacture, use or sell any patented invention that may in any way be related thereto.

CONTENTS

CONTENTS (Continued)

GER 10825

A HIGH PERFORMANCE, LIGHTWEIGHT LUNEBERG LENS

BY

GEORGE WEICH

AND

D. L. BROWN

GOODYEAR AIRCRAFT CORP.

Akron, Ohio

A HIGH PERFORMANCE, LIGHTWEIGHT LUNEBERG LENS

INTRODUCTION

The Luneberg Lens is a variable index, spherically symmetrical structure which will collimate electromagnetic energy. The energy will be focused at a point diametrically opposite the tangency of an impinging plane wave. This is illustrated in figure 1.

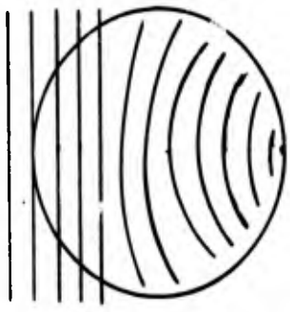

FIGURE I

LUNEBERG LENS WAVE DIAGRAM

To make a spherical lens capable of focusing electromagnetic waves at a given point or at least within a very small area, the refractive index, N, of the dielectric must vary in a precise prescribed manner. The relation between refraction index and radial distance from the center of the sphere for the case where the focal point is on the periphery is shown in the Standard Luneberg Equation.

$$N = \sqrt{2 - \left(\frac{d}{R}\right)^2}$$

where

R = Radius of the lens

d = Distance from the center of the lens.

These lenses offer interesting properties as an antenna for multiple target, aquisition, and tracking systems. Moderate scan speeds can be obtained since only the feed must be moved and a multiplicity of feeds may be operated simultaneously.

Recent developments in artificial dielectric materials and construction designs permit the construction of high performance, lightweight units. The purpose of this presentation is to rather briefly describe the material, its properties, and the construction design. A unique test apparatus for rapidly measuring index of refraction is included because of its importance for precise quality control and cataloging index values necessary to obtain the desired performance. The design and radiation patterns for a 34 inch lens is included to illustrate the results.

ARTIFICIAL DIELECTRIC MATERIAL

Artificial dielectric material is formulated by suspending insulated aluminum slivers or wires in a low density polystyrene foam. This is accomplished by pre-puffing granulated polystyrene into approximately 1/4 inch beads. These beads are thoroughly dried and ionically and mechanically manipulated to produce the desired homogeneity and random sliver orientation. This blend is carefully placed in a mold and foamed into a solid

material. The material is removed from the mold, oven cured to remove moisture and relieve stresses, and precision cut to the specified module size. This complex manufacturing process has been developed to economically produce large quantities of material with a high degree of homogeneity and isotropy.

In general, the slivers load the electric field in a capacitive manner, thereby, increasing the index of refraction. They present little obstruction to the magnetic field so that their effect on the magnetic constant is negligible. For wavelengths long compared to sliver length, the dielectric constant is a fixed ratio dependent mainly on the length of the slivers and on their quantity. Tests of 1/8 inch and 3/16 inch long slivers, over the range of 400 mc to 6000 mc, show a rise of .0008 index points per 100 mc. A typical sliver length selected for the UHF band is 3/8 inch compared to 3/16 in length selected for C band.

High sliver efficiency is obtained by careful selection of the cross section dimension and insulating material. Specifically the importance of the shape factor is shown in the equation

$$E = \left(\frac{\phi}{1-\phi}\right)\left(m\right)$$

where E = efficiency

ϕ = quantity of slivers per unit volume

m = shape factor

A general solution for m can be obtained from the relation

$$m = \frac{a^2}{bc\left[\ell_n \frac{4a}{b+c} - 1\right]}$$

where, a, b, and c sliver lenght, width, and thickness respectively. However, the exact values for m are derived emperically. Figure 2 tabulates measured Tanδ and index values for several sliver coating materials and shape factors at L band, S band, and C band.

SLIVER COATING	DIMENSIONS	TAN	INDEX
L Band			
Polystyrene	3/16x.0045x.00045	.0014	1.387
Polystyrene	3/16x.0023x.0002	.0008	1.314
Polystyrene	3/8 x.0045x.00045	.0003	1.348
Mylar	3/8 x.0045x.00045	.0004	1.345
Mylar	3/16x.0045x.00045	.0007	1.273
Mylar	3/16x.0023x.0002	.0004	1.313
Silane Oxide	3/16x.0023x.0007	.0010	1.335
Polyethylene	3/16x.0023x.00045	.0003	1.345
S Band			
Mylar	3/16x.0023x.00045	.0013	1.387
Mylar	3/16x.0023x.0002	.0012	1.312
Polyethylene	3/16x.0023x.00045	.0004	1.318
C Band			
Polystyrene	3/16x.0023x.0002	.0019	1.350
Mylar	3/16x.0045x.00045	.0015	1.327
Silane Oxide	3/16x.0023x.0007	.0017	1.378
Polyethylene	3/16x.0023x.00045	.0006	1.355

FIGURE TWO

Sliver Coatings, Shape Factors, Electrical Characteristics versus L-Band, S-Band, and C-Band Frequencies.

Figure 3 lists typical characteristics of artificial dielectric material used to construct a C-Band lens.

FIGURE THREE

Typical Characteristics of Artificial Dielectric Material At C-Band

(Suspension Media: 1.5 #/ft^3 polystyrene foam, sliver, aluminum; polyethylene coated)

Sliver Dimensions	3/16" x .0023" x .00045"	
Index Range	1.012	1.400
Index Tolerance*	± 0.0045	
Isotropy **	± 0.010	
Loss Tangent	0.0004	0.0007

* Average of the three orthogonal measurements about zone center.

** Maximum spread between 3 orthogonal measurements about zone center.

CONSTRUCTION DESIGN

The construction design utilizes a small cubical module of material, requiring tens of thousands of cubes per lens, with thirty to forty-five index of refraction values or zones. This concept permits the quality control of very small increments of lens material, a very close approximation of the desired index curve, and a fairly random zone interface to reduce the overall reflection coefficient. These factors were considered necessary design parameters to achieve the high lens performance desired.

For example, the effect of a displaced module will vary for the different directions in which energy goes through a lens, assuming the focal point moves relative to the lens. The angle ϕ, as shown in Figure Four, is the angle between the ray through the center of the improper cube and the line from the center of the lens through the center of the improper cube. This angle may vary from 0° to 180°. For the ideal lens, the parameters satisfy the equation $nr \sin \phi = R \sin \theta$ (1)

which is known as Snell's Law.

FIGURE FOUR

Luneberg Lens with Improper Cube

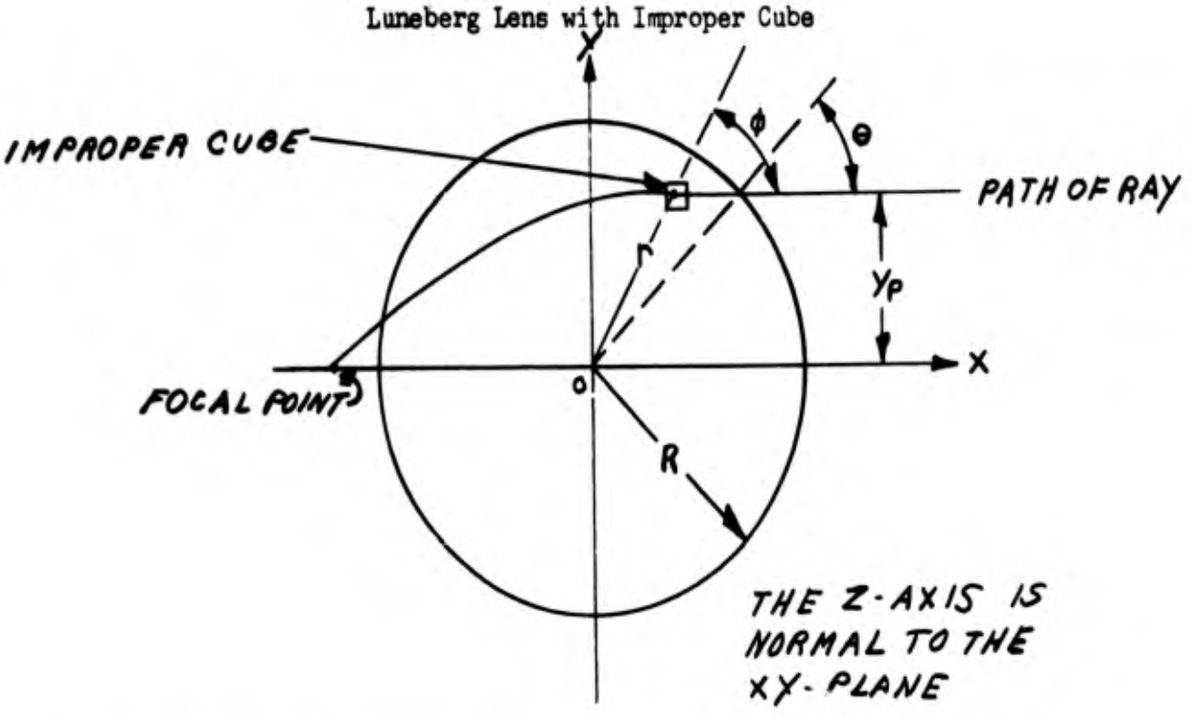

It is assumed that the rays through the defective lens follow the same paths as through an ideal lens and the effect of the improper cube is a perturbation of the phase front in front of the lens. As a first approximation, the magnitude of the perturbation ϕ is given by

$$\phi = \frac{2\pi a (\Delta n)}{\lambda} \qquad (2)$$

where ϕ is measured in radians, a is the length of the edges of the cube, Δn is the difference between the actual and the proper value of the index of refraction for the cube, and λ is the free space wavelength. The area of the perturbation is a^2, the location of which can be determined by equation (1). The center of the improper cube lies in the XY-plane.

It is assumed for the ideal lens that the power is uniformly distributed

over the circle in the X=R plane with the radius R and the Center (R,0,0), and the power density is zero over the rest of the X=R plane. The phase is constant over this circle except for the perturbation. The coordinate Yd for the perturbation may vary from 0 to nr, where n is the proper index of refraction for the improper cube and r is the distance from the center of the lens to the center of the improper cube.

Let E denote the boresight error which is defined as the angle between the axis of the emerging beam and the line from the focal point, or feed point, through the center of the lens. The axis of the emerging beam is found by assuming that it has the same direction as the normal to the best fit plane, using the least squares criterion, for the phase front through the point (R,0,0). The value of E is given by

$$E = \frac{3a^2 Yd}{\pi R^3} (\Delta n) \quad (3)$$

where E is expressed in radians. The maximum value of E is

$$E_{max} = \frac{3a^2 nr}{\pi R^3} (\Delta n) \quad (4)$$

For many lens designs, $nr/R \leq \pi/3$. In this case

$$E_{max} = \frac{a^2}{R^2} (\Delta n) \quad (5)$$

As an example, if (5) is valid, R = 20a and n = 0.01; then

$$E_{max} \leq 0.025 \text{ milliradians} = 0.0014^\circ$$

The solution of the equation $R^2 = X^2 + Y^2 + Z^2$ for the placement of the thousands of 1 inch modules in the lens was accomplished through the use of an IBM-650 computer. A deck of IBM cards for a quarter of the lens was then translated to the quandrant layer drawings used during assembly

of the lens. Such a program readily accepts basic lens design modifications such as shift of focal radius and change of diameters. A typical quandrant layout drawing for the lens equator slice is shown in Figure 5.

FIGURE FIVE

Quandrant - Lens Equator

2	2	1	1	1	1	1	1									
6	6	6	5	4	2	1	1	1								
10	10	9	9	8	6	5	3	1	1	1						
13	13	13	12	11	10	8	7	5	2	1	1					
16	16	15	15	14	13	11	10	8	6	3	1	1				
19	18	18	17	16	15	14	13	11	9	6	3	1	1			
21	21	20	20	19	18	16	15	13	11	9	6	3	1	1		
23	23	22	22	21	20	19	17	15	13	11	9	6	2	1		
25	24	24	23	23	22	20	19	17	15	13	11	8	5	1	1	
26	26	26	25	24	23	22	21	19	17	15	13	10	7	3	1	1
28	27	27	26	26	25	23	22	20	19	16	14	11	8	5	1	1
29	28	28	28	27	26	25	23	22	20	18	15	13	10	6	2	1
30	29	29	28	28	27	26	24	23	21	19	16	14	11	8	4	1
30	30	30	29	28	28	26	25	23	22	20	17	15	12	9	5	1
31	31	30	30	29	28	27	26	24	22	20	18	15	13	9	6	1
31	31	31	30	29	28	27	26	24	23	21	18	16	13	10	6	2
31	31	31	30	30	29	28	26	25	23	21	19	16	13	10	6	2

MATERIAL TEST EQUIPMENT

As mentioned earlier in the construction design discussion, it is necessary to measure index values of a very large quantity of cubes per lens. Each cube is measured in the three orthogonal directions. These three readings are averaged to classify the cube into a zone, then each reading is compared to the zones center value for isotropy tolerance. For completeness, it should be mentioned that tan δ of this material is uniform over a production run and therefore, only sample lots are measured in a standard cubical resonant cavity.

A unique flow through resonant cavity was devised to efficiently perform the large quantity of index measurements and is shown in Figure 6. The electric field configuration of this cavity operating in the fundamental TE 1,C,1 mode is shown in Figure 7. Of course, the index value is derived by noting the cavity resonant frequency with and without the cube in place and the tan δ value is derived by noting the cavity Q with and without the cube in place.

The unique property of this type cavity is the existance of ports in the walls that do not materially affect the cavity resonance characteristics and permit rapid transport of cubes through the cavity. Tubes with cross sectional dimensions which fit the cube to be tested and at least a 1/4 wavelength long, are attached to the cavity ports. The tube cross sectional dimensions are well below the waveguide cut-off at the test frequency.

Figure Six

Flow Through Resonant Cavity

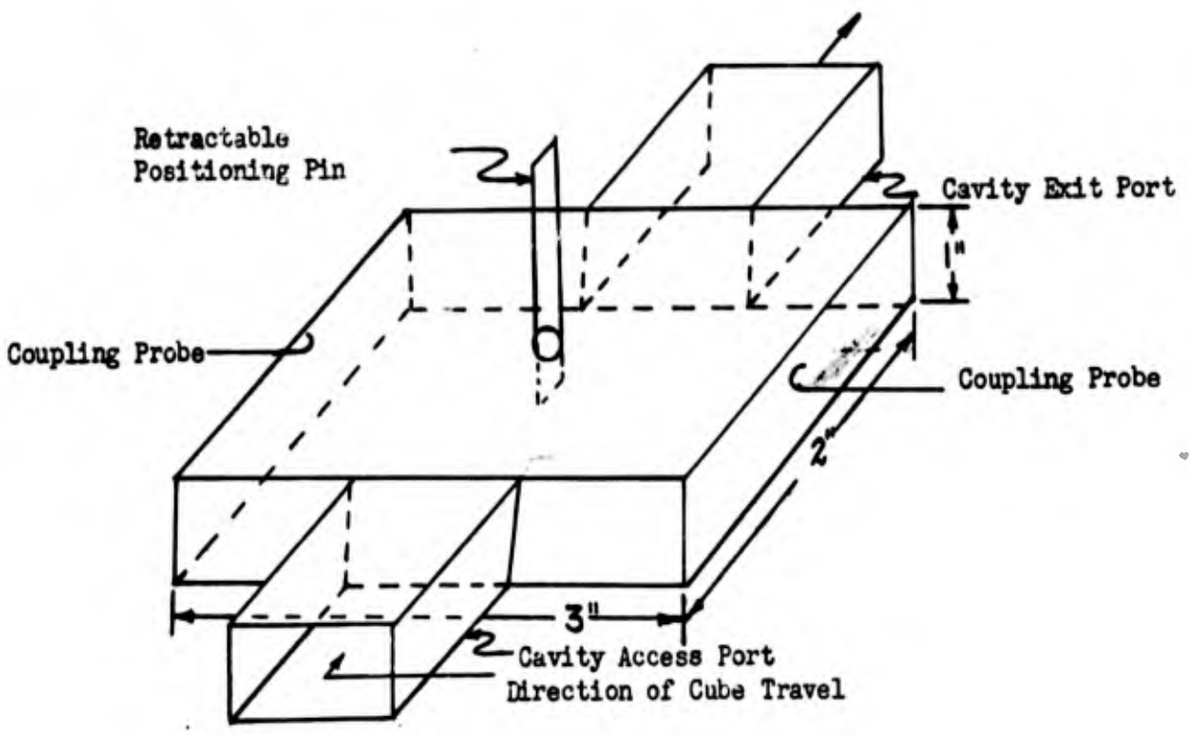

Figure Seven

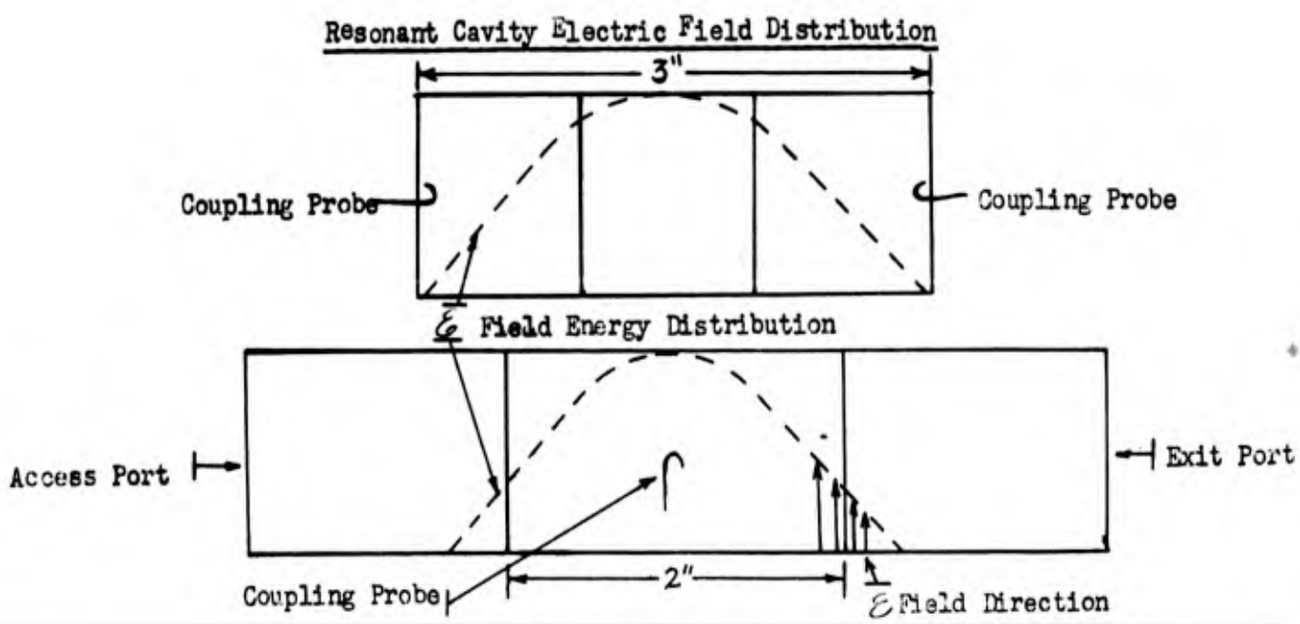

An automated system utilizing this type cavity is shown in Figure Eight.

FIGURE EIGHT

Automatic Dielectrometer

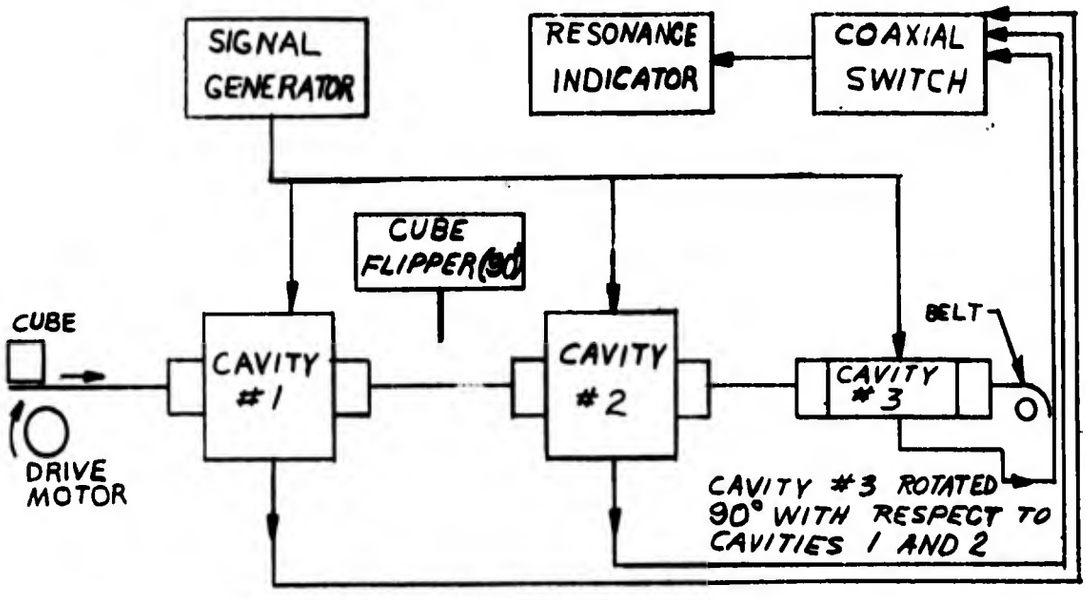

In general, this device consists of 3 identical cavities with access ports. A dielectric conveyor belt of known uniform quality passes through the three cavities, which are orientated as shown. A cube, passing through this device, yields index readings in each orthogonal direction in a minimum of time. Presetting the signal generator and resonance indicator for a specific zone center and isotropy tolerance, allows the device to accept or reject cubes for a precise index level in a matter of seconds.

DESIGN AND TEST RESULTS OF A 34" DIAMETER LUNEBERG LENS

The high performance lens described herein was designed to focus at 1.2

times the lens radius and followed the index distribution as shown in Figure 9. These data are a direct result of the calculations performed and published by S. P. Morgan.[2]

FIGURE NINE

Index Distribution for Focal Point Equals 1.2 Times Lens Radius

ρ = (radius) x (index)	Refractive Index
0.00 (Lens Core)	1.32095
0.05	1.32057
0.10	1.31943
0.15	1.31751
0.20	1.34180
0.25	1.31127
0.30	1.30690
0.35	1.30162
0.40	1.29539
0.45	1.28814
0.50	1.27976
0.55	1.27014
0.60	1.25912
0.65	1.24649
0.70	1.23196
0.75	1.21511
0.80	1.19532
0.85	1.17155
0.90	1.14180
0.91	1.13481
0.92	1.12735
0.93	1.11934
0.94	1.11065
0.95	1.10112
0.96	1.09051
0.97	1.07839
0.98	1.06394
0.99	1.04507
1.00 (Periphery)	1.00000 (Air)

To approximate this theoretical index distribution, the lens was designed to have 31 specific index levels or zones. (Zone 1, of course, consisted of unloaded foamed polystyrene, index = 1.012).

The assembled lens, after being machined to the 17" radius (Spherical within 0.080 inches) was subjected to radiation tests. The results are summarized in figures 9, 10, 11, and 12.

FIGURE 10

34" Luneberg Lens at C Band

Beam Width	1st Null Depth	Boresight	Isotropy	Gain Factor
$\leq$ 0.2 degrees of theoretical	$>$ 40 db	$<$ 0.25 Milliradians	$<\leq$ 1.0 db	$>$ 0.50

* The magnitude of lens isotropy in terms of detected power is measured by off-setting the lens feed from the source - lens line of sight to achieve a received signal 10 db below the peak of the main beam and automatically recording the variation in received signal as the lens is rotated about its center, with the position of the lens feed, lens center, and source held constant.

As indicated in Figure 10, this 34" C-band lens, now one of several, exhibits excellent electrical characteristics. Likewise, these lenses physically are dimensionally precise and lightweight weighing on the order of 18 pounds.

The authors wish to gratefully acknowledge the assistance of Mr. R. B. Higgins for carrying out and documenting much of the experimental work, and Bell Telephone Laboratories and Wheeler Laboratories for their substantial contributions.

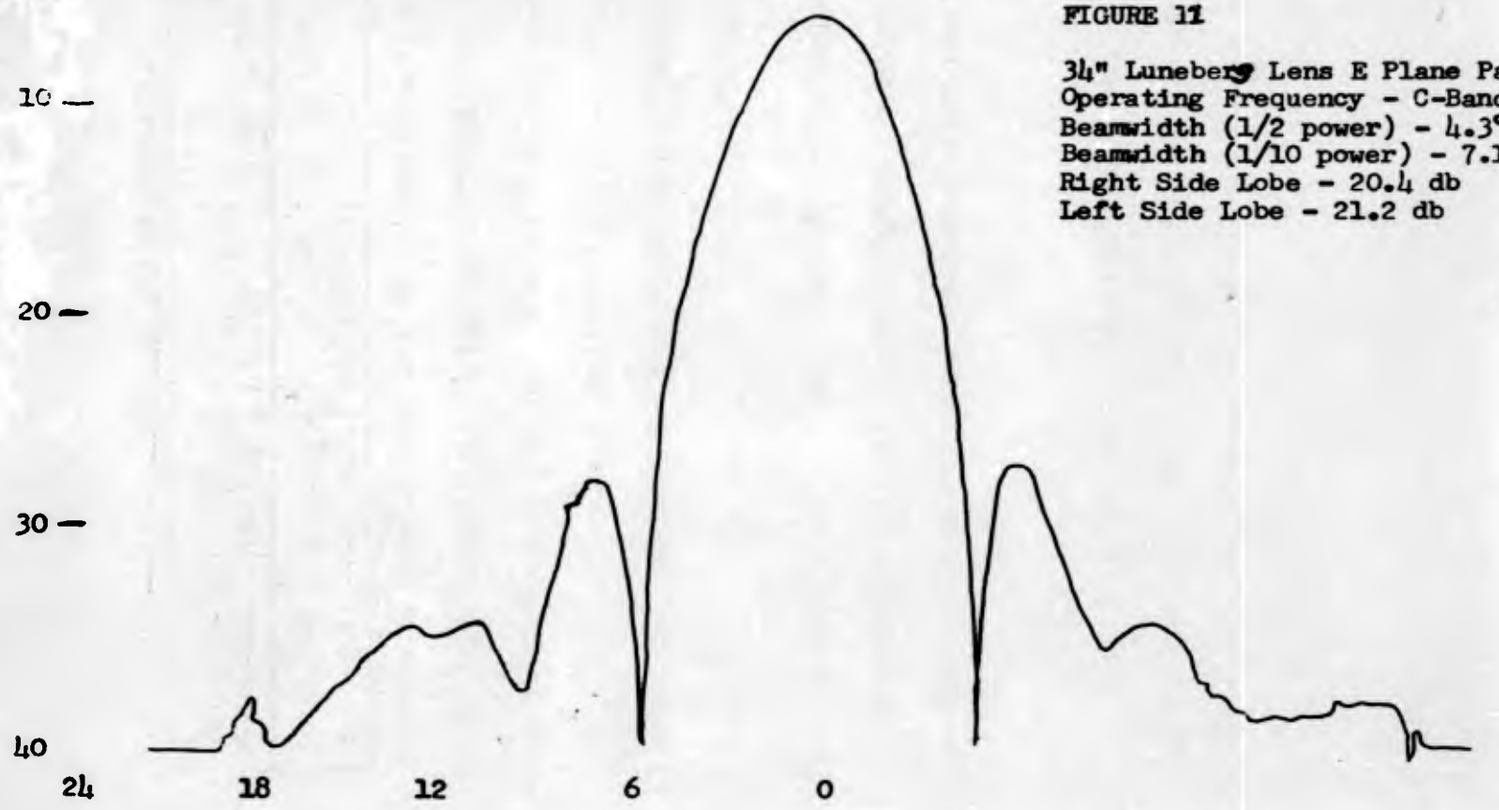

FIGURE 11

34" Luneberg Lens E Plane Patter
Operating Frequency - C-Band
Beamwidth (1/2 power) - 4.3°
Beamwidth (1/10 power) - 7.1°
Right Side Lobe - 20.4 db
Left Side Lobe - 21.2 db

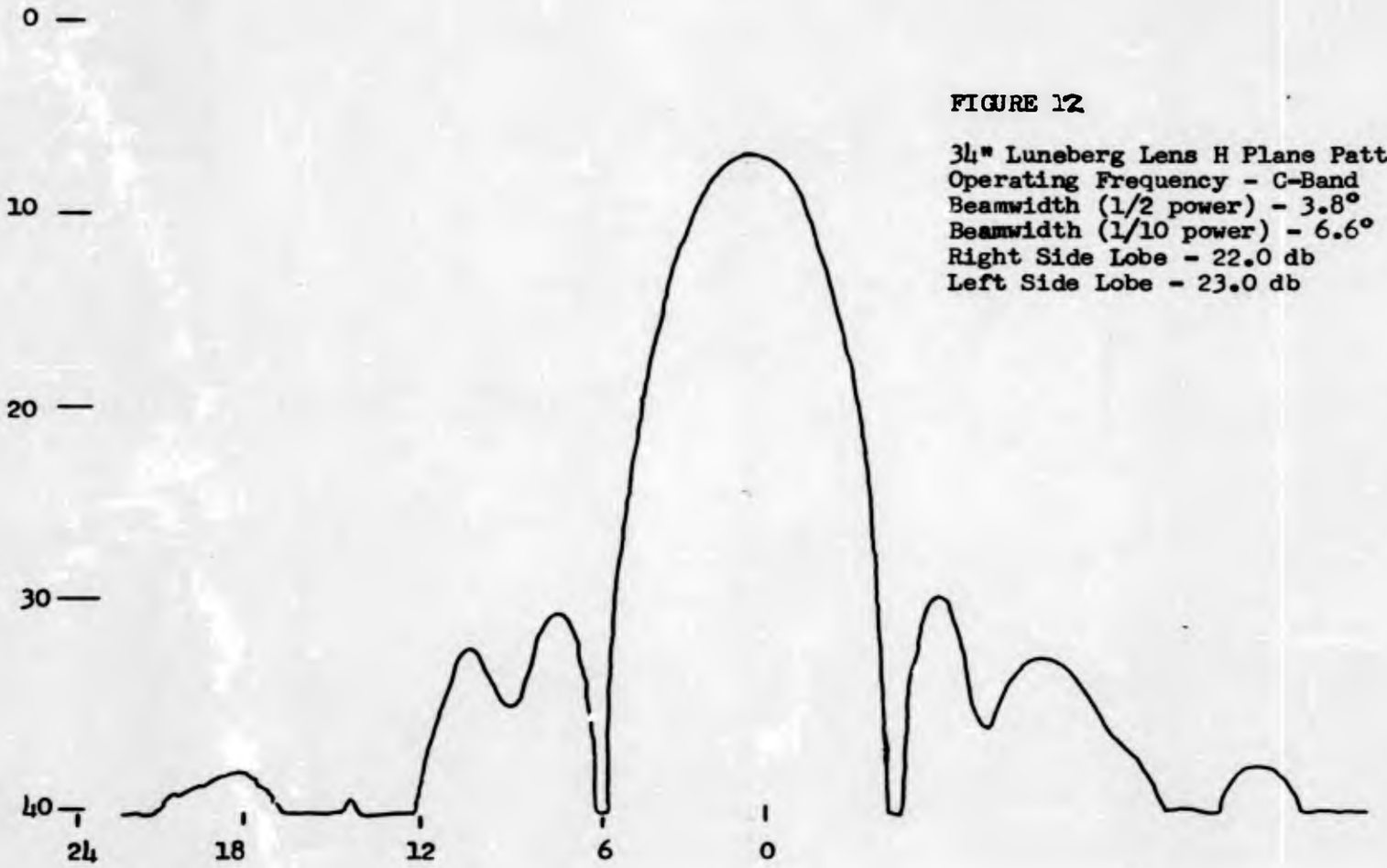

FIGURE 12

34" Luneberg Lens H Plane Pattern
Operating Frequency - C-Band
Beamwidth (1/2 power) - 3.8°
Beamwidth (1/10 power) - 6.6°
Right Side Lobe - 22.0 db
Left Side Lobe - 23.0 db

REFERENCES

1. R. K. Luneberg, Mathematical Theory of Optics, Brown University Press, Providence, 1944; pp. 189-212.

2. S. P. Morgan, General Solution of the Luneberg Lens Problem, Journal of Applied Physics, September 1958.

ABSTRACT

Geodesic Lenses for Flush-mounted Applications

by

R. C. Rudduck, C. H. Walter, and C. E. Ryan, Jr.

Antenna Laboratory
Department of Electrical Engineering
The Ohio State University
Columbus 10, Ohio
October 1962

A class of geodesic lenses having circular symmetry are described. From a single feed such a lens antenna radiates a high gain, fan beam. By utilizing the circular symmetry of the lens it is shown how rapid scanning or simultaneous beams in many directions about the symmetry axis can be obtained. In addition, methods are described for scanning in the orthogonal plane. One alternative is the use of an array of such lenses, each lens designed to radiate in a different direction, giving overlapping beams. A much simpler alternative is the use of a single lens design denoted as the vertical scanning lens which has the interesting property of scanning the beam in the orthogonal plane by radial feed movement. It is shown how these lenses can be readily flush mounted to a flat surface such as an aircraft fuselage or in a surface of revolution such as a nose cone.

Of particular interest is the use of the vertical scanning lens in nose cone applications. Antenna patterns are given for a vertical scanning lens flush mounted in a nose cone which demonstrate the feasibility of scanning over almost an entire hemisphere about the nose axis by feed movement alone. These patterns demonstrate wide frequency band operation in both polarizations. Methods of achieving overlapping beams for monopulse operation are discussed.

GEODESIC LENSES FOR FLUSH-MOUNTED APPLICATIONS

by

R. C. Rudduck, C. H. Walter and C. E. Ryan, Jr.

Antenna Laboratory
Department of Electrical Engineering
The Ohio State University
Columbus 10, Ohio
October 1962

INTRODUCTION

A class of geodesic lenses having circular symmetry is described. Such a lens, when fed from a feed placed at the focal radius, radiates a high-gain fan beam. The direction of the beam maximum is diametrically opposite the feed and at an angle β with respect to the plane of the lens rim. The lens is constructed from two parallel metal plates designed to support the TEM waveguide mode. The closely spaced plates are surfaces of revolution having the ideal lens contour as a mean surface. With no dielectric material between the plates the index of refraction is unity. From a geometrical optics viewpoint the ray paths in the lens follow the "geodesic" or shortest paths on the mean lens surface, hence the name geodesic lens.

A more general class of lenses was derived in Reference 1. In these lenses the index of refraction can be an arbitrary function of radius.

LENS CONTOURS

The beam angle β and the feed radius r_1 are determined by the lens contour. The lens contour consists of two sections; a conical outer shell having a constant slope b and a central portion having a more complex contour. For a normalized lens radius, the outer shell lies in the interval $\cos\beta \leq r \leq 1$ and the central portion lies in the interval $0 \leq r < \cos\beta$. The feed radius must lie in the outer shell, i.e., $r_1 \geq \cos\beta$.

For a feed radius at the inner radius of the outer shell, i.e., $r_1 = \cos\beta$, the lens contour is given by

$$(1) \qquad \sqrt{1+\dot{Z}^2} = \frac{1}{2} + \frac{\pi}{4\beta} - \frac{1}{2\beta}\tan^{-1}\sqrt{\frac{\cos^2\beta - r^2}{1-\cos^2\beta}}\,,$$

$$0 \le r < \cos\beta$$

and the slope of the outer shell is given by

$$\sqrt{1+\dot{Z}^2} = \sqrt{1+b^2} = \frac{\pi}{2\beta}\,, \quad \cos\beta \le r \le 1\,.$$

The contours for several values of β are illustrated in Fig. 1.

For a feed radius within the outer shell, $r_1 > \cos\beta$, the lens contour is given by

$$(2) \qquad \sqrt{1+\dot{Z}^2} = \frac{1}{2} + \sqrt{1+b^2} - \frac{\sqrt{1+b^2}}{\pi}\left[\tan^{-1}\sqrt{\frac{\cos^2\beta - r^2}{r_1^2 - \cos^2\beta}} + \tan^{-1}\sqrt{\frac{\cos^2\beta - r^2}{1-\cos^2\beta}}\right]$$

$$0 \le r < \cos\beta$$

where the slope b of the outer shell is given by

$$\sqrt{1+b^2} = \frac{\pi}{2\left(\beta + \cos^{-1}\dfrac{\cos\beta}{r_1}\right)}\,, \quad \cos\beta \le r \le 1\,.$$

The contours for various values of β are illustrated in Fig. 2.

If the slope b of the outer shell is to be physically realizable then $\sqrt{1+b^2} \ge 1$ which for values of $\beta > 45^\circ$ requires that the feed radius lie in the interval

$$(3) \qquad \cos\beta \le r_1 \le \cot\beta\,.$$

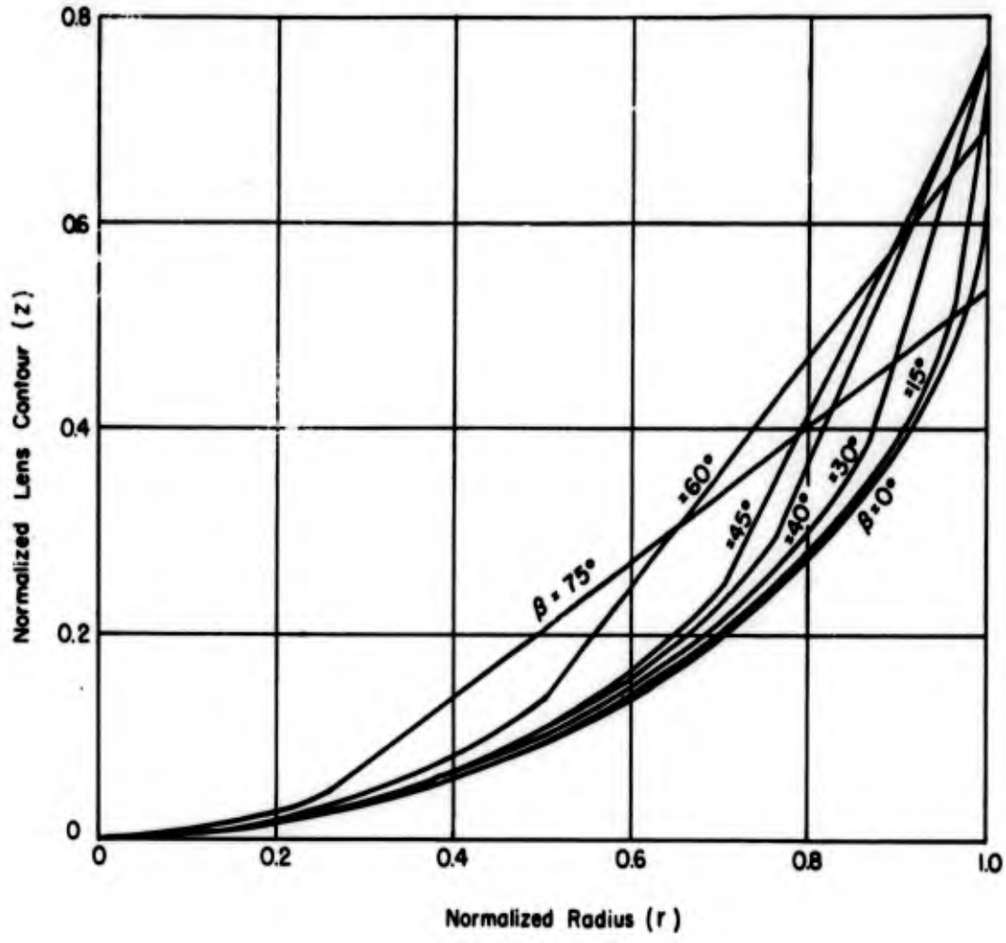

Fig. 1. Unit-index lens contours ($r_1 = \cos \beta$).

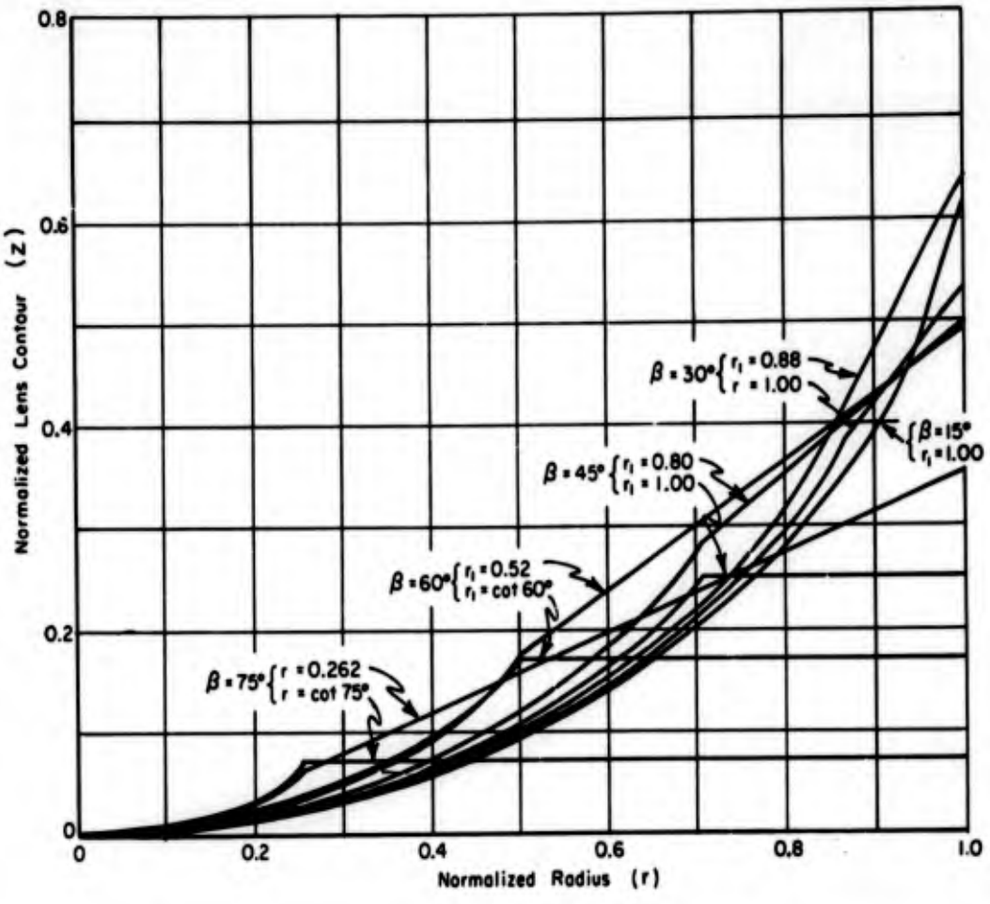

Fig. 2. Unit-index lens contours ($r_1 > \cos \beta$).

ANTENNA PATTERNS

These lenses radiate from a semicircular aperture around the rim opposite the feed point. The antenna patterns of such a lens can be approximated by those of a semicircular line source with the same radius as the lens. The radiated beam can be described in terms of its cross sections in two principal planes. The principal planes are illustrated in Fig. 3. The vertical pattern is considerably broader than the lens-plane

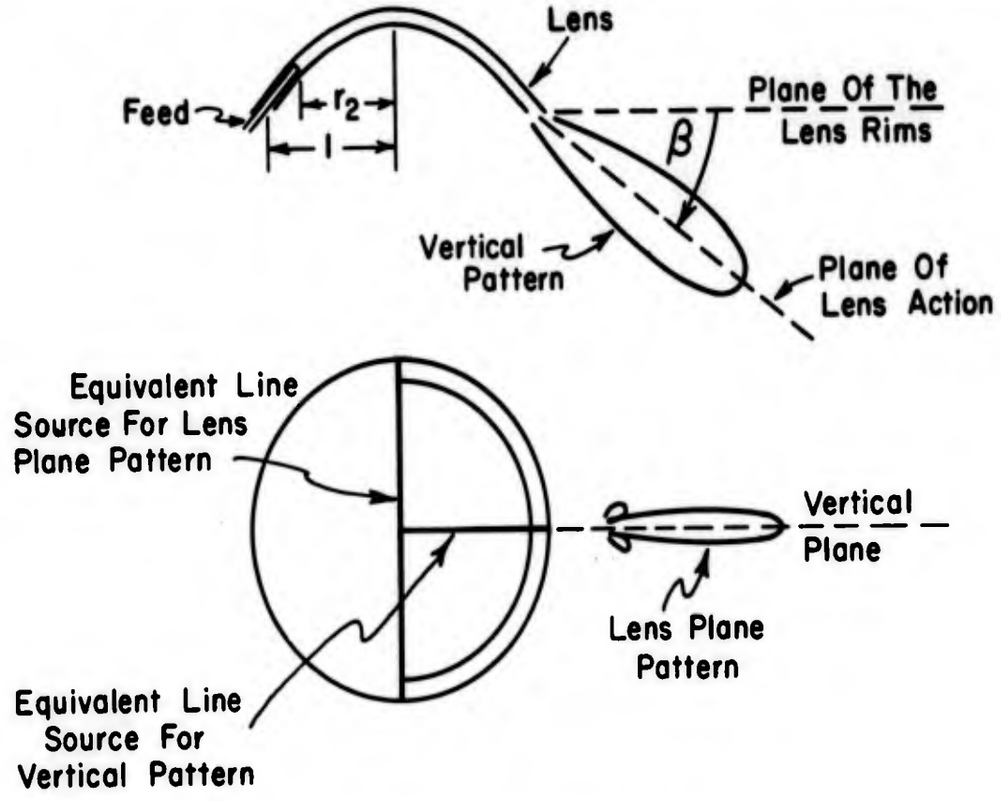

Fig. 3. Description of lens patterns.

pattern because its equivalent source length is one half that for the lens plane pattern, and also the vertical pattern is not broadside to its equivalent source. The phase distribution around the semicircular aperture depends on the angle of maximum radiation, β, and gives an "in phase" condition in the direction of maximum radiation.

Actually this phase distribution is such as to radiate two beams; the other beam is at the angle β on the other side of the plane of the lens rim. For the TEM waveguide mode the direction of the electric field at the aperture produces a dipole element pattern. In many lenses, the

slope of the lens contour at the rim is steep enough that the second beam is effectively eliminated. The patterns also depend on the amplitude distribution around the aperture, which is determined by the effective feed pattern.

EXPERIMENTAL RESULTS

The TEM lens structure has the features of wide bandwidth and high power handling capability. A 3:1 bandwidth is demonstrated in Reference 1. These results were obtained from the lens design of Eq. (1) for which $\beta = 30^{\circ}$.

Due to the circular symmetry of these lenses, rapid scanning or simultaneous beams in many directions about the symmetry axis can be obtained. It is also desirable to scan the beam in the vertical plane. One method is the use of an array of such lenses, each lens designed to radiate at a different angle, giving overlapping beams. A simpler approach is the use of a single lens with a steerable beam. Calculations show that a certain amount of scanning of the beam in the vertical plane can be obtained by moving the feed from its true focal radius. One of the most practical lenses in this respect is the lens design of Eq. (2) for which $\beta = 40^{\circ}$ and $r_1 = 0.82$.

An 18-inch diameter lens of this design was constructed from two parallel copper plates. The lens was tested in three different mounting configurations: mounted on a 24" x 48" rectangular ground plane, mounted without ground plane, and mounted in a sheet metal cone having a cone angle of 45°. The mechanical feasibility of mounting such a lens on a flat surface such as an aircraft fuselage or in a surface of revolution such as a nose cone is illustrated by these mounting configurations.

The beam was scanned from an angle of 25° with respect to the plane of the lens rim to broadside by moving the feed from near the rim to the center of the lens. The feed employed was an open ended X-band waveguide butted between the lens walls, and measurements were taken at 10 kmc.

The patterns for the lens mounted on the ground plane exhibit a lobe about 10° from the plane of the lens rim, caused by currents flowing on the ground plane, as shown in Fig. 4. The ground plane lobe is more pronounced for the beam maximum near the ground plane and decreases as the beam is scanned away from the ground plane. The ground plane also produces ripples in the vertical pattern for lenses radiating a

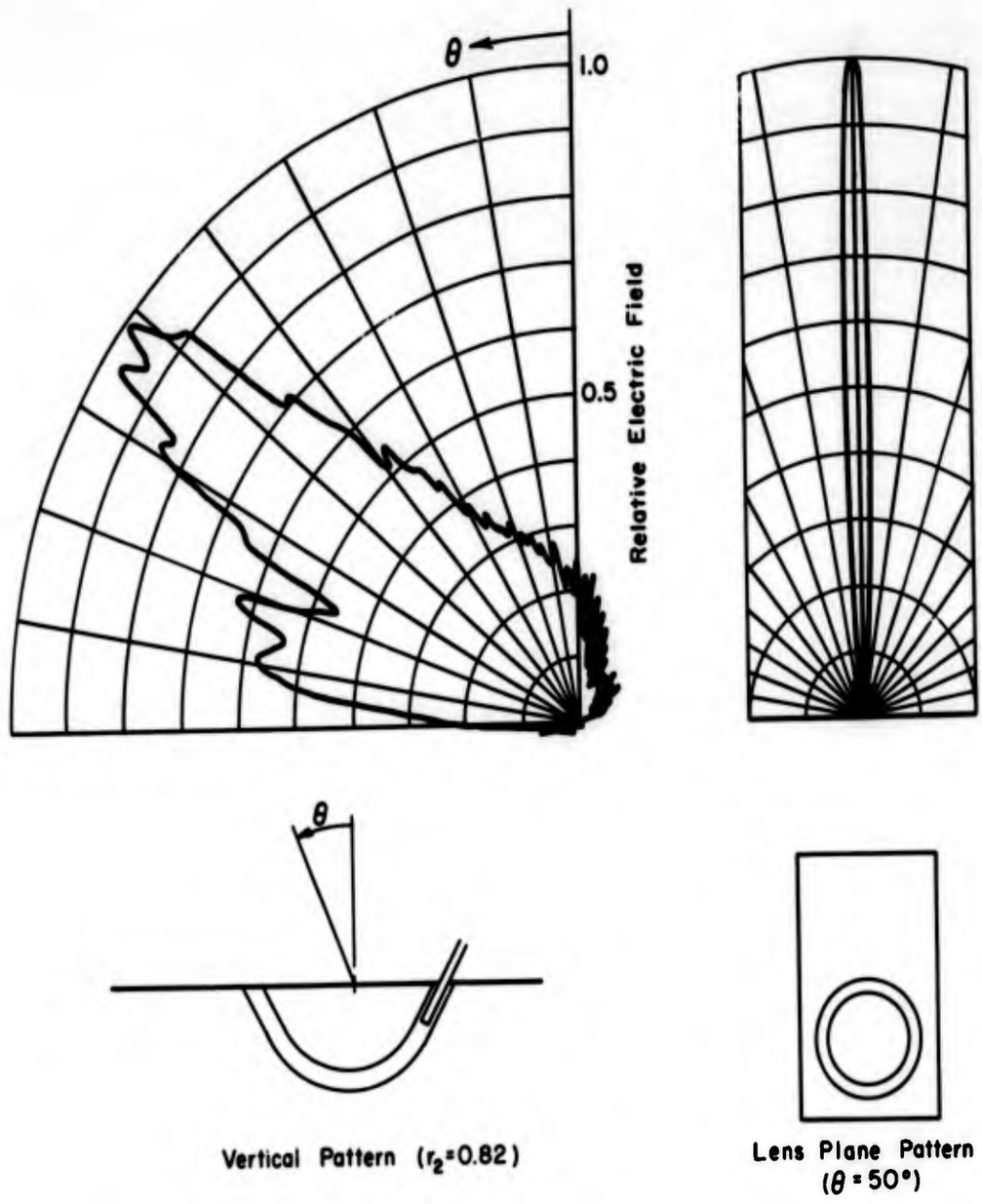

Fig. 4. Patterns of ground plane mounted lens.

vertically polarized electric field. For cleaner vertical patterns and higher gain from ground plane mounted lenses it is probably desirable to use some method of suppression for the ground plane currents, e. g., a corrugated strip on the ground plane adjacent to the lens aperture.

The lens plane patterns were found to be good for all beam positions in each mounting configuration. The vertical patterns of the lens without ground plane, as shown in Fig. 5, demonstrate the improvement obtained by elimination of the ground plane. At beam angles near broadside to the plane of the lens rim, broadening of the vertical pattern is apparently caused by inadequate illumination near the ends of the semicircular aperture. Thus a broader feed pattern is desirable for feed positions near the center of the lens.

The vertical patterns for the cone-mounted lens indicate the presence of the second beam at the angle β on the other side of the plane of the lens rim, as shown in Fig. 6. The magnitude of this beam is greatest for beam positions close to the plane of the lens rim. The second beam is caused by a shift in the dipole pattern of an element of the lens rim relative to its position in the other mounting configurations. This shift was caused by the extension of the inner lens wall in flush mounting the lens to the cone. The undesired beam can be reduced by increasing the directivity of the element pattern. One approach would be to give a horn flare to the lens walls at the rim. These patterns demonstrate the feasibility of scanning the beam over almost an entire hemisphere about the cone axis.

The previously discussed lenses employ the TEM waveguide mode which has a frequency-independent index of refraction, thus providing wide bandwidth for vertical polarization. Horizontal polarization can be obtained by use of the TE_{01} waveguide mode but the index is frequency-dependent. However in a parallel-plate lens of constant plate spacing the index at a given frequency is constant throughout the lens. Thus, for frequencies above cutoff, the beam is still focused as well as the vertically polarized beam but is shifted so that the beam position is given by

$$(4) \qquad \cos \beta_{HP} = \sqrt{1 - \left(\frac{\lambda}{2d}\right)^2} \cos \beta_{VP}$$

where d/λ is the plate spacing in wavelengths and β_{VP} is the beam position for vertical polarization. Thus, if the plate spacing is large enough at the lowest frequency of operation, the horizontally polarized beam can be scanned over nearly the same region as the vertically polarized beam in the vertical scanning lens.

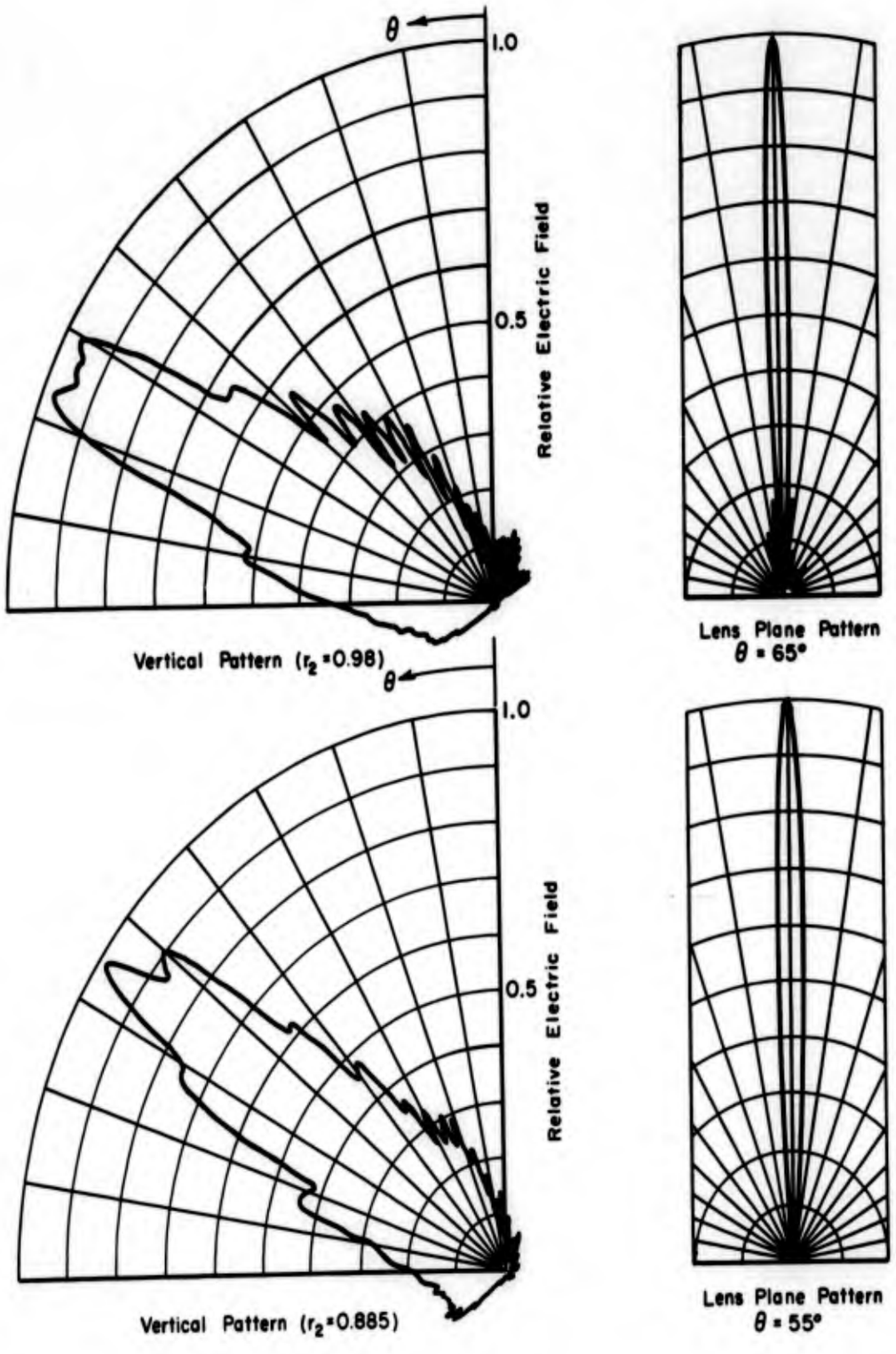

Fig. 5a. Patterns of lens without ground plane.

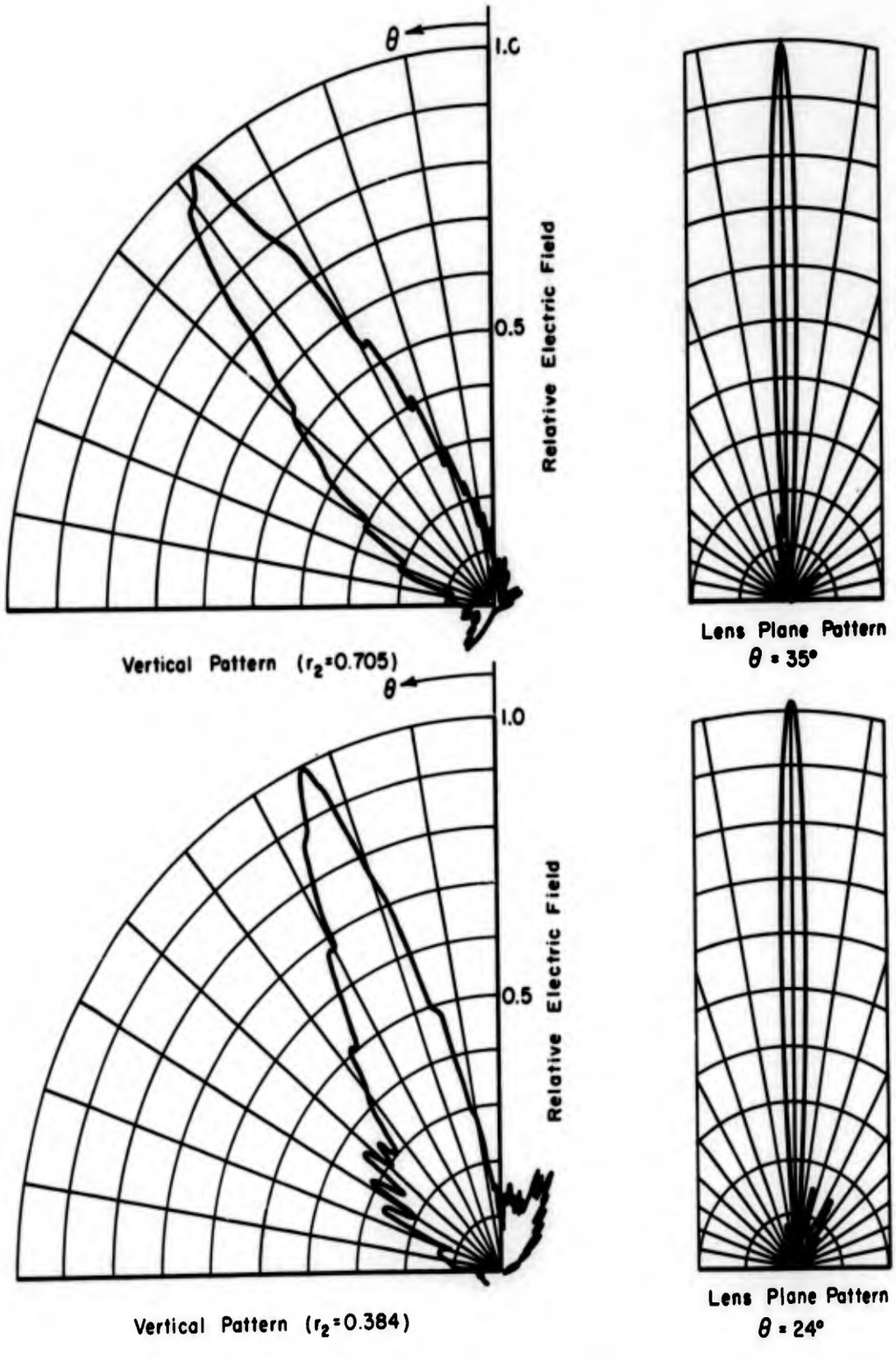

Fig. 5b. Patterns of lens without ground plane.

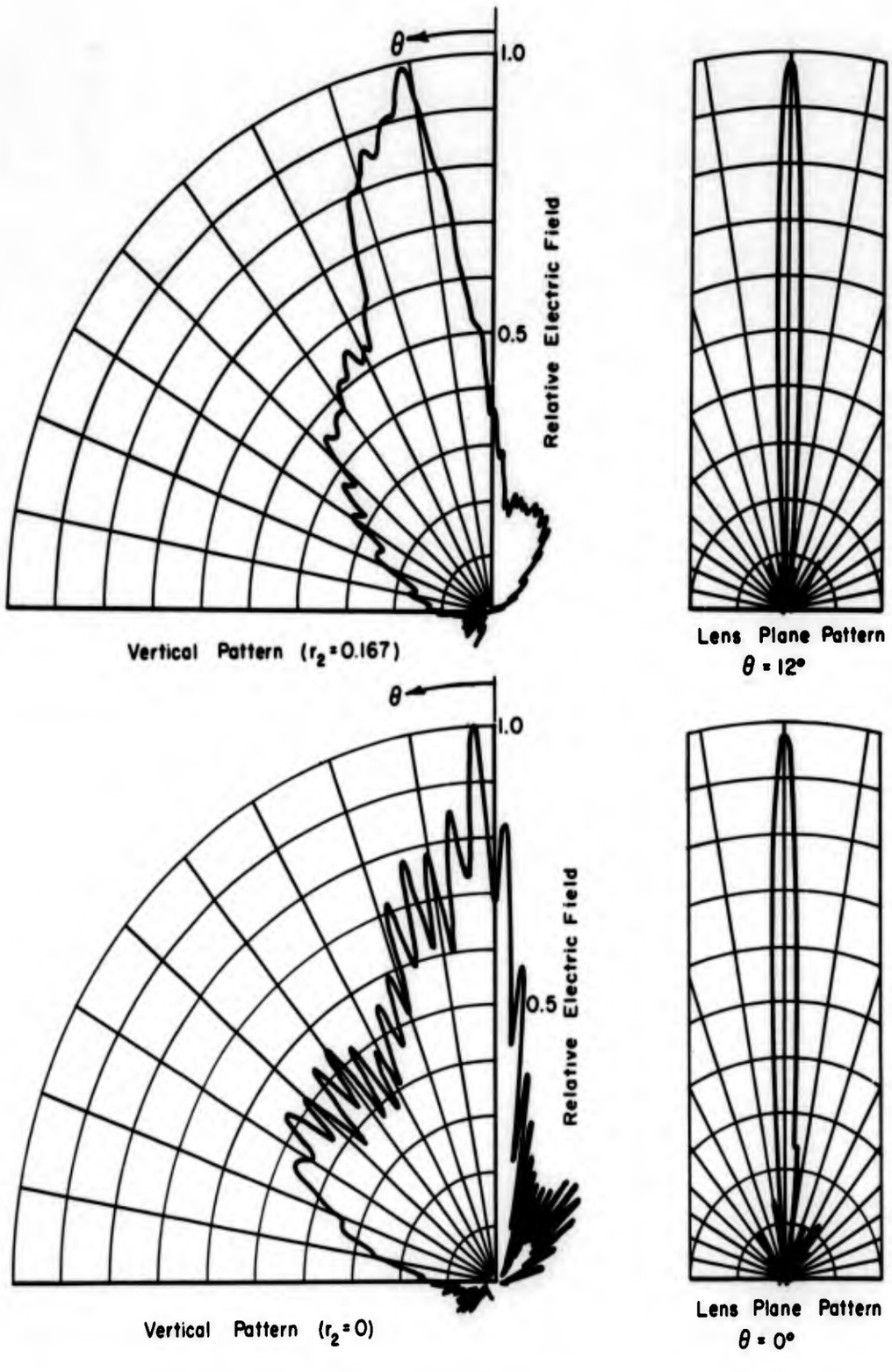

Fig. 5c. Patterns of lens without ground plane.

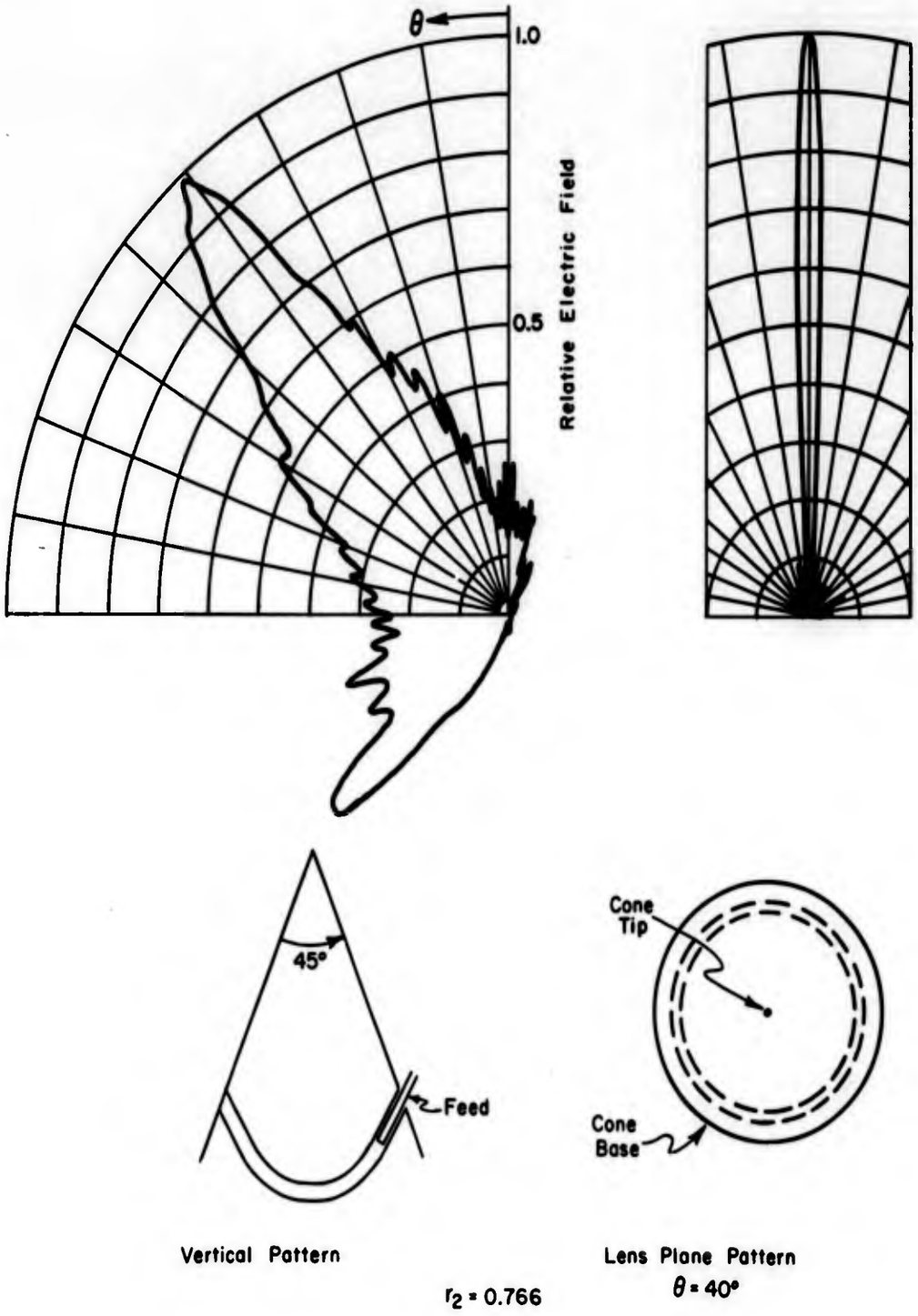

Fig. 6. Patterns of cone mounted lens.

APPLICATIONS

The described lens model demonstrates the potentiality of scanning a high-gain fan beam over a large sector from a flush-mounted antenna installation. The installation might be on the flat surface of a vehicle as suggested in Fig. 4 or in a nose cone as suggested in Fig. 6.

One application might be a single beam radar system in which beam positioning or scanning is obtained by a single feed capable of moving throughout the lens. Several feeds might be used for more versatility and more rapid scanning; each feed designed to cover a particular sector. Use of more than one feed requires that the feeds be positioned so that energy blocking is not a problem.

For monopulse operation, beam overlap in the plane of lens action can be obtained by two adjacent feeds. Beam overlap in the vertical plane might be obtained by use of a second lens in which another pair of feeds are spaced radially behind the feeds in the first lens as illustrated in Fig. 7. One lens plate could be common to both lenses in this case.

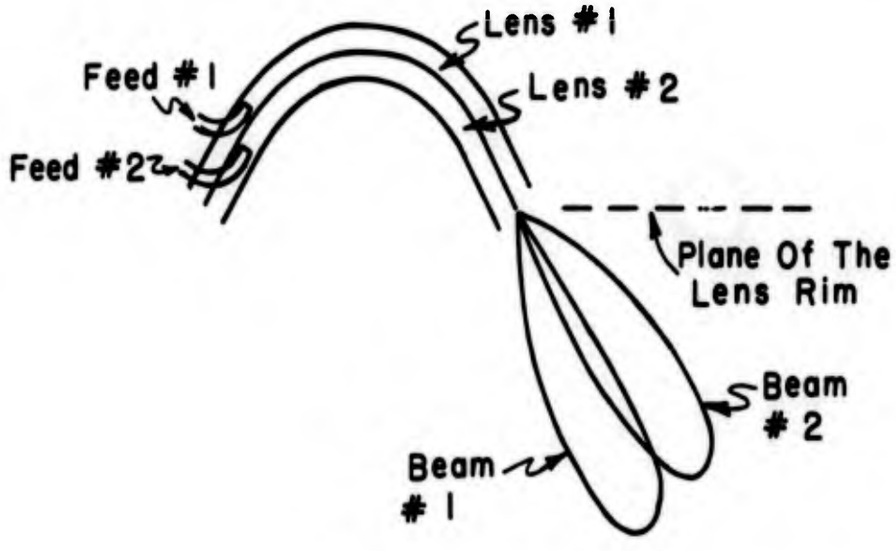

Fig. 7. Vertical beam overlap for monopulse operation.

BIBLIOGRAPHY

1. R. C. Rudduck and C. H. Walter, "A General Analysis of Geodesic Luneberg Lenses," IRE Trans. on Antennas and Propagation, vol. AP-10, No. 4, pp. 444-450, July 1962.

ACKNOWLEDGEMENT

The authors wish to extend their appreciation to Curt Davis who made many of the measurements and calculations.

Fabrication and Testing of Step-Index Luneberg Lenses for Antennas with High Directional Accuracy

By

Eino J. Luoma

Emerson & Cuming, Inc.
Canton, Massachusetts

The design and fabrication of a large, precise spherical Luneberg lens presents many interesting problems. In particular, this paper is concerned with the problem of designing and fabricating a 48-inch lens with a high degree of electrical symmetry and with a precisely located focus. The application is as a computer lens for an antenna system under development by the Systems Management Department of Westinghouse Electric Corporation. It is beyond the scope of this paper to discuss the details of the application.

The achievement of the objectives of this development program divide naturally into the following two problem areas, which are the two main topics:

1. Precise Location of Focal Point
2. Electrical Symmetry

A. Precise Location of Focal Point

The well known Luneberg law is stated as

$$K' = 2 - r^2$$

where K' is the dielectric constant, and r is the distance from a point in the sphere to the center, normalized in terms of the outer radius of the sphere. This defines the dielectric constant required for any point in the spherical lens to make the lens focus at its surface, and would result in

a continuous gradation of dielectric constant from a maximum of 2 at the center to a minimum of unity at the surface.

In practice, there is no known technique for reliably achieving this continuous gradation. Therefore, the lens is actually built with dielectric constant varying in radial steps, approximating the desired gradation. Experience has shown that for lenses 12" or larger operating in the 1 to 10 Gc range, 1/2-inch steps are a good approximation.

To make a 48-inch lens in 1/2-inch steps would require 48 spherical shells. Early in the development program of the precise lens it was felt that this large number of steps would make the achievement of precise focal location and near-perfect symmetry exceedingly difficult. Therefore, a theoretical investigation of the feasibility of a ten-step lens was undertaken to determine whether or not ten steps were sufficient to produce a lens with good focussing properties.

This theoretical investigation consisted of the development of a digital computer program for predicting the performance of a multi-step spherical lens with point-source feed. Performance factors of the lens-feed combination included in the prediction technique included gain, null depth, beamwidth, side lobe level, and deviation of the near field from a plane phase front.

The approach to the prediction was by geometric optics. The point-source feed was assumed to have a cosine amplitude pattern. From this point 50 rays all in one plane separated in equal angular increments were traced mathematically through a multi-step hemi-sphere to the opposite surface. Because of spherical symmetry it is unnecessary to repeat the ray tracing for the other hemi-sphere or for other planes. This mathematical tracing results in information as to the location of each of the 50 ray intersections on the opposite surface and the relative amplitude and phase at each of the intersections. From this information, it is possible to proceed directly to the near-field phase-front prediction. Or, it is also possible to proceed directly to the far-field pattern prediction, which will result in information as to null depths, side-lobe levels, and beamwidths. The gain determination was not an absolute gain determination in the true sense of the word. Dissipation losses and reflection losses were ignored. For the sake of simplicity the gain determination was simply a comparison between the power level at the peak of the predicted pattern with the power level at the peak of the predicted pattern which would have resulted if the lens had been a perfect Luneberg lens. Thus, the loss of predicted power is due only to phase errors resulting from the step design.

To locate the focus of a lens with a proposed stepped-index design, it was necessary to repeat these predictions for several successive incremental locations of the point source. The location of the point source which yielded the deepest first nulls was taken as the focus of the lens.

To design a ten-step lens with the focus in the desired location it is necessary to propose a design and locate its focus by this prediction technique. This was done on several designs. It was found that the design which resulted in a focus at the required location just outside the surface was produced by the use of the following formula for choice of dielectric constant:

$$K' = 2 - \frac{r_1^2 + r_2^2}{2}$$

where K' is the dielectric constant of the shell, r_1 is the outer normalized radius of the shell, and r_2 is the inner normalized radius of the shell. In addition, the radii of the individual shells were chosen in a manner such as to produce 10 shells all of approximately the same thickness.

It was experimentally verified that this 10-step design did indeed produce a lens with good focussing properties and with a focus near the outer surface of the lens. For comparison a more conventional 44-step design was also built and tested. Interestingly the 10-step design was somewhat superior to the 44-step design in many respects.

B. Electrical Symmetry

For the Westinghouse Electric Corporation application it was highly important that the lens be electrically symmetric. A measure of the departure from perfect symmetry of the lens was defined as follows:

1. Record a pattern of the lens-feed combination in the usual fashion.

2. Rotate lens and feed to one of the points 10 db down from peak position.

3. Leaving feed stationary, rotate lens alone through 360°, and record variation of signal as a function of rotation of the lens. This variation expressed in decibels is one measure of asymmetry of the lens. It can easily be converted into an angular measure of directional error by using the pattern to determine what the measured excursion in decibels corresponds to in angular shift of the main lobe.

4. Repeat these steps for three mutually perpendicular rotation axes of the lens.

The degree of symmetry achieved in a large lens is due, of course, to the type of material used in the lens and the techniques for fabricating it into hemispherical shells. The material used in the fabrication of this lens was a previously developed polystyrene foam (EccofoamPS). The density of foam was adjusted to produce the dielectric constants required for each of the 10 steps. The foam is produced by heating polystyrene granules in a mold until they expand to completely fill the mold and adhere to each other forming the hemispherical shell. Dielectric constant of the shell depends on the density of this material. The density is adjusted to the desired values by choice of granule size and by heating schedules. A great deal of experimental work went into these control problems to make it possible to manufacture shells with the desired dielectric constant and with a minimum variation of dielectric constant in each shell.

Early in the program it became evident that, since the dielectric constant of the foam depended very consistently on its density, the electrical asymmetry of a lens should depend directly on the displacement of its center of gravity from its geometric center. This same principle applies also to individual shells. Therefore, mechanical measurement techniques were developed to measure the location of the center of gravity of each of the 10 shells. This information was then used to assemble the lens in a manner such that the center of gravity of the complete assembly was as close to the geometric center as possible. This procedure reduced the electrical asymmetry considerably. The remaining asymmetry was still further reduced by remachining the outer surface of the lens to move the geometric center closer to the electrical center.

C. Test Results

1. The focal radius of the lens varied from 23.19 to 23.36 inches.

2. The total excursion in the symmetry patterns was an average of 2.07 db and never any greater than 2.5 db. This converts to an average beam shift of approximately ± 1.5 mils.

3. Side lobe levels averaged around 18 db down from main lobe peak.

4. The average gain factor was 0.571. $\left[\text{actual gain} = 0.571\left(\frac{\pi D}{\lambda}\right)^2\right]$

D. Conclusions and Recommendations

1. One of the most significant results of this work is the information that a 10-step approximation of the Luneberg law is sufficient to produce a good lens.

2. The computer prediction technique developed under this program is general enough to be applicable to any desired number of steps, and any diameter to wave length ratio. It is available as a Fortran computer program and can be used to design lenses for future applications.

3. The fact that Luneberg lenses can be made with excellent electrical symmetry and directional accuracy as demonstrated by this effort should be kept in mind by system designers.

E. Acknowledgments

1. This work would not have been undertaken without the sponsorship of the Systems Management Department of Westinghouse Electric Corporation. The technical project manager at Westinghouse was Mr. Helmut E. Schrank.

2. The Fortran prediction program was for the most part the work of Professor Samuel J. Mason of the Massachusetts Institute of Technology, acting as a consultant to Emerson & Cuming, Inc.

3. The project engineer at Emerson & Cuming, Inc. was Mr. Russell Stetson.

THE OPTIMUM EXCITATION FOR A PHASE COMPARISON ARRAY

W. H. Nester
General Electric Company

I. INTRODUCTION

Monopulse tracking is performed by using radiation patterns which are either even or odd in direction cosine space. The even pattern is known as the sum or $\sum$-pattern while the odd pattern is known as the difference or Δ-pattern.[1] The rms angular error produced by receiver noise in a skin tracking radar has been shown by Kirkpatrick[2] to be inversely proportional to a sensitivity factor defined by the expression

$$S = KG_{\sum}^{\frac{1}{2}} \tag{1}$$

More explicitly, the sensitivity factor is defined as the product of the sum gain and of the slope of the difference gain. The slope is defined as

$$K = \frac{\partial G_{\Delta}^{\frac{1}{2}}}{\partial \alpha} \tag{2}$$

If the sum and difference excitations can be formed independently, then these excitations can be chosen to give the maximum possible sum gain and difference slope respectively. In this case, the sensitivity has its maximum possible value. The maximum sum gain has been shown by Silver[3] to be produced by a uniform excitation in the case of a cophasal beam; i.e., excluding super gain. Kirkpatrick[4] has shown that the maximum slope is produced by a linear-odd excitation.

(1) D. R. Rhodes, Introduction to Monopulse, McGraw-Hill Book Company, Inc., New York, N. Y., p. 95.

(2) G. M. Kirkpatrick, General Electric Co., Astia Document AD 18458, August, 1952, p. 25.

(3) S. Silver, "Microwave Antenna Theory and Design", M.I.T. Rad. Lab. Series, McGraw-Hill Book Company, Inc., New York, N. Y., vol. 12, pp. 177-178, 1949.

(4) Kirkpatrick, p. 15.

If the maximum value of the sum gain is designated

$$\left[G_{\sum}^{\frac{1}{2}} \right]_{max} = G_o^{\frac{1}{2}} \quad , \tag{3}$$

then the maximum difference slope has the value

$$K_{max} = \frac{G_o^{\frac{1}{2}}}{\sqrt{12}} \tag{4}$$

and the maximum value of the sensitivity factor is found to be

$$S_{max} = \frac{G_o}{\sqrt{12}} \tag{5}$$

Allen[5] has shown that it is indeed possible to produce independent sum and difference excitations in a phased array, which does allow the maximum tracking sensitivity to be achieved. However, the feed structures for independent sum and difference excitations become rather complex. The feed structure can be simplified by using a phase comparison array, but the tracking sensitivity is also reduced. However, if the excitation of the phase comparison array is optimum, then the sensitivity is reduced by less than 1 db from the maximum possible value.

---

(5) J. L. Allen, "The Theoretical Limitations on the Formation of Lossless Multiple Beams in Linear Arrays", I.R.E. Transactions on Antennas and Propagation, vol. AP9, pp. 350-352, July, 1961.

A phase comparison array is defined for the purposes of this paper to be an array in which the odd excitation is formed simply by negating the even excitation over half the aperture. For example, let each quadrant of an array be fed by a corporate feed structure as illustrated in Figure 1. These four feed structures are then combined in a conventional 4-horn comparator. One beam can be identified with each quadrant. The four beams are all parallel but each has a different phase center location; e.g., the center of each quadrant. The resulting large phase center separation is an identifying characteristic of the system. Therefore, this type array has been termed a phase comparison array. The optimum excitation function for such an array is derived in the following section.

II. OPTIMUM EXCITATION FUNCTIONS

A. Two-Dimensional Tracking

Since the sum and difference excitations are not independent in the phase comparison array, the sum gain and the difference slope can not be maximized separately. Rather the product of the two must be maximized by the choice of a single excitation function.

The array geometry used in the analysis is sketched in Figure 2. A rectangular array is located in the x-y plane. The sum pattern is formed along the z-axis by an excitation function which is even in both x and y. Two difference patterns are formed. The one has a central null over the y-z plane and is generated by an excitation function odd in x but even in y. The other difference pattern has a central null over the x-z plane and is generated by an excitation function odd in y but even in x. If the excitation functions are

taken to be separable, then the sum excitation can be expressed as

$$\sigma\left(\frac{x}{X}, \frac{y}{Y}\right) = \sigma_x\left(\frac{x}{X}\right) \sigma_y\left(\frac{y}{Y}\right) \tag{6}$$

where

$$\sigma_x\left(\frac{x}{X}\right) = \sigma_x\left(-\frac{x}{X}\right)$$

$$\sigma_y\left(\frac{y}{Y}\right) = \sigma_y\left(-\frac{y}{Y}\right) \tag{7}$$

Similarly, the difference excitations can be written

$$\delta_1\left(\frac{x}{X}, \frac{y}{Y}\right) = \delta_x\left(\frac{x}{X}\right) \sigma_y\left(\frac{y}{Y}\right)$$

$$\delta_2\left(\frac{x}{X}, \frac{y}{Y}\right) = \sigma_x\left(\frac{x}{X}\right) \delta_y\left(\frac{y}{Y}\right) \tag{8}$$

where

$$\delta_x\left(\frac{x}{X}\right) = -\delta_x\left(-\frac{x}{X}\right)$$

$$\delta_y\left(\frac{y}{Y}\right) = -\delta_y\left(-\frac{y}{Y}\right) \tag{9}$$

Since the optimum excitation is to be used in both the x and y direction, the following equalities hold:

$$\sigma_x\left(\frac{x}{X}\right) \equiv \sigma_y\left(\frac{y}{Y}\right) \equiv \sigma(w)$$

$$\delta_x\left(\frac{x}{X}\right) \equiv \delta_y\left(\frac{y}{Y}\right) \equiv \delta(w) \tag{10}$$

Under these conditions the sum gain is given by the expression

$$G_{\Sigma}^{\frac{1}{2}} = \frac{G_{o}^{\frac{1}{2}} \int_{-\frac{1}{2}}^{+\frac{1}{2}} \sigma(w)\, e^{-j\alpha_x w}\, dw \int_{-\frac{1}{2}}^{+\frac{1}{2}} \sigma(w)\, e^{-j\alpha_y w}\, dw}{\int_{-\frac{1}{2}}^{+\frac{1}{2}} \sigma^2(w)\, dw} \qquad (11)$$

where

$$\alpha_x = \frac{2\pi X}{\lambda} \cos\gamma_x$$

$$\alpha_y = \frac{2\pi Y}{\lambda} \cos\gamma_y \qquad (12)$$

Similarly, the difference gain is given by the expression

$$G_{\Delta}^{\frac{1}{2}} = \frac{G_{o}^{\frac{1}{2}} \int_{-\frac{1}{2}}^{+\frac{1}{2}} j\delta(w) e^{-j\alpha_x w}\, dw \int_{-\frac{1}{2}}^{+\frac{1}{2}} \sigma(w)\, e^{-j\alpha_y w}\, dw}{\left[\int_{-\frac{1}{2}}^{+\frac{1}{2}} \delta^2(w)\, dw \int_{-\frac{1}{2}}^{+\frac{1}{2}} \sigma^2(w)\, dw\right]^{\frac{1}{2}}} \qquad (13)$$

Therefore, the slope of the difference gain is given by the expression

$$K = \frac{\partial G^{\frac{1}{2}}_{\Delta}}{\partial \alpha_x}$$

$$= \frac{G_o^{\frac{1}{2}} \int_{-\frac{1}{2}}^{+\frac{1}{2}} w\,\delta(w)\, e^{-j\alpha_x w}\, dw \int_{-\frac{1}{2}}^{+\frac{1}{2}} \sigma(w)\, e^{-j\alpha_y w}\, dw}{\left[\int_{-\frac{1}{2}}^{+\frac{1}{2}} \delta^2(w)\, dw \int_{-\frac{1}{2}}^{+\frac{1}{2}} \sigma^2(w)\, dw\right]^{\frac{1}{2}}} \qquad (14)$$

Finally, the sensitivity factor for the phase comparison array is obtained by:

(a) Evaluating the integrals in equations (11) and (14) at $\alpha_x = 0$, $\alpha_y = 0$

(b) Converting all integrations over the full interval to twice the integration over half the interval by virtue of symmetry.

(c) Using the defining condition of a phase comparison array; viz.

$$\delta(w) = \sigma(w) \quad , \quad 0 \leq w \leq \frac{1}{2} \qquad (15)$$

(d) Forming the product of equations (11) and (14) according to equation (1).

The expression which results for the sensitivity factor is

$$S = \frac{4G_o \int_0^{\frac{1}{2}} w\,\sigma(w)\,dw \left[\int_0^{\frac{1}{2}} \sigma(w)\,dw\right]^3}{\left[\int_0^{\frac{1}{2}} \sigma^2(w)\,dw\right]^2} \qquad (16)$$

The excitation function $\sigma(w)$ is to be chosen to give the sensitivity factor S its maximum value. According to the calculus of variations, when the excitation function is optimum the variation of the sensitivity factor is zero.

$$\partial S = 0 \qquad (17)$$

Using the same formalism for taking variations as for differentiation, the following result is obtained.

$$\left[\int_0^{\frac{1}{2}} \sigma^2\,dw \int_0^{\frac{1}{2}} \sigma\,dw\right] \int_0^{\frac{1}{2}} w\,\partial\sigma\,dw + 3\left[\int_0^{\frac{1}{2}} \sigma^2\,dw \int_0^{\frac{1}{2}} w\,\sigma\,dw\right] \int_0^{\frac{1}{2}} \partial\sigma\,dw$$

$$- 4\left[\int_0^{\frac{1}{2}} w\,\sigma\,dw \int_0^{\frac{1}{2}} \sigma\,dw\right] \int_0^{\frac{1}{2}} \sigma\,\partial\sigma\,dw = 0 \qquad (18)$$

Since the bracketed quantities are definite integrals involving no variations, they can be expressed as multiples of one another. Accordingly, the following proportionality factors are defined for the optimum excitation:

$$\int_0^{\frac{1}{2}} \sigma^2 \, dw = 4A \int_0^{\frac{1}{2}} w \, \sigma \, dw \tag{19}$$

and

$$3 \int_0^{\frac{1}{2}} \sigma^2 \, dw = 4B \int_0^{\frac{1}{2}} \sigma \, dw \tag{20}$$

Then the variational statement in (18) can be rewritten to give

$$\int_0^{\frac{1}{2}} (Aw + B - \sigma) \, \delta\sigma \, dw = 0 \tag{21}$$

This variational statement is to be true for arbitrary variations in the excitation about its optimum value. In order to insure that the variational integral vanishes for all possible variations, the first factor in the integrand must be identically zero. Therefore, the optimum excitation has the form

$$\sigma = A w + B \quad , \quad 0 \leq w \leq \frac{1}{2} \tag{22}$$

The constants must satisfy equations (19) and (20). Both equations give the same condition; viz.,

$$A^2 + 2AB - 4B^2 = 0 \tag{23}$$

or $$A = (-1 \pm \sqrt{5}) B$$

"B" is an arbitrary constant and can be taken equal to unity for convenience. When the sensitivity factor is evaluated, the choice of the positive sign is found to give the greater sensitivity. Therefore, the optimum excitation function is given by the expression

$$\sigma = (\sqrt{5} - 1)\, w + 1 \quad , \quad 0 \leq w \leq \frac{1}{2} \tag{24}$$

The optimum sum and difference excitations are sketched in Figure 3.

The sum gain can be computed using equations (7), (10), (11) and (24) evaluated at $\alpha_x = \alpha_y = 0$. The result is

$$\left[G_{\Sigma}^{\frac{1}{2}} \right]_{opt} = \frac{3(\sqrt{5} + 3)}{16}\, G_o^{\frac{1}{2}} \tag{25}$$

Therefore, the optimum gain is only 0.16 db below the maximum gain.

Similarly, the difference slope can be computed using equations (9), (10), (14), and (24)

$$\left[k \right]_{opt} = \frac{\sqrt{5} + 2}{16}\, G_o^{\frac{1}{2}} \tag{26}$$

The optimum slope is down 0.76 db from its maximum possible value given in equation (4).

Finally, the optimum sensitivity factor can be computed using equations (16) and (24). The result can also be identified as the product of (25) and (26).

$$\left[s \right]_{opt} = \frac{3(11 + 5\sqrt{5})}{256}\, G_o \tag{27}$$

The optimum sensitivity for the phase comparison array is 0.92 db below the maximum possible value reported in equation (5).

B. One-Dimensional Tracking

The optimum excitation for a one-dimensional tracker is not the same as for a two-dimensional tracker. The most obvious difference is that the optimum excitation in the one direction is uniform. For example, if tracking is to be performed in the x-z plane, then the optimum excitation in the y-direction is uniform

$$\sigma_y \left(\frac{y}{Y} \right) = 1 \qquad (28)$$

The excitation in the y-direction affects the sum gain and the slope of the only difference pattern in an exactly like manner. Since it is known that a uniform excitation produces maximum gain, it follows that the optimum excitation in the y-direction is uniform.

In addition, the optimum excitation in the x-direction, although still piecewise linear, has a greater amplitude taper. The explanation is simple. As the taper of the excitation function is increased, the form of the even excitation departs further from the ideal uniform excitation while the odd excitation more nearly approaches the ideal continuous linear form. Therefore, as the amplitude taper is increased, the sum gain decreases as the difference slope increases. As a result, the product of the two reaches a maximum for a particular value of amplitude taper.

In the two-dimensional tracker where identical excitations are used in both the x and y-directions, the factor reducing the sum gain is squared. However, in the one-dimensional tracker the gain reduction

factor occurs as only the first power. Therefore, the influence on sensitivity by the sum gain is reduced and the influence by the difference slope is increased. Consequently, a greater amplitude taper is needed for an optimum excitation in the one-dimensional tracker than found previously for the two-dimensional tracker.

The analysis of the one-dimensional tracker is outlined in the following paragraphs. The sum gain is given by the expression

$$G_{\sum}^{\frac{1}{2}} = \frac{G_o^{\frac{1}{2}} \int_{-\frac{1}{2}}^{+\frac{1}{2}} \sigma_x(w)\, e^{-j\alpha_x w}\, dw}{\left[\int_{-\frac{1}{2}}^{+\frac{1}{2}} \sigma^2(w)\, dw\right]^{\frac{1}{2}}} \tag{29}$$

The difference slope is given by the expression

$$K = G_o^{\frac{1}{2}} \frac{\int_{-\frac{1}{2}}^{+\frac{1}{2}} w\, \delta_x(w)\, e^{-j\alpha_x w}\, dw}{\left[\int_{-\frac{1}{2}}^{+\frac{1}{2}} \delta_x^2(w)\, dw\right]^{\frac{1}{2}}} \tag{30}$$

The sensitivity factor is given by the expression

$$S = 2G_o \frac{\int_0^{\frac{1}{2}} w\, \sigma_x(w)\, dw \int_0^{\frac{1}{2}} \sigma_x(w)\, dw}{\int_0^{\frac{1}{2}} \sigma_x^2(w)\, dw} \tag{31}$$

Setting the variation of the sensitivity equal to zero gives the following variational statement

$$\left[\int_0^{\frac{1}{2}} \sigma_x^2\, dw \int_0^{\frac{1}{2}} w\sigma_x dw\right]\int_0^{\frac{1}{2}} \partial\sigma_x dw + \left[\int_0^{\frac{1}{2}} \sigma_x^2\, dw \int_0^{\frac{1}{2}} \sigma_x\, dw\right]\int_0^{\frac{1}{2}} w\,\partial\sigma_x\, dw$$

$$- \left[2\int_0^{\frac{1}{2}} \sigma_x\, dw \int_0^{\frac{1}{2}} w\,\sigma_x\, dw\right]\int_0^{\frac{1}{2}} \sigma_x\,\partial\,\sigma_x\, dw = 0 \qquad (32)$$

The coefficients of the variational integrals satisfy the following conditions:

$$\int_0^{\frac{1}{2}} \sigma_x^2\, dw = 2A \int_0^{\frac{1}{2}} w\,\sigma_x\, dw$$

$$\int_0^{\frac{1}{2}} \sigma_x^2\, dw = 2B \int_0^{\frac{1}{2}} \sigma_x\, dw \qquad (33)$$

Then the variational statement can be rewritten to read

$$\int_0^{\frac{1}{2}} (Aw + B - \sigma)\,\partial\sigma\, dw = 0 \qquad (34)$$

Therefore, the optimum excitation has the form

$$\sigma = Aw + B \quad , \quad 0 \le w \le \frac{1}{2} \qquad (35)$$

Equations (32) both give the following relative values for the constants:

$$A = \pm \sqrt{12}\ B \tag{36}$$

Choosing B equal to unity for simplicity and choosing the positive sign for maximum sensitivity gives the following expression for the optimum excitation

$$\sigma = \left(\sqrt{12}\, w + 1 \right) , \quad 0 \leq w \leq \tfrac{1}{2} \tag{37}$$

The optimum sum and difference excitation in the x-direction is sketched in Figure 4. The excitation in the y-direction is uniform. (The result can also be interpreted as the optimum excitation for a linear array). It is interesting to note that the maximum amplitude taper along the diagonals of the array are nearly equal for the one and two-dimensional cases. For the one-dimensional case, the maximum amplitude taper is 2.732:1 or 8.7 db. For the two-dimensional case, the maximum taper is 2.62:1 or 8.3 db.

Using the optimum excitation for the one-dimensional tracker gives the following values for the sum gain, difference slope, and sensitivity factor.

$$\left[G_{\Sigma}^{\frac{1}{2}} \right]_{opt} = \frac{\sqrt{2 + \sqrt{3}}}{2}\ G_o^{\frac{1}{2}} \tag{38}$$

$$\left[K \right]_{opt} = \frac{\sqrt{2 + \sqrt{3}}}{2}\ \frac{G_o^{\frac{1}{2}}}{\sqrt{12}} \tag{39}$$

$$\left[S \right]_{opt} = \frac{3 + 2\sqrt{3}}{24}\ G_o \tag{40}$$

Therefore the optimum sum gain and difference slope are both 0.3 db below their respective upper bounds. The sensitivity is 0.6 db below the maximum possible value.

III. OPTIMUM PATTERNS

Since the excitation was assumed to be separable, the complete radiation pattern can be expressed as the product of the two principal plane patterns. Therefore, only the patterns in the two principal planes need be computed. When the symmetry conditions in (7) and (9) are used together with condition (15) which defines the phase comparison array, then the principal plane patterns are given by the following expressions:

$$\sum = \int_0^{\frac{1}{2}} \sigma(w) \cos \alpha w \, dw \tag{41}$$

and

$$\Delta = \int_0^{\frac{1}{2}} \sigma(w) \sin \alpha w \, dw \tag{42}$$

Using the optimum excitation for the two-dimensional tracker given in equation 24, the sum pattern in either principal plane is found to be given by the expression

$$\sum = \frac{\sqrt{5}+1}{2} \frac{\sin \frac{\alpha}{2}}{\frac{\alpha}{2}} - \frac{\sqrt{5}-1}{4} \left[\frac{\sin \frac{\alpha}{4}}{\frac{\alpha}{4}} \right]^2 \tag{43}$$

The optimum sum pattern is plotted in Figure 5. Note that the first side lobe is down 10.6 db from the sum peak.

The difference pattern for the optimum excitation is given by the expression

$$\Delta = \frac{\sqrt{5}+1}{\alpha}\left[1-\cos\frac{\alpha}{2}\right] - \frac{\sqrt{5}-1}{\alpha}\left[1-\frac{\sin\frac{\alpha}{2}}{\frac{\alpha}{2}}\right] \quad (44)$$

The optimum difference pattern is plotted in Figure 6. Since the square of the excitation function is the same in the even and odd mode, the radiated power is equal for the two modes. Therefore, although the patterns do not give absolute values of gain, relative gain comparisons can be made. Note that the peak difference gain is 2.5db less than the peak sum gain. The first side lobe in the difference pattern is down 10.7db from the difference peak.

The corresponding results for the one-dimensional tracker are presented in Figures 7 and 8. Only one pattern exists in the y-z plane. It has not been included in the figures since it is the familiar $\frac{\sin\alpha/2}{\alpha/2}$ pattern. Figures 7 and 8 give the sum and difference patterns in the x-z plane. The patterns are also given by the following expressions derived from equations (37), (41) and (42).

$$\Sigma_{xz} = \frac{\sqrt{12}+2}{2}\,\frac{\sin\frac{\alpha}{2}}{\frac{\alpha}{2}} - \frac{\sqrt{12}}{4}\left[\frac{\sin\frac{\alpha}{4}}{\frac{\alpha}{4}}\right]^2 \quad (45)$$

$$\Delta_{xy} = \frac{\sqrt{12}+2}{\alpha}\left[1-\cos\frac{\alpha}{2}\right] - \frac{\sqrt{12}}{\alpha}\left[1-\frac{\sin\frac{\alpha}{2}}{\frac{\alpha}{2}}\right] \quad (46)$$

IV. CONCLUSIONS

The optimum excitation of a phase comparison array has been shown to be piecewise linear with the only discontinuity at the center of the array. The excitation increases in amplitude from the center of the array to the edge with a taper in the principal planes of 4.2 db for the two-dimensional tracker and 8.7 db for the one-dimensional tracker. The optimum tracking sensitivities for the two systems are 0.9 and 0.6 db below the maximum value possible for any system. The optimum pattern characteristics were derived and are tabulated below.

TABLE I: OPTIMUM PATTERN CHARACTERISTICS

Pattern Characteristic	2-Dimensional Tracker	1-Dimensional Tracker
Sum Gain Factor	0.16 db	0.3 db
Difference Gain Factor	2.7 db	2.4 db
Difference Slope Factor	0.76 db	0.3 db
Sum Side Lobe Level	10.6 db	8.4 db
Difference Side Lobe Level	10.7 db	11.3 db

(a) ARRAY GEOMETRY

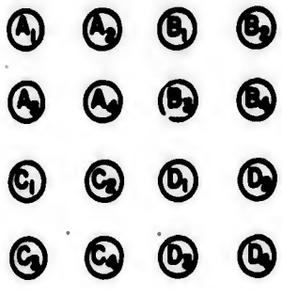

(b) FEED NETWORK

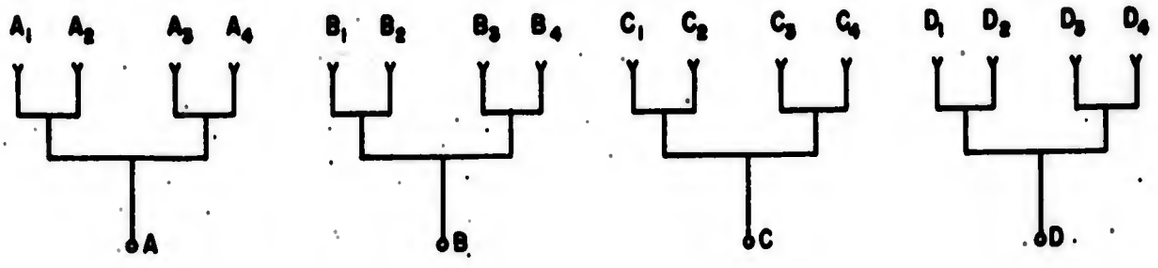

(c) COMPARATOR

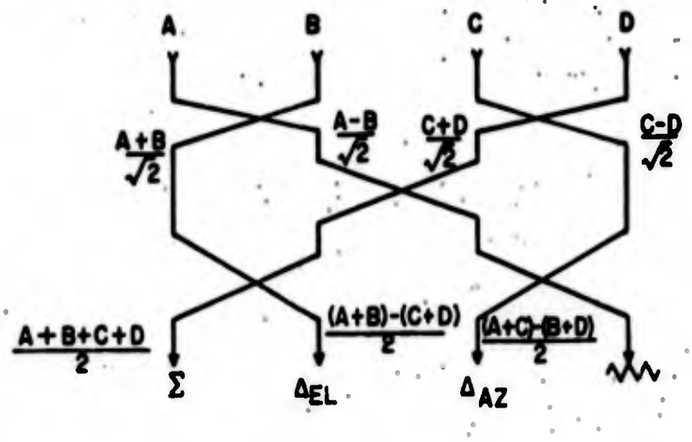

PHASE COMPARISON ARRAY
FIGURE 1

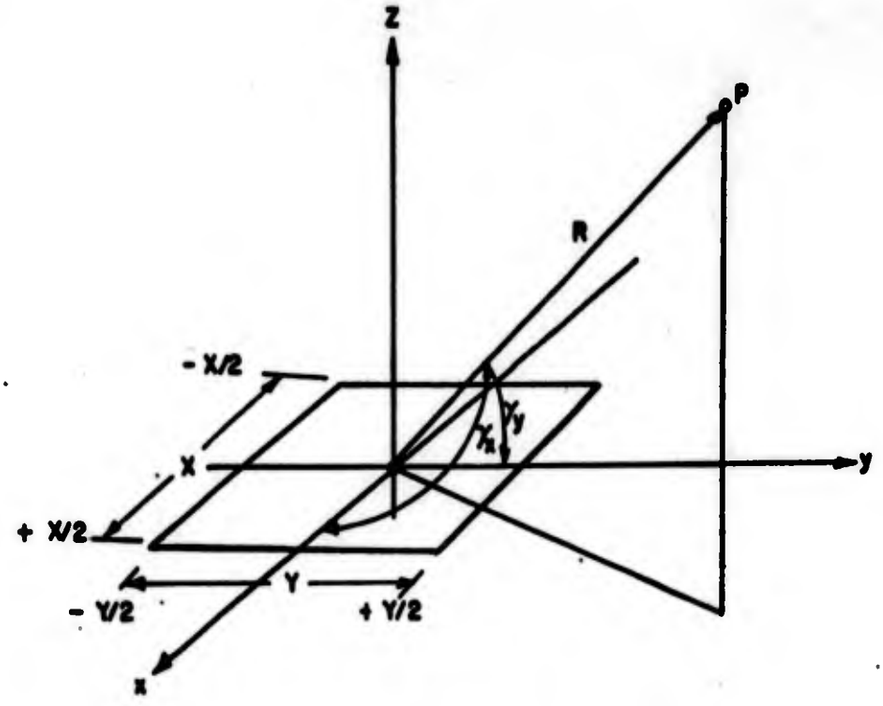

ARRAY GEOMETRY

FIGURE 2

(a) SUM EXCITATION

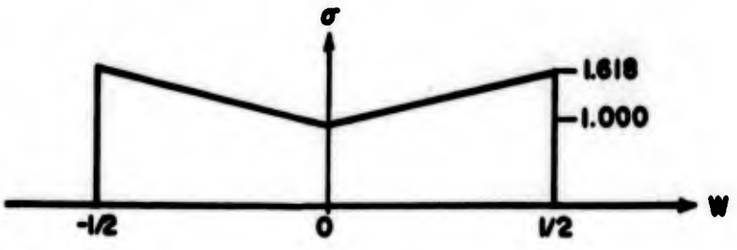

(b) DIFFERENCE EXCITATION

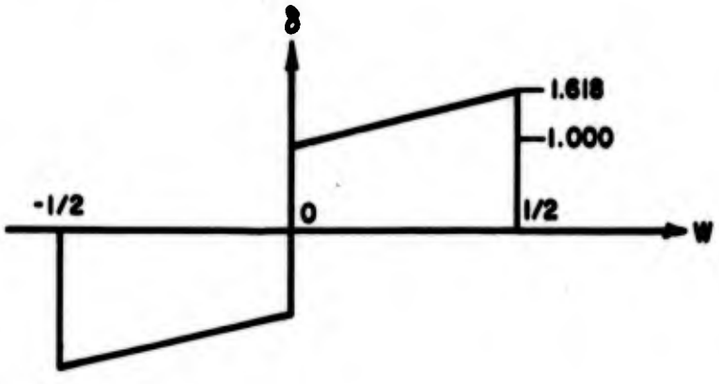

$$\left.\begin{aligned}\sigma(w) &= \sigma_x\left(\frac{x}{X}\right) = \sigma_y\left(\frac{y}{Y}\right)\end{aligned}\right\} \quad \sigma\left(\frac{x}{X},\frac{y}{Y}\right) = \sigma_x\left(\frac{x}{X}\right)\sigma_y\left(\frac{y}{Y}\right)$$

$$\left.\begin{aligned}\delta(w) &= \delta_x\left(\frac{x}{X}\right) = \delta_y\left(\frac{y}{Y}\right)\end{aligned}\right\} \quad \left\{\begin{aligned}\delta_1\left(\frac{x}{X},-\frac{y}{Y}\right) &= \delta_x\left(\frac{x}{X}\right)\sigma_y\left(\frac{y}{Y}\right)\\ \delta_2\left(\frac{x}{X},-\frac{y}{Y}\right) &= \sigma_x\left(\frac{x}{X}\right)\delta_y\left(\frac{y}{Y}\right)\end{aligned}\right.$$

OPTIMUM EXCITATIONS FOR THE TWO DIMENSIONAL PHASE COMPARISON ARRAY

FIGURE 3

(a) SUM EXCITATION

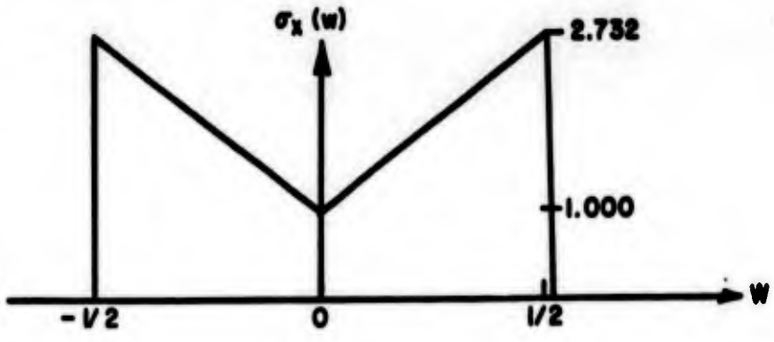

(b) DIFFERENCE EXCITATION

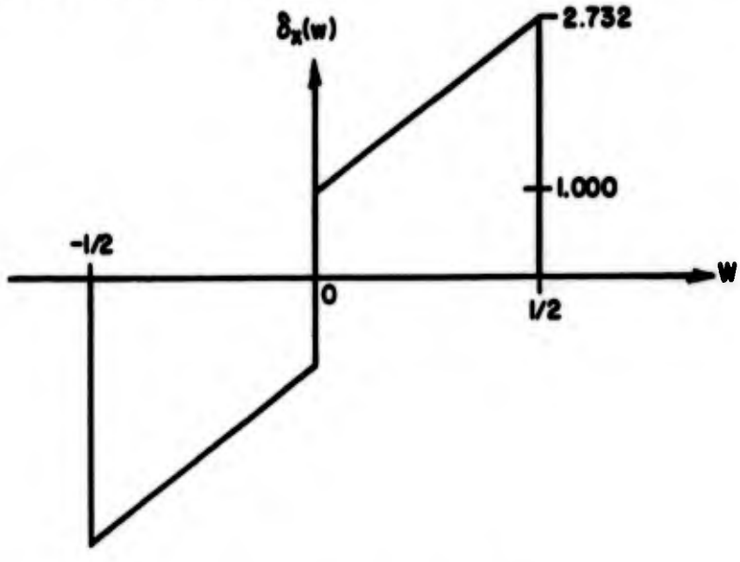

$$\sigma_y(w) = 1 \quad \Big\} \quad \sigma\left(\frac{x}{X}, \frac{y}{Y}\right) = \sigma_x\left(\frac{x}{X}\right)$$

$$\delta_1\left(\frac{x}{X}, \frac{y}{Y}\right) = \delta_x\left(\frac{x}{X}\right)$$

OPTIMUM EXCITATIONS FOR THE ONE DIMENSIONAL PHASE COMPARISON ARRAY

FIGURE 4

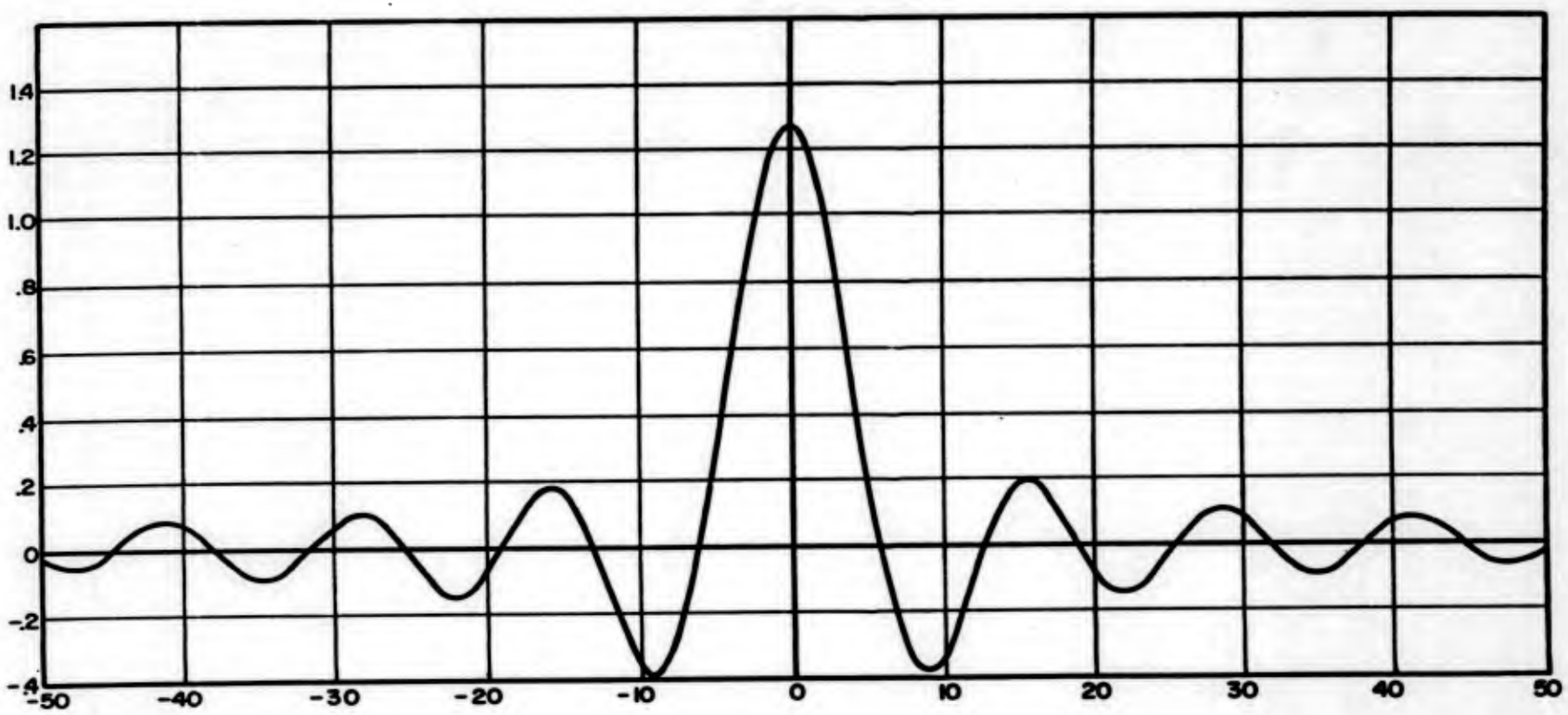

OPTIMUM SUM PATTERN FOR THE TWO DIMENSIONAL TRACKER

FIGURE 5

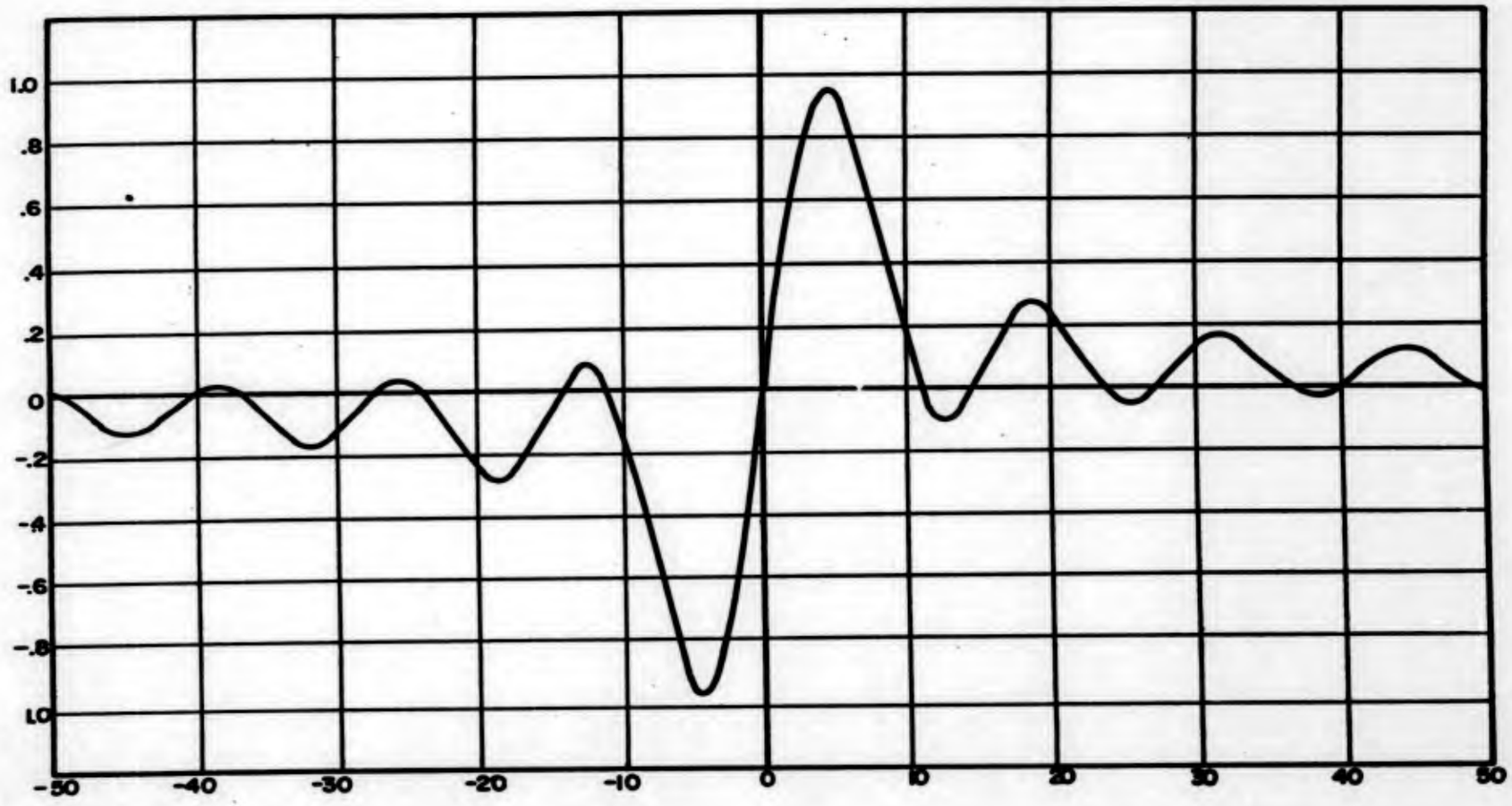

OPTIMUM DIFFERENCE PATTERN FOR THE TWO DIMENSIONAL TRACKER

FIGURE 6

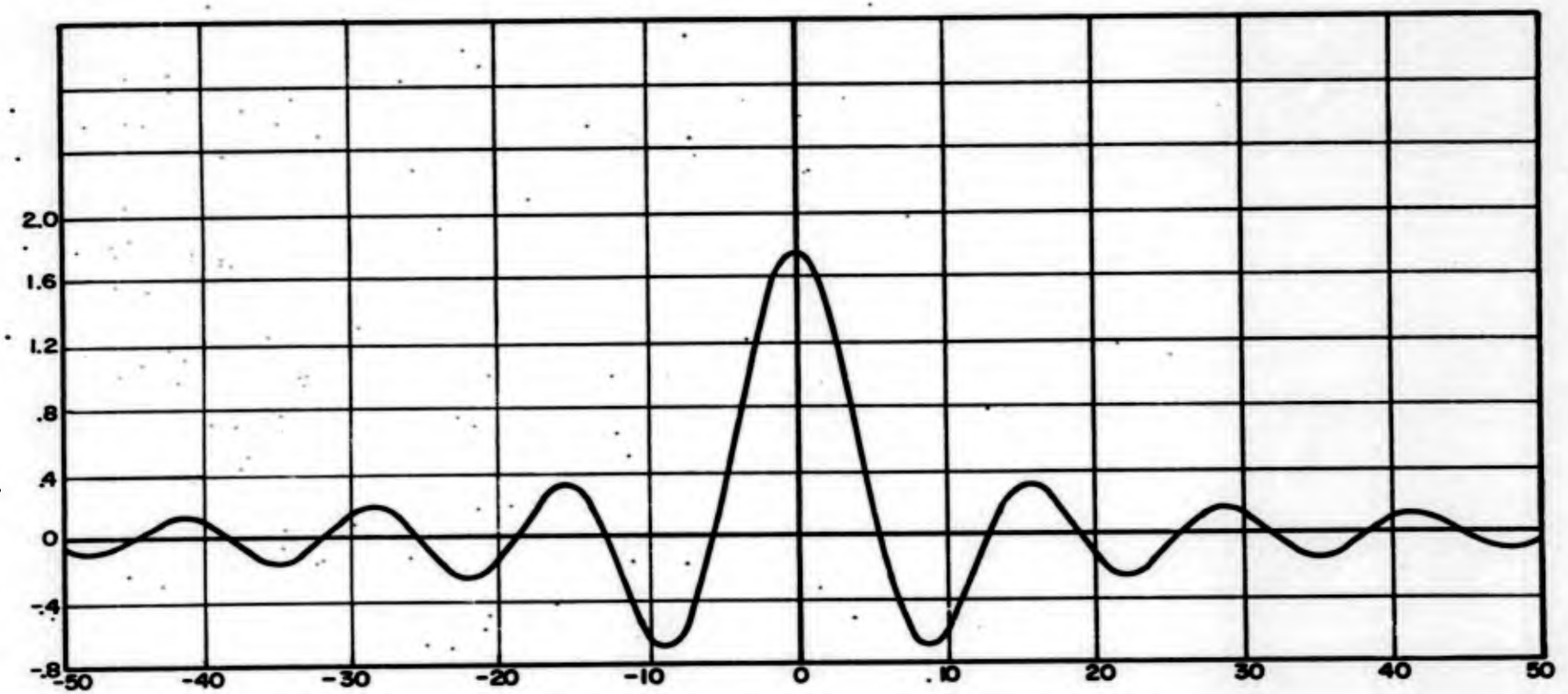

OPTIMUM SUM PATTERN FOR THE ONE DIMENSIONAL TRACKER

FIGURE 7

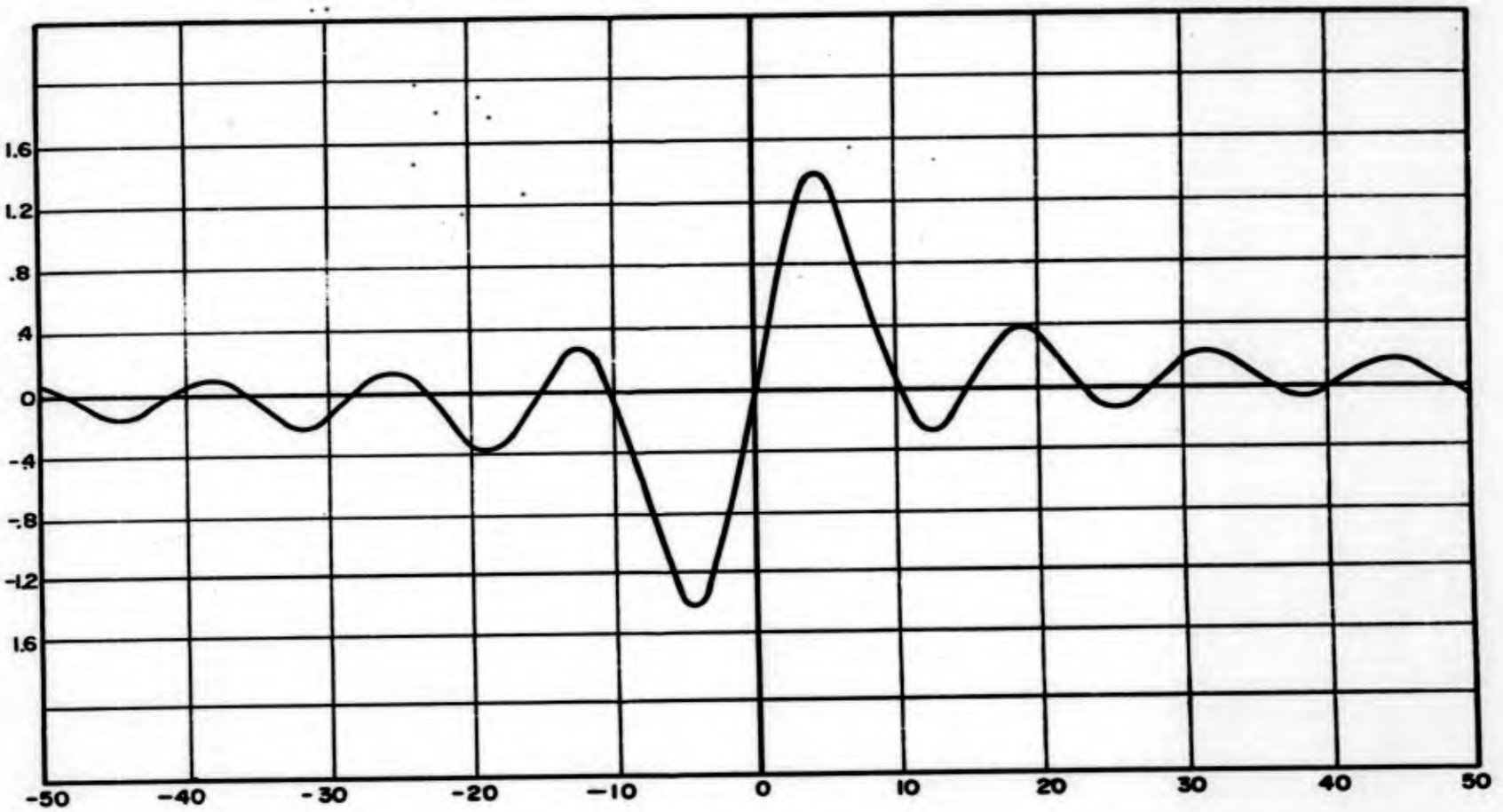

OPTIMUM DIFFERENCE PATTERN FOR THE ONE DIMENSIONAL TRACKER
FIGURE 8

Unclassified Paper

Short Pulse-Fresnel Radiation Patterns of Traveling-Wave Antennas

D. L. Huffman
North American Aviation, Inc.
Columbus Division

A paper for presentation at the Twelfth Annual Symposium on U.S.A.F. Antenna Research and Development at University of Illinois, Robert Allerton Park, Monticello, Illinois on October 16-19, 1962.

The author wishes to express appreciation to North American Aviation, Inc. for their support of this paper. In particular, recognition is given to Mr. John Spies for his work in computer programming on N.A.A. Recomp II, and his verification of derived equations.

I. Introduction

Traveling-Wave Antennas are a class of antenna structures that are prominently considered in applications to radar and communications. Such structures have application because of certain features of design simplicity: Impedance matching (end feeding), and aperture illumination (amplitude and phase) can be more easily controlled by this technique than by the use of other techniques. Alternative approaches would consider the use of a corporate feed structure, with separated radiating elements.

Traveling-Wave Antennas receive consideration in the design of Incoherent Side-Looking Radars; and this paper is concerned with the inherent limitation of their use in Side-Looking Radars. There are two fundamental limitations when application is considered. The limitations are the short pulse effect and the defocussing effect (resulting from Fresnel Radiation).

Short Radar Pulses, and Long End-Fed Linear Antenna Arrays are employed for the purpose of producing high range and angular resolution. The conventional consideration in the design of antenna arrays is the selection of the required aperture distribution of energy that will yield desirable values for C.W. Far Field Gain in relationship to low side lobe levels. However, transient radiating fields that exist during the times of incomplete antenna excitation, will have a perturbing effect on the contemplated radiation pattern, if the antenna excitation time is an appreciable percentage of the pulse duration time. If Short Radar Pulses and Long End-Fed Arrays are employed, then this condition is produced. In addition, Side-Looking Radars often contain ground mapping modes of operation which lie at ranges in the Fresnel field of the antenna.

L. L. Bailin* has studied the short pulse effect that is created by a transient radiating field from a long array, and his work is suggestive of the importance of the short pulse effect. An earlier statement of the problem presented in this paper suggested to M. S. Wheeler and D. K. Alexander** a related study. Their study is restricted to the Far Field Transmit Pattern, and calculations are given for the case of uniform, and cosine illumination.

This paper formulates the short pulse effect in terms of the Transmitting Fresnel Radiation Pattern; and derives the expression for the Short Pulse Radar Return Pattern. A computer program has been given for a generalized aperture distribution of the form:

$$f(x) = C_0 + C_1 \cos\frac{\pi}{2}x + C_2 \cos\pi x \qquad -1 \leq x \leq +1$$

A close approximation to Taylor Aperture Excitation can be obtained by selection of the coefficients C_0 , C_1 , and C_2 . North American Aviation's Recomp II has been used for computer calculations.

Computed examples are given for the following antenna parameters:

Antenna Length: 13 ft. at K_a Band

Taylor Aperture Excitation: -28 db. side lobe level

Radar Pulse Duration: 0.04 and 0.10 μsec.

A discussion is given of the detrimental effect of Short Pulse-Fresnel Radiation on Side-Looking Radar System performance. The Short Pulse-Far Field Radar Return Pattern is plotted for the case of Uniform Aperture Excitation.

* Bailin, L. L., "Fundamental Limitations of Long Arrays", Tech Memo 330, Hughes Aircraft Corporation, 27 October 1953, Contract AF 19(604)-262 F-16

** Wheeler and Alexander, "Short Pulse Effects in Traveling-Wave Antennas", Westinghouse Electric Corporation, Symposium Paper for the 8th Annual Radar Symposium, 6-8 June 1962, Ann Arbor, Michigan.

II. Traveling-Wave Antenna Model

Fig. 1 depicts the nature of a Traveling-Wave Antenna in the form of a primary end-fed waveguide array.

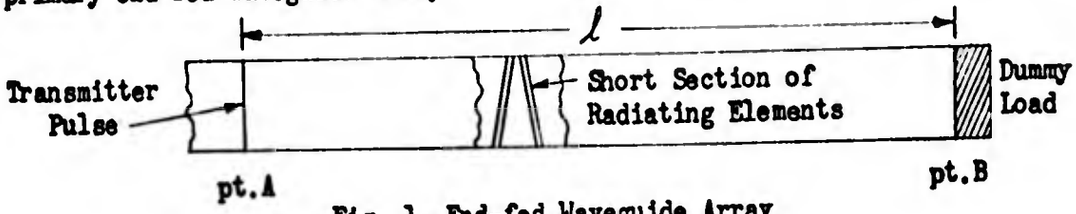

Fig. 1 - End-fed Waveguide Array

Fig. 1 indicates the length of the waveguide array, and a short section of radiating elements of the array are shown as inclined slots in the side of the radiating waveguide. The transmitter pulse enters the waveguide at pt.A and any remaining transmitter energy that is not radiated is absorbed at pt.B in the Dummy Load.

Figure 2 illustrates the relationship between transmitted pulse length τ, and waveguide excitation time τ_d.

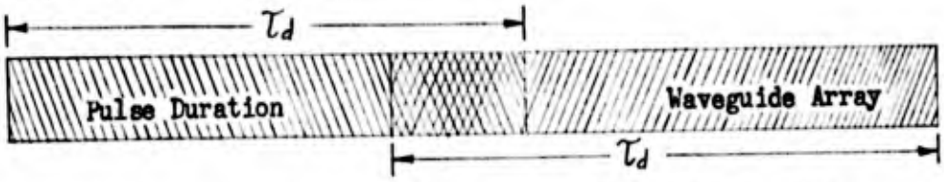

Fig. 2 - Pulse Duration in Waveguide, during instant of imcomplete Aperture Excitation

A square shaped transmitter pulse is assumed, and the value of τ is restricted to $\tau > 2\tau_d$, since there is not any practical design application if $\tau < 2\tau_d$.

Fig. 3 indicates the standardized representation of a line source in the Fresnel Field*, where f(x) is the aperture distribution; and u is a dimensionless parameter equal to $\frac{\pi \ell}{\lambda}\sin\theta$ with ℓ, the array length, and λ, the operating wavelength, and θ, the angle measured from the normal to the array. The coefficient β is equal to $\frac{\pi \ell^2 \cos^2\theta}{4R\lambda}$ with R, the operating range.

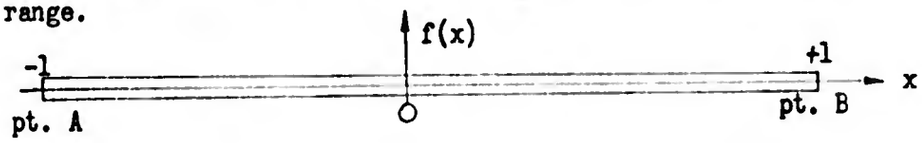

Radiated Field Strength for angular position, u : $\int_{-1}^{+1} f(x)\, \epsilon^{j(ux-\beta x^2)} dx$

Fig. 3 - Steady State Representation of a Line Source

* Jasik, Antenna Engineering Handbook, 2-30 McGraw-Hill Book Company, Inc., 1961

Fig. 3 will be interpreted for the time of incomplete aperture excitation, and the result is shown in Fig. 4. The waveform of the transmit pattern is given by Eqns. I-a, I-b, and I-c; with time t, measured from the start of the pulse.

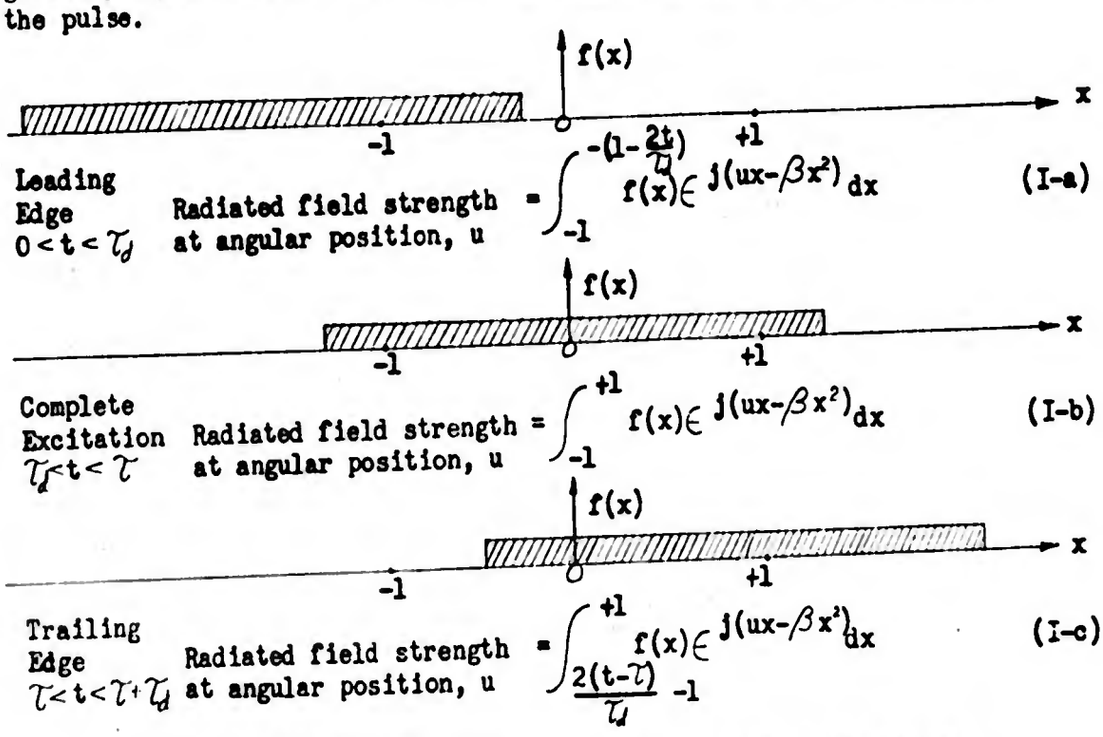

Fig. 4 Transient Representation of an End-Fed Line Source

The total transmitted energy is proportional to the time integral of the square of the absolute value of the transmitted field intensity as given in Eqn. II (with the assumption that f(x) is symmetric).

$$(\tau-\tau_d)\left[\left|\int_{-1}^{+1} f(x)\in^{j(ux-\beta x^2)}dx\right|^2\right] + 2\int_0^{\tau_d}\left|\int_{-1}^{-(1-\frac{2t}{\tau_d})} f(x)\in^{j(ux-\beta x^2)}dx\right|^2 dt \qquad \text{(II)}$$

Antenna reciprocity states that the receive pattern can be obtained by retransmitting the transmit wave form of Eqns. I-a, I-b, and I-c. When this is performed, the waveforms have the following form, as written in Eqn. III.

Signal Return $0<t<\tau_d$

$$\int_{-1}^{-(1-\frac{2t}{\tau_d})}\int_{-1}^{2(\frac{t}{\tau_d}-1)-x} f(x)f(z)\in^{j\left[u(x-z)-\beta(x^2-z^2)\right]}dxdz \qquad \text{(III-a)}$$

$\tau_d<t<2\tau_d$

$$\int_{-3+\frac{2t}{\tau_d}}^{+1}\int_{-1}^{2(\frac{t}{\tau_d}-1)-x} f(x)f(z)\in^{j\left[u(x-z)-\beta(x^2-z^2)\right]}dxdz + \int_{-1}^{-3+\frac{2t}{\tau_d}}\int_{-1}^{+1} f(x)f(z)\in^{j\left[u(x-z)-\beta(x^2-z^2)\right]}dxdz \qquad \text{(III-b)}$$

$2\tau_d<t<\tau$

$$\int_{-1}^{+1}\int_{-1}^{+1} f(x)f(z)\in^{j\left[u(x-z)-\beta(x^2-z^2)\right]}dxdz \qquad \text{(III-c)}$$

Signal Return .
$\tau < t < \tau + \tau_d$ Waveform identical to Eqn. III-b because of f(x) symmetry (III-d)

$\tau + \tau_d < t < \tau + 2\tau_d$ Waveform identical to Eqn. III-a because of f(x) symmetry (III-e)

The total received energy proportional to the time integral of the square of the absolute value of the return field intensity, as given in Eqn. IV (with the assumption that f(x) is still symmetric).

$$2\int_0^{\tau_d}\left|\int_{-1}^{-(1-\frac{2t}{\tau_d})}\int_{-1}^{2(\frac{t}{\tau_d}-1)-x} F(x)F(z)dxdz\right|^2 dt$$

$$+ 2\int_{\tau_d}^{2\tau_d}\left|\int_{-3-\frac{2t}{\tau_d}}^{+1}\int_{-1}^{2(\frac{t}{\tau_d}-1)-x} F(x)F(z)dxdz + \int_{-1}^{-3-\frac{2t}{\tau_d}}\int_{-1}^{+1} F(x)F(z)dxdz\right|^2 dt$$

$$+ (\tau - 2\tau_d)\left|\int_{-1}^{+1} F(z)dz\right|^4 \qquad \text{(IV)}$$

where F(x) and F(z) represent

$F(x) = f(x)\epsilon^{j(ux-\beta x^2)}$; $F(z) = f(z)\epsilon^{j(uz-\beta z^2)}$

Eqn. II and IV are used in computed calculations.

III. Mathematical Formulation

Short Pulse-Fresnel Equation, Transmit Pattern

Eqn. II is rewritten as Eqn. II-a for the purpose of interpretation and discussion of permissible mathematical simplifications:

$$\left[\left|\int_{-1}^{+1} f(x)\epsilon^{j(ux-\beta x^2)}dx\right|^2\right] + \frac{2}{\tau-\tau_d}\int_0^{\tau_d}\left|\int_{-1}^{-(1-\frac{2t}{\tau_d})} f(x)\epsilon^{j(ux-\beta x^2)}dx\right|^2 dt \quad \text{(II-a)}$$

The first term of Eqn. II-a is the Fresnel Radiation Pattern, while the second term is the complete short pulse correction to the Fresnel Radiation Pattern. The second term contains in it, a second order type of correction in the form of a short pulse correction to the Fresnel correction. This second order correction can be neglected for computational simplification, with the use only of a first order short pulse correction. In other words, the simplification can be made that

$$\int_0^{\tau_d}\left|\int_{-1}^{-(1-\frac{2t}{\tau_d})} f(x)\epsilon^{j(ux-\beta x^2)}dx\right|^2 dt \approx \int_0^{\tau_d}\left|\int_{-1}^{-(1-\frac{2t}{\tau_d})} f(x)\epsilon^{jux}dx\right|^2 dt$$

The validity of the simplification can be checked by the use of graphical integration and numerical tables for the Fresnel Integral. Graphical integration studies have indicated the validity of this assumption for values of $\tau > 2\tau_d$ and $\beta < \pi/2$. Further reasoning indicates that, if the second order correction (or the interaction between the short pulse and the defocussing effect) was not negligible, then the calculated results would indicate an unuseable antenna pattern shape, for side-looking radar applications. Therefore, Eqn. II-a can then be simplified to a tractable form of Eqn. II-b

$$\left[\left|\int_{-1}^{+1} f(x)\epsilon^{j(ux-\beta x^2)}dx\right|^2\right] + \frac{2}{\tau-\tau_d}\int_0^{\tau_d}\left|\int_{-1}^{-(1-\frac{2t}{\tau_d})} f(x)\epsilon^{jux}dx\right|^2 dt \quad \text{(II-b)}$$

A computer program using Eqn. II-b was written using North American Aviation's Recomp II.

Short Pulse-Radar Return Pattern

The general solution f(x) to Eqn. IV has not been considered because of the inherent complexity of the required computer program. In addition, the radar return pattern has no direct application to ground mapping radars. Ground mapping targets are extended terrain targets (land, water, and random scatterers), and not point targets (large corner reflectors), that are assumed in the radar return pattern.

However, a restricted solution to Eqn. IV has been optained for the far field pattern of a uniformly illuminated aperture. The result for this restricted case is given by Eqn. IV-a:

$$\frac{\sin^4 u}{u^4} + \frac{\tau_1}{\tau u^2}\left\{\left[\frac{\cos 2u}{2} - 1\right]\left(-\frac{1}{u^2} + \frac{\sin 2u}{u^3} - \frac{\cos 2u}{u^2}\right) + \frac{1}{3}\right\} \qquad \text{(IV-a)}$$

Specific Aperture Distribution

The aperture distribution: $f(x) = C_0 + C_1 \cos\frac{\pi}{2}x + C_2 \cos \pi x$ was selected for development in Eqn. II-b. The result is stated here as Eqn. V, for the particular value of $\beta = 0$.

$$G(u) + \frac{2}{\tau - \tau_1}F(u) \qquad \text{(V)}$$

with

$$G(u) = \frac{2(1-\cos 2u)}{u^2}C_0^2 + \frac{\pi^2(1+\cos 2u)}{2(u^2 - \frac{\pi^2}{4})^2}C_1^2 + \frac{2u^2(1-\cos 2u)}{(u^2-\pi^2)}C_2^2$$

$$- \frac{2\pi \sin 2u}{u(u^2 - \frac{\pi^2}{4})}C_0 C_1 - \frac{4(1-\cos 2u)}{u^2 - \pi^2}C_0 C_2 + \frac{2\pi u \sin 2u}{(u^2 - \frac{\pi^2}{4})(u^2 - \pi^2)}C_1 C_2$$

$$\text{and } F(u) = \tau_d \left\{ \frac{2\left(1-\frac{\sin 2u}{2u}\right)}{u^2} C_o^2 + \left[\frac{1+\frac{\sin 2u}{2(u+\pi/2)}}{2(u+\pi/2)^2} + \frac{1+\frac{\sin 2u}{2(u-\pi/2)}}{2(u-\pi/2)^2} - \frac{1+\frac{\sin 2u}{2(u+\pi/2)}+\frac{\sin 2u}{2(u-\pi/2)}}{2(u^2-\pi^2/4)} \right] C_1^2 \right.$$

$$+ \left[\frac{1-\frac{\sin 2u}{2(u+\pi)}}{2(u+\pi)^2} + \frac{1-\frac{\sin 2u}{2(u-\pi)}}{2(u+\pi)^2} + \frac{1-\frac{\sin 2u}{2(u+\pi)}-\frac{\sin 2u}{2(u-\pi)}}{2(u^2-\pi^2)} \right] C_2^2$$

$$+ \left[\frac{\frac{\cos 2u+1}{2(u-\pi/2)} - \frac{1-\cos 2u}{2u} + \frac{2}{\pi}}{u(u-\pi/2)} + \frac{\frac{1-\cos 2u}{2u} - \frac{\cos 2u+1}{2(u+\pi/2)} + \frac{2}{\pi}}{u(u+\pi/2)} \right] C_o C_1$$

$$+ \left[\frac{\frac{\sin 2u}{2u} + \frac{\sin 2u}{2(u+\pi)} - 1}{u(u+\pi)} + \frac{\frac{\sin 2u}{2u} + \frac{\sin 2u}{2(u-\pi)} - 1}{u(u-\pi)} \right] C_o C_2$$

$$+ \left[\frac{\frac{\cos 2u+1}{2(u+\pi/2)} - \frac{1-\cos 2u}{2(u+\pi)} + \frac{2}{\pi}}{2(u+\pi/2)(u+\pi)} - \frac{\frac{1-\cos 2u}{2(u-\pi)} - \frac{\cos 2u+1}{2(u-\pi/2)} + \frac{2}{\pi}}{2(u-\pi/2)(u-\pi)} \right.$$

$$\left. \left. + \frac{\frac{\cos 2u+1}{2(u-\pi/2)} - \frac{1-\cos 2u}{2(u-\pi)} - \frac{2}{3\pi}}{2(u+\pi/2)(u-\pi)} + \frac{\frac{1-\cos 2u}{2(u+\pi)} - \frac{\cos 2u+1}{2(u-\pi/2)} - \frac{2}{3\pi}}{2(u-\pi/2)(u+\pi)} \right] C_1 C_2 \right\}$$

A computer program for computation of the first part, or Fresnel Integral of Eqn. II-b has been written, but the expression will not be given. The results of this computer program, with the expression of Eqn. V, permits calculation of the Short-Pulse-Fresnel Transmit Pattern.

IV. Computer Results

The calculations that are included as enclosures represent applications of the derived formulas to a particular assumed antenna example; and the values chosen could be considered as typical of the present radar state of the art development:

Antenna Length: 13 ft. at K_a Band (with excitation time, τ_d = 0.0166 μsec.)

Pulse Length: 0.04 and 0.10 μsec. for approximated Taylor Weighting of Side Lobe Level = -28 db, $\bar{n}$ = 6

Figs. 5-a and 5-b represent transmitting pattern calculations for conventional aperture distributions of uniform, cosine, and cosine squared illumination. It is interesting to compare the pattern results with Figs. 2-21 a, 2-21 b, and 2-21 c of Ref. 3; the cited figures are plots of Fraunhofer, and Fresnel Patterns for the same aperture distributions of: Uniform, Cosine, and Cosine Squared aperture illumination. Figs. 5-a and 5-b are normalized to zero at u = 0, in order to emphasize relative values for side lobe levels; and the change in the pattern gain for a given aperture distribution and pulse length is not shown. (The gain factor loss can be obtained from this paper.)

Fig. 6 represents the transmitting pattern for approximated Taylor Weighting (Side Lobe Level = -28 db., $\bar{n}$ = 6). The short pulse-far field results are plotted for the pulse lengths: 0.04 and 0.10 μsec., and zero decibel power reference is taken at u = 0. The suitability of the approximation is indicated by the fact that the first and second null positions of the approximated Taylor pattern are identical to the Taylor Far Field Pattern ($\bar{n}$ = 6, -28 db.), and the approximated magnitudes of the first four side lobes are close to -28 db.

Figs. 7-a and 7-b represent transmitting Fresnel pattern calculations for a more generalized Taylor Weighting Aperture Distribution:

$$J_0\left(j\pi B\sqrt{1-x^2}\right); \quad -1 \leq x \leq 1$$

for the side lobe level -28 db. See 2-28 of Ref. 3. The loss in gain due to the defocussing effect is shown in Figs. 7-2, and 7-b. The combined detrimental effect of short pulses and Fresnel defocussing are indicated by a comparison with the short pulse-far field curve. Figs. 7-a and 7-b are considered as preliminary information, and they represent the first data from the computer program.

Figs. 9-a and 9-b are discussed in Section V of this paper.

V. Pattern Effect on Radar System Performance

System Resolution: Range and Azimuth

The system resolution of a radar is a function of particular radar parameters describing the radar receiver units.

System range resolution is a function of the pulse duration, I.F. and Video Bandwidth, the C.R.T. spot size, and recording resolution (optics and film). The expressions derived in this paper indicate that the return radar pulse is changed from the original square pulse length of τ to a distorted pulse length of $\tau + 2\tau_d$. The primary limitation to good system range resolution at the present time is considered to be the C.R.T. spot size, and not the pulse length. Range resolution is not considered in this paper, although the expressions necessary for plotting the shape are derived in this paper.

System azimuth resolution is a function of the antenna beamwidth, the C.R.T. spot size. Therefore, the short pulse study, considering the azimuth effect, has greater application to radar system performance than the range resolution effect.

Graphical Presentation: Effect on Azimuth Resolution

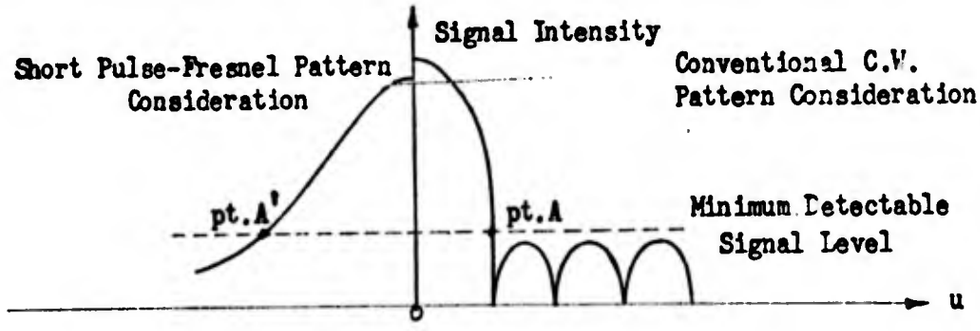

Fig. 8 - Effect on Azimuth Resolution

Fig. 8 presents in a qualitative manner the Short-Pulse-Fresnel effect on azimuth resolution. The conventional antenna design consideration assumes that the side lobe intensity level of the radiation pattern will be below the minimum detectable signal level of the radar receiver. Thus, the position for azimuth resolvability, pt. A is defined at the threshold level of signal detectability. Short Pulse-Fresnel considerations indicate a general increase in the side lobe level, with the result that the position for azimuth resolvability is now at pt.A', according to the above definition of angular resolvability. This decrease in angular resolvability is evident from the graphical presentation of Fig. 8.

Furthermore, the lobular structure of the conventional C.W. pattern is absent in the short pulse pattern, with an accompanying increase in the probability of radar target detection.

Radar Pattern: Far Field-Uniform Aperture Excitation

Figs. 9-a and 9-b are plots of the Radar Pattern for Uniform Excitation (see enclosures). Comparison patterns are shown for the Two Way Transmit Patterns with 0.04 and 0.10 μ sec. pulse lengths. The further deterioration of the pattern shape on receive is explained from a brief look at the return pulse shape. Although the original square pulse length τ, is distorted to a length $\tau + 2\tau_d$, there is relatively little return energy in the leading and trailing portions of the return waveform. The energy of the return signal occurs mostly in the portion associated with complete waveguide excitation, with a time duration of $\tau - 2\tau_d$; therefore, the further deterioration on receive seems to be plausible.

Ground Mapping Performance - Elevation Coverage: $\csc^2 \theta \cos^{\frac{1}{2}} \theta$

The cited reference* derives the elevation coverage of the form $\csc^2 \theta \cos^{\frac{1}{2}} \theta$ (θ, horizontal depression angle) for the condition for uniform ground mapping. It is stipulated that the effective azimuth beamwidth $\Delta\beta(\theta)$ is independent of the depression angle of coverage θ. This fact can be interpreted as a statement that the desired elevation coverage is a function of the effective azimuth beamwidth. The effective azimuth beamwidth is a function of the Short Pulse-Fresnel Pattern Effect, so that the desirable form of elevation coverage is related to the Short Pulse-Fresnel Pattern Effect.

VI. Conclusion

The techniques for evaluation of the Short Pulse-Fresnel Effect have been indicated in this paper.

The mathematical formulation for the transmit condition has been given for a generalized aperture distribution: $f(x) = C_0 + C_1 \cos \frac{\pi}{2} x + C_2 \cos \pi x$. The coefficients C_0, C_1, and C_2 can be selected from knowledge of the values of the first and second side lobe levels of the C.W. Far Field Patterns.

An evaluation of Radar System Performance can be made from a knowledge of the requirements of minimum detectable signal, and a knowledge of the anticipated dynamic range for radar ground return.

* Terrain Handbook, Report 694-9, Section 2-2, Feb. 1, 1959
The Ohio State University Research Foundation, Columbus 10, Ohio

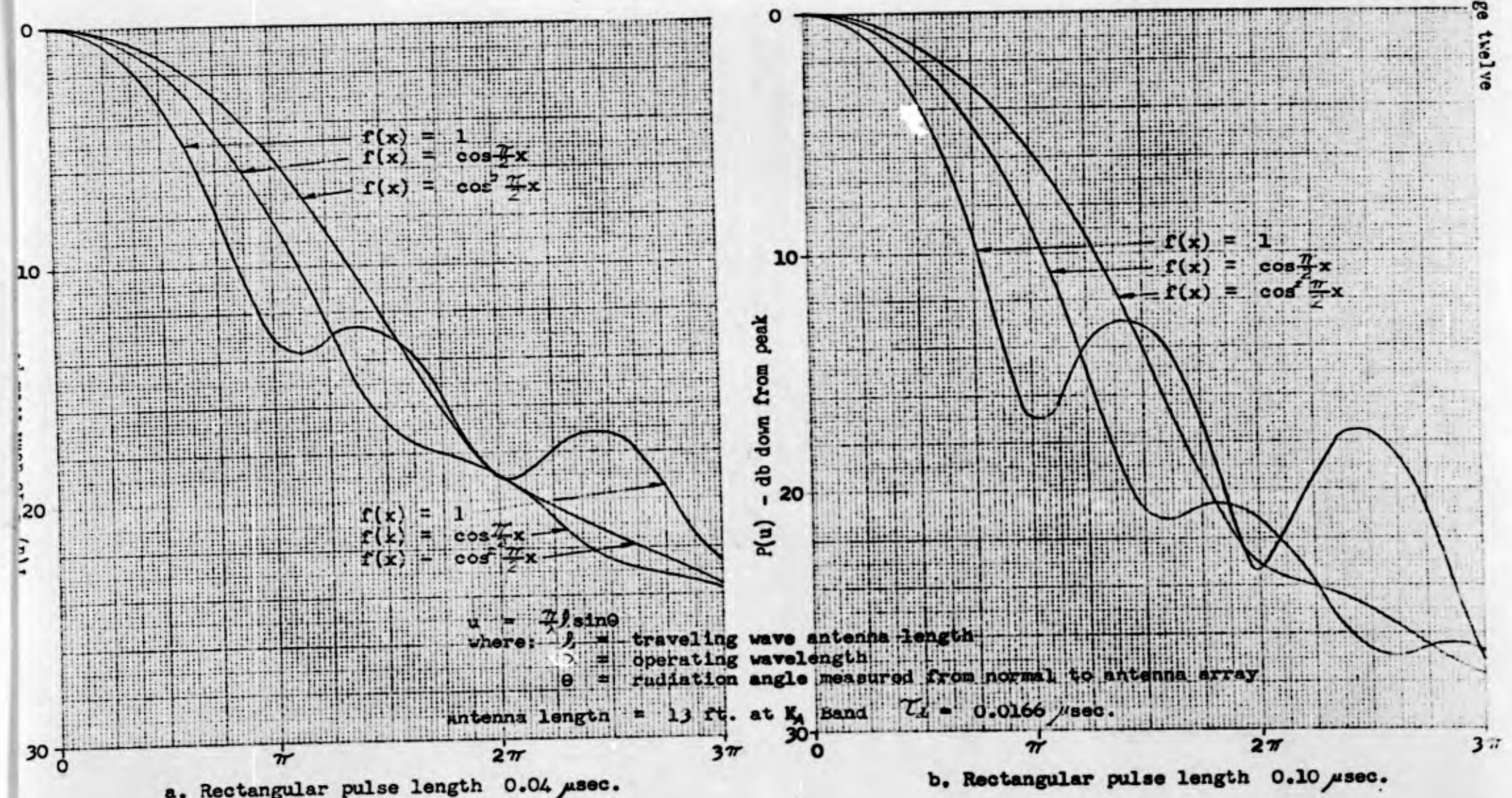

a. Rectangular pulse length 0.04 μsec.

b. Rectangular pulse length 0.10 μsec.

Fig. 5 Transmitting Short Pulse Far Field Pattern

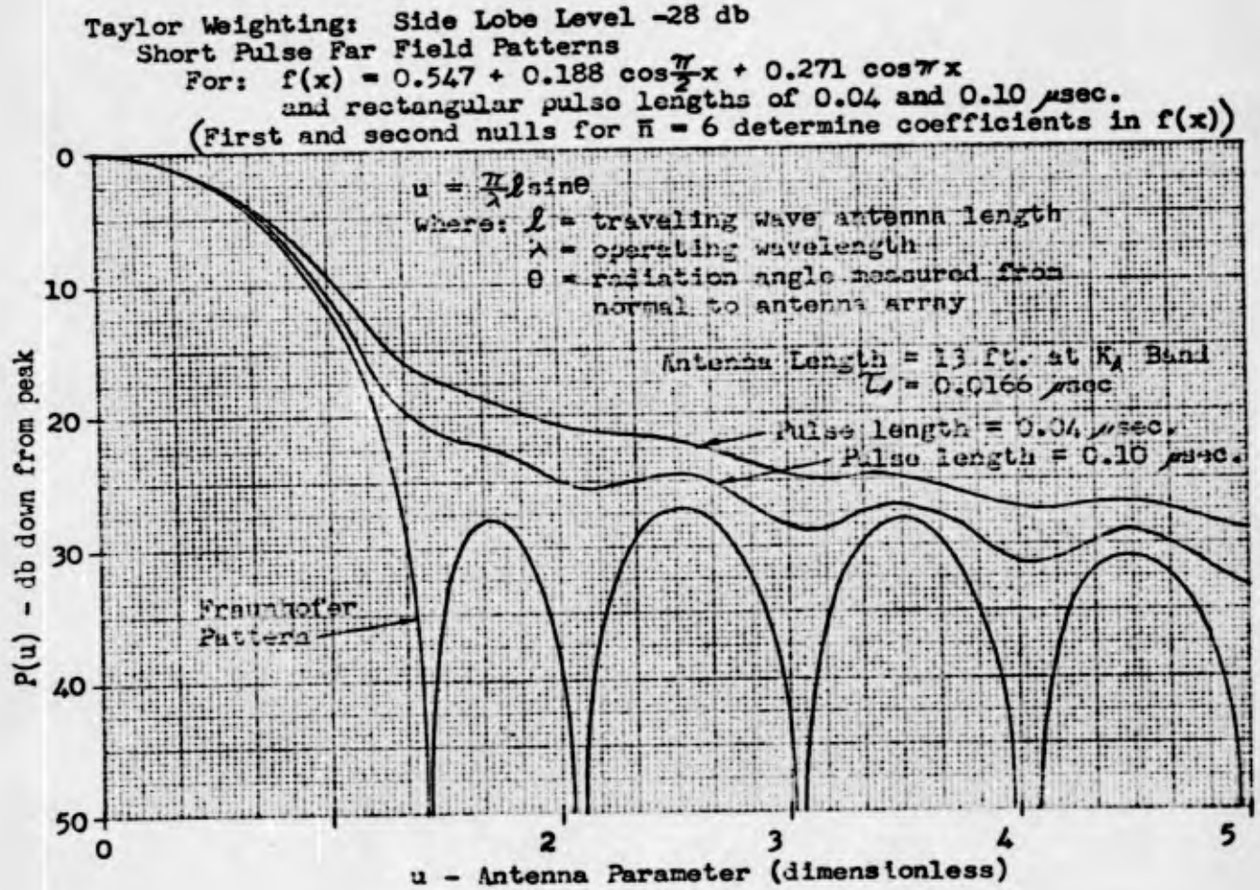

Fig. 6 Transmitting Radiation Pattern for Approximated Taylor Weighting

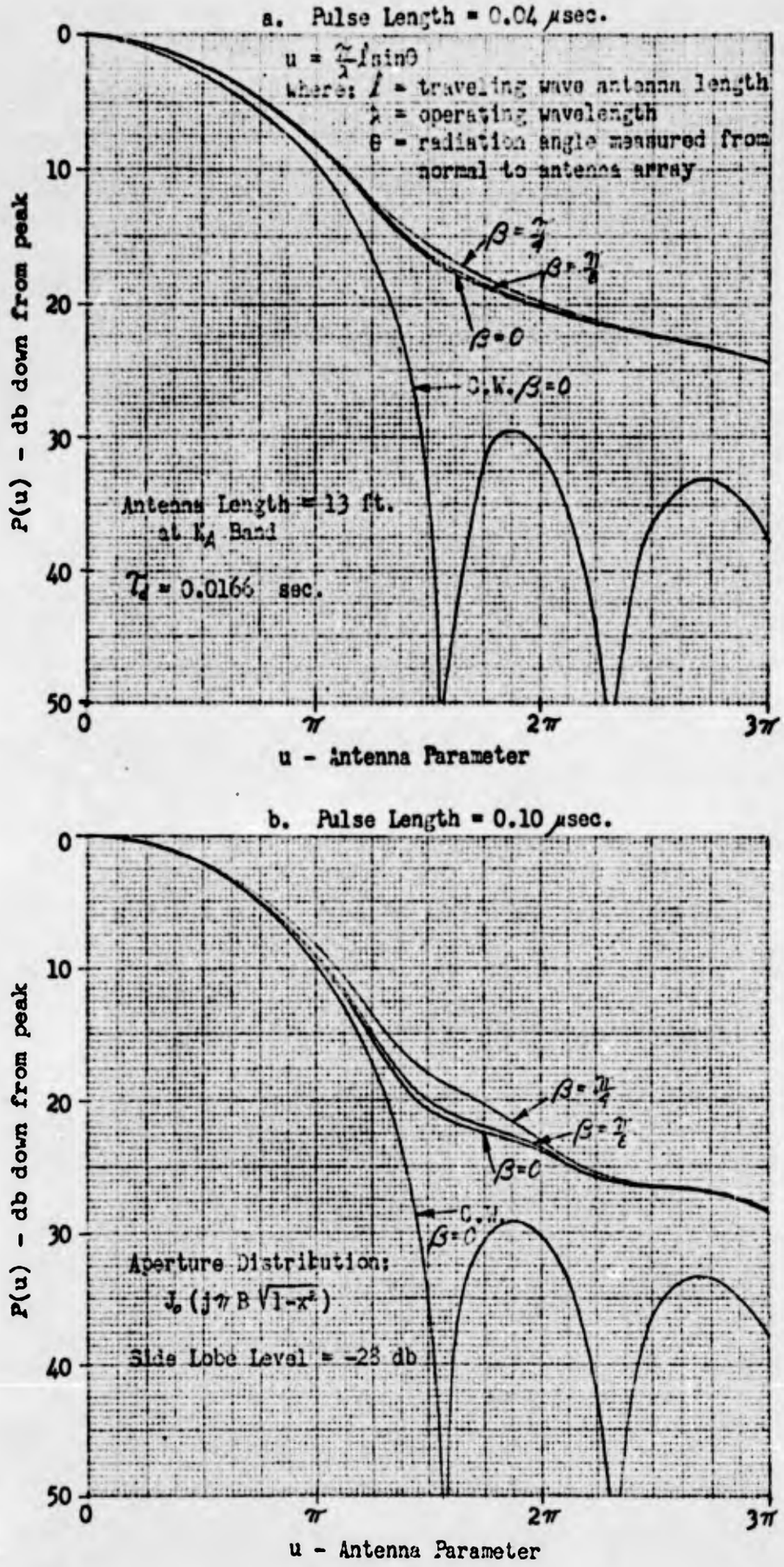

Fig. 7 Short Pulse - Fresnel Patterns for Approximated Taylor Weighting

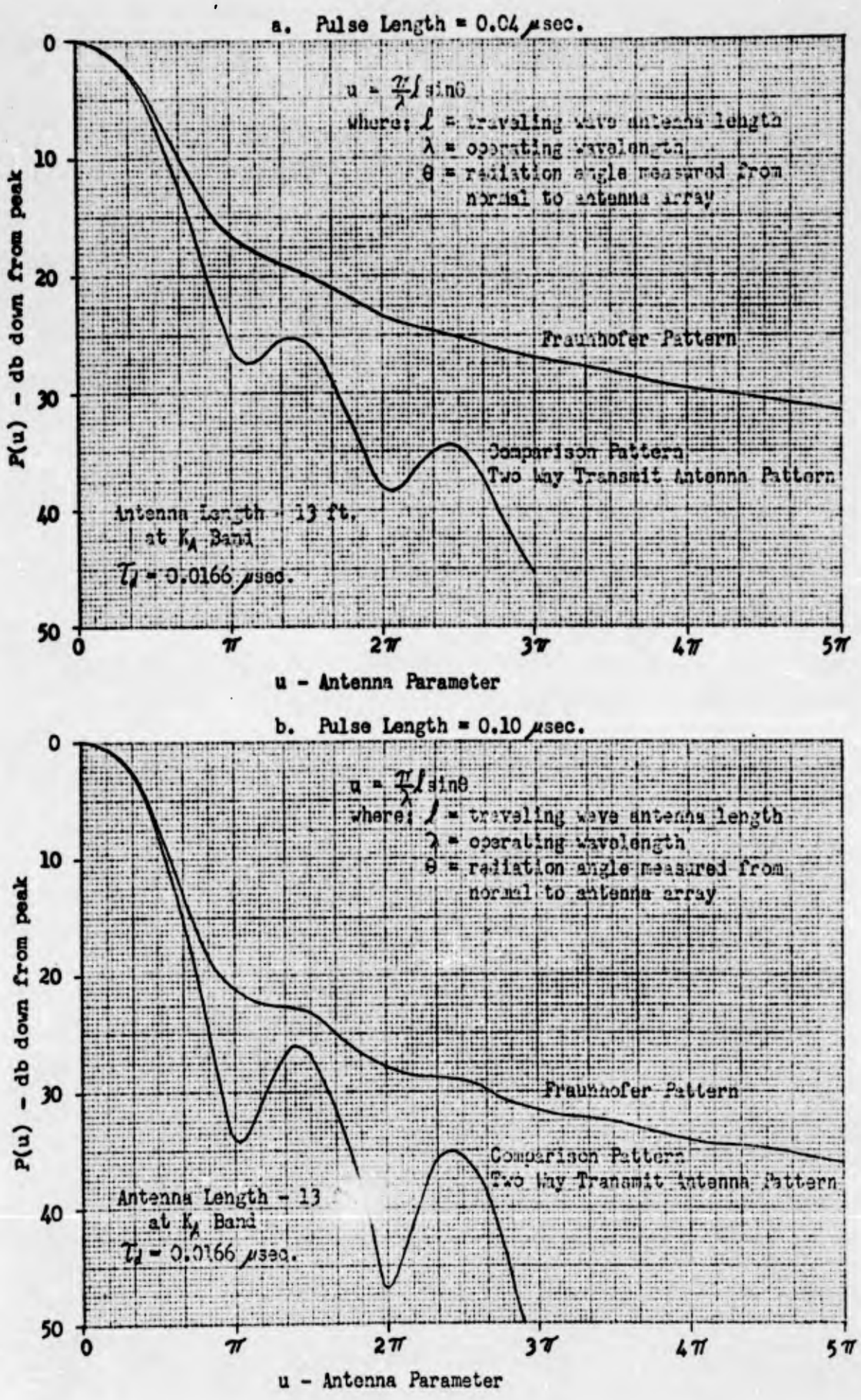

Fig. 9 Radar Pattern - Short Pulse Effect for Uniform Excitation

STATISTICAL DESIGN OF SPACE TAPERED ARRAYS

S. J. Rabinowitz - Columbia University
Electronics Research Laboratory

and

R. F. Kolar - RCA Moorestown Missile
and Surface Radar Division

Statistical Design of Space Tapered Arrays

S. J. Rabinowitz and R. F. Kolar

Phased arrays are generally accepted as having many advantages, particularly where high resolution or multi-beam requirements make more conventional antennas impractical. However, obtaining low sidelobes can be a problem with phased arrays. The discontinuity at the edge of a uniformly illuminated aperture results in undesirably high sidelobes. In reflector type antennas, the primary patterns can be shaped to lower the sidelobes by reducing the edge illumination. In an array, the same effect can be obtained by attenuating the currents in the elements near the edge.

This solution is inefficient since power is wasted when separate modules are used for each element. A more desirable way to taper the current density is by eliminating elements near the aperture edges and fully driving those remaining. This process is known as space tapering, since it approximates a continuous tapered illumination function by a discrete distribution of uniformly illuminated elements, closely spaced near the center of the array and more widely separated near the edges.

Design Method

The space tapering procedure described here results in an approximation of a known low sidelobe amplitude tapered "design array". Other solutions to the problem, are available,[1,2] but the method described here can be programmed for a digital computer which automatically furnishes designs having predictable characteristics.

It is necessary that no periodicities exist in the illumination function since they would cause high sidelobes. This suggests the use of a random process.

Consider a square lattice containing M X N element locations where the separation, ℓ, has been established by grating lobe considerations. The coordinates for a circular array are shown in Figure 1. The possible element locations (m,n) are at the intersection of lines of a square grid. Irregular separations are not considered here since they would complicate the calculation of mutual impedance effects.

Let the excitation of the m,nth element be $A_{m,n}$ where

$$A_{m,n} = 1 \text{ with probability } P_{m,n}$$
$$A_{m,n} = 0 \text{ with probability } q_{m,n} = 1 - P_{m,n} \qquad (1)$$

That is, the excitation of each element is a random variable which can have the value of 1 when the element is present in the array or zero when it is deleted. Only one element can reside at any of the lattice points. This constraint on element position is necessary if identical element modules are to be used.

The far field power pattern is found by multiplying the field intensity by its conjugate

$$F(\theta,\phi) = \sum_{m} \sum_{n} \sum_{r} \sum_{s} A_{m,n} A_{r,s} \, e^{j\left[(m-r)\, u + (n-s)\, v\right]} \qquad (2)$$

$$\text{where } u = \frac{2\pi\ell}{\lambda} \left[\sin\theta \cos\phi - \sin\theta_0 \cos\phi_0\right]$$

$$v = \frac{2\pi\ell}{\lambda} \left[\sin\theta \sin\phi - \sin\theta_0 \sin\phi_0\right]$$

and θ_0 and ϕ_0 are the angular coordinates of the main beam.

Since the $A_{m,n}$ are random variables, the expected value $\overline{F(\upsilon,\varphi)}$ of $F(\upsilon,\varphi)$ is given by

$$\overline{F(\upsilon,\varphi)} = \sum_m \sum_n \sum_r \sum_s \overline{A_{m,n}A_{r,s}}\; e^{j\left[(m-r)\,u + (n-s)\,v\right]} \tag{3}$$

If all the A_{mn} are independent random variables, then

$$\overline{A_{m,n}\,A_{r,s}} = \overline{A_{m,n}}\;\overline{A_{r,s}}\,(1 - \delta_{m,r}\,\delta_{ns}) + \overline{A^2_{m,n}}\,\delta_{mr}\,\delta_{ns}, \tag{4}$$

where $\delta_{i,j}$ is the Kronecker delta defined by

$$\delta_{i,j} = 1 \qquad \text{if } i = j$$
$$\delta_{i,j} = 0 \qquad \text{if } i \neq j$$

Equation (4) says that the expected value of the product $A_{m,n}A_{r,s}$ is equal to the product of the expected values of A_{mn} and A_{rs} separately unless $m = r$ and $n = s$, i.e., unless the two A's refer to the same element in the array. If $m = r$ and $n = s$, then $A_{m,n}A_{r,s} = A^2_{mn}$.

From equation 1, it follows that

$$\overline{A}_{mn} = P_{mn}$$
$$\overline{A}_{rs} = P_{rs}$$
$$\overline{A^2}_{m,n} = P_{mn} \tag{5}$$

The substitution of Equation (5) into (4) yields, after terms are combined,

$$\overline{A_{m,n}A_{r,s}} = P_{m,n}P_{r,s} + P_{m,n}\,q_{m,n}\,\delta_{m,r}\,\delta_{n,s} \tag{6}$$

The substitution of Equation (6) into (3) yields

$$\overline{F(\upsilon,\varphi)} = \left|\sum_m \sum_n P_{mn}\, e^{j(mu + nv)}\right|^2 + \sum_m \sum_n P_{mn}\,q_{mn} \tag{7}$$

Equation (7) is the basis for the statistical design of a space tapered array and is interpreted as follows:

The term $\left| \sum_m \sum_n P_{mn} e^{j(mu + nv)} \right|^2$ is recognized as the pattern of a fully occupied amplitude tapered array where the excitation coefficients are equal to the $P_{m,n}$ i.e., where the excitation coefficient of the m,n^{th} element of the amplitude tapered array is equal to the probability that the m,n^{th} element of the space tapered array is present. The second term in Eq. (7) is the average sidelobe level due to space tapering and is independent of angle. If now the $P_{m,n}$ are made proportional to the amplitudes of an amplitude tapered distribution which produces a pattern having negligible sidelobes, it follows that $\overline{F(\theta,\phi)}$ is a pattern which has a main lobe identical to that of the amplitude tapered array plus equal sidelobes in all directions. This does not mean that any particular antenna designed in this manner will have constant sidelobes since random fluctuation will occur. However, in a large array, it has been found that the probability of any sidelobe peak exceeding the average sidelobe by more than 7 db is extremely small.

The design of the array is accomplished as follows: A random number is generated for each matrix point. The random numbers are compared with the $P_{m,n}$ which are proportional to the amplitude of a known low sidelobe amplitude tapered distribution at the same point. If and only if the random number is equal to or less than $P_{m,n}$ is an element located at m,n. In this way, the probability that an element exists at a given location is equal to the amplitude of a low sidelobe amplitude tapered distribution.

The design array must have sidelobes below the required level since as is shown by equation 7, the space tapering process will raise them.

In any array designed in this manner, some deviation from the average values can be expected, but if the array is large, statistical regularity will insure that the deviations will be small. In any event, if a particular design exhibits characteristics markedly at variance with the expected values, that design can be discarded and a new one made by generating another set of random numbers and comparing them with the desired excitation coefficients. This prodedure can be repeated as often as necessary until an average design is achieved. A large array will require fewer trial designs than a small one.

An indication of the quality of a design is given by the number of elements in the array. One having very nearly the expected number will have characteristics closely approximating those predicted.

Number of Elements

The average number of elements to be expected from many designs is equal to the average value of the selected excitation function times the total number of element locations. The mean illumination for the continuous amplitude tapered distribution is given by

$$I_{AV} = 2 \int_0^1 I_r \, r \, d \, r \tag{8}$$

where r is the normalized radius and Ir is the amplitude of the design illumination function at a distance r from the center of the array.

The expected value of the total number of elements in the space tapered array is then

$$N_{ST} = 2\pi N_r^2 \int_0^1 I_r \, r \, d \, r \tag{9}$$

where N_r is the number of elements on a radius.

Gain

The array gain of the continuous circular amplitude tapered array can be calculated from

$$G_{AT} = \frac{2 N_r^2 \pi \left[\int I_r \, r \, dr \right]^2}{\int I_r^2 \, r \, dr} \tag{10}$$

For a space tapered array, the elements are all fully driven so its efficiency is 100% and the array gain is simply equal to the total numbers of elements.[3]

$$G_{ST} = N_{ST} \tag{11}$$

Sidelobes

The term in equation 7 which gives the sidelobe level due to space tapering is not a function of angle. The sidelobe energy is equally distributed in all directions including that of the main lobe. The average sidelobe level, relative to the main lobe, and subject to the condition that the sidelobes of the amplitude tapered array are negligible, is

$$\overline{SL}^{-1} = \frac{\text{Sidelobe Power + Main lobe power}}{\text{Sidelobe Power}} \tag{12}$$

$$= \frac{\left(\sum_m \sum_n P_{m,n} \right)^2}{\sum_m \sum_n P_{m,n} \, q_{m,n}} + 1 \tag{13}$$

which after substituting gain equations for arrays of discrete elements[3] becomes

$$\overline{SL} \text{ (db)} = -10 \log \frac{G_{ST}}{1 - \frac{G_{ST}}{G_{AT}}} \tag{14}$$

where G_{AT} is the gain of the fully occupied amplitude tapered design array.

Discussion

Equations have been developed which can be used for predicting the characteristics of space tapered arrays after a design array function has been selected. Just as in amplitude tapered arrays, the major factor controlling gain and beamwidth is the array size. As a designer strives for reduced sidelobes, it is inevitable that the beamwidth will be increased. The tapering function worthy of primary consideration is the Taylor[4] taper which yields the optimum compromise between beamwidth and sidelobe level. Illuminations having peak sidelobes of -40 db, satisfy the requirement that the sidelobe level of the design array be negligible for most applications. A small amount of control over the gain and beamwidth is available by changing the value of $\bar{n}$ in Taylor's equations. High values of $\bar{n}$ produce high gain and low beamwidth.

Equation 9 shows that the expected number of elements in an array of a specified diameter is proportional to the average value of the illumination of the design array. For a -40 db Taylor taper, this value will vary between 0.394 and 0.435 so that available control over the maximum array gain for a specified aperture size is small. If slightly increased sidelobes can be tolerated, values of $I_{av} = 0.50$ can be realized from -35 db taper.

The average excitations for all low sidelobe amplitude tapers are lower than their efficiencies so although the space tapered antenna has 100% efficiency, its gain is still below that of the amplitude tapered array. This in no way limits the gain which can be achieved by space tapering since the gain of the design array can be made as large as desired by increasing the size of the array.

Any low sidelobe level amplitude distribution can be used to achieve any given space taper antenna gain. Nevertheless, it is advantageous to use a high efficiency amplitude taper since this will lead to a space taper design with the lowest average sidelobe level for a fixed gain.

Example

As an example an array based on a -40 db circular taper with $\bar{n} = 10$ was designed according to the method described above. A graphical presentation of the expected values of gain, beamwidth, and sidelobe level for arrays based on this function is shown in Figure 2.

An aperture having a radius of 62 elements separated 0.57λ was selected. The array diameter is 70.68λ. The expected value of the beamwidth, β, is found from the curve at a value of $2a/\lambda = 70.68$. The result is 1.03 degrees. The expected gain and rms sidelobe level depend upon the number of elements and not on their separation. (Mutual effects are neglected here). The curve at $N_R = 62$ gives an expected gain value of 37 db and an rms sidelobe level of -40.6 db. Adding 7 db to the expected rms sidelobe level results in expected peak sidelobes of -33 db.

The resulting array has 4991 elements or a gain of 36.98 db. The beamwidth and sidelobe level of the computed patterns shown in Figure 3 agree very well with the expected values.

The equivalent amplitude tapered array would have a gain of 39.5 db but would require 12076 driven elements with some means provided to reduce the current in most of them.

Conclusions

A method has been described for designing arrays with low sidelobes without resorting to attenuating the current in some elements. This is accomplished by using fewer elements near the edge of the array then near its center. The elements are located by a pseudo-random method to prevent the occurance of any periodicities which would result in high sidelobes. The design is based on a

known low sidelobe amplitude tapered distribution and a digital computer is used to locate the elements. The gain, beamwidth, and sidelobe level of the space tapered array can be reliably predicted for large arrays. An example of an array having all sidelobes below -30 db with a gain of 36.9 db and a beamwidth of about 1° is given.

References

1. Robert E. Willey, "Space Tapering of Linear and Planar Arrays", IRE Trans. on Antennas and Propagation, Vol. AP-10, pp. 369-377, July, 1962.

2. Frank C. Ogg, "Steerable Array Radars," IRE Trans. on Military Electronics, Vol. MIL-5, pp. 80-94, April, 1961.

3. Allen, J. L., et al, "Phased Array Radar Studies," 1 July 1960 to 1 July 1961, Tech. Rpt. 236 MIT Lincoln Laboratory, Lexington, Mass., (Nov. 1961).

4. T. T. Taylor, "Design of Circular Aperture for Narrow Beamwidth and Low Side Lobes", IRE Trans. on Antennas and Propagation, Vol. AP-8, pp. 17-22, January, 1960.

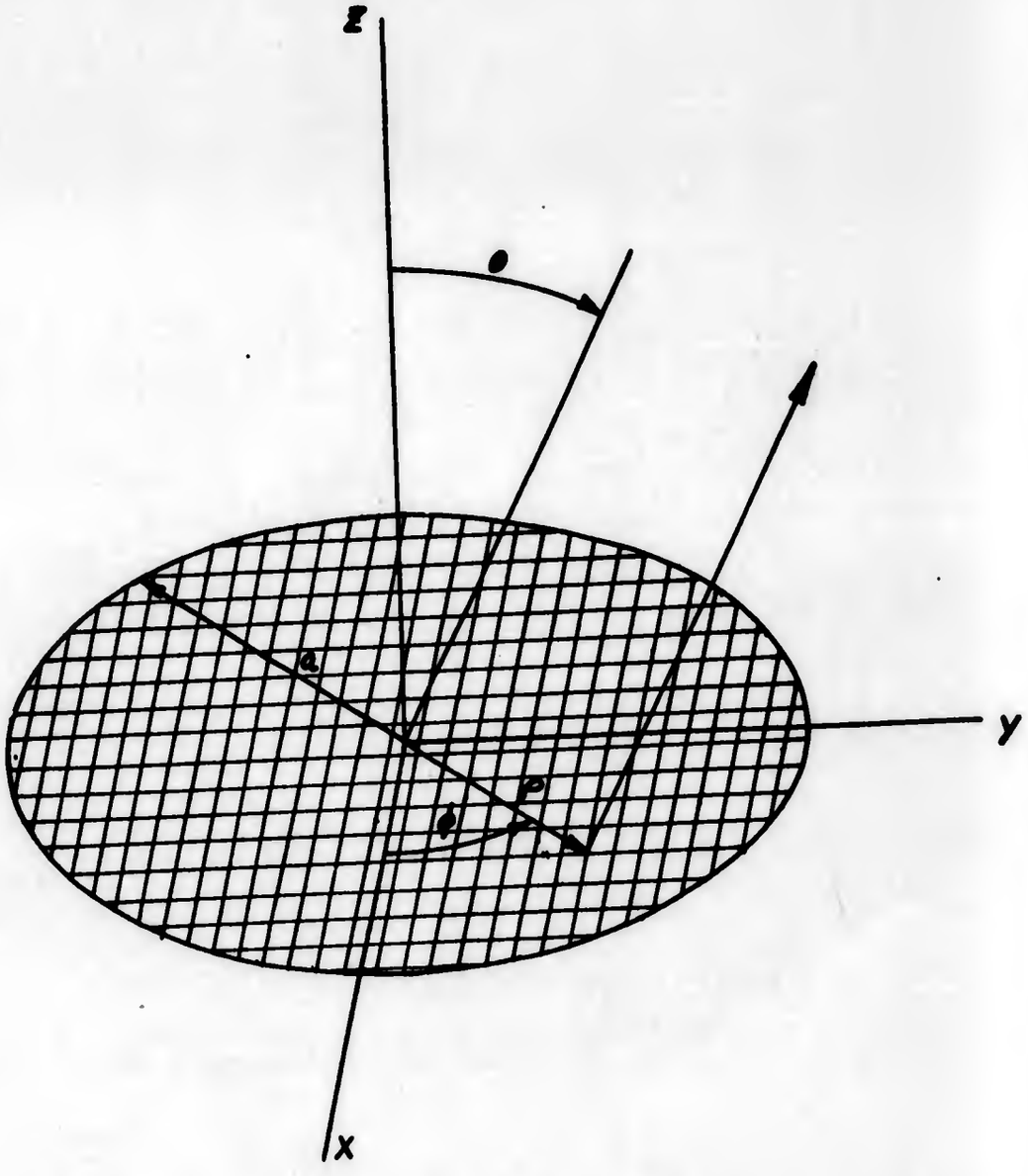

FIG. 1 ARRAY CONFIGURATION

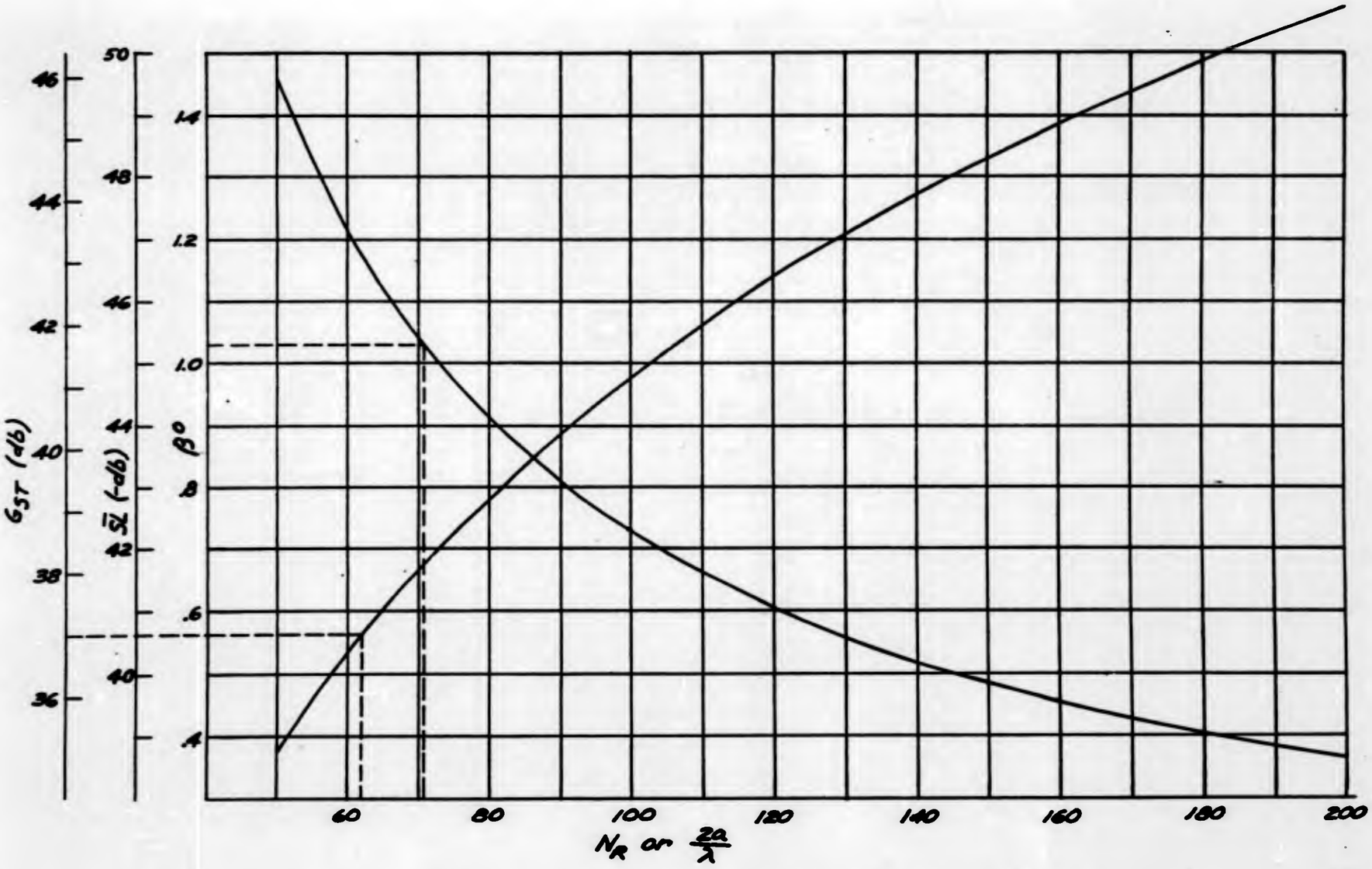

FIG. 2 SPACE TAPER DESIGN CURVES FOR -40 DB $\bar{n} = 10$ TAYLOR TAPER

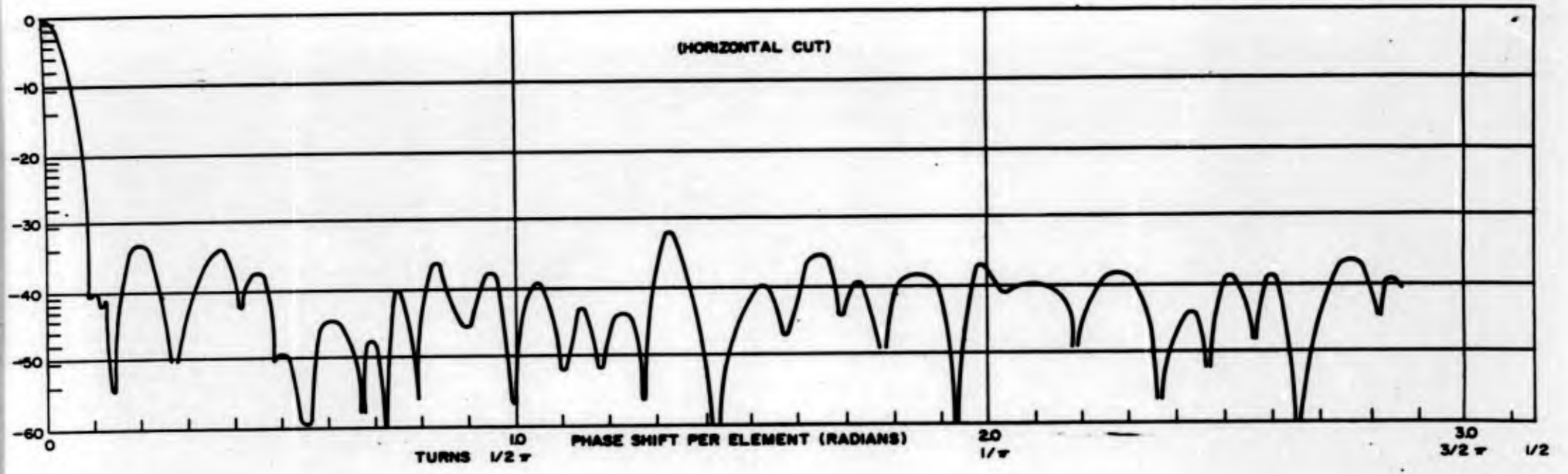
(HORIZONTAL CUT)
0
-10
-20
-30
-40
-50
-60
0
1.0
TURNS 1/2π
PHASE SHIFT PER ELEMENT (RADIANS)
2.0
1/π
3.0
3/2π
1/2

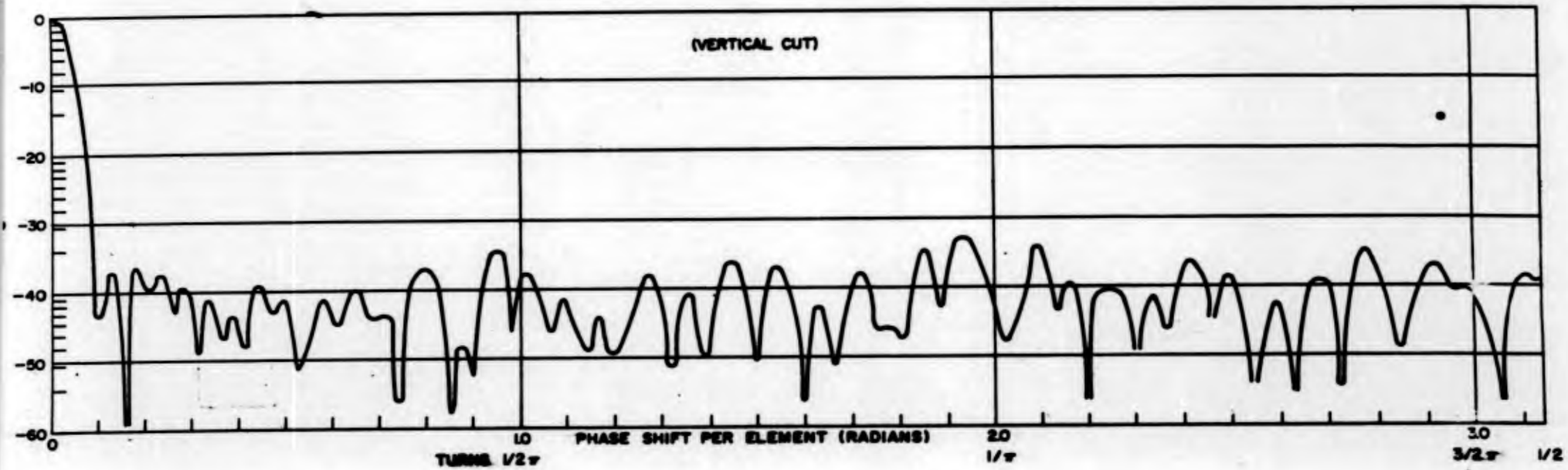
(VERTICAL CUT)
0
-10
-20
-30
-40
-50
-60
0
1.0
TURNS 1/2π
PHASE SHIFT PER ELEMENT (RADIANS)
2.0
1/π
3.0
3/2π
1/2

ANTENNA DESIGN WITH DIGITAL COMPUTERS

Presented at

The Twelfth Annual Symposium on U.S.A.F. Antenna
Research and Development
Robert Allerton Park, Monticello, Illinois
16-19 October, 1962

Prepared by

Conway A. Bolt, Jr.

INTRODUCTION

The design procedure for shaped reflector mapping antennas offers numerous opportunities for application of the digital computer to significantly reduce design time and effort. A group of computer programs which were written to aid in the design of line source fed, singly curved reflector ("shaped-beam") antennas will be outlined. Results from these programs have been verified experimentally both in laboratory model and production antenna designs. Although the computer programs were originally intended for application to a specific class of antennas, many of them are sufficiently general to apply to a variety of designs.

In establishing the design of a singly curved cylindrical reflector antenna, two essentially independent design areas are investigated. The first of these is the determination of the reflector contour and primary radiator parameters required to give a specific vertical plane secondary radiation pattern. The second is the determination of the proper line source feed dimensions to produce the required narrow-beam horizontal plane secondary pattern.

REFLECTOR CONTOUR COMPUTATION PROGRAMS

The reflector contour required to produce the specified vertical plane radiation pattern is determined by geometric optics techniques. The method of calculating the contour of a singly curved reflector (and the closely related problem of the doubly curved reflector) is adequately pre-

sented in the literature[1,2] and will consequently only be summarized.

If the primary radiation pattern (in units of power ratio) is specified by $I(\phi)$ and the secondary radiation pattern is specified by $G(\theta)$, the energy in any incident wedge of the primary pattern is proportional to the energy in the corresponding wedge of the secondary pattern by principles of energy conservation, or:

$$K\, I(\phi)\, d\phi = G(\theta)\, d\theta \qquad (1)$$

Since all of the primary pattern energy intercepted by the reflector appears in the secondary pattern, the proportionality constant K may be evaluated by solving equation (1) over the appropriate limits. Once the constant has been evaluated for given primary and secondary patterns, the relationship between the primary pattern angle ϕ and the secondary pattern angle θ is determined from equation (1).

The differential equation of the reflector contour (derived from the law of optical reflection) is:

$$\frac{d\rho}{\rho} = \tan \frac{\phi - \theta}{2}\, d\phi \qquad (2)$$

in which ρ, ϕ are the polar coordinates of the reflector as shown in Figure 1. Equation (2) may be solved for the coordinates of points on the reflector contour when values of θ as a function of ϕ are known from equation (1).

1. S. Silver, Microwave Antenna Theory and Design, McGraw-Hill, New York 1949, pp. 497-500 and 502-508.

2. A.S. Dunbar, "Calculations of Doubly Curved Reflectors for Shaped Beams", Proc. I.R.E., Vol. 36, pp. 1289-1296, October, 1948.

For purposes of calculation, a primary illumination distribution

$$I(\phi) = \cos^m(\phi - \phi_o) \qquad \phi_p \leq \phi \leq \phi_s$$

$$I(\phi) = 0 \text{ elsewhere}$$

and a secondary radiation pattern

$$G(\theta) \propto \csc^2 \theta \qquad \theta_p \leq \theta \leq \theta_s$$

$$G(\phi) = 0 \text{ elsewhere}$$

are assumed.

Inputs to the reflector contour computer program are the primary illumination distribution, the specified idealized secondary radiation pattern, the feed normalization angle ϕ_o, the dimension from the feed to a reference point on the reflector surface ρ_s, and the desired increment for calculating the reflector coordinates $\Delta\phi$. Outputs from the program are the polar coordinates of points on the reflector surface and their corresponding cartesian coordinates. Machine time for a typical case of 100 points on the reflector contour is roughly 1/10 second for the IBM 7090 computer.

Typical shaped reflectors for mapping antennas are parabolic over a considerable portion of their contour, and in general this parabolic region is less sensitive to small changes in dimensions than the "shaped" portion of the reflector. Consequently, the computer program starts in the "shaped" portion of the reflector and works toward the parabolic portion to allow any cumulative errors to accumulate in the parabolic region where they will have less effect on the secondary radiation pattern.

The reflector contour calculated in this manner is of course subject to the "infinite frequency" approximation of ray theory, and the specified idealized secondary pattern can only be approached for a finite aperture. The effects of polarization and the diffraction effects of pattern ripple and secondary lobes for a given reflector contour and primary radiator combination must be investigated analytically by physical optics techniques.

A pattern regeneration program based on approximate physical optics techniques, using as its inputs the geometric optics reflector contour, the polarization, and the wavelength, is employed to calculate the secondary radiation pattern which would be produced by the given reflector and feed combination. The secondary radiation pattern may be determined from the surface-current distribution induced on the reflector by the field of the primary radiator. These techniques are also presented in detail in the literature[3,4] and will therefore be summarized briefly.

The far field radiation pattern of a line source fed cylindrical reflector (as shown in Figure 2) in the vertical plane, $E(\Theta)$ is given by

$$E(\Theta) = \text{Const.} \int_{\phi_p}^{\phi_s} \rho^{1/2} F(\phi)\, d\phi \exp. \left\{-jk\rho\left[1 + \cos(\phi - \Theta)\right]\right\} \quad (3)$$

for horizontal polarization, and by

3. S. Silver, op. cit. pp. 144-145 and pp. 500-502 (note typographical error in equations (15) and (16) page 501).

4. L. Thourel, The Antenna, John Wiley and Sons, New York 1960, pp. 209-212.

$$E(\Theta) = \text{Const.} \int_{\phi_p}^{\phi_s} \rho^{1/2} F(\phi) \left[\cos(\phi - \Theta) + \sin(\phi - \Theta) \tan \angle i\right] d\phi$$

$$\exp. \left\{-jk\rho \left[1 + \cos(\phi - \Theta)\right]\right\} \qquad (4)$$

for vertical polarization (assuming that the reflector is in the cylindrical wave region of the line source feed).

In these equations, ρ, ϕ are the coordinates of the reflector, $F(\phi)$ is the vertical plane primary field distribution, $\angle i$ is the angle between and the normal to the reflector surface, and Θ is the secondary pattern angle. The secondary pattern expressions differ for the two polarizations because the horizontally polarized vector is parallel to the generatrix of the shaped reflector; whereas the vertically polarized vector is perpendicular to the generatrix of the shaped reflector and its reflection characteristics are modified from the simple geometric optics condition.

Ordinarily, the ρ of equations (3) and (4) - or more correctly $\rho(\phi)$ - is not presented in functional form since the reflector contour is calculated only at specific points. For this reason the integrals must be evaluated numerically.

The integrals of equations (3) and (4) are in vector form and may be solved approximately by vector summation of their components at a large number of points over the entire reflector surface. The summation process must be repeated for every angle (Θ_q) at which the secondary radiation pattern is to be calculated. For accuracy, the primary pattern increment $\Delta\phi$ must be small so that a large number of points on the reflector surface are summed.

The pattern regeneration program is combined with the geometric optics reflector contour program to avoid having a large number of points on the reflector surface to be read into the computer as inputs. Inputs, in addition to those of the contour calculation program, are wavelength and the desired range and increment of the secondary pattern angle Θ. Machine time for the pattern regeneration program is approximately 5 minutes for the IBM 7090 for a typical horizontal polarization case and slightly longer for vertical polarization.

The regeneration program is of course subject to the limitations imposed by the approximations involved in its derivation. The effects of diffraction at the edges of the reflector, back radiation from the primary radiator, and aperture blocking by the primary radiator structure have been neglected.

The pattern regeneration program is of definite value in enabling a shaped reflector antenna design to be thoroughly evaluated to assure compliance with pattern requirements before any experimental models need be constructed and tested. The program may also be used with minor modifications to investigate the effect on the secondary pattern of dimensional errors in the reflector contour.

LINE SOURCE FEED COMPUTATION PROGRAMS

The second area for using the digital computer in the design of shaped reflector mapping antennas is the design of the line source feed. A slotted waveguide one-dimensional array is customarily employed as a feed for a cylindrical reflector antenna. A non-resonant array having a specified illumination distribution (for example; Taylor, or uniform) is assumed.

Since waveguide losses are significant for long X and K band arrays, these losses must be included in calculating the slot coupling coefficients.

A general series expression for the slot coupling coefficients (defined as the ratio of power radiated by an element to the power passed on to succeeding elements) has been derived by extending an analysis by Norwood[5]. The expression for the coupling coefficient for the K^{th} element is:

$$\gamma_K = \frac{\left[e^{-2(N-1)\alpha L} - P_T\right] C_K}{e^{-2(K-1)\alpha L} \sum_{S=1}^{N} C_S e^{-2(N-S)\alpha L} - \left[e^{-2(N-1)\alpha L} - P_T\right] \sum_{S=1}^{N} C_S e^{-2(K-S)\alpha L}} \qquad (5)$$

in which:

- N = the number of elements
- C_K = the power distribution coefficients
- α = waveguide attenuation in nepers per unit length
- L = the element spacing (assumed to be uniform)
- P_T = the power to the termination expressed as a fraction of the input power.

For the practical case of an array with a relatively large number of shunt elements which are individually resonant and loosely coupled to the feeding waveguide, the coupling coefficients are numerically equivalent to the normalized shunt conductance.

5. V.T. Norwood, "Note on a Method for Calculating Coupling Coefficients of Elements in Antenna Arrays", I.R.E. Trans. A.P., Vol. AP-3, pp. 213-214, October, 1955.

The required slot dimensions are determined directly from the calculated values of conductance either analytically or by utilizing measured data relating conductance and pertinent slot dimensions obtained from groups of identical slots. The latter method offers the advantage of taking into account the effects of mutual coupling.

These operations are combined in a single computer program which calculates the required edge slot dimensions for a given number of elements with a given illumination distribution. Machine time for this program which includes a "plug in" program for calculating the Taylor coefficients, is approximately 0.03 second per element with the IBM 7090.

The slot dimension program has also been modified by the incorporation of the transmission line equations to enable the input S.W.R. as a function of frequency of the line source feed to be calculated.

Finally, the computer has been utilized extensively to determine the deleterious effects of reflector bending as a function of weight or G loading upon the horizontal plane radiation pattern for the case of a typical two point mounting structure. The reflector (or array) is assumed to be a uniform beam with known cross-sectional moment of inertia and Young's modulus. Its deflections from a perfectly flat condition are determined as a function of its weight and the pressure loading applied at its ends and center. The deflections are converted to variations from uniform phase and are used in calculating the far-field radiation pattern. Machine time for this program is typically 1/4 second per element for the IBM 7090 computer.

The computer programs outlined have been utilized extensively in the design of a number of low-ripple airborne mapping antennas including a dual altitude design employing dual feed structures with a common reflector. Measured results show extremely good agreement with the computed results.

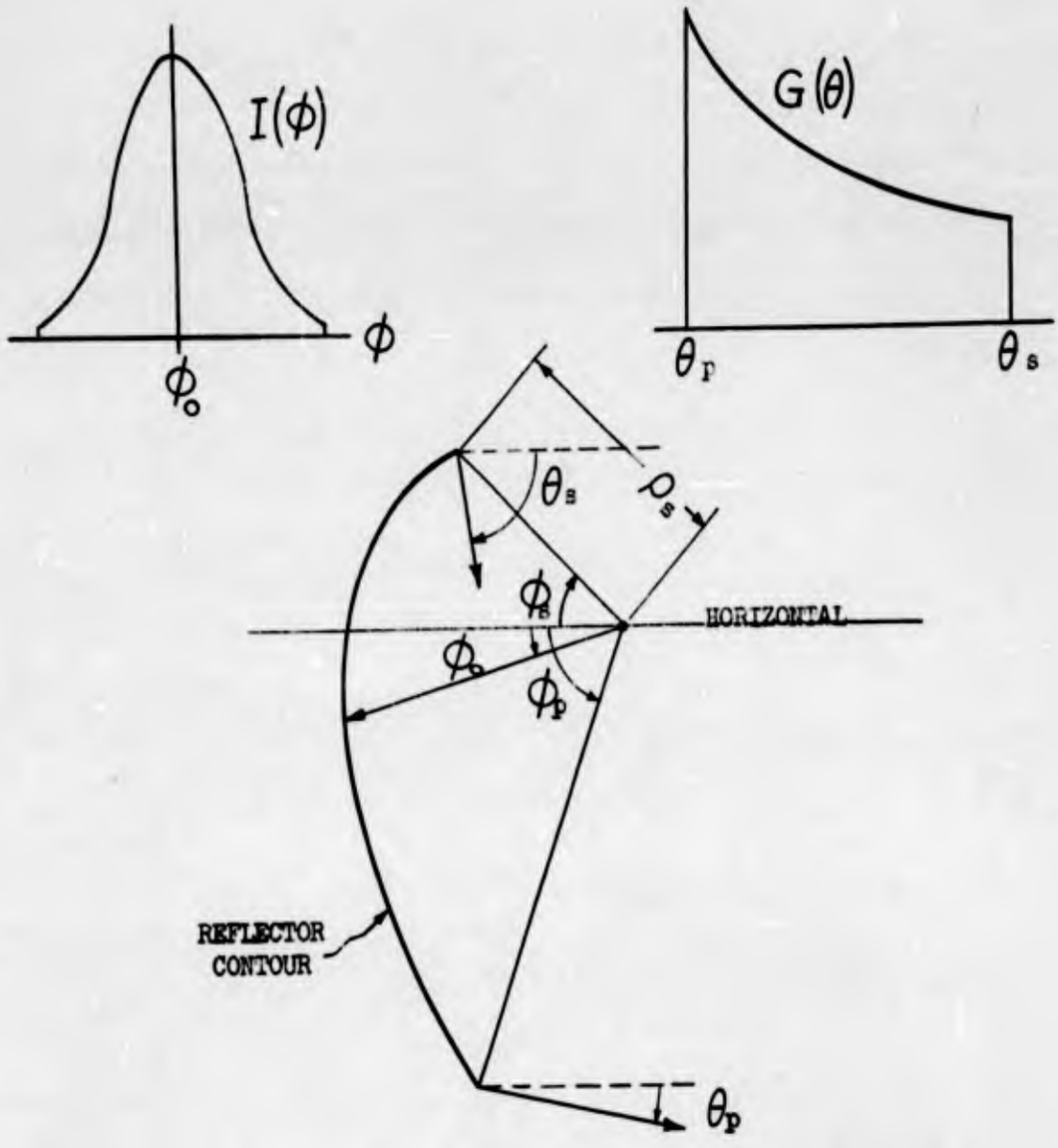

Figure 1

Geometry of Singly Curved Reflector for Contour Calculation Program

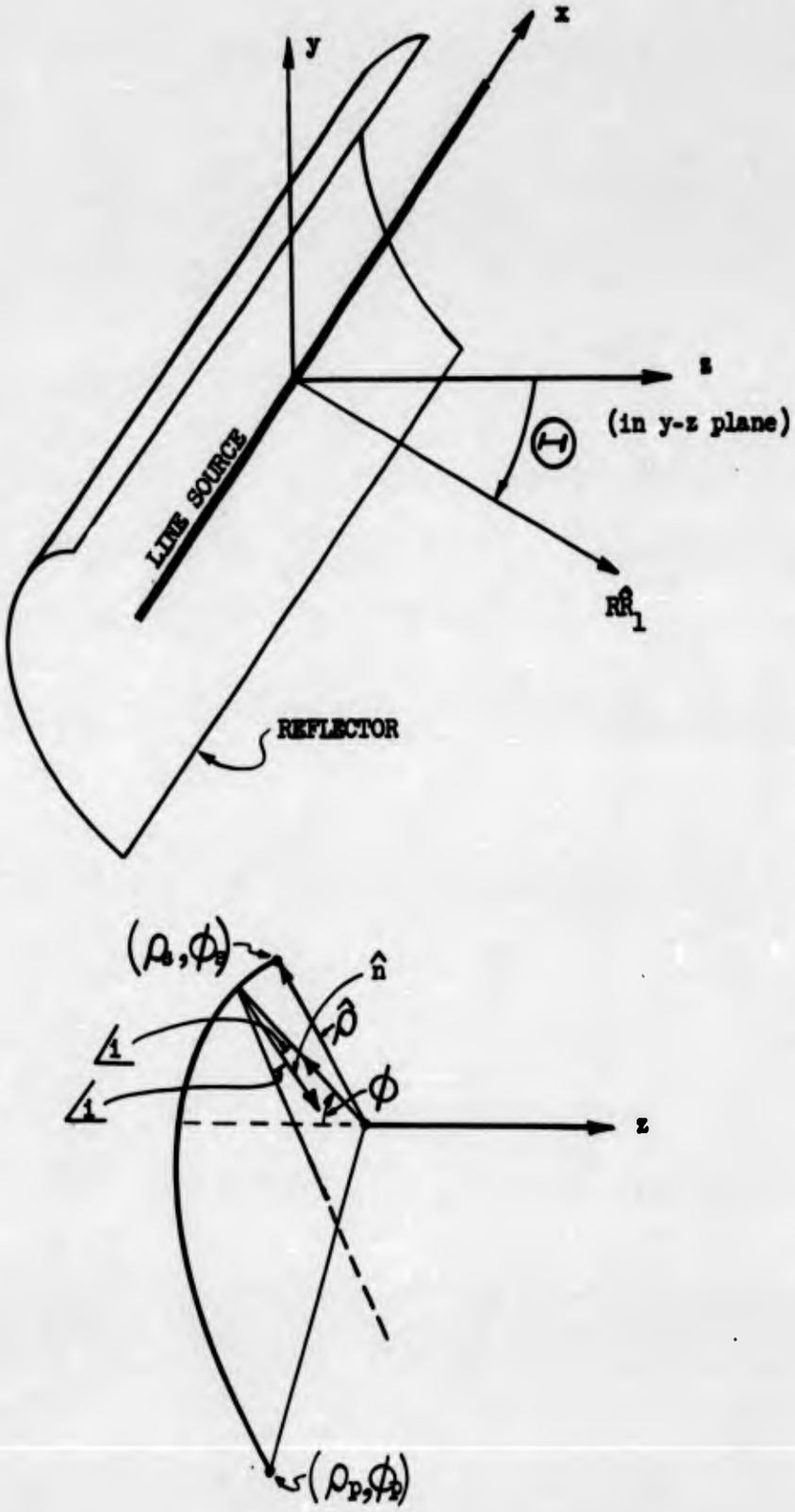

Figure 2

Geometry of Singly Curved Reflector and Line Source Feed for Pattern Regeneration Program

THE APPLICATION OF NON-LINEAR PROGRAMMING TO PATTERN SYNTHESIS PROBLEMS

Richard A. Micholson
James W. Schomer

THE BOEING COMPANY
Transport Division
Technology Section

I

INTRODUCTION

A designer of antenna arrays is presented with an increasing number of synthesis problems today for which there are no well developed methods of solution. Equal-spaced linear arrays present few problems, but the realization that many patterns from these arrays can be approximated quite closely by using a fewer number of unequally spaced elements has created a considerable interest in unequal-spaced arrays. A significant reduction in the number of elements in a very long array is attractive from the economic point-of-view, but there are electrical advantages as well. The bandwidth-steerability product of unequal spaced arrays can be increased significantly over that of equal-spaced arrays.[1] Side lobe suppression is also possible by spacing the elements unequally.[2] Synthesis techniques for the design of unequal spaced arrays however, are in their early stages of development[3], and the array designer who intends to use an unequal-spaced array, for whatever purpose, must approach his design by what amounts to a "cut-and-try" process.

Similar problems are encountered in the design of non-linear arrays. Only in very special cases can the patterns for non-linear arrays be synthesized with presently available techniques. The increasing interest in siting very long arrays over uneven ground contours, with appropriate phase correction of the elements, presents an extremely complicated problem of pattern synthesis.

The theoretical solutions to these problems will undoubtedly take many years, but methods of synthesis can be developed which effectively bypass some of the complex theoretical questions and provide quite useful techniques for the design of these arrays.

The technique described in this report considers pattern synthesis simply as a curve fitting problem, in which the desired pattern and the pattern obtained from the pattern function for the array are the two curves. The problem then is to find a set of values for the variables in the pattern function which provides a pattern that is a "good" fit to the desired pattern.

A non-linear programming technique is employed to fit the two curves, using an IBM 7090 digital computer. There are three sets of variables within the pattern function that can be used for fitting; the amplitudes and phases of excitation, and the element positions. The constants in the problem are the curve along which the elements are dispersed, and the number of elements.

There are two problems here that need mentioning. For an equal spaced linear array of isotropic sources, Dolph and Riblet have ascertained the optimum pattern. But, in most instances, it is not known what the optimum pattern is for given array, nor what the optimum array is for a specified pattern. Since both the desired pattern and the pattern function for the array must be known before the curve-fitting technique can be applied, there is no assurance that either an optimum pattern has been synthesized for a given array or that the simplest array has been selected to produce the desired pattern. A discussion of a program modification that may circumvent this difficulty is contained later in this report.

The following sections contain a formulation of the array pattern function, a discussion of the non-linear programming technique, and several examples of synthesis for a variety of arrays.

II

FORMULATION OF THE PATTERN FUNCTION

Consider an equal-spaced array of 2N+1 elements located along the arc of a curve as shown in Figure 1. If the elements are numbered from -N to N from left to right and fed with complex currents I_p, $(p = -N,\ldots,N)$, then the space factor for the array is given by,

$$F(\phi) = \sum_{p=-N}^{N} f_p(\phi) I_p \exp\left(j \Psi_p(\phi)\right) \quad . \tag{1}$$

where

$$\Psi_p(\phi) = \beta d_p(\phi)$$

and

$$\beta = \frac{2\pi}{\lambda} \quad .$$

The function, $\Psi_p(\phi)$, is the phase difference between the radiations from the p-th element and element 0, that is due to the position of element p in the array.

It can be shown by elementary trigonometry that:

$$d_p(\phi) = X_p \sin \phi + Y_p \cos \phi$$

The function, $f_p(\phi)$, is the element factor of the p-th source. Since the elements in general are arrayed on an arc of a curve rather than along a straight line, usually

$$f_p(\phi) \neq f_{p+1}(\phi) \quad .$$

The remaining sections of this report consider only symmetric arrays. The synthesis technique to be described however, is just as applicable to non-symmetric configurations. This condition was imposed only to take advantage of the

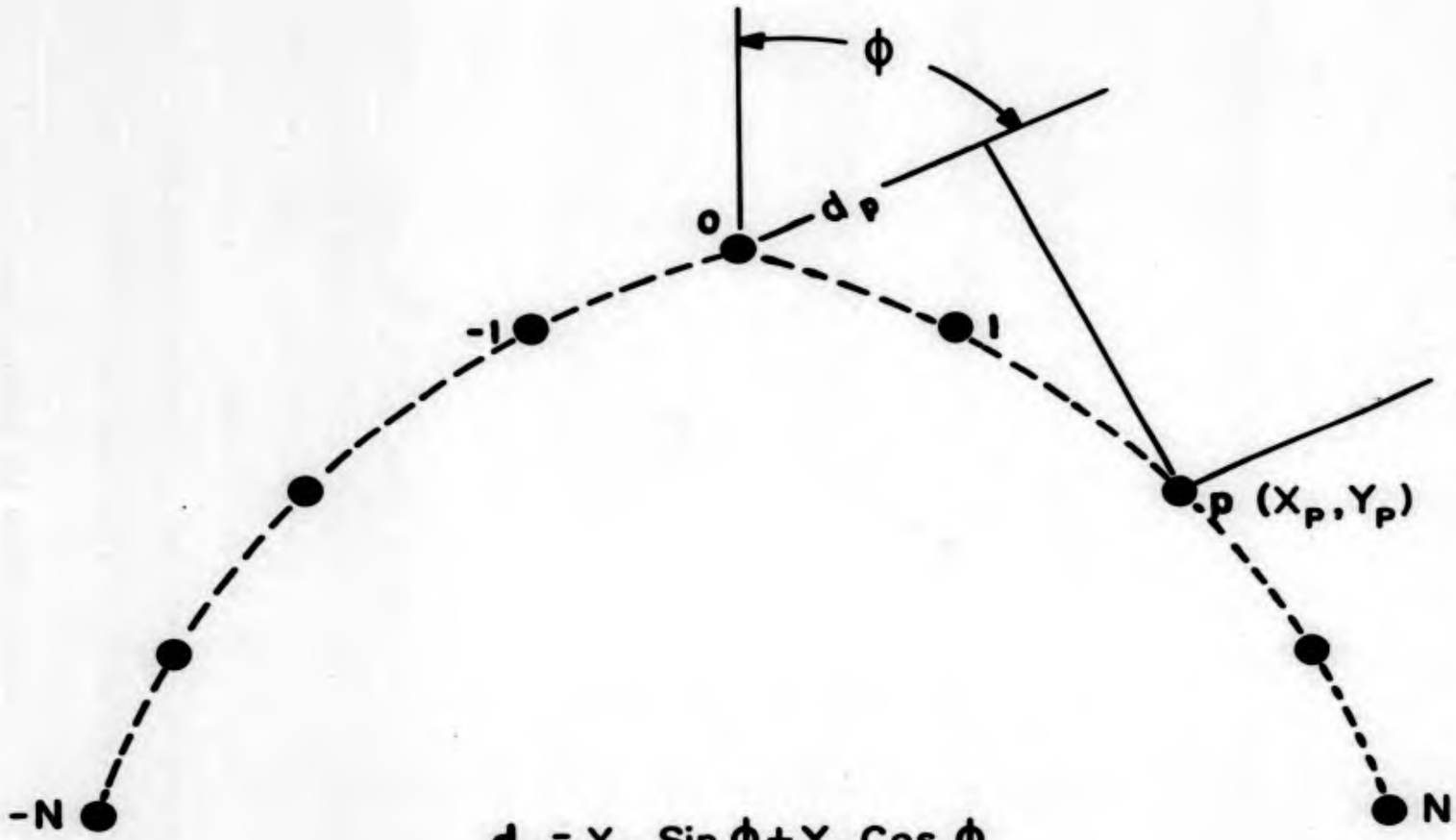

FIG. 1
GEOMETRY OF NON-LINEAR ARRAY

resulting simplifications in the mathematical expressions that follow.

Under conditions of symmetry then, it is assumed that,

$$I_{-p} = I_p \quad \text{for } p = 0,1,2,\ldots,N \ ,$$

and further that

$$f_{-p}(\phi) = f_p(-\phi) \quad \text{for } p = 0,1,2,\ldots,N \ .$$

The curve along which the elements are dispersed enters the pattern function in the expression for $d_p(\phi)$. For linear arrays this becomes,

$$d_p(\phi) = X_p \sin \phi \ .$$

If the array is along a curve whose graph is

$$Y = f(X)$$

then the expression for $d_p(\phi)$ is given by

$$d_p(\phi) = X_p \sin \phi + f(X_p) \cos \phi \ .$$

If I_o is taken as reference (i.e., $I_o = 1 + jo$), then Equation (1) can be rewritten as:

$$F(\phi) = f_o(\phi) + \sum_{p=1}^{N} I_p \left[f_p(\phi) \exp(j \Psi_p(\phi)) + f_{-p}(\phi) \exp(j \Psi_{-p}(\phi)) \right] .$$

THE FUNCTIONING OF THE NON-LINEAR PROGRAM

The application of non-linear programming to pattern synthesis was based on the proposition that, if the area of the region bounded by the graphs of two continuous functions of ϕ and the lines $\phi = \pm \delta$ is zero, then the two functions coincide on the interval $-\delta \leq \phi \leq \delta$.

The three sets of variables in equation (3) that can be used to synthesize a pattern are the magnitudes and phases of the currents I_p, and the X_p's. Letting

$$I_p = a_p e^{j\theta_p} \qquad p = 1,2,\ldots N$$

define

$$\vec{B} = (a_1, a_2, \ldots, a_N, \theta_1, \ldots, \theta_N, X_1, \ldots, X_N)$$

remembering that:

$$a_{-p} = a_p ,$$

$$\theta_{-p} = \theta_p ,$$

and $$X_{-p} = -X_p .$$

Equation (3) can now be rewritten as

$$\bar{F}(\phi,\vec{B}) = f_o(\phi) + \sum_{p=1}^{N} a_p \exp(j\theta_p)\Big[f_p(\phi)\exp(j\beta(X_p \sin\phi + f(X_p)\cos\phi))$$

$$+ f_{-p}(\phi) \exp(j\beta(-X_p \sin\phi + f(-X_p)\cos\phi))\Big] \qquad (4)$$

The area of the region under discussion then, is expressed by,

$$A(\vec{B}) = \int_{-\delta}^{\delta} \Big| |\bar{F}(\phi,\vec{B})| - |G(\phi)| \Big| d\phi \qquad (5)$$

This expression is referred to as the "objective function"of the non-linear program and is illustrated in Figure 2. The graph of $|G(\phi)|$ is the desired pattern over the interval $-\delta \leq \phi \leq \delta$ and the graph of $|\bar{F}(\phi,\vec{B})|$ is the pattern obtained from the set of a_p's, θ_p's and X_p's corresponding to $\vec{B}$. Clearly $A(\vec{B})$ is the area between these two graphs on this interval. Now if there exists $\vec{B}$ such that $A(\vec{B}) = 0$ (and if this $\vec{B}$ can be found) then the synthesis of $|G(\phi)|$ has been accomplished.

The real problem, of course, is to find a set of variables such that this integral will be zero. If a technique could be found whereby, from some starting set of variables corresponding to $\vec{B}_1$, a second set corresponding to $\vec{B}_2$ could be selected, such that $A(\vec{B}_2) < A(\vec{B}_1)$, then by successively employing this technique to select additional sets of variables corresponding to $\vec{B}_k$, the values of the integral $A(\vec{B}_k)$ could be made to converge on the value $b \geq 0$.

If $b > 0$, then a $\vec{B}_k$ was not found such that the pattern of the space factor corresponding to the variables determined by $\vec{B}_k$ is $|G(\phi)|$. But this does not mean that a "good" approximation to $|G(\phi)|$ cannot be attained. If b is "small" and evenly dispersed over the interval $[-\delta,\delta]$, then the approximation would be "good".

If A is not a convex* function, then two different initial $\vec{B}$'s may lead to two different final values for b, or two different final $\vec{B}$'s with the same value of b. Future effort will be directed toward determining a set of conditions on A to insure its convexity.

G. Zoutendijk** devised a non-linear programming technique for minimizing functions of n variables that utilizes the method of "steepest descent".

---

*A function A on a region R is convex on R if for each B_1, B_2 in R and for all non-negative λ and μ such that $\lambda + \mu = 1$ it follows that $A(\lambda B_1 + \mu B_2) \geq \lambda A(B_1 + \mu A(B_2)$.

**The general method was sketched by G. Zoutendijk, "Maximizing a Function in a Convex Region", Journal of Royal Statistical So., Ser. B., Vol. 21, (1959). The method, a variant of the method of steepest ascent, was expanded by A. Bhatia and B. Foster, "An Application of the Method of Feasible Directions to the Non-Linear Maximization Problem with Non-Linear Constraints", The Boeing Company, Document D6-7133, (1961).

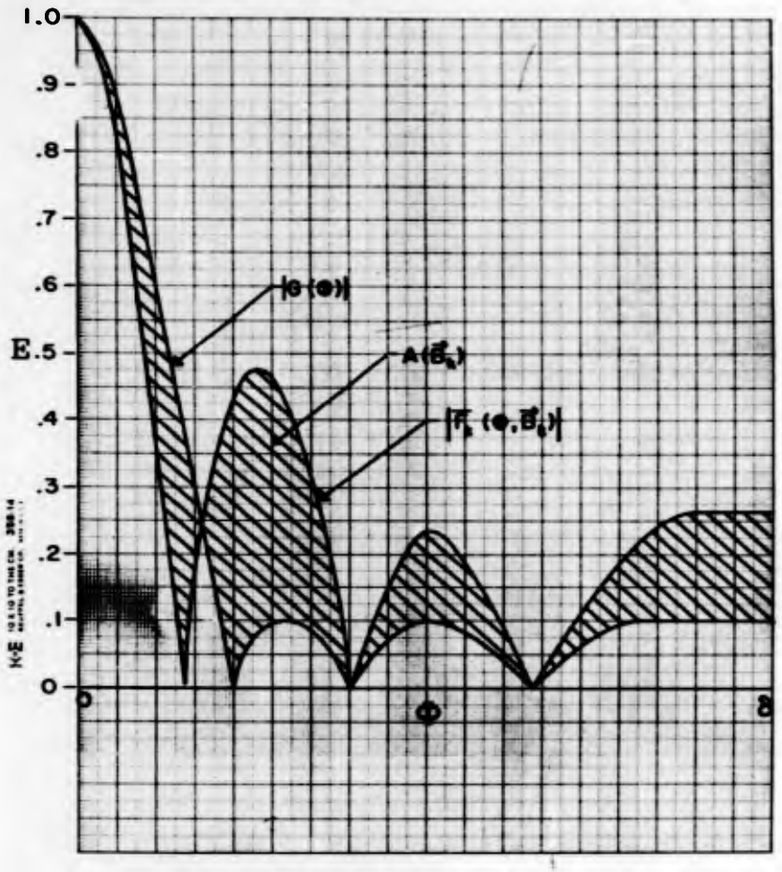

$$A(\vec{B}_k) = \int_{-\delta}^{\delta} \left| |\bar{F}_k(\Phi, \vec{B}_k)| - |G(\Phi)| \right| d\Phi$$

FIG. 2

THE OBJECTIVE-FUNCTION FOR THE NON-LINEAR PROGRAM

A program based on this technique was written for an IBM 7090 computer and was employed for a solution to the pattern synthesis problem. The program is in the form of a "walk" in the direction of steepest descent which is determined by the gradient vector of $A(\vec{B})$. From a starting set of variables corresponding to $\vec{B}_1$, the partial derivatives of $A(\vec{B}_1)$ are evaluated with respect to its 3N real variables. If some of the variables in $\vec{B}$ are held as constants, then the partial derivatives of $A(\vec{B})$ with respect to these are zero. The gradient vector of $A(\vec{B})$ is determined by these partials and the first "step" in the walk is taken in the direction of this vector. Successive steps are taken in the same fashion until the difference of the value of A after two successive steps is less than some preassigned number ε.

The above process could be described simply as "curve-fitting where the measure of fit is given by the objective function, equation (5), which is just the area between the two curves.

The functioning of the program was evaluated by synthesizing an optimum Tchebycheff pattern for a linear array of seven equi-spaced isotropic sources with $\frac{\lambda}{2}$ spacing. In this case,

$$F(\phi,\vec{B}) = f(\phi)\left[1 + 2\sum_{p=1}^{N} a_p \exp(j\theta_p)\cos(\beta X_p \sin\phi)\right]$$

where $f(\phi) = 1$.

The pattern to be synthesized is given by

$$G(\phi) = T_6\left(Z_o \cos\left(\frac{\beta d \sin\phi}{2}\right)\right)$$

where $Z_o = 1.127$ for -20 db side lobes and $d = \frac{\lambda}{2}$.

The array excitation was held uniform in phase and only the amplitudes were allowed to vary. In this way, a comparison could be made between the amplitudes of excitation synthesized by the non-linear program package and those synthesized by the more conventional technique of Dolph.

The initial $\vec{B}$ for this run, denoted by $\vec{B}_1$ (remembering that all element variables are normalized to the center element) was

$$\vec{B}_1 = (2,3,4,0,0,0,.5,1.0,1.5)$$

At the end of the 24th step, the improvement in the objective function value was less than 0.10 per cent which terminates the walk.

The synthesized $\vec{B}$,

$$\vec{B}_{25} = (.915075, .694234, .544039, 0,0,0,.5,1.0,1.5)$$

A comparison of the excitations contained in $\vec{B}_{25}$ and the excitation synthesized by using the method of Dolph is shown below:

AMPLITUDE OF EXCITATION

Element No.	Program Synthesis	Dolph Synthesis
0	1.000000	1.000000
1	0.915705	0.915708
2	0.694234	0.694235
3	0.544039	0.544041

For array design purposes, the two sets of excitations are identical. The patterns obtained from the starting and final excitations are shown in Figure 3 together with a few of the patterns obtained from intermediate excitations. A listing of the excitations producing the patterns shown in Figure 3 is given below, together with the objective function values. To permit comparisons, the total area under $|G(\phi)|$ is 2.810922.

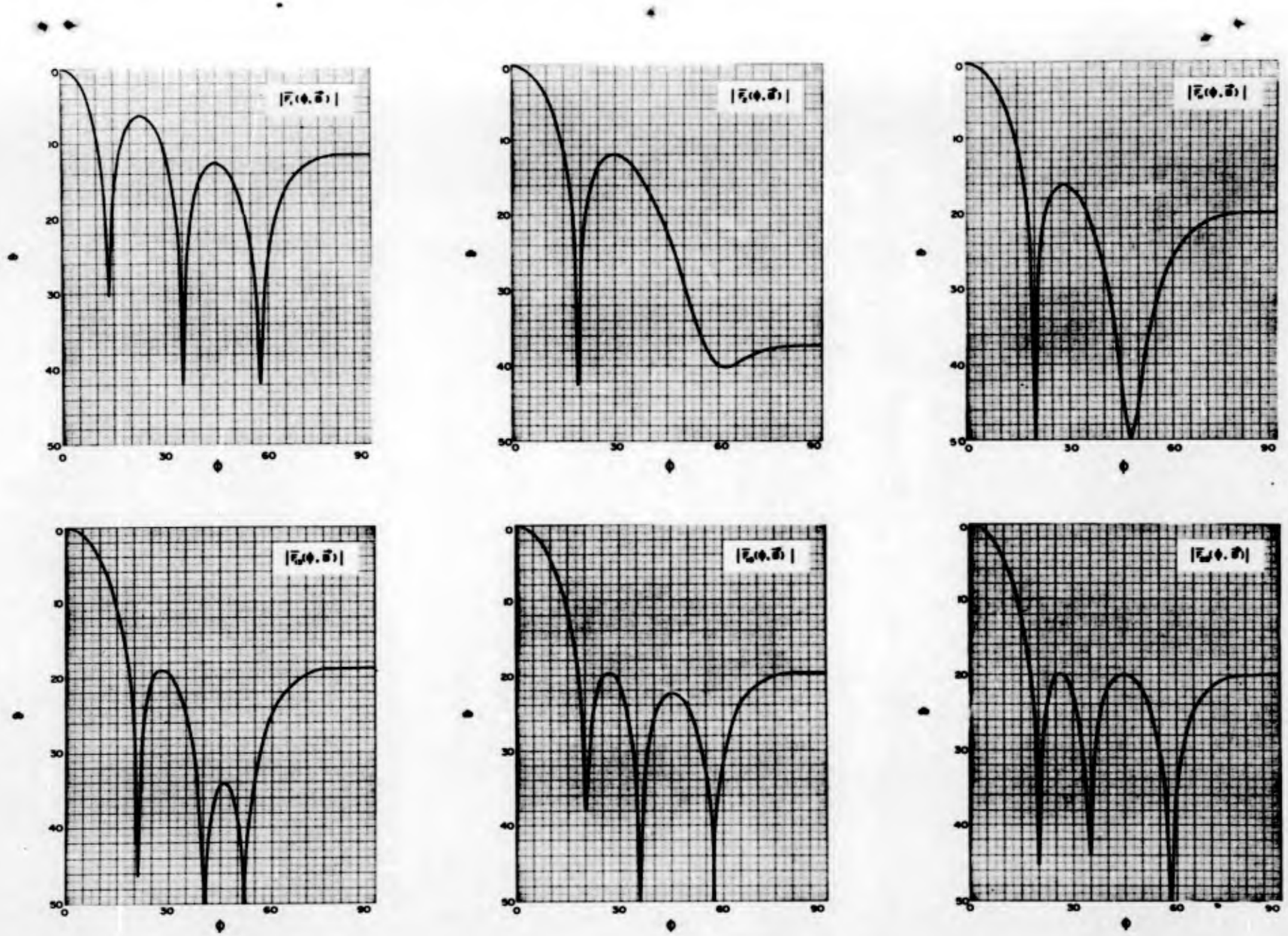

FIG. 3
SYNTHESIS OF T_e PATTERN FOR A LINEAR ARRAY OF 7 EQUI-SPACED ISOTROPIC SOURCES (VARYING AMPLITUDE ONLY)

k	a_p's	$A(B_k)$
1	2.000000	
	3.000000	
	4.000000	.231537
2	1.525813	
	1.534016	
	0.564319	0.18317617
10	1.283195	
	1.007229	
	0.559094	0.10522996
12	1.156021	
	0.816606	
	0.512072	0.10011706
14	0.980544	
	0.730156	
	0.534363	0.03308119
24	0.915705	
	0.694234	
	0.544039	$0.11737032 \times 10^{-5}$

The ability of the non-linear program package to synthesize an array pattern with this degree of precision was very encouraging, and it was decided to try to synthesize this same 20 db T_6 pattern with other linear arrays and combinations of variables.

IV

SYNTHESIS OF LINEAR ARRAY PATTERNS

A. Seven-Element Array of Unequal Spaced Isotropic Sources

When arrays are designed for the purpose of obtaining pattern gain only, an optimum pattern in The Tchekycheff sense is not required and a uniform excitation can be employed. The -13.5db sidelobe level of a uniform array, however, is objectionable for some applications. The sidelobe levels can be reduced by tapering the amplitude of excitation, but this also broadens the main-beam and adds considerably to the complexity of the array feed system.

It would be desirable to be able to reduce the sidelobe levels of uniform arrays without appreciably affecting the main-beam. Harrington devised a perturbational procedure for doing this that employs unequal element spacing.

It was felt that the non-linear program could be utilized for this type of problem by simply holding the amplitudes and phases of excitation constant, and varying only the element positions. The seven element array of isotropic sources was used for this exercise.

It was decided to use the 20 db T_6 pattern for $|G(\phi)|$ rather than Harrington's modified sin u/u. It is true that the main-beam of the T_6 pattern is broader than that obtained from a uniform array, but the consequent reduction in gain is only about 0.2 db.

The array was assigned a uniform excitation in both amplitude and phase and these were held constant while the inter-element spacing was allowed

to vary from an initial value of one-half wave length. The patterns obtained from the initial and final element positions are shown in Figure 4. All of the sidelobes in the final pattern are below -16 db. This level was obtainable, however, at the expense of some beam broadening.

The synthesized element positions, measured from the center element, are:

Element No.	Position (wave length)
1	0.382176
2	0.827978
3	1.391014

In these positions the inter-element spacing of the first two elements is less than one-half wave length (.38 and .45 wave lengths respectively). This is undesirable because of the mutual effects among actual array elements which conspire to increase the problems of excitation and reduce the operating bandwidth of the array. It was thought that suitable constraints on element position can be inserted in the program to prevent the inter-element spacing from becoming too small, but attempts to do this so far have interfered with the synthesis procedure.

B. Five-Element Array of Isotropic Sources

It was of interest to determine how good an approximation to the 20 db T_6 pattern could be obtained, using less than seven elements, and an attempt was made to synthesize this pattern using five isotropic sources with various sets of variables. The first program was run with a uniform excitation held constant and varying only the element position. The second program was run with five equal-spaced elements, (having an inter-element spacing of .75 wave lengths) varying the amplitude only with uniform phase. And the third program was run varying both amplitude

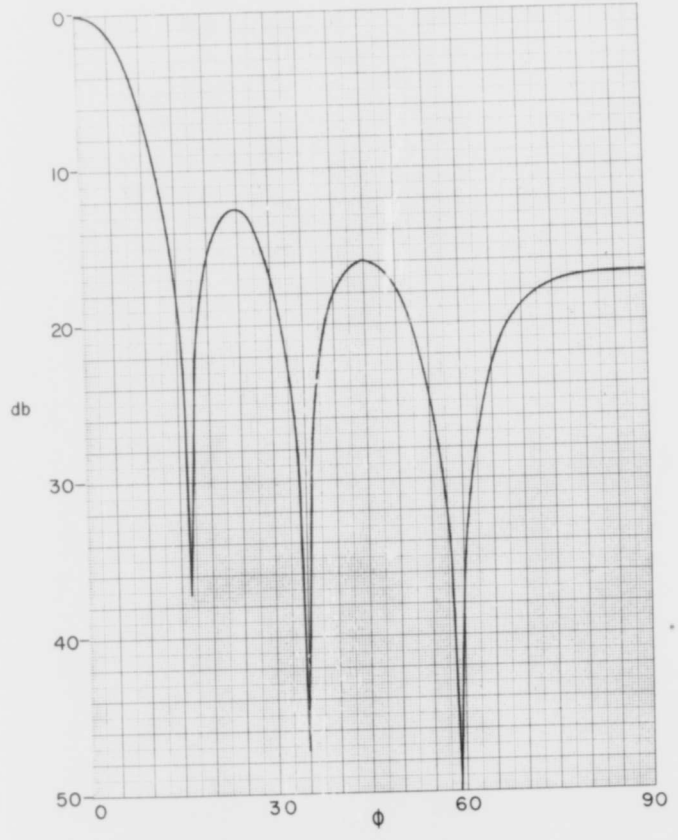

INITIAL PATTERN

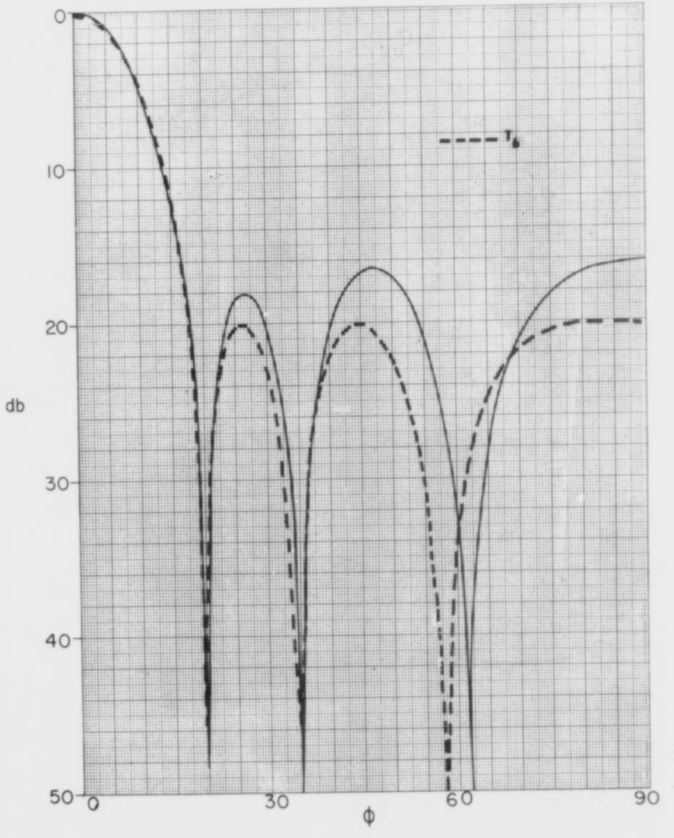

FINAL PATTERN

FIG. 4

SYNTHESIS OF T_6 PATTERN FOR A LINEAR ARRAY OF 7 ISOTROPIC SOURCES (VARYING SPACING ONLY)

and element position with uniform phase. The patterns for the final values of the variables are shown in Figure 5 and the variables are given below.

Program No.	Element Position	Amplitude of Excitation
1	0.566149 1.243376	amplitude held constant
2	element position held constant	.878209 .546137
3	0.707374 1.409077	0.834876 0.533945

The additional pattern control afforded by varying inter-element spacing is quite evident in Figure 5. The pattern obtained by varying the element position along with the amplitude is a good approximation to the T_6 pattern. It should be noted that the elements in the array producing this pattern are very nearly equal-spaced at .7λ.

C. Four Element Array of Unequal-spaced Isotropic Sources

The successful synthesis of the T_6 pattern from only 5 elements encouraged further experimentation with the program package. A synthesis of this pattern was again attempted but with only four elements allowing both amplitude and element position to vary while holding the phase uniform. The initial and final patterns are shown in Figure 6. The synthesized element positions and amplitudes are given below. The element positions are measured from the array centerline.

Element No.	Element Position	Amplitude
1	0.414	.999313
2	1.139	.908749

The synthesized pattern has a mainbeam that is a good approximation to the mainbeam of the T_6 pattern but the sidelobe structures are not a good fit.

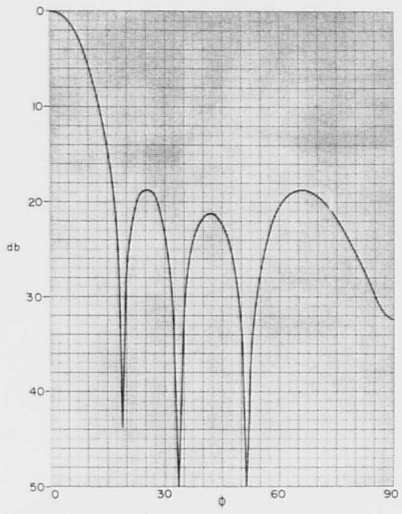

VARYING AMPLITUDE ONLY

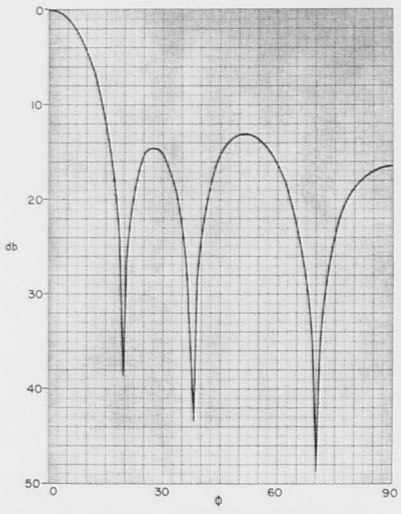

VARYING SPACING ONLY

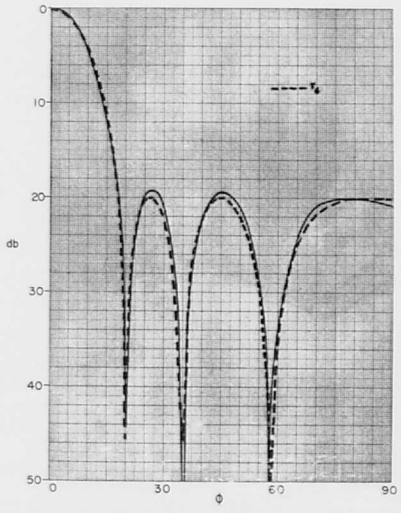

VARYING AMPLITUDE & SPACING

FIG.5

SYNTHESIS OF T_6 PATTERN FOR A LINEAR ARRAY OF 5 ISOTROPIC SOURCES

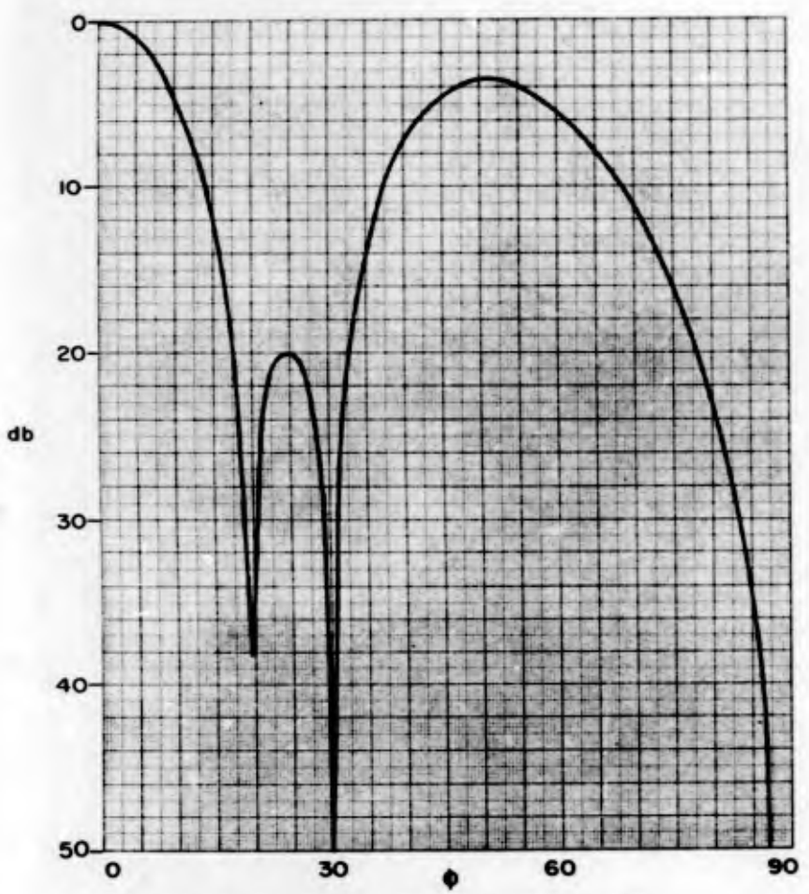

INITIAL PATTERN

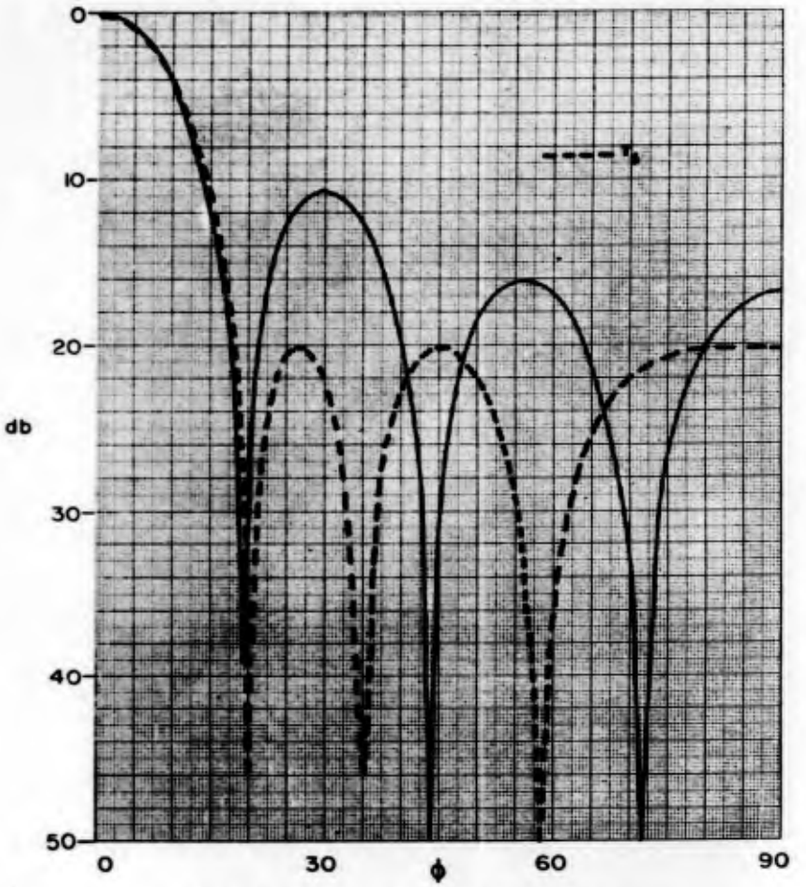

FINAL PATTERN

FIG. 6

SYNTHESIS OF T_6 PATTERN FOR A LINEAR ARRAY OF 4 ISOTROPIC SOURCES (VARYING AMPLITUDE & SPACING)

SUMMARY AND CONCLUSIONS

It has been demonstrated that a non-linear programming technique can be employed to synthesize linear array patterns. This technique can be applied to equi-spaced arrays or to those having unequal element spacing. Whenever the pattern to be synthesized can be specified and the pattern function for the array can be formulated, an approximation to the desired pattern is available through the medium of the program.

The degree of approximation obtainable by this technique is influenced by many factors, some within the program package itself and others inherent in the capabilities of the particular array chosen to produce the pattern.

Because of the optimization problem mentioned in the Introduction, the investigation of this technique commenced with a linear array of equi-spaced isotropic sources, where the optimum pattern for the array was known from the work of Dolph. It was then determined that the five element array was also capable of reproducing this same T_6 pattern quite closely, if the element positions were allowed to vary as well as the amplitudes of excitation. A four element array however, was only capable of reproducing the main-beam of the pattern and failed to produce the desired sidelobe structure.

The ability of the present technique to synthesize a T_6 with five elements instead of the usual seven elements has instigated the creation of a dynamic programming technique which will contain the present technique along with the ability to vary the number of elements to be utilized in the synthesis. This technique should provide a means of selecting the simplest array to reproduce a given pattern.

Some examples of pattern synthesis for arrays on circular and parabolic arcs were planned for inclusion in this report, but a preoccupation with the linear arrays and some unforeseen difficulties with the formulation and programming of the curved array problems precluded this.

REFERENCES

(1) M. G. Andreasen, "Linear Arrays with Variable Inter-Element Spacings", IRE Trans. on Antennas and Propagation, Vol. AP-10, pp. 137-143; March, 1962.

(2) R. F. Harrington, "Side-lobe Reduction by Nonuniform Element Spacings", IRE Trans. On Antennas and Propagation, Vol. AP-9, pp. 187-192; March, 1961.

(3) D. D. King, R. F. Packard, and R. K. Thomas, "Unequally-spaced, Broadband Antenna Arrays", IRE Trans. on Antennas and Propagation, Vol. AP-8 pp. 380-384; July, 1960.

ACKNOWLEDGEMENTS

The non-linear program was written by Mr. Donald Ecker, and the programs for the various problems considered here were executed by Mr. Chin Kim. Their efforts are greatly appreciated.

A special thanks goes to Mr. Daryl Stone for the preparation of the figures and supervision of the report reproduction.

MUTUAL EFFECTS BETWEEN CIRCULARLY POLARIZED ELEMENTS

Leonard I. Parad and Randall W. Kreutel

Sylvania Electronic Systems

A Division of Sylvania Electric Products Inc.

Waltham, Mass.

ABSTRACT

An analysis which describes two identical circularly polarized antenna elements having circularly symmetric apertures is presented in this paper. The specific situation studied is that of open ended circular waveguides propagating the TE_{11} mode.

The solution to the problem is obtained by dividing the circularly polarized wave incident upon the aperture of the excited element into two appropriately orientated linearly polarized waves. The properties of the fields that exist in the excited and coupled antenna elements are then obtained by symmetry arguments.

If the coupled fields are divided into right and left hand circularly polarized waves, then the phase of the polarization picked up by the probe of the coupled element is dependent upon twice the angle that the coupled element makes with the excited element and a reference line. However, the other polarization is independent of this angle. An element placed in the middle of $N(N \geq 3)$ equispaced in phase elements on the circumference of a circle will couple no energy to the probe of the center element. It is also shown that if only the center element is driven, the mutual coupling will cause a serious degradation of the on-axis circularity of the radiation pattern.

I. Introduction

Arrays of circularly polarized antenna elements are desired for many applications. When the beam is not electronically steered, the element on-axis pattern and input impedance design is relatively simple. For an electronically steered array, the entire element pattern is important and the input impedance is a function of the steering angle. The design of a circularly polarized element

for an electronically steered array is a complex problem and it is useful to have an analytical understanding of the different effects to be encountered. Once a reasonable understanding of the phenomenon has been obtained, it is often possible to separate problem areas experimentally and thus solve them more easily.

II. Analysis of Two Identical Elements With Identical Orientations

The antenna element to be analyzed is the probe fed circular waveguide operating in the TE_{11} mode with circularity obtained by placing a quarter-wave plate between the input probe and the aperture as shown in Figure 1. The results to be derived will apply equally well to any circularly symmetric antenna that has a one cycle angular dependence. The situation to be investigated is shown in Figure 2.

Let the input probe of element #1 be excited with a voltage V = K volts causing the TE_{11} mode with radial electric field component.

$$1. \qquad E_r = \sqrt{2}\, J_1(k_c r) \cos\phi \cos\omega t = J_1(k_c r)\left[\sin(\phi + 45) + \cos(\phi + 45)\right]\cos\omega t$$

to be generated. Upon passing through the quarter-wave plate, the cos (ϕ + 45) component is delayed 90° more than the sin (ϕ + 45°) component so that the field incident upon the aperture of element #1 is given by

$$2. \qquad E_{inc} = J_1(k_c r)\left[\sin(\phi + 45)\cos(\omega t - b) + \cos(\phi + 45)\sin(\omega t - b)\right]$$

$$= J_1(k_c r)\sin(\omega t + \phi + 45 - b)$$

where the constant "b" accounts for the phase shift that the sin (ϕ + 45°) component incurs in travelling from the input probe to the aperture. At the aperture, the incident wave is reflected, radiated, and coupled over to the adjacent aperture. The reflected component, as will be seen later, produces some unexpected results. However, we will first examine the coupled component which produces a TE_{11} mode in the adjacent aperture. First, equation 2 will be expressed in terms of fields which have maximum radial electric field intensities in the directions $\phi = \phi_o \pm 45°$. The purpose of this transformation is to provide a field symmetry which is independent of ϕ_o. Rewriting equation 2, we have:

3. $$E_{inc} = J_1(k_c r)\Big\{\Big[\sin(\phi - \phi_o + 45)\cos\phi_o + \cos(\phi - \phi_o + 45)\sin\phi_o\Big]\cos(\omega t - b) + \Big[\cos(\phi - \phi_o + 45)\cos\phi_o - \sin(\phi - \phi_o + 45)\sin\phi_o\Big]\sin(\omega t - b)\Big\}$$

$$= J_1(k_c r)\ \sin(\phi - \phi_o + 45)\cos(\omega t - b + \phi_o) + \cos(\phi - \phi_o + 45)\sin(\omega t - b + \phi_o)$$

From the symmetry equations of Figure 2, the TE_{11} mode fields coupled to aperture #2 due to E_{inc} in element #1 are:

4. $$E_{coupled} = J_1(k_c r)\sin(\phi - \phi_o + 45)\Big[C_1\cos(\omega t - b + \phi_o) + C_2\sin(\omega t - b + \phi_o)\Big] + J_1(k_c r)\cos(\phi - \phi_o + 45)\Big[C_1\sin(\omega t - b + \phi_o) + C_2\cos(\omega t - b + \phi_o)\Big]$$

where C_1 is the coupling between parallel polarized fields and C_2 is the coupling between the perpendicularly polarized fields. Combining terms of equation 4, we have:

5. $$E_{coupled} = J_1(k_c r)\Big[C_1\sin(\omega t - b + \phi + 45) + C_2\cos(\omega t - b + 2\phi_o - \phi - 45)\Big]$$

Examining equation 5, it is noted that the C_1 coupled field is rotating in the same sense as E_{inc} and is independent of ϕ_o while the C_2 coupled field is rotating in the opposite sense and has a phase dependence of $2\phi_o$. Thus, C_1 is the coupling coefficient between similarly polarized fields while C_2 is the coupling coefficient between oppositely polarized fields. The C_1 and C_2 fields in the aperture of antenna #2 cause two waves, a radiation (scattered) wave and a wave incident upon the quarter-wave plate of antenna #2. The scattered portion of the C_1 field will be of the same sense as the original incident wave while that of the C_2 fields will be of the opposite sense. To determine the waves that the coupled fields produce at probe #2, we first express equation 5 in terms of linearly polarized waves with maximum radial electric field in the directions $\phi = \pm 45°$ yielding:

6. $$E_{coupled} = J_1(k_c r)\Big\{C_1\Big[\sin(\omega t - b)\cos(\phi + 45) + \cos(\omega t - b)\sin(\phi + 45)\Big] + C_2\Big[\cos(\omega t - b + 2\phi_o)\cos(\phi + 45) + \sin(\omega t - b + 2\phi_o)\sin(\phi + 45)\Big]\Big\}$$

Remembering that the cos (ϕ + 45) field is delayed 90° more than the sin (ϕ + 45) field it is seen that the field incident upon probe #2 is:

$$7. \qquad E = \sqrt{2}\, J_1(k_c r)\left[C_1 \sin\phi \cos(\omega t - 2b) + C_2 \cos\phi \sin(\omega t - 2b + 2\phi_o)\right]$$

Comparing equation 7 to equation 1, it is seen that the C_2 coupling will cause a voltage $V_c = C_2 K$ volts at the output of probe #2, while the C_1 coupled field will be completely reflected at the probe and reradiate. Since the C_1 field is orthogonal to probe #2, the field radiated will be of the incorrect sense. Thus we have seen that the C_1 coupling (coupling of like polarizations) produces two radiated fields, that due to scattering from the aperture which is of the correct sense and radiation from the wave which is reflected at probe #2 which is of the incorrect sense. The C_2 coupling produces a scattered field of the incorrect sense and a coupled voltage at the feed of the adjacent antenna. The effects of aperture mismatch have been neglected up to this point and only first order effects have been considered. An approximation of aperture mismatch effects will now be derived. Let us first consider the effects of having aperture #2 mismatched. A wave incident upon aperture #2 is the C_1 coupled wave that has been reflected by probe #2 (see equation 7). Because of the aperture reflection coefficient Γ, a portion of the incident C_1 field will be reflected causing the wave $\sqrt{2}\,\Gamma C_1 J_1(k_c r) \cos\phi \cos(\omega t - 4b)$ to be incident upon probe #2. Now, consider the effect of aperture #1 having the reflection coefficient Γ. It may be shown that the portion of the incident wave reflected by aperture #1 will cause a wave $\sqrt{2}\,\Gamma \sin\phi \cos(\omega t - 2b)$ to be incident upon probe #1. Comparing this field to the C_1 field of equation 7, it is seen that after being reflected at probe #1 towards the aperture #1, coupled over to aperture #2 via C_1 coupling, and passing through the quarter-wave plate, a field $\sqrt{2}\, C_1 \Gamma J_1(k_c r) \cos\phi \cos(\omega t - 4b)$ will be incident upon the probe #2 due to aperture #1 being mismatched. Summing the two fields due to aperture mismatch with the field due to direct coupling (the C_2 portion of equation 7), the total voltage at the output of probe #2 is:

$$8. \qquad V_{total} = K\left[C_2 \sin(\omega t - 2b + 2\phi_o) + 2\Gamma C_1 \cos(\omega t - 4b)\right]$$

Thus, while one may expect the magnitude of the coupling between two circularly polarized antennas to be independent of the angle between them, equation 8 shows this to be true only if the apertures are matched.

III. Analysis of Two Identical Elements With Different Orientations

In this section, two elements of the type illustrated in Figure 1 will again be investigated, but this time the relationship between the coupled fields and the angle through which the coupled antenna has been rotated will be found. The configuration used is shown in Figure 3 where it is noted that ϕ_o has been set equal to zero for convenience. On a physical basis, one would expect that rotating element #2 $\theta°$ should change the phase of the C_1 and C_2 coupling coefficients by $\theta°$ in magnitude, but in opposite directions since rotating a circularly polarized antenna corresponds to a phase shift. This result will now be determined mathematically.

Exciting element #1 with a voltage V = K volts will cause the circularly polarized wave

$$9. \qquad E_{inc} = J_1(k_c r)\sin(\omega t + \phi + 45° - b)$$

to be incident upon aperture #1. At the aperture, the incident wave is reflected, radiated and coupled over to the adjacent aperture. The TE_{11} mode fields formed in aperture #2 due to E_{inc} is:

$$10. \qquad E_{coupled} = J_1(k_c r)\Big\{\sin(\phi + 45)\Big[C_1\cos(\omega t - b) + C_2\sin(\omega t - b)\Big] + \cos(\phi + 45)\Big[C_1\sin(\omega t - b) + C_2\cos(\omega t - b)\Big]\Big\}$$

Expressing the coupled fields in terms of fields which have maximum radial electric fields in the directions $\phi = \theta \pm 45°$, we have:

$$11. \qquad E_{coupled} = J_1(k_c r)\Big\{\Big[\sin(\phi + 45 - \theta)\cos\theta + \cos(\phi + 45 - \theta)\sin\theta\Big]\Big[C_1\cos(\omega t - b) + C_2\sin(\omega t - b)\Big] + \Big[\cos(\phi + 45 - \theta)\cos\theta - \sin(\phi + 45 - \theta)\sin\theta\Big]\Big[C_1\sin(\omega t - b) + C_2\cos(\omega t - b)\Big]\Big\}$$

From Figure 3, it is seen that the cos $(\phi + 45 - \theta)$ terms will be delayed by 90° more than the sin $(\phi + 45 - \theta)$ terms so that the field incident upon probe #2 is:

$$12. \quad E = J_1(k_c r)\Big\{\sin(\phi + 45 - \theta)\Big[C_1 \cos(\omega t - 2b + \theta) + C_2 \sin(\omega t - 2b - \theta)\Big] + \cos(\phi + 45 - \theta)\Big[C_2 \sin(\omega t - 2b - \theta) - C_1 \cos(\omega t - 2b + \theta)\Big]\Big\}$$

$$= \sqrt{2}\, J_1(k_c r)\Big[C_1 \cos(\omega t - 2b + \theta) \sin(\phi - \theta) + C_2 \sin(\omega t - 2b - \theta) \cos(\phi - \theta)\Big]$$

Examining equation 13, it is seen that the C_2 fields are completely absorbed and the C_1 fields completely reflected by the probe. To account for aperture mismatch effects, the C_1 coupled fields must be traced as was done in Section II. The result of these computations leads to the output voltage of probe #2 as:

$$13. \quad V = K\Big[C_2 \sin(\omega t - 2b - \theta) + 2\Gamma C_1 \cos(\omega t - 4b + \theta)\Big]$$

This result is similar to equation 8 in that the coupled voltage is dependent upon the angle of rotation if the aperture is not matched.

IV. A Seven Element Array

Consider an array of seven identically orientated elements, six located on the vertices of a hexagon with the seventh in the center (Figure 4). To a first approximation the coupling between the center element and one of the outer elements is independent of the other five elements and the results of Section II will apply. Two situations will be considered. One, the center element is fed and some element pattern effects are noted and two, the six outer elements are fed, and the voltage appearing at the center element probe is determined.

We will first determine some mutual coupling effects when the center element is fed. It is noted from equation 8 that the voltage measured at the other six probes consists of both C_2 and C_1 coupling so that coupling values should repeat every 180° rather than being independent of ϕ_o. If it is desired to separate the C_1 and C_2 components, a probe perpendicular to the existing probe is placed in each antenna element. This probe will measure the C_1 component while the original probe will measure the C_2 component.

Another effect that occurs when feeding the center element is that of TE_{11} mode scattering by the outside ring of elements. This effect can be determined by noting the discussion following equation 5. Since the scattering from the C_1 component is independent of ϕ_o and is of the proper sense, the scattering from the six outside elements will add in phase at broadside. Assuming that the scattered energy is of the same order of magnitude as that which couples into the guide, the on-axis field will be $1 + 6C_1$ and it is seen that for C_1 coupling 30 db down, it is possible to change the on-axis power density by ±1.5 db. Scattered C_2 fields are dependent upon $2\phi_o$ and hence cancel on-axis and partially add off-axis. Since these fields are of the wrong sense, they degrade the off-axis circularity of the element pattern.

The final radiated field to be considered is the C_1 component that is coupled from the center element into the outside elements, reflected from the probes and then radiated. The radiated fields in this instance are all in phase and of the wrong sense so that they seriously degrade the element pattern on-axis circularity. If the scattered C_1 fields are neglected, the on-axis circularity is:

$$14. \qquad C = 20 \log \frac{1 + 6C_1}{1 - 6C_1} \text{ db.}$$

Thus, it is seen that if the C_1 coupled energy is -30 db, the on-axis circularity ratio will be worse than 3 db. The scattered C_1 fields are not considered in equation 14 since neither their exact amplitude nor phase relationship with the original transmitted field are known.

The voltage excited at the center element probe due to coupling from the outer six elements will now be computed. In the computation, it will be assumed that the aperture is well matched. Since only C_2 coupling is involved, the magnitude of the output voltage of the center element is:

$$15. \qquad V = \left| C_2 \sum_{k=1}^{6} V_k e^{j2\phi_{ok}} \right|$$

Where V_k is the input voltage to the k^{th} element and ϕ_{ok} is the angle between the line joining the k^{th} element to the center element and the X axis.

Choosing the voltages V_k equal in magnitude to unity with phase to steer the beam in the XZ plane, equation 15 becomes:

16. $$V = \left| C_2 \left\{ 2e^{j180} + e^{j\alpha} \left[e^{j420} + e^{j300} \right] + e^{-j\alpha} \left[e^{j60} + e^{j660} \right] \right\} \right|$$

$$= 2 \left| C_2 (1 - \cos \alpha) \right|$$

where $\alpha = \sqrt{3}\, \pi d/\lambda \sin \theta_s$, d is the element spacing and θ_s is the main beam pointing angle.

If the center element were driven with a unity amplitude signal, equation 16 would represent the active reflection coefficient seen looking into the center element as a function of steering angle. Equation 16 is plotted in Figure 5.

From the previous discussion, it should be apparent that an aperture mismatch makes it difficult to interpret measured data. In the actual design of an element, the aperture configuration is often varied in an attempt to reduce the C_1 and C_2 coupling coefficients while maintaining a reasonable element pattern. If the aperture had to be rematched for every trial configuration, a very long experimental procedure would result. However, if the elements are designed with a set of orthogonal probes so that both the C_1 and C_2 components can be absorbed, aperture mismatch effects are almost negligible. Therefore, it is felt that a useful design procedure for circularly polarized elements is to provide ports that may receive both C_1 and C_2 couplings, vary the aperture configuration to minimize these couplings, and then match the aperture in the presence of the other elements.

V. Experimental Results

A number of measurements were made with circularly polarized antennas. The antennas were coaxial waveguides operating in the TE_{11} mode with a single probe feed and were spaced about 0.6λ apart. Coupling measurements indicated that both the C_1 and C_2 couplings were on the order of -28 db. The coupling varied drastically from element to element and it is expected that in addition to C_1 and C_2 coupling interactions a small amount of TEM mode energy also influenced the coupling measurements.

Antenna patterns were taken of the element by itself (Figure 6) and the element surrounded by six identical elements whose probes were terminated in matched loads (Figure 7). The antenna patterns were taken by using a linearly polarized transmitting antenna which is physically rotated. The rapid variations in the signal received by the test element is a measure of the test element circularity. Thus, it is seen that for a single element, the on-axis circularity is almost perfect while the element pattern in the array has an on-axis circularity ratio of about 10 db. These patterns illustrate the magnitude of the change of an element pattern when taken by itself and when taken in an array of elements. It is apparent that relatively little effort should be put into obtaining a good element aperture match or pattern when the element is isolated. Instead, a reasonable aperture match and pattern should be obtained for the isolated element and the main effort be put into designing the element in the array environment. In the case of the coaxial waveguide element, it was found that after small changes in the aperture configuration reduced the coupling by a couple of db and the aperture was matched in the array, a significantly improved pattern was obtained.

Acknowledgements

The authors express thanks to both Dr. Lechtreck and Kenneth Rau. Dr. Lechtreck helped formulate the problem in early discussions on the mutual coupling problem while Kenneth Rau suggested that aperture mismatch effects could cause the coupling to vary as a function of the angle ϕ_o.

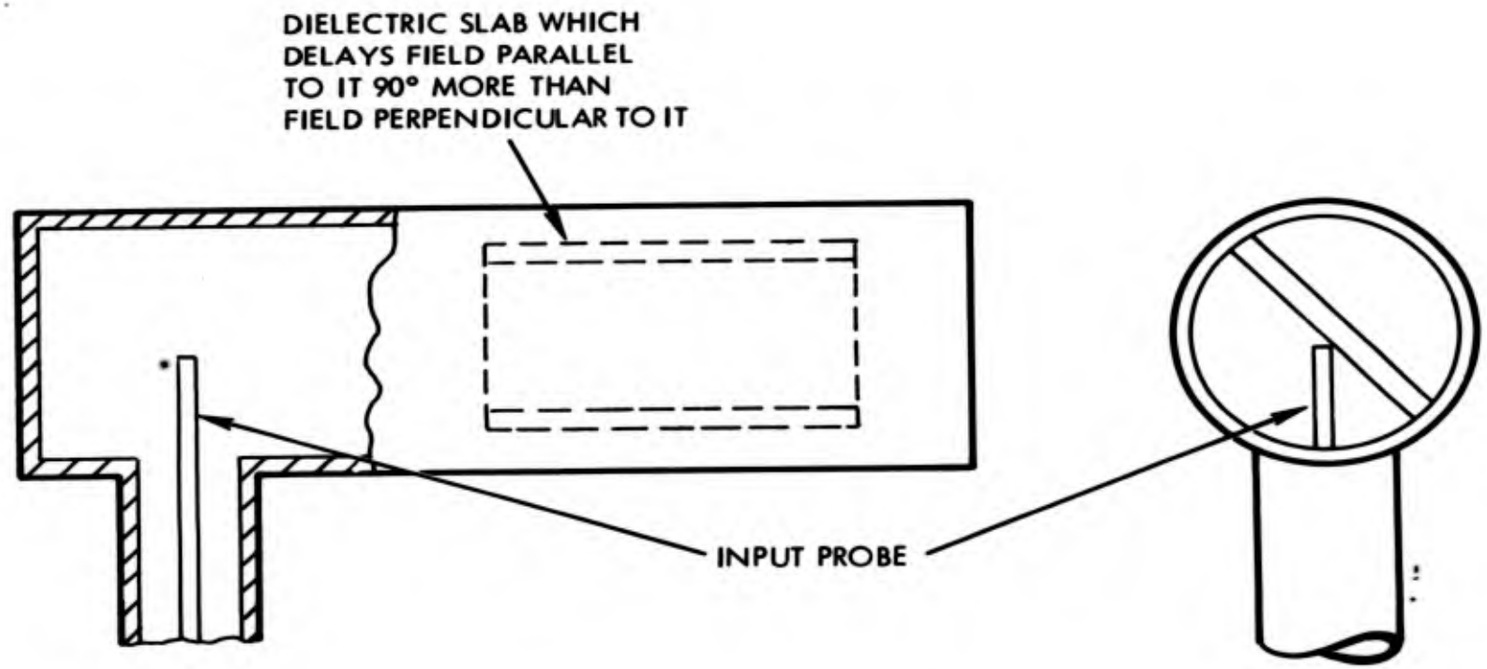

PROBE FED CIRCULAR WAVEGUIDE
ANTENNA

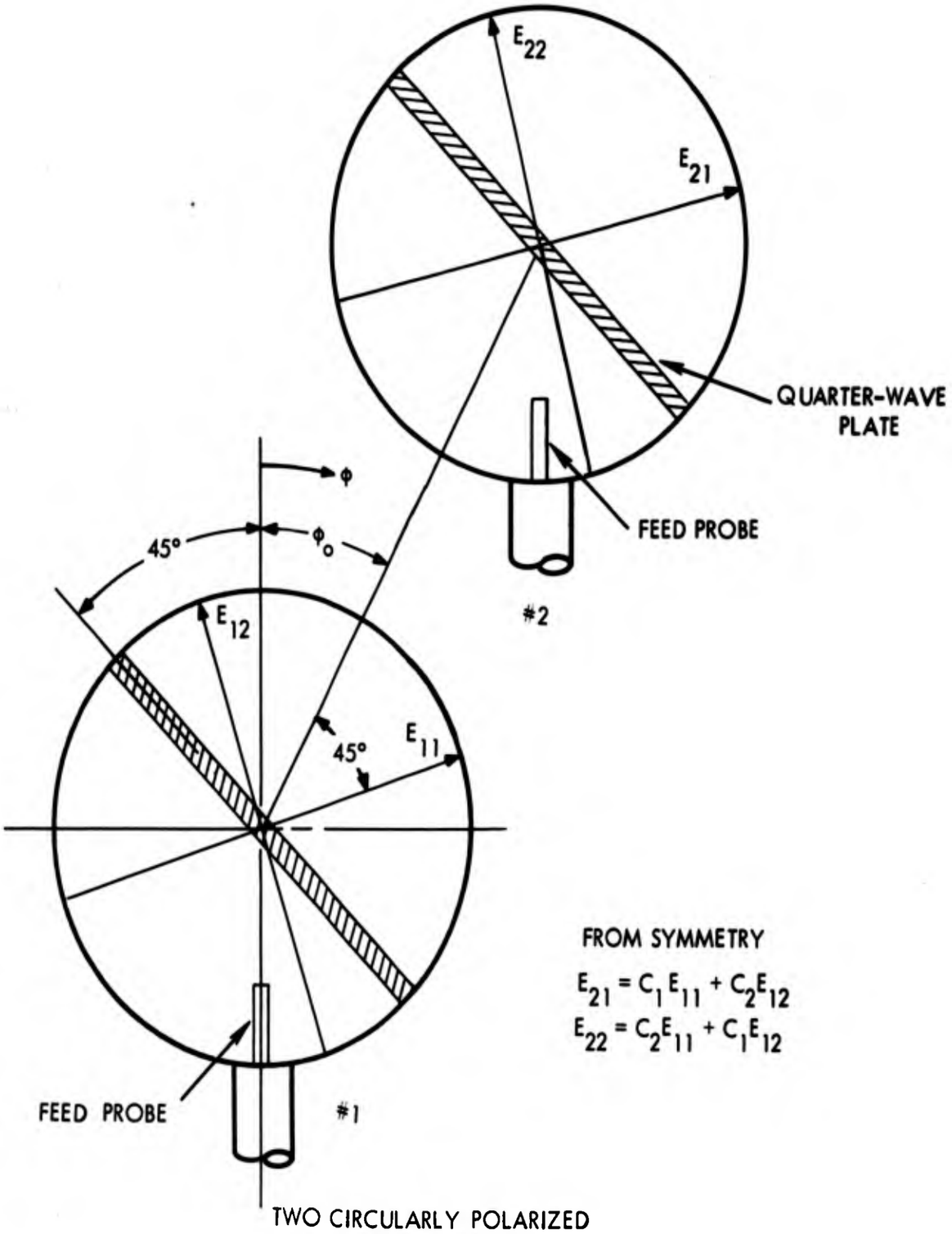

FROM SYMMETRY

$E_{21} = C_1 E_{11} + C_2 E_{12}$

$E_{22} = C_2 E_{11} + C_1 E_{12}$

TWO CIRCULARLY POLARIZED ELEMENTS WITH IDENTICAL ORIENTATIONS

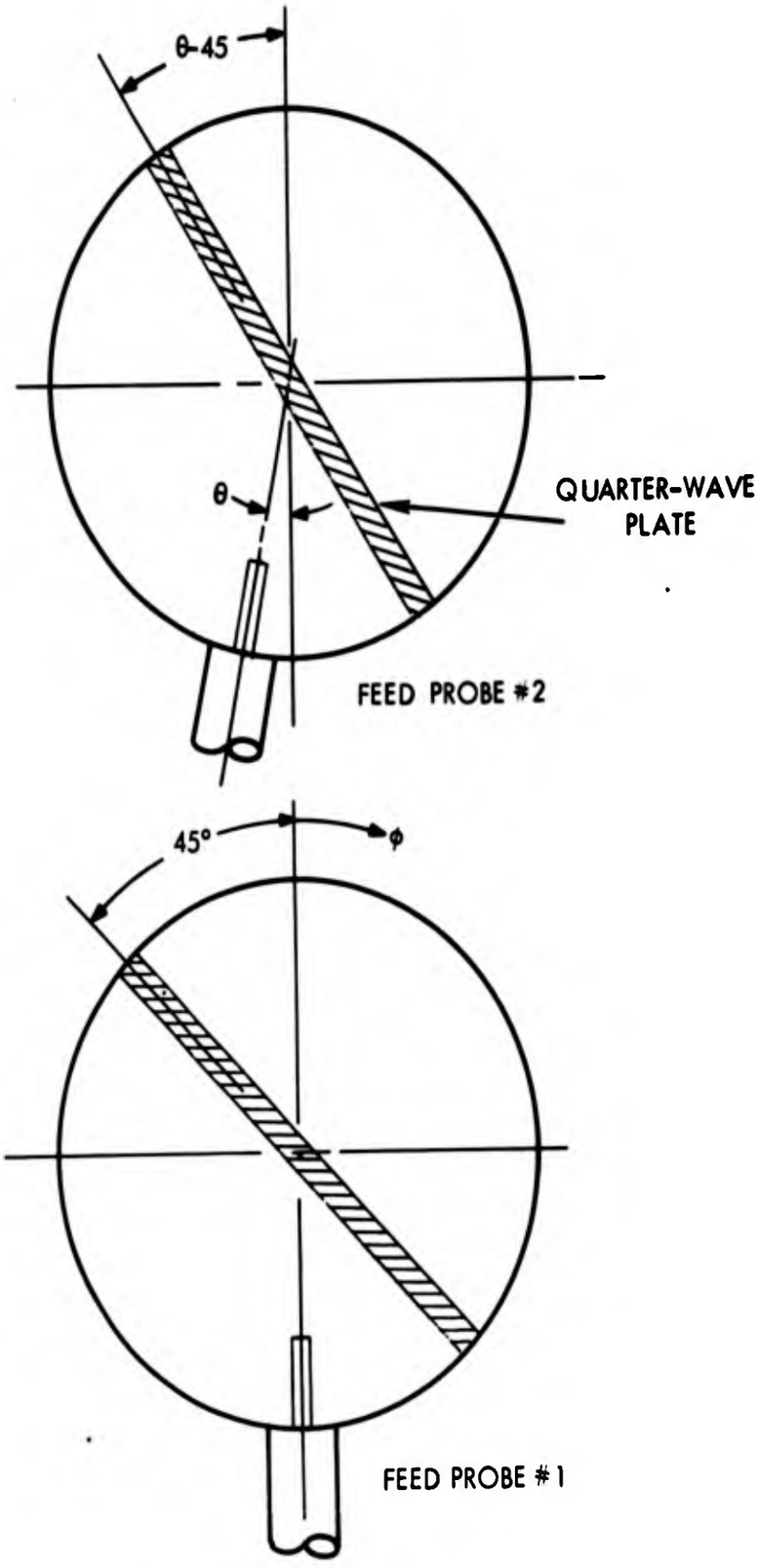

TWO CIRCULARLY POLARIZED ELEMENTS WITH DIFFERENT ORIENTATIONS

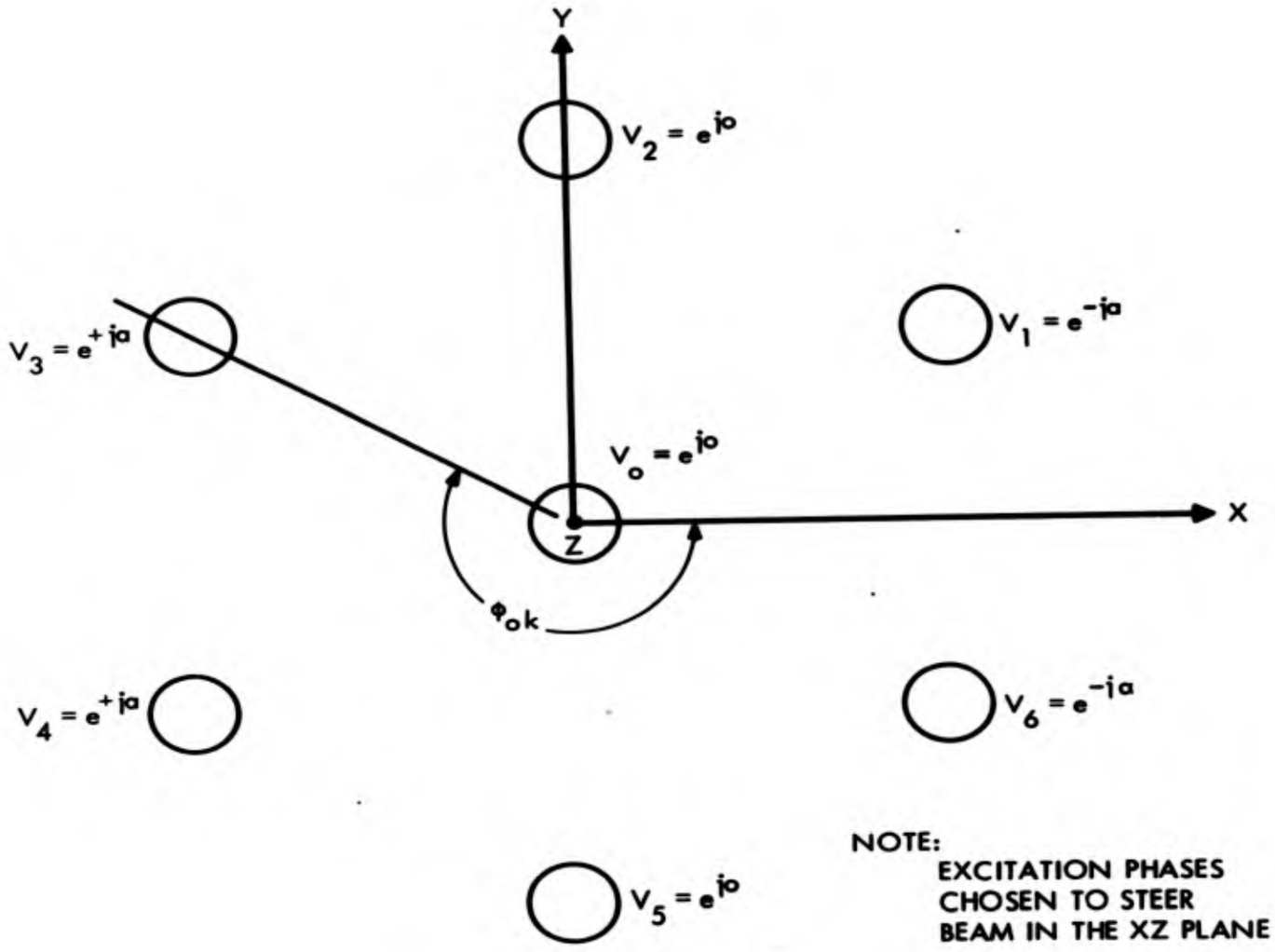

SEVEN ELEMENT PHASED ARRAY

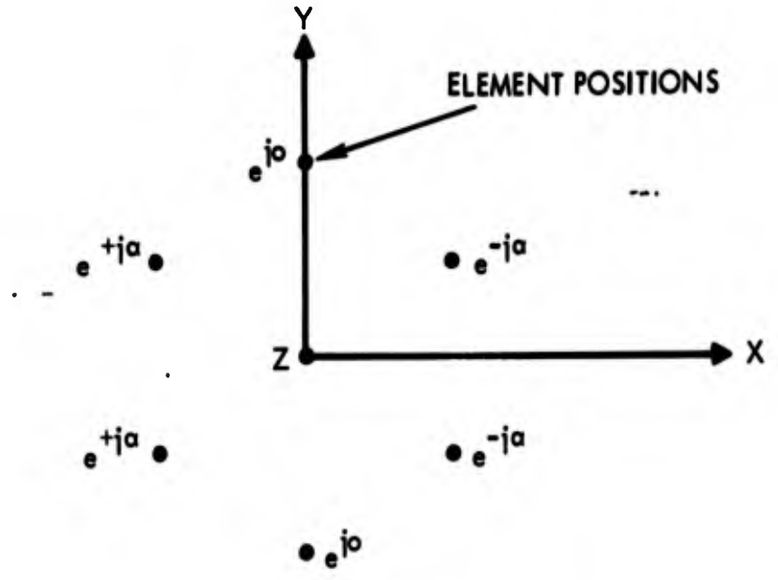
Y
ELEMENT POSITIONS
$e^{j\alpha}$
$e^{+j\alpha}$
$e^{-j\alpha}$
Z
X
$e^{+j\alpha}$
$e^{-j\alpha}$
$e^{j\alpha}$

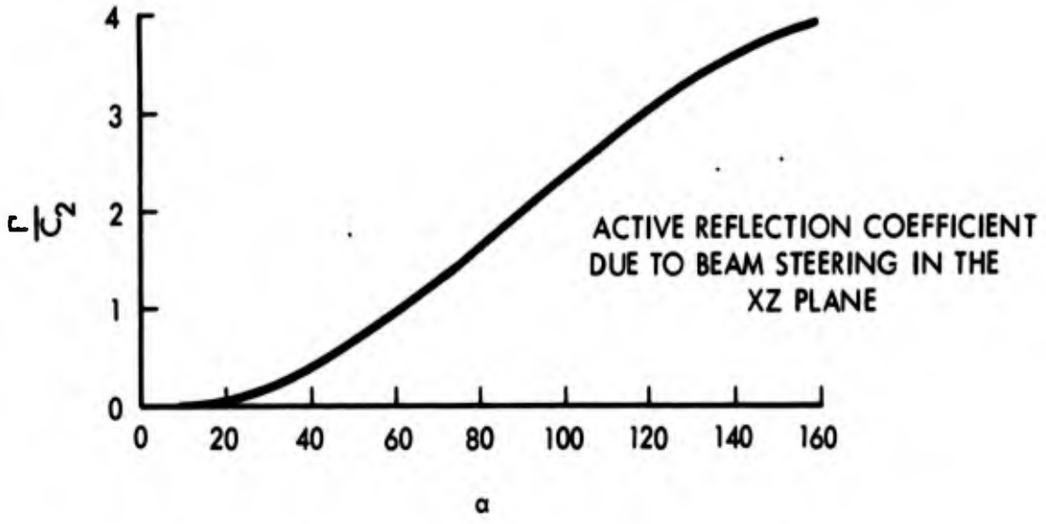
4
3
2
1
0
$\Gamma|^2$
0
20
40
60
80
100
120
140
160
α
ACTIVE REFLECTION COEFFICIENT
DUE TO BEAM STEERING IN THE
XZ PLANE

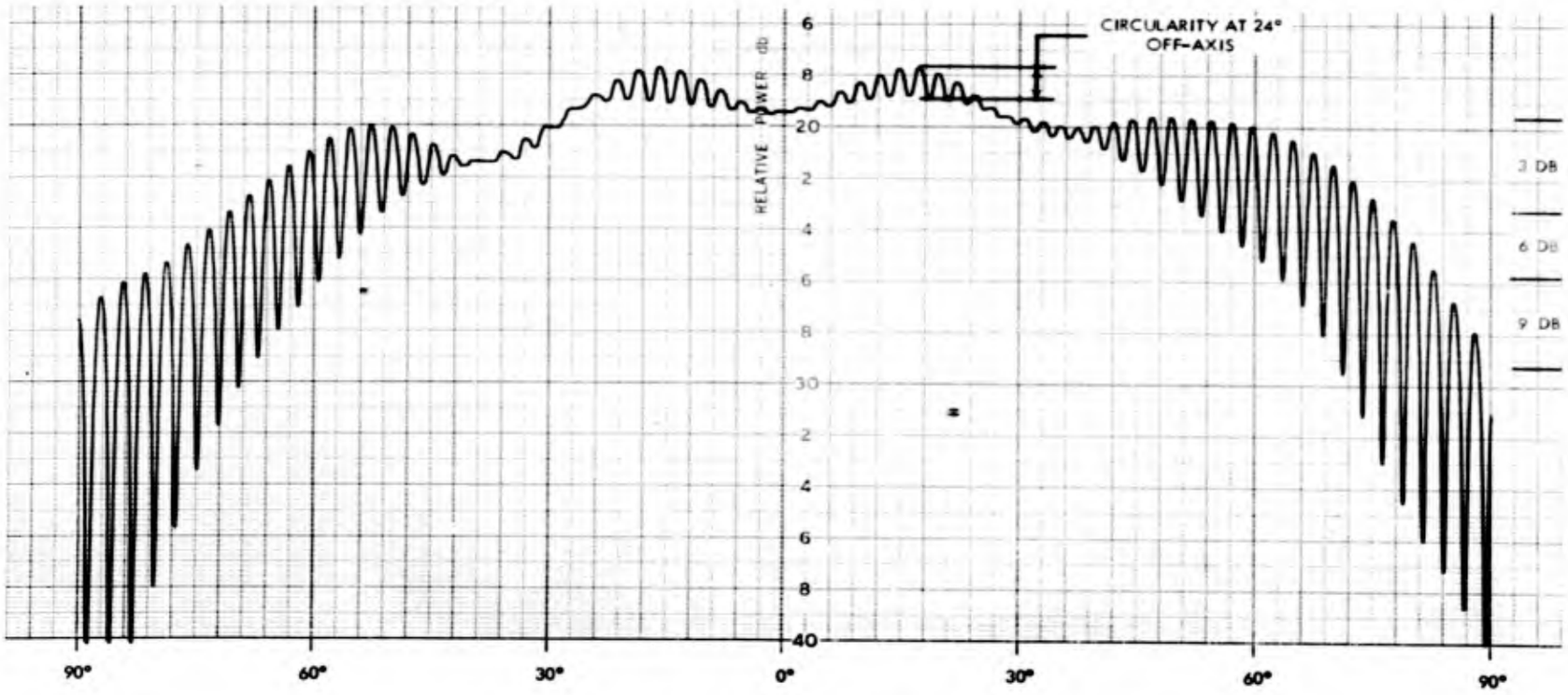

PATTERN OF A SINGLE ELEMENT IN A LARGE GROUND PLANE

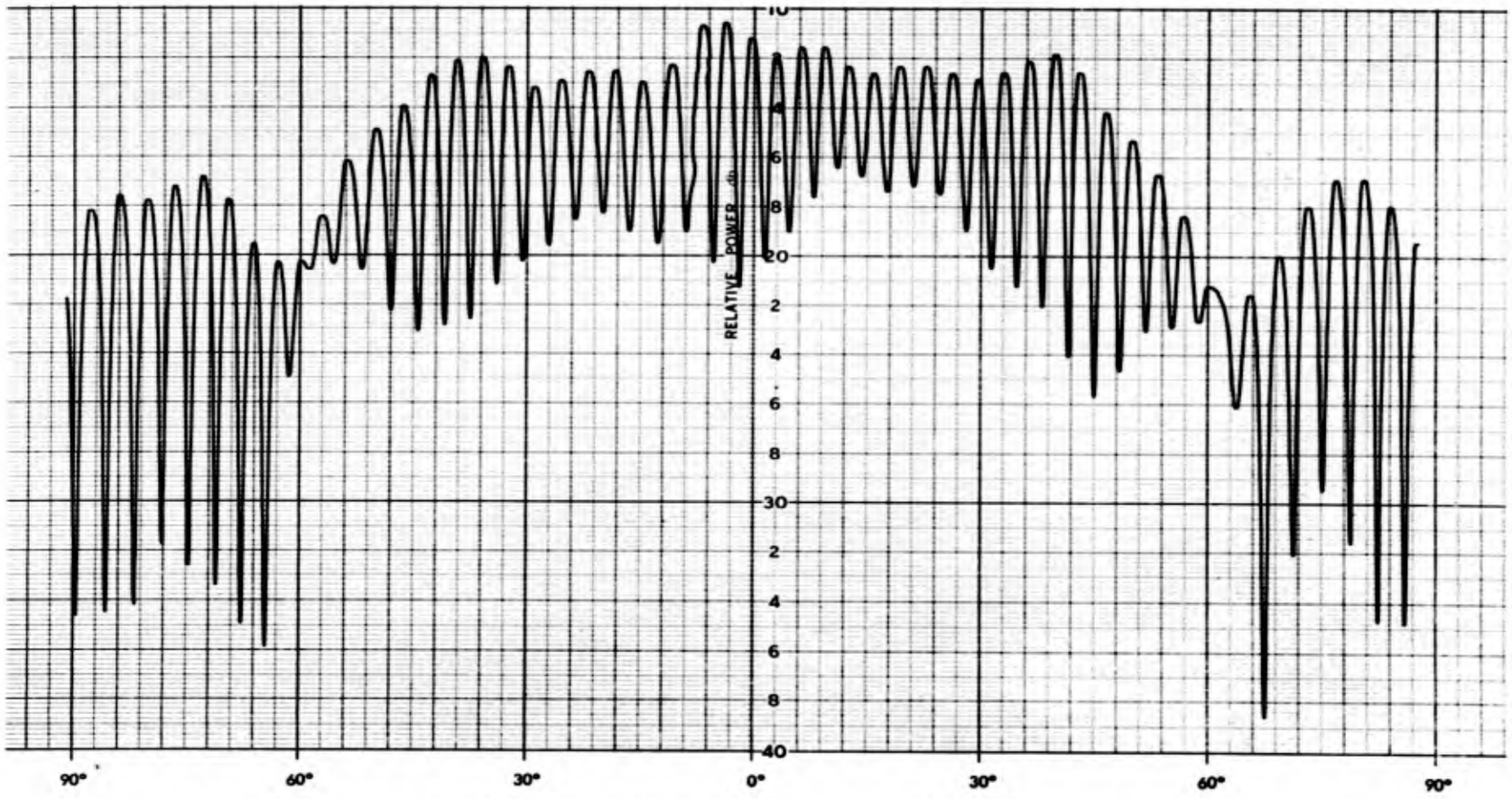

PATTERN OF SEVEN ELEMENT ARRAY WITH ONLY CENTER ELEMENT FED

A NEW BROADBAND TRACKING ANTENNA

● LaVergne E. Williams

Radiation Incorporated
Melbourne, Florida
August 1962

(Unclassified)

A NEW BROADBAND TRACKING ANTENNA

By: LaVergne E. Williams
Radiation Incorporated
Melbourne, Florida

SUMMARY

A new type of broadband automatic tracking phase monopulse antenna is described. The antenna is capable of simultaneously receiving orthogonal linear polarization or circular polarization of either sense over a frequency band of a decade or more, utilizing the full physical aperture over the entire band.

Basically, the antenna is an array of parabolic reflectors, each of which contains a "frequency independent" log-periodic feed. The reflector and feed constitute an element of the array and the element has a normalized pattern that is essentially frequency independent. (Of course, the beamwidth scale varies inversely with frequency.) The normalized array pattern is also frequency independent, hence the normalized product of the element and the array pattern is frequency independent.

Error signals for automatic tracking are generated by combining the element signals so as to produce sum and difference signals as in conventional phase monopulse tracking systems.

Both theoretical and experimental performance data are presented for a four-reflector array. Experimental data consists of the results from model studies and measurements made on a full-scale antenna utilizing four ten-foot diameter reflectors and a feed capable of operation from 200 to 2300 mcs.

INTRODUCTION

As space programs develop, a larger portion of the total frequency spectrum is being used to fulfill the multitudinous requirements for command, telemetry surveillance and communications. There is an increasing requirement for larger antennas with more gain, polarization diversity capability, automatic tracking capability, and, in addition, very broad frequency coverage.[1,2,3] The frequency independent antennas such as the logarithmically periodic and conical spiral types, have provided a partial solution to this problem. While it is true that they are capable of broad frequency coverage, they are essentially low gain devices with gains of the order of 10 db. Some success has been achieved in arraying log periodic and spiral elements such that array factors and element patterns are frequency independent but for decade bandwidths the maximum realizable gain appears to be below 20 db.[4,5] In this latter case, the total pattern of the array is essentially frequency independent, which means the effective aperture is only a fraction of the total physical aperture at the high-frequency end of the band.

A second approach to the problem has been to array a number of end-fired elements with fixed phase-center spacing. The number of elements in the array can be increased to achieve the required gain and the mechanical configuration of the elements, plus the power distribution to the elements, can be varied to achieve the desired pattern characteristics. Unfortunately, the end-fired elements suitable for this configuration, such as the axial mode helix, the disc-on-rod, and the yagi, are limited to bandwidths somewhat under an octave because the element patterns degrade with frequency. In addition, the number of elements required becomes unwieldy when a gain in excess of about 24 db is required.[6]

The combination of a log periodic or conical spiral feed on axis in a parabolic reflector provides good aperture efficiency with satisfactory secondary patterns, is frequency independent, and utilizes the full physical aperture over the frequency band. By means of feed design it is possible to develop error signal information for automatic tracking via either the conical scan or amplitude monopulse routes utilizing this approach. The over-all system performance, however, is appreciably degraded by the restrictions placed on a tracking feed system. Aperture efficiency is reduced, side lobes increased, and the mechanical complexity increased.

BASIC CONFIGURATION

The antenna to be considered is an array of parabolic reflectors, each of which contains a frequency independent feed.* The combination of parabolic reflector and frequency independent feed will be considered as an array element with a constant "normalized" element pattern in which the beamwidth varies inversely

---

* Patent pending by author assigned to Radiation Incorporated

with frequency. An array pattern of isotropic elements also has a "normalized" pattern that is frequency independent. The total pattern of the antenna is the product of the element pattern and the array pattern, and if these two vary as the same function of frequency, the normalized total pattern will be frequency independent.

There are many variations of the array worthy of consideration, ranging from two elements to many elements, but this paper will be primarily concerned with a simple four-element array. The reflectors are overlapped as shown in Figure 5 and the feeds are mounted with their axes aligned with the axes of the paraboloids.

To analyze the secondary pattern of two circular apertures, consider the configurations shown in Figure 1. Uniform illumination is assumed. The top figure illustrates two circular apertures located in the same plane with their edges tangential. A plot of the calculated pattern shows the first sidelobe approximately 10.7 db below the main lobe. The bottom pattern is that which would be produced if the two apertures completely eclipsed so as to produce a single circular aperture. The sidelobe level for the uniformly circular aperture is the well known 17.6 db. The center figure illustrates a configuration in which the circular apertures are partially overlapped and the calculated pattern is plotted. In this instance, the first sidelobe level is approximately 16.5 db below the peak of the main beam. The pattern produced by the partially overlapped configuration illustrates that uniformly illuminated circular apertures can be arrayed by slightly overlapping them and a reasonably low side level of 16.5 db can still be maintained.

In the sections to follow, three different primary feed illumination tapers will be considered in order to evaluate the trends in over-all antenna performance as a function of primary feed pattern. These are uniform illumination, tapered illumination with 10 db edge illumination, and a $(1 - r^2)^2$ with zero edge illumination. These were selected because they are fairly representative of the measured performance of an actual feed design to be described later. The normalized E- and H-plane voltage patterns of the feed are shown in Figure 2(a) and the three assumed aperture illuminations are shown in Figure 2(b). Experimental E-plane secondary patterns were made with an array having an F/D of 0.3. These conditions can be approximated by the $(1 - r^2)^2$ illumination taper. The assumed taper with 10 db edge illumination is an approximation of an average E- and H-plane distribution with an F/D of about 0.4. Uniform illumination is the limit reached when the F/D becomes large.

In Figure 3 the normalized secondary patterns are plotted for each of the three primary feed illuminations described above. In the calculations to follow, the single dish secondary patterns will be considered as element patterns and will be multiplied by array patterns to calculate total patterns.

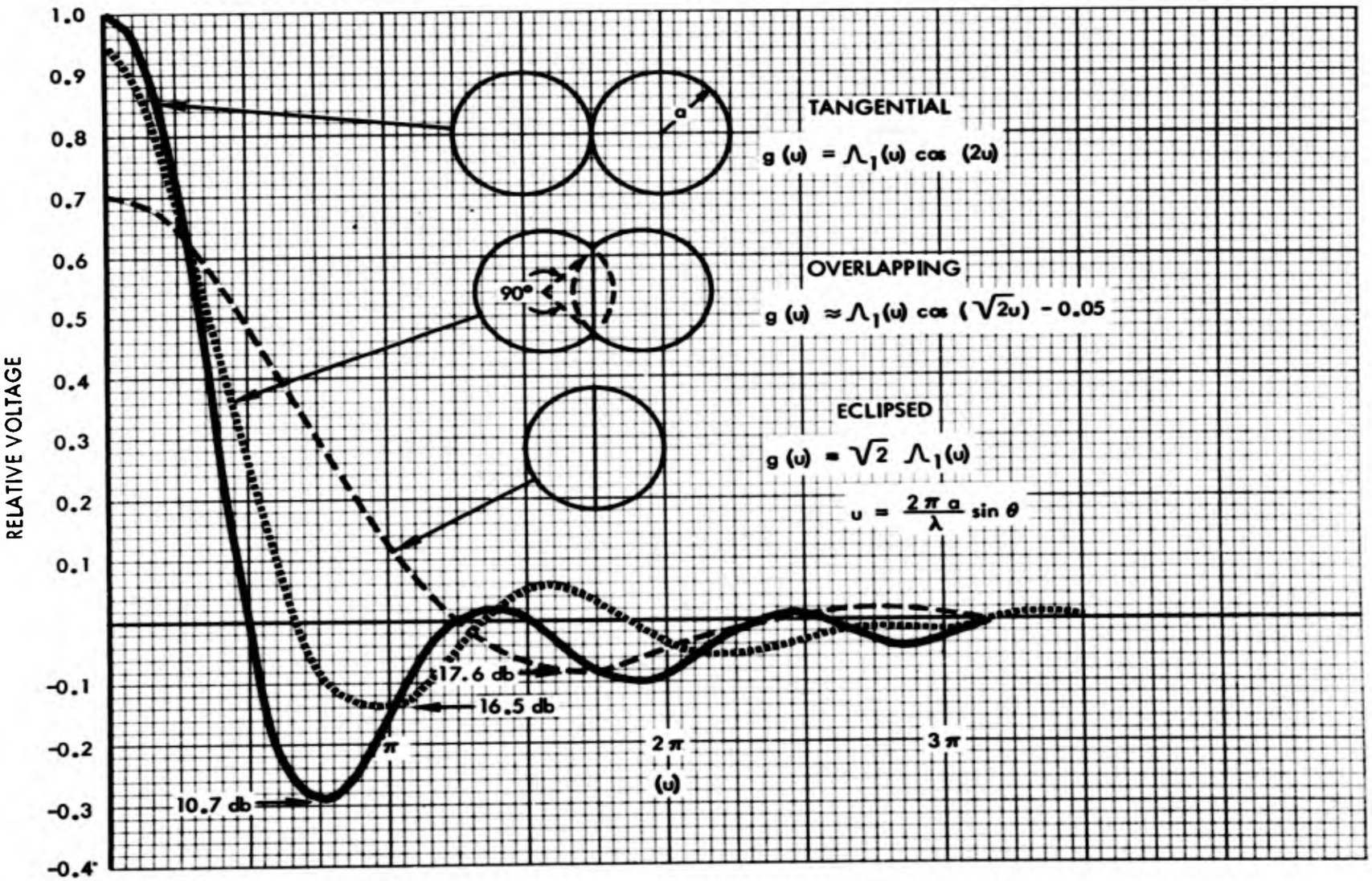

Figure 1. Figure Showing Effect on Secondary Patterns of "Overlapping" Uniformly Illuminated Circular Apertures

35402

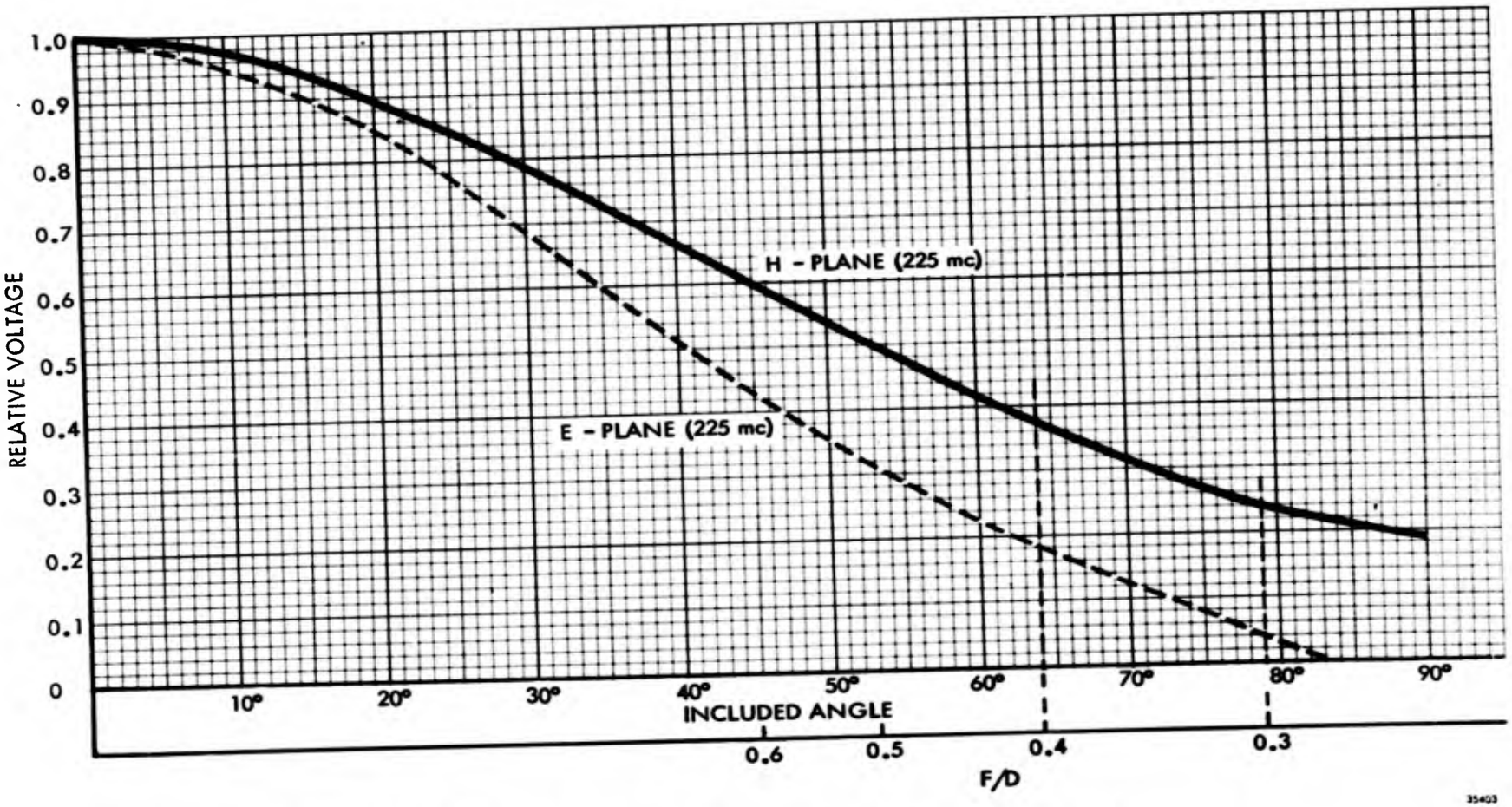

Figure 2 (a). Primary Patterns of Triangular Tooth Log-Periodic Feed

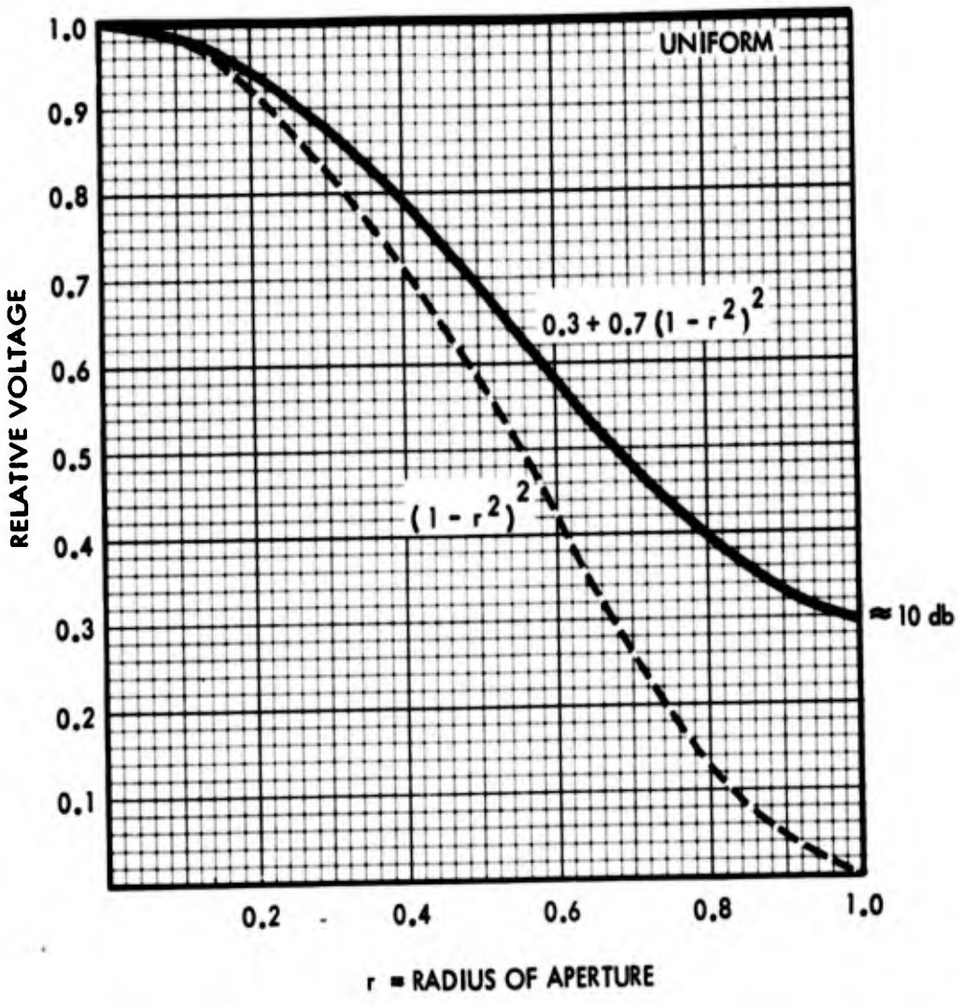

Figure 2 (b). Curves Showing Three assumed Aperture Distributions Used in the Calculations

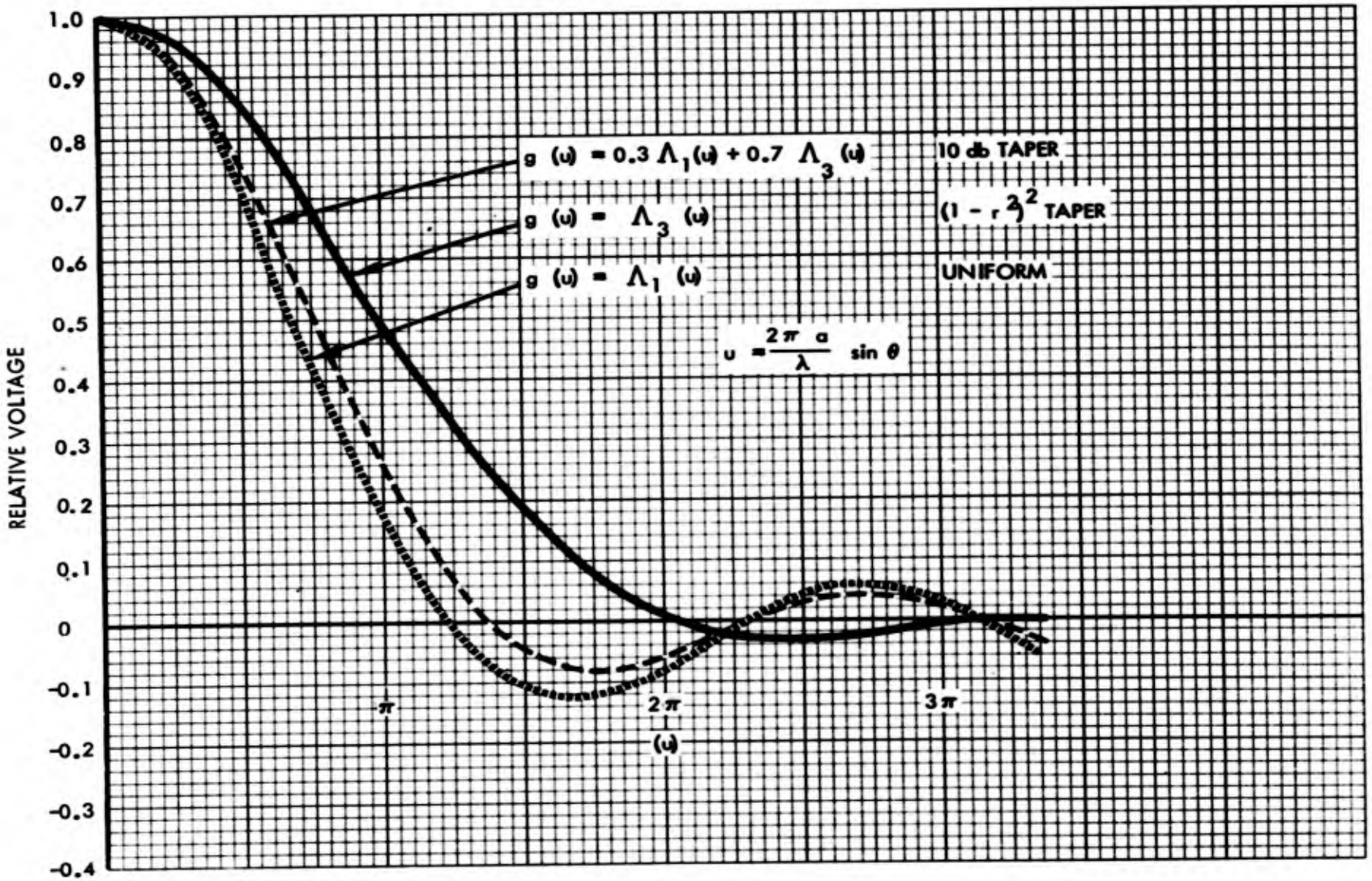

Figure 3. Secondary Patterns for Circular Apertures with Three Different Illumination Tapers

35405

Figure 4 shows the effect of overlapping two circular apertures as a function of aperture illumination. It is noted that a severe taper such as the $(1 - r^2)^2$ tends to produce a high first side lobe level (10 db). The first side lobe level produced with both uniform illumination and the 10 db edge taper is approximately the same or 16.5 db. An aperture illumination with a 10 db edge illumination is entirely feasible and represents a good compromise between side lobe levels, spillover, and aperture efficiency. With two apertures, the area of overlap is only 9% of the total circular area and with the edge illumination down 10 db the amount of power spillover from dish-to-dish is exceedingly small.

Two array configurations will be considered as shown in Figure 5. The patterns calculated for the square array are essentially the same as the 45° patterns calculated for the diamond array and vice versa. The only essential difference in operation is the method by which the elevation and azimuth error signals are generated in the phase monopulse comparator. In the square array, the azimuth error signal is the difference between (A + D) and (B + C), while in the diamond array it is given by simply (C - D). Similarly, elevation error is (A + B) - (C + D) for the square array and simply (A - B) for the diamond array.

The hybrid circuitry for producing the sum and difference signals is shown in Figure 5.

ANTENNA PATTERNS

The total patterns for various array configurations were calculated by multiplying the array patterns by the element patterns, assuming the elements were circular apertures, and then subtracting the pattern effects caused by the areas of overlap. For example, the sum pattern for the square array was calculated by the method illustrated in Figure 1. The region of overlap in the center illustration of Figure 1 is assumed to reduce the on-axis power gain of the antenna by an amount equal to the ratio of the overlap area to the area of the two circular apertures. In this instance, the area of overlap was assumed to produce a broad pattern, with respect to the total pattern, and when subtracted from the pattern of two circular apertures, will reduce the on-axis voltage gain by 5%. The area of overlap between the two top and two bottom dishes of the square array will have a pattern very similar to the array pattern in the region near the main beam and first few side lobes. Its effect on the total pattern will be quite small when the patterns are normalized and is therefore assumed to be negligible. Figure 6 illustrates the calculations for the total pattern of the diamond array with uniform illumination. The areas of overlap are assumed to have sinusoidal distribution and are accounted for by subtracting their effect from the total pattern of the four circular apertures.

The effect of the overlap area on total patterns is significant although not particularly great with uniform illumination, but it is much less significant when

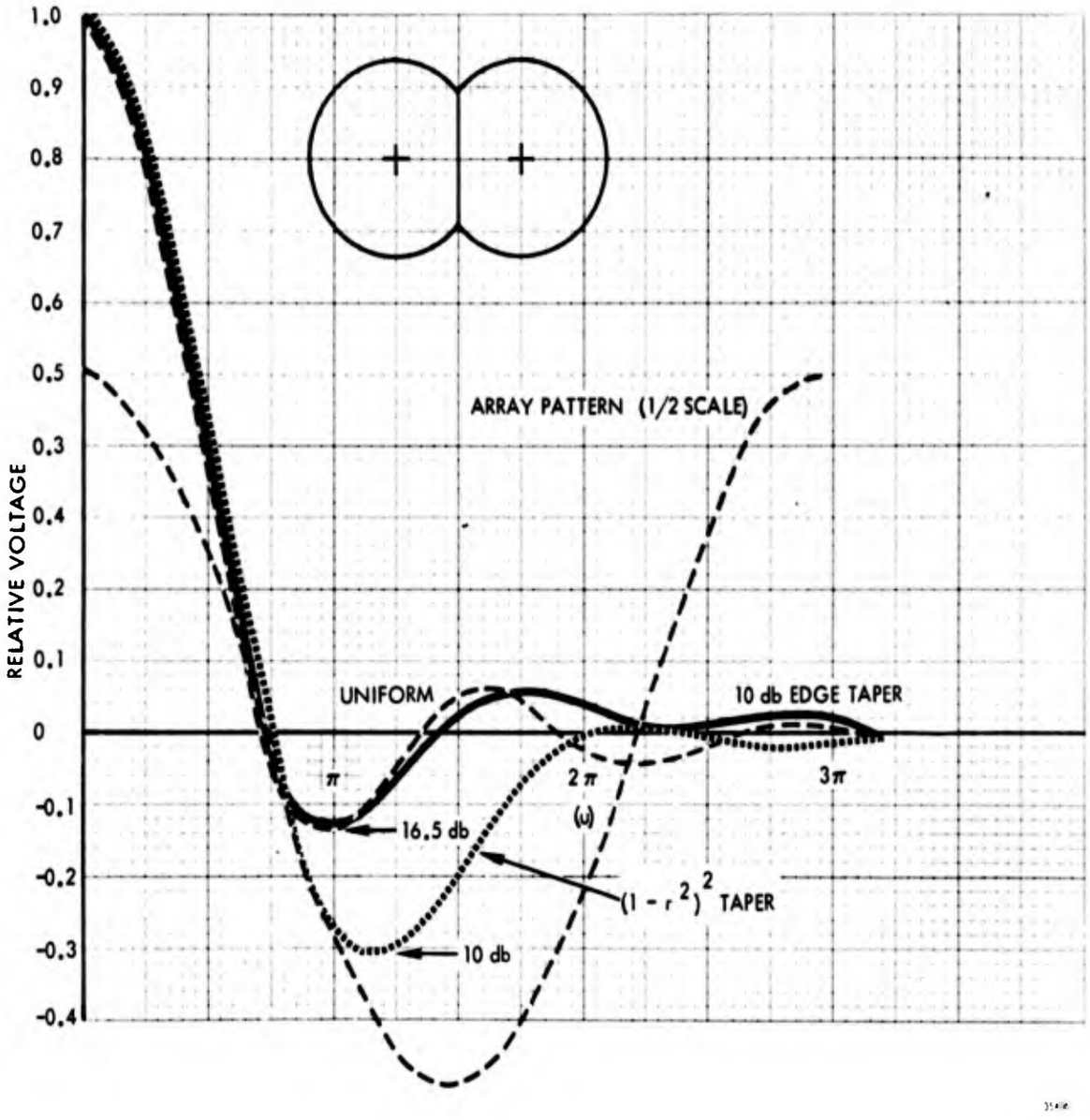

Figure 4. Calculated Patterns Showing the Effect of Aperture Illumination on Secondary Patterns of a Two Element Array

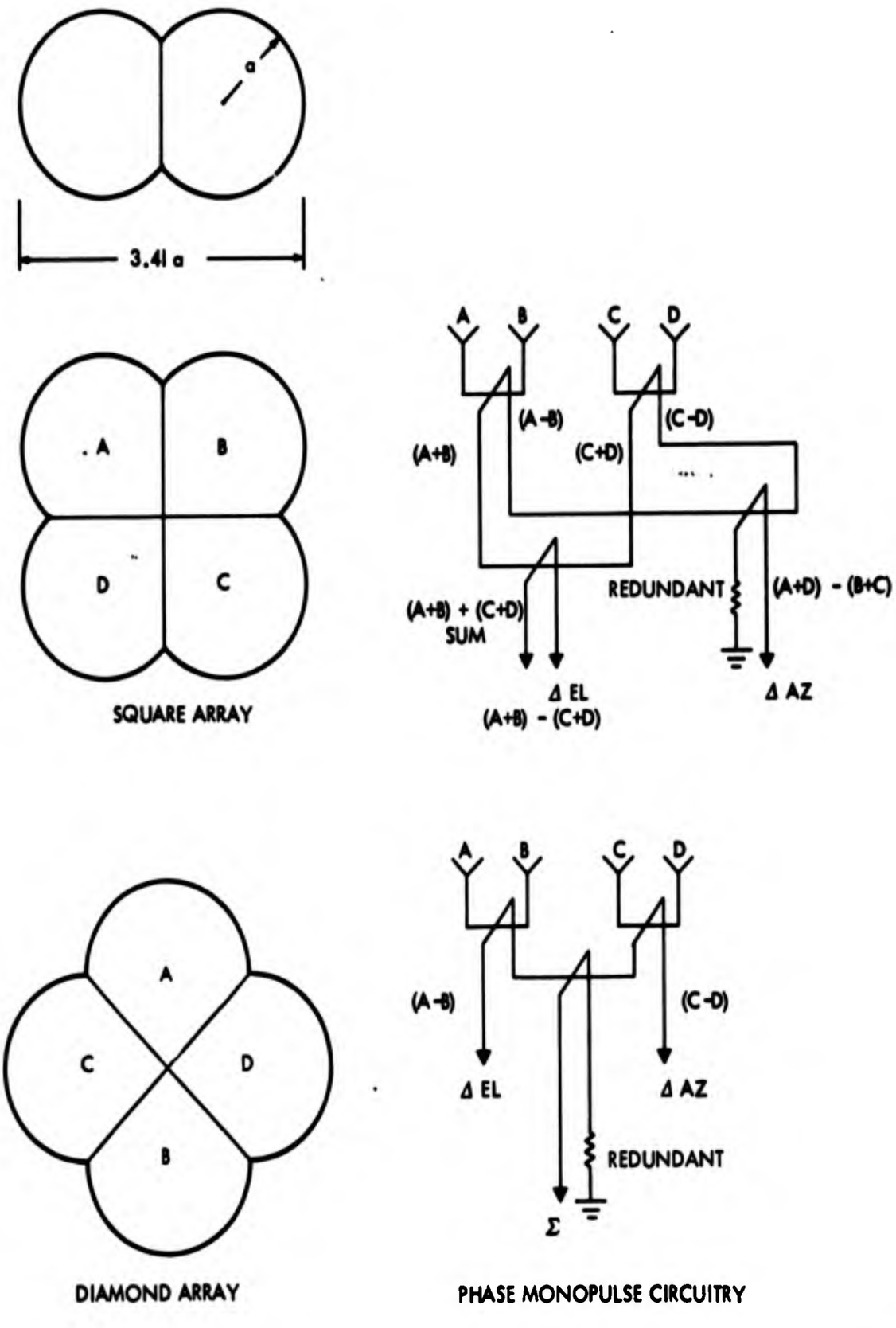

Figure 5. Figure Showing the Square and Diamond Arrays and Associated Circuitry for Generating Phase Monopulse Sum and Difference Signals (The Coefficients of Terms are Omitted)

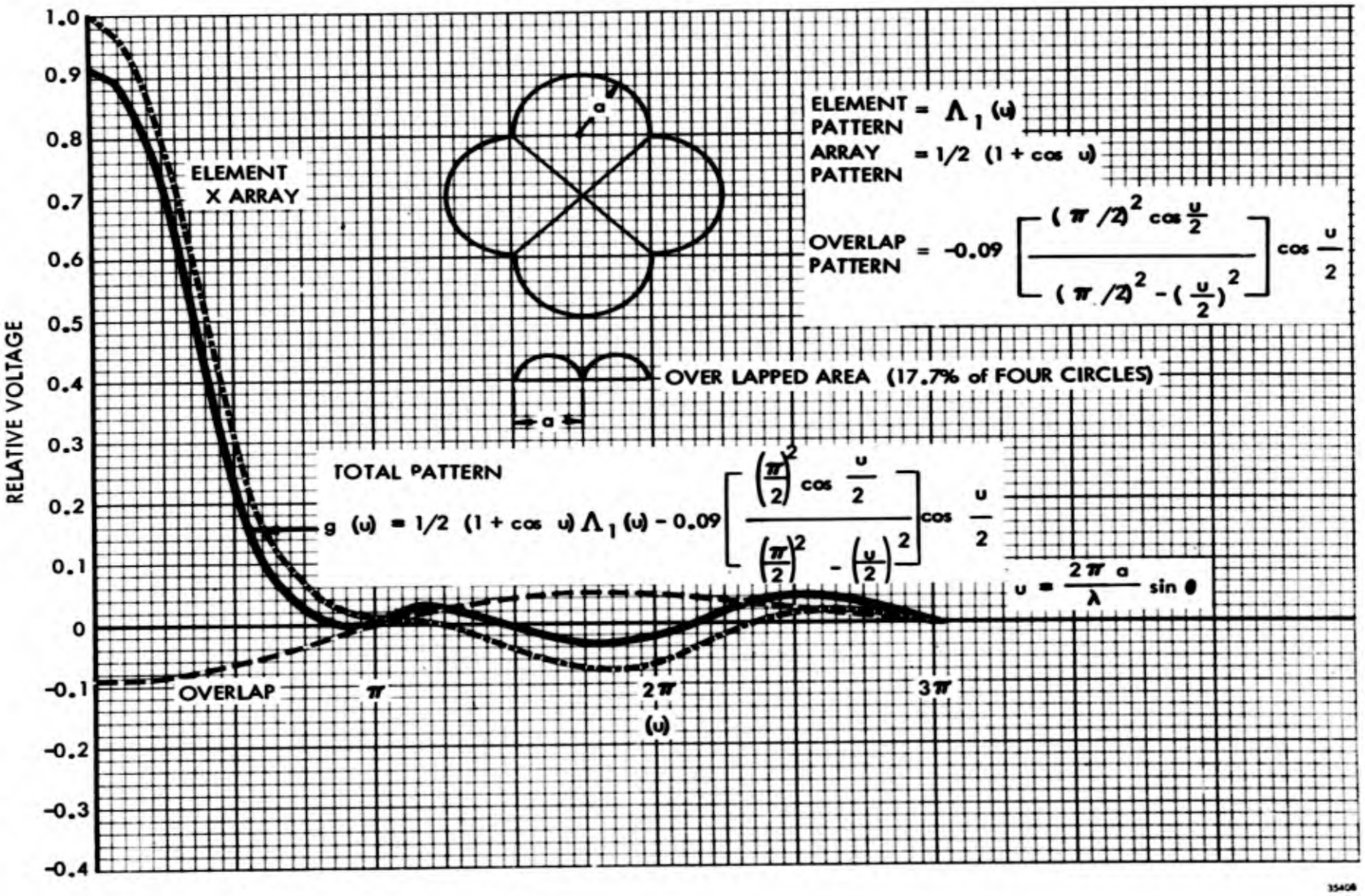

Figure 6. Calculated Secondary Pattern for the Four Dish Diamond Array with Uniform Illumination

the edge illumination of the dish is down by 10 db or more. For this reason, the contribution of the overlapped area to the total patterns is neglected in calculating the total patterns for the 10 db edge illumination and the 0 edge illumination condition. Figures 7 through 12 show the calculated sum and difference patterns for the square array and the diamond array with the three assumed illumination tapers. It should be noted that these curves were calculated assuming no aperture block and no defocusing of the feed.

Examination of the antenna patterns will show that the shape of the main beam and the location of the first null is largely determined by the array pattern. The half power beamwidths are given very closely by the following equation for both the square and the diamond array:

$$\theta_{HP} \approx \frac{64\lambda}{D} \text{ degrees}$$

where

D = maximum over-all dimension of the array

λ = wavelength

The physical area of the array is equal to 0.818 times the area of an enclosing circle that is tangent to the four edges of the array.

Also of interest is the fact that the slope of the difference channel in the null is practically the same for the two arrays.

APERTURE BLOCK

When the feed of the individual element is comparable in size to the reflector diameter, as is the case with four 10-foot diameter reflectors at a frequency of 215 mcs, the aperture block has a significant effect on patterns and must be considered. Figures 13 through 16 illustrate the calculated effect of aperture block on the sum patterns of both the square and diamond array with the two assumed illumination tapers. The three values of aperture block assumed were 0%, 19%, and 36% of the total effective aperture. The curves illustrate how aperture block by the feed at the center of the elements can be responsible for changing relative side lobe levels.

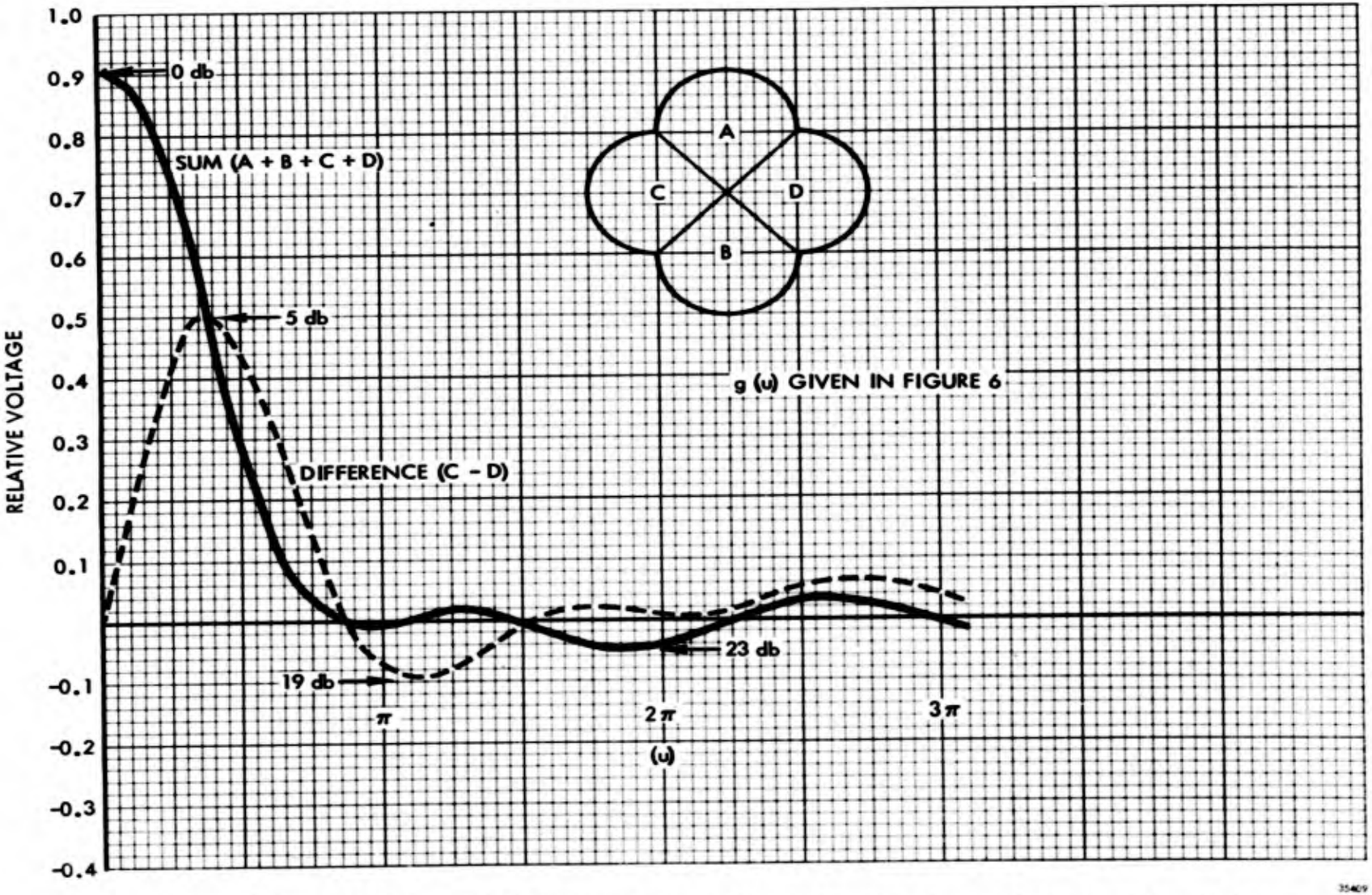

Figure 7. Calculated Sum and Difference Patterns for the Diamond Array with Uniform Illumination – No Aperture Block

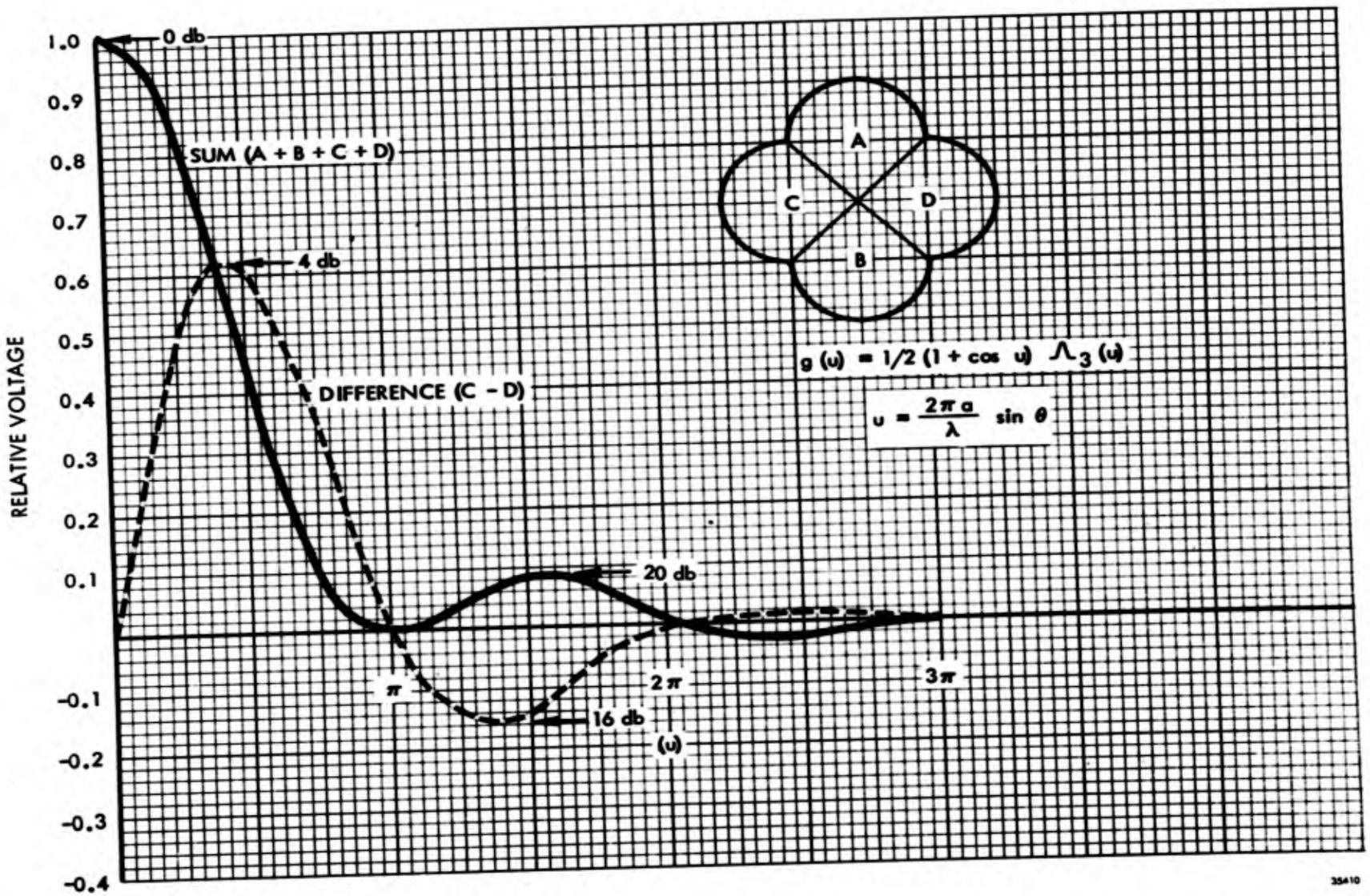

Figure 8. Calculated Sum and Difference Patterns for Diamond Array with $(1 - r^2)^2$ taper - No Aperture Block

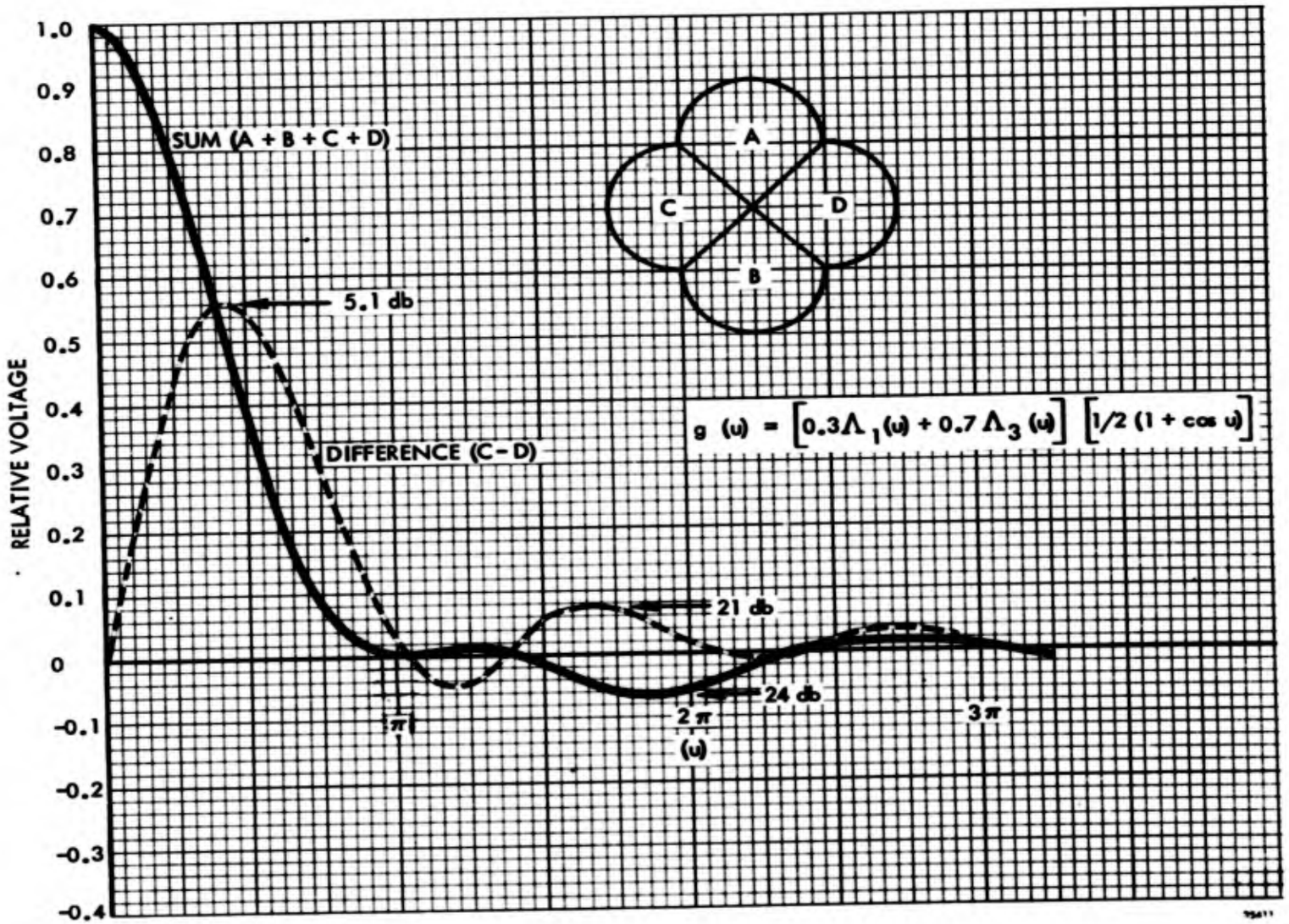

Figure 9. Calculated Sum and Difference Patterns for Diamond Array with 10 db Edge Illumination - No Aperture Block

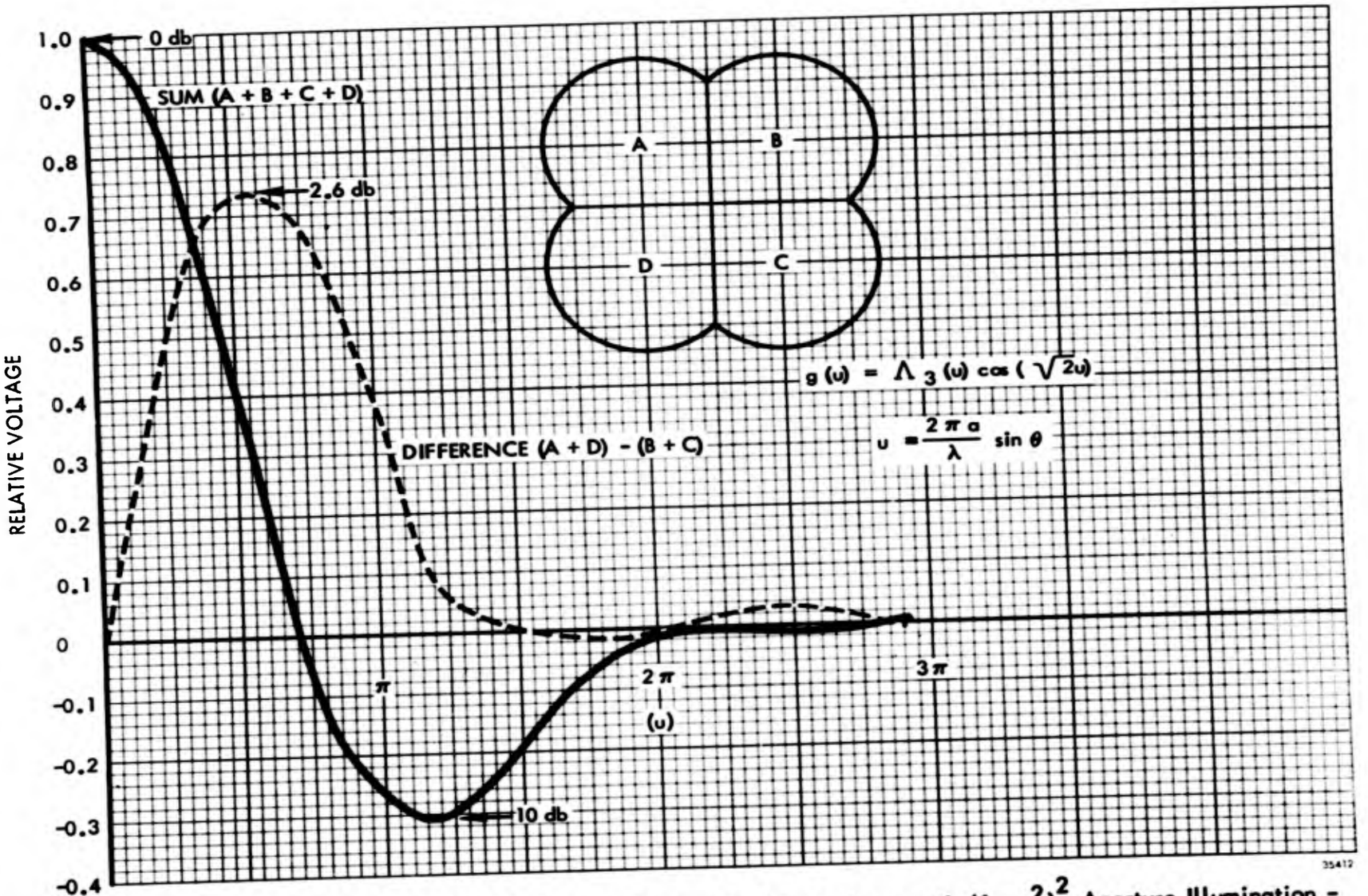

Figure 10. Calculated Sum and Difference Patterns for Square Array with $(1 - r^2)^2$ Aperture Illumination - No Aperture Block

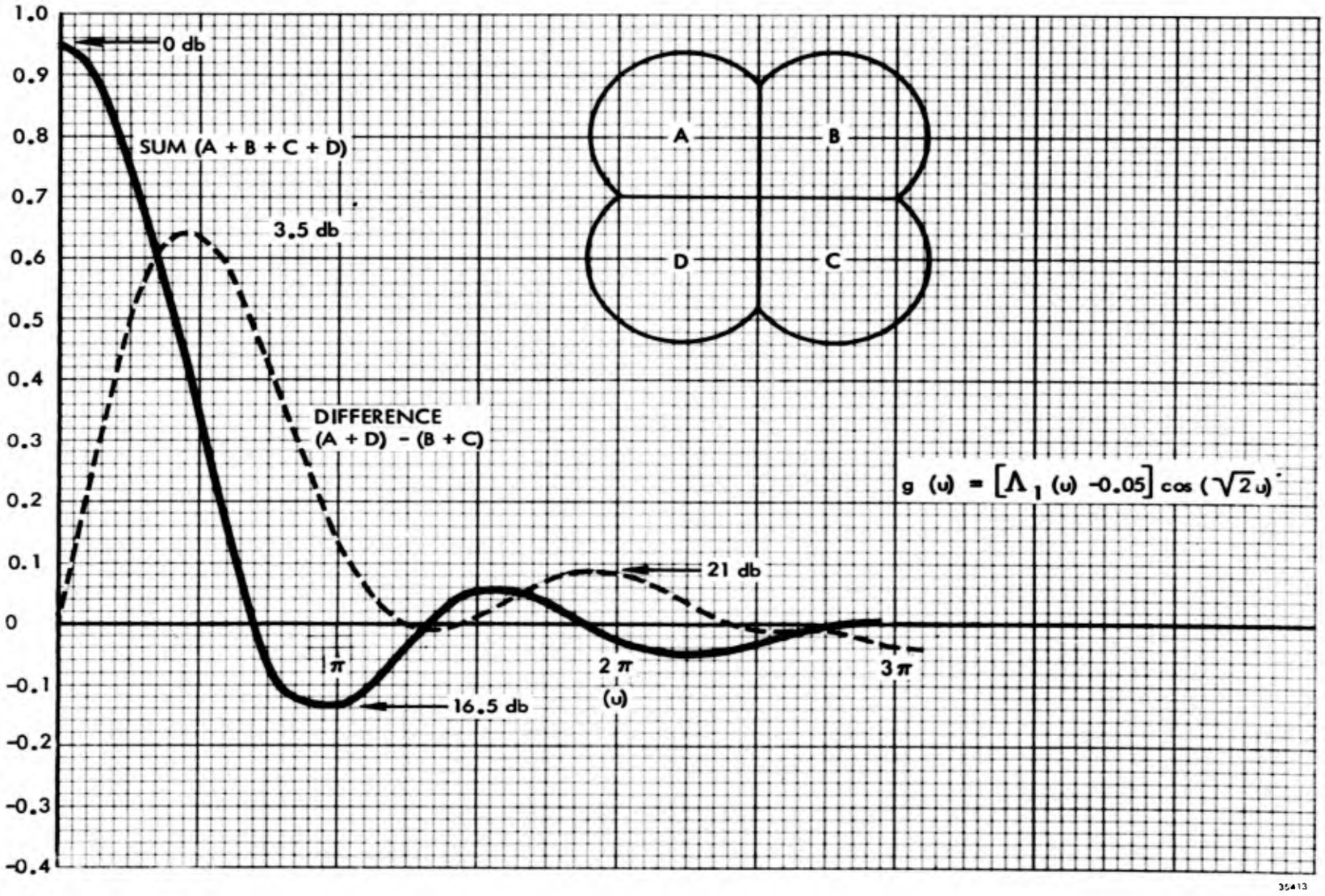

Figure 11. Calculated Sum and Difference Patterns for Square Array with Uniform Illumination - No Aperture Block

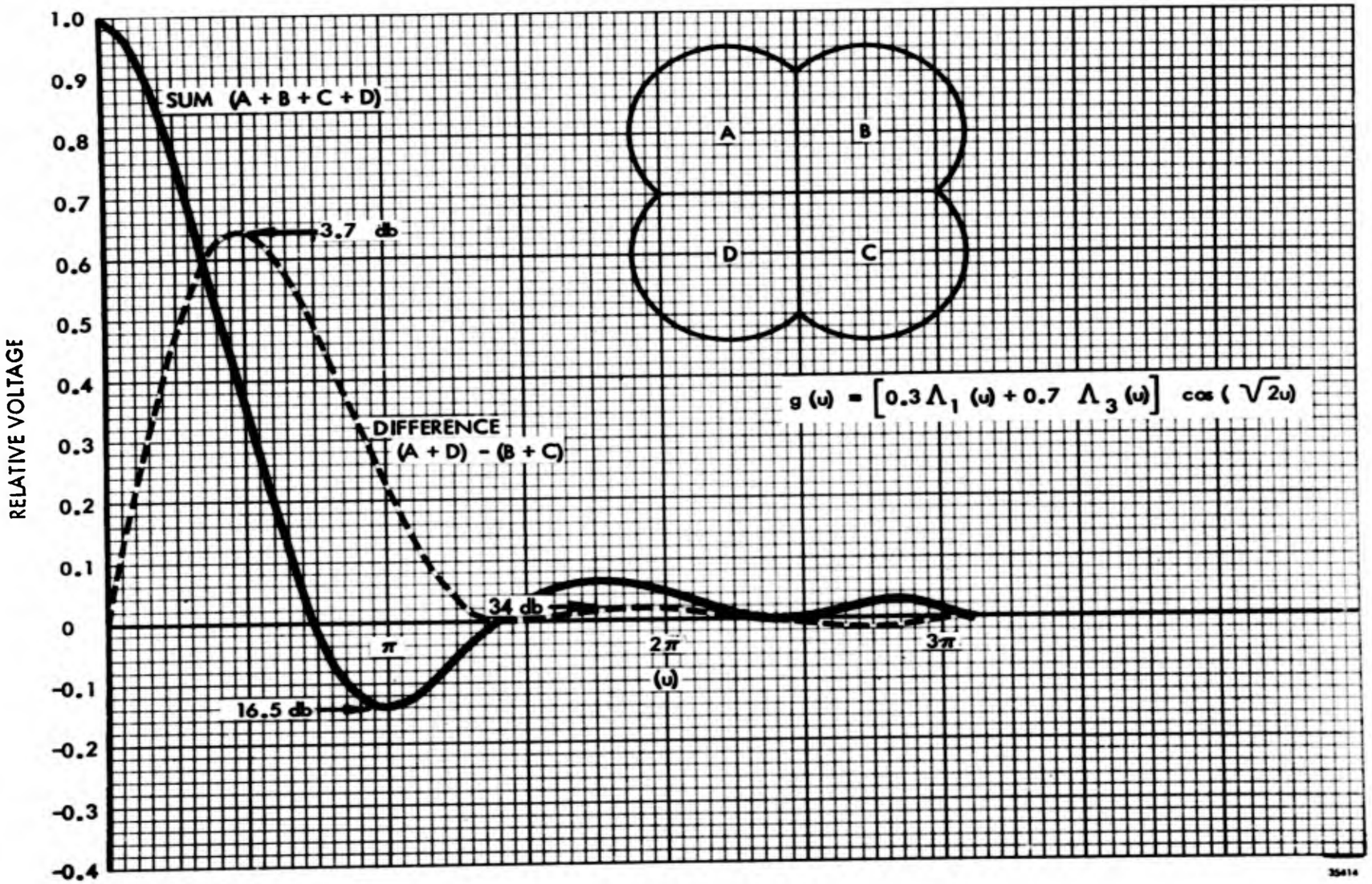

Figure 12. Calculated Sum and Difference Patterns for Square Array with 10 db Edge Illumination - No Aperture Block

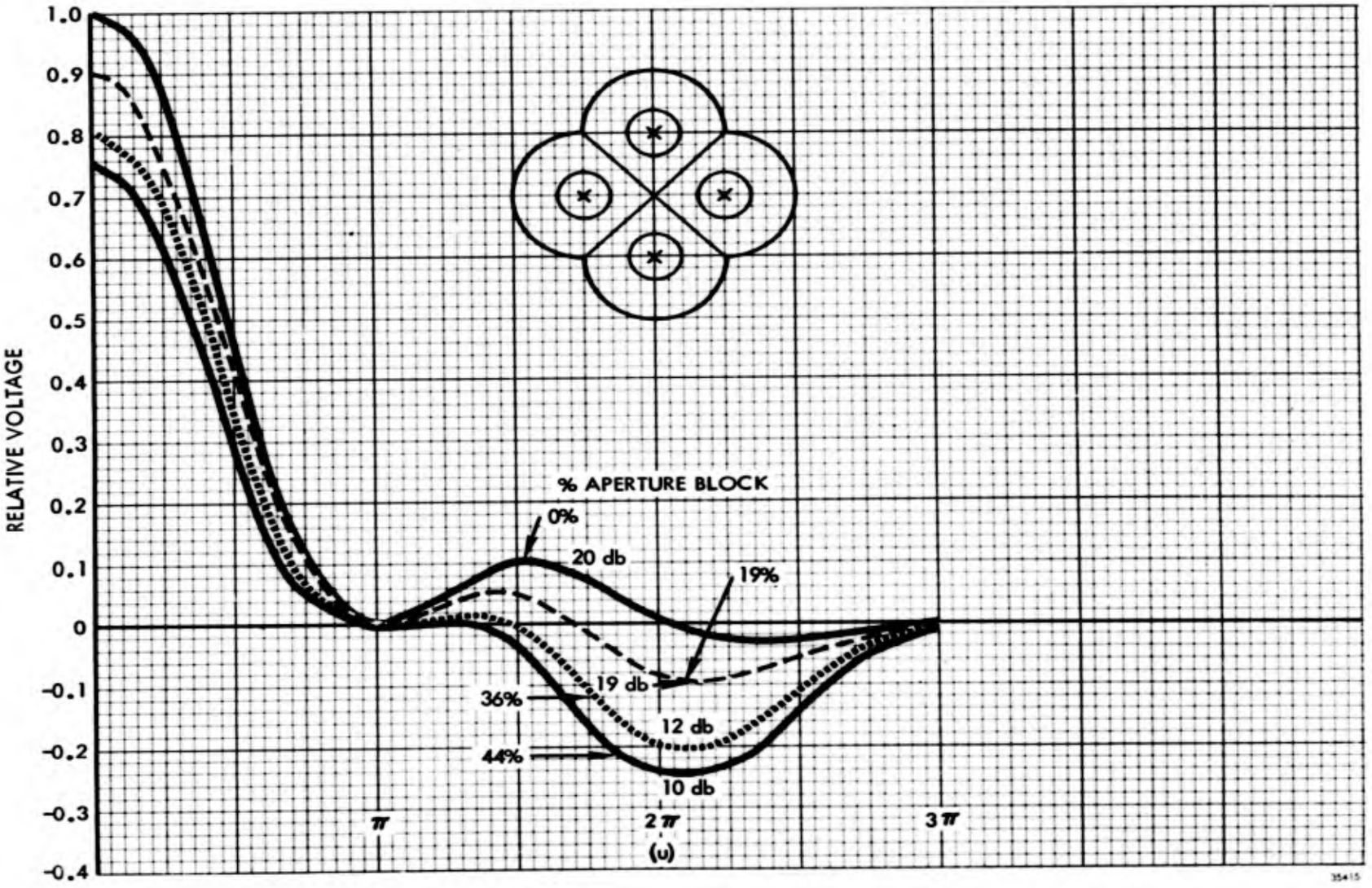

Figure 13. Calculated Sum Patterns for Diamond Array with $(1 - r^2)^2$ Taper and Several Different Values of Aperture Block

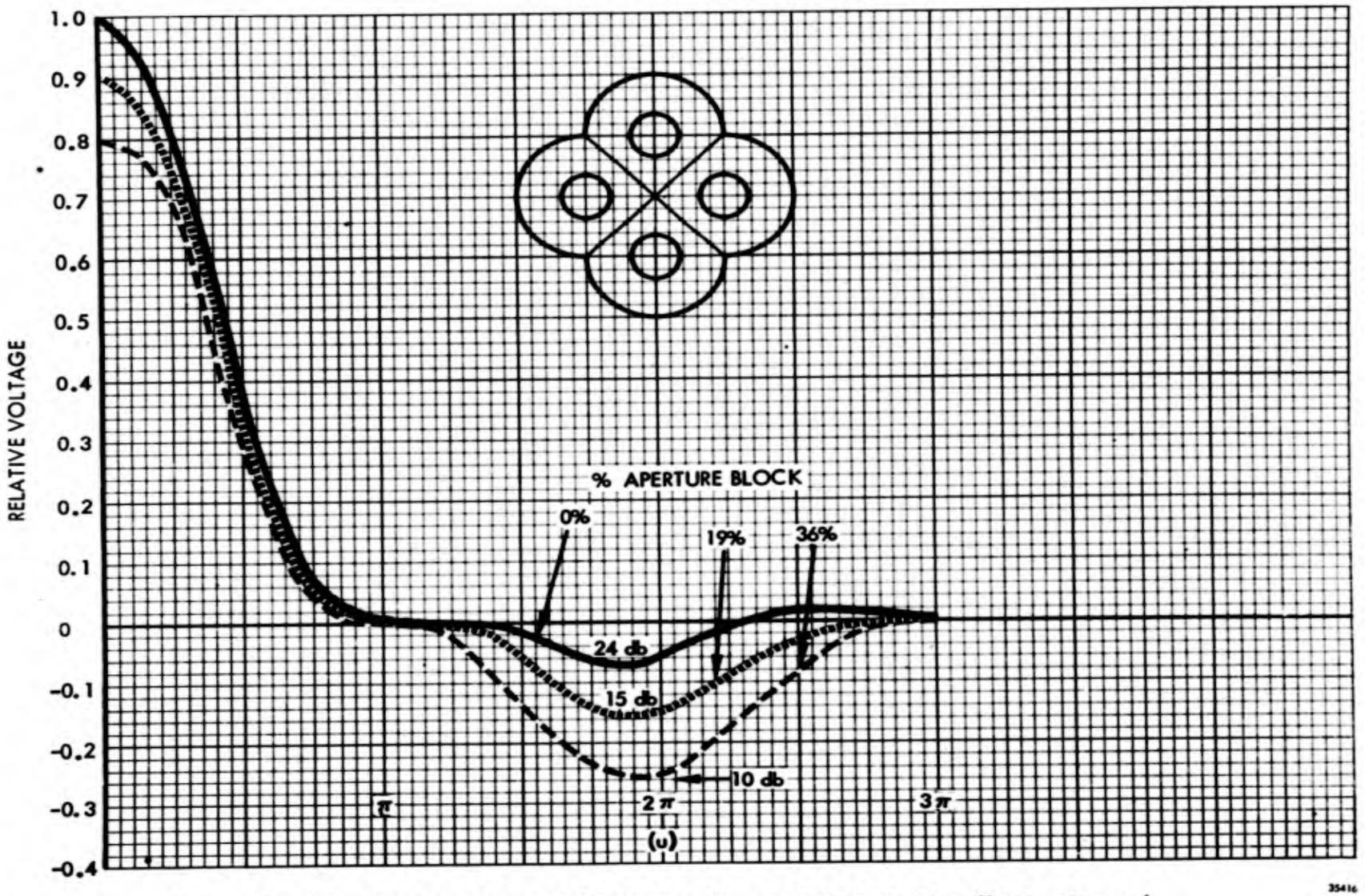

Figure 14. Calculated Sum Patterns for Diamond Array with 10 db Edge Illumination and Different Values at Aperture Block

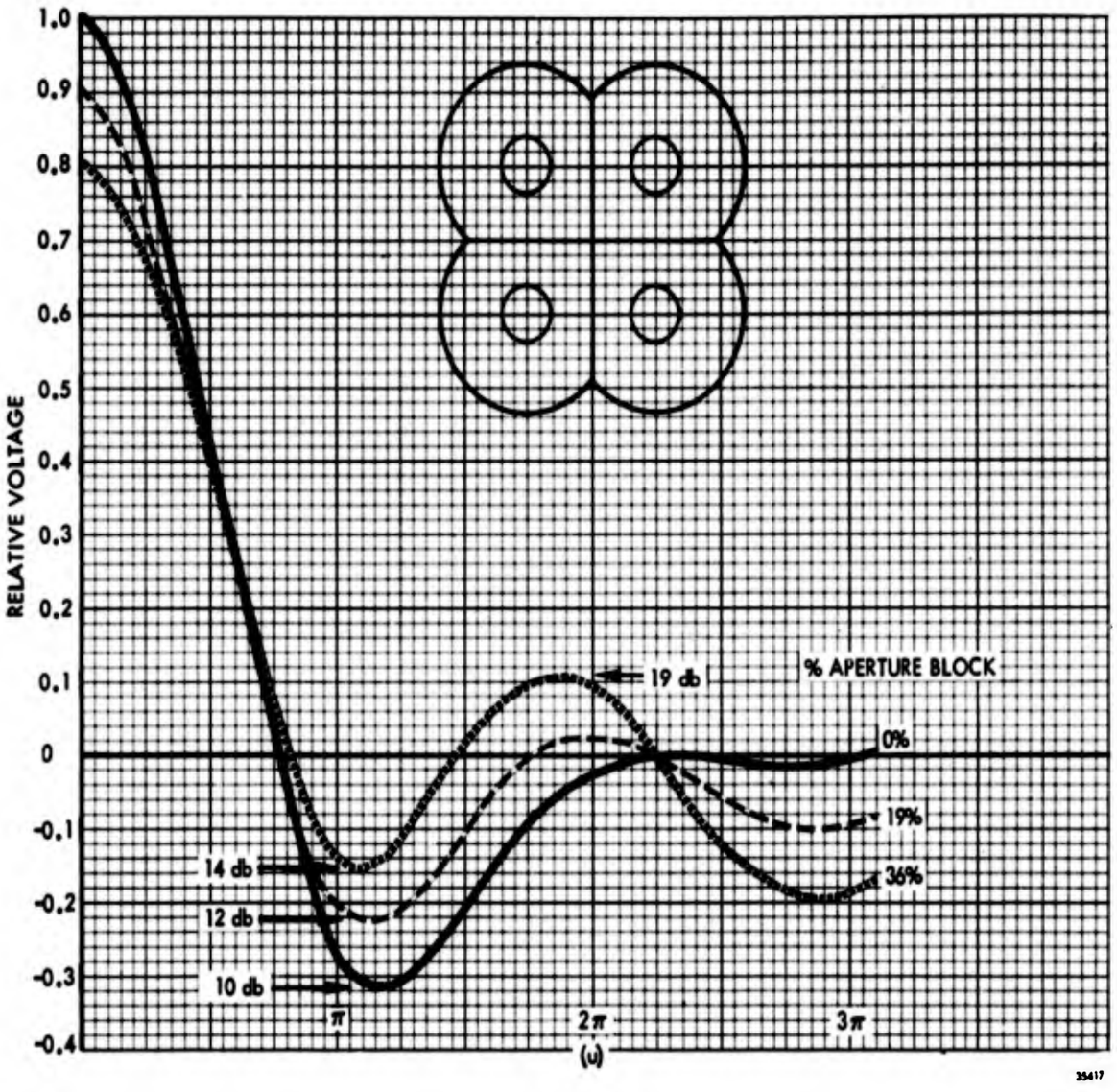

Figure 15. Calculated Sum Patterns for Square Array with $(1 - r^2)^2$ Taper and Three Different Values of Aperture Block

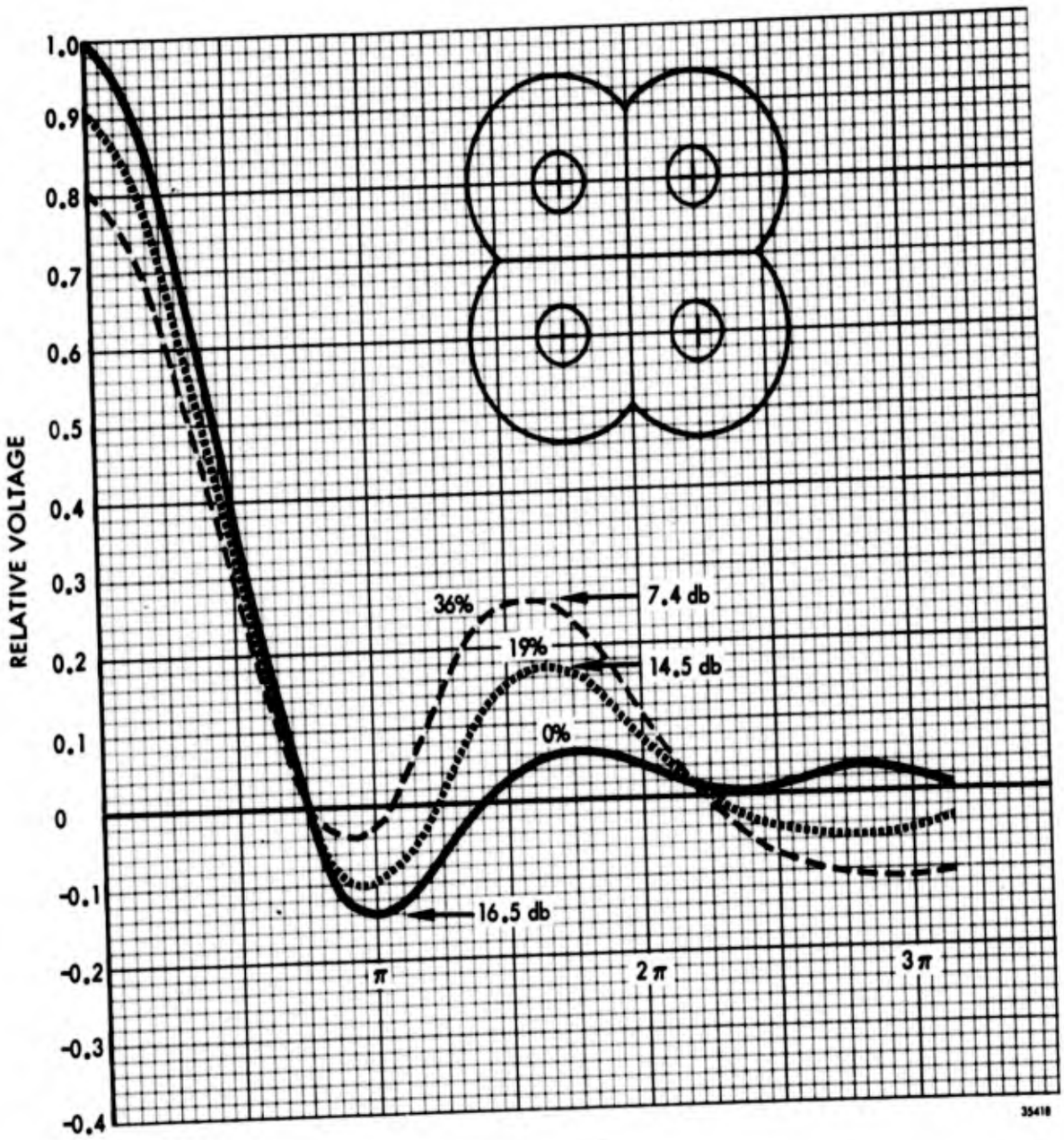

Figure 16. Calculated Sum Patterns for Square Array with 10 db Edge Illumination and Three Values of Aperture Block

THE LOG PERIODIC FEED

A feed development program was conducted to obtain a log-periodic feed for the antenna system that would provide nearly equal E- and H-plane patterns over a frequency bandwidth from 216 to 2300 mcs, provide orthogonal linear polarization, and one which would also have a minimum displacement of the phase center as a function of frequency to minimize defocusing effects.

The final feed design utilized orthogonal, triangular tooth elements with an alpha angle of 83°. With this configuration, the amount of defocusing is approximately one-quarter wavelength at any frequency if the apex of the feed is placed at the focus of the parabola. The triangular tooth structure also was found to be relatively free from pattern distortion caused by higher order radiation modes when the frequency band exceeds 3:1. A typical set of feed patterns over the frequency range are shown in Figure 17. The VSWR of the feed elements were less than 3 to 1 over the 10 to 1 frequency band. The completed feed weight was approximately 20 pounds.

APERTURE EFFICIENCY

The theoretical aperture efficiency of the antenna will be very nearly equal to the theoretical efficiency of the individual elements. The efficiency of an element utilizing the triangular tooth log-periodic feed in a parabolic reflector was calculated for various values of maximum aperture angles and corresponding F/D utilizing the graphical integration method described by P.D. Potter.[7,8] The aperture efficiency is given by the following equation:

$$\eta = \cot^2\left(\frac{\Psi}{2}\right) G_{of} \left| \frac{1}{N} \sum_{n=1}^{n=N} \int_{o}^{\Psi} E_{fn}\left(\psi, \xi\right) \tan\left(\frac{\psi}{2}\right) d\psi \right|^2$$

where

Ψ = maximum aperture angle

G_{of} = absolute gain of the feed (also computed by graphical integration)

N = number of pattern cuts integrated (In this case N = 2, E-plane and H-plane)

$E_{fn}(\psi, \xi)$ = voltage feed pattern

ψ = angle between axis of paraboloid and a line from the focus to a point on the parabolic surface

ξ = angle measured in plane of the aperture between radius reference and a point in the aperture

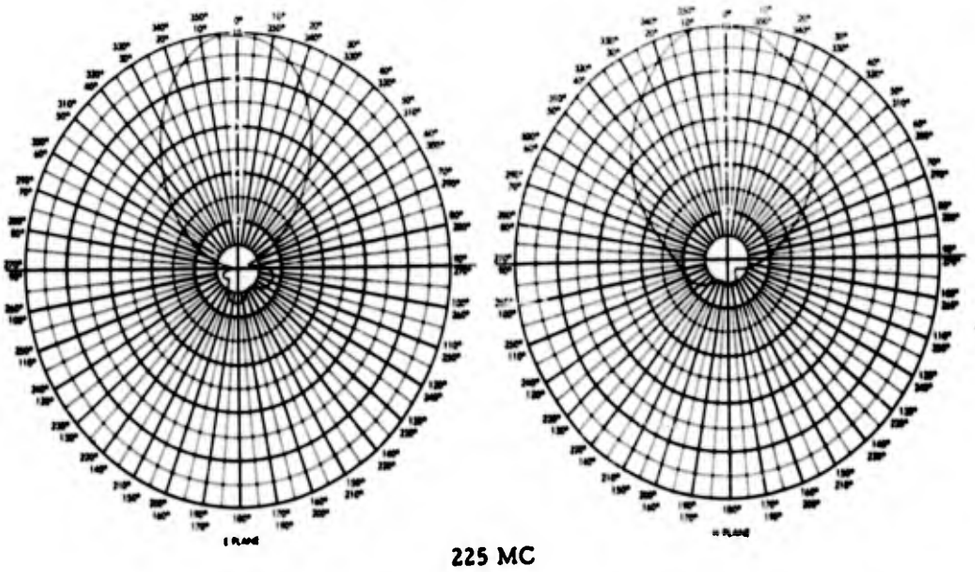

225 MC

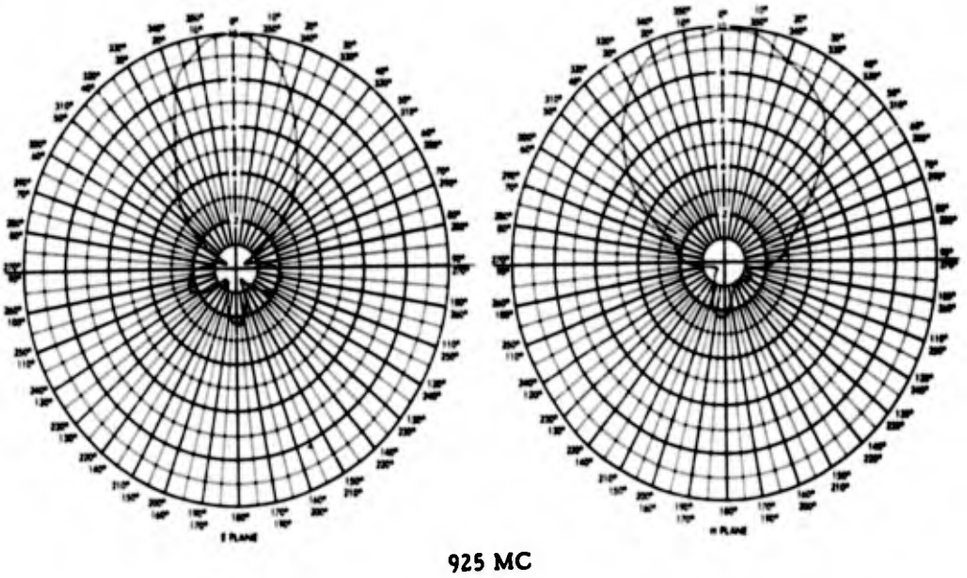

925 MC

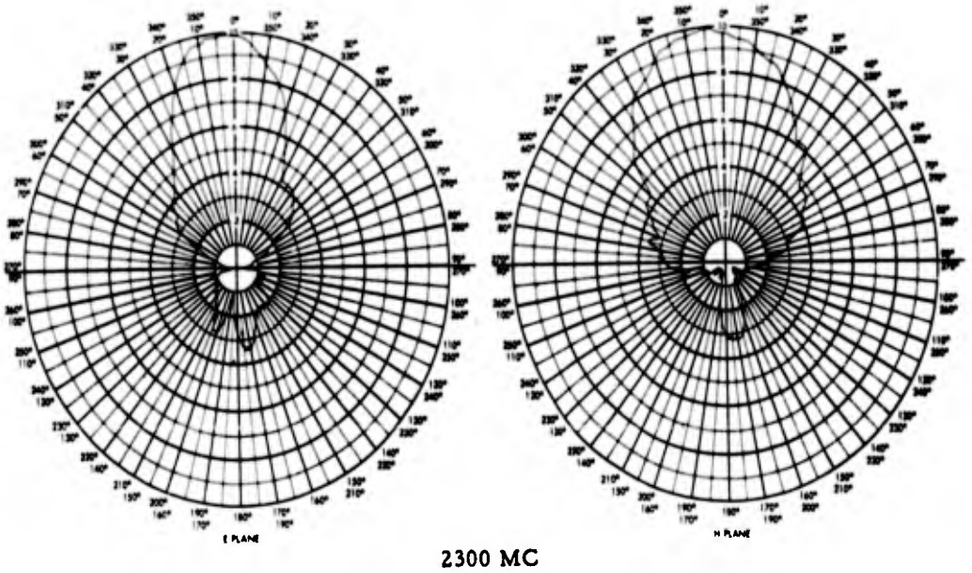

2300 MC

35419

Figure 17. "Zig-A-Log" Feed Primary Patterns (E- and H-Plane)

The summation was carried out for two values of n corresponding to the E- and H-plane patterns of the feed at a frequency of 225 mc. The calculated curves are shown in Figure 18. The effect of defocusing the feed phase center by one-quarter wavelength is estimated and shown on the graph. From the calculated curves the optimum F/D ratio for the triangular tooth feed falls between 0.4 and 0.5 and there is appreciable loss in efficiency when the F/D of the parabola is as low as 0.3. The calculated aperture efficiency neglects cross-polarized effects, losses resulting from surface tolerances, aperture block and losses in the feed and transmission lines.

EXPERIMENTAL RESULTS

In the early phases of this program a two element array was constructed utilizing log-periodic dipole feeds and reflectors 2-feet in diameter. A photo of this antenna is shown in Figure 19 and some of the patterns from this model are shown in Figure 20; and, although the characteristics of the log-periodic dipole feed were not the same as the triangular tooth feed, certain trends in the patterns are apparent. Figure 21 contains characteristic patterns obtained with a diamond array utilizing a triangular tooth log-periodic feed and 2 foot diameter reflectors with an F/D of 0.375. It should be noted that the reflectors were only two wavelengths in diameter at the lowest design frequency of the feed and serious aperture block resulted. Also, the small physical size made it difficult to hold mechanical tolerances.

Figure 22 is a photograph of a full-scale antenna utilizing four 10-foot diameter reflectors with an F/D of 0.3 and triangular tooth log-periodic feeds capable of covering the frequency band from 216 mcs to 2300 mcs. A typical measured pattern at 2200 mc is shown in Figure 23 and a measured pattern for 245 mcs is shown in Figure 24. Unfortunately, the choice of 0.3 for the F/D of this array was made before the characteristics of the feed were known, and it is now apparent that it was a poor choice. The small F/D ratio gives rise to a relatively large aperture block and the one-quarter wavelength defocusing produces a serious phase error.

The combination of large aperture block, incorrect F/D and small reflector size in terms of wavelengths all tend to raise sidelobes and decrease aperture efficiency. Figure 25 shows the calculated aperture efficiency for the actual antenna including the effect of aperture block, phase error, and other miscellaneous losses such as the effects which occur when a reflector diameter is small in terms of wavelengths, cross-polarization, etc. The lower shaded area represents the calculated theoretical aperture efficiency of the antenna over the frequency range with the F/D = 0.3 and includes the above mentioned losses. Although the F/D of the antenna does not change, the large size of the feed relative to the reflector at the low frequency end of the band and its associated defocusing of phase center is equivalent

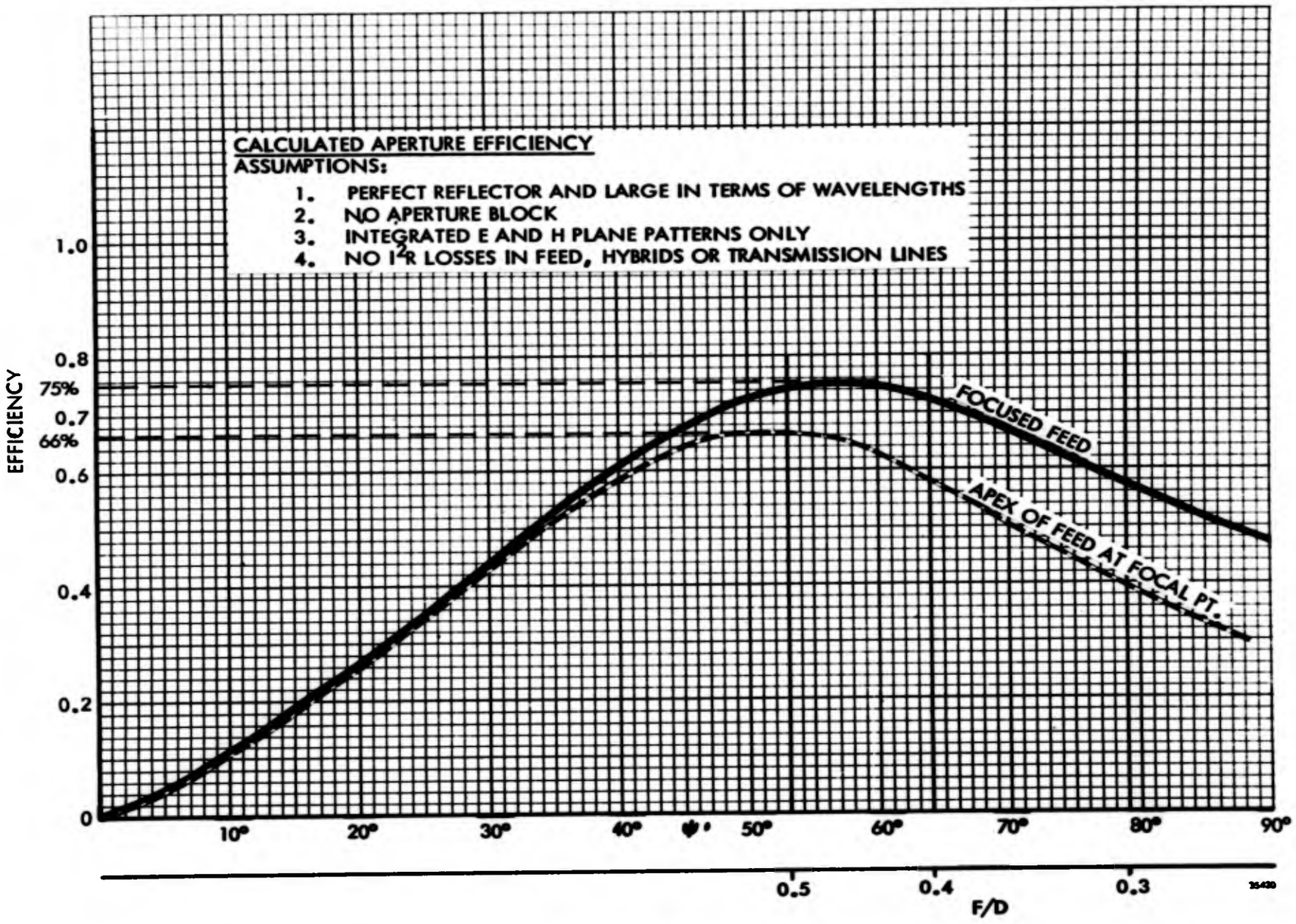

Figure 18. Calculated Aperture Efficiency

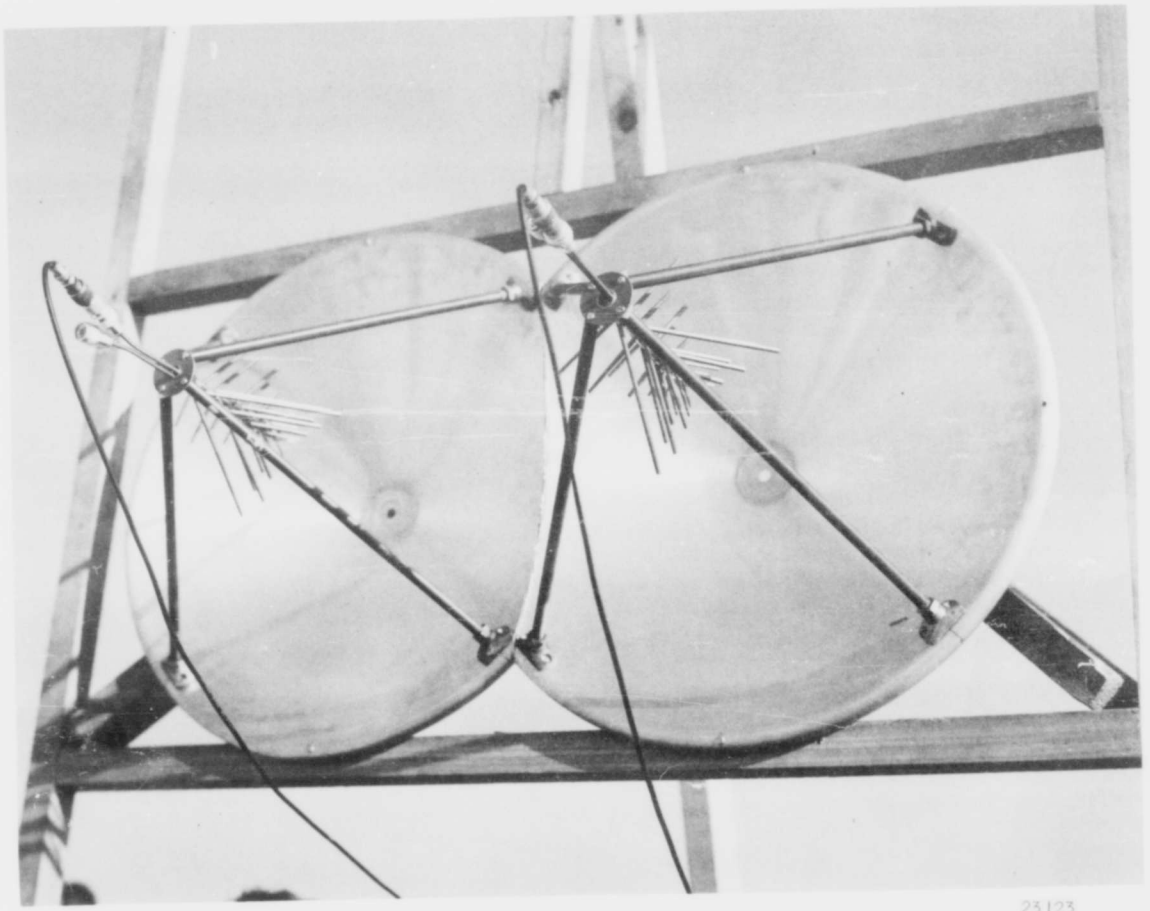

Figure 19. Broadband Monopulse Antenna Model with Log-Periodic Dipole Feeds and Two-Foot Diameter Reflectors

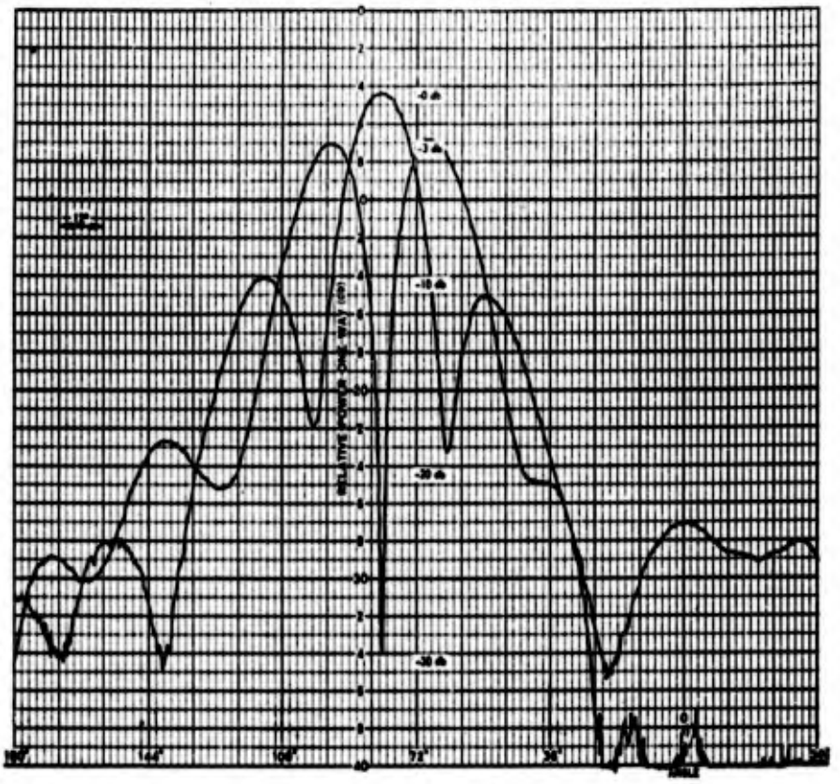

Sum and Difference Patterns - E-Plane (1000 MC) Broadband Monopulse

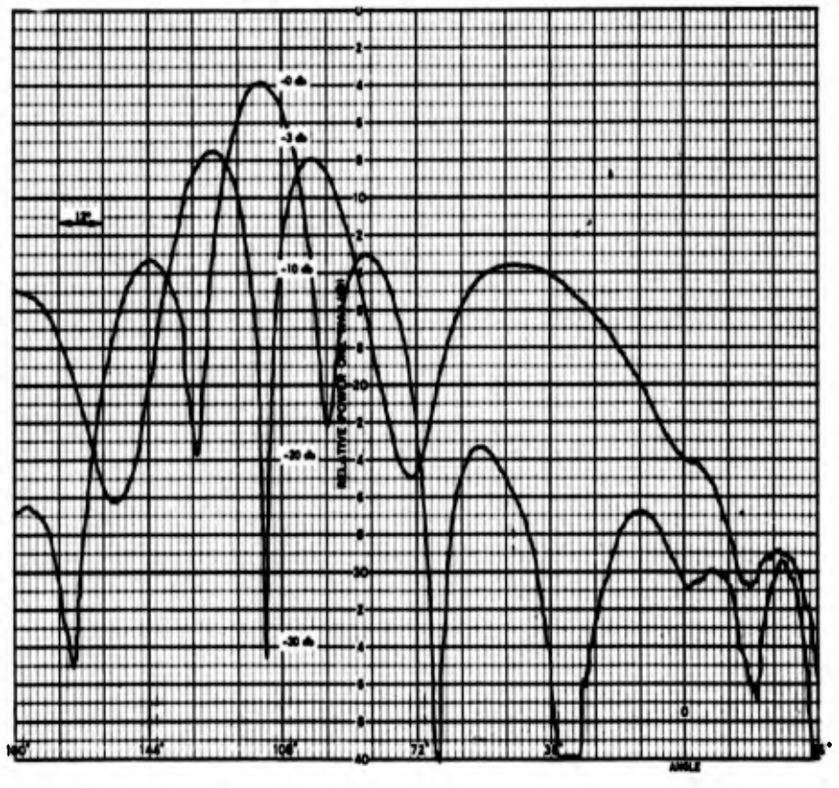

Sum and Difference Patterns - H-Plane (1000 MC) Broadband Monopulse

35421

Figure 20. Typical Experimental Patterns with Two Reflectors Two-Feet in Diameter

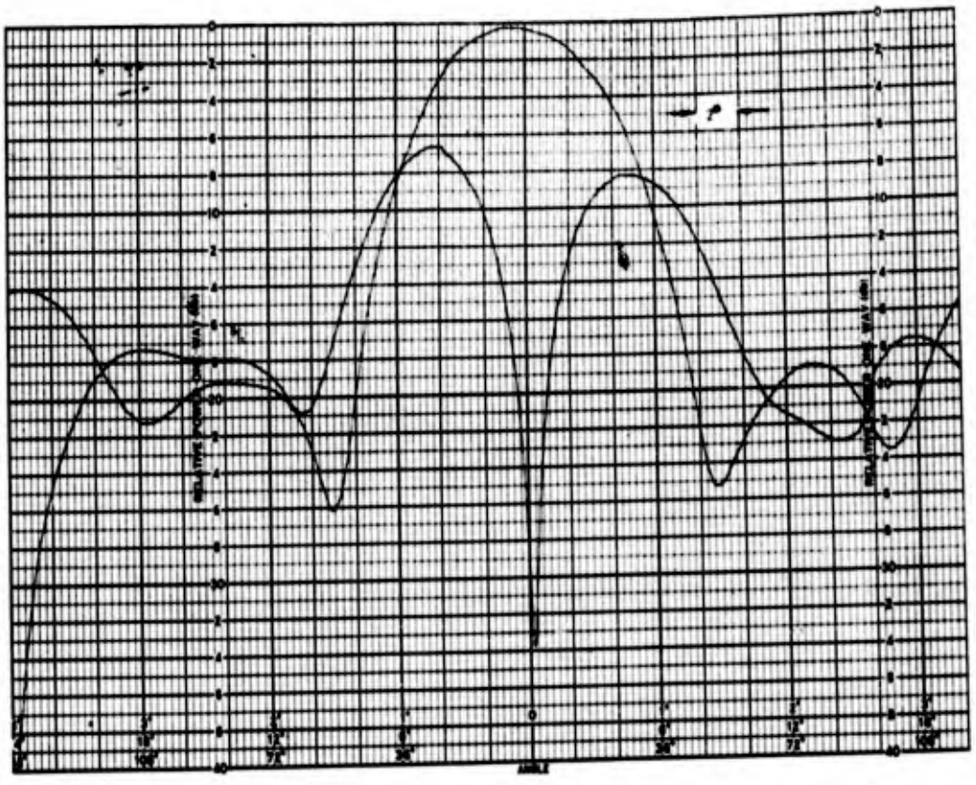

H-Plane patterns, Diamond Array, 4-2ft. diameter reflectors, 2200mc

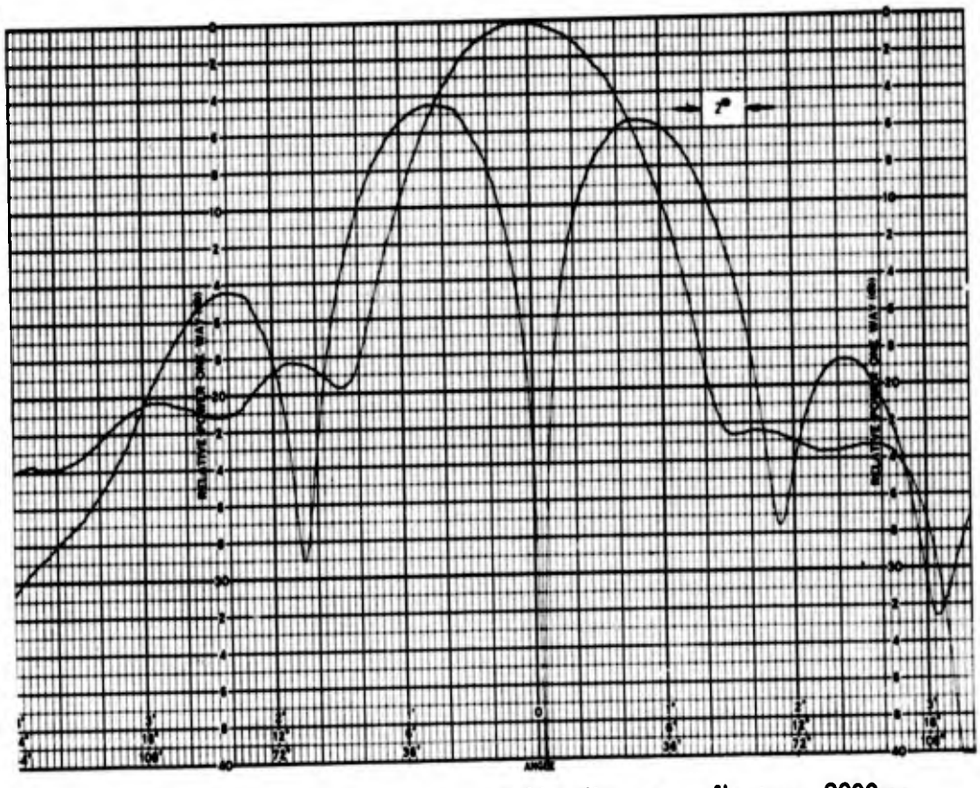

E-Plane patterns, Diamond Array, 4-2ft. diameter reflectors, 2200mc

29855

Figure 21. Experimental Patterns Made with Diamond Array and Two-Foot Diameter Reflectors using Triangular Tooth Feeds F/D = 0.375

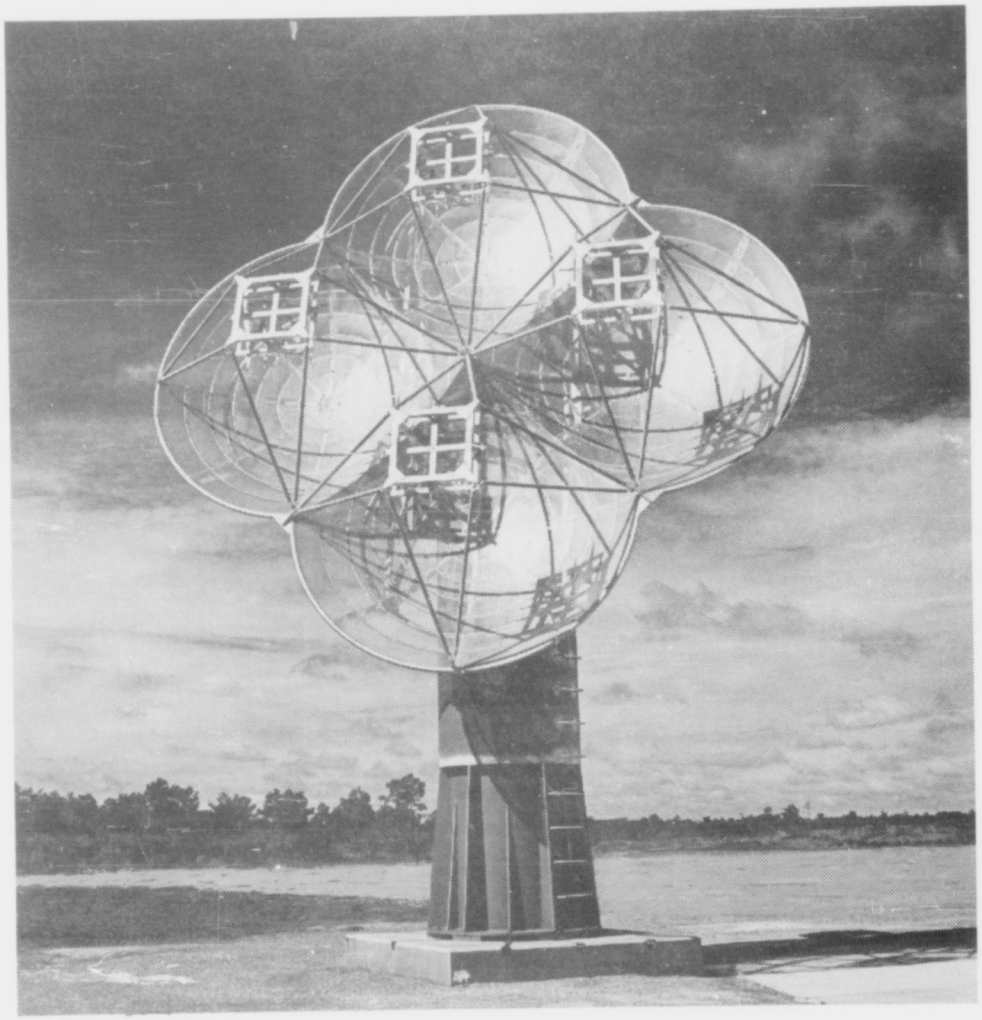

33635

Figure 22. Photograph of Experimental Four-Element Array

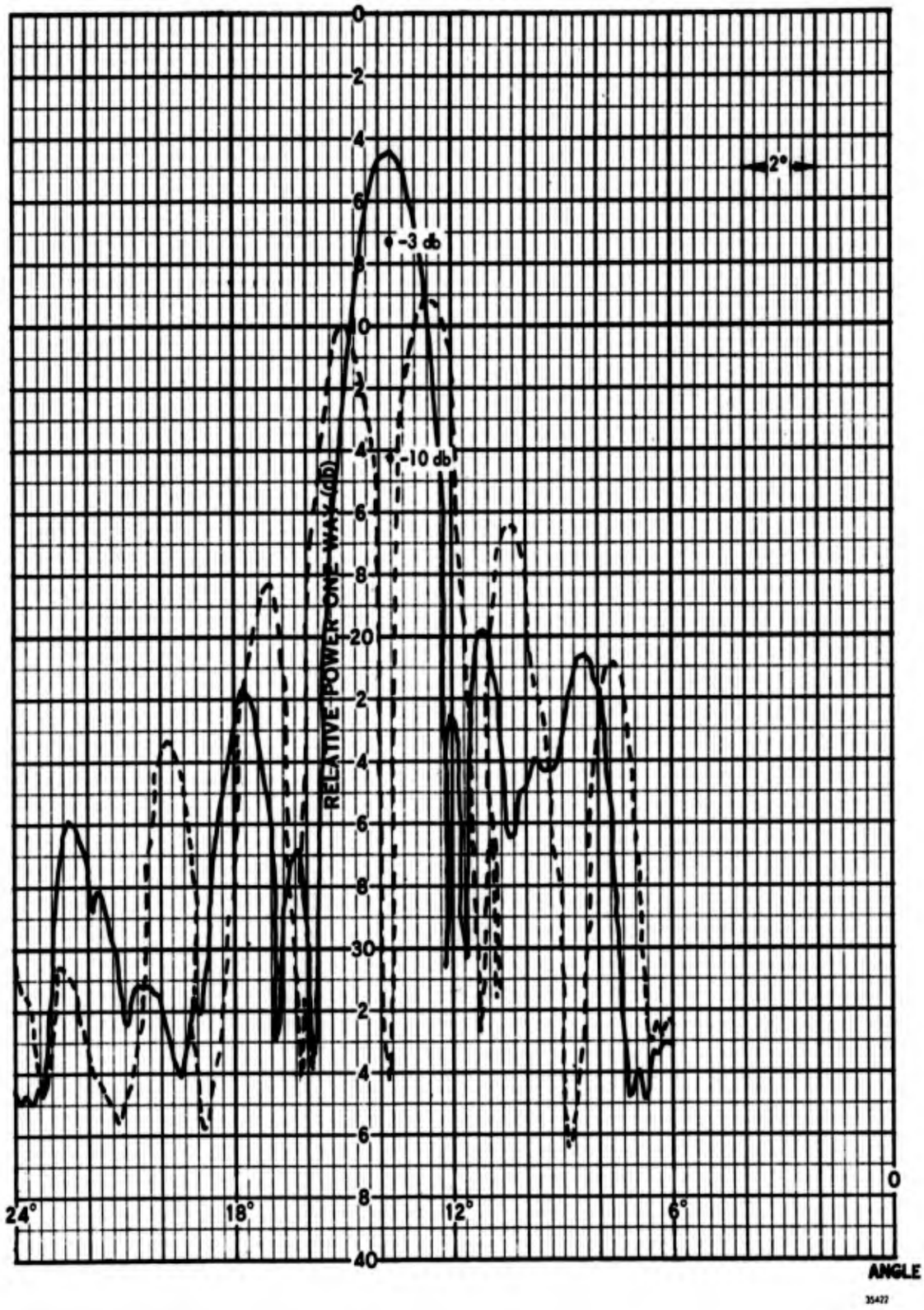

Figure 23. Measured Sum and Difference E-Plane Patterns of Diamond Array Utilizing Four Ten-Foot Diameter Reflectors at 2250 mc. F/D = 0.3

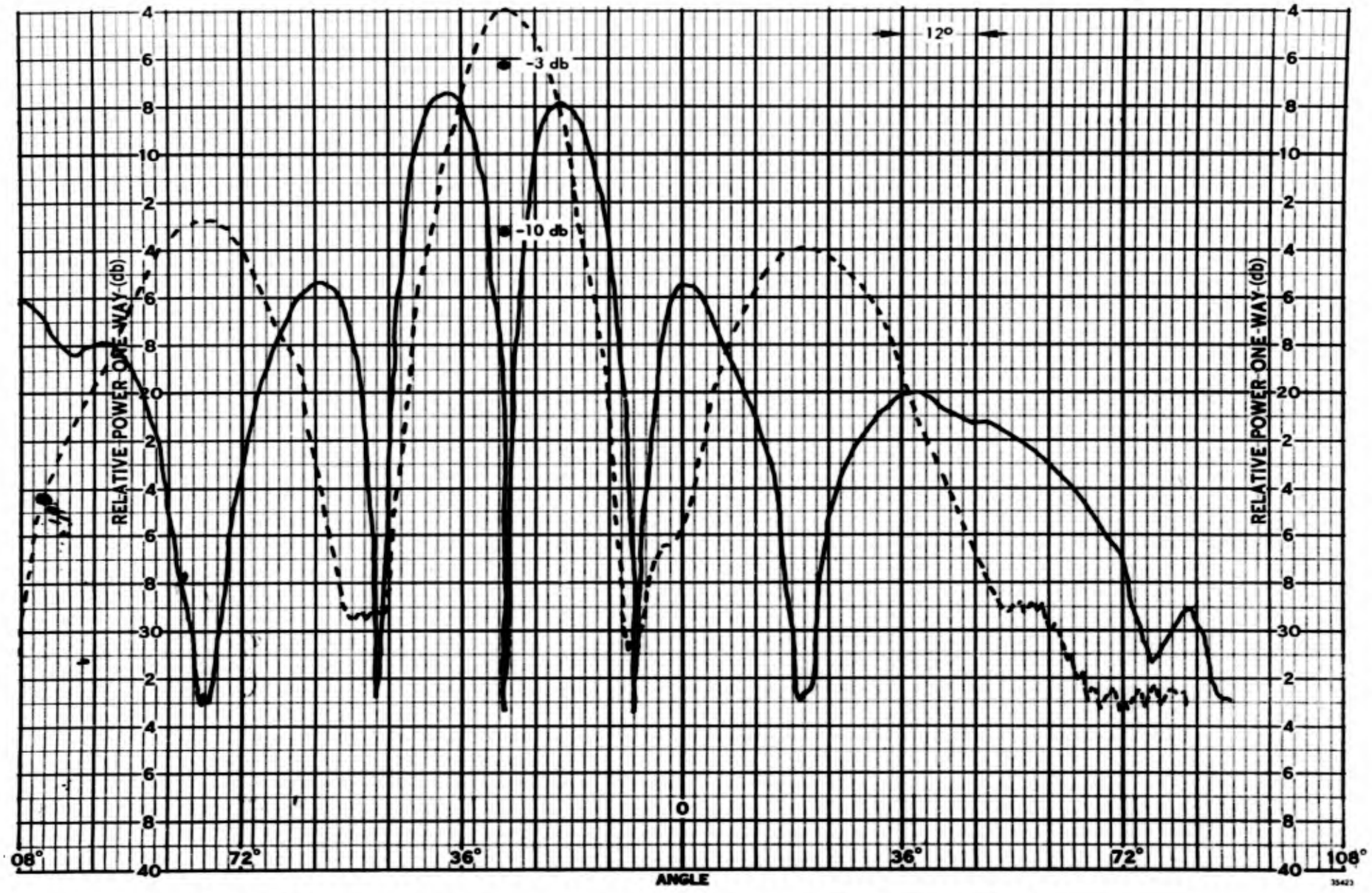

Figure 24 (a). Measured Sum and Difference E-Plane Patterns of Diamond Array Using Ten-Foot Diameter Reflectors at 245 mc

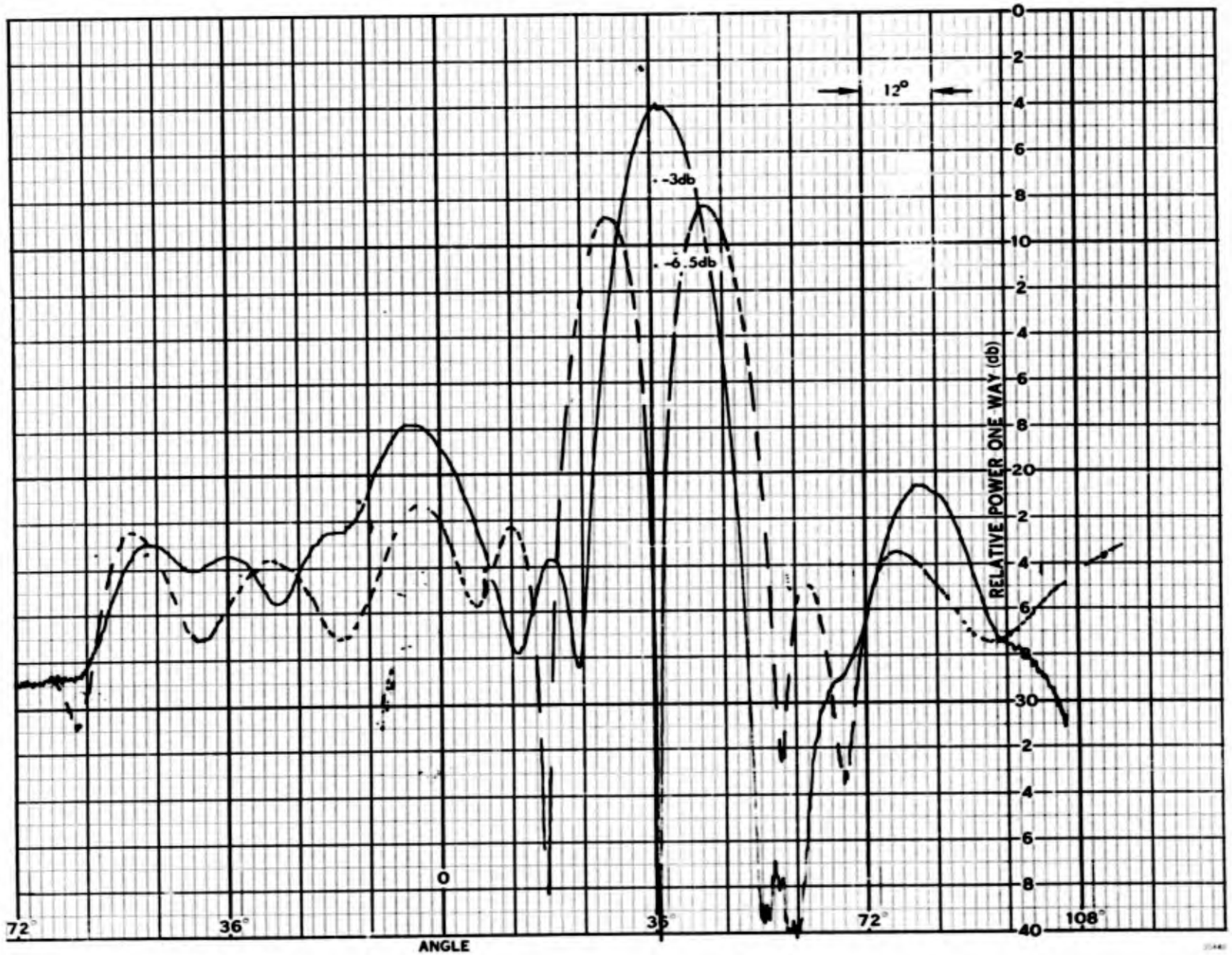

Figure 24 (b). Sum and Difference Measured H-Plane Patterns for Diamond Array of Four Ten-Foot Diameter Reflectors at 245 mc

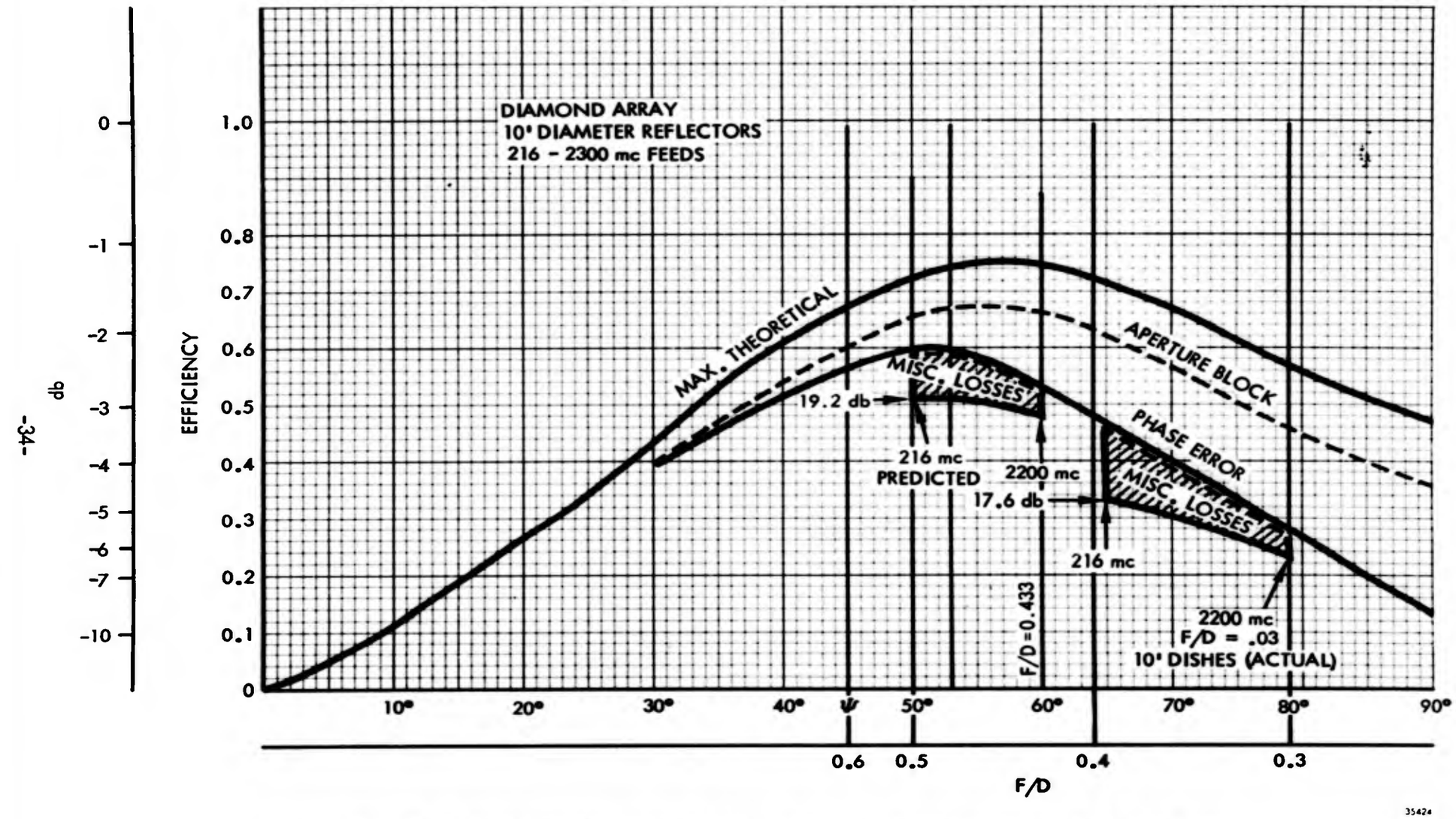

Figure 25. Theoretical Calculated Aperture Efficiency for Array Containing Four Ten-Foot Diameter Reflectors and Improvement to be Expected with Corrected F/D Ratio

to increasing the effective F/D of the antenna. The calculated gain at 245 mcs is approximately 17.6 db, and the gain measured by several methods averaged to approximately the same value. The calculated effect of increasing the F/D of the individual reflectors from 0.3 to 0.433 is shown in the Figure as the top shaded area. It appears that an additional gain of nearly 2 db and aperture efficiency in the order of 50% can be achieved at this higher F/D ratio utilizing the same reflector size and same feeds.

ADVANTAGES

The antenna system possesses a number of distinct advantages over the conventional types of broadband tracking systems utilizing conical scan or amplitude monopulse. Some of these are:

- No moving or rotating parts are required to develop error signal information.
- The primary feed systems are relatively simple, lightweight, and are fixed in position.
- Orthogonal linear polarizations are easily achieved and these can be combined to produce circular polarization of either or both senses.
- The shape of the array structure is more desirable mechanically than a single reflector because the structure is shallower and the center of gravity can be located appreciably closer to the elevation axis. This results in less counterweight and lower moments of inertia which, in turn, will yield better mechanical performance or a more economical structure, or both. Also, wind loading is less.
- With a conventional antenna utilizing a single reflector and feed, feed sag results directly in an angular pointing error. Since the error signals of the phase monopulse system are based on the relative phase of the arriving signals at each feed, feed sag in a plane parallel to the aperture may squint the element patterns slightly but does not produce a comparable boresight shift.

CONCLUSIONS

The antenna array described is capable of operating over a frequency band of a decade or more and it utilizes the full aperture at all frequencies. Sum and difference patterns can be used to generate error signal information by conventional phase monopulse methods. The calculations show that the electrical performance, in terms of sidelobes and aperture efficiency, is a function of F/D, aperture block, feed characteristics, and the physical size of the reflectors in terms of wavelength.

Although the experimental results using the four 10-foot diameter reflectors agreed quite well with the predicted theoretical values the calculations indicated that the F/D was not optimum and considerable improvements should result when a larger value of F/D is used.

ACKNOWLEDGEMENTS

The author wishes to acknowledge the many contributions made to this program by various members of the RF Division, Radiation Incorporated, and particularly to Marvin Livingston for his work on the feed system and William Corry for the mechanical design.

REFERENCES

1. Bresler, A. D., Jaski, H., Kampinsky, A., "A Wide Band Conical Scan Antenna Feed System", Microwave Journal, Vol. 4, No. 12, Dec. 1961, pg. 97-104.

2. DuHamel, R. H., and Ore, F. R., "Log-Periodic Feeds for Lens and Reflectors", 1959 IRE National Convention Record, Part 1, pp 128-137.

3. Webster, R. E., Lyles, J. F., "Application of Frequency Independent Feeds to Automatic Tracking Antennas" Abstract of the Eleventh Annual USAF Antenna Research and Development Program, Oct. 1961.

4. Dyson, J. D., "An Antenna to Cover the 220 through 2400 mc Telemetry Bands", Proc. of the 1962 National Telemetering Conference, Vol. 1, Sect. 9-4, May 23-25, 1962.

5. DuHamel, R. H., Berry, D. G., "Logarithmically Periodic Antenna Arrays", IRE Wescon Convention Record 1958.

6. Williams, L. E., "The Case for the Big Dish", GSE Magazine, Vol. 2, No. 5, Oct/Nov 1960.

7. Potter, P. D., "The Aperture Efficiency of Large Paraboloidal Antenna as a Function of their Feed-System Radiation Characteristics", Jet Propulsion Lab., Technical Report No. 32-149, 25 Sept. 1961.

8. Silver, S., "Microwave Antenna Theory and Design", Radiation Lab. Series, Vol. 12, McGraw-Hill Book Co., Inc. 1949.

THE BACKFIRE BIFILAR HELICAL ANTENNA

W. T. Patton*
University of Illinois
Urbana, Illinois

ABSTRACT

The backfire bifilar helical antenna, consisting of two opposed helical wires fed with balanced currents at one end, is a new type of circularly polarized antenna. Operated above the cutoff frequency of the principal mode of the helical wave guide, the bifilar helix produces a beam directed along the structure toward the feed point. The term "backfire" is used in contrast with "endfire" which denotes radiation away from the feed point.

Radiation patterns, measured for a wide range of helix parameters, show maximum directivity slightly above the cutoff frequency. The pattern broadens with frequency, and, for pitch angles near 45 degrees, the beam splits and scans toward the broadside direction.

Near-field measurements show the current decaying rapidly to a level about 20 decibels below the feed-point level at a rate that increases with frequency. Phase measurements show that the feed-region current has a backward-wave character. The measured phase progression is toward the feed point, while the energy flows away from the feed point.

A theoretical analysis has been obtained. It is based upon the semi-infinite model, using linearizing assumptions. These assumptions consist of replacing the wires with a current at their center lines and satisfying the boundary conditions along one line of the conducting surface. The results predict the patterns of the experimental study and show the effect of wire size on antenna performance.

---

* Radio Corporation of America, Moorestown, New Jersey. Formerly with Antenna Laboratory, University of Illinois, Urbana, Illinois.

1. INTRODUCTION

The backfire bifilar helical antenna shown in Figure 1 is constructed of two helical wires wound on a right circular cylinder with a constant pitch angle ψ. At any cross section the wires appear at the ends of a diameter of the cylinder. At the feed point the wires are brought inward along a diameter to a balanced transmission line on the helical axis. The helical conductors extend beyond the feed point for seven to fifteen turns depending upon the frequency of operation. The exact length of the antenna is not a critical factor in its performance.

The backfire bifilar helical antenna is distinguished from the endfire helical beam antenna of Kraus[1] by the method of feed and the direction of radiation. The Kraus type helix is fed against a ground screen at one end and the radiated beam is directed along the structure away from the feed point.

The study of the backfire antenna is a part of a larger investigation of the properties of periodic radiating structures. The investigation of periodic structures was started in an effort to learn more about the behavior of log-periodic antennas[2-4]. In this connection it has been suggested[5] that the properties of a log-periodic antenna, as a function of distance from the apex, are related to those of a periodic structure whose period is given by the local period of the log-periodic structure. In this sense, the bifilar helix is an analog of the two arm equiangular spiral antenna[4]. This antenna and periodic antennas in general, however, have many useful properties and deserve study in themselves.

The portion of a log-periodic antenna, nearest the feed point at or near the apex of the structure, acts as a transmission line carrying the energy to the larger portion. The energy is carried to the so-called "active region"

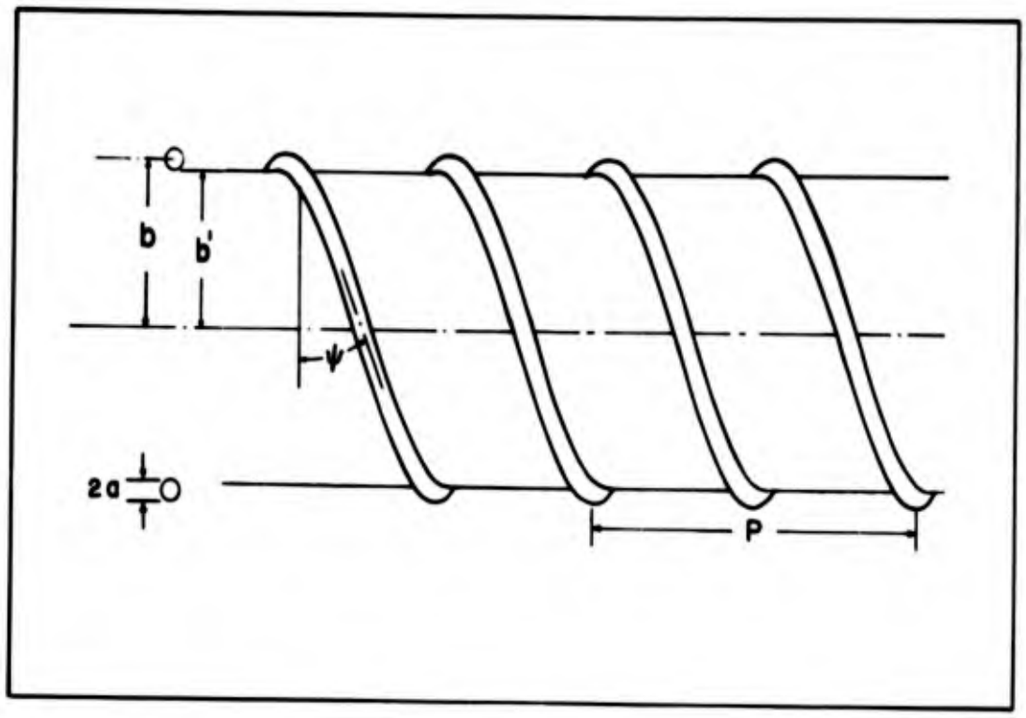

Figure 1. The geometry of the bifilar helix

of the structure whose position and size varies inversely with frequency. This region is thought to be primarily responsible for the radiation from the structure. Beyond this region the current decays very rapidly with distance. The direction of the main beam of a log-periodic antenna is along the structure toward the feed point. It can be shown that if the antenna radiated in the direction of the structure, the current would not decay rapidly enough to avoid a large reflection from the large-end truncation of the structure. These characteristics of the log-periodic antenna are observed for the bifilar helix when variation of distance from the apex is replaced with a variation of frequency.

2. THE HELICAL WAVE GUIDE

The operation of a helix as a wave guide is well known[6,7]. The propagation constant of the current relative to axial displacement, is given approximately by

$$\beta = k/\sin\psi$$

until the edge of the visible range is reached, that is, until

$$k/\sin\psi = \tau - k$$

where

$$\tau = 2\pi/p$$

$$p = \text{pitch of helix}$$

This equation defines the cutoff frequency of the principal wave guide mode for infinitely thin helical conductors. This critical frequency, normalized

with respect to τ, is called x to avoid confusion with the critical frequency, k_c; for finite-size helical conductors. It is given explicitly by

$$x = \frac{\sin \psi}{1 + \sin \psi}$$

The critical frequency marks the boundary between the frequency range for which the helical structure is primarily a wave guide and that for which it is a backfire antenna.

Several models of the bifilar antenna were constructed for a range of x between 0.05 and 0.4. The physical dimensions of these models are given in Table I. These are based upon a frequency of 1.5 Gc. The pitch of the helix is determined from the wavelength at the base frequency by

$$p = x \lambda$$

The pitch angle is given by

$$\psi = \sin^{-1}\left(\frac{x}{1 - x}\right)$$

and the mean radius of the helix is given by

$$b = \frac{\lambda}{2\pi}\sqrt{1 - 2x}$$

The dispersion curves for these models were obtained by sampling the fields near the antenna by a current loop moving parallel with the helical axis. A typical amplitude response of this loop as a function of distance from the feed point is shown in Figure 2. Below the critical frequency the propagation constant of the wave guide mode is determined easily by the standing wave on

TABLE I

The Physical Parameters of the Experimental Models of the Bifilar Helical Antenna

Code Name		Pitch p(CM)	Radius b(CM)	Relative Wire Size δ*	Pitch Angle ψ (degrees)
BBH-1	0.1	2	2.663	.0227	6.38
BBH-2	0.15	3	2.847	.0242	10.18
BBH-3	0.2	4	2.465	.02620	14.49
BBH-4	0.25	5	2.251	.0287	19.47
BBH-5	0.30	6	2.013	.0323	25.37
BBH-6	0.35	7	1.743	.0371	32.60
BBH-7†	0.40	16	2.85	.0226	41.82

* No. 16 AWG tinned copperwire was used in the construction of the models.

† The base frequency for this model was changed from 1.5 Gc to .75 Gc for mechanical reasons.

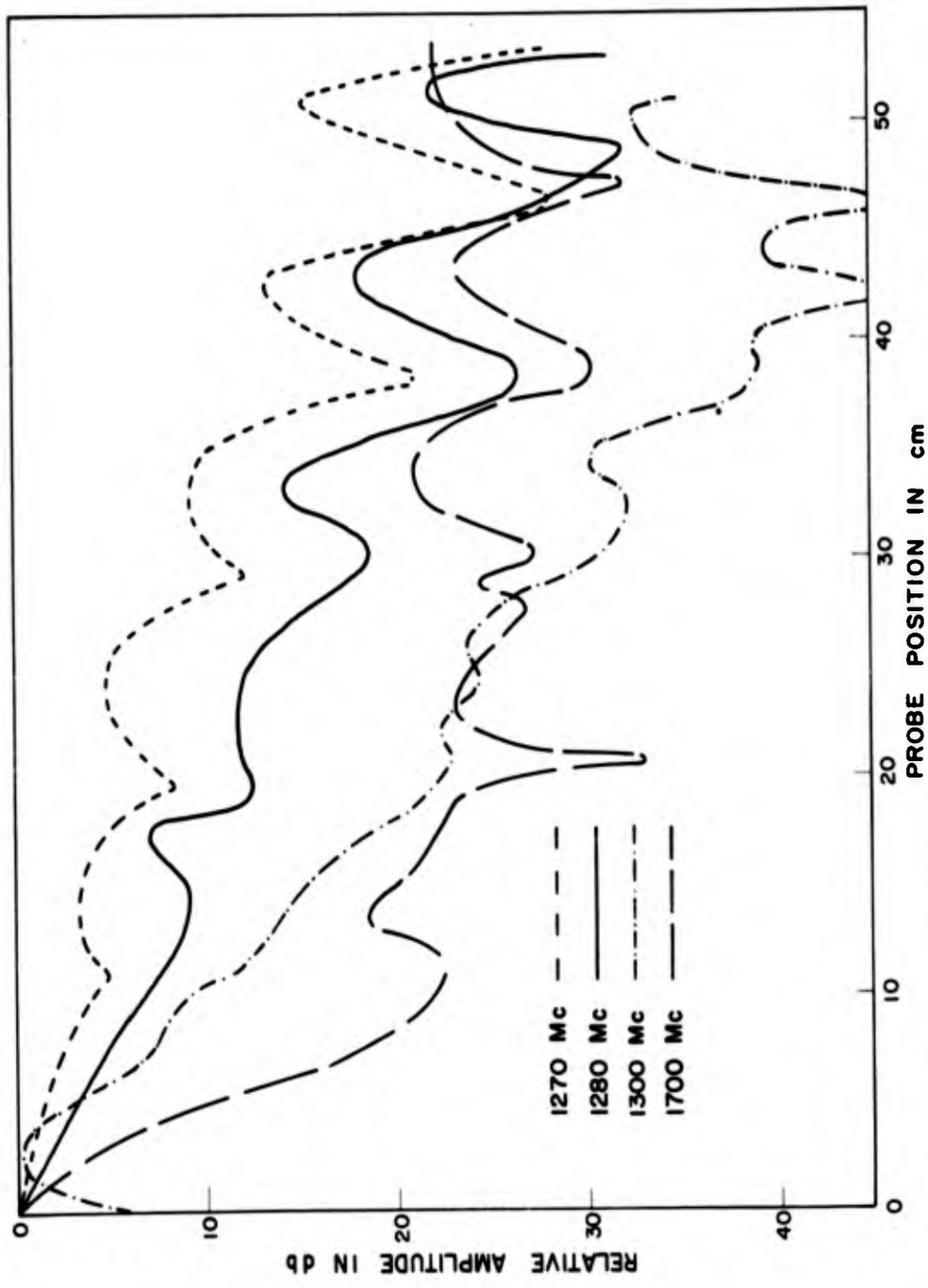

Figure 2. Current amplitude distribution above the critical frequency

the structure. The propagation constants measured in this way are shown in Figure 3. It is noted that the cutoff frequency for each of these models is below x due to the finite wire thickness. The cutoff frequencies for the models used in this investigation are plotted as a function of ψ in Figure 4.

The dispersion curve for a periodic structure has been called the Brillouin diagram. A typical computed Brillouin diagram is shown in Figure 5. The dispersion curve departs from the asymptotes near the critical frequency by an amount depending upon the relative wire size, δ, which is the ratio of wire radius, a, to mean helix radius b. The Brillouin diagram for the bifilar helix represents the roots of the determinantal equation

$$Z(\beta) = (\beta^2 - k^2) \sum_{n \text{ odd}} B_n(\beta) - \frac{k^2 \cot^2 \psi}{2} \sum_{n \text{ even}} [B_n(\beta-\tau) \cdot B_n(\beta-\tau)]$$

where

$$B_n(\beta) = I_n(b' \gamma_n) K_n(b\gamma_n)$$

$$\gamma_n = \sqrt{(\beta + n\tau)^2 - k^2}$$

$$b' = b - a = (1-\delta) b$$

A more convenient form of this equation for graphical solution is

$$\frac{\sum_{n \text{ even}} [B_n(\beta+\tau) + B_n(\beta-\tau)]}{2 \sum_{n \text{ odd}} B_n(\beta)} = \text{Tan}^2 \psi \quad \frac{\beta^2}{k^2} - 1$$

A typical solution of this expression is presented in Figure 6 where

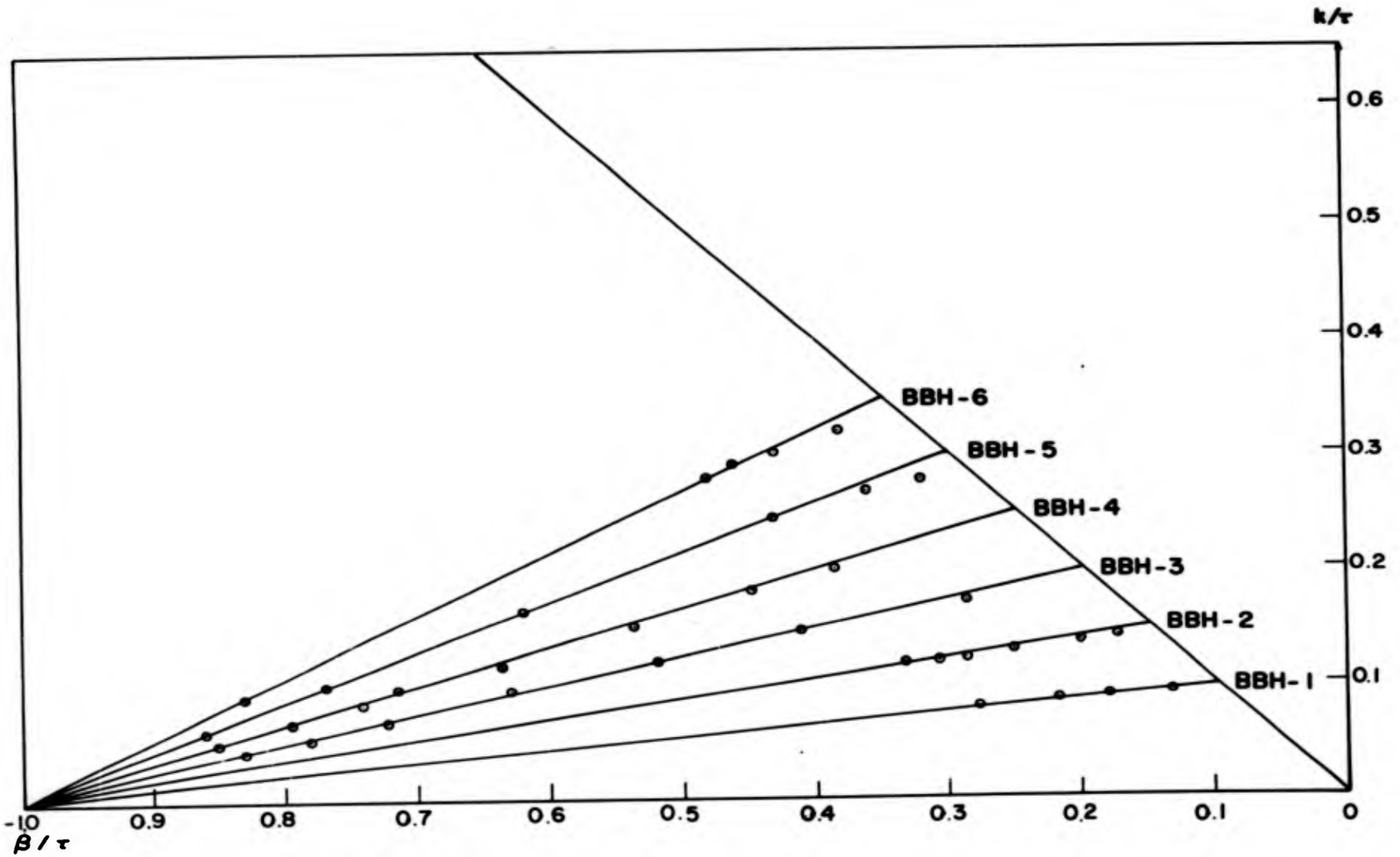

Figure 3. Measured propagation constants of the principal waveguide mode on the bifilar helix

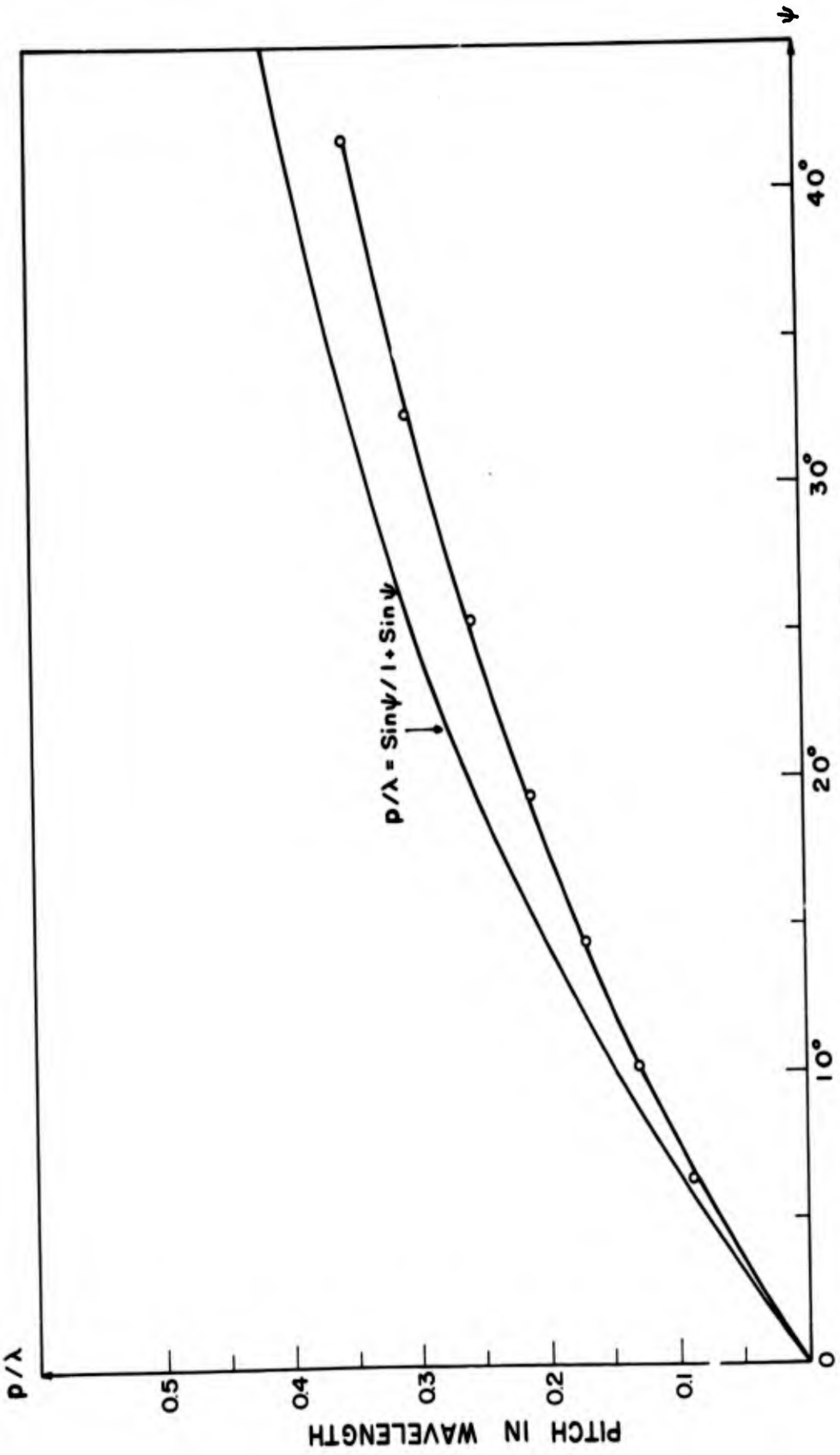

Figure 4. Measured values of the principal-mode cut-off frequency for the bifilar helix

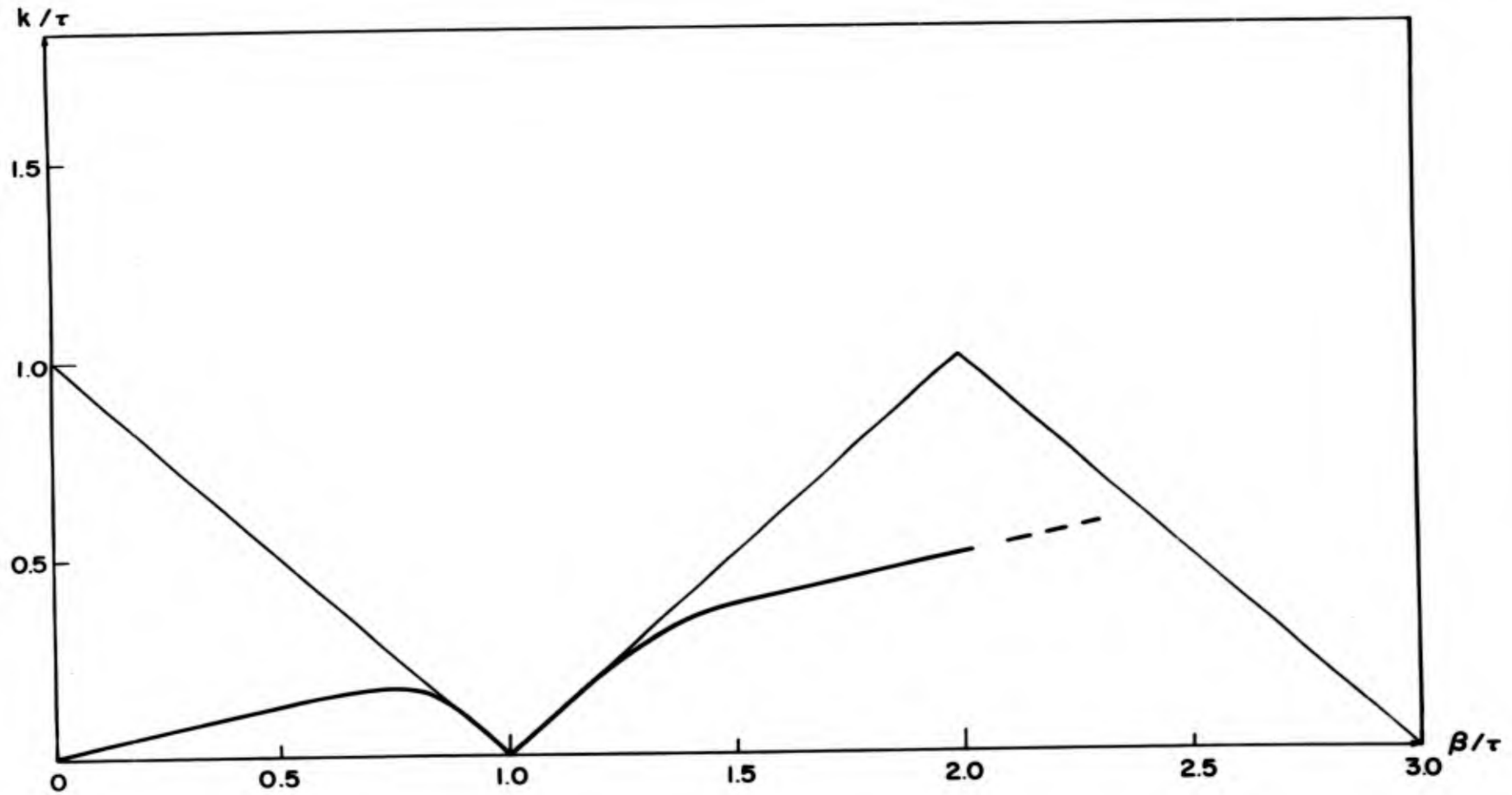

Figure 5. Brillouin diagram for a monofilar helical waveguide

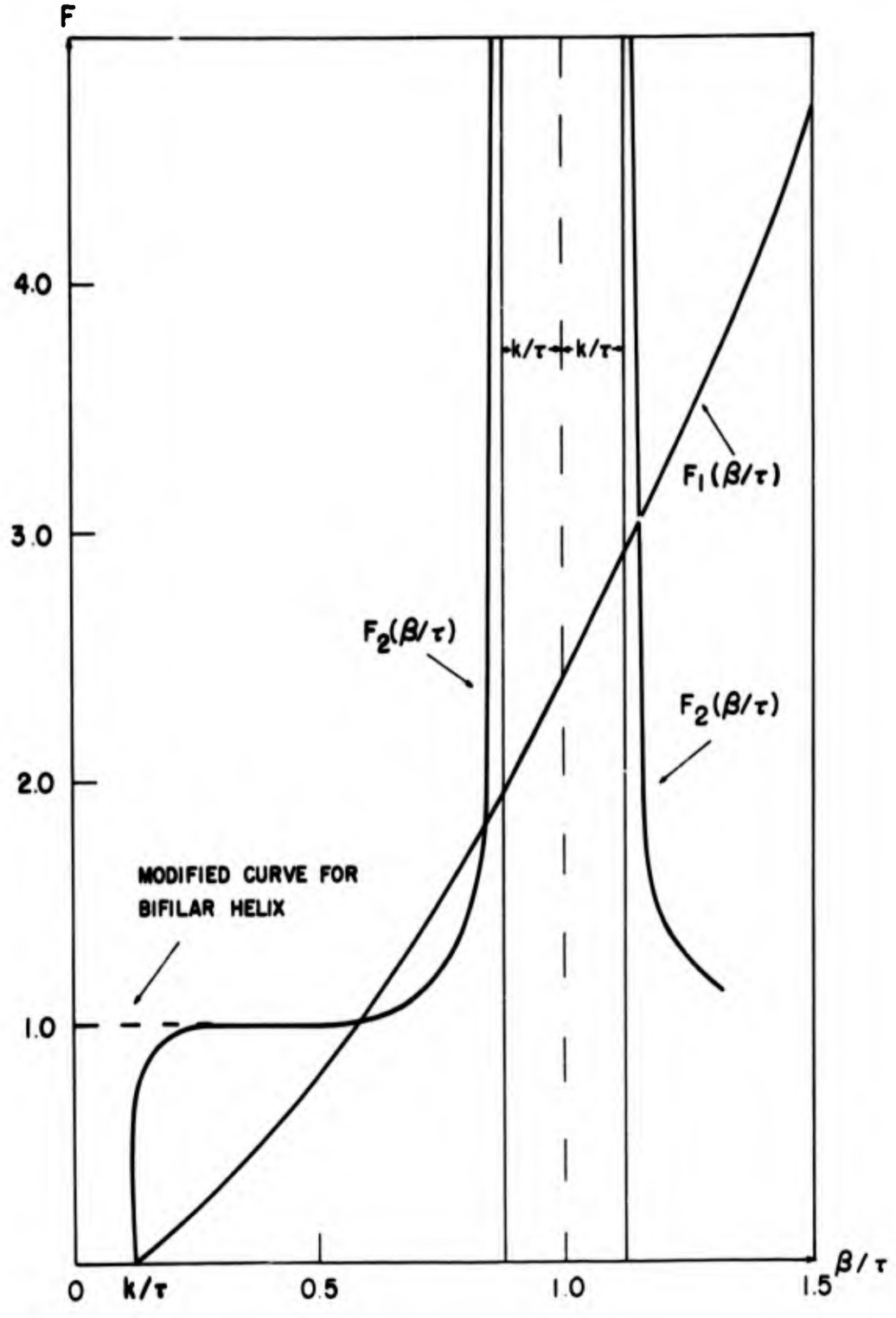

Figure 6. Graphical solution for the roots of the helix determinantal equation when $k < k_c$

$$F_2 = \frac{\sum_{n\ \text{even}} [B_n(\beta+\tau) + B_n(\beta-\tau)]}{2 \sum_{n\ \text{odd}} B_n(\beta)}$$

and

$$F_1 = \tan^2 \psi \left[\frac{\beta^2}{k^2} - 1 \right]$$

It can be seen in Figure 6 that F_2 is approximately one except near

$$\beta = \tau \pm k$$

where F_2 becomes logarithmically infinite. The curvature of F_2 near these singular points causes the Brillouin diagram to depart from its asymptotes.

An unusual feature of the standing wave pattern of the wave guide mode on the bifilar helix was noted during the course of the measurements. The apparent guide wavelength increases with frequency from a minimum at zero frequency equal to the pitch of the helix to a maximum, somewhat less than the free space wavelength, at the cutoff frequency. This indicates that the principal mode on the bifilar helix is a backward wave. The phase constant decreases with increasing frequency, and therefore, the phase velocity and group velocity must have opposite signs.

The measured and computed Brillouin diagrams can be brought into agreement by shifting the axis by $\beta = \tau$. The computed curve corresponds to a phase measurement along the wire while the experimentally derived diagrams were measured along the helical axis. The additional phase shift of 2π radians per pitch distance results from the curvature of the wire. This is just the phase shift one obtains in rotating a linear element through a circle in a

circularly polarized field. Thus while the current represents a forward wave along the helical wires, the fields associated with this current are backward waves.

3. THE BACKFIRE HELICAL ANTENNA

It can be seen in Figure 2 that, above the cutoff frequency, the standing-wave has vanished and is replaced with a wave with decaying amplitude distribution. As frequency is increased, the rate of decay increases. This is shown in greater detail in Figure 7. At these higher frequencies, a standing-wave distribution again appears with a maximum amplitude about twenty decibels below the input level. This is the higher-order helical wave guide mode. The excitation of this mode increases with frequency from a negligible level near the cutoff frequency of the principal mode. The development of this mode places an upper limit on the frequencies for which the bifilar helix behaves as a backfire antenna.

Phase measurements made in the near field above the cutoff frequency are shown in Figure 8. In this figure the phase is normalized to the free space propagation constant and is plotted in centimeters. The first curve shows that the phase is leading as the probe moves away from the feed point. In other words, the direction of phase progression is toward the feed point. The first curve, slightly above the critical frequency, k_c, shows leading phase over most of the length of the structure. As frequency is increased, the direction of phase progression near the end of the structure changes and is away from the feed point. The point at which the phase progression changes from leading to lagging moves toward the feed point as frequency is increased. This corresponds to the point at which the feed region currents have decayed to the level of the higher order helical wave guide mode.

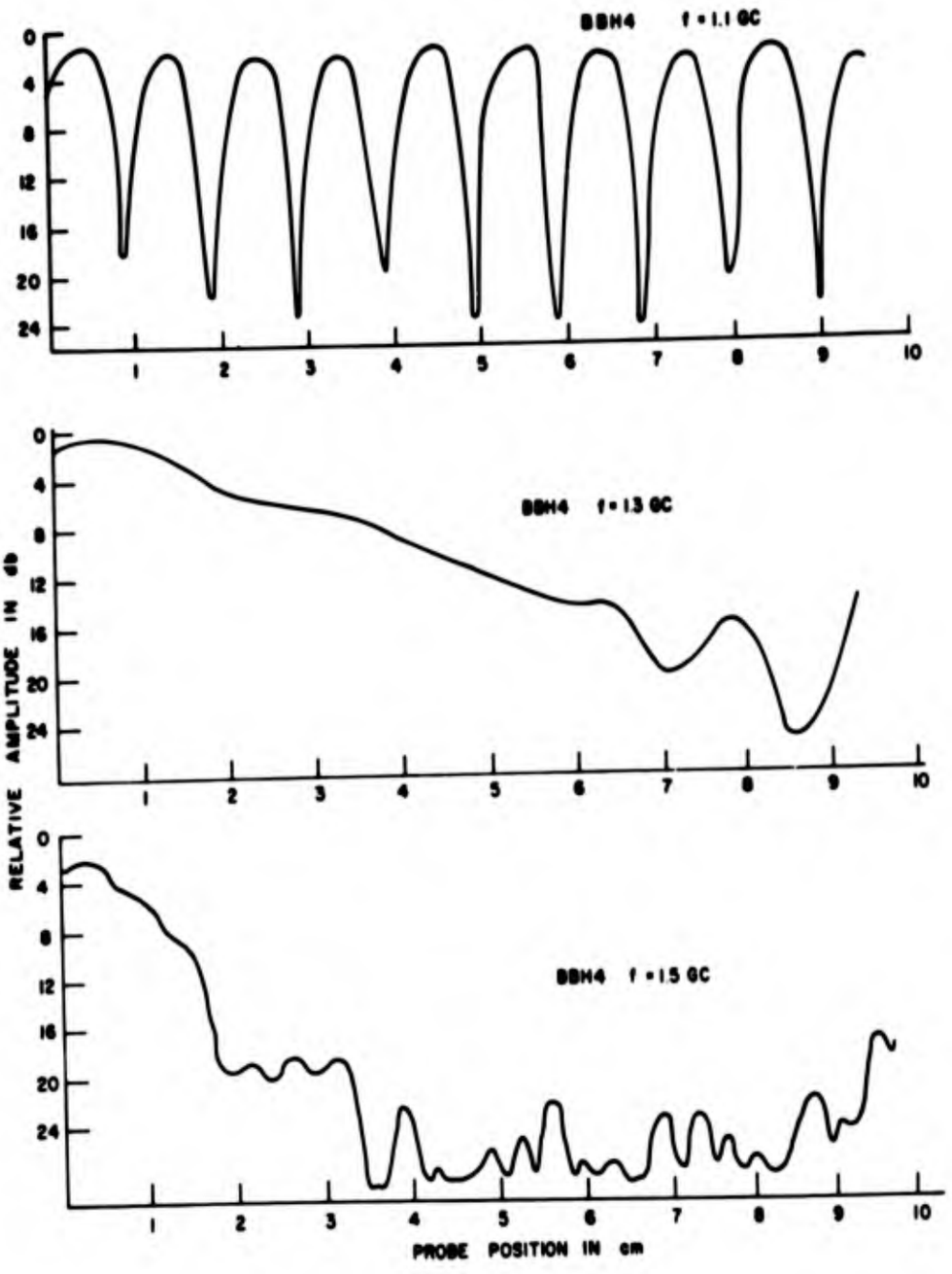

Figure 7 Current amplitude distribution on a bifilar helix

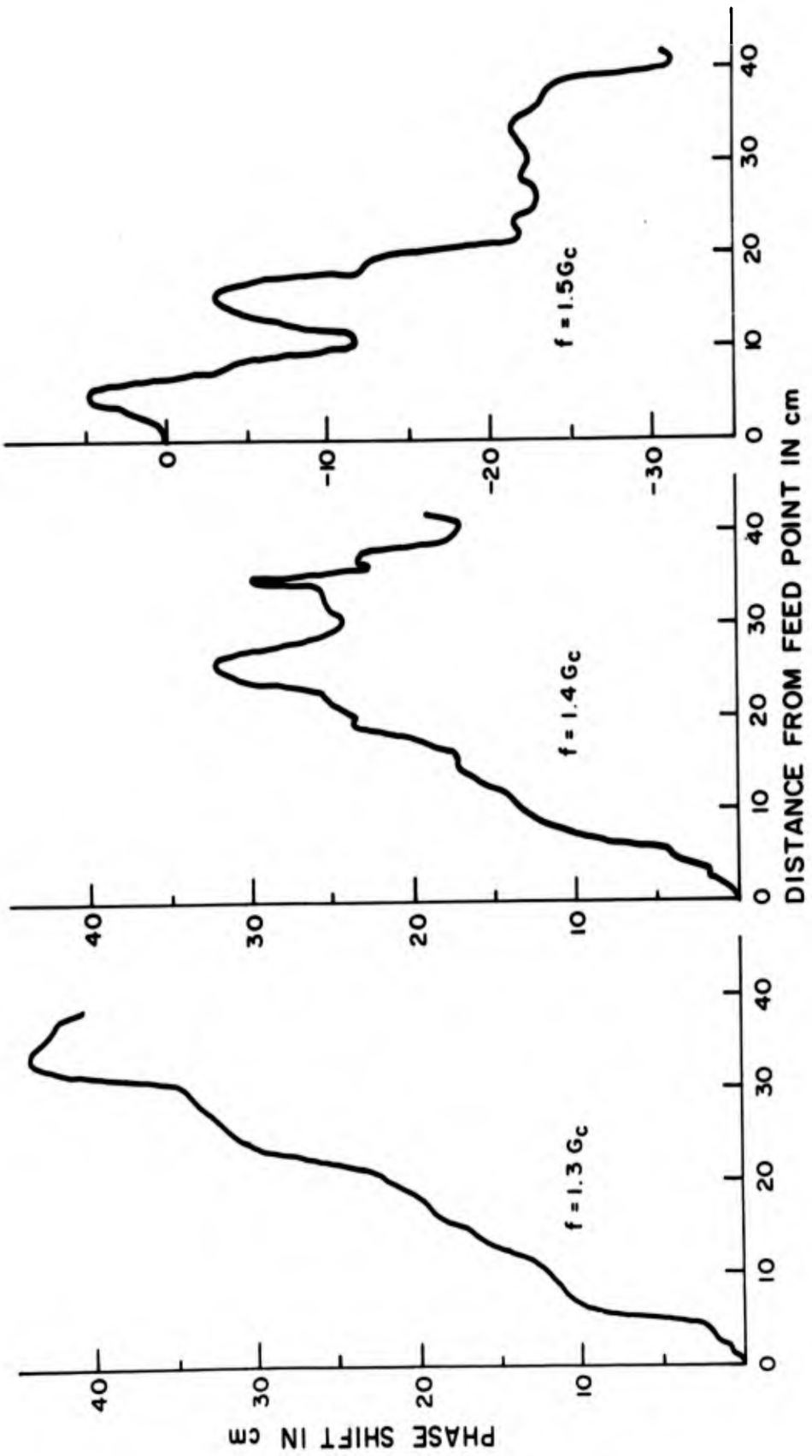

Figure 8. Near-field phase measurements for the bifilar helix BBH-4

The near field phase measurements indicate that, although it does not correspond to a proper mode, the feed region current has a backward wave character above critical frequency. The leading phase characteristic persists as long as the feed region current is dominant on the structure. On the remainder of the structure the higher order mode, with its lagging phase or forward-wave characteristic, dominates the current distribution. The fact that in the feed region the direction of phase progression is toward the feed point is consistent with the "backfire" radiation of the bifilar helical antenna, since an antenna tends to radiate in the direction of the phase progression of the current

The measured radiation patterns for the backfire bifilar helical antennas are presented in Figure 9 The patterns are plotted so that their centers give the helix radius and pitch in wavelengths at the frequency for which the pattern was measured. Two curves are also provided for reference to the Brillouin diagram for the bifilar helix The curve

$$\frac{b}{\lambda} = \frac{\sqrt{1 - 2\frac{p}{\lambda}}}{2\pi}$$

gives the frequency at which the propagation-constant asymptote

$$\beta = k/\sin\psi$$

intersects the edge of the visible range given by

$$\beta = \pi - k$$

This corresponds to the cutoff frequency of the principal mode on the helical wave guide with infinitely thin conductors The curve

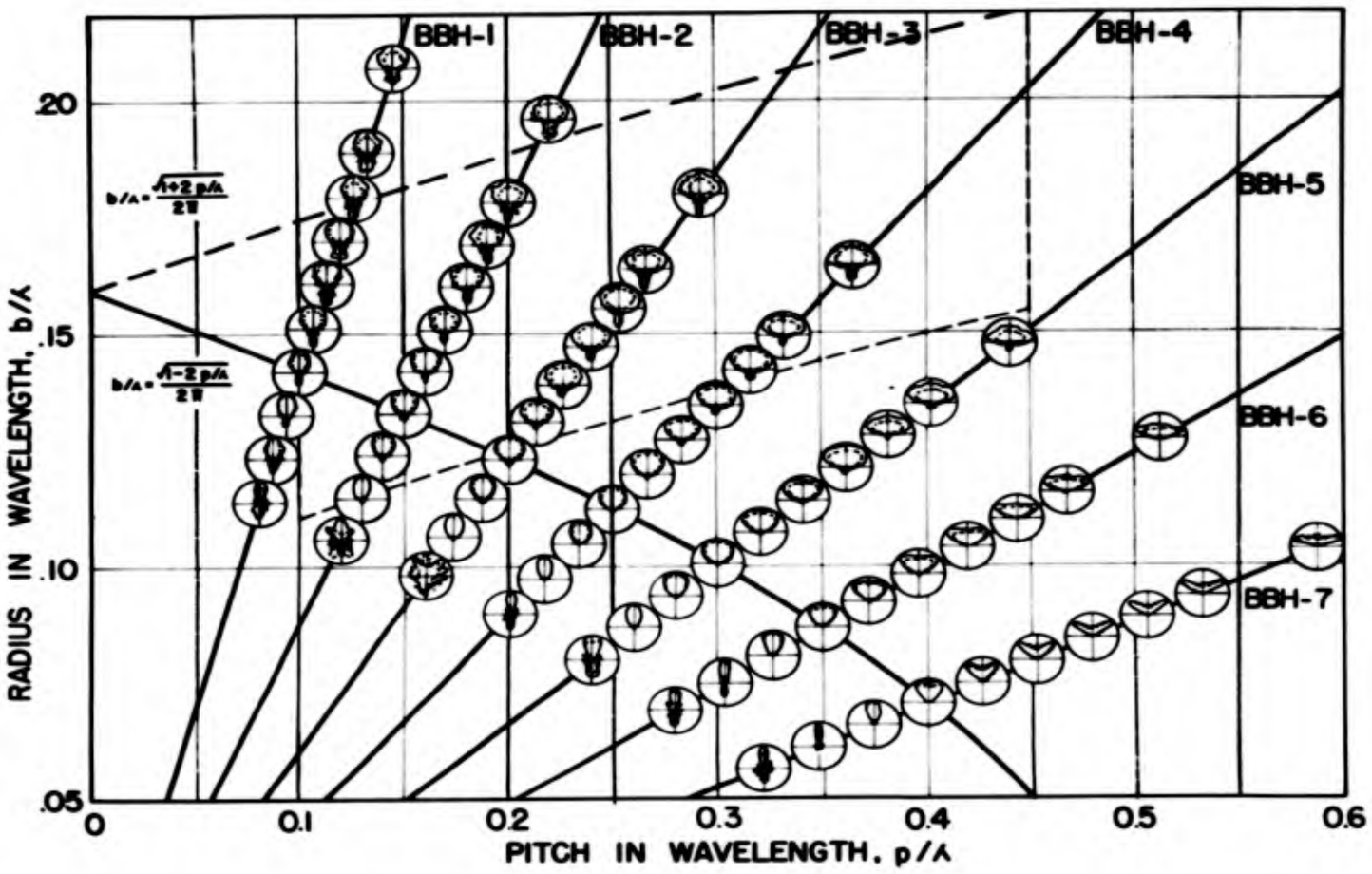

Figure 9. Measured radiation patterns of the backfire bifilar helical antenna

$$\frac{b}{\lambda} = \frac{\sqrt{1 + 2\frac{p}{\lambda}}}{2\pi}$$

gives the frequency for which the propagation-constant asymptote intersects the edge of the visible range given by

$$\beta = \tau \cdot k$$

This curve is given by Kraus[8] as the upper frequency limit for beam mode operation of the Kraus-type helical antenna. The range of parameters for this antenna, given by Kraus, is indicated by the broken line

The critical frequency can be determined by studying the radiation patterns shown in Figure 9. As the critical frequency is approached from above, the patterns show increasing directivity characterized by a single lobe with little or no "endfire" radiation or "back lobe". Below the critical frequency, the patterns have many lobes, and the pattern shape changes rapidly with frequency. This indicates the standing-wave current distribution on the antenna. As the frequency is increased, the patterns tend to broaden and, for larger pitch angles, tend to form a split beam. This is due to two effects: first, the phase velocity in the feed region tends to become faster than light velocity, and second, the rate of current decay increases, decreasing the effective aperture of the antenna. The splitting of the main beam is not observed for smaller pitch angles because the effective aperture is too small to form distinct beams. For larger pitch angles the rate of current decay is smaller, and the larger effective aperture can produce a well defined beam.

4. ENDFIRE RADIATION FROM THE BACKFIRE HELIX

Endfire radiation from the backfire bifilar helical antenna is due to the higher order wave guide mode. The extent of its contribution is controlled by the length of the antenna and the excitation of this mode. The excitation of the higher-order mode is inversely proportional to derivative of $Z(\beta)$ at the root, β_o, of the determinantal equation corresponding to this mode. Since $Z(\beta)$ is logarithmically singular at $\beta_1 = \tau \cdot k$, the slope of $Z(\beta)$ is large when β_o is near β_1. The excitation of the higher-order mode is small when β_o is near β_1. This occurs at the critical frequency. The value of β_o and with it the excitation of the higher order mode increase with frequency above the cutoff frequency. This is also evident in the near-field amplitude measurements.

Typical patterns showing the effect of helix length are shown in Figure 10. The size of the back lobe decreases with decreasing length with little change in the main beam until the antenna becomes too short to support the feed region current. Shortening the antenna beyond this point will generally broaden the main beam pattern. Front-to-back ratios obtained for several lengths are shown in Figure 11. The sinusoidal curve in this figure represents the predicted radiation of the higher order mode as a function of antenna length.

At frequencies well above the critical frequency there is an optimum length for the backfire bifilar helical antenna for each frequency. This optimum length is just that required to support the feed region current. A longer length will decrease the front-to-back ratio. At frequencies near the critical frequency the feed region current penetrates the structure to a much greater length. The lowest frequency that can be used in the backfire mode

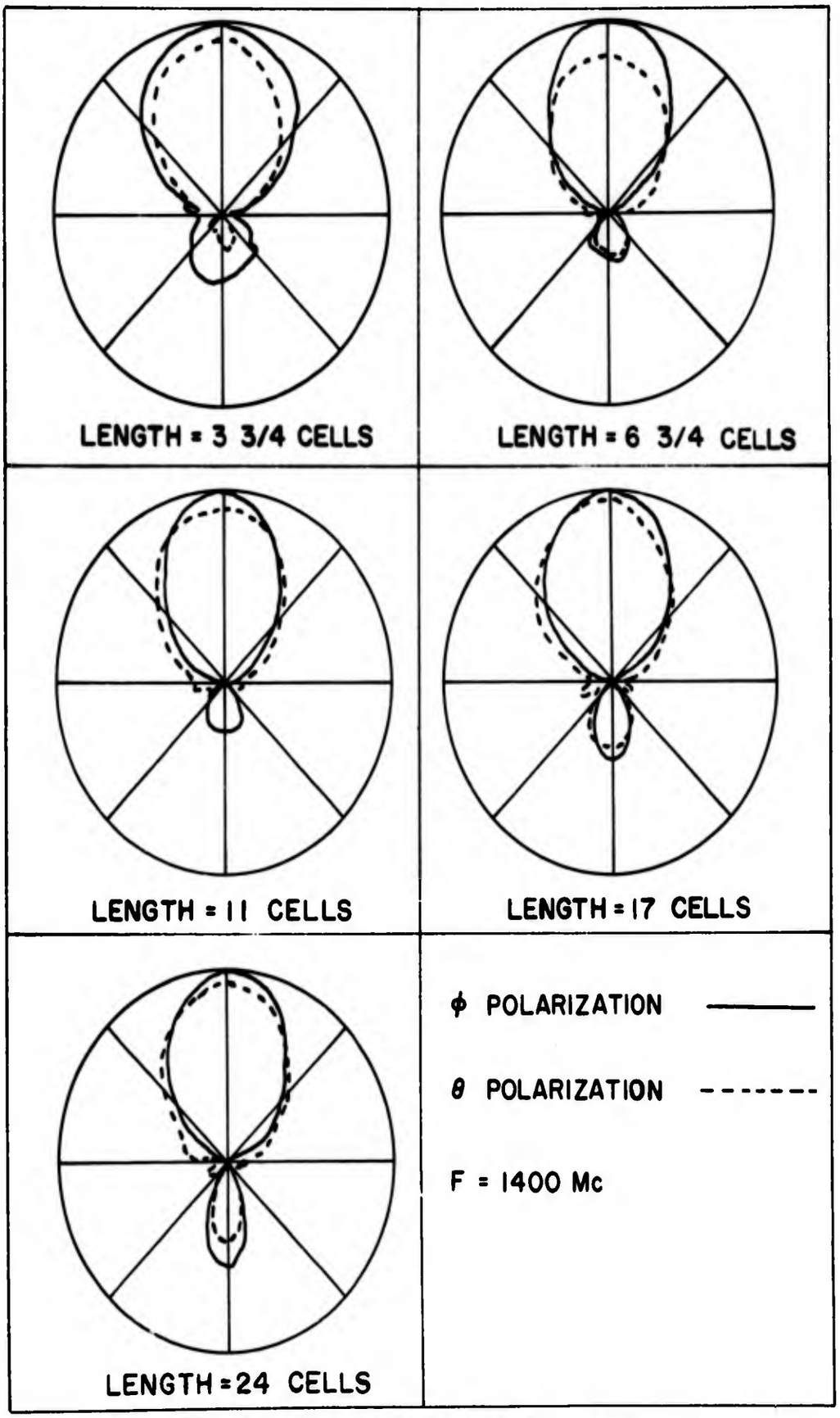

Figure 10. Radiation patterns showing the effect of changing the length of the antenna

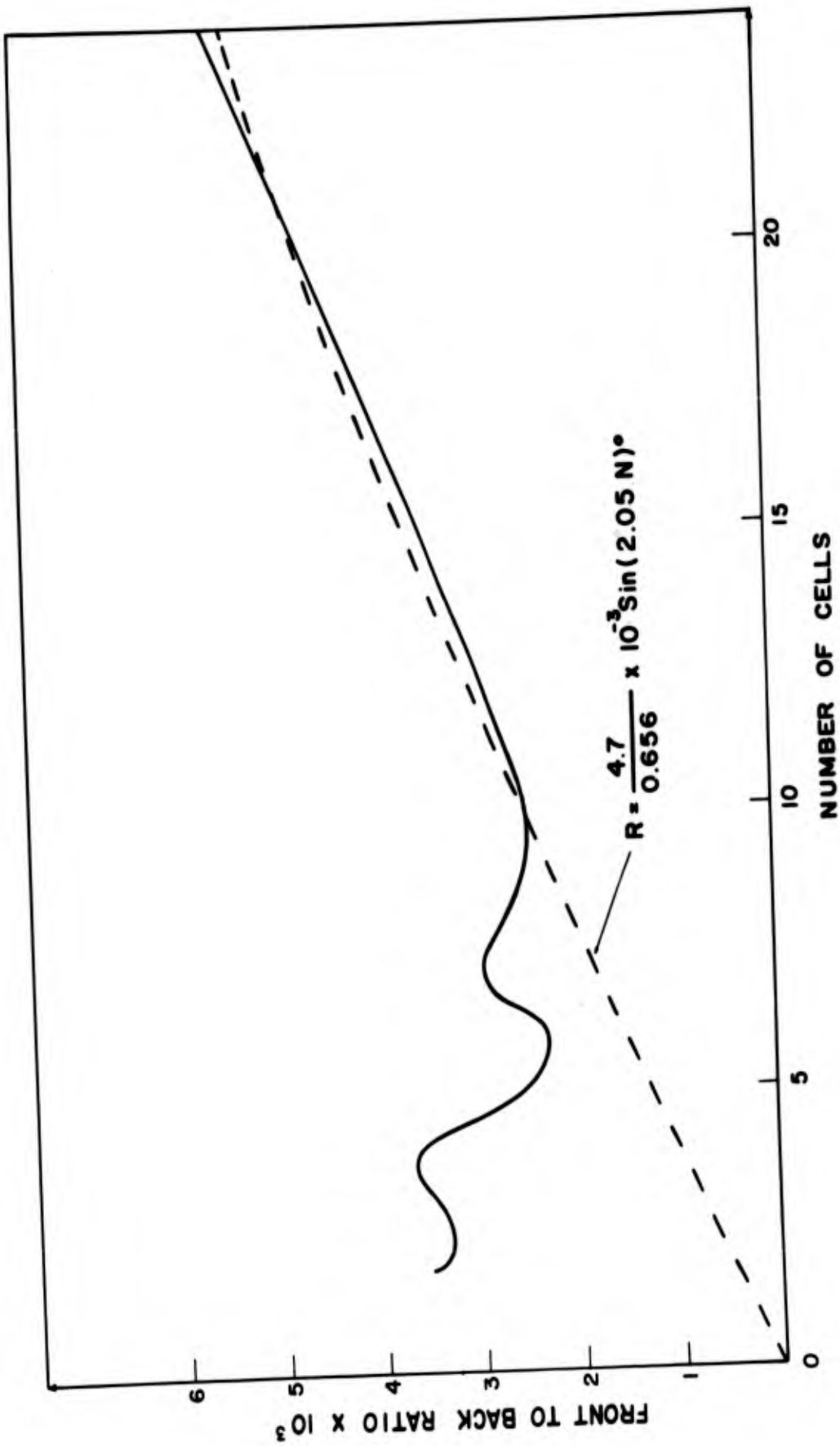

Figure 11. Front-to-back ratio as a function of antenna length

on a particular model depends upon the length of the antenna. the required length, however, changes so rapidly as the critical frequency is approached that the cutoff frequency determined from pattern measurements on an antenna of reasonable length (10 to 15 turns) is in error less than one percent. An infinitely long antenna is required to support the feed region currents at the cutoff frequency.

5. HIGH GAIN BACKFIRE HELICAL ANTENNAS

Backfire bifilar helical antennas with large pitch angles tend to give the greatest directivity. To provide more information on this property, two antennas were built with a pitch angle of forty-five degrees. BBH-8a was constructed of number twenty-two wire wound on a 1-inch diameter plexiglass tube 48 inches long. BBH-8b was constructed of number thirty-two wire wound on a 0.475-inch diameter pyrex glass tube, 48 inches long. The patterns obtained for these antennas are shown in Figure 12.

The pattern for BBH-8a at 1.315 Gc has a twenty-eight degree beamwidth. The length of the antenna at this frequency is 5 35 wavelengths. Using the approximate relation between beam width and gain given by Kraus[9]

$$D = \frac{41{,}253}{\theta_H \theta_E}$$

the gain of the antenna at this frequency is 52 5 (17.2 db). This gives a ratio of gain to length in wavelengths of 9.82.

The beamwidth of BBH-8b at 2 575 Gc is twenty degrees, and the length is 10.45 wavelengths. The gain of the antenna is 103 1 (20.1 db) and the gain-to-length ratio is 9.9 This result can be compared with the expression given by Schelkunoff and Friis[10] for the gain of a long array of isotropic radiators

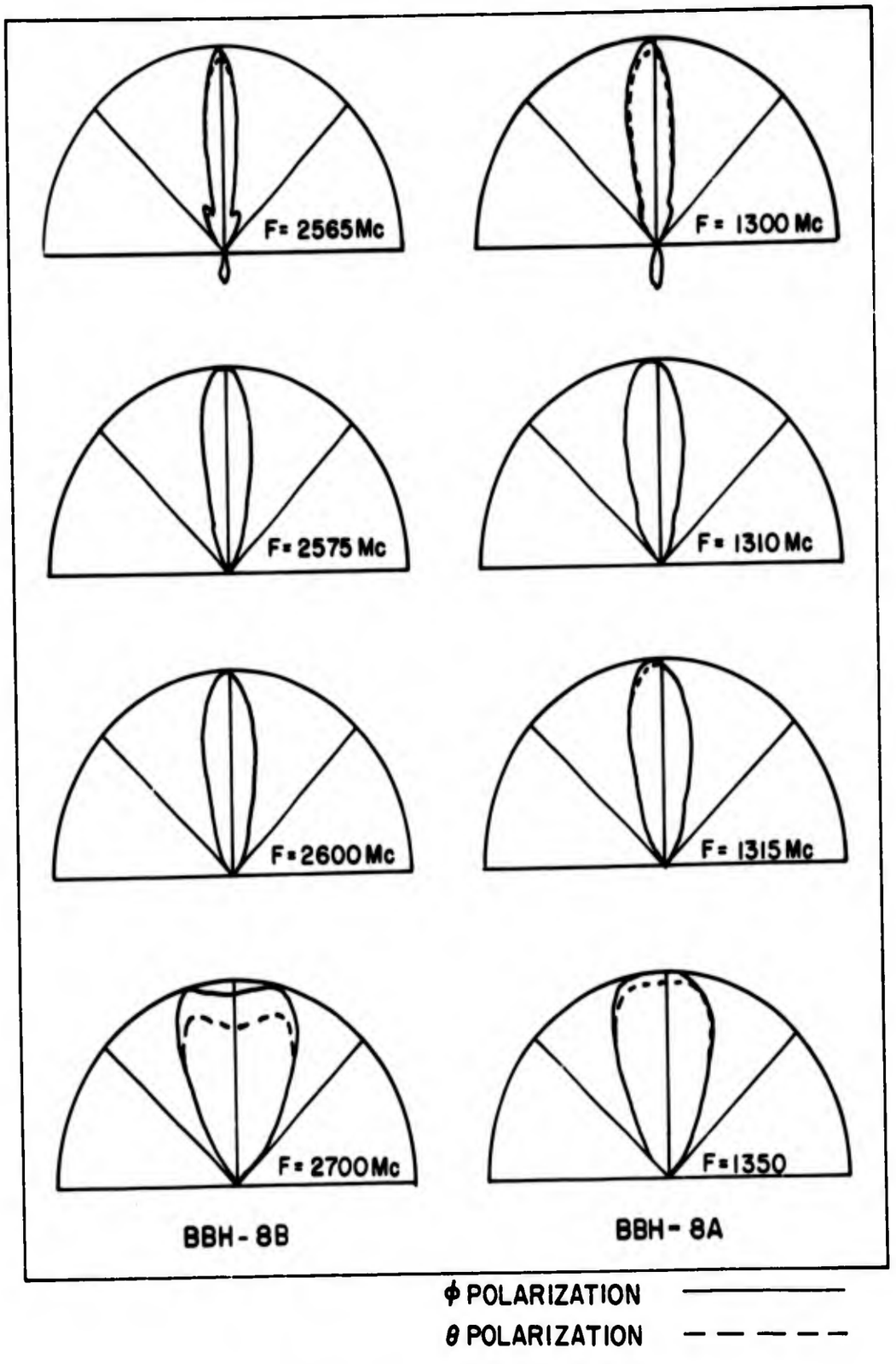

Figure 12. High-gain patterns measured for BBH-8

in terms of its length

$$g = 7.2 \frac{\ell}{\lambda}$$

This gain results when Hansen-Woodyard excess phase shift (2.94 radians) is used in the array feed. The backfire helix provides a gain about 1.375 times as great without side lobes. If side lobes were permitted as shown in Figure 12 for the lower frequencies, the gain is increased 1.7 times.

The backfire bifilar helix is obviously a supergain antenna when operated near the critical frequency. The usual instability associated with supergain antennas takes the form of a very rapid widening of the beam for the backfire helix. One half percent increase in frequency increases the beamwidth two degrees.

6. THE TAPERED HELIX--LOG-SPIRAL ANTENNA

In an attempt to retain some part of the high gain performance of the antennas described above and, at the same time, increase the bandwidth, an 8-foot long antenna was built, tapered from 1/2 inch diameter at one end to 1 inch diameter at the other end. A Rexolite 1422 core was used with number twenty wire wound at a pitch angle of forty-five degrees

Patterns obtained for this antenna are shown in Figure 13. This antenna has an average gain of 36 (15.6 db) in a forty-five percent bandwidth. Thus, tapering slows the rate with which the patterns vary with frequency and, at the same time, reduces the maximum gain that can be achieved This is the result expected since this antenna is a conical log-spiral antenna with a very small cone angle.

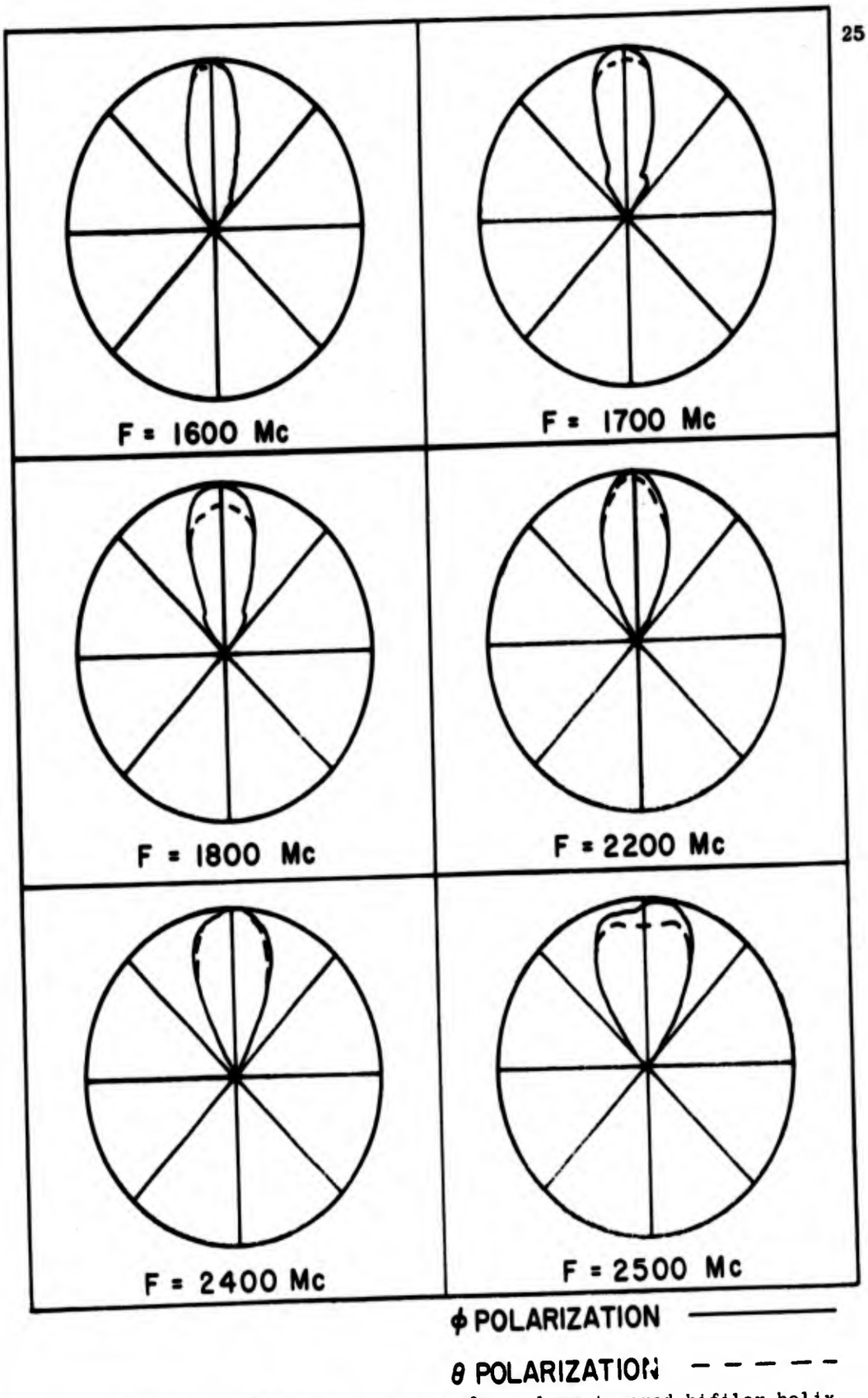

Figure 13. Measured patterns for a long tapered bifilar helix

7. THE BACKFIRE MONOFILAR HELICAL ANTENNA

The operation of a helical antenna in the backfire mode is not dependent upon the number of helical conductors used in its construction. To illustrate this, a backfire monofilar helical antenna, shown in Figure 14, was built. This model used the parameters of BBH-2. The conductor in this case was a Microdot cable which was also used to carry energy from the feed point to the receiver. At the feed point, the Microdot cable was brought radially from the perimeter of the helix to the axis. The center conductor of the cable was connected to the center of a straight wire, ten centimeters long, placed on the axis of the helix.

The patterns obtained for the monofilar helix are shown in Figure 15. These patterns are very similar to those obtained for the bifilar BBH-2. This demonstrates that the monofilar helix will operate in the backfire mode, although it is more difficult to feed than the bifilar helix.

8. A BACKFIRE HELIX WITH A CONDUCTING CORE

The backfire bifilar helix model BBH-4 has a diameter of 1.77 inches. Patterns obtained for this model, when a series of brass rods were placed inside the helix and coaxial with it, are shown in Figure 16. The cores were of the same length as the antenna and ranged from 1/2 inch to 1 1/2 inches in diameter in 1/4 inch steps. These patterns are for the frequency 1.4 Gc. When the 1 1/2 inch rod was used the thickness of the dielectric, polystyrene foam, between the core and the wires was 0.11 inch. This is 0.013 wavelengths at 1.4 Gc.

The main beam of the patterns shows little change with increasing core diameter except for some asymmetry due to misalignment of the core axis and

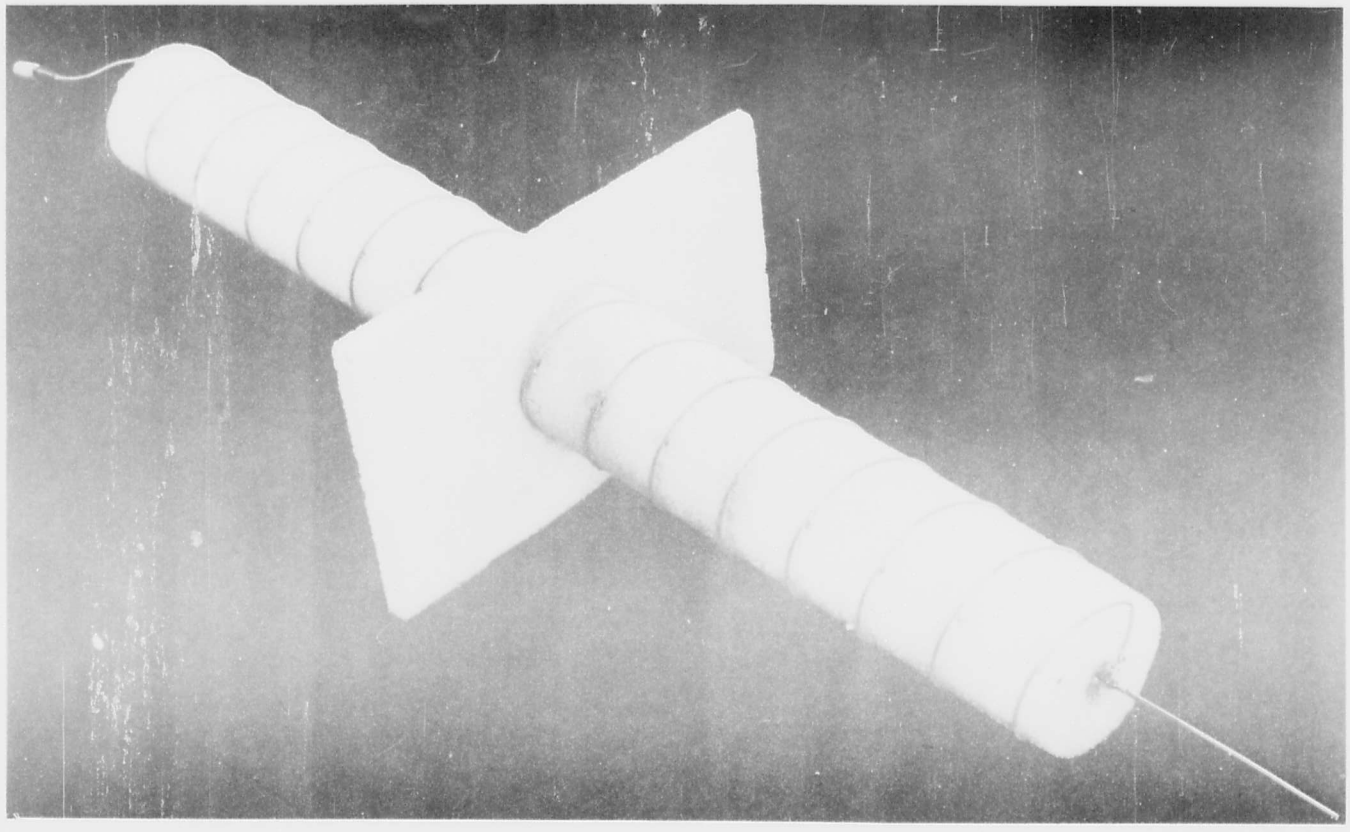

Figure 14. Picture of a backfire monofilar helical antenna

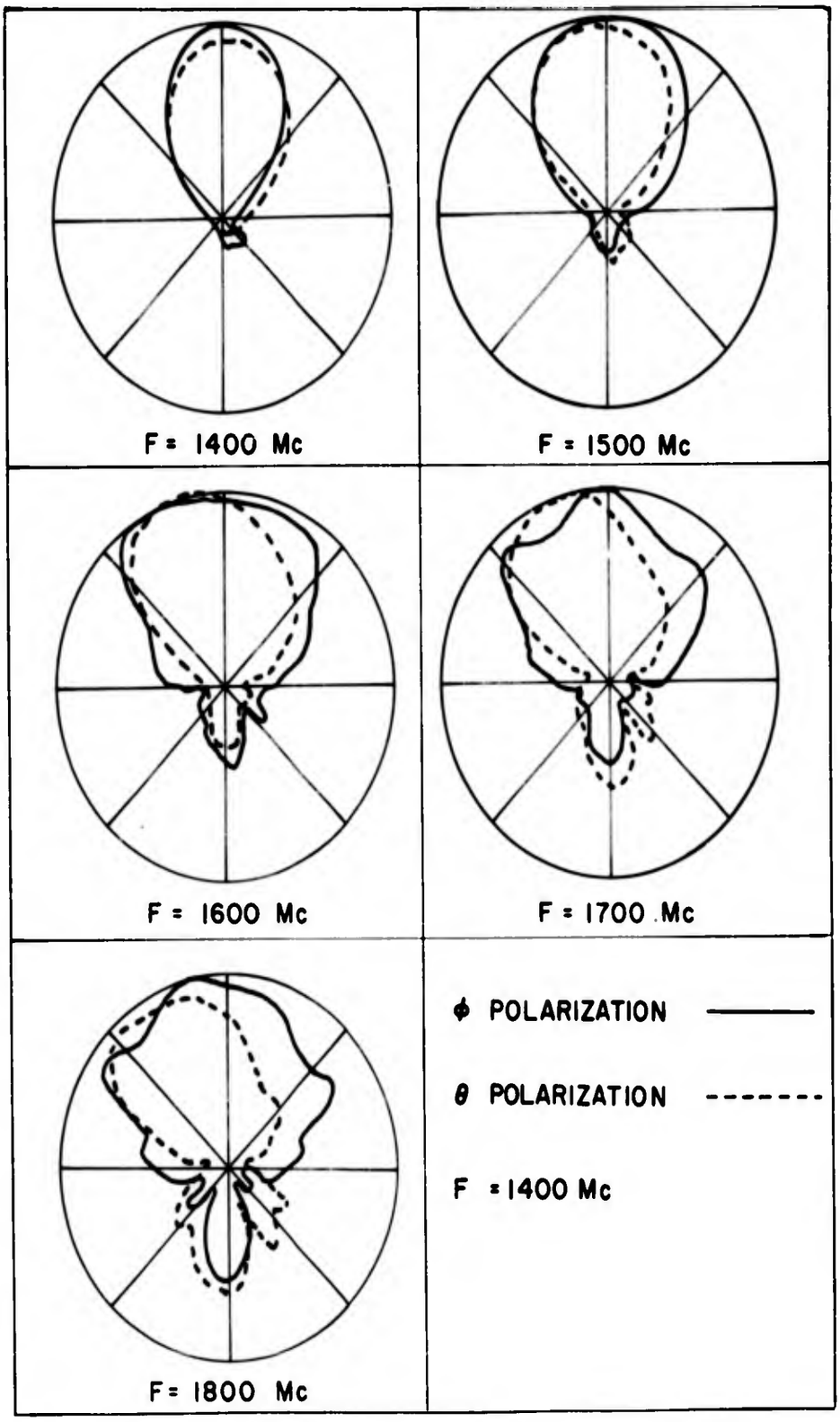

Figure 15. Radiation patterns measured for a backfire monofilar helix

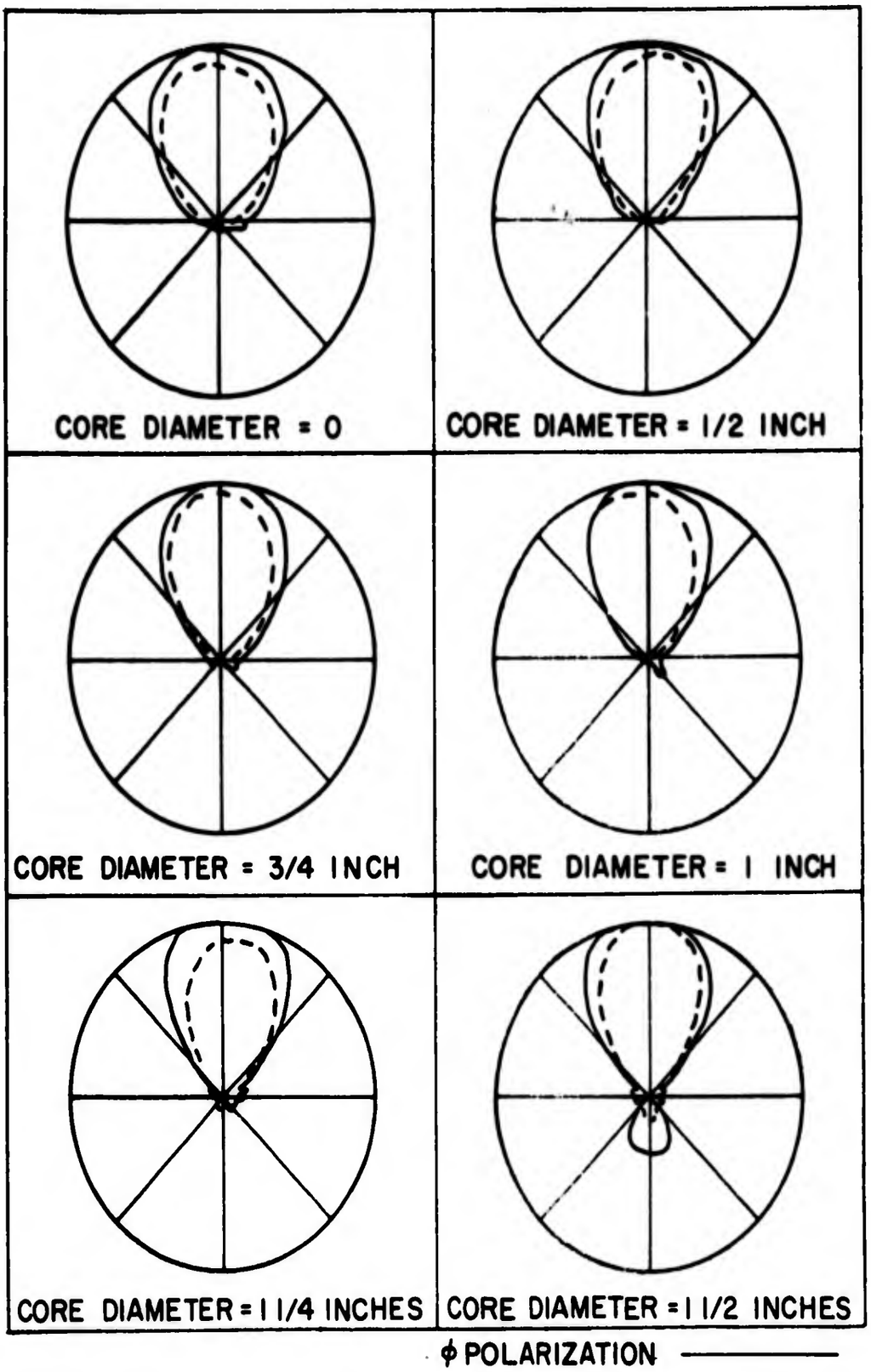

Figure 16. Patterns of BBH-4 with a conducting coaxial core

some improvement in the circularity of the polarization on the axis. The principal effect of the core is to increase the excitation of the higher-order wave guide mode. This is indicated by the increase in endfire radiation.

The increase in endfire radiation is significant only when the conducting core nearly fills the center of the helix. It is expected that a further increase in core diameter would rapidly change the character of the radiation pattern, but, for the core diameters used in this investigation surprisingly little effect was noted.

9. CONCLUSION

A theoretical solution for the patterns of the backfire bifilar helical antenna has been obtained. This solution, appropriate for a semi-infinite bifilar helix, is based upon a Wiener-Hopf factorization of the determinantal equation for the bifilar helix. This solution predicts the main beam radiation from an antenna of finite length. This analysis is described in Technical Report No. 61, AF33(657)-8460, Antenna Laboratory, University of Illinois, Urbana, Illinois.

The study of the backfire bifilar helical antenna is important for several reasons. Not the least of these is the fact that the antenna is a useful practical device in itself. It provides circularly polarized fields with a single lobed pattern of almost any desired gain. When pitch angles near forty-five degrees are used, the antenna can provide circularly polarized fields with a pattern that is omnidirectional in azimuth with high vertical directivity.

This study also provides further insight into the operation of the conical log-spiral antenna, and it is the first simply periodic backward wave or backfire antenna for which a theoretical solution has been obtained. The study

of other types of periodic antenna structures that operate in the backfire mode will aid in understanding the operation of known log-periodic antennas and will suggest new ones. These structures are important in themselves for their unidirectional single lobe patterns and their frequency scanning characteristics, as well as for the insight they give in the operation of log-periodic structures.

ACKNOWLEDGEMENT

The author wishes to thank all members of the staff of the Antenna Laboratory of the University of Illinois for their help and encouragement during this study. The guidance of Professor G. A. Deschamps, and the suggestions of Professor P. E. Mayes are particularly appreciated.

Thanks are also due to Samuel C. Kuo who assisted in the data reduction and prepared the illustrations, and to Bradley Martin, Calvin Evans, and Edward Young, who assisted in the experimental measurements. This work was sponsored by the United States Air Force, Aeronautical Systems Division, Wright-Patterson Air Force Base, under contract AF33(616)-6079 and AF33(657)-8460, for whose support the author is grateful.

REFERENCES

1. J. D. Kraus, "Helical Beam Antenna," Electronics, Vol. 20, April, 1947, pp. 109-111.

2. D. E. Isbell, "Non-Planar Logarithmically Periodic Antenna Structures," Antenna Laboratory, University of Illinois, Urbana, Tech. Report No. 30, Contract AF33(616)-3220, February, 1958.

3. R. H. DuHamel and F. R. Ore, "Logarithmically Periodic Antenna Designs," IRE National Convention Record, pt. 1, 1958; pp. 139-151.

4. J. D. Dyson, "The Unidirectional Equiangular Spiral Antenna," IRE Transactions on Antennas and Propagation, Vol. AP-7, Oct. 1959, pp. 329-334.

5. P. E. Mayes, G. A. Deschamps, and W. T. Patton, "Backward Wave Radiation from Periodic Structures and Application to the Design of Frequency-Independent Antennas," Proceedings of the IRE, Vol. 49, May, 1961; pp. 962-961.

6. S. Sensiper, Electromagnetic Wave Propagation on Helical Conductors, Ph. D. Thesis, Massachusetts Institute of Technology, 1951.

7. S. Kh. Kogan, "The Propagation of Waves Along an Endless Helix," Compt. Rend. Acad. Sci. (USSR), Vol. 66, June 1949; p. 867.

8. J. D. Kraus, Antennas, McGraw-Hill, New York, 1951; p. 176.

9. Ibid; p. 25.

10. S. A. Schelkunoff and H. T. Friis, Antennas; Theory and Practice, John Wiley and Sons, New York, 1952; p. 559.

NEAR-FIELD MEASUREMENTS ON BACKFIRE PERIODIC DIPOLE ARRAYS

P. E. Mayes and P. G. Ingerson*
University of Illinois
Urbana, Illinois

1. INTRODUCTION

Although notable progress has been made in recent years in achieving frequency-independent performance from antennas, the understanding of the basic principles of operation of most of the practical frequency-independent antennas remains incomplete. It has been proposed that studies of uniform periodic structures which correspond geometrically to the several successful undirectional log-periodic and log-spiral antennas can yield information which will aid in developing the basic concepts.[1] Preliminary measurements have been made on a number of periodic radiating structures at the University of Illinois Antenna Laboratory. Two of these structures, the helix and periodic dipole array, are amenable to analysis and parallel theoretical investigations by Patton[2], Mittra[3], Klock and Laxpati (unpublished) have yielded corroborating results.

It has been found that the near-fields on the uniform periodic structures can often be represented by simple wave functions. Brillouin diagrams, plots of frequency versus propagation constant, for these waves yield valuable information about the operation of the corresponding log-periodic structure. The variation with frequency of the propagation constant along the uniform periodic structure corresponds to the variation with distance of the propagation constant along the log-periodic structure. Of particular interest are the frequency bands where the propagation constant is complex. The purpose of this paper is to display the Brillouin

---

*Antenna Laboratory, University of Illinois, Urbana, Illinois

diagram for the uniformly periodic counterpart of the highly useful log-periodic dipole array[4,5] and to compare the form of this diagram with those obtained from some other periodic structures.

2. DESCRIPTION OF THE MEASUREMENTS

The backfire periodic dipole array consists of an array of identical coplanar dipoles equally spaced along a transposed feeder as shown in Figure 1. The transposed feeder is known to be required for successful frequency-independent operation of the log-periodic dipole array. A comparison of the Brillouin diagrams for this case with that for a monopole array with single feed line (equivalent to a two wire feeder not transposed) will clarify the importance of the transposition.

In order to probe the near-field with minimum disturbance the uniform dipole array was constructed as shown in the sketch in Figure 2. The dipole elements were made from 0.1875-in. diameter brass tubing and were silver-soldered to twin booms which were made from 0.425-in. diameter coin-silver tubing. The twin booms served both as support and balanced feeder. The excitation signal was brought to the input terminals by means of a coaxial cable in one of the booms. The other boom was slotted to allow a small probe to move along, sampling the voltage between the feeder conductors. The probe was connected to a length of rigid cable which could be accurately positioned from the back end of the antenna. The methods used for measuring both phase and amplitude of the probe signal were standard techniques which are described elsewhere[5,6]. The antenna used for most of the measurements reported here had sixteen dipoles spaced 6.3 cm apart. The basic length of each half-dipole was 27.25 cm, but moveable inserts were employed to make the

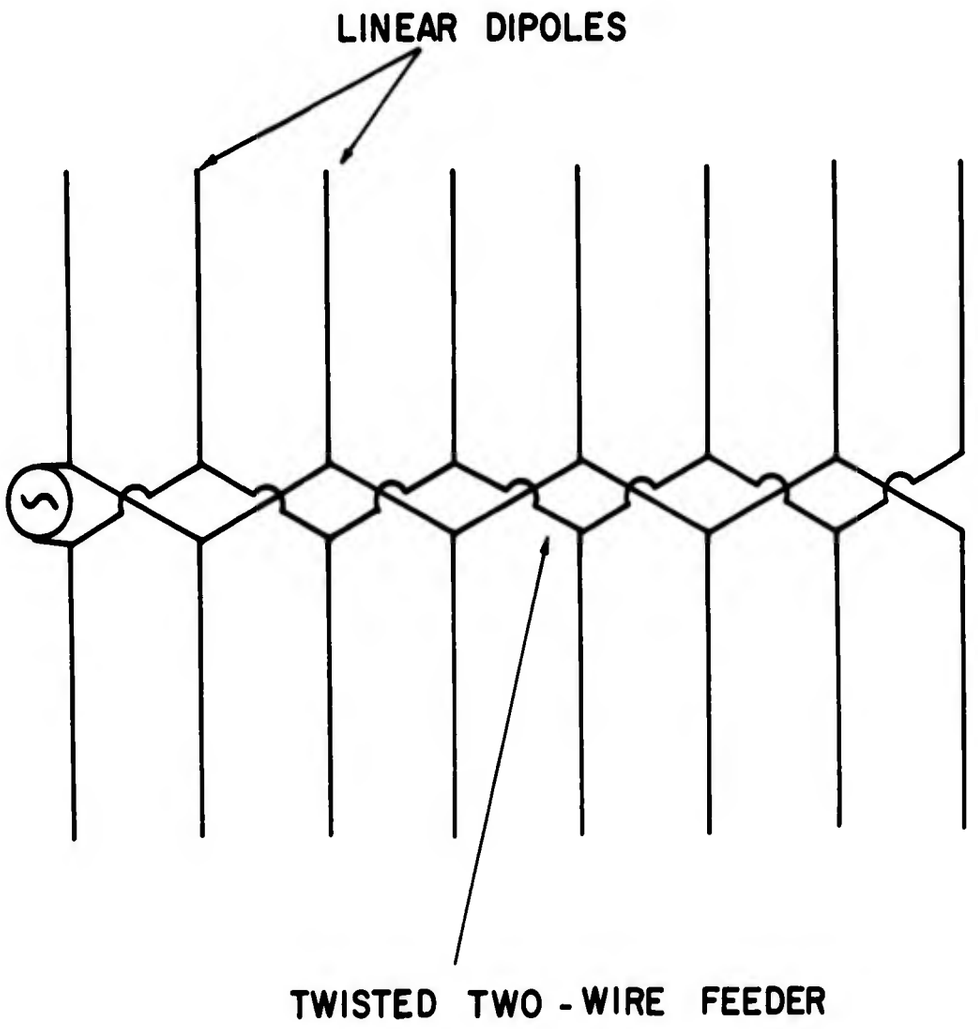

Figure 1 The Backfire periodic dipole array

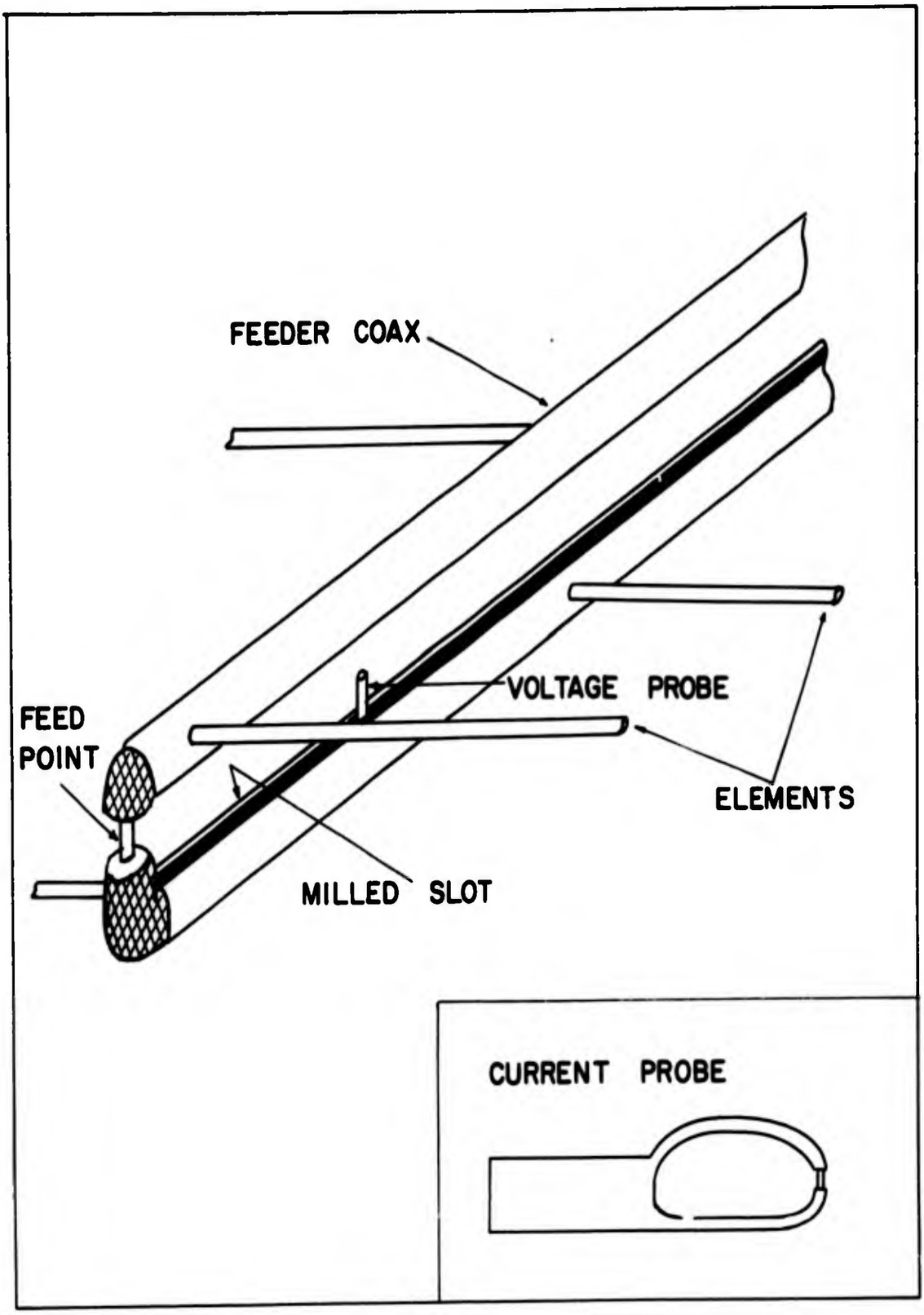

Figure 2 The near-field, probing system

dipole length adjustable.

3. INTERPRETATION OF RESULTS

In certain frequency bands the dipole-loaded line acts as a transmission system, i.e. a wave propagates along the structure with negligible attenuation. In other frequency bands the feeder voltage is rapidly attenuated. The behavior of the voltage versus distance at these latter frequencies is similar to that of the field in a periodically-loaded waveguide when the frequency is in the stopband. Hence we shall refer to the bands with undamped propagation as passbands and those with attenuation as stopbands.

Examples of these different types of behavior are shown in Figures 3 and 4. Figure 3a shows a typical standing wave pattern which is measured in the passbands. Since the feed line was terminated in a conducting plate which was an effective short-circuit, almost perfect reflection was obtained at the end of the structure opposite the feedpoint. This accounts for the standing wave of voltage when there is small attenuation. From the distance between nulls a guide wavelength can be determined which demonstrates that the loaded line supports an undamped slow wave at 237 Mc. The average distance between nulls in Figure 3a is 20.4 cm, which corresponds to a phase velocity along the line which is 32% of the free space value.

The decaying voltage shown in Figure 3b shows that the frequency 253 Mc is in the stopband. The attenuation has increased to the point where the field is negligible at the termination and the standing waves are no longer attributable to reflections from the terminal plate since the field amplitude is attenuated to negligible values at a point some distance from the plate. Even so, the alternate maxima and minima indicate the presence of two waves on the transmission line. A similar situation is observed at 255 Mc as

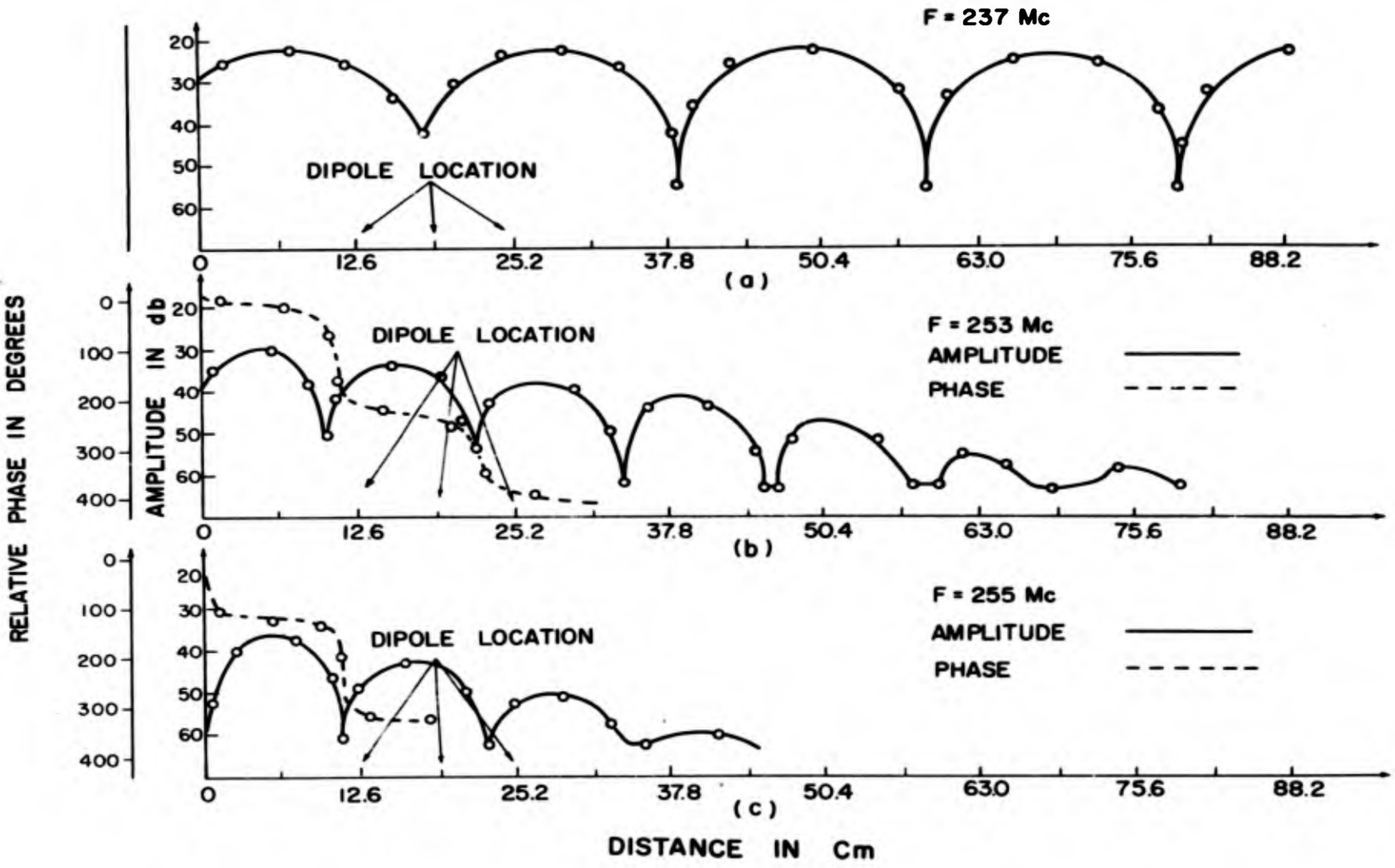

Figure 3 Measured feeder line voltage amplitude and phase versus distance from feed point on periodic dipole array

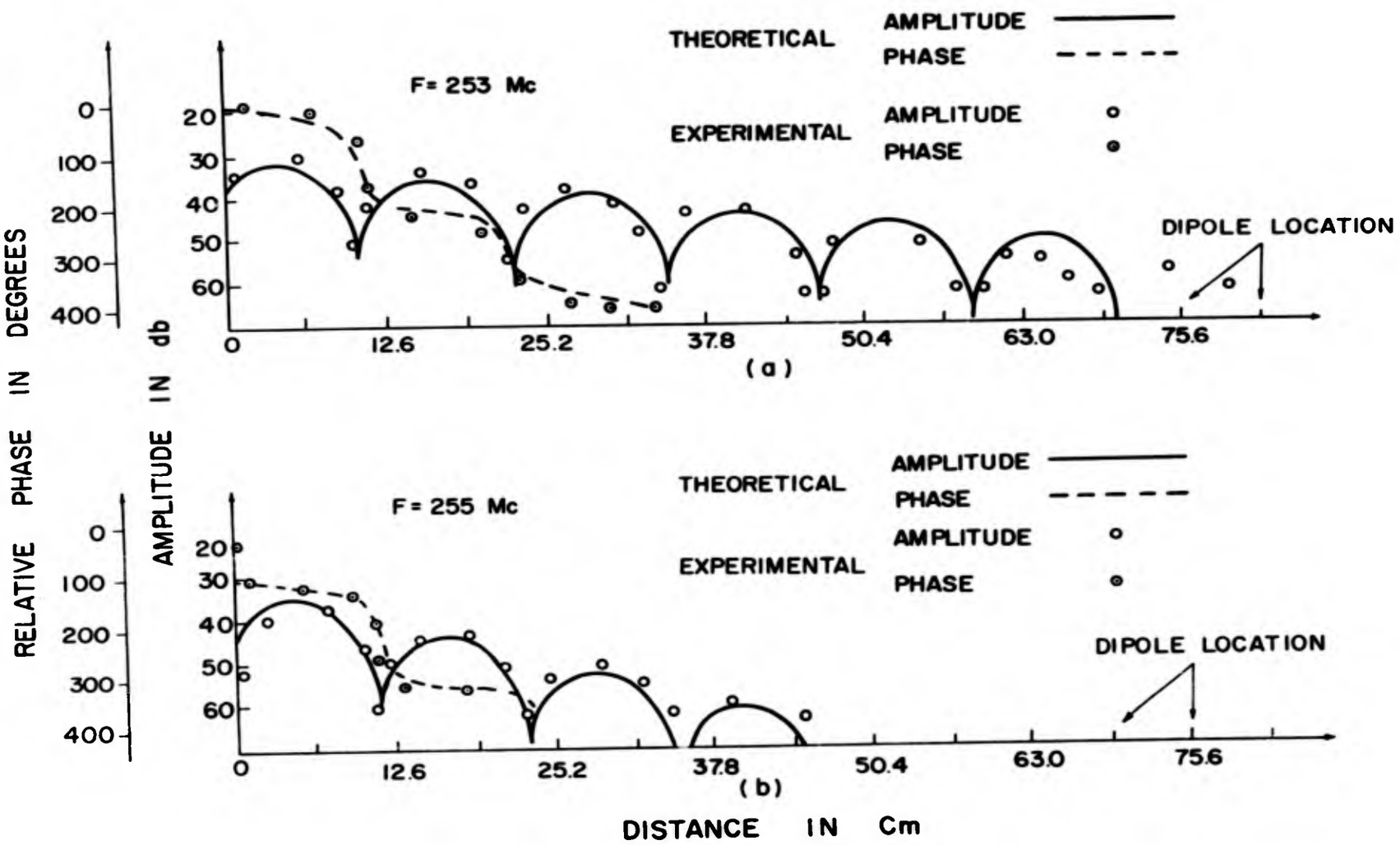

Figure 4 Measured feeder line voltage amplitude and phase versus distance from feed point on periodic dipole array

shown in Figure 3c. Note, however, that the attenuation has increased significantly in this small (2Mc) frequency increment.

The voltage amplitudes and phases shown in Figures 3b and 3c have been analyzed to determine the properties of the separate waves. Assuming the voltage to be of the form

$$V(x) = e^{-\alpha x}(e^{-j\beta x} + Ke^{+j\beta x})$$

produces a calculated voltage versus distance plot which is shown as the solid lines in Figures 4a and 4b. The constants α, β and K have been chosen to produce a good fit to the experimental points shown on the same figure.

Figure 5 shows the voltage amplitude and phase as frequency is increased further. The standing wave pattern with still higher attenuation is shown in Figure 5a for 265 Mc. At 275 Mc, however, (Fibure 5b) the standing wave has disappeared and the phase shift between cells has reduced to a small value. At 290 Mc the attenuation has begun to decrease and the phase shift between dipoles is practically zero. As frequency is further increased the attenuation decreases to negligible values as standing waves are again formed by reflections from the end. The phase constant in this second passband is determined by distance between nulls as before.

In the vicinity of the three half-wavelengths resonance of the dipoles the stopband characteristics are repeated. Figure 6 shows the voltage plots at 768, 815, and 831 Mc which display forms very similar to those in the lower stopband. Further plots showing the decreasing attenuation and small phase shift as the frequency approaches a third passband are shown in Figure 7.

The Brillouin diagram affords a convenient way of summarizing the above

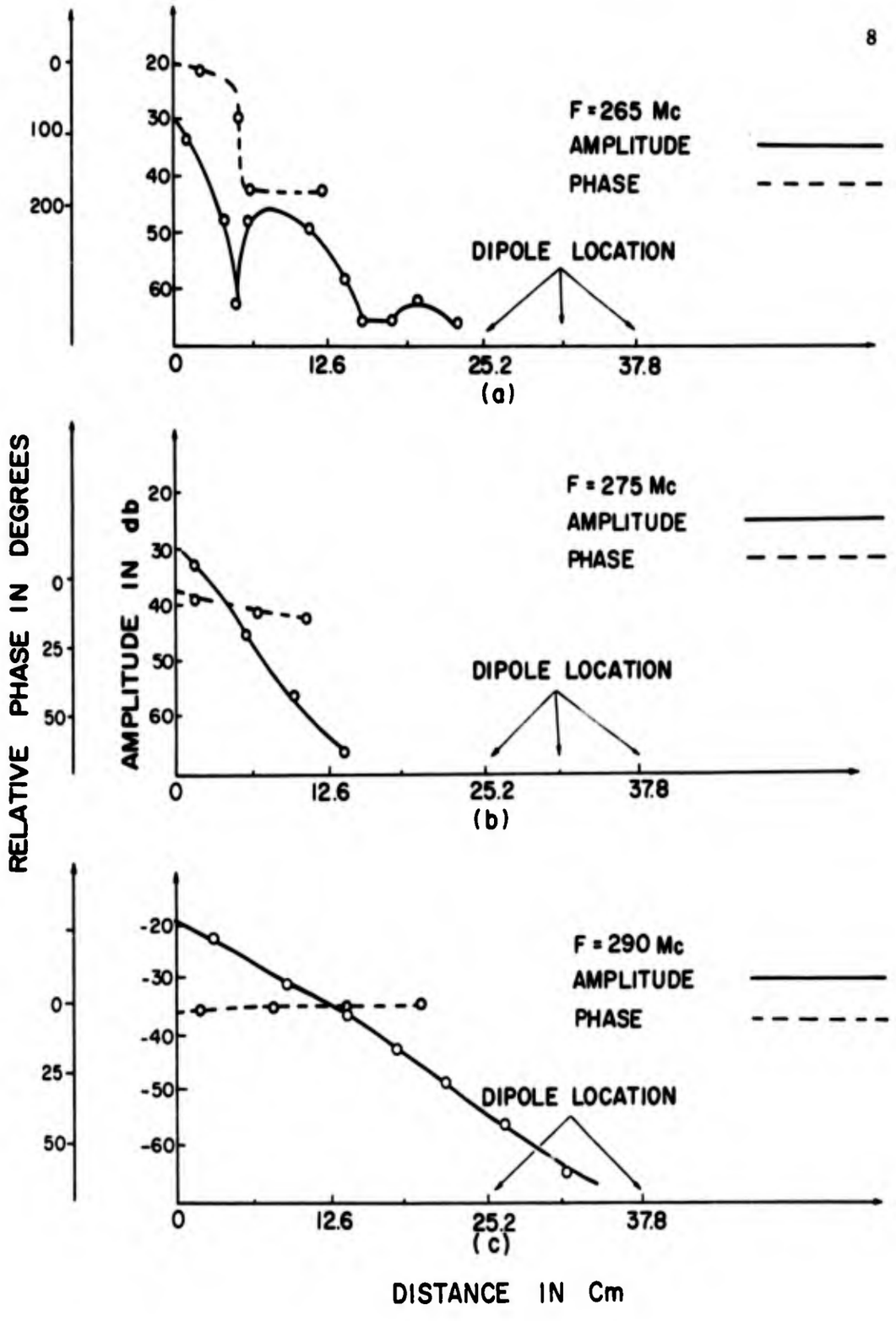

Figure 5 Measured feeder line voltage amplitude and phase versus distance from feed point on periodic dipole array

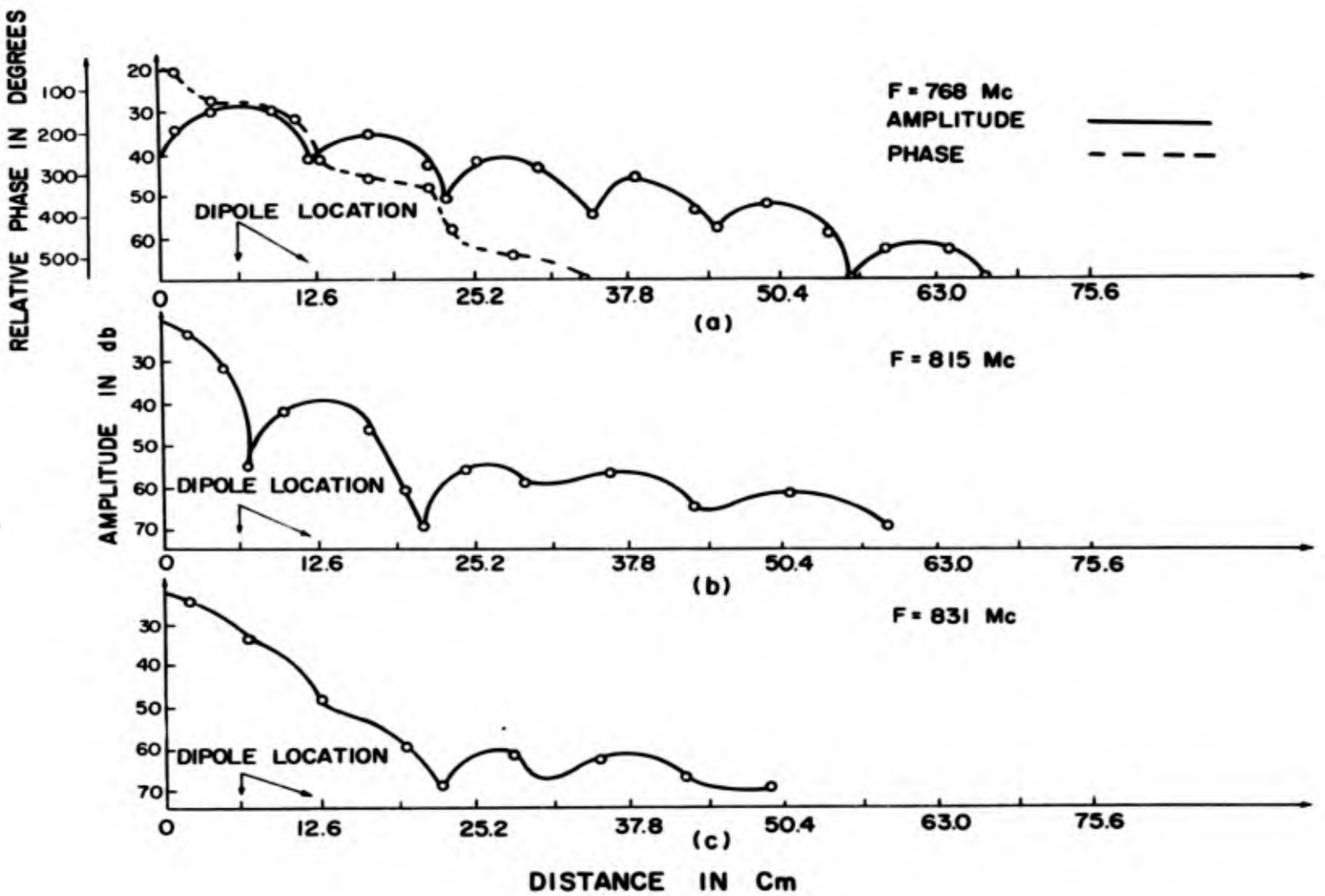

Figure 6 Measured feeder line voltage amplitude and phase in second stopband versus distance from feed point on periodic dipole array

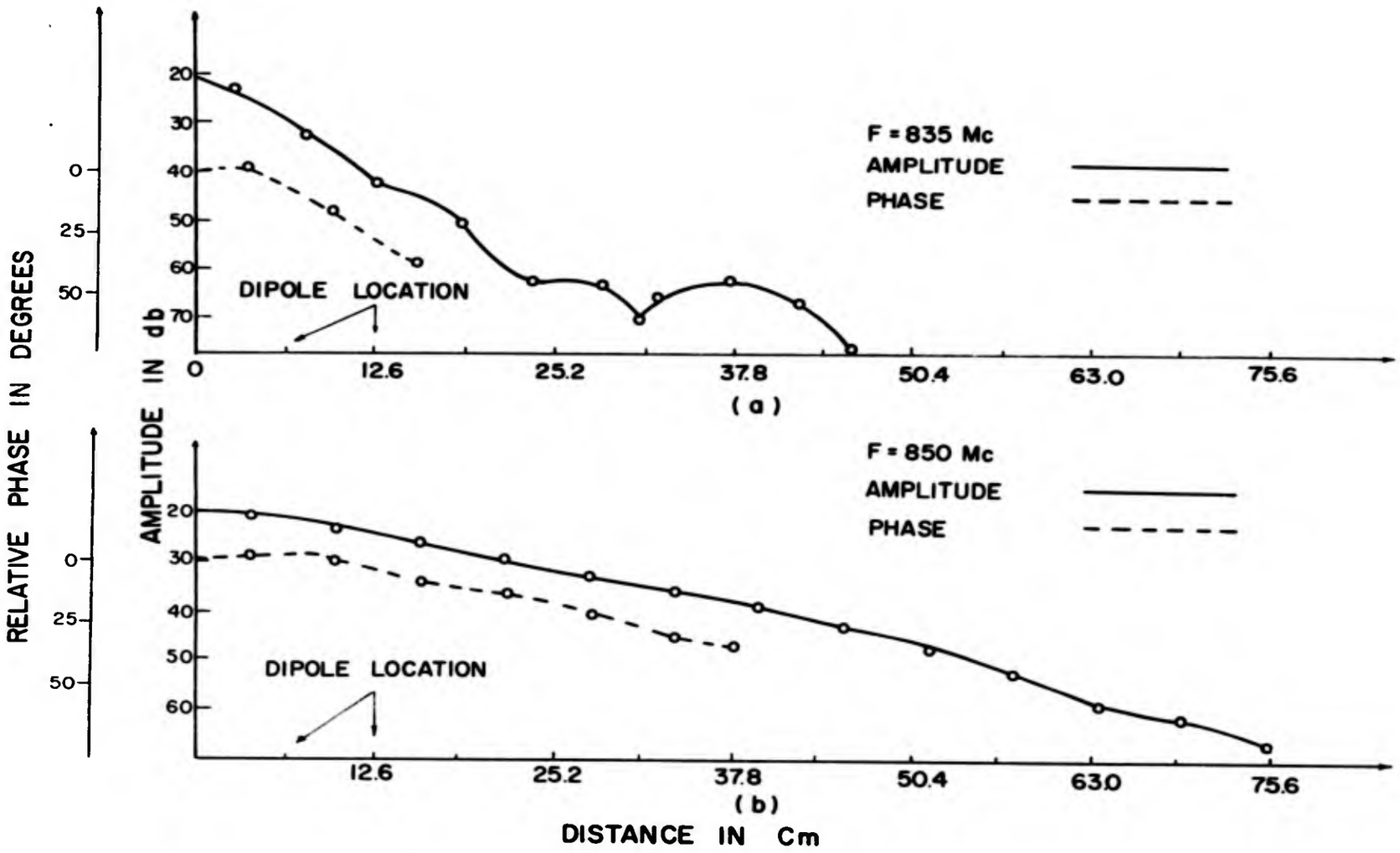

Figure 7 Measured feeder line voltage amplitude and phase in second stopband versus distance from feed point on periodic dipole array

data together with that taken at a number of other frequencies. Figure 8 shows such a diagram based upon the phase shift between adjacent dipoles. Also shown in Figure 9 is the attenuation of the voltage wave in the distance between adjacent dipoles. These diagrams have forms similar to those calculated for a transmission line loaded with shunt elements which have multiple resonances similar to those of the dipoles.[3] The numerical agreement is greatly improved, however, if the calculations are performed using expressions for the actual dipole admittance and including the effect of mutual coupling between the elements.[7]

Because of the complications involved by the existence of more than one wave at the lower edge of the stopbands, the determination of the phasing of the dipole currents is not directly obtained from the voltage plots given above. Since sensitivity of the current probe is somewhat less than that of the voltage probe, only limited data have been obtained for the current distribution. Figure 10 shows the current distribution measured along the feeder at 255 Mc, the edge of the first stopband. Note that the phase shift between adjacent dipoles at 255 Mc is approximately 90 degrees. When this 90 degree phase progression exists from dipole to dipole along the feeder, the actual phase progression of the dipole currents is likewise 90 degrees per dipole, but in the opposite direction due to the transposed feeder. This agrees with the result obtained by Carrel[5] in the "active region" of the log-periodic dipole array. Thus the dipoles are phased for backward-wave radiation so long as this phasing condition is maintained. The dramatic change in the antenna patterns which is observed at the edge of the lower stopband where the above conditions are first established is illustrated in Figure 11. Similar action takes place in the second stopband and a backward-wave pattern is produced there also. Prior use has been made of this

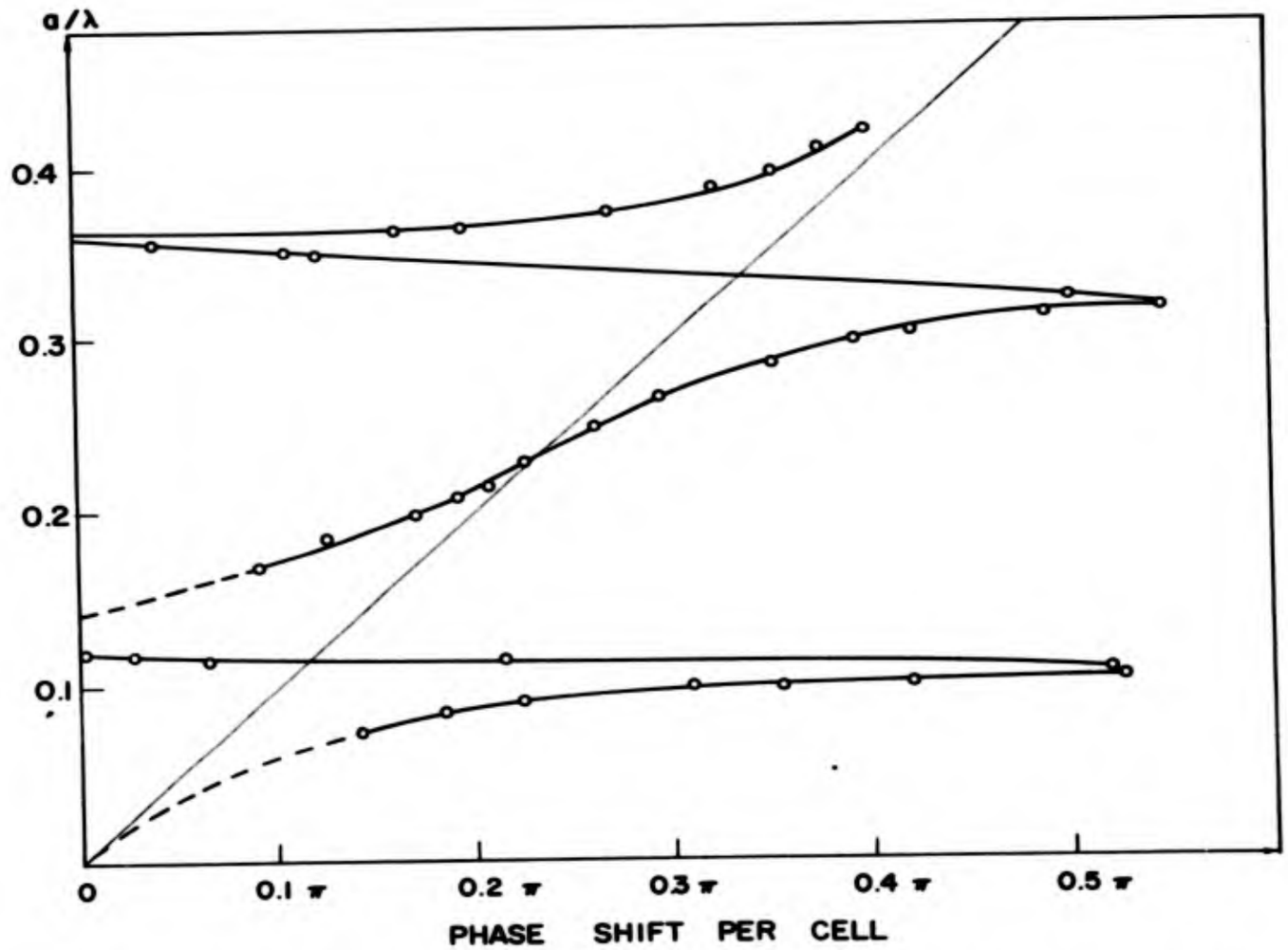

Figure 8 Brillouin Diagram for waves along feeder of uniform periodic dipole array

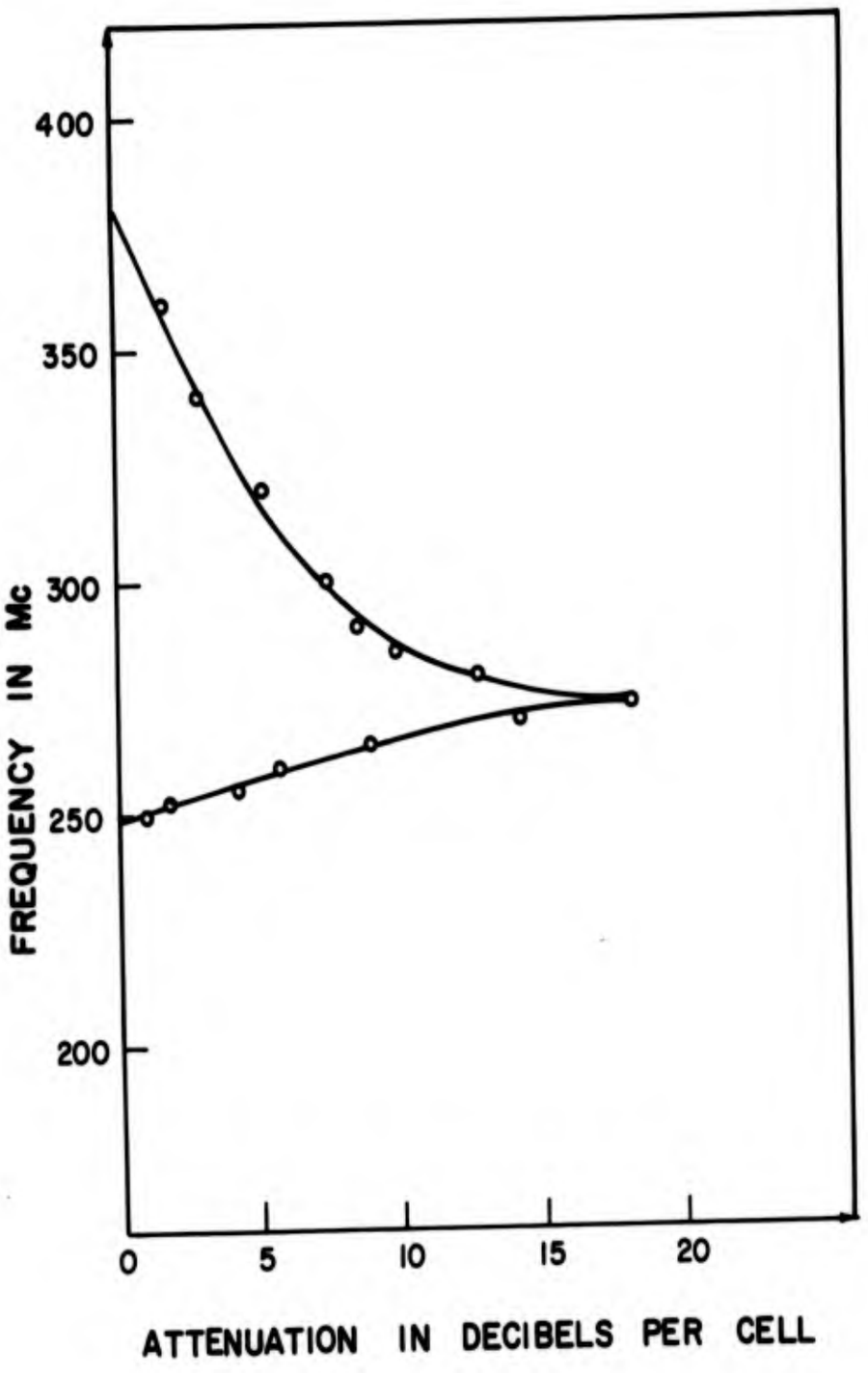

Figure 9 Attenuation of feeder voltage in first stopband of uniform periodic dipole array

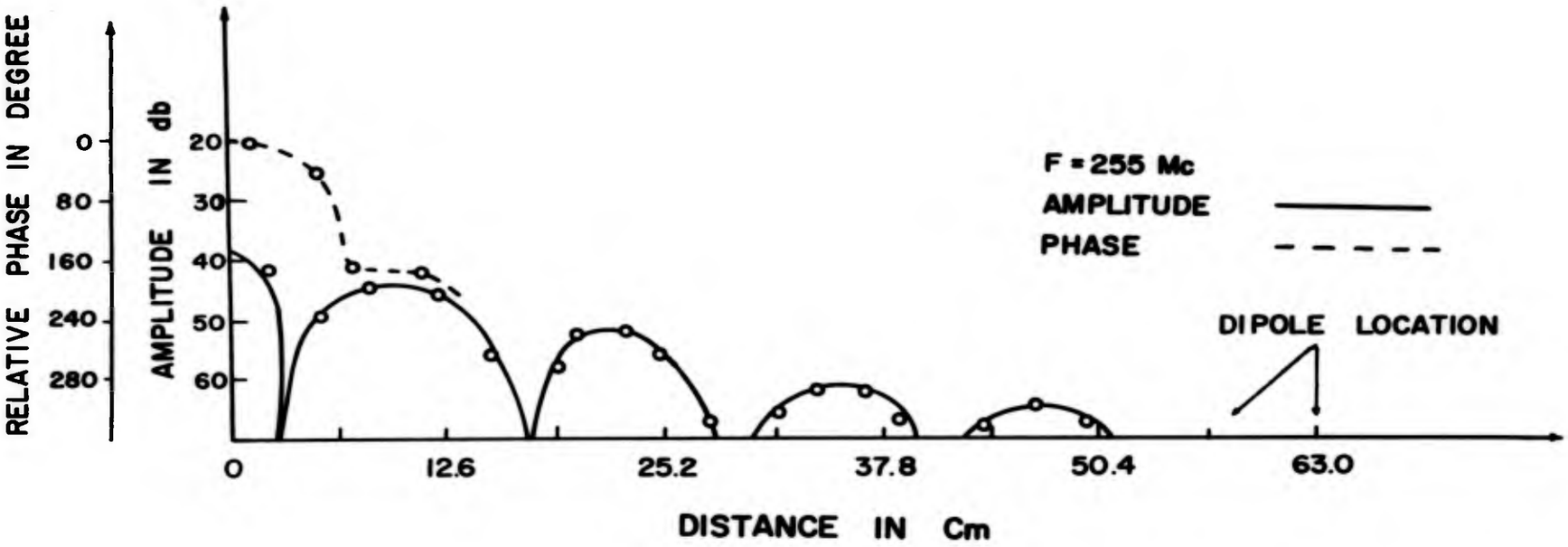

Figure 10 Measured feeder line current amplitude and phase versus distance from feed point on periodic dipole array

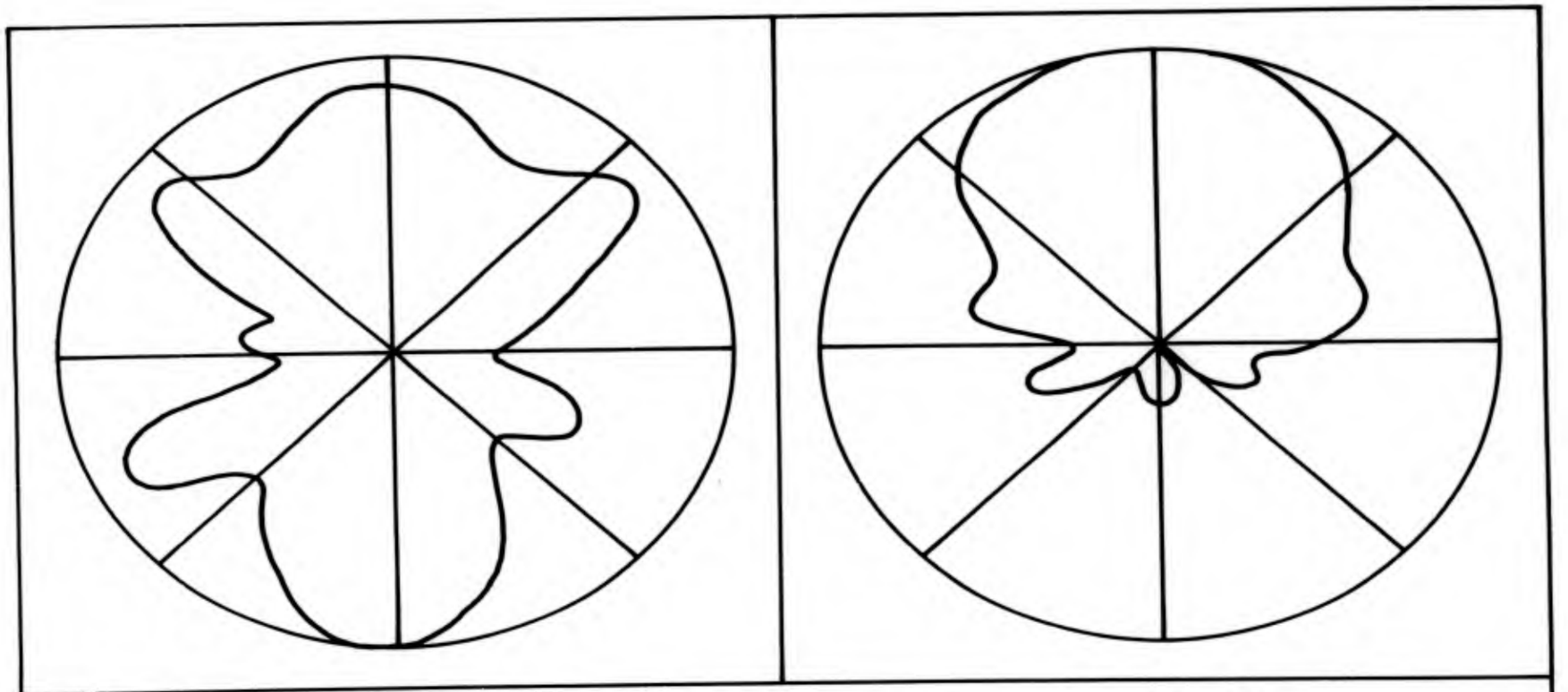

Figure 11 H-plane radiation patterns of uniform periodic dipole array in passband (252.5 Mc) and stopband (255 Mc)

phenomenon in the design of multimode log-periodic antennas.[8]

To illustrate how the periodic dipole array characteristics differ from other periodic structures we consider next the simple periodic monopole array and briefly present some results obtained by E. Hudock. Figure 12 is the Brillouin diagram obtained from measurements on an array of 13 monopoles 5.7 cm long spaced 4.5 cm apart on a straight single-wire feeder spaced 1/4 in above a ground plane. Again the general features of pass and stopband are present, but the phase shift per cell at the onset of the first stopband is nearly 180 degrees rather than 90 degrees as in the dipole array with transposed feeder. Hence, although this structure has a complex propagation constant in the stopband region the phase constant there does not produce backfire radiation.

As a further contrast of log-periodic structures which are both successful frequency independent antennas we consider the bent zigzag shown in Figure 13 which has been investigated by J. W. Greiser.[9] The Brillouin diagram for a zigzag made of .048-in diameter wire with a period of 2.0 in spaced 1/4 in above a ground plane is shown in Figure 14. The vertical elements were 3 in high; the horizontal elements, 1 3/4 in long. In this case, the phase constant is approximately given by assuming free-space phase velocity along the wire. These values are shown as a dashed line on Figure 14. Inside the triangles shown the fundamental wave and all of its space harmonics are slow waves and the phase constant can be determined by probing the standing wave produced by a short-circuit termination. Several points determined in this way are located by dots inside the triangles shown in Figure 14. The points outside the triangle were determined from radiation pattern measurements. At each of these frequencies there is a space

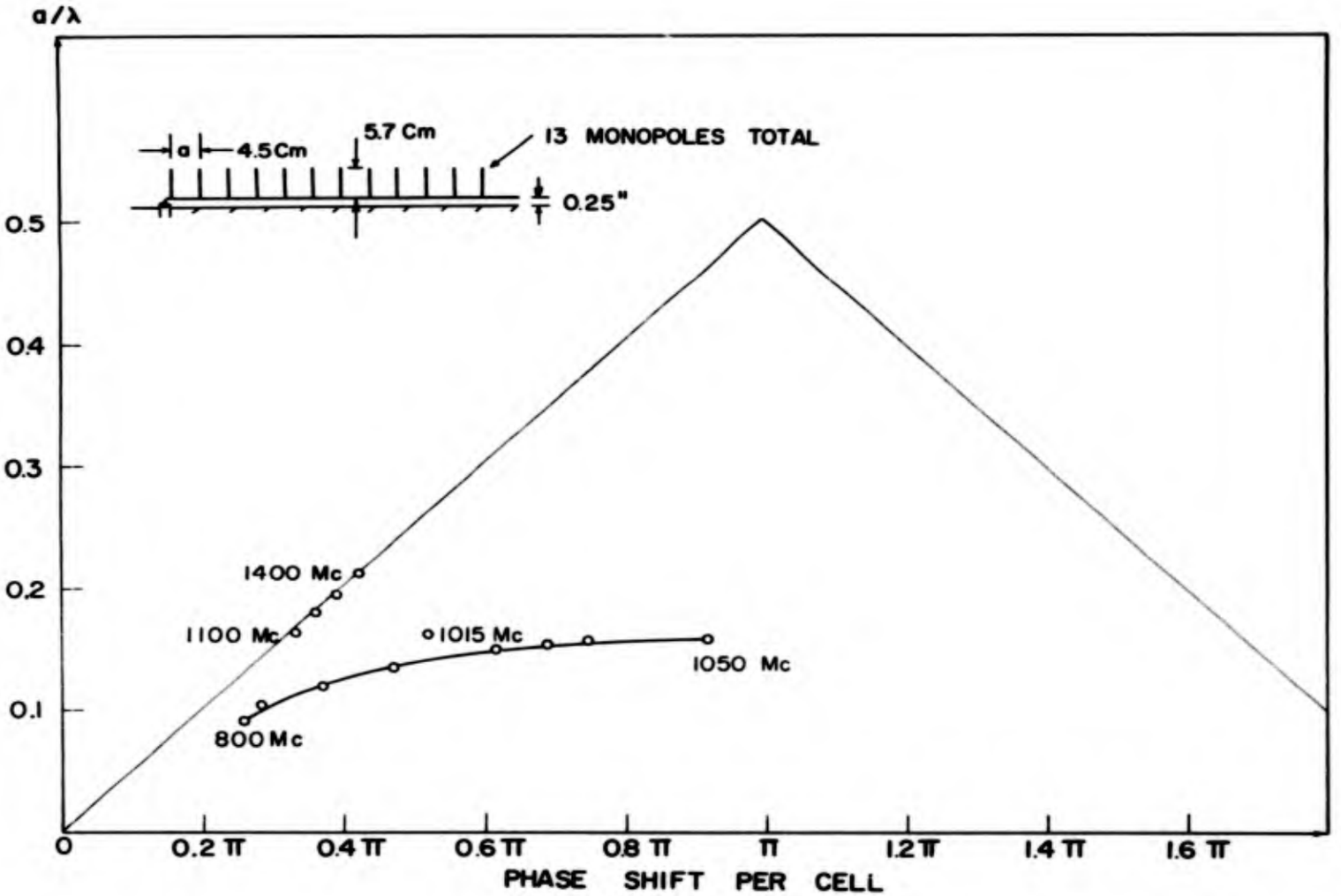

Figure 12 Brillouin diagram for periodic array of monopoles

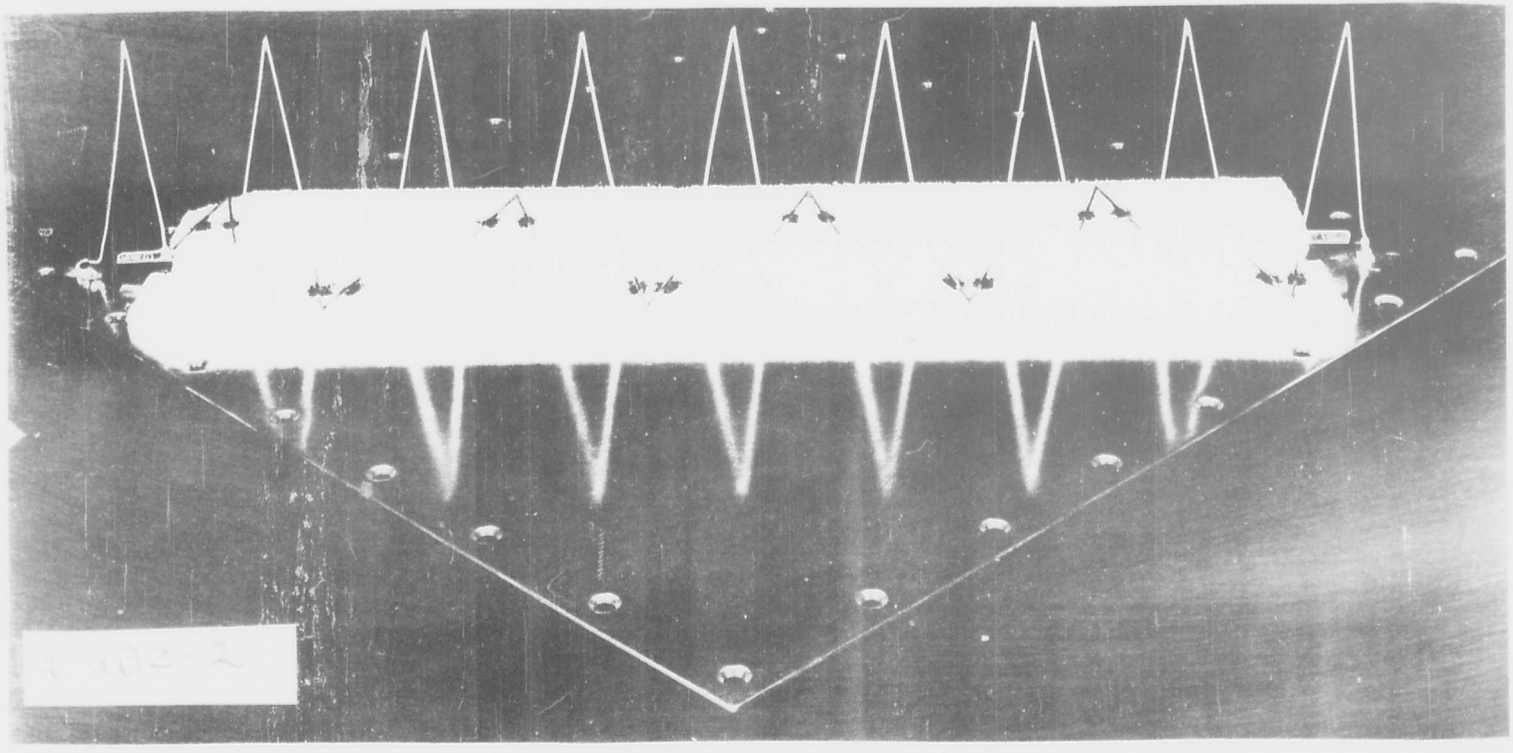

Figure 13 A uniform periodic bent zigzag antenna

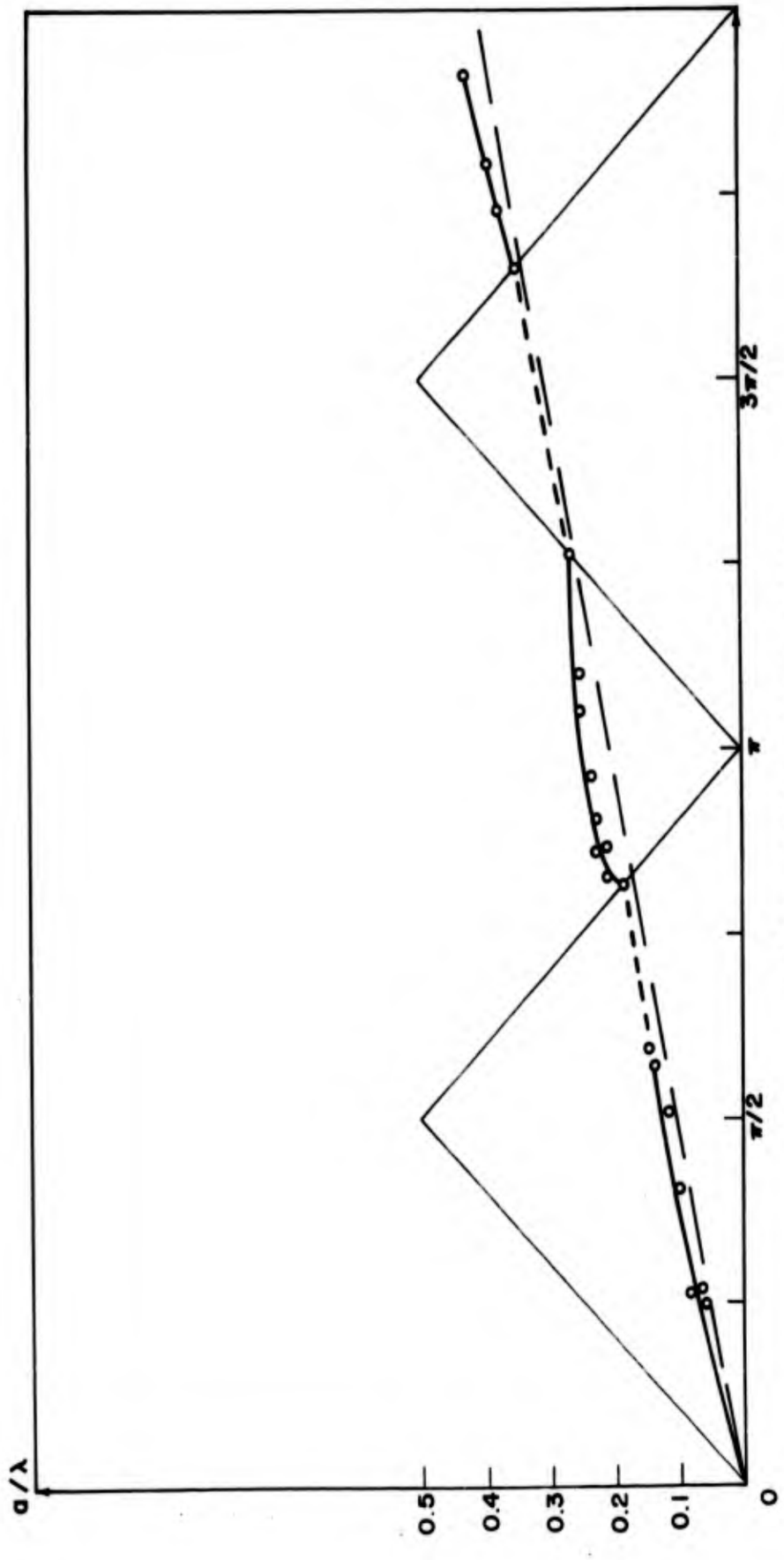

Figure 14 Brillouin diagram for uniform periodic bent zigzag antenna

harmonic which is a fast wave having a direction of propagation corresponding to the direction of maximum radiation.

$$\frac{\beta_n}{k} = \cos\theta \qquad \beta_n = \beta_o + \frac{2\pi n}{a}$$

k = free-space phase constant
θ = angle of maximum radiation
a = period
n = integer

We therefore see that the Brillouin diagram for this nonresonant structure is quite different from either of the resonant structures. A space harmonic in the field can produce backward wave radiation when the proper relation exists between the period of the structure and the operating wavelength. In this backfire region the propagation constant along the zigzag is complex as also it is in the stopband of the periodic dipole array.

5. SUMMARY

We have demonstrated here that the feeder voltage and current of a dipole-loaded transmission line is closely given by simple waves with frequency-dependent propagation constants. Backfire radiation occurs in frequency bands where the propagation constant is complex but the phase progression of the dipole currents from element to element is much greater than that corresponding to propagation in free-space. In this respect the dipole array differs from other nonresonant frequency-independent antennas such as the log-periodic zigzag and the conical log-spiral.

We have thus attempted to clarify the role of complex propagation constants as they affect the performance of frequency-independent antennas. From these considerations it is hoped that improved tehcniques for analysis and design of frequency-independent antennas will be evolved.

ACKNOWLEDGEMENT

The authors gratefully acknowledge helpful discussions with Professor G. A. Deschamps. They also are indebted to E. Hadock and J. W. Greiser for the use of their data. This work was sponsored by USAF Aeronautical Systems Division, Wright-Patterson AFB, Ohio under Contract AF 33(657)-8460.

REFERENCES

1. P. E. Mayes, G. A. Deschamps, and W. T. Patton, "Backward Wave Radiation from Periodic Structures and Application to the Design of Frequency-Independent Antennas", Proc. I.R.E., (correspondence), Vol. 49, No. 5, May 1961, pp. 962-963. Also, Tech. Rept. No. 60, Contract No. AF33(657)-8460, Antenna Laboratory, University of Illinois, Urbana, Illinois, October, 1962.

2. W. T. Patton, "The Backfire Bifilar Helix", Technical Report No. 61, Contract No. AF(33(657)-8460, Antenna Laboratory, University of Illinois, Urbana, Illinois, October, 1962.

3. R. Mittra, "Theoretical Study of a Class of Logarithmically Periodic Circuits", Technical Report No. 59, Contract No. AF33(657)-8460, July, 1962, Antenna Laboratory, University of Illinois, Urbana, Illinois.

4. D. Isbell, "Log-Periodic Dipole Arrays," IRE Trans., Vol. AP-8, No. 3., May, 1960, pp. 260-267. Also Technical Report No. 39, Contract No. AF33(616)-6079, June, 1959, Antenna Laboratory, University of Illinois, Urbana, Illinois.

5. R. L. Carrel, "Analysis and Design of the Log-Periodic Dipole Antenna," Technical Report No. 52, Contract AF33(616)-6079, October 1961, Antenna Laboratory, University of Illinois, Urbana, Illinois.

6. O. L. McClelland, "An Investigation of the Near Fields on the Conical Equiangular Spiral Antenna, Technical Report No. 55, AF33(657)-8460, Antenna Laboratory, University of Illinois, Urbana, Illinois, May, 1962.

7. K. E. Jones and R. Mittra," A Survey of Continuously Scaled and Log-Periodic Transmission Lines with Application to Antenna Problems", 1962 Fall URSI-IRE Meeting, Ottawa, Ontario, Canada, October 1962.

8. P. E. Mayes, R. L. Carrel, "Logarithmically Periodic Resonant-V Arrays," Technical Report No. 47, Contract No. AF33(616)-6079, Antenna Laboratory, University of Illinois, Urbana, Illinois, 15 July 1960.

9. J. W. Greiser and P. E. Mayes, "Vertically Polarized Log-Periodic Zigzag Antennas", Proc. National Electronics Conference, Vol. 17, pp. 193-204, October 1961.

AUTOMATIC MEASUREMENT OF THE PHASE CENTERS OF ANTENNAS*

John D. Dyson

and

Robert E. Griswold

University of Illinois

Urbana, Illinois

ABSTRACT

An approach to the measurement of the phase centers of antennas has been developed which depends upon the comparison of information received from a detector which is sensitive to the amplitude and phase of the radiated field, with one sensitive only to the amplitude of this field. These patterns may be automatically recorded on standard antenna range equipment. The system can materially reduce the time required to determine the phase center and can be a useful tool in the study of antennas for which a unique phase center does not exist.

---

*Presented at the Twelfth Annual USAF Symposium on Antenna Research and Development, sponsored by the Aeronautical Systems Division, AFSC., 16-19 October 1962.

1. INTRODUCTION

There are many applications of antennas which demand a knowledge of the phase as well as the amplitude characteristics of the radiation field. For any given antenna an expression for one component of this field can be put in the form

$$E = cf(\theta,\phi)\,\frac{e^{j(\Psi(\theta,\phi) - \beta r_o)}}{r_o} \qquad (1)$$

where c is a constant depending on the amplitude of excitation and units used, and r_o is the distance from the chosen origin of coordinates to the point of observation. In this expression θ is the elevation angle and ϕ the azimuthal angle in a spherical coordinate system.

The directive pattern of the amplitude function $f(\theta,\phi)$, and the directive pattern of the phase function $\Psi(\theta,\phi)$, represent the far field. It is well known that a shift in the origin to which the coordinates are referred, by a distance which is small compared to r_o, can be neglected in the expression for the amplitude of this field, but this same shift in origin can not be neglected when considering this phase of the radiated field. Thus, although the form of the amplitude function, $f(\theta,\phi)$ is considered to be independent of the exact origin of coordinates, the phase function $\Psi(\theta,\phi)$ is not.

For some antennas there does exist an origin such that the phase function $\Psi(\theta,\phi)$ is constant, independent of θ and ϕ[1]. Such an origin is defined to be the phase center of that antenna. The choice of another component of the radiated field will in general lead to a different phase center.

The present study was initiated to determine the phase center, if one existed, for the conical log-spiral antennas. Such information would help to provide a better understanding of the mechanism of radiation from these structures, and also permit their use in complex systems, such as feeds for reflectors and in complex array geometries.

For most antennas and in fact for the logarithmic spiral and logarithmic periodic antennas, a unique phase center apparently does not exist. For such antennas there may exist, however, a limited surface, over which the phase function is essentially constant. Associated with this surface, there exists an origin or center of curvature which we will define to be the "apparent phase center" for this limited surface. This limited surface may in some cases degenerate into an arc of a given angular width. For example the phase of the far field of the conical spiral antennas is known to vary linearly with the azimuthal angle ϕ. Hence, observations must be made in a plane of constant ϕ.

This concept of an "apparent phase center" is nevertheless a useful parameter in the practical application of these antennas since it has been observed that the movement of this center, as the angle of observation is changed, may be very small in terms of wavelengths. An apparent phase center must, however, be specified in terms of the polarization of the incident field, the plane of observation, and a range of angular coordinates associated with that plane.

In this context we will present a method of experimentally determining the phase center of an antenna if one exists, or the apparent phase center for a given surface if a unique phase center does not exist.

2. DETERMINATION OF THE PHASE CENTER

Assume that an antenna is given that has a phase center on the axis of the structure. If a phase pattern is recorded for this antenna about some origin, or center of rotation, which coincides with the phase center, this pattern will be a constant, i.e., a circle on a polar plot or straight line on a rectangular plot.

If now a phase pattern in a plane of constant ϕ (the azimuthal angle around the axis of the antenna) is recorded for this antenna about some origin which lies along the axis of the structure, but is displaced a distance r from the phase center, the phase of the field of the antenna will be modulated by a sinusoidal function of the elevation angle, θ. When r is very small with respect to the distance to the point of observation, this modulation function, as shown in Figure 1 may be expressed as

$$\Phi \cong \beta r(1 - \cos \theta) \qquad (2)$$

If the pattern is normalized to the phase of the signal received when the phase center is at position A in Figure 1a, the resultant phase pattern will be as shown in Figure 1b. Normalization to the phase of the signal received when the phase center is at position B in Figure 1c will produce a phase pattern as shown in Figure 1d.

One of the conventional methods of determining the phase center is to measure the phase of the signal received when the antenna is at a position such as A in Figure 1; and then vary the angle θ in small steps about this point by rotating the antenna, measuring the phase of the received signal at each of these points[2]. A plotted curve of these measured values will normally be of a sinusoidal form. In theory the position of the phase

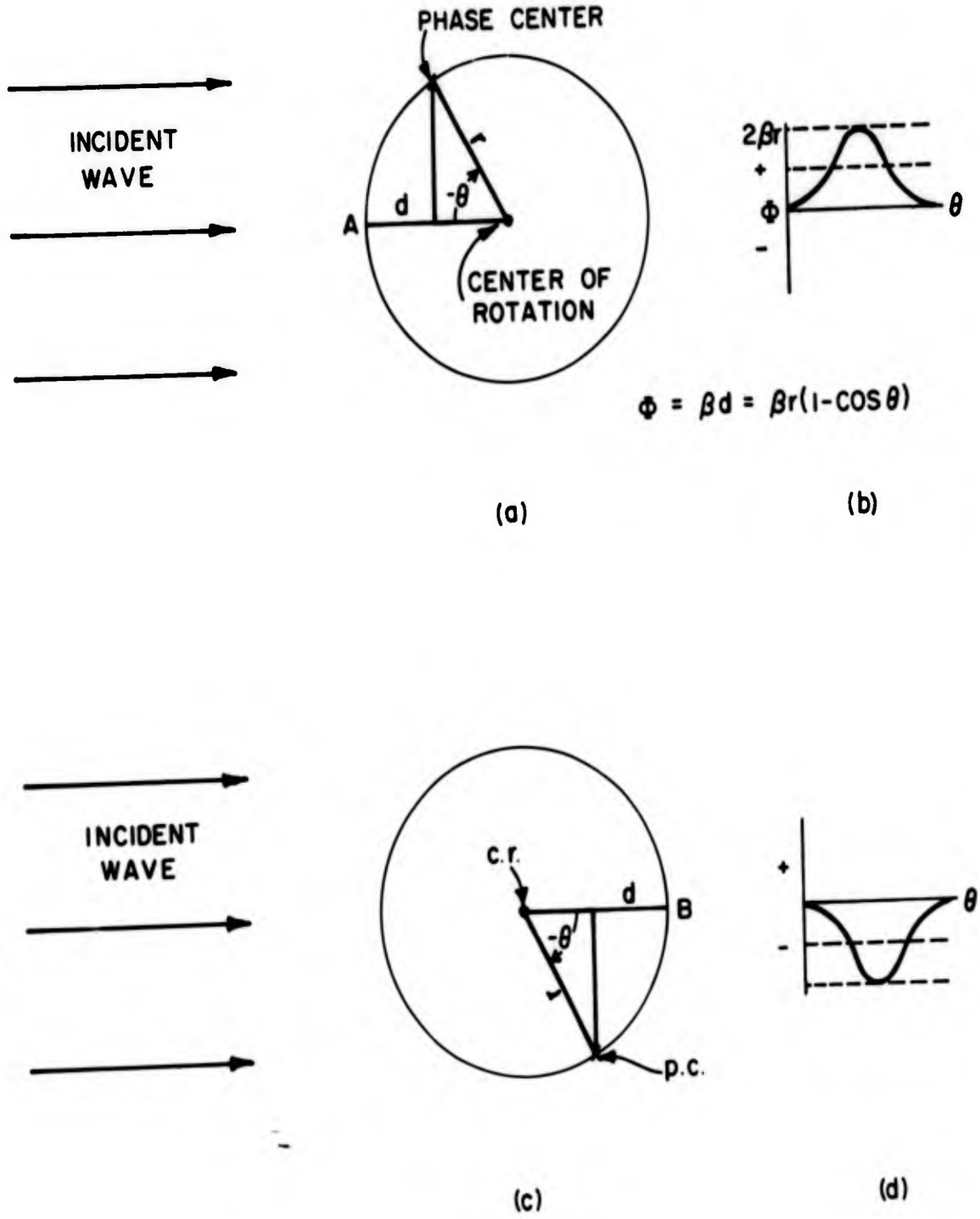

Figure 1. Phase modulation of the electric field where antenna is rotated about an origin displaced from the phase center

center can be calculated from one such curve. In practice it is frequently necessary, because of experimental anomalies or because the antenna has no phase center, to reposition the antenna along a radial line directed toward the source of radiation and record sufficient data to plot several curves to bracket a curve with minimum variation, i.e., in the idealized case a straight line, before a decision can be made. A second method of determining the phase center depends upon plotting equiphase contours.[3,4] Unless these methods are automated they involve many individual measurements and are tedious and time consuming.

3. AN AUTOMATIC PHASE COMPARISON SYSTEM

Phase measurements in the UHF or microwave region are all relative measurements in which two r.f. voltages are usually combined by addition or subtraction to obtain an interference pattern or a null[5,6]. For voltages which are not equal in magnitude the greatest sensitivity to small changes of the phase of one signal can be achieved by a system which provides a null when the two r.f. voltages are in phase quadrature. One such system is shown in Figure 2.

An r.f. voltage is generated at the desired frequency, modulated, filtered and monitored in the usual manner. A reference voltage, E_R, is extracted with a directional coupler and the remainder of the original signal is radiated as the transmitted field. The antenna under test is placed in the far field on a positioner that is capable of precise rotation about a point and of precise translation along an axial line between the transmitting and receiving positions.

The reference voltage, E_R, which can be varied in amplitude and phase, is combined with the unknown voltage, E_S, in a hybrid circuit. If we let

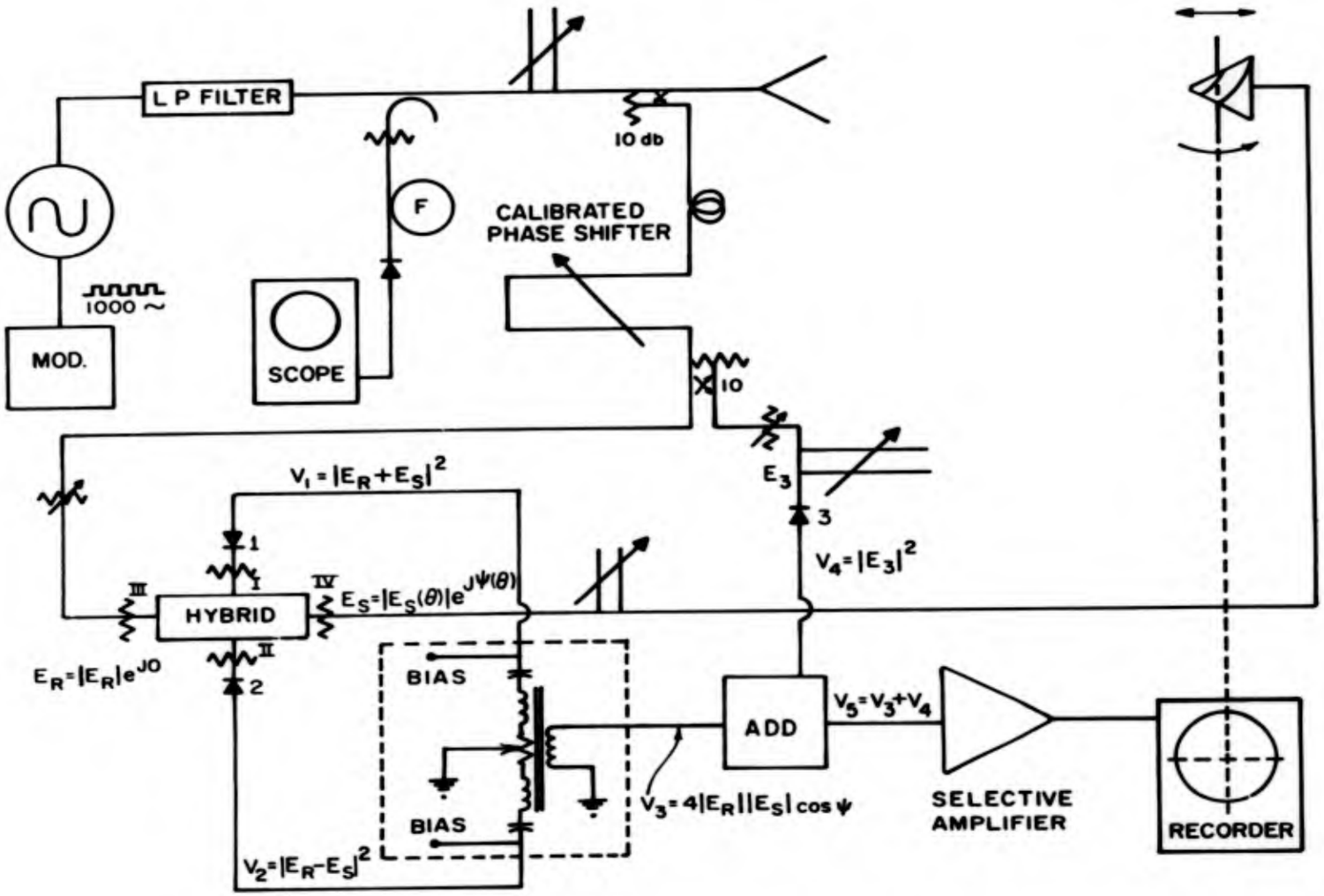

Figure 2. Diagram of equipment for measurement of phase centers

$$E_R = |E_R| \, e^{j0} \tag{3}$$

$$E_S = |E_S(\theta,\phi)| \, e^{j\psi(\theta,\phi)} \tag{4}$$

where ψ is the relative phase delay between E_R and E_S, the output from the side arms of the hybrid will be

$$E_R + E_S = |E_R| + |E_S| \cos\psi + j\,|E_S| \sin\psi \tag{5}$$

$$E_R - E_S = |E_R| - |E_S| \cos\psi - j\,|E_S| \sin\psi \tag{6}$$

These outputs when detected by matched square law detectors will give

$$V_1 = (|E_R| + |E_S| \cos\psi)^2 + (|E_S| \sin\psi)^2 \tag{7}$$

$$V_2 = (|E_R| - |E_S| \cos\psi)^2 + (|E_S| \sin\psi)^2 \tag{8}$$

The difference between V_1 and V_2 may be taken with an audio transformer to yield,

$$V_3 = 4\,|E_R| \, |E_S| \cos\psi \tag{9}$$

Since the reference voltage, $|E_R|$ is constant, the voltage, V_3, is proportional to the amplitude, $|E_S(\theta,\phi)|$, and the cosine of the phase, $\psi(\theta,\phi)$, of the unknown signal.

If we assume both $|E_S|$ and $|E_R|$ are constant, Figure 3 indicates the relative magnitudes of the voltages V_1 and V_2 at the side arms of the hybrid as the angle ψ varies from 0 to π. At $\psi = \pi/2$ these voltages are equal, and

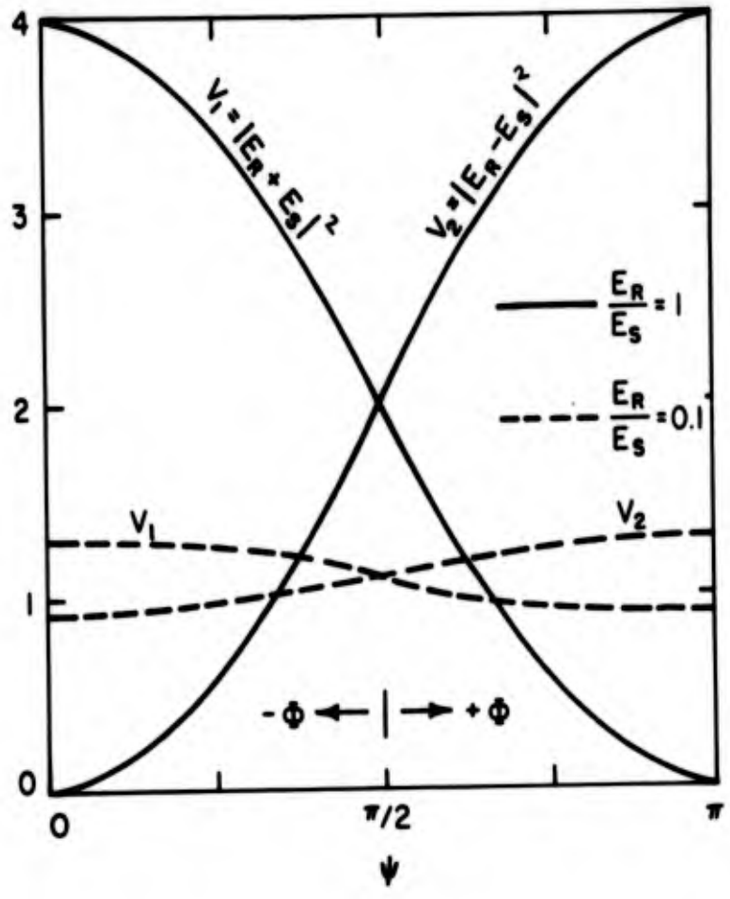

Figure 3. Relative magnitude of voltages at side arms of hybrid

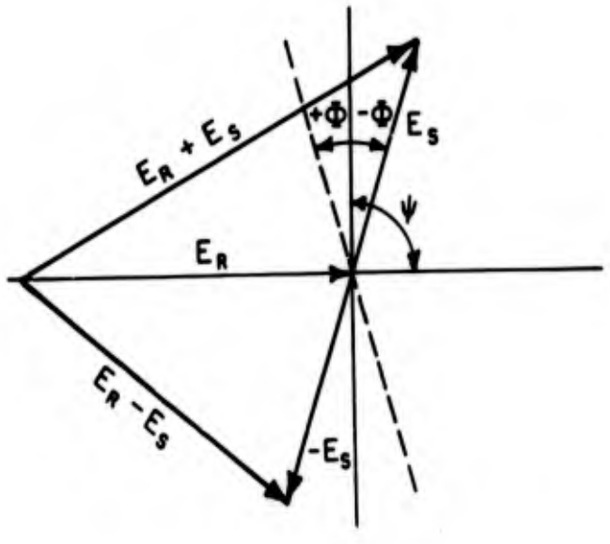

Figure 4. Voltages at the terminals of the hybrid

as indicated by Equation (9), $V_3 = 0$. This system has been used for the measurement of relative phase[7,8]. In this measurement the system is balanced to a null when $\psi = \pi/2$. A change in phase of the unknown voltage is then compensated for by a change in phase of the calibrated phase shifter in the reference line. As Figure 4 indicates, since the system is balanced to a null when the reference and unknown voltages are in phase quadrature, it has good sensitivity to small changes in ψ in the neighborhood of $\psi = \pi/2$ even though there are large differences in the relative magnitudes of these voltages.

From Equation (2), $\Phi = 0$ at $\theta = 0$ and, since to null the system we force ψ to be $\pi/2$ at $\theta = 0$,

$$V_3 = 4 \mid E_S(\theta) \mid \mid E_R \mid \cos\left(\frac{\pi}{2} \pm \Phi\right) \tag{10}$$

The voltage V_3 could be plotted on a recorder as a function of the angle θ. If the system is nulled at $\theta = 0$ and the phase center is displaced from the center of rotation, the recorded voltage would appear as in Figure 5a on polar and rectangular plots for an omnidirectional antenna ($\mid E_S \mid = 1$). Similar plots are shown in Figure 5b for an antenna with a bidirectional cos θ radiation pattern. If a radial displacement of the antenna produces some origin or center of rotation, such that these patterns reduce to a point, or a straight line respectively, this center of rotation coincides with the phase center.

Figure 1 indicates that there is a polarity, or sense, associated with the change in phase, Φ, with a change of θ. This polarity depends upon whether the system is nulled at point A or B, that is to say, whether the signal is normalized to zero when the phase center is ahead of or behind

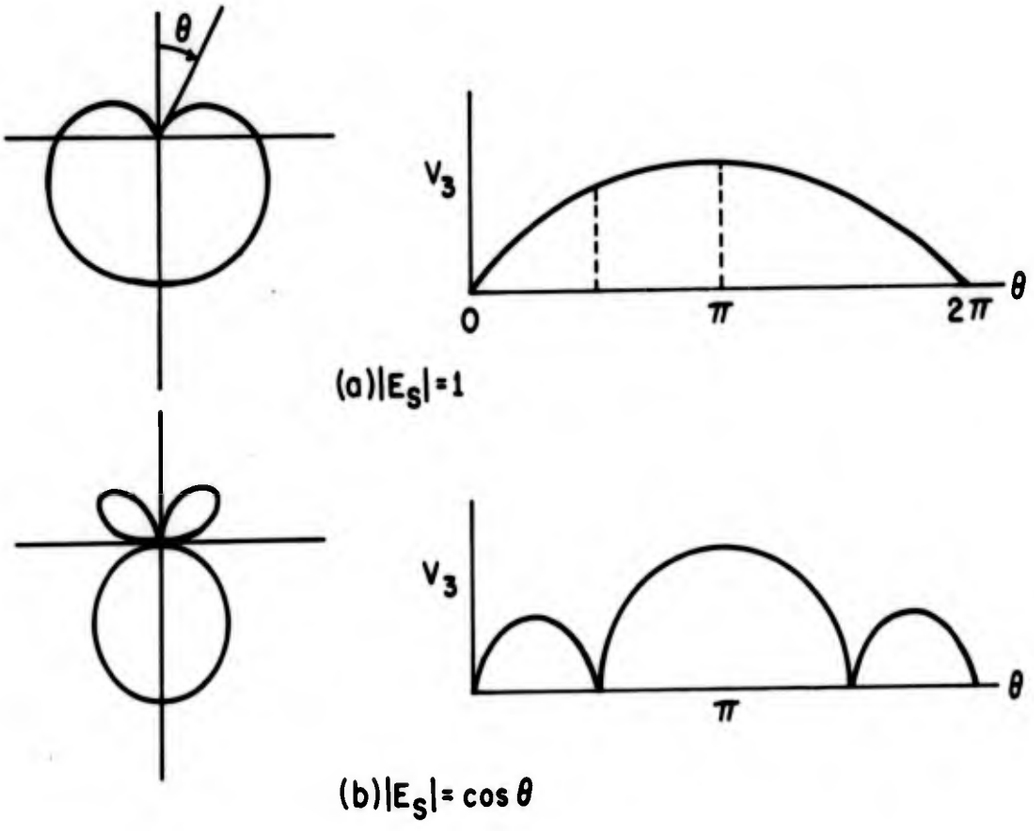

Figure 5. Magnitude of V_3 as a function of elevation angle θ

the center of rotation. An important advantage of the system outlined above is that this sense of the phase angle Φ is preserved through the system up to V_3 as indicated in Figures 3 and 4. However, the patterns of Figure 5 would be the same for either sense of Φ.

To preserve the sign of Φ a constant voltage E_3 may be taken from the reference line and, after detection, added to V_3 in a conventional audio mixer that provides adequate isolation between the two input signals. This, in effect, biases V_3 from a null condition at balance. If the magnitude of this bias voltage, V_4, is for convenience, set equal to $|E_R|$ in this mixer, we have from Equation (10)

$$V_5 = V_4 + V_3$$

$$= |E_R| [1 + 4|E_S| \cos (\psi \pm \Phi)] \qquad (11)$$

This voltage, recorded as a function of the angle θ, will take the form of Figure 6 for the unidirectional antenna with a cos θ radiation pattern. Note that this plot, which we will identify as the "modified phase pattern," preserves the sign of the phase modulation function Φ. Thus, after a simple calibration of the system, one recorded modified phase pattern will, under ideal conditions, i.e., if a phase center exists and is on the axis of the structure, predict the exact distance the phase center is in front of or in back of the center of rotation. Under practical conditions, and for antennas without a phase center, several patterns may again be required, to obtain a pattern that closely approximates the unit circle. The time required however, for balancing the system and recording an entire pattern is on the order of

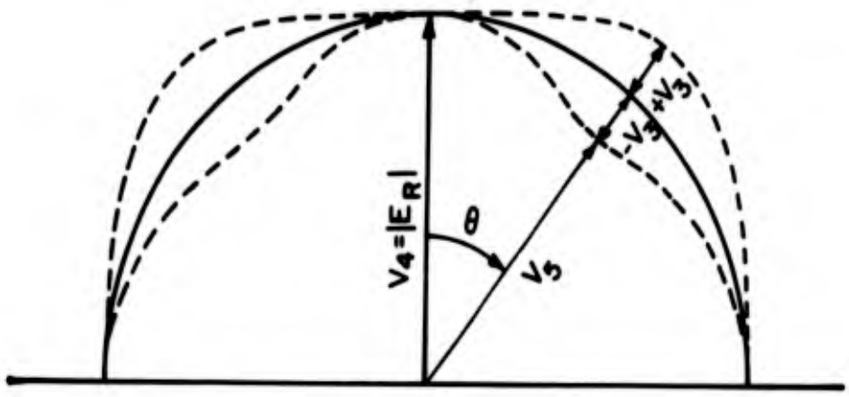

Figure 6. Modified phase pattern indicating voltage relationships

that required for a similar balancing and the measurement of the relative phase at one point with a point by point system.

Figure 7 is a rectangular plot of this modified phase pattern over one quadrant, and indicates the relative sensitivity of the system as a function of the directivity of the radiation pattern when the phase center is displaced only .05 λ from the center of rotation.

4. ADJUSTEMNT AND CALIBRATION OF THE SYSTEM

The system may be used over any frequency range where suitable components are available. Measurements have, however, been confined between 450 and 900 Mc with coaxial equipment.

Detectors 1 and 2 in Figure 2 are bolometers in matched wideband mounts selected to have an output within 1/2 db of each other for a given input signal. To provide a better match to the side arms of the hybrid, precision, well matched coaxial attenuators were inserted between these ports and the detectors. Increased isolation in the hybrid could be secured by inserting tuning stubs between one of the side ports and its attenuator. With E_S applied to port IV and a detector connected to port III, the stubs are tuned for a null at this detector.

Since the modified phase patterns that will be recorded will be functions of the amplitude of the radiation pattern, this pattern may be recorded by terminating ports II and III of the hybrid and disconnecting V_4 from the audio mixer. Thus $|E_S|^2$ is available at the recorder. Since at this laboratory a standard linear-square root pattern range recorder was used, the voltage pattern, $|E_S|$, was recorded with the amplitude adjusted to some suitable normalized value at $\theta = 0$.

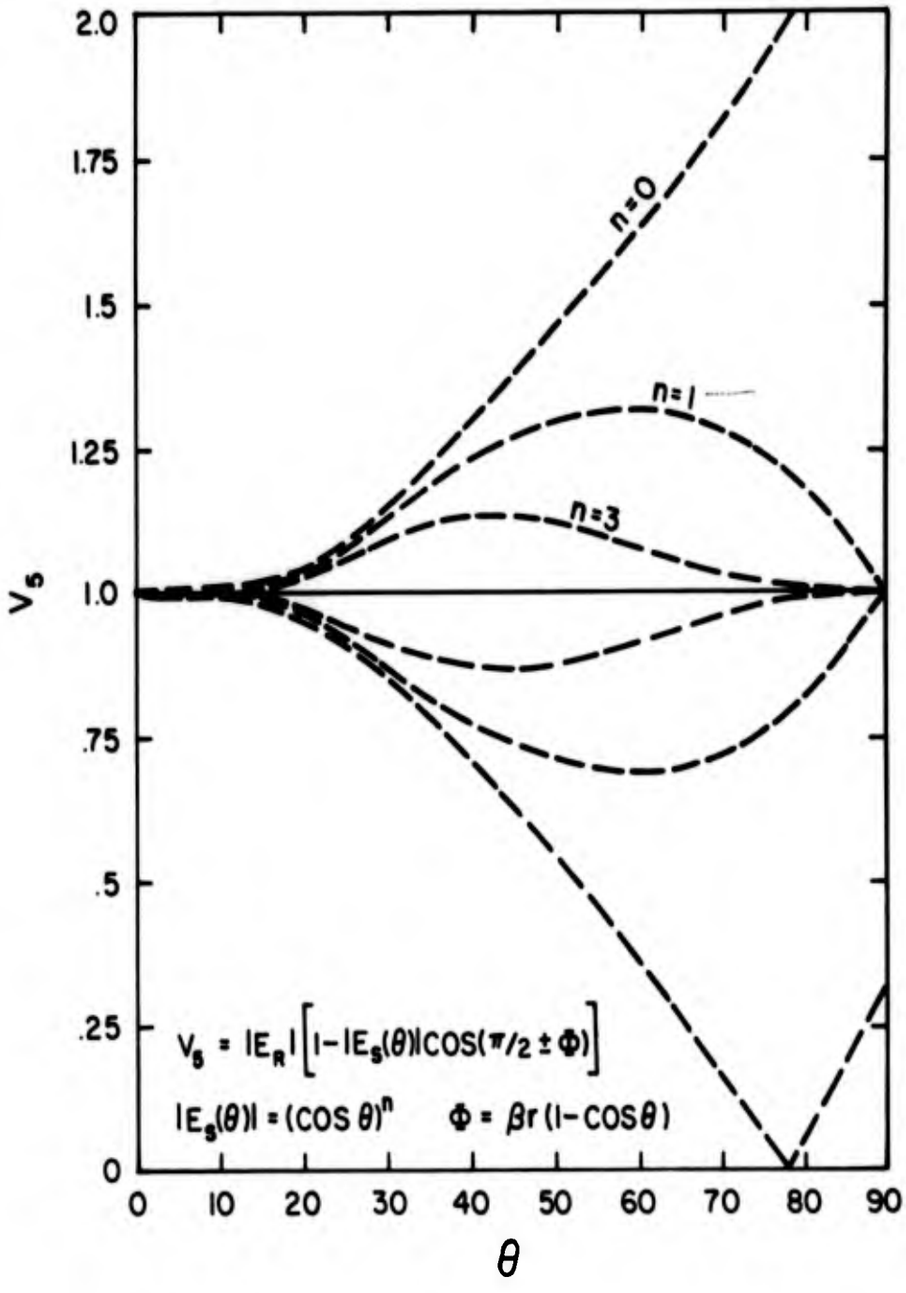

Figure 7. Relative sensitivity of modified phase pattern as a function of the directivity of the radiation pattern, $S(\theta)$. $r = .05\ \lambda$.

To insure suitable sensitivity to small changes in Φ, E_S is disconnected from the hybrid, ports II and IV are terminated, and E_R adjusted to give a deflection on the recorder equal to $|E_S|$ at $\theta = 0$ with the recorder set for linear amplification. The exact level of E_R is not critical unless the relationship between E_R and E_S is used later in the phase pattern interpretation.

To balance the audio signals, E_S is connected to the hybrid, and the padded detectors are connected to ports I and II, with port III terminated. Potentiometer P is now adjusted for a minimum indication on the recorder. For the greatest accuracy of measurement this audio null could be improved by modulating only the unknown signal E_S[8]. With the reference signal unmodulated the only undesired signal produced by the bolometers due to this reference signal is a dc signal which is rejected by the transformer.

The hybrid is reconnected as shown in Figure 2 and the phase of E_R adjusted to produce a null on the recorder, after which V_4 is connected and adjusted in magnitude to give a deflection of the recorder equal to $|E_R|$. Thus at $\theta = 0$, $V_4 = |E_R| = |E_S|$.

To initially determine the direction of the deflection of the recorder for a given input, the antenna is moved a small distance away from the transmitter and the direction of the movement of the pen noted. If the deflection of the pen is toward zero the vector relationship shown in Figure 4 applies and, as is the usual case, the audio voltage V_4 is in phase with V_3. This movement of the antenna corresponds to conditions in Figure 1a. A deflection below the unit circle or below the normalized $\theta = 0$ line on a rectangular recorder, as θ is varied, indicates that the phase center is in front of the center of rotation, i.e., between the transmitter and the center of rotation. Deflection above this line indicates the phase center is in back of the center of rotation.

If, when the antenna was initially moved back, the deflection of the pen was in the opposite direction to that just established, it indicates that E_R is 180^o out of phase with the initial assumption, or that V_4 may be out of phase with V_3. These conditions do not modify the system except that now all movement of the pen below the established reference circle or line indicates that the phase center is behind the center of rotation, and movement above this circle or line indicates that the phase center is in front of the center of rotation.

After this initial adjustment and calibration, successive modified phase patterns may be recorded for different positions of the antenna along a radial line from the source. The system is re-nulled at $\theta = 0$ by an adjustment of the phase of E_R, and if necessary, a slight adjustment is made in the magnitude of V_4.

5. INTERPRETATION OF THE RECORDED PHASE PATTERNS

To aid in the interpretation of recorded patterns, the functions defining Φ and V_3 have been plotted over a limited range of values in Figure 8. As an example of the use of these graphs, assume a recorded modified phase pattern has a normalized amplitude of 1.3, and the electric field radiation pattern has an amplitude of 0.8 at $\theta = 30^o$. We enter Figure 8 at $V_3 = 0.3$ and intersect the line $S = 0.8$. Corresponding to this intersection we read $\Phi = 5.5^o$. We then follow this vertical line to intersect the horizontal line at $\theta = 30^o$ to read a value of r between .10 and .12λ. If the prior calibration of the system indicates that a deflection greater than one indicates the phase center is behind the center of rotation we should expect it to be approximately .11λ back of the known center of rotation. A pattern or two recorded after the

antenna has been moved approximately .11λ toward the transmitter should establish the phase center of the antenna at that particular frequency. If the existence of a phase center has not been determined, the application of these curves should be limited to the neighborhood of the point of normalization.

Figure 8 could, of course, be used with a single measurement at a given angle, θ, and under ideal conditions the position of the phase center could be determined. Recording the complete modified phase pattern becomes of greatest value when the antenna does not have a phase center and an effort is being made to determine the apparent phase center for a given range of the angular coordinates about the structure.

The phase angle Φ may also be measured directly by varying the calibrated phase shifter in the reference line to rebalance the system at any point on the curve. Alternatively, calibration points may be automatically plotted on the modified phase pattern. If it is desired to calibrate a plotted curve that deflects below the unit circle or line, a fixed calibration angle, δ, of the opposite sign may be inserted in the system by changing the phase of E_R. Thus

$$V_5 = |E_R| \, [1 - 4 |E_S(\theta)| \cos (\pi/2 + \delta - \Phi)] \qquad (12)$$

A new phase pattern is now plotted and when this new pattern crosses the unit circle, $\Phi = \delta$.

6. MEASURED PATTERNS

Figure 9 indicates the type of information that is obtainable. Modified phase patterns were recorded for a log-periodic dipole array. The pattern is

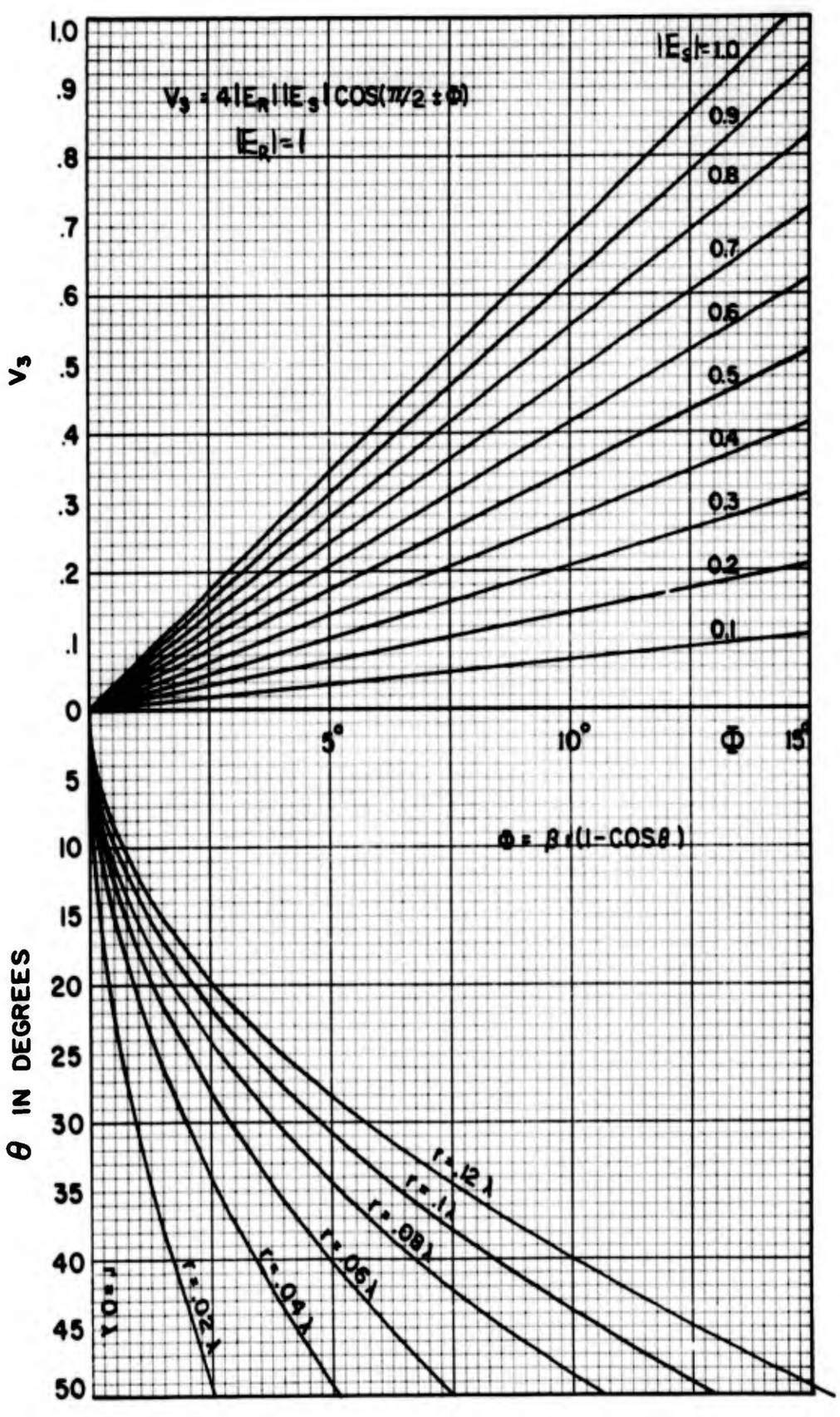

Figure 8. Modulation function Φ, and pattern deflection, V_3 for given displacement of phase center from center of rotation.

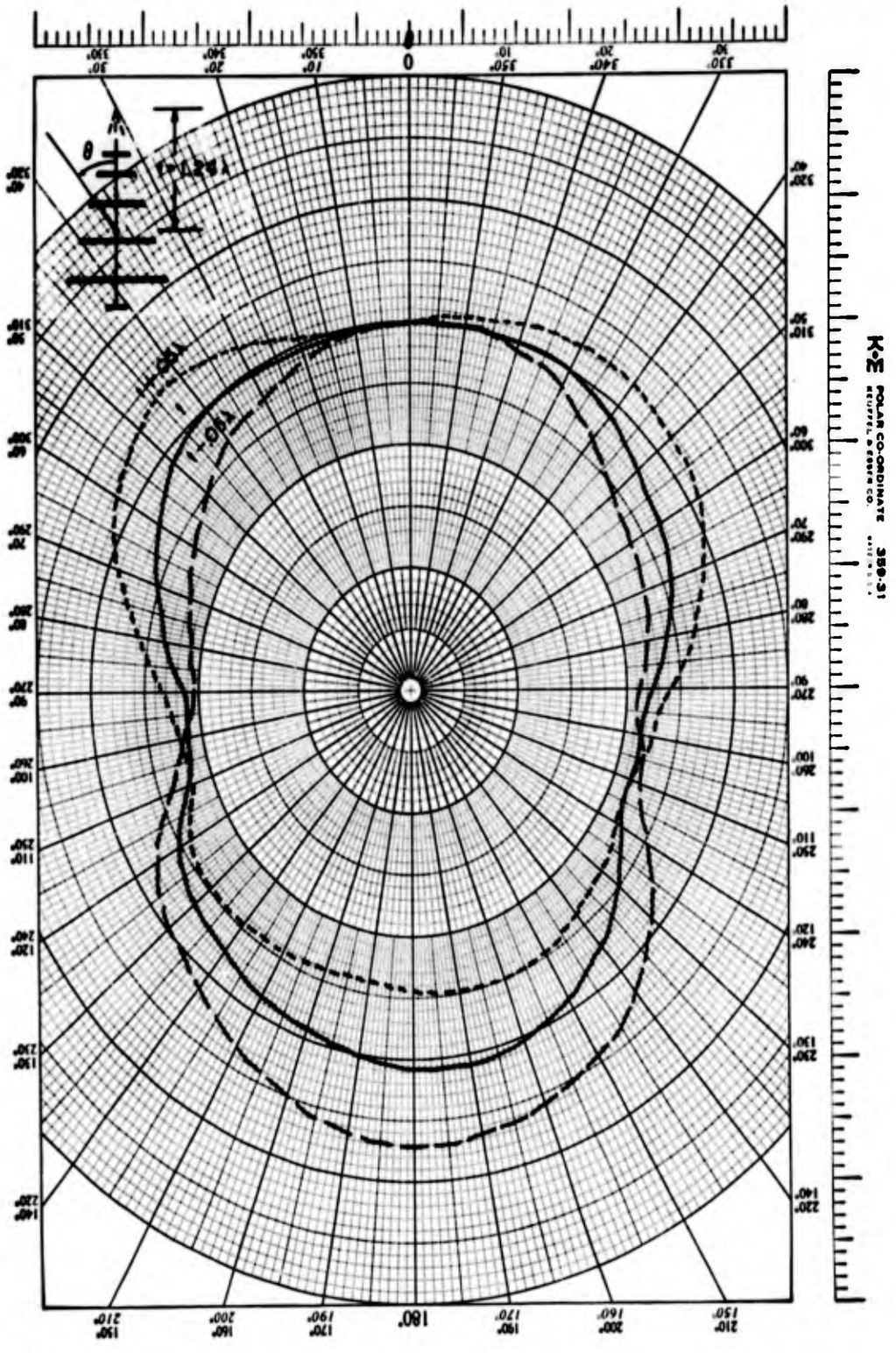

Figure 9. Recorded modified phase patterns for a log-periodic dipole array for three positions of the center of rotation

normalized to one at $\theta = 0$. At this particular frequency the antenna has an apparent phase center on the axis of the structure over a range of at least $\pm 30^{\circ}$ off the axis of the antenna. The sensitivity of the system is indicated by the two curves recorded for a displacement of the center of rotation by $\pm$ .05 λ from this apparent phase center. The resolution of the system is such that a displacement of the phase center of 0.1 in, is easily discernible at 600 Mc i.e., a displacement of approximately 1/200 wavelength.

Figure 10 again shows the modified phase pattern for this antenna, recorded with the center of rotation 1.24λ from the apex and calibration curves for 2°, 5°, and 10° variations in Φ. This curve indicates that for $53^{\circ} \geq \theta \geq 314^{\circ}$ in a plane perpendicular to that of the elements, there is a phase contour that varies no more than +0, -2° from a circle. Associated with this phase contour we can identify an "apparent phase center" 1.24 λ from the apex.

Note that beyond this range of θ the modified phase pattern rapidly departs from the unit circle. This would indicate that the phase front in this region is distorted from a spherical surface and that the center of curvature for any given segment of this phase front has moved away from the apparent phase center measured for the main portion of the radiated beam.

Modified phase patterns for one conical log-spiral antenna are shown in Figure 11. These indicate that over a range of $40^{\circ} \geq \theta \geq 325^{\circ}$ for this particular ϕ-constant cut, there is an apparent phase center located on the axis 0.798 wavelengths from the tip of the cone. There is less than a 2° variation in the phase contour associated with this center from $50^{\circ} \geq \theta \geq 305^{\circ}$.

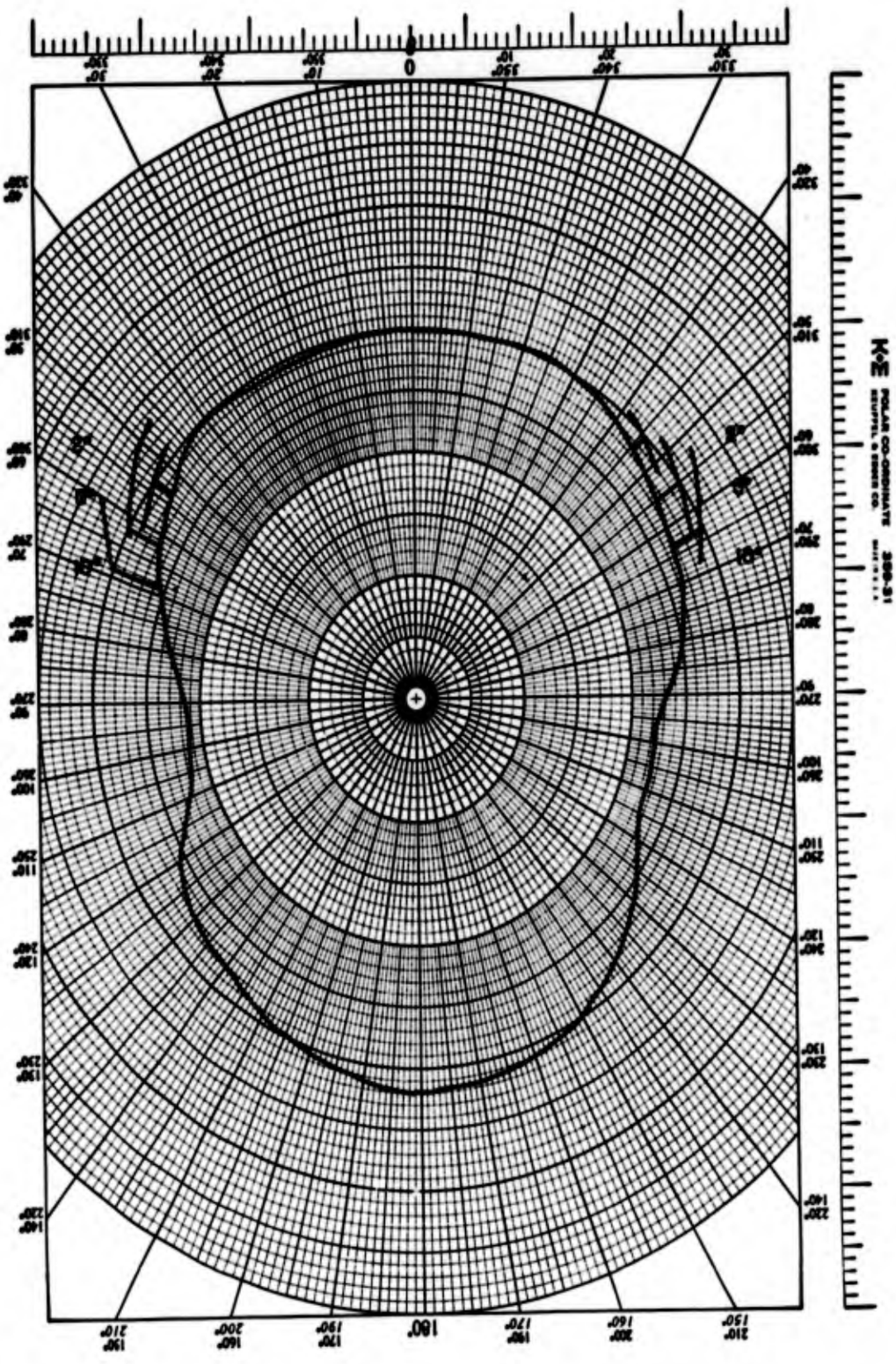

Figure 10. Modified phase pattern for L-P dipole array with calibration curves at 2^{o}, 5^{o}, and 10^{o}

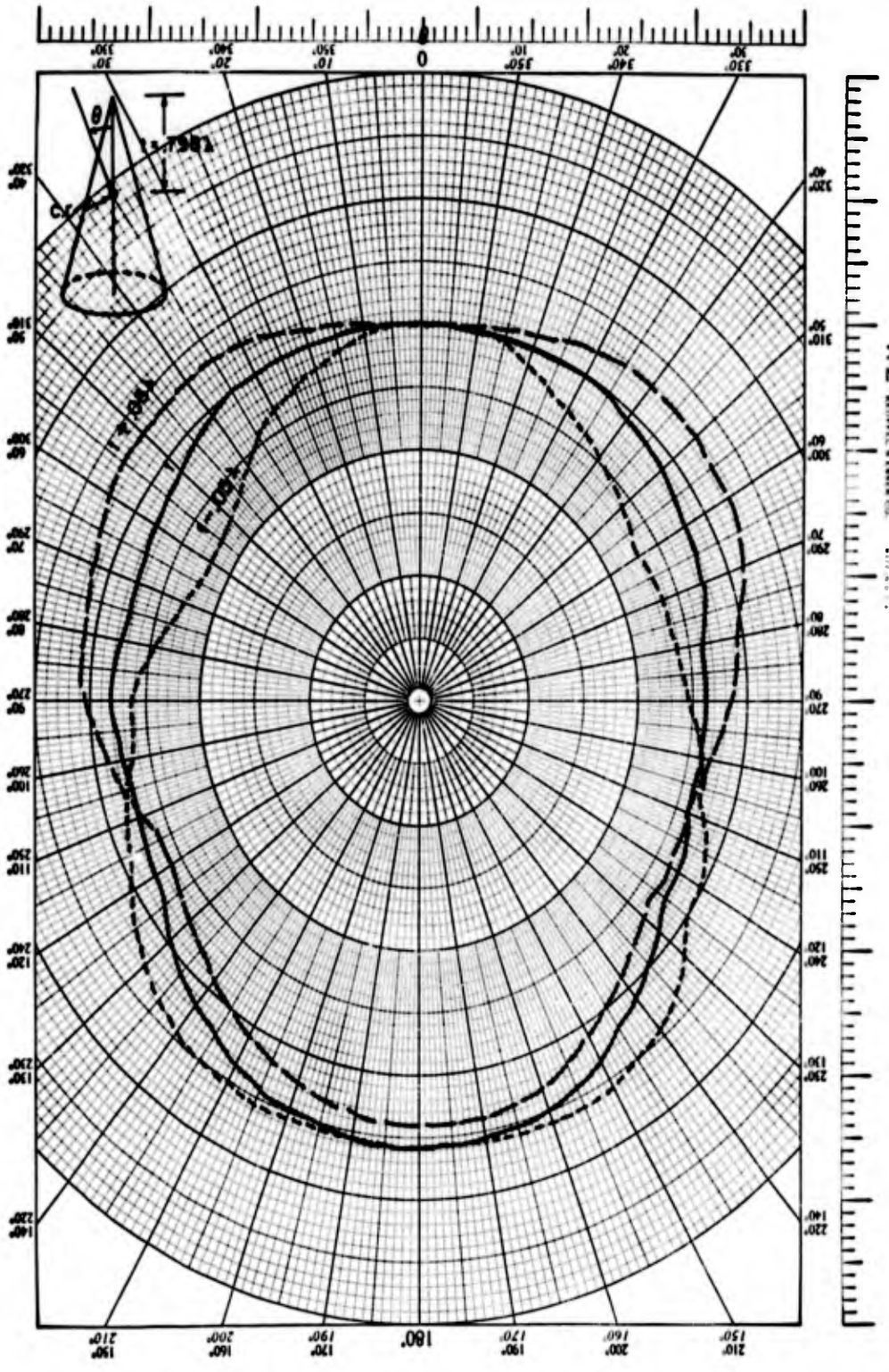

Figure 11. Modified phase pattern of one conical spiral antenna for three positions of the center of rotation

The fact that all three curves in Figures 10 and 11 mutually intersect at θ equal to approximately $\pm 100^{o}$, at a point below the unit circle, would indicate that the apparent phase center around this angle of incidence is on the other side of the axis of the antenna from the incident wave. This is in agreement with the theoretical solution obtained by Carrel for the log-periodic dipole array[9]. A detailed study of the phase centers of some of the frequency independent antennas using these techniques will be the basis of a subsequent paper.

7. A VARIATION IN THE SYSTEM

One variation of the system that permits an interesting display is to sample voltage E_3 from the unknown signal E_S instead of from the reference signal. If detector No. 3 in Figure 1 is changed to a linear detector we can make

$$V_4 = |E_S(\theta)| \tag{13}$$

From the audio mixer the signal becomes,

$$V_5 = |E_S(\theta)| \; [1 - 4|E_R| \cos(\pi/2 \pm \Phi)] \tag{14}$$

Equation (14) indicates that displacement of the phase center from the center of rotation will cause a deviation of the shape of the modified phase pattern from that of the amplitude pattern, $|E_S(\theta)|$. Further the sense of Φ is preserved. Thus depending upon the initial calibration, a displacement of the phase center in front of the center of rotation will cause a deviation greater than the amplitude pattern, and displacement of the phase center in

back of the center of rotation will produce a modified phase pattern that is narrower than the amplitude pattern. This display may have importance in the study of antennas which have "rough" amplitude patterns and hence rapid variations in $|E_S|$ that might make the interpretation of modified phase patterns made with the original system difficult to interpret.

8. CONCLUSION

A new approach to the measurement of the phase center of antennas has been developed. In essence this consists of comparing the recorded radiation pattern made with a detector sensitive to only the amplitude of the radiated field, with one made with a detector sensitive to the amplitude and phase of this field. Deviations of this latter pattern from a unit circle or straight line (or as a modification, from the amplitude pattern), may be interpreted from curves supplied, to show the position of the phase center from the known center of rotation used to obtain the patterns.

There are many antennas, including the log-periodic and log-spiral antennas, that do not have a unique phase center. For these antennas an "apparent phase center" is defined over a limited range of space surrounding the antenna. This measurement technique permits a continuous display of the effective position of this "apparent phase center" for all angles off the axis of the antenna in the particular plane in which patterns are recorded.

The system can materially reduce the time required to determine the phase center of antennas and should be a useful tool in the study of those antennas for which a unique phase center does not exist.

REFERENCES

1. Vol'pert, A. R., "On the Phase Centers of Antennas," Radiotekhnika, Vol. 16, No. 3, 1961, pp. 3-12.

2. Sander, S., and Cheng, D. K., "Phase Center of Helical Beam Antennas," Syracuse University Research Institute, Report No. EE393, 56121, Contract AF30(602)-1463, 31 October 1956.

3. Hu, Yueh-Ying, "Phase Centers of Electromagnetic Horns," Syracuse University Research Institute, Final Report, Contract AF30(602)-926-EE19, 30 September 1954.

4. Barbano, N., "Phase Center Distributions of Spiral Antennas," IRE WESCON Convention Record, 1960, Part I.

5. Wind, M. and Rapaport, H., "Handbook of Microwave Measurements," Polytechnic Institute of Brooklyn, Vol. I & II, 1954.

6. Montgomery, C. G., "Technique of Microwave Measurements," McGraw-Hill, 1947.

7. Morita, T., and Sheingold, L. S., "A Coaxial Magic-T," Trans. of IRE, Vol. MTT-1, No. 2, November 1953, pp. 17-23.

8. Richmond, J. H., "Measurement of Time-Quadrature Components of Microwave Signals," Trans. of IRE, Vol. MTT-3, No. 3, 1955, pp. 13-15.

9. Carrel, R. L. "Analysis and Design of the Log-Periodic Dipole Antenna," Antenna Laboratory, University of Illinois, Technical Report No. 52, Contract AF33(616)-6079, October 1961, AD 264 558.

BALANCED FLUSH MOUNTED LOG-PERIODIC ANTENNA FOR AEROSPACE VEHICLES

Abstract of Paper
Presented at Twelfth Annual Symposium
on USAF Antenna Research
and Development
University of Illinois
16-19 October 1962

By: Paul F. Stang
at Lockheed-California Company

Summary:

The antenna described here is a log-periodic, cavity backed tooth structure radiating in a quasi-endfire mode with a forward pointing beam. It covers the frequency range from 1.0 Gc to 10 Gc. The structure is suitable for flush mounting in an airframe. The size is

length = 11.3"

width = 8.0"

depth = 3.0"

The VSWR is less than 3:1 over the band. The lobe of the radiation pattern is nearly the same at all of the test frequencies and appears independent of the applied frequency. Two antenna halves are used and are fed against each other with a teflon filled logarithmically tapered line balun. To avoid cavity resonance the cavity on all sides and on its bottom is covered with absorbing material. The feedpoint is at the vertex of the two antenna halves and is not connected to the cavity.

This antenna produced a beam which is in the direction in which the vertex of structure points. The take-off angle of the main lobe depends on the vertex angle of the structure in the same manner as the well known log-periodic antennas.

Design Parameters

The well known log-periodic antenna has two parts which are fed against each other and both of its halves radiate, when the antenna is mounted in free space. To have radiation from only one half of the structure a

terminating cavity must be provided on the side from where radiation is to be barred. Such a cavity was built replacing one half structure. But tested over a 10 to 1 band the result was not promising because of cavity resonance, and, therefore, the radiation patterns were found multilobed of certain frequencies. This means that the antenna cannot be halved and have the same performance as the balanced model. To avoid any cavity resonance the cavity was covered with non-reflecting material on all sides and on the bottom, and a balanced antenna type was used. Both antenna halves were inserted. One of the antenna halves was located inside of the non-reflecting cavity; the other antenna halves were flush mounted on the cavity lid. The feedpoint is on the vertex of the two antenna halves and is not connected to the cavity.

This is the important point! Both antenna halves radiate the energy. The flush mounted antenna half radiates the energy into free space, and the one inside the cavity radiates its energy into the non-reflecting material. This part looks like a matched dummy antenna. The whole antenna system is therefore well balanced, and no resonance from the cavity occurred. The angle between the two halves is approximately 20 degrees. It should be noted that the impedance of such an arrangement shifts with the vertex angle ψ and the angle α of the structure. In our present case the antenna was matched to the 50 ohm cable with a teflon filled logarithmically tapered line balun.

The Figure No. 1 shows the trapezoidal teeth structure.

$R_1 = 7.15"$, $t = 0.7$, $\sqrt{t} = 0.838$, $\alpha = 45°$, $\beta = 15°$

The low frequency cutoff occurs approximately when the longest tooth is 1/4 wavelength long and the high frequency cutoff occurs when the shortest tooth is somewhat less than 1/4 wavelength long.

Two of these antenna halves were built and mounted in the non-reflecting cavity with a vertex angle of 20 degrees (see Fig. 4a and 4b).

The space on the vertex is confined; therefore, a logarithmic tapered line balun was built which is shown in Fig. No. 2 and 3. The inner conductor is constant in its size. The outer conductor is logarithmically cut off in its length and converts the coaxial structure slowly into a parallel wire transmission line.

Such a transformer is used to match the antenna to the 50 ohm cable. The transformer runs along at the center of the antenna halves. The outside of the conductor is in contact with the antenna halves which are located inside of the cavity. The center conductor of the transformer is connected at the upper antenna halves.

The Non-reflecting Cavity

To minimize cavity resonance the cavity on its inside is covered with absorbing material (Emerson & Cuming Type AN73 3/8"). Two layers of this material are applied, but the contacting sheet is scraped off at the first layer and a coated cardboard inserted between the two layers of absorbing material. This is made to increase the bandwidth of the absorbing material.

This is made to increase the bandwidth of the absorbing material. The cavity resonance is practically eliminated over a wide frequency band. At the lower end of the frequency band the cavity resonance was found to be not critical. Anyway, at the higher end of the frequency band the cavity resonance without the non-reflecting sheet was recognized as very troublesome. (See Fig. 5 and 6.)

VSWR Measurements

In steps of 500 Mc the over-all VSWR was measured. The maximum VSWR is 3:1 of approximately 8 Gc. In Fig. No. 7 the result is plotted over the frequency band from 1 Gc to 10 Gc.

Antenna Patterns

The patterns of the antenna were measured over the ten to one frequency band (1000 Mc to 10000 Mc.) In principal, the main beam pointed up approximately 20° above the plane at the antenna window at all of the tested frequencies. In the range from 6500 Mc to 7500 Mc greater side lobes become apparent, but the main beam still points up into the 20 degree direction.

The beam width is smaller at the higher frequency band and wider in the lower frequency band as expected. At an angle of 10° up, at all of the tested frequencies the decrease in gain never goes below 3 db from the maximum.

Conclusion

The antenna presented here is very useful for wide-band signal reception and is particularly suited for ECM application. Other applications seem to be promising, as the beam can be broadened or narrowed by different design of the structure, and the "take off angle" can be varied with the vertex angle between the two antenna halves.

A continuation of the study, which so far has not been funded, is indicated in view of possible application for ASW, radar homing and others.

Bibliography

1. Du Hamel, R. H. and D. E. Isbell, "Broadband Logarithmically Periodic Antenna Structures," Technical Report No. 19, Antenna Laboratory, University of Illinois, May 1957.

2. Du Hamel, R. H. and F. R. Ore, "Logarithmic Periodic Antenna Design," Collins Radio Comp. Technical Report CTR-198, March 1958.

3. Du Hamel, R. H. and D. E. Isbell, "Broadband Logarithmically Periodic Antenna Structures," 1957 IRE National Convention Record, March 1957.

4. Du Hamel, R. H. and D. E. Isbell, "Logarithmically Periodic Antenna Design," 1958 IRE National Convention Record, March 1958.

5. Du Hamel, R. H. and F. R. Ore, "Logarithmic Periodic Feeds for Lens and Reflectors," 1959 IRE National Convention Record, March 1959.

6. Webster, Robert and Jesse F. Lyles, "Application of Frequency Independent Feed in Automatic Tracking Antennas," Dynatronics, Inc., Orlando, Fla., 11th Annual Symposium USAF, Illinois, October 1961.

LOCKHEED AIRCRAFT CORPORATION
CALIFORNIA DIVISION

REPORT

Fig. No. 1

TRAPEZOIDAL TOOTH STRUCTURE

1 KMc to 10 KMc

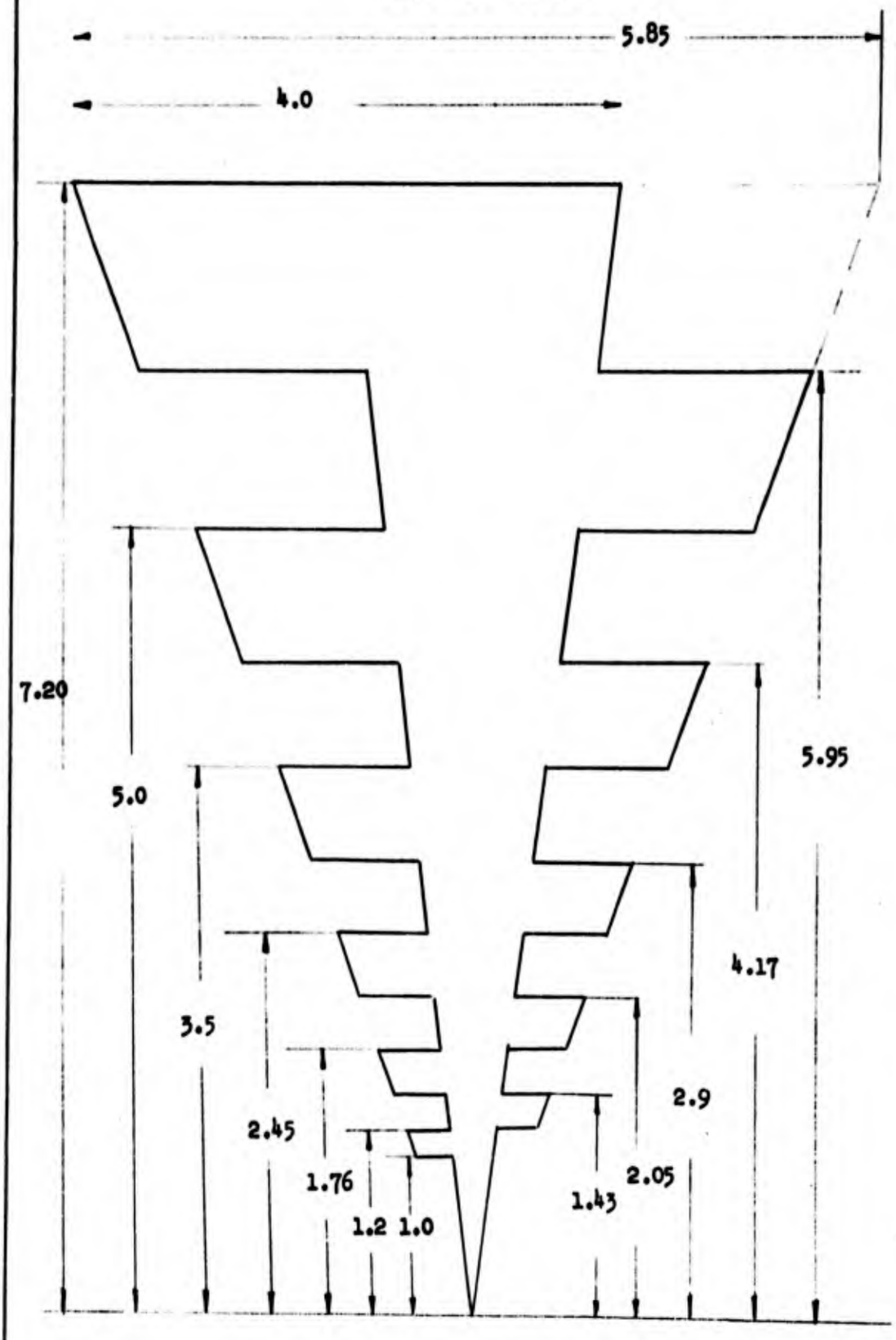

Form 5767-1

Fig. No. 2

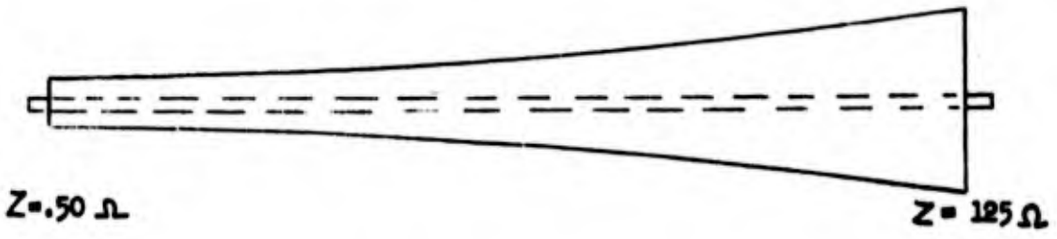

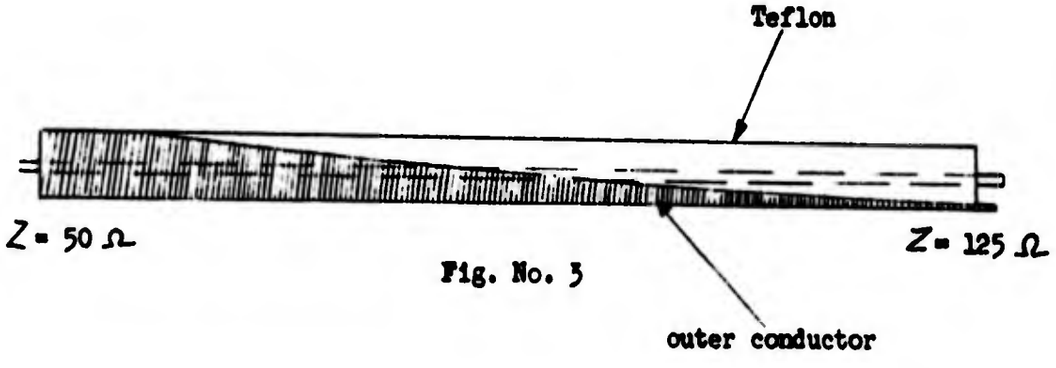

Fig. No. 3

Coaxial logarithmic tapered line transformer

Trapezoidal - tooth log periodic structure

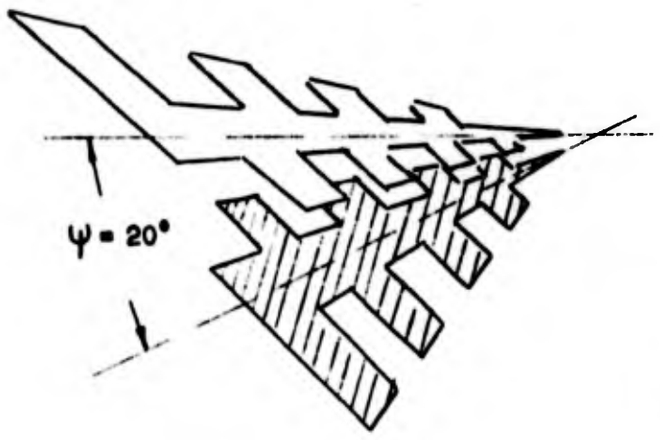

Fig. No. 4a

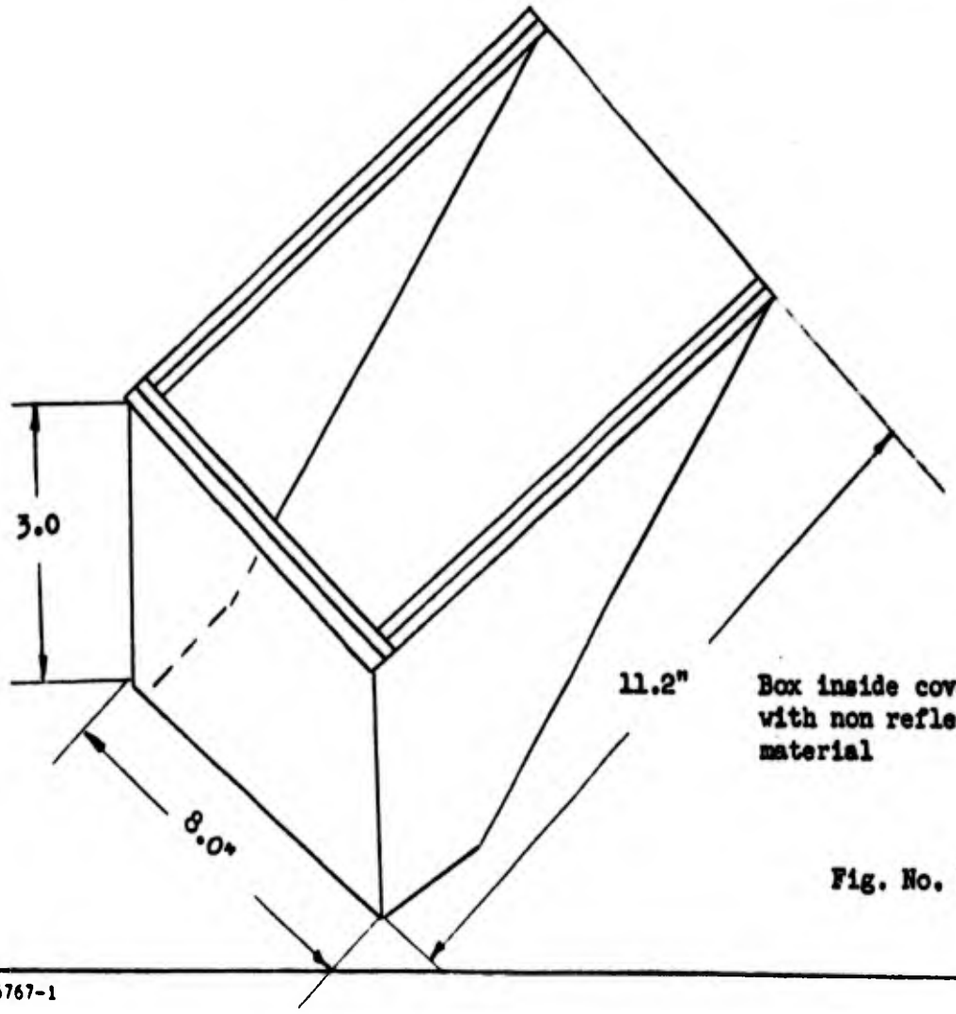

Box inside covered with non reflecting material

Fig. No. 4b

LOGARITHMIC PERIODIC ANTENNA

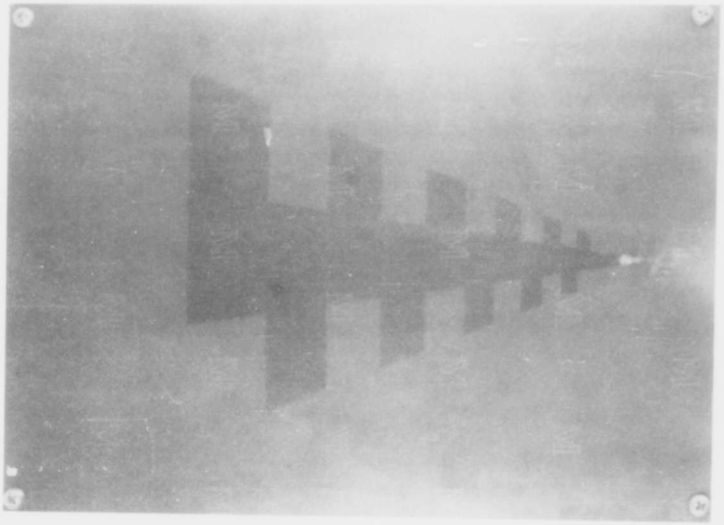

72 406R

Fig. No 5

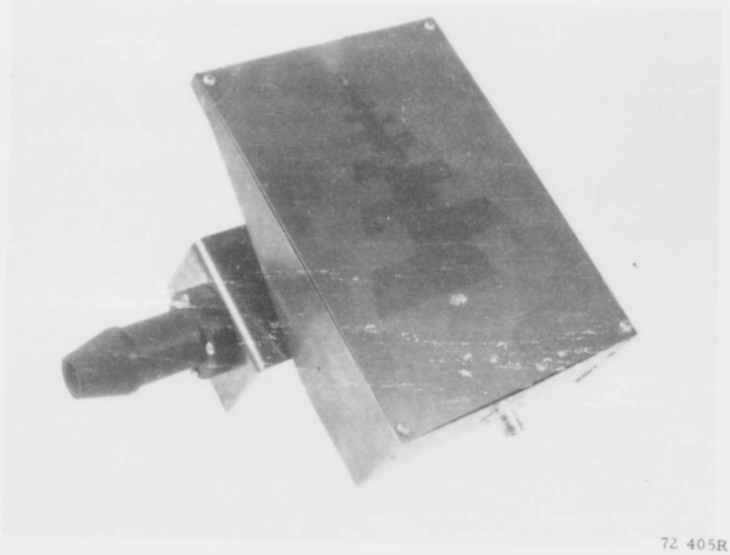

72 405R

Fig No 6

Fig. No. 2

VSWR of Log Trapezoidal - Antenna

with tapered line balun. 50 to 125 Ω

Antenna is flush mounted

cavity 8 x 11.2 inches ψ = 20° vertex angle

Depth 0.5 to 3.0 inches

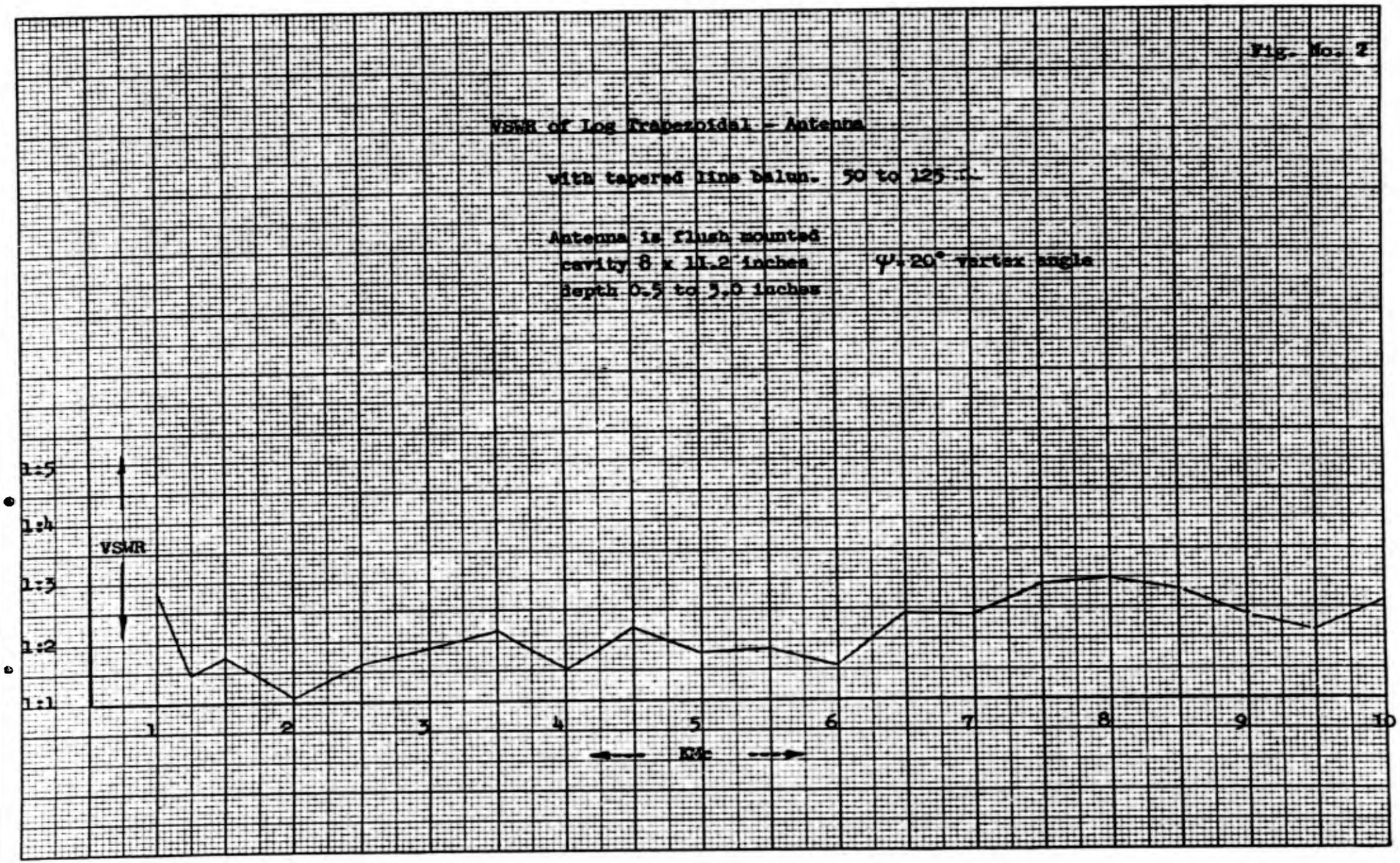

Antenna pattern log periodic tooth structure

E - plane 45° cut.
vertex angle $\psi = 20°$

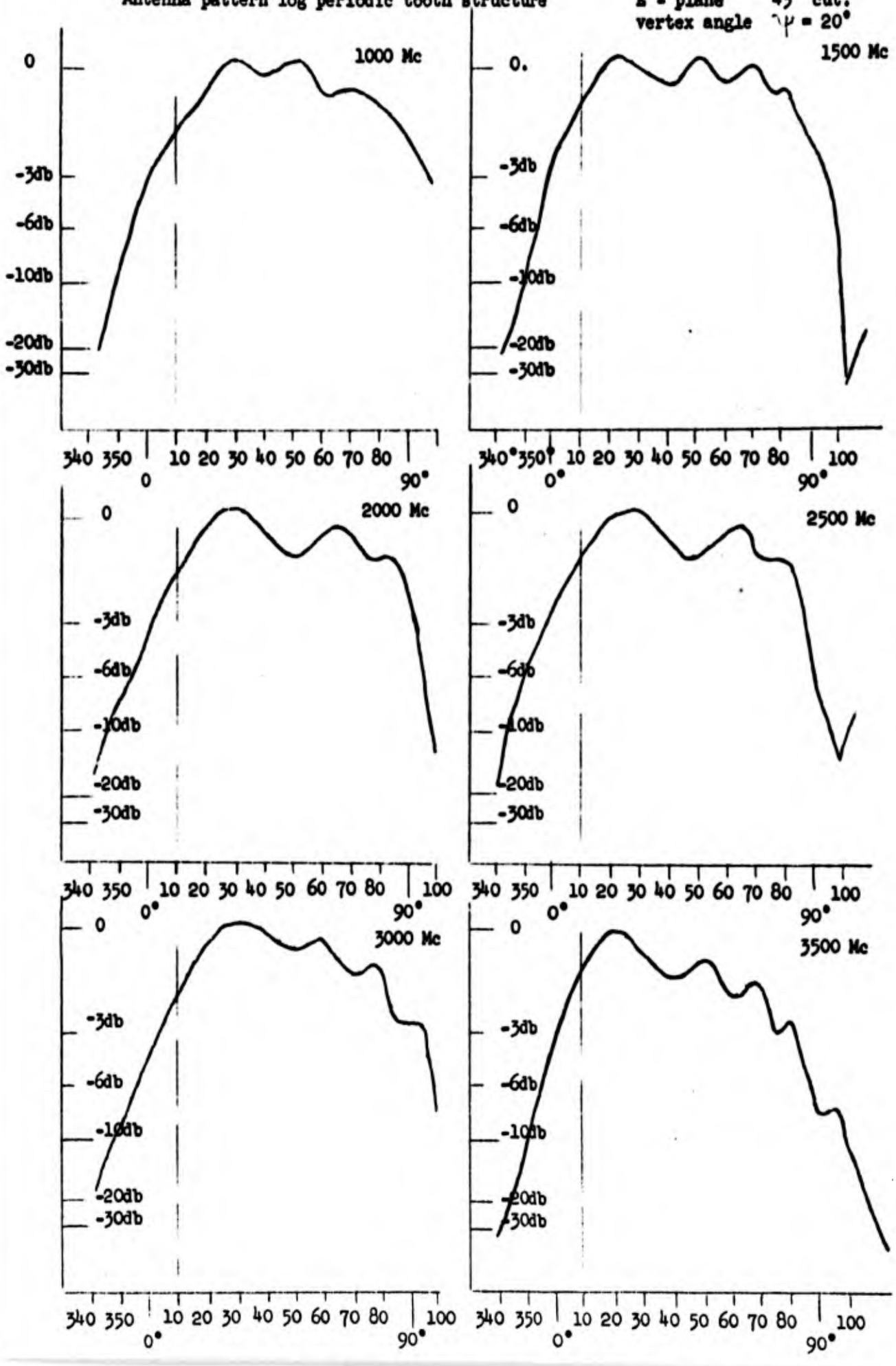

Antenna pattern log periodic tooth structure

E - plane 45° cut.
vertex angle $\psi = 20°$

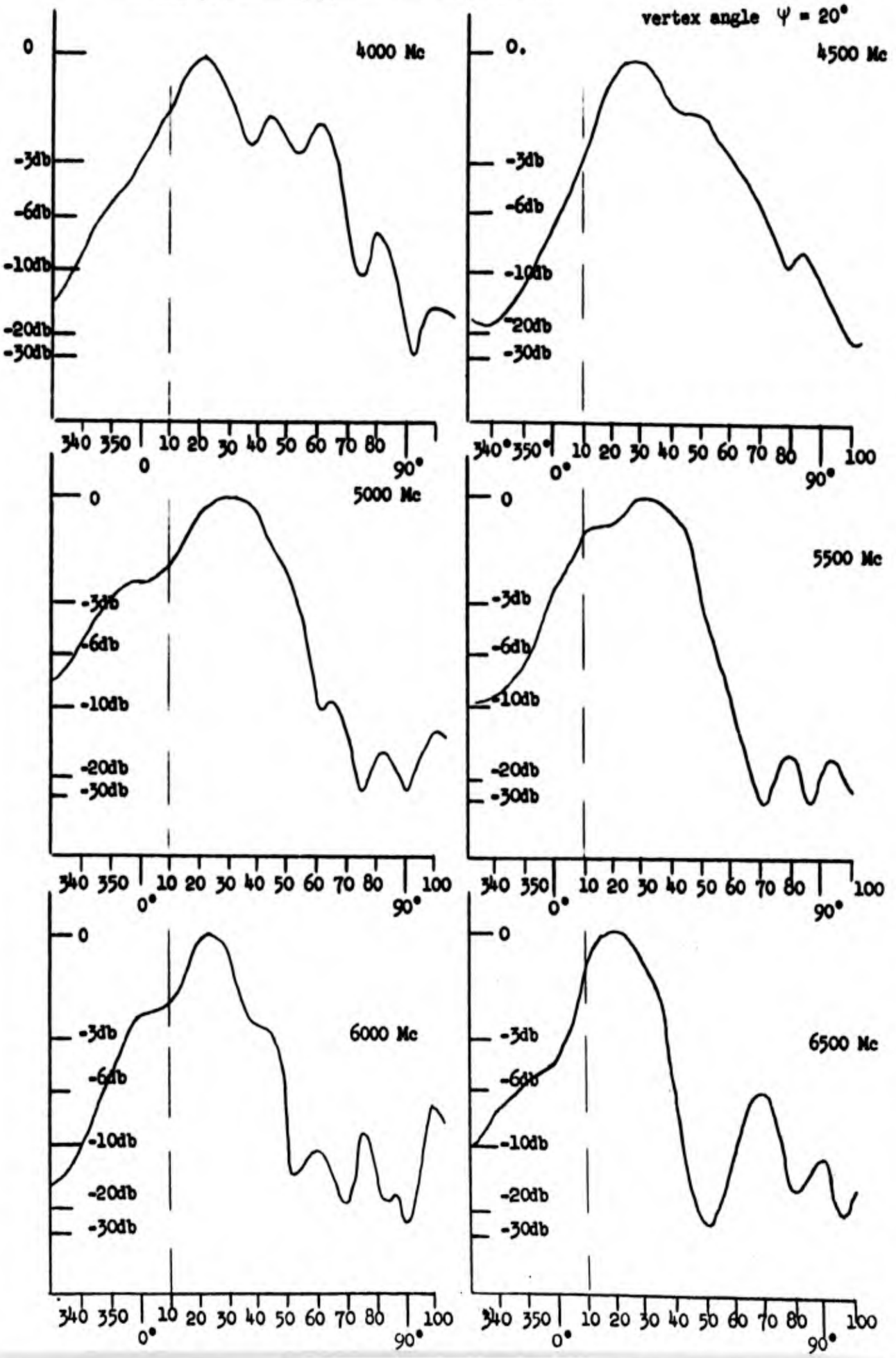

Antenna pattern log periodic tooth structure

E - plane 45° cut.

vertex angle $\psi = 20°$

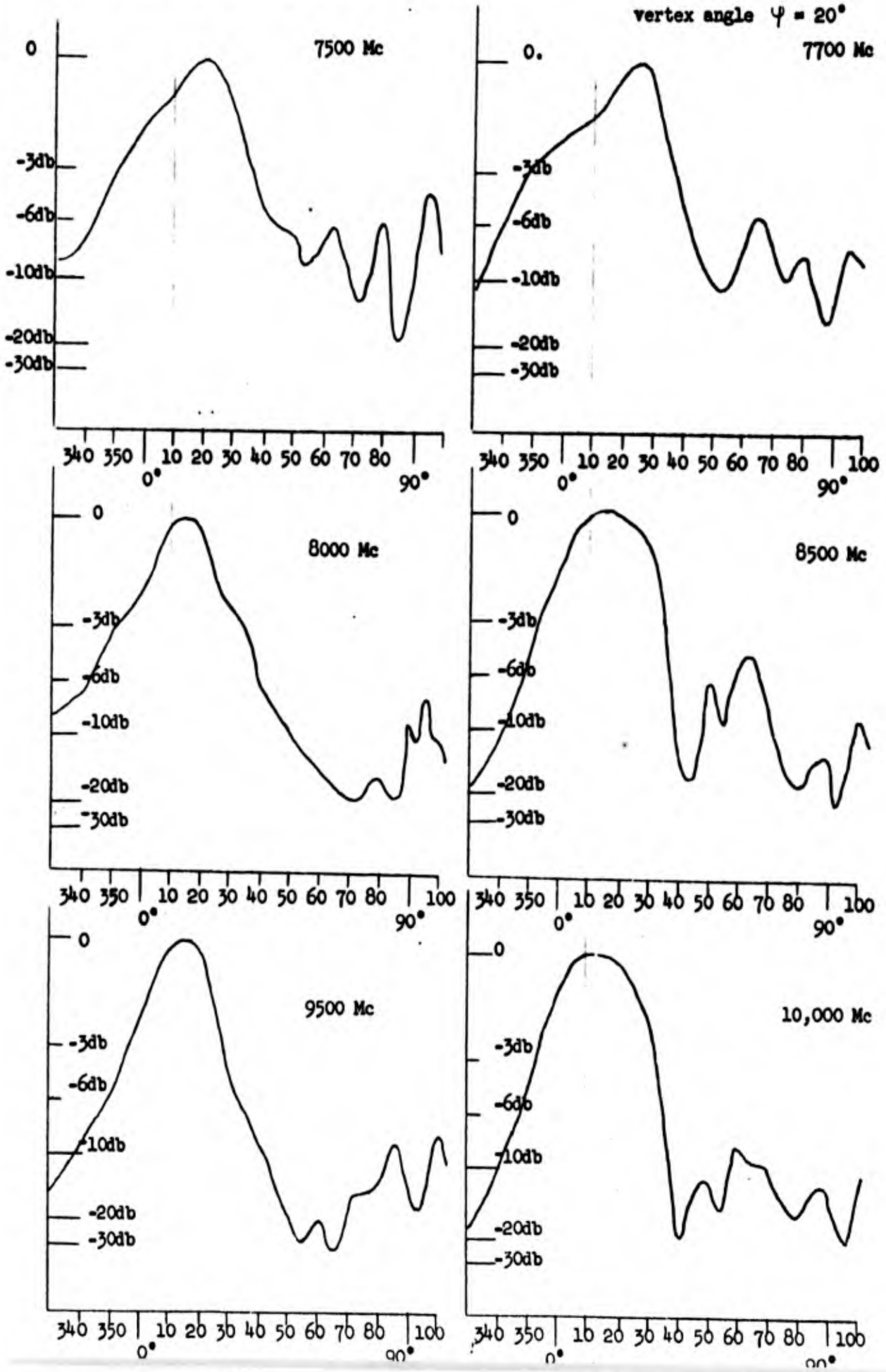

ANALYSIS OF AN ELECTRICALLY AND MAGNETICALLY LOADED LOOP ANTENNA

By M. A. Islam*

1. INTRODUCTION

This paper is an outcome of the author's investigation of low-frequency magnetic antennas and of whether or not a permeable core (a ferrite core, for example) can improve the performance of such an antenna. As a natural consequence of the inquiry, the first problem to be solved was that of solving Maxwell's equations with prescribed boundary conditions. For this, one could use the electric-field and magnetic-field quantities, or use suitably-defined vector and scalar potentials. The second method was chosen in the present case. Only rationalized MKS units have been used throughout this paper.

The method involves the solution of the homogeneous wave equation with the harmonic time variation in terms of a complete set of harmonic functions with unknown coefficients. Then, proper boundary conditions are imposed on this set of solutions to determine the unknown coefficients.

Among the various possible configurations, a cylindrical material core, excited by a loop of current, might be of particular practical interest. While the prolate spheroid represents the nearest approximation to a cylindrical core of finite length realizable with orthogonal coordinate surfaces, we will discuss in this paper the mathematically simpler case of an infinite cylindrical core and indicate how the method can be extended to the prolate spheroid.

* Laboratory For Electronics, Inc., Boston, Mass.

2. STATEMENT OF THE PROBLEM

The problem is to find an expression for the retarded vector potential $\vec{A}$, due to a current loop of radius "a" meters whose axis coincides with the z axis, and is located at $z = z_0$. (See Figure 1.) A homogeneous and isotropic core of radius "b" meters ($b \leq a$) is coaxial with the loop and extends along the z axis from $-\infty$ to $+\infty$. Thus, the problem is to solve equation (1), subject to boundary conditions (2).

$$\nabla^2\vec{A} + k^2\vec{A} = 0 \tag{1}$$

$$\hat{n} \times (\vec{E}_2 - \vec{E}_1) = 0 \tag{2}$$

$$\hat{n} \times (\vec{H}_2 - \vec{H}_1) = \text{true surface current}$$

where

$\vec{A}$ = Vector Magnetic Potential

$k = \omega/v$ = Wave Number

$\vec{E}$ = Electric Field Intensity

$\vec{H}$ = Magnetic Field Intensity

$\hat{n}$ = Unit Vector Normal to the Boundary Surface.

The solutions obtained must obviously be finite, single valued, and an outgoing wave at infinity.

Since this study is directed toward relatively low frequency applications for which the dimensions of the loop are small compared to the free-space wavelength, we assume the current to be uniform over the loop.

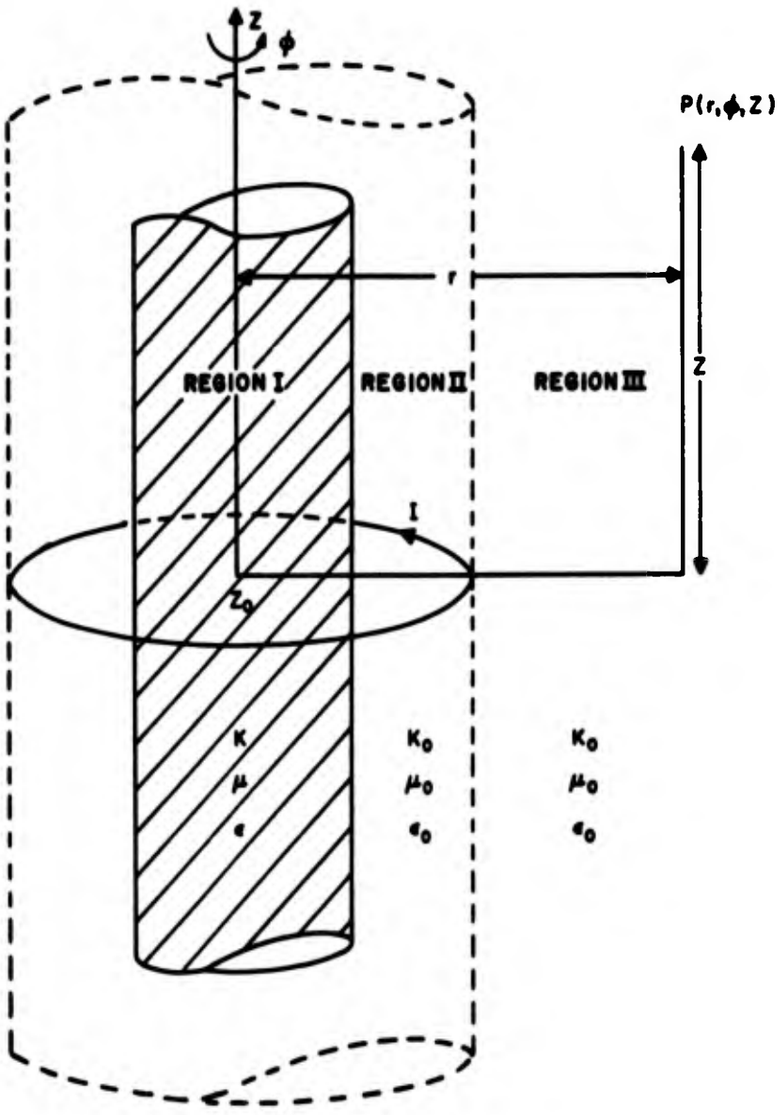

Figure 1. Current Loop and Infinitely Long Core

3. OUTLINE OF SOLUTION FOR THE VECTOR POTENTIAL

Due to the cylindrical symmetry of the loop with assumed uniform current, only the A_ϕ component exists, and $\partial/\partial\phi = 0$.

Under these conditions, (1) reduces to

$$\frac{\partial^2 A_\phi}{\partial z^2} + \frac{\partial^2 A_\phi}{\partial r^2} + \frac{1}{r}\frac{\partial A_\phi}{\partial r} - \frac{1}{r^2} A_\phi + k^2 A_\phi = 0 \quad .$$

Here, one may use the standard method of separation of variables and let $A_\phi = R(r)Z(z)$.

The separated equations are

$$\frac{d^2R}{dr^2} + \frac{1}{r}\frac{dR}{dr} + [(k^2 - \lambda^2) - \frac{1}{r^2}]\, R = 0 \quad .$$

$$\frac{d^2Z}{dz^2} + \lambda^2 Z = 0 \quad .$$

Where λ is the separation constant.

A solution to (1) may then be written as:

$$A_\phi = [BJ_1(\sqrt{k^2 - \lambda^2}\, r) + CH_1(\sqrt{k^2 - \lambda^2}\, r)]\, e^{i\lambda|z-z_0|} \quad .$$

Here, B and C and constants, $J_1(\ )$, $H_1(\ )$ are the Bessel and Hankel functions. Because there are no restrictions on λ, the complete solution is given by

$$A_\phi = \int_0^\infty [B(\lambda) J_1(\sqrt{k^2 - \lambda^2}\, r) + C(\lambda) H_1(\sqrt{k^2 - \lambda^2}\, r)]\, e^{i\lambda|z-z_0|}\, d\lambda \quad . \quad (3)$$

In Eq. (3), it is obvious that λ could be either smaller or larger than k, because the integral over λ runs from zero to infinity and, hence, permissible solutions are only J_1's in region I (which includes the line r = 0), and H_1's in region III (which includes $r = \infty$). In region II, obviously, both J_1's and H_1's are permissible. Therefore, the solutions are

$$A_\phi^{(1)} = \int_0^\infty B(\lambda)\, J_1(\sqrt{k^2 - \lambda^2}\, r)\, e^{i\lambda|z-z_o|}\, d\lambda \quad \text{for } r \le b$$

$$A_\phi^{(2)} = \int_0^\infty [C(\lambda)\, J_1(\sqrt{k_o^2 - \lambda^2}\, r) + D(\lambda)\, H_1(\sqrt{k_o^2 - \lambda^2}\, r)]\, e^{i\lambda|z-z_o|}\, d\lambda \quad \text{for } b \le r \le a$$

$$A_\phi^{(3)} = \int_0^\infty E(\lambda)\, H_1(\sqrt{k_o^2 - \lambda^2}\, r)\, e^{i\lambda|z-z_o|}\, d\lambda \quad \text{for } r \ge a \quad . \tag{4}$$

Superscripts (1), (2), and (3) with A_ϕ indicate the regions where the solutions for A_ϕ's are valid. The terms $B(\lambda)$, etc., are constants for particular λ's, and are to be determined from the boundary conditions.

The boundary conditions [Eq. (2)] between regions may now be applied.

Continuity of tangential electric fields leads to

$$A_\phi^{(2)} = A_\phi^{(1)} \tag{5a}$$

and continuity of tangential magnetic fields leads to

$$\frac{1}{\mu_o r} \frac{\partial}{\partial r}(rA_\phi^{(2)}) - \frac{1}{\mu r} \frac{\partial}{\partial r}(rA_\phi^{(1)}) = 0 \tag{5b}$$

where μ, μ_o are permeabilities in the core and in free space, respectively.

Substituting Eq. (4) into (5), using the Bessel and Hankel function identity

$$v \frac{dR_1(v)}{dv} + R_1(v) = vR_o(v) \tag{6}$$

and equating coefficients of exp $[i\lambda|z - z_o|]$, one obtains

$$D(\lambda) = C(\lambda) \left\{ \frac{k_m \sqrt{k_o^2-\lambda^2}\, J_o(\sqrt{k_o^2-\lambda^2}b)\, J_1(\sqrt{k^2-\lambda^2}b) - \sqrt{k^2-\lambda^2}\, J_1(\sqrt{k_o^2-\lambda^2}b)\, J_o(\sqrt{k^2-\lambda^2}b)}{\sqrt{k^2-\lambda^2}\, J_o(\sqrt{k^2-\lambda^2}b)\, H_1(\sqrt{k_o^2-\lambda^2}b) - k_m \sqrt{k_o^2-\lambda^2}\, J_1(\sqrt{k^2-\lambda^2}b)\, H_o(\sqrt{k_o^2-\lambda^2}b)} \right\} \tag{7}$$

where

$$k_m = \frac{\mu}{\mu_o} = \text{relative permeability}$$

In applying Eq. (2) on the surface r = a, one observes that the only true surface current occurs at the loop $z = z_o$. This current may be represented by the Dirac Delta function. We then obtain

$$\frac{\partial}{\partial r}\,(rA_\phi^{(2)}) - \frac{\partial}{\partial r}\,(rA_\phi^{(3)}) = \mu_o r I\,\delta(z - z_o) \text{ at } r = a \quad .$$

Using

$$\delta\,(z - z_o) = \frac{1}{\pi}\int_o^\infty \exp\,[i\lambda|z - z_o|]\;d\lambda \quad , \tag{8}$$

the identity

$$J_o(v)\,H_1(v) - H_o(v)\,J_1(v) = \frac{-2i}{\pi v} \quad ,$$

Eq. (6), and again equating coefficients of $e^{i\lambda|z-z_o|}$ one obtains finally from Eq. (4)

$$A_\phi^{(3)} = \frac{i\mu_o Ia}{2}\left\{\int_o^\infty J_1(\sqrt{k_o^2-\lambda^2}\,a)\,H_1(\sqrt{k_o^2-\lambda^2}\,r)\exp\,[i\lambda|z - z_o|]\;d\lambda\right.$$

$$+\int_o^\infty \frac{k_m\sqrt{k_o^2-\lambda^2}\,J_o(\sqrt{k_o^2-\lambda^2}\,b)\,J_1(\sqrt{k^2-\lambda^2}\,b) - \sqrt{k^2-\lambda^2}\,J_1(\sqrt{k_o^2-\lambda^2}\,b)\,J_o(\sqrt{k^2-\lambda^2}\,b)}{\sqrt{k^2-\lambda^2}\,J_o(\sqrt{k^2-\lambda^2}\,b)\,H_1(\sqrt{k_o^2-\lambda^2}\,b) - k_m\sqrt{k_o^2-\lambda^2}\,J_1(\sqrt{k^2-\lambda^2}\,b)\,H_o(\sqrt{k_o^2-\lambda^2}\,b)}$$

$$\left.\cdot\,H_1(\sqrt{k_o^2-\lambda^2}\,a)\,H_1(\sqrt{k_o^2-\lambda^2}\,r)\exp\,[i\lambda|z - z_o|]\;d\lambda\right\} \tag{9}$$

Eq. (9) is the desired solution for the retarded vector potential for the point P (r, ϕ, z), (r > a).

Letting k approach k_o in Eq. (9), k_m approaches unity and the second integral in Eq. (9) approaches zero. Therefore, the first integral in

Eq. (9) represents the contribution of an unloaded loop, and the second integral represents the contribution due to the presence of the core.

Utilizing the behavior of the Bessel function for small arguments, one can carry out the integration in the first integral, and after transformation into spherical coordinates, arrive at the familiar form for the loop:

$$A_\phi \simeq \frac{\mu_o I a^2}{4} \left\{ \frac{1}{R^2} - \frac{ik_o}{R} \right\} \exp[ik_o R] \sin\theta \quad .$$

4. OUTLINE OF SOLUTION FOR THE POYNTING VECTOR AND THE RADIATION IMPEDANCE

The rather formidable looking solution (9) may be summarized as

$$A_{\phi}^{(3)} = \int_0^{\infty} f(\lambda)\, H_1(\ell_0 r) \exp[i\lambda\, |z - z_0|]\, d\lambda \qquad (10)$$

where

$$\ell_0 = (k_0^2 - \lambda^2)^{1/2}$$

and

$f(\lambda)$ includes all the terms of (9) not specifically indicated in (10).

From

$$\vec{E} = -\frac{\partial \vec{A}}{\partial t} - \nabla\phi$$

$$\vec{B} = \nabla \times \vec{A}$$

$$\nabla\phi = 0$$

one obtains, for every point in the far field, E and H, and hence the Complex Poynting Vector

$$\vec{P} = \frac{1}{2}\, \vec{E} \times \vec{H}^*$$

Integration of the Complex Poynting Vector over a surface enclosing the antenna yields a complex number, the real part of which is identified with the dissipated power and the imaginary part is identified with $2\omega \times$ the difference of mean values of magnetic and electric energies.

Since it appears difficult to reduce the expressions for E and H, obtainable from (9) as simple functions of r and z, numerical integration methods were considered. It turns out that calculation of the radiated energy by first computing E and H for a set of sample points on the surface, and then summing the Poynting Vectors over the sample points, leads to a numerical double integration requiring an excessive amount of numerical operations.

Using (10), and the identity (6)

$$\vec{H} = \frac{\vec{B}}{\mu_o} = \frac{\hat{r}}{\mu_o} \frac{\partial A_\phi^{(3)}}{\partial z} + \frac{\hat{z}}{\mu_o} \left(\frac{\partial A_\phi^{(3)}}{\partial r} + \frac{1}{r} A_\phi^{(3)} \right)$$

$$= \hat{r} H_r + \hat{z} H_z$$

where

$$H_r = - \frac{1}{\mu o} \int_o^\infty f(\lambda) H_1 (\ell_o r) \frac{\partial}{\partial z} e^{i|z-z_o|} d\lambda$$

$$H_z = \frac{1}{\mu o} \int_o^\infty \ell_o f(\lambda) H_o (\ell_o r) e^{i\lambda |z-z_o|} d\lambda \qquad (11)$$

thus

$$\vec{P} = \frac{\vec{E} \times \vec{H}^*}{2} = - i \frac{\omega \hat{z}}{2} A_\phi H_r^* + \hat{r} i \frac{\omega}{2} A_\phi H_z^* \qquad (12)$$

$$= \hat{z} P_z + \hat{r} P_r$$

We propose to integrate the normal component of $\vec{P}$ over an infinite cylinder of radius ρ ($\rho > a$), coaxial with the antenna core.

The total radiated energy W is

$$W = \int_{-\infty}^{\infty} P_r \, 2\pi\rho \, dz \qquad (13)$$

+ contributions of ends located at infinity. The last item in the above expression is zero. Combining (10), (11), (12), and (13) gives

$$W = \frac{1}{2} \int_{-\infty}^{\infty} dz \, 2\pi\rho i\omega \int_o^\infty f(\lambda_1) H_1(\ell_{o1}\rho) e^{i\lambda_1 |z-z_o|} d\lambda_1 \int_o^\infty \frac{\ell_{o2}^*}{\mu} f^*(\lambda_2)$$

$$\times H_o^*(\ell_{o2}\rho) e^{-i\lambda_2 |z-z_o|} d\lambda_2 \qquad (14)$$

Using the properties of delta functions

$$2\pi \, \delta(\lambda_1 - \lambda_2) = \int_{-\infty}^{\infty} e^{i(\lambda_1 - \lambda_2) z} dz$$

and

$$\int g(\lambda_1)\,\delta(\lambda_1-\lambda_2)\,d\lambda_1 = g(\lambda_2)$$

reduces (14) to the final expression.

$$W = \pi^2 \frac{i\omega\rho}{\mu_o} \int_o^\infty d\lambda\, \ell_o^*\, f^*(\lambda)\, H_o^*(\ell_o\rho)\, f(\lambda)\, H_1(\ell_o\rho) \tag{15}$$

5. OUTLINE OF SOLUTION FOR THE RADIATION IMPEDANCE BY INDUCED EMF METHOD

For a loss less conductor, the voltage drop across the current loop can also be obtained from

$$V = \oint \vec{E} \cdot d\vec{\ell} = 2\pi a E_\phi$$

where E_φ is given as

$$E_\phi = -\frac{\partial A_\phi}{\partial t} = -i\omega A_\phi$$

and A_ϕ is given by Eq. (9) for $r = a$, $z = z_o$. Thus the input impedance

$$Z = R + iX = \frac{V}{I} \tag{16}$$

is obtained directly.

For loss less cores, the real part of Eq. (16) must equal the radiation resistance obtained from Eq. (15).

6. ANALYSIS OF PROLATE SPHEROID AND CURRENT LOOP

In order to get a more realistic model, the geometry of Figure 2 was also studied. It turns out that for the special case $\partial/\partial_\phi = 0$, the vector wave equation is separable in the Prolate Spheroidal coordinate system.

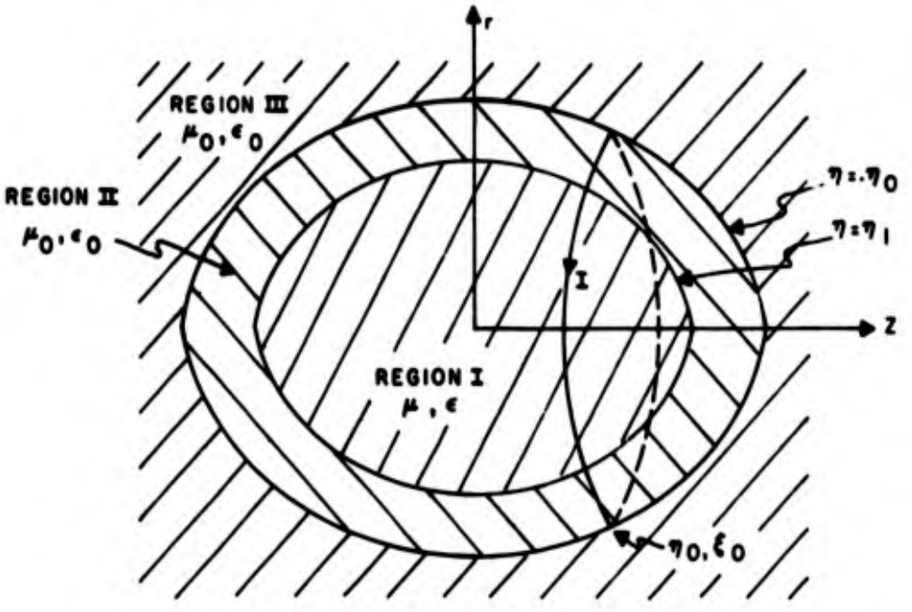

Figure 2. Prolate Spheroid and a Current Loop. A Typical Division of Regions for Applying Boundary Conditions.

Following procedures similar to the ones outlined in the cylindrical case, the vector potential was obtained in terms of spheroidal wave functions. In this case the separation constant assumes a set of discrete values, and the resultant potential is a summation rather than an integral. It seems reasonable to expect that procedures similar to the cylindrical case can be worked out, which would simplify the problem of integration of the resulting Poynting Vector.

7. NUMERICAL RESULTS

For the following set of parameters, Eq. (15) was evaluated using a digital computer, the results of which are indicated below.

Loop: radius a = 1 m, frequency : 300 Kc

Core: radius b = 1 m, $K_m = 100$, $\sigma_{core} = 0$

The radiation resistance (which is independent of the radius of the cylindrical surface over which the Poynting Vector is integrated) was 3.13×10^{-3} ohms. This shall be compared with the radiation resistance of the unloaded loop of the same dimensions, which is 3.08×10^{-7} ohms.

Using the induced EMF method, the input impedance was found to be $Z = 3.13 \times 10^{-3} - i12.5$ agreeing in its real part with the result obtained above. Thus the Q of the loaded loop is of the order of 4000, and the bandwidth accommodated by this arrangement is about 100 Cps.

REFERENCES

(1) W.K.H. Panofsky and M. Phillips, "Classical Electricity and Magnetism," Addison-Wesley Publishing Co. Inc., Reading, Mass., 1956.

(2) W.R. Smythe, "Static and Dynamic Electricity," McGraw-Hill Book Co. Inc., New York, 1950.

(3) P.M. Morse and H. Feshbach, "Methods of Theoretical Physics," Part I and Part II, McGraw-Hill Book Co., Inc., New York, 1953.

ERRATA

Omit the last paragraph, "Using the induced EMF method, . . . ," and substitute:

"Using the induced EMF method, the real part of the input impedance was found to agree with the result obtained above."

PATTERN AND EFFICIENCY STUDIES OF MINIATURIZED SLOT ANTENNAS UTILIZING HIGH "Q" MATERIALS

By

A. T. Adams, J. A. M. Lyon
and J. C. Palais

The University of Michigan
Ann Arbor, Michigan

SUMMARY

In the introduction possible uses and limitations of loaded electrically small antennas are discussed. Theoretical results are obtained for the beam patterns of loaded rectangular slot antennas utilizing simplified aperture-diffraction theory. Experimental data are presented on the beam patterns of loaded and unloaded cavity slot antennas. These pattern data represent a first step in a detailed investigation of the effect of ferrite loading on beam patterns. In general the patterns of a ferrite loaded antenna at frequency f_0 have turned out to be quite similar to the patterns of the same antenna unloaded at a frequency $f_0 \sqrt{\mu_r \epsilon_r}$. The value of $\sqrt{\mu_r \epsilon_r}$ for the ferrite powder was approximately 2.5. In general the half-power beam width increased by a factor of 10 to 30 percent with ferrite loading and side lobe level also increased. In some cases a multi-lobed pattern becomes a single-lobed pattern with ferrite loading. The effect of flange size and shape appears to be more critical with the loaded than with

the unloaded antennas. Specifically, the effects of any physical asymmetries become more pronounced with the addition of ferrite loading. Impedance and efficiency data are presented for the rectangular slot antenna.

INTRODUCTION

This paper covers several aspects of electrically small antennas.* The authors have pursued a general study program dealing with the use of ferrite and dielectric materials as part of the radiating structure. The use of ferroelectric, dielectric, and ferrite materials to reduce the size of antennas has been studied over a period of several years. Brownell and Kendall[1] have presented some information on dielectrically loaded slots. Other important papers related to this subject are listed in Refs. 2-8. In this paper the authors present data on the beam pattern, impedance, and efficiency of two ferrite loaded slot antennas; a rectangular slot antenna and a single ridge slot antenna.

The effectiveness of an antenna in terms of directivity, impedance, efficiency, etc. are related to the size of the antenna in wavelengths. In general high directivity and high efficiency together with desirable impedance characteristics are obtainable only with antennas having linear dimensions comparable to a wavelength.

---

*Work performed with the support of the Electromagnetic Warfare and Communications Laboratory, ASD, Wright-Patterson AFB, Ohio.

Electrically small antennas based upon the wavelength in air generally have poor characteristics. The reasons which account for this situation are as follows:

(1) Low directivity is caused by the difficulty of producing rapid phase and amplitude oscillations in a small physical distance. This difficulty is the same one encountered in producing super gain antennas, which have been discussed at some length in the literature.

(2) Poor impedance match is caused by cutoff-like phenomena. In the case of a waveguide this cutoff phenomena is theoretically sharp and occurs at a distinct frequency. In the case of a horn the cutoff phenomena is gradual and there is no distinct frequency of cutoff. Other antennas such as the dipole, spiral, etc. also have a low frequency behavior corresponding to a type of cutoff phenomena, although in many cases a complete mathematical description of the phenomenon is not available.

(3) The low efficiency of an electrically small antenna is usually ascribed to a low radiation resistance or, more precisely, to a low ratio of radiation resistance to loss resistance. This description is primarily a mathematical one giving very little physical insight into the loss mechanism. Certainly one cause of this

loss is that only a small part of the energy traveling out to the end of the antenna is radiated while the metal losses are roughly proportional to the total energy. In this way the poor impedance characteristic and the poor efficiency characteristic are related.

One of the expected advantages with ferrite loading is a reduction in the linear dimensions of the antenna. This reduction in size is apparent in the antennas described here. A brief listing of the possible advantages accruing from the use of ferroelectric, dielectric and ferrite materials would be as follows: the wavelength for a given frequency is reduced according to the relationship that the wavelength in a material medium is inversely proportional to the square root of the product of the permittivity and permeability. Another possible advantage would be the change in the intrinsic impedance of the material medium as contrasted with the free space intrinsic impedance. For plane waves this impedance is equal to the square root of the permeability divided by the permittivity of the medium. Such a change in impedance level is strictly correct only for plane waves. Still another possible advantage in the use of a material medium in and surrounding metallic antenna elements would be that the medium serves to match the antenna to the transmission line feeding the antenna. Frequently the need for matching may be the paramount reason for utilizing the material. In the consideration of the transmission of power to

the aperture the use of material medium may frequently permit a given size antenna to operate above cutoff frequency whereas without such material the transmission mode feeding the antenna would be below cutoff.

Another possible advantage of ferrite loading is related to the usual dispersive characteristics of ferrite. The change of permeability with frequency is such as to reduce the change of wavelength with frequency. The permeability of ferrite materials generally decreases with increasing frequency. Since the wavelength in ferrite is $\frac{\lambda_0}{\sqrt{\mu_r \epsilon_r}}$, it might be possible to develop a material whose rate of change of μ with frequency is such that wavelength remains constant over a broad frequency range. The implications for broadband matching are obvious. Figure 1 shows a graph of the permeability of a particular ferrite material. The straight line on the graph indicates the values necessary to maintain a constant wavelength. There are serious problems in developing a useful material of this type; the authors have noted this effect but have not yet utilized it in experimental antennas.

THEORETICAL RESULTS

Theoretical beam patterns for a rectangular waveguide radiator loaded with materials described by the permeability μ and the permittivity ϵ are shown in Fig. 2 for several combinations of values

for μ and ϵ. These results are based upon the assumption that only the dominant (TE_{10}) mode is present in the aperture field. Also exterior wall currents are neglected in an analysis similar to that used by Silver.[9] The designation of coordinates is as shown in Fig. 3.

By considering elementary Huygens sources over the aperture and the use of a Hertzian magnetic vector it is possible to derive the following equations which give the electric field exterior to the waveguide:

E Plane, $\phi = \pi/2$:

$$E_\phi = 0$$

$$E_\theta = \mu_r \sqrt{\frac{\mu_o}{\epsilon_o}} \frac{2a^2 b}{\pi \lambda_o^2 R} \left[1 + \frac{\beta_{10}}{\omega \mu_r \sqrt{\epsilon_o \mu_o}} \cos\theta + \Gamma \left(1 - \frac{\beta_{10} \cos\theta}{\omega \mu_r \sqrt{\epsilon_o \mu_o}} \right) \right] \cdot \frac{\sin(\frac{\pi b}{\lambda_o} \sin\theta)}{\frac{\pi b}{\lambda_o} \sin\theta} \cdot e^{-jkR}$$

H Plane, $\phi = 0$:

$$E_\theta = 0$$

$$E_\phi = -\mu_r \sqrt{\frac{\mu_o}{\epsilon_o}} \frac{\pi a^2 b}{2\lambda_o^2 R} \left[\cos\theta + \frac{\beta_{10}}{\omega \mu_r \sqrt{\epsilon_o \mu_o}} + \Gamma \left(\cos\theta - \frac{\beta_{10}}{\omega \mu_r \sqrt{\mu_o \epsilon_o}} \right) \right] \cdot \frac{\cos \frac{\pi a}{\lambda_o} \sin\theta}{(\frac{\pi a}{\lambda_o} \sin\theta)^2 - (\frac{\pi}{2})^2} \cdot e^{-jkR}$$

where:

λ_o = free space wavelength

Γ = reflection coefficient at aperture.

The results of this analysis are shown in Fig. 2 for several combinations of relative permeability and relative permittivity. As can be seen there is some broadening of the pattern compared to the same unloaded antenna for $\mu_r = \epsilon_r = 3$ and $\mu_r = \epsilon_r = 10$. The patterns are changed more radically for μ_r different from ϵ_r. If the relative permeability is very much greater than the relative permittivity the H-plane pattern is similar to the air case for θ between 0 and 90^o. Note that a high backlobe results for this case. In the E-plane the pattern is practically omni-directional. For the case of relative permittivity much greater than relative permeability the situation is reversed with a narrow beam in the E-plane and a broad beam in the H-plane.

EXPERIMENTAL RESULTS; RECTANGULAR SLOT

Figures 4 and 5 show an experimental model of a rectangular cavity slot antenna. The transition from coaxial cable to waveguide consists of a ball probe type of feed. The dimensions of the antenna are shown in Fig. 6. The length of the cavity was chosen to be

approximately a wavelength in order to cut down higher modes and provide a reasonable comparison with theoretical results.

Figure 3 shows the beam pattern coordinate system. Figures 7 and 8 show radiation patterns of this antenna without ferrite loading whereas Figs. 9 and 10 show patterns with ferrite loading. Tables I and II summarize the beam pattern data. In addition, Figs. 7-10 show the theoretical curves utilizing the assumption of a dominant mode only in the aperture and neglecting exterior wall currents as previously described. The theoretical curves shown assume a material with $\mu_r = \epsilon_r = 3$. The experimental curves have been drawn averaging right and left hand values about $\theta = 0^o$. The curves were reasonably symmetrical except for the E-plane patterns of the loaded rectangular cavity without flange. The effect of the flange in the air case is very similar to that predicted by Butson and Thompson.[10] Complete antenna beam patterns are taken on the rectangular slot antenna with and without ferrite loading and with and without flanges. The ferrite powder utilized has a magnetic Q of approximately 6 at 260 Mcs. This relatively low Q placed a very severe restriction on conclusions to be drawn from impedance data. However, the losses occasioned by the low Q do not limit the interpretation of the beam-pattern data. The beam patterns are very close to those that would occur using a lossless ferrite material.

Consider the case of a rectangular cavity slot antenna filled

with lossy ferrite. The eigenvalue solutions for the modes that can exist in the wave guide are exactly the same except that Γ (propagation constant) and k (wave number) are complex. The radiated fields depend only upon the E field in the plane of the aperture. For any given single mode the effect of adding losses to this system will be to introduce an additional E field component 90^{o} out of time phase but with the same spatial distribution. This change from the lossless to the lossy case can be summarized by multiplying the original distribution by some complex number. The radiated field can be found from the aperture field by one of several methods of integration. In each case the complex number can be removed from the integration to yield a radiated field which is also multiplied by the same complex number. The resultant radiated field for the lossy case is equal to the radiated field in the lossless case multiplied by a complex number. Thus the radiation pattern is independent of losses for each single mode aperture field which is assumed. Strictly speaking, in any complex geometry the losses will change the boundary value problem and the resultant complex ratios of mode coefficients will change thereby. The beam pattern tests show that for the rectangular cavity slot antenna the patterns of a loaded antenna at frequency f_0 are similar to the patterns of the same antenna in the unloaded condition but operating at a frequency of $f_0 \sqrt{\mu_r \epsilon_r}$. It is to be noted that the half-power beamwidth is increased by a factor of 10 to 30 percent with ferrite loading and

also the side lobe level is increased. With loading the antenna becomes more sensitive to physical asymmetries. For instance, the E-plane patterns of the loaded rectangular cavity slot antenna are highly asymmetric for the unflanged case.

EXPERIMENTAL RESULTS; RIDGED SLOT ANTENNA

Complete antenna beam patterns were taken on a ridge antenna, with and without ferrite loading and with and without flanges. The ferrite powder used was identical to that used in the rectangular slot tests described above. The ridged slot antenna is shown in Figs. 11 (without flange) and 12 (with flange). Figure 13 shows the dimensions of the ridged slot. The dominant mode cutoff frequency unloaded is 582 megacycles and the cutoff frequency of the next higher mode is about 3,000 megacycles. The length of this antenna is 13-1/2". Feed design is of the type described by S. Cohn.[11]

BEAM PATTERNS; UNLOADED CASE

The beam patterns of this antenna are shown in Figs. 14-17. The patterns of the unloaded antenna are of some interest because little data has been published on this type of antenna. The H-plane patterns consist of a single lobe in the unflanged case with relatively high backlobes. The flange eliminates the back lobe, narrows the beam slightly, and at some frequencies, produces multiple peaks in the

major lobe as predicted by Butson and Thompson.[10] The E-plane patterns are quite irregular due to the fact that the ridge produces considerable physical asymmetry in the plane. The only single-lobed pattern occurs at 2,000 Mcs in the unflanged condition.

BEAM PATTERNS; LOADED CASE

The radiation patterns of the loaded ridged slot antenna are mostly single lobed patterns for the flanged case. The patterns are somewhat broader than the unloaded patterns. The effect of the flange in the H-plane patterns is to narrow the beam slightly and reduce the side lobe level. The E-plane patterns in the unflanged case have pronounced asymmetry with the major lobe occurring at about 80^{o}. The flange mostly eliminates these asymmetries and reduces the side lobe level.

EXPERIMENTAL RESULTS; IMPEDANCE AND EFFICIENCY

High-Q ferrite powder was used for these experiments. The magnetic Q was greater than 70 at 200 megacycles. The characteristics of the solid ferrite from which the powder was made are shown in Table III. The characteristics of the powder are not known exactly. It is expected that relative permeability is about two, relative permittivity is about three, and that the magnetic and electric Q's

are higher than those of the solid ferrite. Accurate measurements of the powder characteristics are being made.

Figures 18 and 19 show preliminary experimental data on VSWR of a rectangular slot radiator. The radiator is similar to that shown in Figs. 4 and 5 with the exception that the "b" dimension has been reduced to 3" and the length has been reduced to 12". Figure 18 shows the VSWR of the unloaded radiator. Figure 19 shows the VSWR of the loaded radiator. The bandwidth is reduced by a factor of about four. The reason for this reduction in bandwidth is that there is considerable reflection from the ferrite-air interface at the end of the antenna. Preliminary results on the solution by variational techniques of a related problem (Fig. 20) confirm the fact of high reflection coefficients at the aperture. This places a basic limitation on such loaded slot antennas. Size may be reduced, but only at the expense of bandwidth. It must be noted, however, that the model tested represents a preliminary design which has not been optimized for the actual impedance of the ferrite-air interface. It is to be expected that a considerably greater bandwidth would be obtained from an optimized design. For instance, doubling the b/a ratio would increase the unloaded bandwidth by a factor of about two. Theoretical results from the variational problem of Fig. 20 indicate that, with the use of solid ferrite of higher permeability and permittivity, greater size reduction can be effected however, with a greater reduction in bandwidth.

The efficiency of the loaded and unloaded rectangular slot antennas was measured using reflection techniques. The method used is described in Ref. 12 and is analogous to that described by Deschamps[13] for transmission line components. In this method, a circle on the Smith chart is defined which, with the impedance of the antenna, completely determines the efficiency. The efficiency of the loaded antenna whose VSWR is shown in Fig. 19 was 57 percent at 300 Mcs, 55 percent at 310 Mcs, and 51 percent at 320 Mcs. A double stub tuner was used in these measurements. Its losses are included in the efficiency figures, which thus represent a lower bound on the efficiency. The efficiency of the unloaded rectangular slot antenna whose VSWR is shown in Fig. 18 was 89 percent at 800 Mcs. Four aluminum boxes of different sizes were used in the experiments. In all cases a large portion of the Smith Chart Circle was defined and accuracy is estimated at ± 10 percent.

REFERENCES

1. F. P. Brownell and D. E. Kendall, "Miniaturized Cavity Fed Slot Antennas," 1960 WESCON Record, Part 1, pp. 158-166.

2. J. Herman, "Thin Wire Loop and Thin Biconical Antennas in Finite Media," Diamond Ord. Fuze Lab. Tech. Report No. TR-462, May 1957.

3. O. R. Cruzan, "Radiation Properties of a Thin Wire Loop Antenna Embedded in a Spherical Medium," IRE Trans. PGAP, October 1959, pp. 345-352.

4. Saburo Adachi, "Impedance Characteristics of a Uniform Current Loop Having a Spherical Core," The Ohio State University Research Foundation Report No. 662-26, April 15, 1959.

5. C. T. Tai, "Radiation From a Uniform Circular Loop Antenna in the Presence of a Sphere," Stanford Res. Inst., Tech. Report No. 32, 1952.

6. D. M. Grimes, "Miniaturized Resonant Antenna Using Ferrites," J. of App. Phys., Vol. 29, No. 3, March 1958, p. 401.

7. C. Polk, "Resonance and Supergain Effects in Small Ferromagnetically or Dielectrically Loaded Biconical Antennas," IRE Trans. PGAP, December 1959.

8. S. A. Schelkunoff and H. T. Friis, Antenna: Theory and Practice, Wiley and Sons, 1952, p. 325.

9. S. Silver, Microwave Antenna Theory and Design, Rad. Lab. Series, Vol. 12, McGraw-Hill, New York, 1951, p. 341.

10. P. C. Butson and G. T. Thompson, "The Effect of Flanges on the Radiation Patterns of Waveguide and Sectoral Horns," IEE, July 1959, pp. 422-426.

11. S. B. Cohn, "Design of Simple Broad Band Wave-Guide-to-Coaxial-Line Junctions," Proc. IRE, September 1947, p. 920.

REFERENCES (Cont.)

12. Interim Engineering Report of Research on Miniature Zero Drag Broadband Tunable Cavity Antennas - 1 July to 30 Sept., 1953, University of Oklahoma Research Institute Contract AF 33(038)-10405.

13. G. A. Deschamps, "Determination of Reflection Coefficients and Insertion Loss of a Wave-Guide Junction," JAP, Vol. 24, No. 8, August 1953, p. 1046.

Half Power Beam Width

Frequency (Mc)	λ/λ_c	Theoretical		Experimental			
				No Flange		Flange	
		E_θ	E_ϕ	E_θ	E_ϕ	E_θ	E_ϕ
592	.85	144^o	86^o	155^o	72^o	134^o	66^o
629	.80	136^o	84^o	174^o	76^o	120^o	68^o
671	.75	130^o	82^o	174^o	80^o	126^o	67^o
719	.70	124^o	78^o	120^o	84^o	164^o	64^o
774	.65	120^o	76^o	120^o	68^o	138^o	56^o
839	.60	116^o	72^o	104^o	45^o	116^o	53^o
Average BW		128^o	80^o	141^o	69^o	133^o	62^o

E-Plane - E_θ

H-Plane - E_ϕ

Table I. Unloaded rectangular cavity antenna - theoretical and experimental results.

Half Power Beam Width

Frequency (Mc)	λ/λ_c	Theoretical		Experimental			
				No Flange		Flange	
		E_θ	E_ϕ	E_θ	E_ϕ	E_θ	E_ϕ
237	.85	160^o	108^o		154^o	102^o	84^o
251	.80	152^o	110^o		92^o	92^o	78^o
269	.75	146^o	112^o		96^o	94^o	84^o
287	.70	146^o	114^o		90^o	120^o	102^o
310	.65	138^o	114^o		78^o	82^o	78^o
335	.60	136^o	114^o		68^o	90^o	78^o
Average BW		146^o	112^o		96^o	97^o	84^o

E-Plane - E_θ

H-Plane - E_ϕ

Table II. Loaded rectangular cavity antenna theoretical ($\mu_r = \epsilon_r = 3$) and experimental ($\mu_r = \epsilon_r = 2.5$) results.

Frequency (Mcs)	μ'	μ''	Q_{MAG}	ϵ'	ϵ''	Q_{ELEC}
200	6.32	.087	72.6			
350	6.66	.236	28.3			
375	6.91	.276	25			
400	6.71	.276	24.2			
425	6.83	.256	26.5			
450	6.87	.315	21.8			
475	6.87	.354	19.4			
500	6.87	.393	17.5			
20				12.00	.0040	3000
500				12.59	.0047	2680

Table III. Characteristics of a high Q ferrite material (mfg. by Motorola Phoenix).

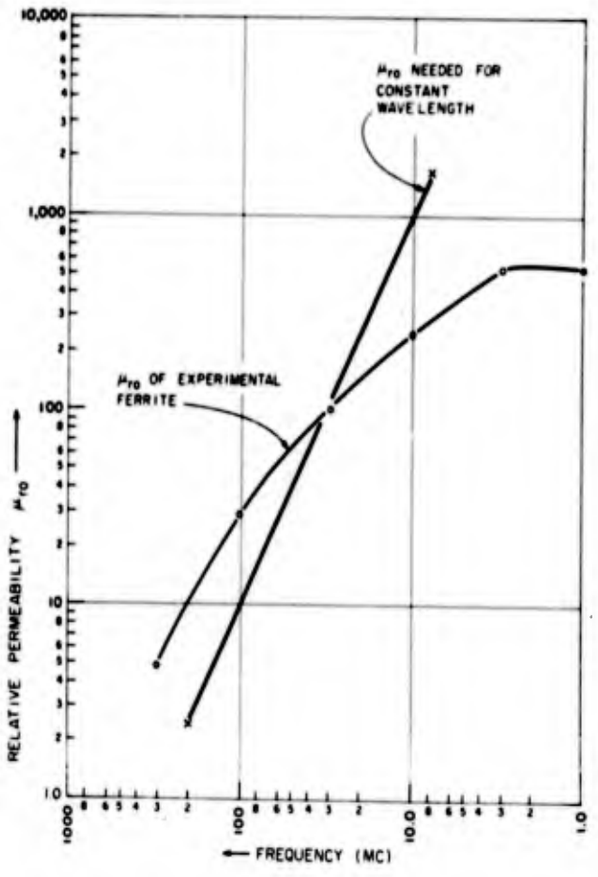

Fig. 1. Dispersive characteristics of ferrite material.

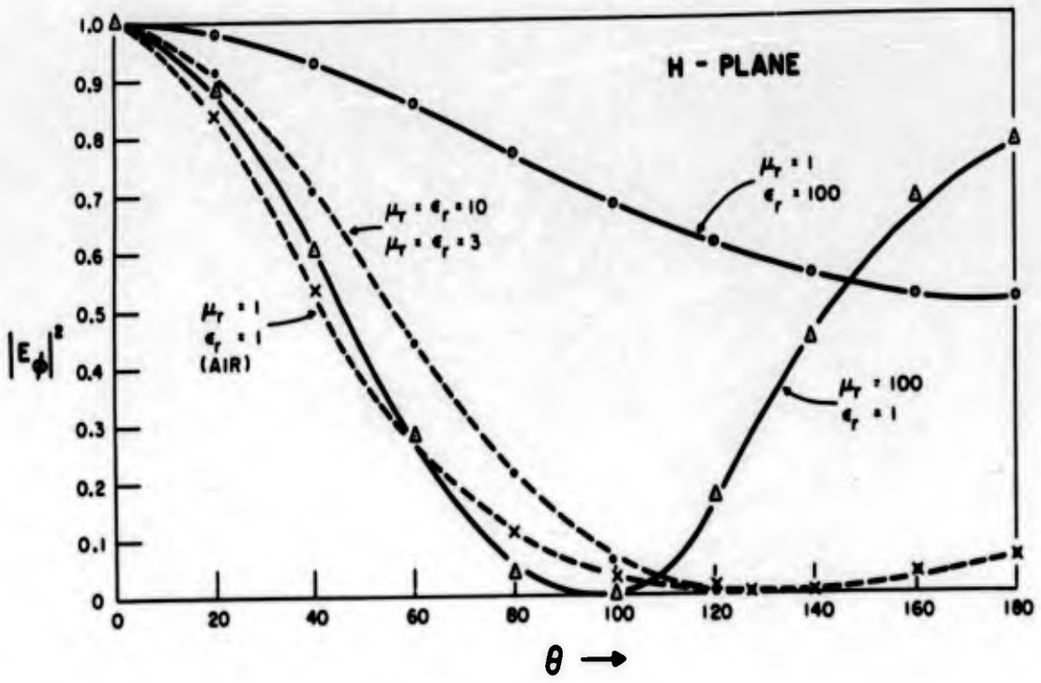

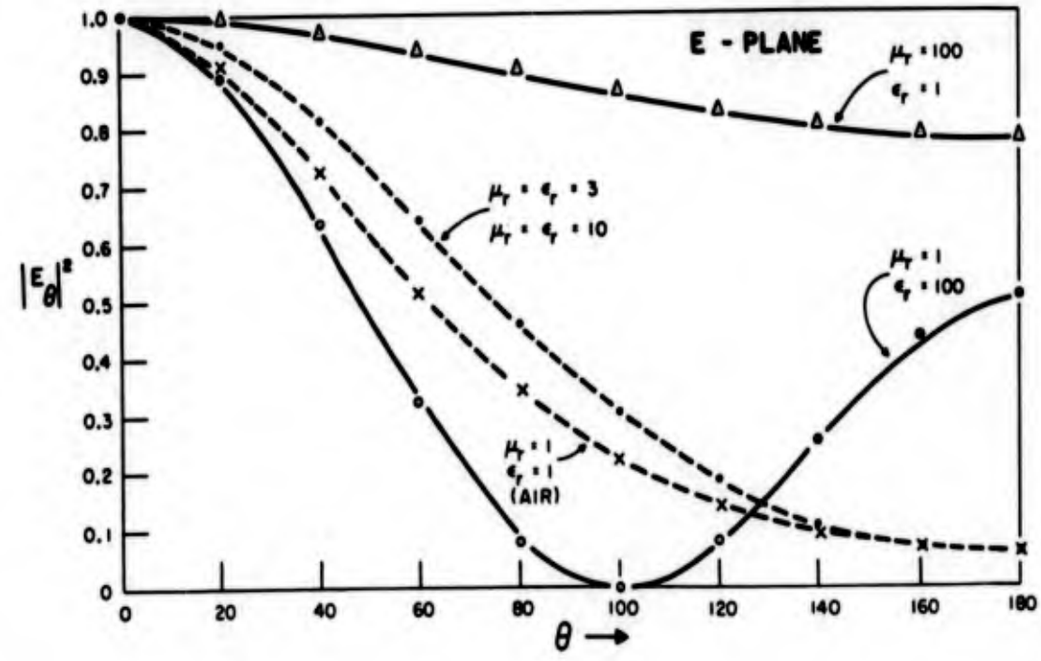

Fig. 2. Theoretical results - loaded waveguide radiation patterns.

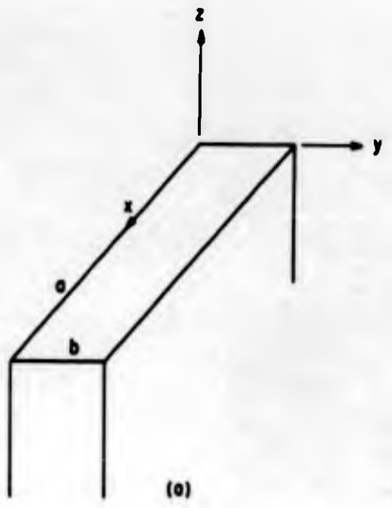

(a)

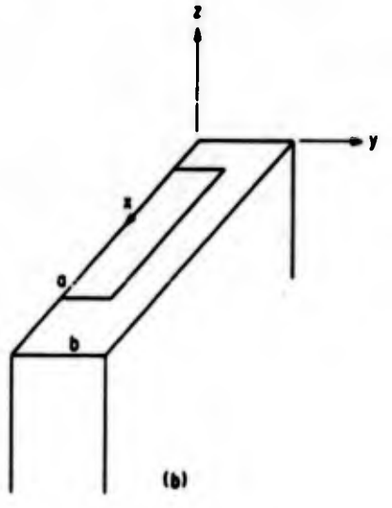

(b)

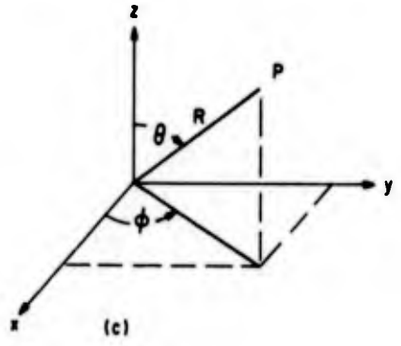

(c)

Fig. 3. Slot antenna coordinate systems.

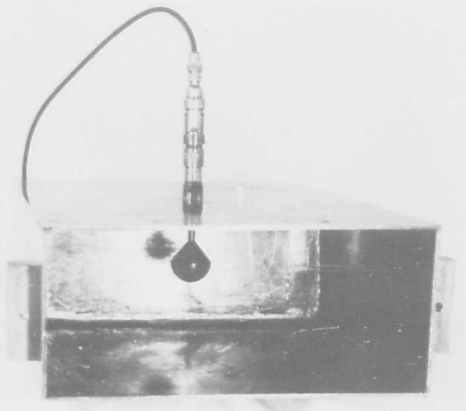

Fig. 4. Rectangular cavity slot antenna (no flange).

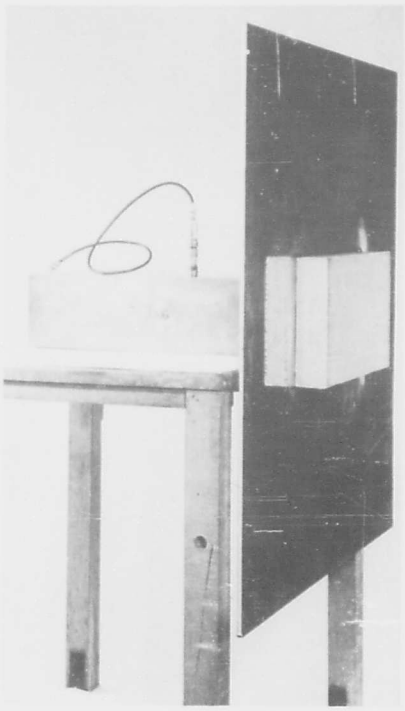

Fig. 5. Rectangular cavity slot antenna (with flange).

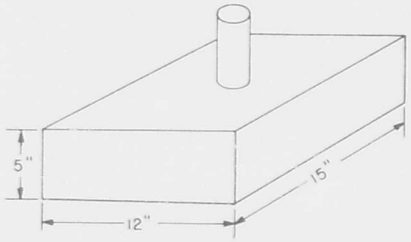

Fig. 6. Dimensions of rectangular cavity slot antenna.

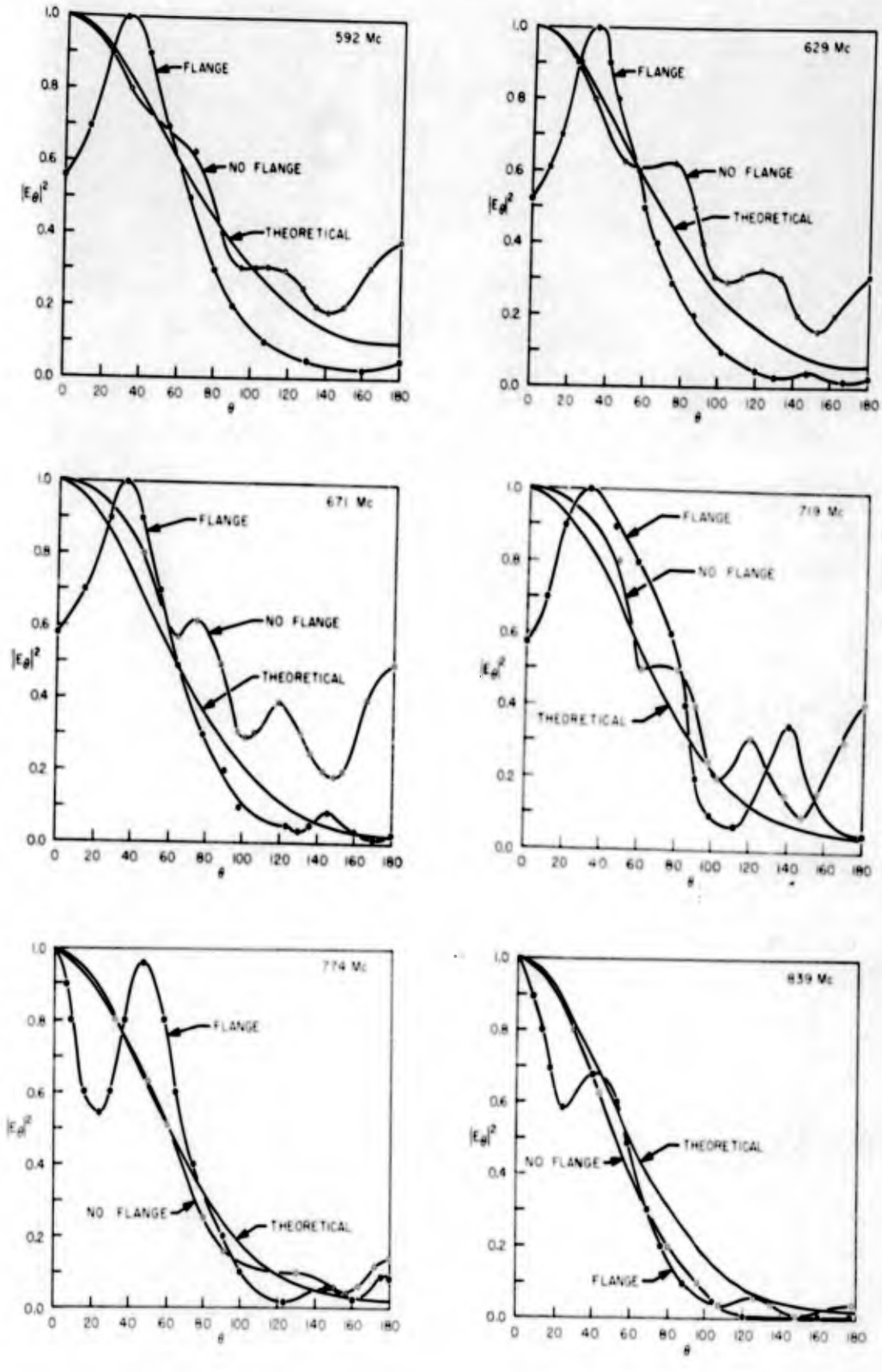

Fig. 7. Unloaded rectangular-cavity slot antenna; theoretical and experimental results. E-plane patterns.

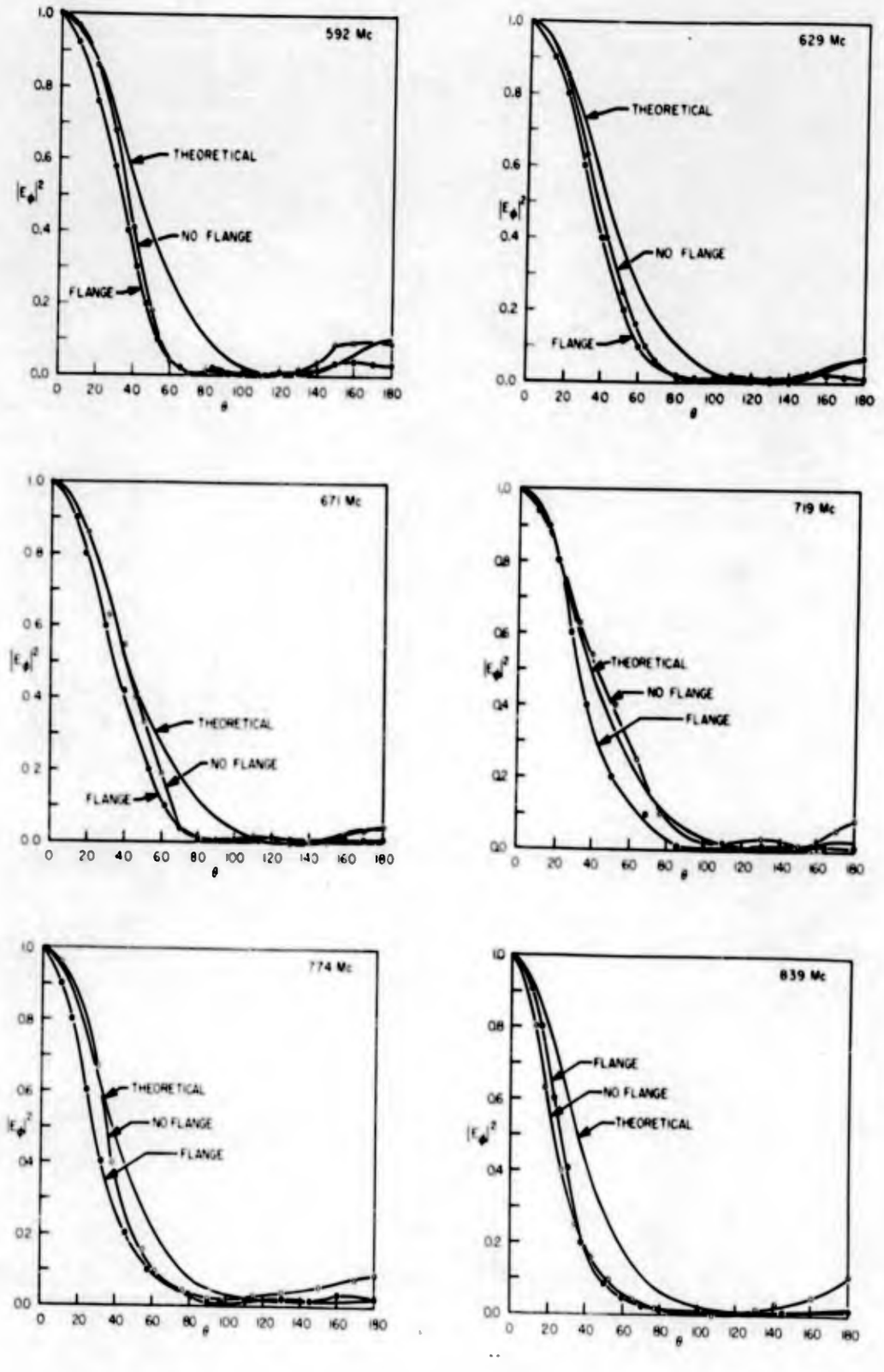

Fig. 8. Unloaded rectangular-cavity slot antenna;
theoretical and experimental results.
H-plane patterns.

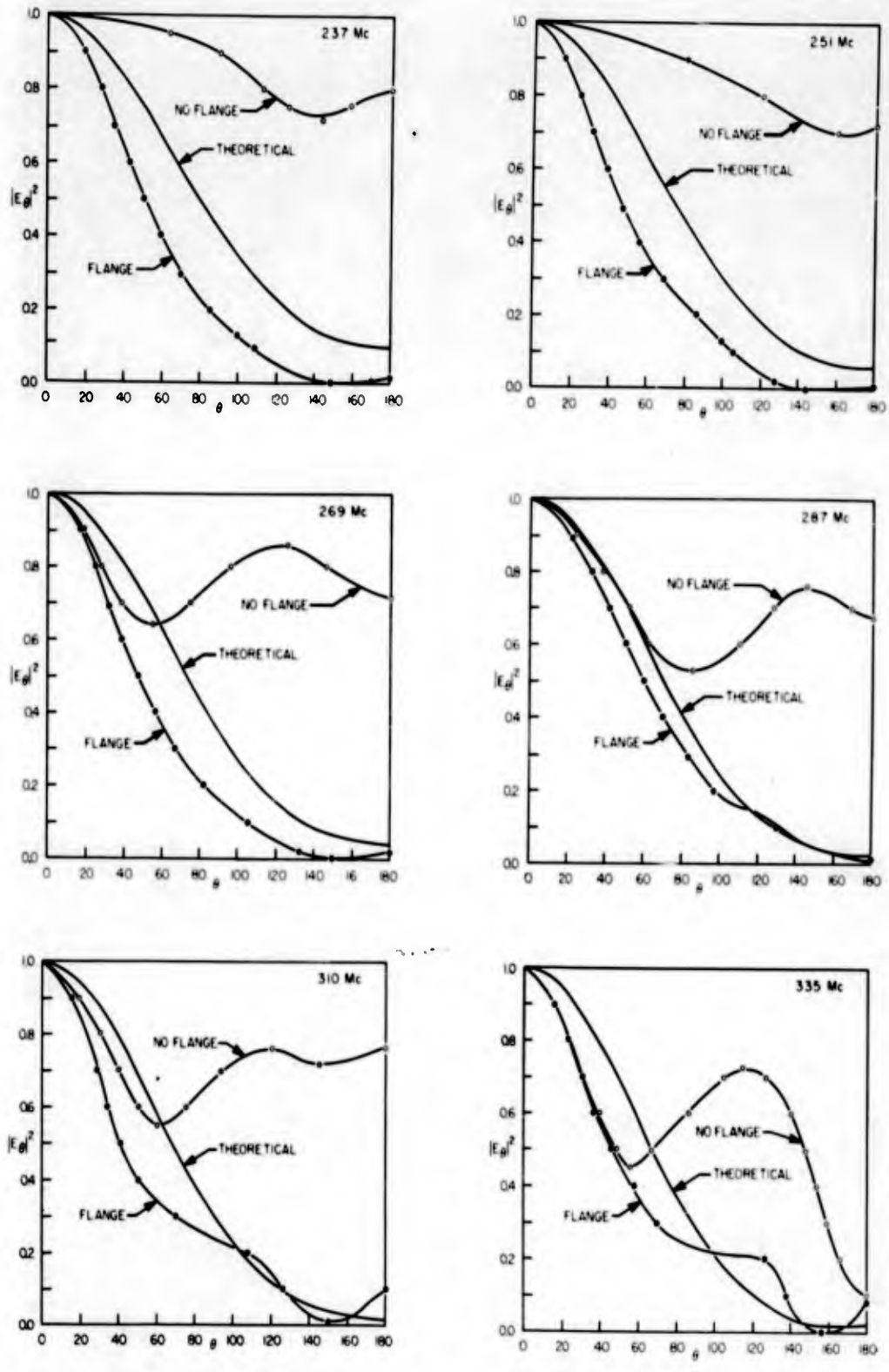

Fig. 9. Loaded rectangular-cavity slot antenna; theoretical and experimental results. E-plane patterns.

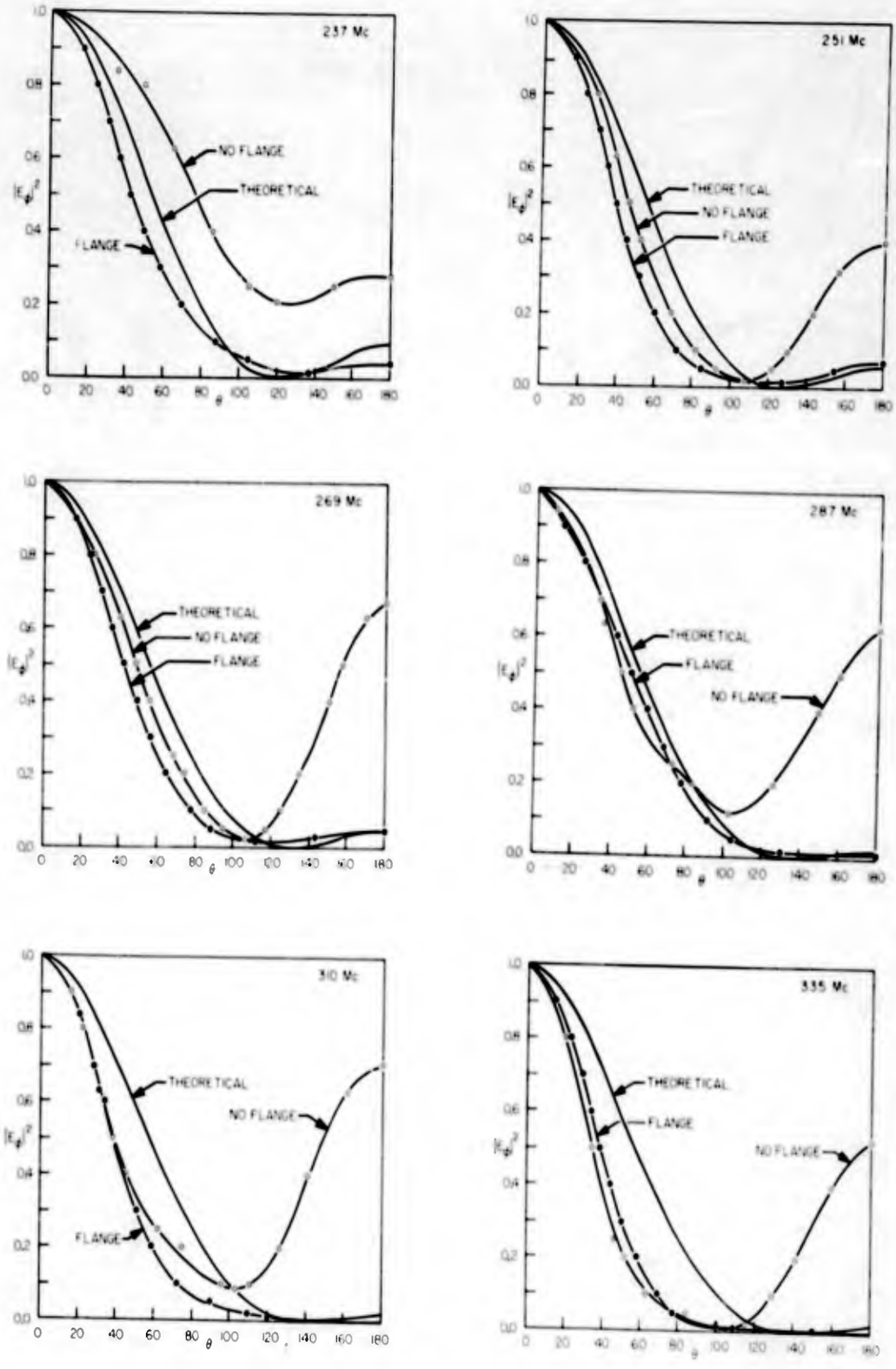

Fig. 10. Loaded rectangular-cavity slot antenna; theoretical and experimental results. H-plane patterns.

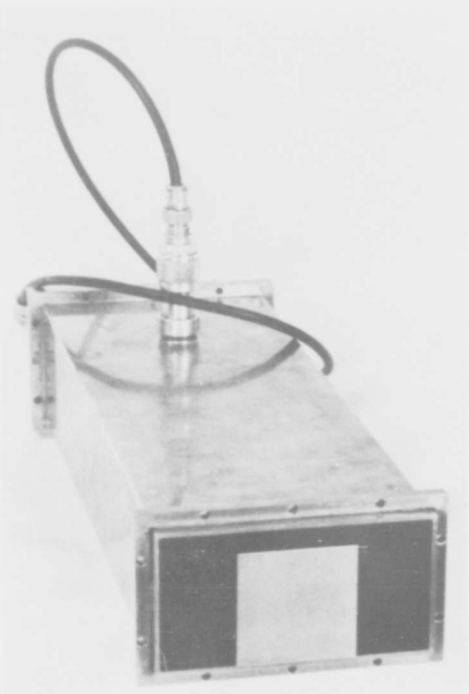

Fig. 11. Ridged slot antenna (without flange).

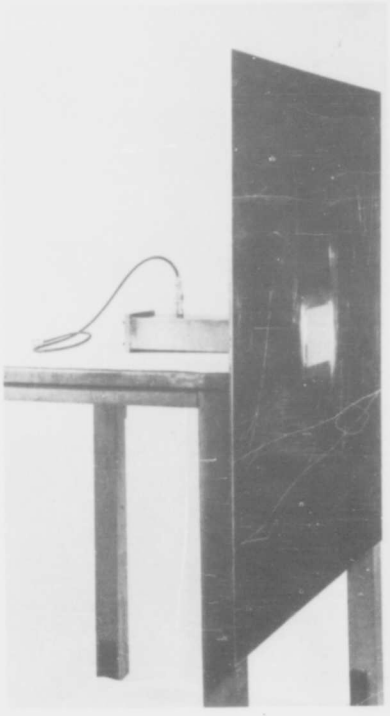

Fig. 12. Ridged slot antenna (with flange).

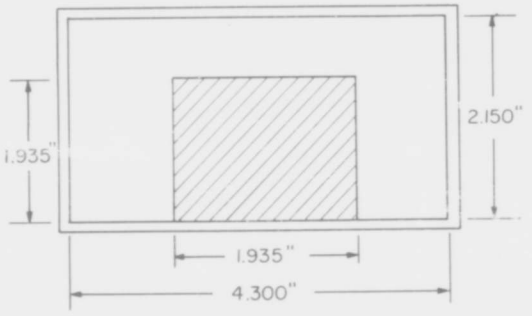

Fig. 13. Dimensions of ridged slot antenna.

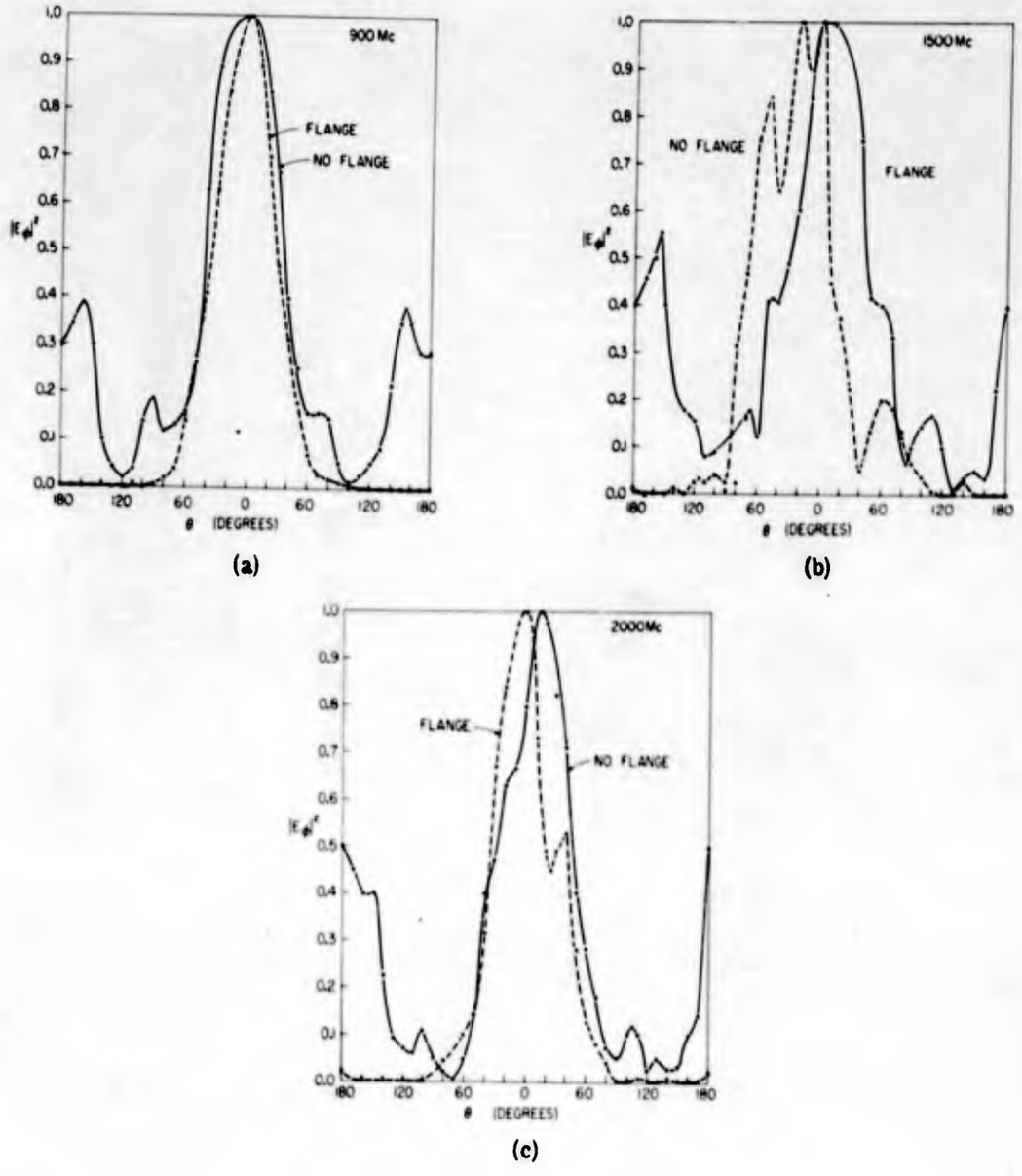

Fig. 14. Ridged cavity slot antenna - unloaded - H-plane patterns.

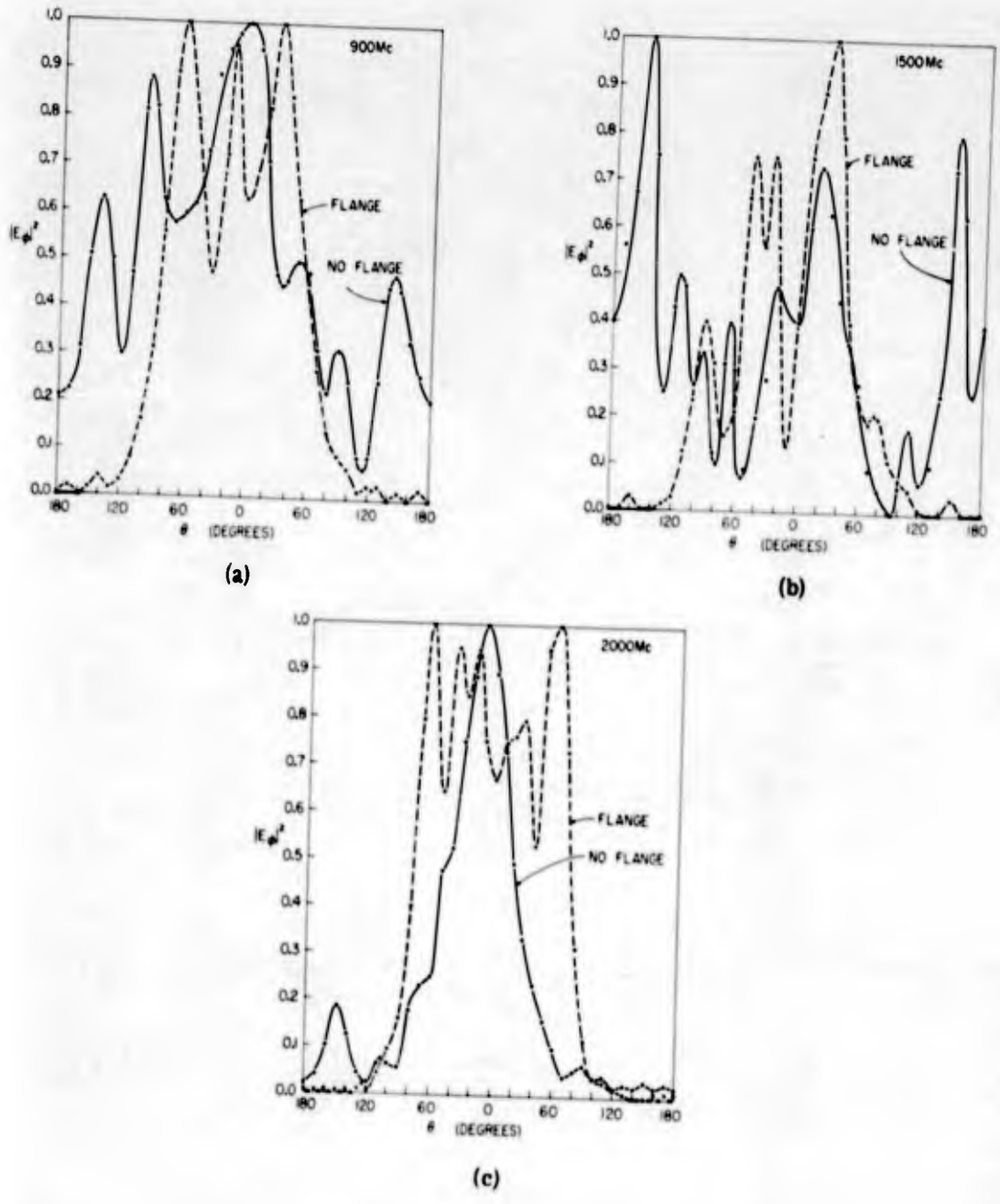

Fig. 15. Ridged cavity slot antenna - unloaded - E-plane patterns.

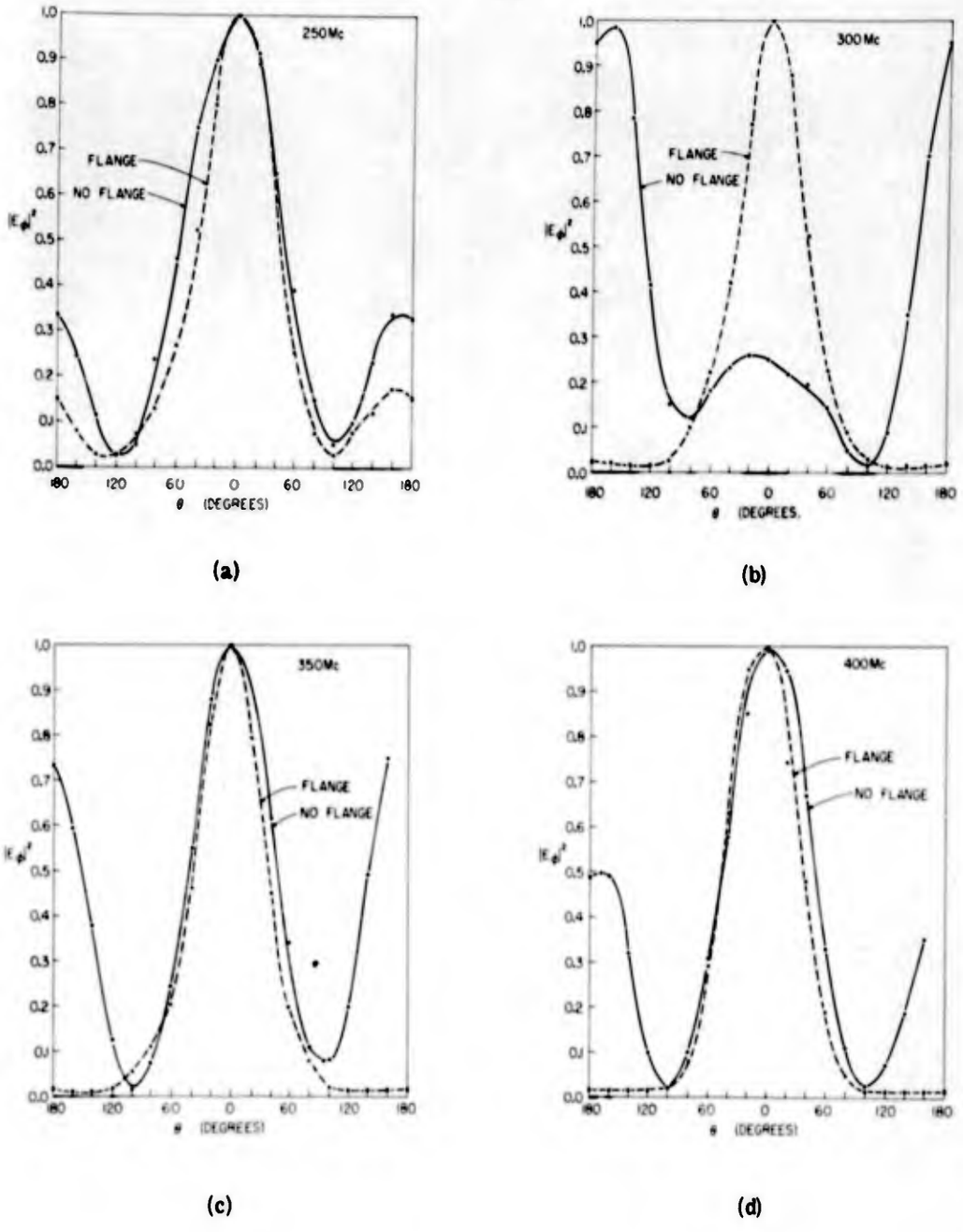

Fig. 16. Ridged cavity slot antenna - loaded - H-plane patterns.

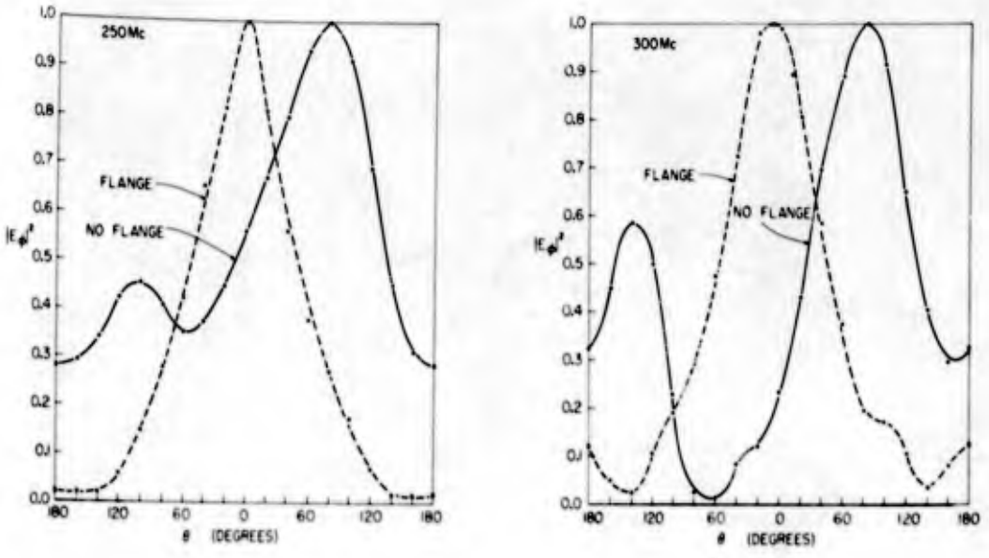

(a) (b)

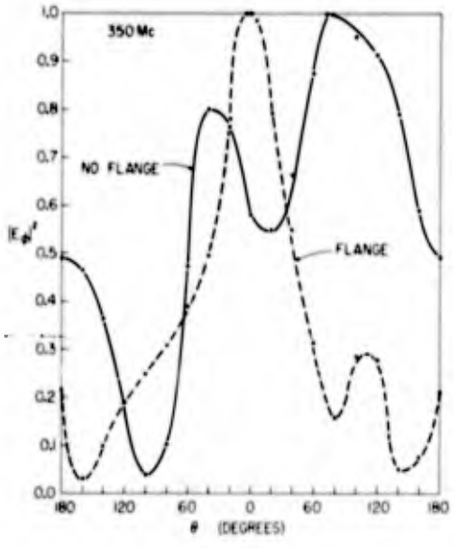

(c)

Fig. 17. Ridged cavity slot antenna - loaded - E-plane patterns.

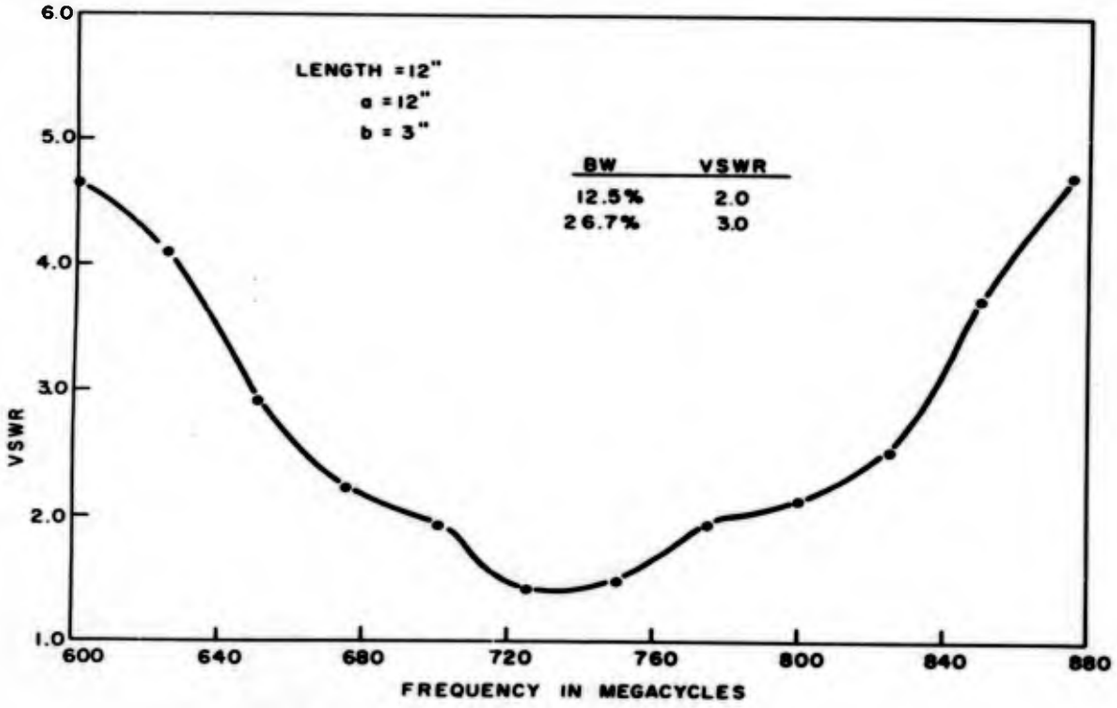

Fig. 18. VSWR of unloaded rectangular slot radiator.

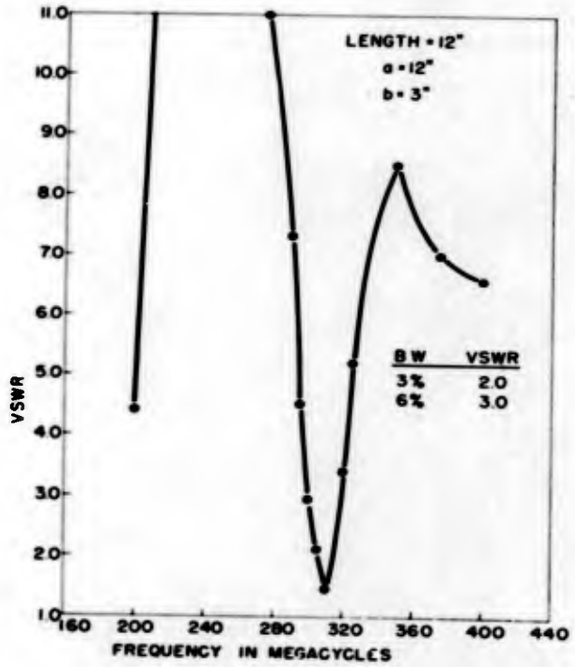

Fig. 19. VSWR of loaded rectangular slot radiator.

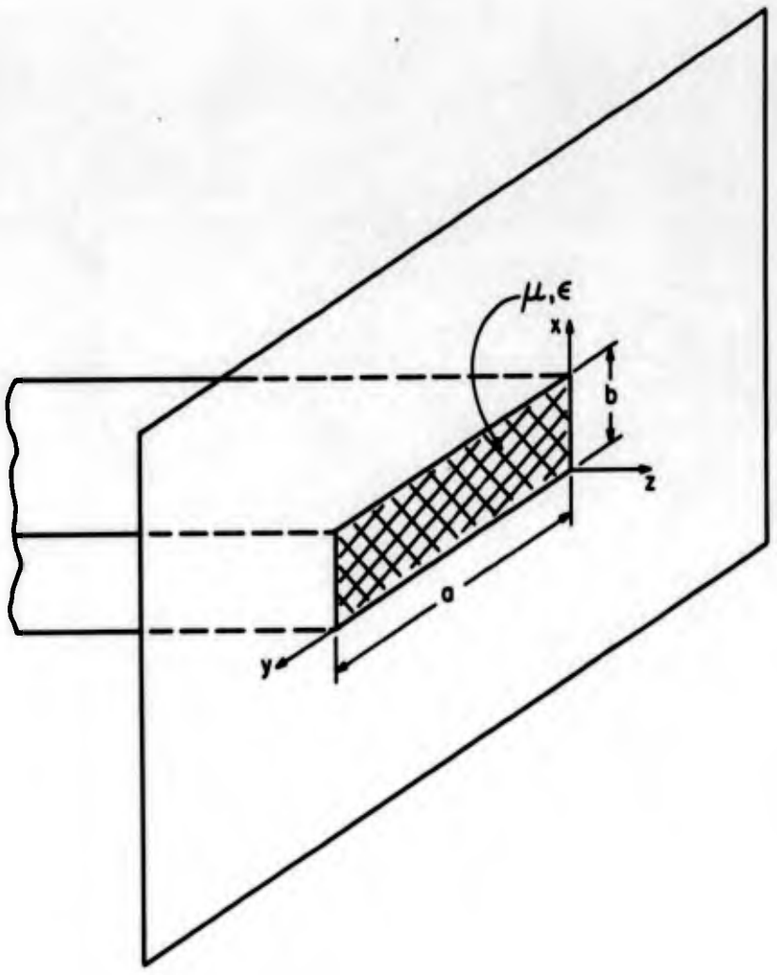

Fig. 20. Rectangular waveguide slot radiator loaded with isotropic ferrite material.

ABSTRACT

Antennafiers for Echo Area Control

by

J. R. Copeland, W. J. Robertson, R. B. Green, S. Mikuteit

Antenna Laboratory
Department of Electrical Engineering
The Ohio State University
Columbus, Ohio
October 1962

A novel hybrid-coupled parametric amplifier for the VHF-UHF range has been developed which exhibits absolute stability with regard to its input termination.

This amplifier has been combined with a pair of orthogonal T-bar slot antennas in a ground plane so that a signal arriving through either antenna is amplified and reradiated from the other.

Echo area measurements of this system are presented, and the general problem of echo area control with integrated antenna-active element systems is discussed.

A few applications in the fields of radar enhancement and camouflage, passive or pseudo-passive satellite communications, and ground-based repeaters are mentioned.

ANTENNAFIERS FOR ECHO AREA CONTROL

by

J. R. Copeland, W. J. Robertson, R. B. Green, S. Mikuteit

Antenna Laboratory
Department of Electrical Engineering
The Ohio State University
Columbus, Ohio
October 1962

I. INTRODUCTION

An approach to echo area control is to treat the radar target as if it were a receiving antenna, whose scattering characteristics are determined by the way in which currents are excited on the antenna and its surrounding structure. Clearly, then, the scattering from such a target is a function of load impedance at the antenna terminals, and the choice of location for these terminals sometimes can be made to simplify the analysis. This approach is used in studying echo control by means of active antennas (antennafiers).

II. ANTENNAFIER SCATTERING

With the introduction of active devices to an antenna, greater control of reflection from the antenna can be achieved. In particular, with the integrated antenna-amplifier, or antennafier, the power retransmitted from the antenna can be many times that from a passive system, allowing cancellation of scattering from a proportionally larger surrounding structure, or permitting considerable echo enhancement from the target, whichever is desired. In addition, aside from the enhancement and camouflage applications of such a system, the amplifier easily may be modulated with information which could be displayed on the radar viewing the target. Such a system would have the potential advantage of being simpler than a conventional radar transponder, and would be adaptable to a wide range of types of information to be transmitted.

III. HYBRID T-BAR SLOT ANTENNAFIER

In order to demonstrate the feasibility of controlling the echo area of antennas with active loads, the input and output ports of a hybrid parametric amplifier were connected to a pair of T-bar slot antennas placed orthogonally in a ground plane. Figure 1 is a sketch of one of the

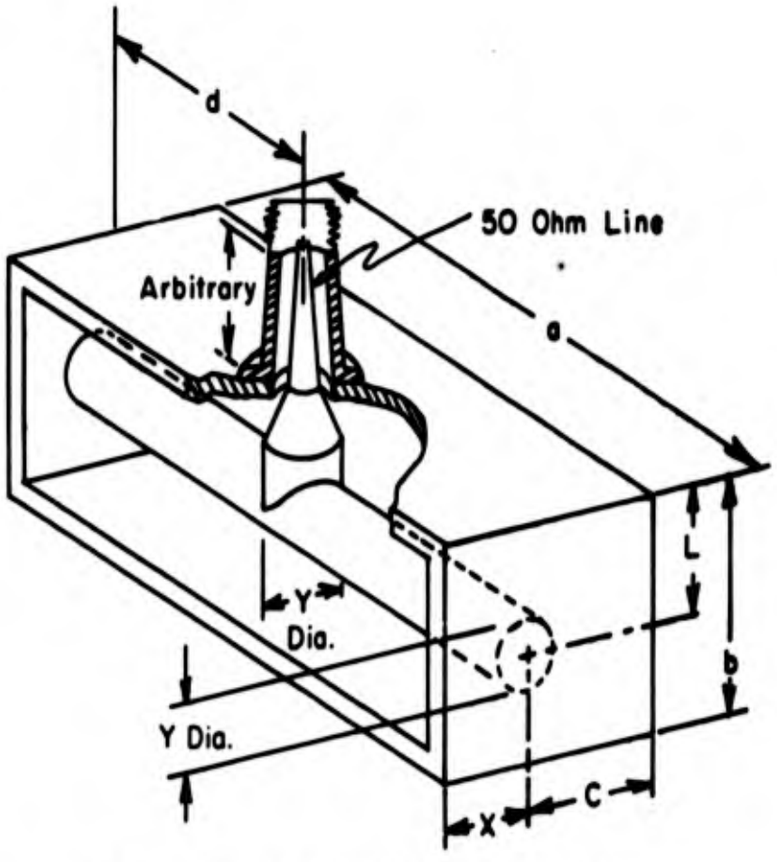

Fig. 1. T-bar compensated slot antenna.

antennas, and Fig. 2 illustrates their placement in the ground plane. Isolation between these two antennas is in excess of 70 db.

Because of the bilateral nature of the hybrid amplifier, the signal received by either antenna is amplified and radiated from the other, with orthogonal polarization. An advantage of the antenna orthogonality is that it permits discrimination between the antennafier scattering and the ground plane structure scattering. However, if sufficient isolation can

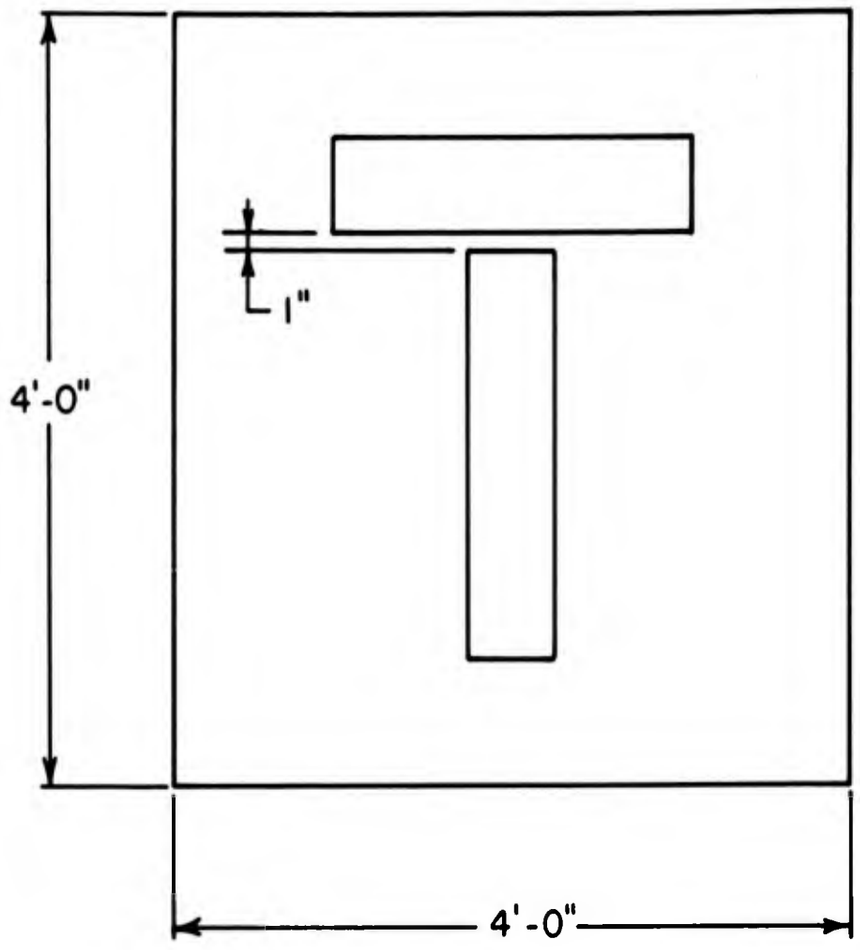

Fig. 2. T-bar slot antennas in ground plane.

be maintained for a required system gain, any other orientation of antennas is permissible.

With the orthogonal antennas and with the radar transmitter and receiver polarized horizontally and vertically, respectively (parallel to the two T-bar slot antennas) the echo from the ground plane is returned cross-polarized to the receiver, but the antennafier echo is matched to the receiving antenna.

However, if the radar transmitter and receiver polarizations are parallel, and aligned to a 45^{o} angle with respect to the polarizations of the T-bar slot antennas, the radar receiver is matched to the combined echo from the ground plane and the antennafier.

Figure 3 shows the echo pattern of the T-bar slot antennafier alone, using the polarization properties to suppress the flat plate echo. The pattern is considered reliable only near the broadside region ($\pm 45^{o}$) because the suppression of the flat plate echo becomes poor near the edge-on aspects.

Also shown in Fig. 3 is the echo pattern of the ground plane alone, taken with the antennafier inoperative, but located in the ground plane. It is seen in this particular case that only near broadside incidence the echo from the ground plane exceeds that from the antennafier. In general the relative values of antennafier scattering and structural scattering are determined by antenna gain, amplifier gain and structure size and shape.

Figure 4 shows the combination pattern of the ground plane with the operating hybrid T-bar slot antennafier, and as expected, the main lobe of the ground plane pattern is virtually unaffected by the presence of the antennafier, while the nulls are filled in and the first side lobes are considerably enhanced.

It was also noted during this experiment that 1000 cps modulation applied to the klystron pump source for the parametric amplifier was clearly audible at the radar receiver throughout the range of target aspect angles occupied by the antennafier echo pattern shown in Fig. 3, even at broadside where the echo level from the active system was considerably lower than that of the flat ground plane. This effect could be of advantage in certain transponder or repeater applications where it would be necessary to encode various types of information on the returning radar echo.

IV. PASSIVE ANTENNA SCATTERING

As an example of the passive antenna-mode scattering concept, a conducting flat plate with a resonant slot in its center was chosen. This particular example was used because:

1. The echo area of flat plates has been studied extensively.

2. Terminals may be introduced conveniently in the form of a slot antenna, and considerable information is available on slot antennas in ground planes.

3. The load may be placed behind the ground plane so as to minimize its effect on the echo area but yet be readily accessible.

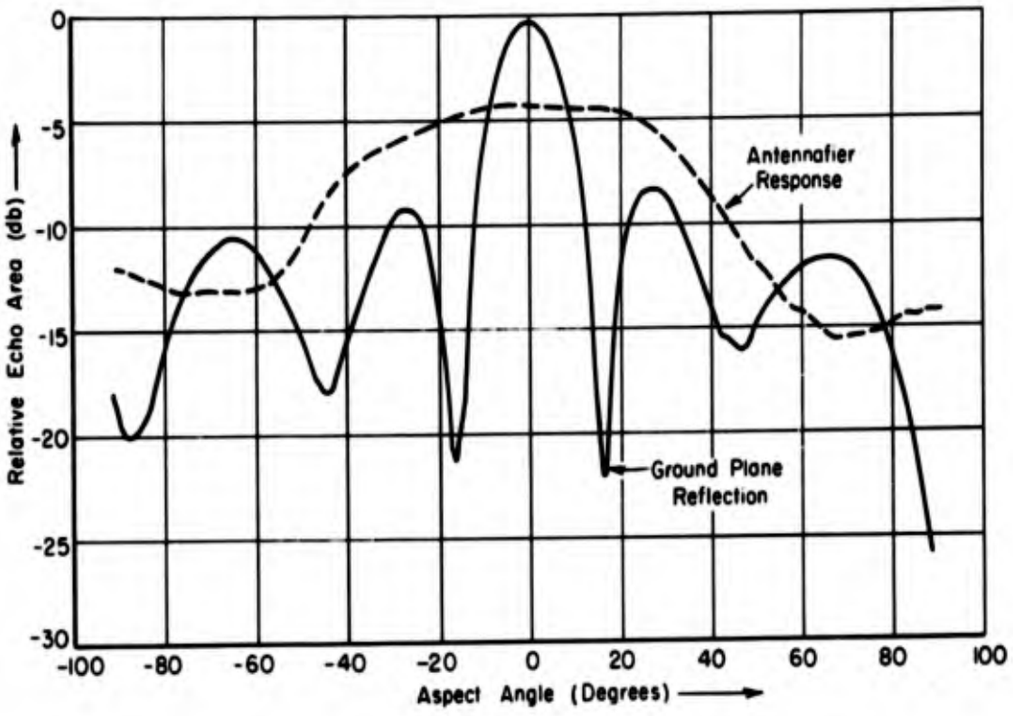

Fig. 3. Echo area of the hybrid T-bar slot antennafier, and the 4-foot ground plane.

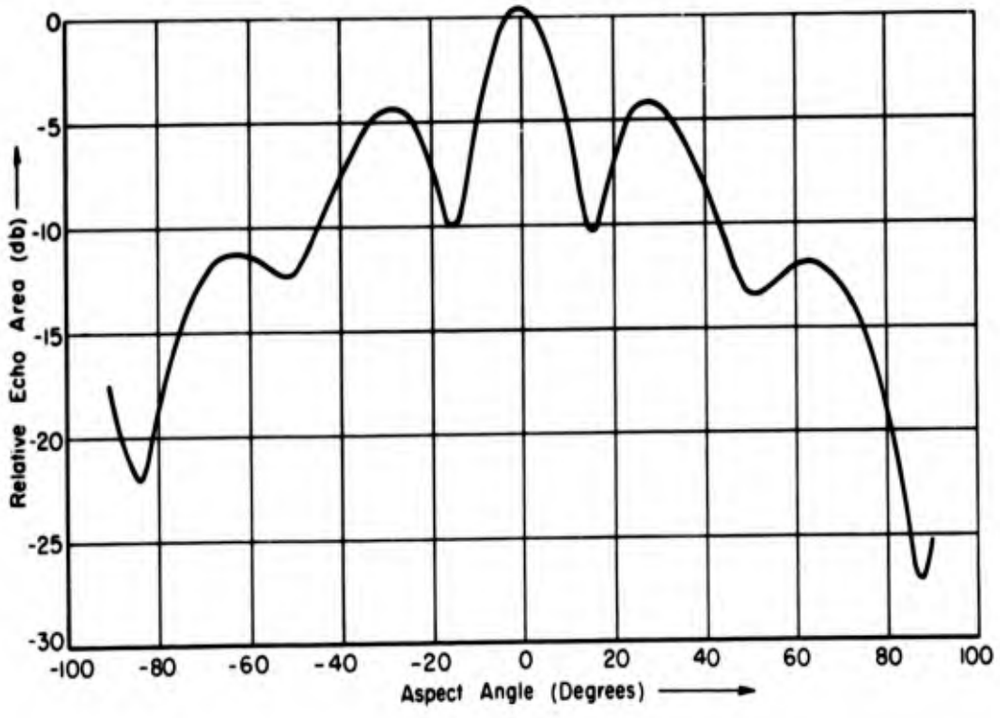

Fig. 4. Echo area of the combined ground plane and hybrid T-bar slot antennafier.

4. The small rectangular flat plate may, with care, be considered as a fundamental unit of area of a more complicated object.

A flat plate 1/2λ x 3/4λ was chosen because its echo pattern would correspond over a considerable range of aspects to the antenna-mode echo area one could expect from a 1/10λ x 1/2λ slot placed in the plate. The device was modelled at X-band, and measured echo patterns of the plate, the plate with a slot, and the slotted plate with a short across the center of the slot are compared in Fig. 5. At broadside a reduction of 13 db was obtained by introducing the slot. Shorting the slot brought the echo area back up to the echo area of the whole plate.

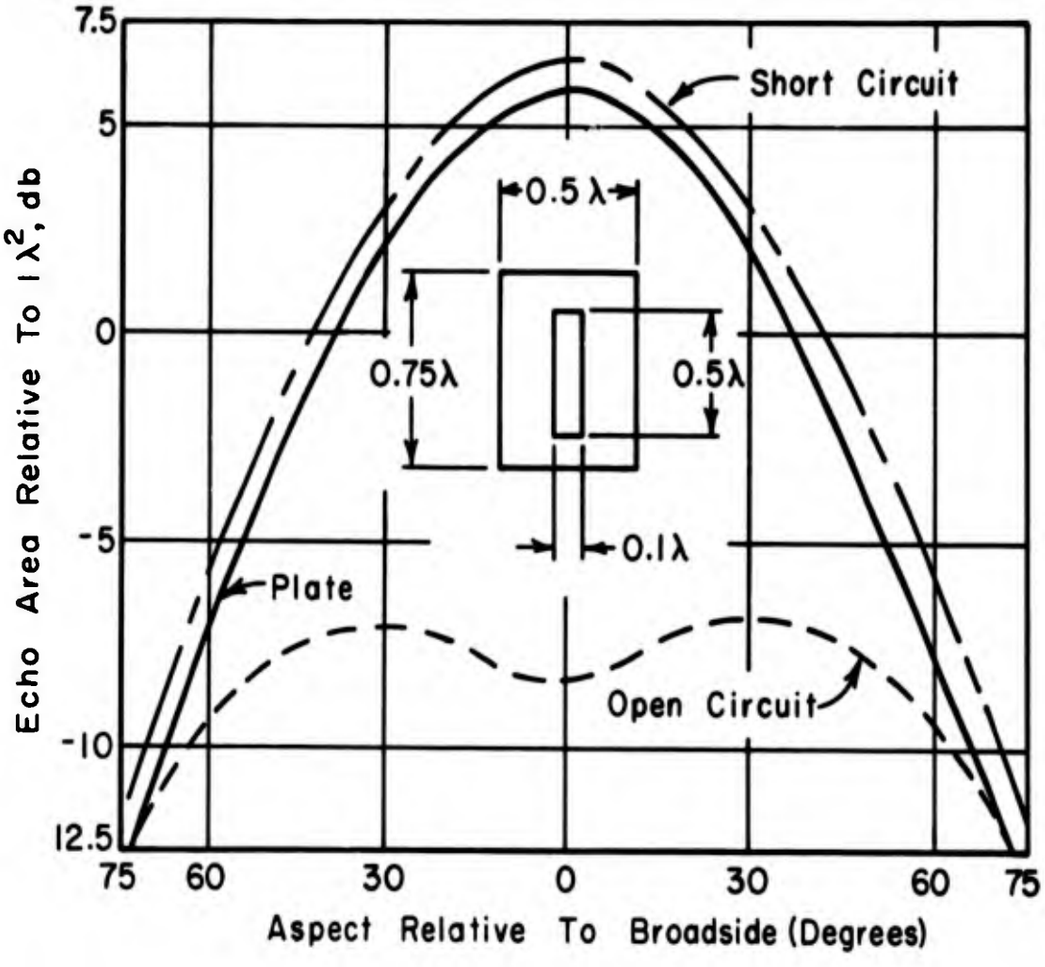

Fig. 5. E-plane echo patterns of a slot-plate configuration.

V. HYBRID PARAMETRIC AMPLIFIER

The amplifier used in the antennafier scattering measurements was a hybrid coupled parametric amplifier as shown in Fig. 6. The details of the parametric diode reflection amplifier assemblies are shown in Fig. 7. The resonating inductance is used to tune out the fixed shunt capacity of the varactor diode and holder. Figure 8 is a photograph of the reflection amplifier.

Since the effective shunt capacity of the varactor diode depends on the DC bias voltage across it, this amplifier element is voltage tunable. In this particular instance, however, the idler circuit was a resonant cavity and had to be retuned for each new signal frequency because the pump source was held fixed. The tuning range was in excess of 100 Mc centered on 420 Mc.

The hybrid coupled parametric amplifier, composed of two matched reflection amplifiers connected to their source and load by a broadband strip-line hybrid junction, operates with stability independent of its input termination, including both open and short circuits. The amplifier operates with a noise figure near 2 db, at a gain of 9 db at 422 mc.

The noise figure deteriorates to 3.5-4.0 db at a stable gain figure of 20 db, and gain near 30 db can be obtained, but instability shows up in this region because of the limited directivity of the hybrid junction used.

VI. UHF RADAR FACILITY

Radar measurements of antennafier systems are complicated by difficulties in constructing scale models. Consequently a CW radar measurement facility has been assembled for full scale echo measurements at 420 mc. A block diagram of the system is shown in Fig. 9.

The transmitting and receiving antennas are 15 element Yagi arrays mounted so their polarizations can be adjusted independently to any angle between horizontal and vertical. Sensitivity of the system is limited only by the depth of the null obtained by phasing a small amount of transmitter signal against that picked up by the receiving antenna when the target is removed.

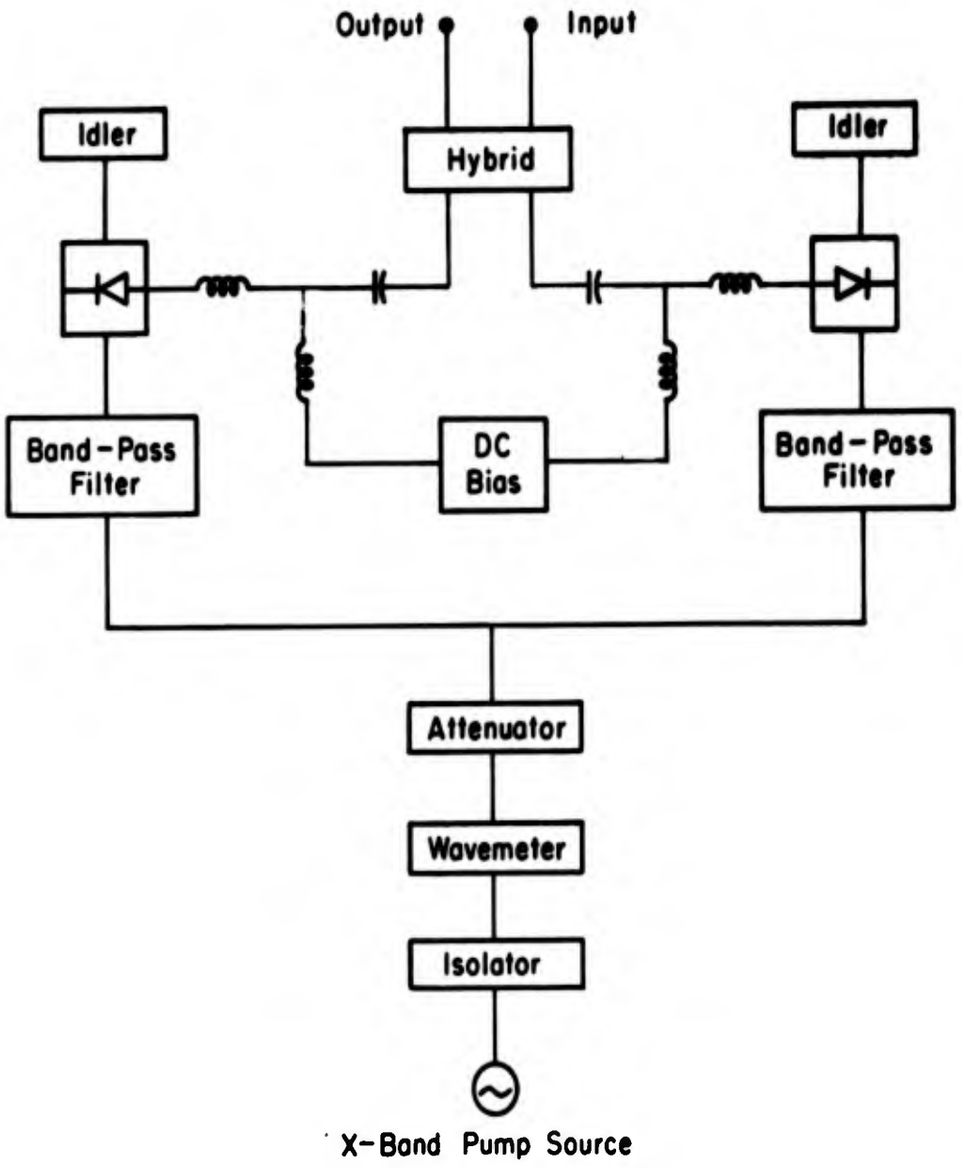

Fig. 6. Voltage-tunable hybrid-coupled parametric amplifier.

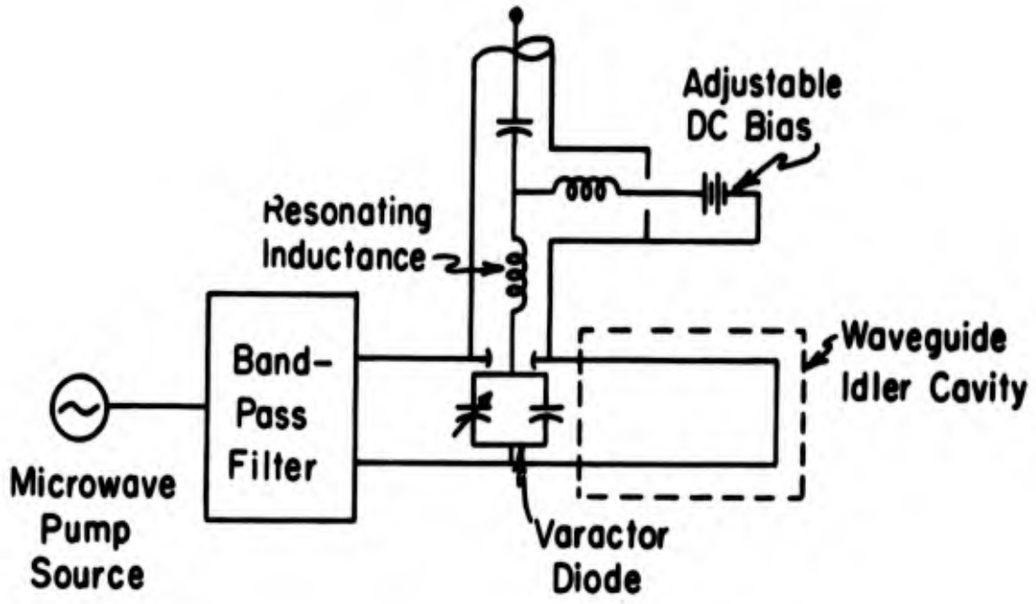

Fig. 7. Schematic diagram of voltage-tunable reflection-type amplifier.

The antennas and the target are located on towers 90 feet apart, approximately 30 feet above the roof of the two story building on which they stand.

No attempts have been made as yet to measure targets as small as half wave dipoles with this system, but its performance is entirely adequate for measurements of the antennafier system described in this paper.

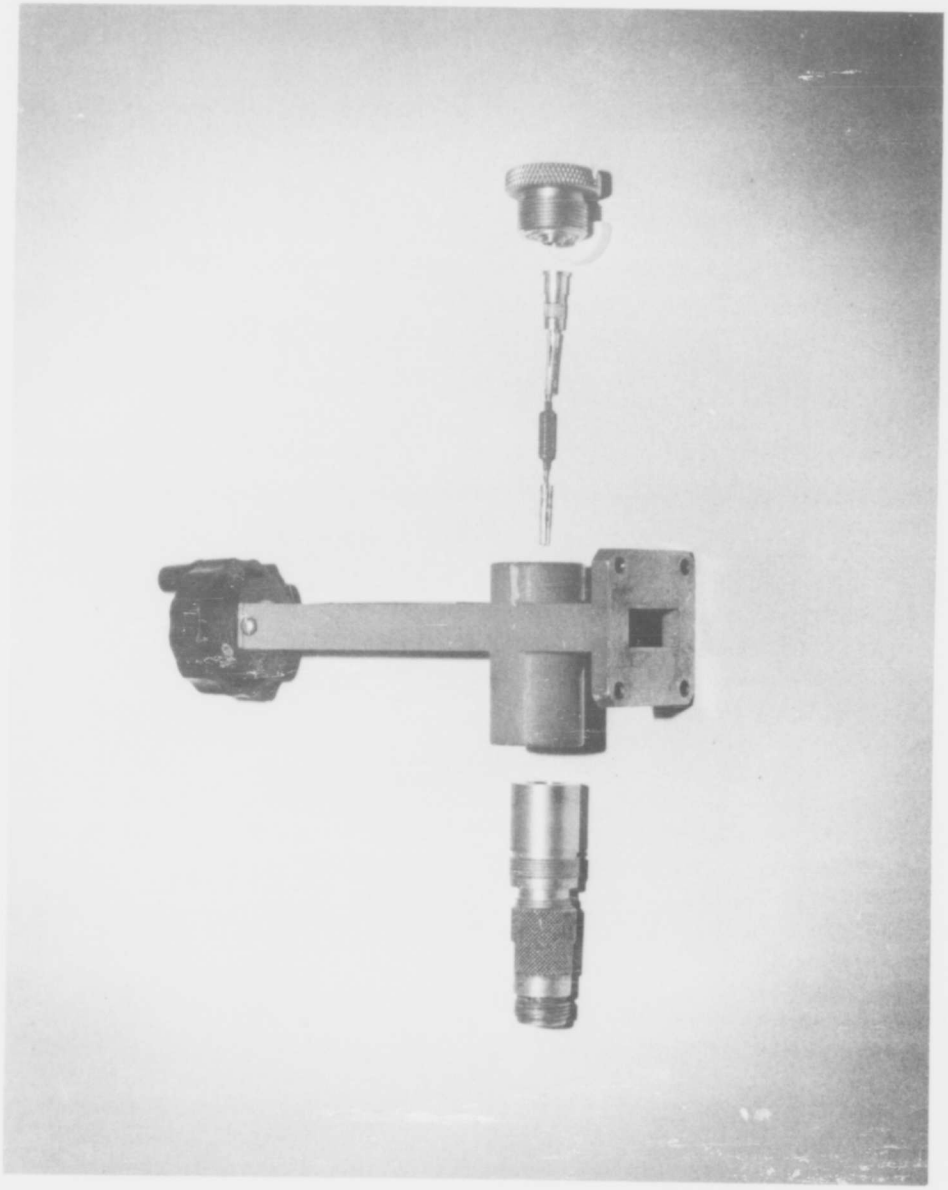

Fig. 8. Exploded view of voltage-tunable reflection amplifier

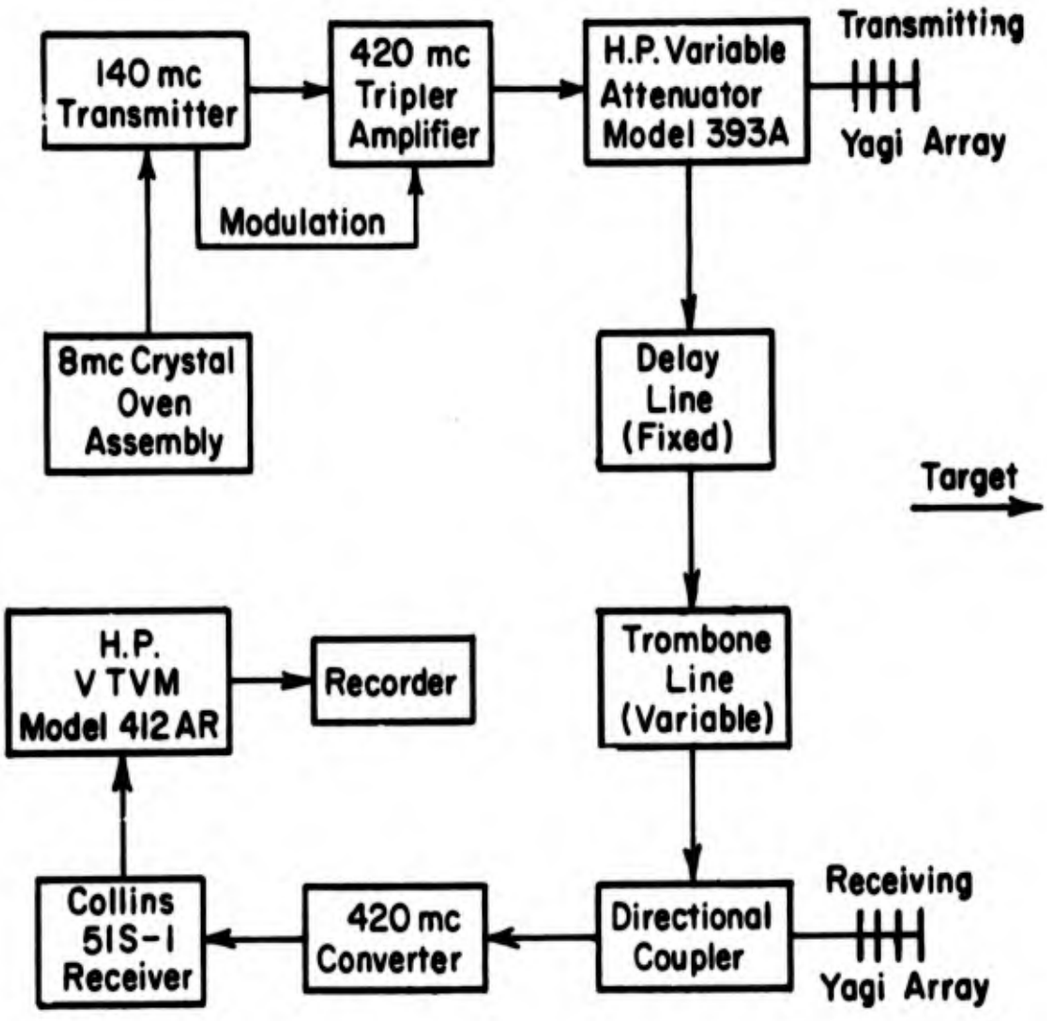

Fig. 9. Block diagram of 420 Mc reflection measuring installation.

VII. CONCLUSIONS

The antennafier system discussed here is potentially useful in bilateral repeater applications, since the signal entering either antenna is amplified and reradiated from the other antenna. The maximum tolerable gain of the system is limited only by the isolation between antennas, which can be extremely good. The model which was discussed here had limited gain because of the modest directivity of the broadband hybrid junction used, but two or more identical hybrid parametric amplifiers could be used in tandem for increased gain. This is possible because of the remarkable stability exhibited by the amplifier circuitry that has been described.

The use of amplifying circuitry in antenna structures can be used for radar enhancement or camouflage of an antenna and its surrounding structure, at least over a narrow band of frequencies. For any particular application, such parameters as antenna gain, coverage pattern and polarizations, surrounding structure, amplifier type, gain, etc., would be chosen according to specific requirements. Other types of active circuits, such as switching diodes, could be used to modify the electrical characteristics of most types of antennas for camouflage purposes over much wider frequency ranges.

ACKNOWLEDGEMENTS

This work was supported by United States Air Force Contract No. AF 33(616)-6211. The authors are pleased to acknowledge the suggestions and encouragement of Mr. E. M. Turner of ASD, and Dr. C. H. Walter of the Ohio State University Antenna Laboratory.

LOW FREQUENCY, SUBSURFACE RADIATING STRUCTURES

BY

A. W. GUY AND G. HASSERJIAN

THE BOEING COMPANY
AERO SPACE DIVISION
PHYSICS TECHNOLOGY DEPARTMENT

P.O. Box 3707
Seattle 24, Washington

ABSTRACT

This paper is a discussion of practical, low frequency subsurface radiating antenna arrays for ground wave propagation. An analysis is made for antenna arrays placed in a semi-infinite homogeneous, conducting medium where the conduction currents are assumed to be larger than the displacement currents. Measured data taken from both model antennas submerged in salt water and full scale antennas buried in the earth are compared with data computed from the theoretical design equations. The axial propagation properties for a single, insulated, infinitely long wire submerged in a semi-infinite conducting medium are derived and expressed in a generalized form. The equations are expressed in terms of wire cross section, depth of burial, and skin depth of the conducting medium. The input impedance and current distribution of a long but finite, length of such an insulated wire can then be determined by standard transmission line expressions. By combining these expressions with the radiation field expressions for a short horizontal dipole below the interface, the radiation efficiency for a single long wire subsurface antenna is determined. The results are presented in the form of generalized curves which may be used to design an optimum antenna for any given set of uncontrollable variables, such as ground conductivity and frequency.

With the long insulated wire considered as an element, it is shown that a closely spaced set of such elements can be used to improve radiation efficiency. The input impedance and current distribution parameters for each element are determined for this case by considering the effect of mutual coupling

on the axial propagation properties first, and then the results are used in standard transmission line expressions.

Theoretical data and experimental data taken from model antennas submerged in salt water show good agreement, and the performance of a full scale buried antenna array in the earth matched all design expectations.

I. INTRODUCTION

The contents of this paper are in part a condensation of the results of a study motivated by the requirement of a reliable hardened antenna system to be used for underground missile sites[1,2,3]. Although many schemes have been proposed for hardening surface antennas and constructing retractable vertical dipoles, the simplicity and reliability of completely buried antennas makes them appealing for the frequency range and distances where the ground wave is an important mode of propagation. In general for this case, where the earth conduction currents are much larger than the displacement currents, the insulated dipole or coaxial antenna was found to be superior to all other types of completely submerged antennas. The horizontal insulated antenna provides the most practical design of the buried antenna from the standpoint of practicability, low cost and maximum efficiency. The geometric shape of the antenna allows simple solutions to be obtained for both the immediate fields and the ground wave field.

Part II of the paper will discuss the development of the theory, Part III will compare the theory with the results of experimental measurements made on models submerged in salt water,

Part IV will discuss design consideration, and Part V will discuss the design and operation of an experimental full scale antenna buried in the earth.

II. THEORY OF THE BURIED INSULATED WIRE ANTENNA

1. Introductory Remarks

The theory of operation of a buried antenna may be divided into two categories. The first category involves the fields immediately adjacent to the antenna which determine the transmission line properties such as current distribution and input impedance. The second category involves the coupling of the energy from the antenna to the radiation and ground wave fields. In this analysis, it is assumed that the ground conductivity is sufficiently high so that the displacement currents are much smaller than conduction currents. It is also assumed that the only contribution to the far zone field is the ground wave.

The coupling factor to the ground wave may be found by first determining the ground wave field due to an infinitesimal source and then integrating over the current distribution of the antenna. A measure of launching efficiency for the antenna may be determined by comparing the resulting ground wave field to that obtained from a short vertical dipole above the ground, fed with identical power.

2. Ground Wave Fields of Small Electric Dipoles

The ground wave field expressions for the various electric dipoles with dipole moment $Id\ell$ shown in Figure 1 are

Vertical Dipole[4,5,6]

$$E_z = j60KId\ell F \frac{e^{-jKR}}{R} \quad (1)$$

$$E_r = uE_z \quad (2)$$

where F is the well known ground wave attenuation factor

$$u = \sqrt{j\frac{\omega\epsilon_0}{\sigma}}$$

K = Phase constant of plane wave in free space

ω = Angular frequency

ϵ_0 = Permittivity of free space

σ = Conductivity of the earth

Horizontal Dipole at Earth's Surface[4,5,6]

$$E_z = j60KId\ell F\cos\phi\, u \frac{e^{-jKR}}{R} \quad (3)$$

$$E_r = uE_z \quad (4)$$

Buried Horizontal Dipole[7]

$$E_z = j60KId\ell F\cos\phi\, u \frac{e^{-jKR - \frac{h}{\delta}}}{R} \quad (5)$$

$$E_r = uE_z \quad (6)$$

where h = burial depth and $\delta = \sqrt{\frac{2}{\omega\mu_0\sigma}}$ is the skin depth in the conducting medium.

Note that the ground wave field due to a buried horizontal dipole is identical to that of a horizontal dipole at the

interface except for the "depth loss factor" $e^{-h/\delta}$. Noting also that the vertical field expressions for the vertical and horizontal electric dipoles are identical except for the factor u cos ϕ and the fact that Norton's ground wave propagation curves for vertical electric dipoles have become standard for radio communication system design, one may use the short vertical dipole as a standard for comparing the launching efficiencies of buried antennas.

3. Transmission Line Properties of a Single Wire

In order to determine the ground wave fields in terms of input power for a buried antenna of arbitrary length, it is necessary to know its current distribution and input impedance. For a simple cross-section of the antenna, as shown in Figure 2, the derivation of the field expressions are quite simple for the assumed case where $\sigma/\omega\epsilon_o$ is very large compared to the earth dielectric constant, ϵ_g. The local field characteristics for an infinitely long antenna surrounded by an infinite conducting medium with skin depth δ are first expressed. These characteristics are then modified to account for the presence of the air-conducting medium interface. Finally, with the use of standard transmission line equations, one can determine the input impedance and current distribution. We now consider a new coordinate system (r', ϕ', Z') and the antenna cross section shown in Figure 2 with dielectric constant ϵ_r, dielectric radius b, center conductor radius a, and center conductor skin depth δ_1. The assumption is made that $a/\lambda < b/\lambda \ll 1$ (where λ is a free space wavelength) which is valid for all practical buried antennas. First considering a conducting medium that is infinite in extent, the electric fields may be derived by a standard method[8] and simplified by

the above assumptions to

In the Dielectric (Region 2)

$$E_2 \approx E_{r'2} \approx \frac{\Gamma}{j\omega\epsilon_0\epsilon_r} \frac{I}{2\pi r'} e^{j(\omega t - \Gamma z)} \tag{6}$$

and

In the Conducting Medium (Region 3)

$$E_3 \approx E_{z'3} \approx \frac{I\sqrt{-j2}}{2\pi\sigma b\delta} \frac{H_0^{(2)}\left(\frac{\sqrt{-j2}r}{\delta}\right)}{H_1^{(2)}\left(\frac{\sqrt{-j2}b}{\delta}\right)} e^{j(\omega t - \Gamma z)} \tag{7}$$

where the propagation constant Γ may be expressed in the generalized form

$$\frac{\Gamma}{\sqrt{\epsilon_r}k} = \frac{\alpha}{\sqrt{\epsilon_r}K} + j\frac{\beta}{\sqrt{\epsilon_r}K}$$

$$= \left[-1 - \frac{je^{-j\frac{\pi}{4}}}{\sqrt{2}\ln\frac{b}{a}}\left(\frac{\delta}{b}\frac{H_0^{(2)}\left(\frac{b}{\delta}\sqrt{-j2}\right)}{H_1^{(2)}\left(\frac{b}{\delta}\sqrt{-j2}\right)} - \frac{\delta_1}{a}\frac{J_0\left(\frac{a}{\delta_1}\sqrt{-j2}\right)}{J_1\left(\frac{a}{\delta_1}\sqrt{-j2}\right)}\right)\right]^{\frac{1}{2}} \tag{8}$$

The above expressions may be modified to account for the presence of the interface by representing the total field E_z below the surface as the sum of two components

$$E_z = E_p + E_s \tag{9}$$

where E_p is the primary field corresponding to that of a wire at infinite depth, and E_s is a secondary field resulting from the effect of the boundary. This representation is valid if one restricts the wire burial depth to be at least ten wire radii. Considering the coordinate system in the sketch of a

wire near the interface in Figure 3, the primary field given by equation (7) may be expanded into a known Fourier integral form

$$E_p = \frac{I\sqrt{-j2}}{2\pi^2\sigma b\delta}\,\frac{e^{j(\omega t-\Gamma z)}}{H_1^{(2)}\left(\frac{\sqrt{-j2}\,b}{\delta}\right)}\int_{-\infty}^{\infty}\frac{e^{j\zeta x-j(y+h)\sqrt{\frac{-j2}{\delta^2}-\zeta^2}}}{\sqrt{\frac{-j2}{\delta^2}-\zeta^2}}\,d\zeta \qquad (10)$$

and the secondary field may be represented by an unknown Fourier integral form

$$E_s = \int_{-\infty}^{\infty} E(\zeta)\, e^{j\zeta x+j(y-h)\sqrt{\frac{-j2}{\delta^2}-\zeta^2}}\,d\zeta \qquad (11)$$

where $E(\zeta)$ must be determined. By expressing the remaining E and H fields in terms of Fourier integrals, applying boundary conditions, and taking the inverse transforms, the solution

$$E(\zeta) = \frac{I\sqrt{-j2}}{2\pi^2\sigma b\delta H_1^{(2)}\left(\frac{\sqrt{-j2}\,b}{\delta}\right)\sqrt{\frac{-j2}{\delta^2}-\zeta^2}}\left[\frac{\sqrt{\frac{-j2}{\delta^2}-\zeta^2}-\sqrt{K^2-\zeta^2}}{\sqrt{\frac{-j2}{\delta^2}-\zeta^2}+\sqrt{K^2-\zeta^2}}\right] \qquad (12)$$

is obtained.

The total field therefore may be expressed as

$$E_z = \frac{I\sqrt{-j2}\,H_0^{(2)}\left(\frac{\sqrt{-j2}\,r}{\delta}\right)}{2\pi\sigma b\delta H_1^{(2)}\left(\frac{\sqrt{-j2}\,b}{\delta}\right)} f(x,y,h) \tag{13}$$

where

$$f(x,y,h) = 1 + \frac{1}{\pi H_0^{(2)}\left(\frac{\sqrt{-j2}\,r}{\delta}\right)} \int_{-\infty}^{\infty} \frac{\sqrt{\frac{-j2}{\delta^2} - \zeta^2} - \sqrt{K^2 - \zeta^2}}{\sqrt{\frac{-j2}{\delta^2} - \zeta^2} + \sqrt{K^2 - \zeta^2}} \frac{e^{j\zeta x + j(y-h)\sqrt{\frac{-j2}{\delta^2} - \zeta^2}}}{\sqrt{\frac{-j2}{\delta^2} - \zeta^2}} d\zeta \tag{14}$$

where $r = \sqrt{x^2 + (y+h)}$

Since $\left|\frac{-j2}{\delta^2}\right| \gg K^2$

from the assumption that $\frac{\sigma}{\omega \epsilon_0 \epsilon_g} \gg 1$

and by a change in variable, equation (14) may be simplified to

$$f(x,y,h) = 1 + \frac{j}{\pi H_0^{(2)}\left(\sqrt{-j2}\,\frac{r}{\delta}\right)} \int_{-\infty}^{\infty} \frac{\sqrt{j+\xi^2} - |\xi|}{\sqrt{j+\xi^2} + |\xi|} \frac{e^{j\xi\frac{x\sqrt{2}}{\delta} + (y-h)\frac{\sqrt{2}}{\delta}\sqrt{j+\xi^2}}}{\sqrt{j+\xi^2}}\, d\xi \qquad (15)$$

The new propagation constant corresponding to this case may be derived by assuming that the transverse fields in the dielectric (region 2) of the antenna are unmodified by the interface which is reasonable for a burial depth of at least ten wire radii.

The generalized propagation constant may then be expressed as

$$\frac{\Gamma}{\sqrt{\epsilon_r}K} = \left[-1 - \left(\frac{j e^{-j\frac{\pi}{4}} H_0^{(2)}\left(\frac{b}{\delta}\sqrt{-j2}\right)}{\frac{b}{\delta}\sqrt{2}\,\ln\frac{b}{a}\,H_1^{(2)}\left(\frac{b}{\delta}\sqrt{-j2}\right)}\right. \right. f(b,-h,h)$$

$$\left. \left. - \frac{\delta_1}{a} \frac{J_0\left(\frac{a}{\delta_1}\sqrt{-j2}\right)}{J_1\left(\frac{a}{\delta_1}\sqrt{-j2}\right)}\right)\right]^{\frac{1}{2}} \qquad (16)$$

For the case where $b/\delta \ll 1$ and $a/\delta_1 \gg 1$ which is true for practical buried antennas, equation (16) reduces to the simpler expression

$$\frac{\Gamma}{\sqrt{\epsilon_r}K} = \frac{\alpha}{\sqrt{\epsilon_r}K} + j\frac{\beta}{\sqrt{\epsilon_r}K}$$

$$= \left[\frac{1}{\ln\frac{b}{a}}\left(0.230 + \ln\frac{b}{\delta}\right) - 1 - \frac{I\left(\frac{h}{\delta}\right)}{2\ln\frac{b}{a}} + \frac{j}{2\ln\frac{b}{a}}\left(\frac{\pi}{2} + \frac{\delta_1}{a}\right)\right]^{\frac{1}{2}} \qquad (17)$$

where the integral

$$I\left(\frac{h}{\delta}\right) = \int_{-\infty}^{\infty} \frac{\sqrt{1+\xi^2} - |\xi|}{\sqrt{1+\xi^2} + |\xi|} \frac{e^{-2\sqrt{2}\frac{h}{\delta}\sqrt{1+\xi^2}}}{\sqrt{1+\xi^2}} \, d\xi \tag{18}$$

has been evaluated on a digital computer and is plotted in Figure 3. Figure 4 shows a plot of $\Gamma/\sqrt{\epsilon_r}\,K$ as a function of b/δ and b/a for the case where $h/\delta > 1.6$ ($I(h/\delta) \approx 0$) and δ_1/a is negligibly small (no center conductor loss). Since this plot was made from equation (16), no restriction exists for the size of b/δ. For small values of b/δ, the generalized phase constant $\beta/\sqrt{\epsilon_r}\,K$ is very large compared to the generalized attenuation constant $\alpha/\sqrt{\epsilon_r}\,K$. In fact, the major contribution to $\beta/\sqrt{\epsilon_r}\,K$ is that due to $\frac{1}{\ln\frac{b}{a}} \ln\frac{b}{\delta}$ in equation (17). Since $I(h/\delta)$ is small compared to $\ln b/\delta$, the phase constant, β/k, will change by only a few percent as depth is varied. The major contribution to α/k on the other hand is due to the imaginary components in the bracketed portion of equation (17). Since these components are of much less magnitude than the real components, the imaginary part of $-I(h/\delta)$, which is maximum at approximately 0.3 skin depths, will have a much greater effect on α/k. At zero depth and depths greater than 1.6 skin depths, however, the imaginary part of $I(h/\delta)$ is zero so β/k should not be affected. One may therefore conclude that the transmission line properties for a

single buried insulated wire very close to the interface is nearly identical to those for a wire buried at large depths, but the attenuation constant will vary for intermediate depths.

The characteristic impedance of the buried antenna is expressed as

$$Z_0 = \frac{a\int^{b} E_{r2}' \, dr'}{I} = \frac{60\,\Gamma}{j\,er\,K} \ln\frac{b}{a} \tag{19}$$

The input impedance and current distribution for any length dipole ℓ and any termination Z_L at the dipole ends may now be easily found from standard transmission line equations. The two cases of interest corresponding to the most efficient buried antenna configurations are the cases where the dipole ends are terminated in a short (ground rod) or an open (insulated end). The impedances may be put into generalized forms which are convenient for antenna design purposes. These forms are

$$\frac{\frac{\beta}{k}}{g} R_{in} = 15\pi \left[\frac{\frac{\beta}{\alpha} \sinh\frac{\alpha}{\beta}\frac{2\pi\ell}{\lambda_c} \pm \sin\frac{2\pi\ell}{\lambda_c}}{\cosh\frac{\alpha}{\beta}\frac{2\pi\ell}{\lambda_c} \pm \cos\frac{2\pi\ell}{\lambda_c}} \right] \tag{20}$$

$$\frac{\frac{\alpha}{k}}{g} X_{in} = \pm 15\pi \left[\frac{\sin\frac{2\pi\ell}{\lambda_c} \mp \frac{\alpha}{\beta}\sinh\frac{\alpha}{\beta}\frac{2\pi\ell}{\lambda_c}}{\cosh\frac{\alpha}{\beta}\frac{2\pi\ell}{\lambda_c} \pm \cos\frac{2\pi\ell}{\lambda_c}} \right] \tag{21}$$

where R_{in} = Input resistance

X_{in} = Input reactance

$\lambda_c = 2\pi/\beta$

and $$g = \frac{8\alpha\beta}{\pi\sigma_r K^2} \ln\frac{b}{a} \qquad (22)$$

The top sign of the double sign in the equations refers to a dipole terminated in a short while the bottom sign refers to a dipole terminated in an open.

The above generalized forms are plotted in Figures 5 and 6 for all significant values of ℓ/λ_c and α/β. It is significant to note that the function g is in general a function of three variables: b/δ , a/δ_1 , and h/δ . For small values of b/δ , however, it reduces to the form

$$g = g\left(\frac{a}{\delta_1}, \frac{h}{\delta}\right) = 1 + \frac{2}{\pi}\left(\frac{\delta_1}{a} - \mathrm{Im}\left[I\left(\frac{h}{\delta}\right)\right]\right) \qquad (23)$$

where $I_m[\ \ ]$ denotes "imaginary part of".

One may note that for an antenna at an infinite depth with negligible center conductor loss, $\delta_1/a = 0$, $I(h/\delta) = 0$ and $g = 1$.

Since it can be shown that the distributed series resistance of the antenna is $g15\pi k$, we may interpret the function g as "geometry loss factor", indicating the increase in antenna resistance and loss in antenna efficiency due to center conductor loss and proximity to the interface of the surrounding conductor.

It will be shown later that mutual coupling between elements in an array will also cause an increase in g. One may also show by substituting values from Figure 4 into equation (22) that g will decrease when b/δ becomes greater than 0.1. This is due to the greater cross sectional area that the current is forced to flow through around the antenna.

The current distribution of the antenna may easily be obtained from standard transmission line equations.

4. Efficiency of a Single Buried Antenna

In order to provide a basis for comparing the buried dipole to the vertical dipole above the earth, the expression for the vertical field in the air, at the surface of the earth, due to a buried dipole of arbitrary length ℓ and terminating impedance Z_L must be obtained. Figure 7 shows the top view of an insulated antenna, buried at depth h. Noting that the ground wave field due to the infinitesimal section of the antenna dz' is given by equation (5), integration over the antenna current distribution $I(Z')$ gives for the ground wave field

$$E_z = j60\sqrt{\frac{P}{R_{in}}}\ F\ u\ \frac{e^{-jKR-\frac{h}{\delta}}}{R}\ f(\phi) \qquad (24)$$

where

$$f(\phi) = \frac{K\cos\phi}{I_0}\int_{-\frac{\ell}{2}}^{\frac{\ell}{2}} I(z')\, e^{jKz'\cos\phi}\, dz' \qquad (25)$$

and P is antenna input power, and R_{in} is the antenna input resistance. The horizontal $f(\phi)$ of most practical single wire buried antennas is predominantly a cos ϕ variation with

a maximum off the end of the antenna. One may compare the efficiencies of various underground antenna configurations in launching energy to the surface wave by comparing the vertical fields of the underground antenna and a vertical electric dipole above the earth. The launching efficiency of the buried antenna is defined as

$$\mathcal{E} = \left| \frac{E_{zh}}{E_{zv}} \right|^2 \tag{26}$$

where E_{Zh} and E_{Zv} are the respective vertical electric fields of the buried antenna and the short vertical antenna above the ground for the same input power. Noting that the radiation resistance of a short vertical dipole of length $d\ell$ is $400\ (d\ell\ /\lambda)^2$, the efficiency expression becomes

$$\mathcal{E} = \frac{2}{9} \times 10^{-8}\ \frac{f}{\sigma}\ \frac{|f(\phi)|^2}{R_{in}}\ e^{-2\frac{h}{\delta}} \tag{27}$$

For computational purposes, the above expression may be put into the form

$$\frac{\sigma}{f}\, e^{2\frac{h}{\delta}}\, \mathcal{E} = E\left(\frac{\ell}{\lambda}, \frac{\beta}{k}, \frac{\alpha}{\beta}\right) \tag{28}$$

where E is a function of the antenna length in wavelengths and the antenna propagation constant. Equation (28) has been plotted in Figures 7 and 8 for both open end and shorted end dipoles. The curves are plotted for the typical case of $\alpha/\beta = 0.05$, as a function of β/k and ℓ/λ. For values of $\alpha/\beta \leq 0.2$, the curves will change very little for values of ℓ/λ from 0 to values corresponding to the first maximum of E.

Therefore, the curves may be used for most practical design problems. Note that the efficiency varies inversely with the "geometry loss factor" g and directly with the depth attenuation factor $e^{-2h/\delta}$. The relative refraction loss is accounted for by the factor f/σ . The impedance and efficiency curves in Figures 5, 6, 7 and 8 are not only useful for predicting the performance of a single wire antenna but are equally useful for predicting the performance of antenna arrays discussed in the following section.

5. Buried Antenna Arrays

The efficiency of a buried antenna array increases with the number of parallel elements. In order to determine the input impedance and current distribution of each element in an array, one must know the mutual coupling between the elements. Since the local fields of the antenna are due to the dominant TM mode, the mutual impedance between elements may be derived by the use of coupled wave theory. It is easy to derive the self and mutual impedance expressions for a pair of coupled wires since it involves only two coupled wave equations. For n elements, however, one must solve n coupled wave equations to determine the mutual coupling expressions. For buried arrays with a large number of elements, this is very cumbersome and impractical. One may obtain a good approximation of the mutual coupling effects for a large loosely coupled array, however, by considering each element as if it were in an infinite array with the same spacing between elements. The infinite number of wave equations then become identical, and it is only necessary to solve a single wave equation. Actual measurements have shown that this assumption yields fairly reliable results if the spacing between elements is greater

than a skin depth which is true for practical antenna arrays. For spacings less than a skin depth, however, the approximation breaks down since there are lateral variations in environment for the elements in the array. That is, the environment for the edge elements is quite different than that for the center elements. The experimental measurements shown in Figures 12 and 13 discussed in section V illustrate this quite clearly.

Considering an infinite number of elements as shown in Figure 9, we assume that the distance between the antenna, s, is such that $b \ll s$ and $\ell > s$. The latter condition is required to justify the assumption that cylindrical waves couple the energy between the antennas. Other assumptions are that the radial dependence of an individual antenna field in the conducting media is unmodified by the presence of other elements, and each element is excited with the same current.

For such a situation, the antenna mutual coupling occurs by longitudinal currents so the voltage $V(Z) = \int_a^b E_{r'_2}(Z)\, dr$ and the current $I(Z)$ for any wire are related as

$$\frac{dV(z)}{dz} = -\left(z_{11} + \sum_{j=2}^{\infty} z_{1j}\right) I(z) \tag{29a}$$

and

$$\frac{dI(z)}{dz} = -y_{11} V(z) \tag{29b}$$

where Z_{11} is the distributed series self impedance, Z_{1j} is the distributed series mutual impedance between wire 1 and wire j,

and Y_{11} is the distributed shunt admittance for each wire. Equations (29a) and (29b) yield impedance and current distribution solutions identical to those discussed previously with the exception that the new propagation constant denoted by Γ_∞ will be

$$\Gamma_\infty = \sqrt{\left(z_{11} + \sum_{j=2}^{\infty} z_{1j}\right) Y_{11}} \tag{30}$$

When wire spacings are greater than ten wire radii, it is reasonable to assume that z_{11} and Y_{11} will be identical with the corresponding distributed series impedance and shunt admittance for a single isolated line. Γ_∞ may therefore be expressed in terms of the propagation constant $\Gamma = \sqrt{z_{11}\, Y_{11}}$ of a single line by the equation

$$\Gamma_\infty = \Gamma \sqrt{1 + \frac{1}{z_{11}} \sum_{j=2}^{\infty} z_{1j}} \tag{31}$$

The distributed self impedance is

$$z_{11} = Z_0 \Gamma = \frac{-j\Gamma^2 \omega \mu_0 \ln \frac{b}{a}}{2\pi \epsilon_r K^2}$$

and from equation (13)

$$\sum_{j=2}^{\infty} z_{1j} = \frac{\sqrt{-j2}}{\pi \sigma b \delta H_1^{(2)}\left(\frac{\sqrt{-j2}\, b}{\delta}\right)} F\left(\frac{s}{\delta}, \frac{h}{\delta}\right) \tag{32}$$

where

$$F\left(\frac{s}{\delta}, \frac{h}{\delta}\right) = \sum_{n=1}^{\infty} H_0^{(2)}\left(\frac{ns\sqrt{-j2}}{\delta}\right) f\left(\frac{ns}{\delta} - h, h\right) \tag{33}$$

Since $H_1^{(2)}(X) \approx -j\frac{2}{\pi X}$ for $X \ll 1$ Γ_∞ may be reduced to the generalized form

$$\frac{\Gamma_\infty}{\sqrt{\epsilon_r}K} = \sqrt{\frac{\Gamma^2}{\epsilon_r K^2} + \frac{j\pi}{\ln\frac{b}{a}}F\left(\frac{s}{\delta},\frac{h}{\delta}\right)} \tag{34}$$

or, from equation (17)

$$\frac{\Gamma_\infty}{\sqrt{\epsilon_r}K} = \left[\frac{1}{\ln\frac{b}{a}}\left(0.230+\ln\frac{b}{a}\right)-1-\frac{I\left(\frac{h}{\delta}\right)}{2\ln\frac{b}{a}}+\frac{j}{2\ln\frac{b}{a}}\left(\frac{\pi}{2}+\frac{\delta_1}{a}+2\pi F\left(\frac{s}{\delta},\frac{h}{\delta}\right)\right)\right] \tag{35}$$

For this case, the "geometry loss factor" is

$$g_\infty = g_\infty\left(\frac{s}{\delta},\frac{h}{\delta},\frac{a}{\delta_1}\right) = 1+\frac{2\delta_1}{\pi a}-\frac{2}{\pi}\,\mathrm{Im}\left[I\left(\frac{h}{\delta}\right)\right]+4\,\mathrm{Re}\left[F\left(\frac{s}{\delta},\frac{h}{\delta}\right)\right] \tag{36}$$

The equation $F(s/\delta\ ,\ h/\delta\ )$ has been evaluated on a digital computer for all applicable values of s/δ and h/δ , and the results are plotted in Figure 10. Equations (35) and (36) may now be used with the previous equations or curves for efficiency and impedance for a single wire to predict the performance of each element in an antenna array. The total maximum efficiency $\mathcal{E}_T$ of the array corresponding to $\phi = 0$ will be proportional to the number of elements or

$$\mathcal{E}_T = n\mathcal{E} \tag{37}$$

where $\mathcal{E}$ is the efficiency of a single element of the array determined from Γ_∞ and g_∞.

Where previously the pattern of the array was f (Ø)/f(0), corresponding closely to cos Ø pattern, it will now be[9]

$$\frac{f(\phi)}{f(0)} \frac{\sin\left(\frac{nKS\cos\phi}{2}\right)}{n\sin\left(\frac{KS\cos\phi}{2}\right)} \qquad (38)$$

III. EXPERIMENTAL RESULTS FROM MODEL ANTENNAS

Most of the model experimental measurements were made on standard RG 58 coaxial cable with the outer shield removed. The wires were allowed to protrude through a ground image plane into a 10'x6'x2' tank containing a salt solution. Current distribution measurements were made by energizing the wires with a signal at the desired frequency while a small current measuring loop connected to a receiver was moved along the wires. The maximum to minimum current ratio and the position of the minimum was used to determine the wire propagation constants from standard transmission line equations. The impedances of single wires were measured directly at the ground plane feed through point with a bridge. The input impedance of wires in an array was measured by joining all wires at a common point with equal length coaxial cables. The impedance of each wire was calculated from the resultant measurement at the common point, taking account of the line lengths and number of wires. Model antenna efficiencies measured at a salt water site on Puget Sound agreed well with theory. Rather than include model efficiency measurements in this paper, data is presented in part V on the efficiency of a full scale antenna buried in the earth.

Figures 11a and 11b show a comparison between measured and theoretical propagation constants for typical model antennas as a function of loss tangent. The data shown in the first figure was a result of varying frequency while that of the second was a result of varying conductivity of the surrounding medium. Figure 12 shows the measured current distribution for the elements of a large array with spacings greater than a skin depth while Figure 13 shows the same data for spacings less than a skin depth. Note that the distributions for the former case are identical except for the edge wire while that for the latter case vary with the position of each wire. Figure 14 shows a comparison between the values of propagation constant computed from the current distribution for large spacings and that computed from theory for the infinite array. Figure 15 shows data for the same case with depth as a variable parameter. This data, taken for array widths 20 to 50 skin depths wide, supports quite well the use of the infinite array mutual coupling expressions for finite width arrays. Figure 16 shows a comparison between measured and theoretical input impedance versus ℓ/λ_c for a typical model buried antenna, and Figure 17 shows the impedance comparison for a large array as a function of spacing.

IV. DESIGN CONSIDERATIONS

1. Antenna Wire Size

The theoretical expressions and curves discussed in the previous section may be used to optimize the design of either a single element or multi-element buried antenna. First considering a single element buried antenna very close to the surface such that $g = 1$, an examination of the efficiency

curves in Figure 7 show that antenna efficiency is not dependent on β/k for small antenna lengths, but becomes increasingly dependent on the parameter as length increases. Computations not included in this paper show that this is equally true for the parameter α/β. It is also true that the magnitude of the maxima of the efficiency curves increase markedly with decreasing β/k, but very slowly with decreasing α/β. This would seem to indicate that the most ideal situation would be an antenna wire with β/k equal to or nearly equal to unity. The propagation constant curves in Figure 4, however, show that the insulation wire required for this situation would have to be excessively thick and have a dielectric constant near unity. If such a wire were available, one could obtain the maximum possible efficiency for a single wire antenna. Examination of the curves will reveal, however, that this situation does not correspond to an efficient use of wire since greater efficiencies per unit length are obtainable with shorter lengths of wire with higher values of β/k.

For many multi-element array designs, the higher value of efficiency per unit length of wire is more desirable than maximum efficiency obtained from optimum lengths corresponding to a low value of β/k. Ideal wire for this application is standard types of coaxial cable such as RG 8 and RG 17, with the outer shield removed. The center conductor size should be of sufficient size to keep the loss down (negligible effect from the a/δ_1 in the expressions for $\frac{\Gamma}{\sqrt{\epsilon_r}k}$ and g).

2. Antenna Length and Termination

The antenna efficiency follows a series of maxima and minima when plotted as a function of length. The first maximum for

$\phi = 0°$ is of greatest importance since it corresponds to the maximum attainable efficiency for the cos ϕ type pattern. Although greater efficiencies are possible with longer antennas, the patterns become multi-lobed, and the efficiency per unit length of antenna is greatly reduced. We will therefore restrict our attention to antenna lengths not exceeding the value required to give the first maximum of the efficiency.

The open-ended antenna is superior from a standpoint of gaining maximum efficiency for a given β/k while the efficiency and efficiency per unit length of the shorted antenna is greater than the open-ended antenna for short lengths up to the first maximum of the shorted antenna. A major disadvantage of the latter is the necessity of using grounding or shorting rods which must be 0.5 to 1 skin depths in length. Also, converging currents of large magnitude would produce additional losses at location of the rods and, in addition, the effectiveness of the shorting rods is susceptible to changing ground parameters, corrosion and other unpredictable factors. From a standpoint of efficiency, therefore, it appears that the open-ended antenna is superior. For certain applications, however, the antenna with shorted ends may be preferred from an impedance standpoint.

The impedance curves in Figures 5 and 6 indicate that the magnitude of the antenna $Q = X_{in}/R_{in}$ increases without limit for the open antenna as the length becomes increasingly small. On the other hand, the Q of the shorted antenna approaches 11.4 for the typical case of $\alpha/\beta = 0.05$ as the length decreases. When the Q of the open antenna becomes excessive, it cannot

be matched properly to a source or load without loss in the matching network.

From an impedance standpoint, therefore, the shorted antenna is preferable for short antenna lengths where the Q of the open antenna is excessively high. For most transmitting antennas, one does not run into this problem since long lengths are required to obtain the necessary efficiency. But, for receiving antennas where required efficiencies and lengths are much less, the shorted antennas are more efficient due to the lower Q, provided effective grounding can be obtained.

3. Burial of Antenna Wire

The antenna should be buried at a depth sufficiently large to provide the desired degree of hardening. The efficiency will deteriorate with depth, h, by the amount of $e^{-2h/\delta}$. The efficiency will also be reduced by the increase in "geometry loss factor" g, due to depth. The function g reaches a maximum at 0.3 skin depths. For greater depths, it will decrease reaching a minimum for depths greater than 1.6 .

4. Antenna Arrays

Substantial improvements in antenna efficiency may be obtained by arraying a group of parallel wires. The use of wire spacings of several skin depths will eliminate mutual coupling and allow an increase in efficiency proportional to the number of elements n. Since $\delta << \lambda$, a great number of elements may be arrayed without changing the cos ϕ pattern characteristic of a single element. Antenna arrays may be optimized

according to two different criteria, the first making the most efficient use of a fixed ground area and the other making the most efficient use of a fixed length of wire or number of elements n. Considering the first case, we note that

$$\mathcal{E} \sim \frac{n}{g(s/\delta)} = \frac{\delta/s\, W}{g(s/\delta)}$$

where W = the allowed width of the array in skin depths and s is the element spacing which must be optimized. Figure 18 shows a plot of the relative values of $\frac{\delta/s}{g(s/\delta)}$ in db versus s/δ for the model antenna characteristics given in Figure 18. Note that $\frac{\delta/s}{g(s/\delta)}$ increases to a constant value for element spacings less than 1.5 skin depths. This signifies that element saturation is reached for this spacing, and no further increase in efficiency can be obtained by adding more elements. This corresponds to the case where the fixed area is covered with a current sheet uniform in magnitude in a direction lateral to the elements. For the other case with a fixed number of elements and no restriction on area

$$\mathcal{E} \sim \frac{1}{g(s/\delta)}$$

A plot of the relative values of $1/g(s/\delta)$ for the same antenna characteristics is also given in Figure 18. One may note for this case that maximum efficiency is obtained only for spacings greater than ten skin depths, but the efficiency is only 0.7 db less than ideal for spacings of 3 skin depths. There is nearly 3 db degradation in efficiency, however, for the 1.5 skin depth spacing that was ideal for the previous case. In practical cases, however, both area and number of elements must be taken into account. A good compromise

appears to be a spacing of 3.0 skin depths which results in a -0.7 db degradation from maximum efficiency obtainable from either a fixed number of elements or a fixed area. In theory, the array efficiency may be made to increase indefinitely as width increases. In practice, however, as array width increases, feed problems become more complex with greater feed line losses, and the resultant antenna pattern would narrow. As an example, consider the case where an omnidirectional coverage is obtained by feeding two arrays of n elements each in space quadrature and fed 90° out of phase. Since the field strength of each array for a constant input power is proportional to

$$\frac{\sin\left(\frac{nsk\cos\theta}{2}\right)}{\sqrt{n}\ \sin\left(\frac{sk\cos\theta}{2}\right)}$$

the maximum field strength at $\phi = 0°$, 90°, 180° and 270° is proportional to $\sqrt{n}$. The field strength corresponding to $\phi = 45°$, 135°, 225° and 315° on the other hand is proportional to

$$\frac{\sin\left(\frac{nsk\sqrt{2}}{4}\right)}{\sqrt{n}\ \sin\left(\frac{sk\sqrt{2}}{4}\right)}$$

which is maximized for an array width of $ns \approx 0.525\lambda$. Thus, for the omnidirectional coverage, the width of each array must be limited to 0.525λ due to pattern characteristics. A wide variety of pattern shapes are obtainable by varying the number of elements of one array with respect to another. It can be shown that the greatest efficiency is obtained by feeding all elements with currents of equal magnitude.

The following is a summary of how the theoretical data of the previous section may be used for optimizing and predicting the performance of an antenna array design.

1. Determine the geometry loss factor g from equation (36) versus s/δ using the given wire and ground characteristics b/a, b/δ, a/δ_1, h/δ and ϵ_r. The required values of $I(h/\delta)$ and $F(s/\delta, h/\delta)$ are obtained from Figures 3 and 10 respectively.

2. Establish the optimum spacing for the best compromise between optimum efficiency per unit area and per foot of wire.

3. Determine the values of α/β and β/k for this spacing from equation (35).

4. Use the efficiency curves in Figure 7 for determining the optimum antenna length for maximum efficiency and the efficiency $\mathcal{E}$ per element.

5. Use the impedance curves in Figure 5 for determining the input impedance to each element. The length of the elements may also be chosen on the basis of obtaining desirable impedance characteristics by choosing lengths that are less than those obtained in step 4.

6. The desired total efficiency $\mathcal{E}_T$ will be determined by the number of elements n by the relation

$$\mathcal{E}_T = n\mathcal{E}$$

7. The antenna array pattern is determined from the expression

$$\frac{f(\phi)}{f(0)} \frac{1}{n} \frac{\sin\left(\frac{nsk\cos\phi}{2}\right)}{\sin\left(\frac{sk\cos\phi}{2}\right)}$$

V. FULL SCALE ANTENNA ARRAY

Several full scale antenna arrays were tested in the earth at various test sites near Kansas City, Missouri. The arrays included cases where lengths were based on obtaining maximum efficiency and cases where lengths were less than ideal in order to obtain different impedance characteristics. In all cases, good agreement between measured and theoretical parameters were obtained. The measured results of a typical 8x8 element omnidirectional array shown in the construction stage in Figure 19 agreed well with theory. The antenna had the following parameters:

Wire type - RG/8 with outer conductor removed

b = 0.1425" b/a = 3.68 ϵ_r = 2.25

Element length, ℓ = 660 feet

Element spacing, s = 76 feet (s/δ = 4.15)

Burial depth, h = 4 feet

Soil Conductivity, σ = 0.04 mhos/meter

Frequency, f = 180 kc

Array type - Two arrays buried in space quadrature consisting of 8 elements and fed 90° out of phase to give omnidirectional coverage.

Theoretical Data

Propagation Properties (assuming mutual coupling effects)

β/k = 3.87 and α/β = 0.0626

$g(h/\delta , s/\delta , a/\delta_1)$ = 1.38

Theoretical efficiency of array $\mathcal{E}$ = -36.5 db

Measured efficiency $\mathcal{E}$ = -35.6 db

Figure 20 shows a comparison between theoretical and measured impedances of a single element of the antenna versus frequency. The slight differences in impedance are assumed to be due to the slight mutual coupling which would be difficult to predict for the case of the measured element adjacent to non-energized elements.

Figure 21 shows a comparison between theoretical and measured values of field strength for the antenna versus distance. The experimental data results from measurements taken at different times with various field strength instruments in different radial directions from the antenna. The antenna patterns shown in Figures 22, 23 and 24 agree with the shapes expected from the theory.

VI. CONCLUSIONS

The use of arrays of long insulated wires provides a simple method of maximizing the efficiency of a completely buried "hard" antenna in terms of either optimum utilization of a given area of earth or a given total length of buried wire. Experimental data verifies that the ground wave field expression for the infinitesimal buried horizontal dipole may be applied through integration to specify the field due to a long wire insulated antenna. Experimental data also verifies that the dominant TM mode equations provide a reliable and simple means of predicting the impedance properties of either single or multiple element buried antenna arrays consisting of insulated dipoles buried in a conducting homogeneous earth. The theoretical data has been presented in a generalized form that allows a straightforward method of facilitating the design of optimum buried antenna arrays.

For more detailed information on past and recent work on buried antennas, including other type configurations, the reader is referred to a paper by R. C. Hansen[10] which contains an excellent survey and a complete list of referneces on the subject.

REFERENCES

1. A. W. Guy and G. Hasserjian, "Design Criteria for Buried Antennas", Document D2-7760, The Boeing Company, 1961.

2. A. W. Guy, "Experimental Data on Buried Antennas", Document D2-90051, The Boeing Company, 1961.

3. T. L. Johnson, "Phase I Final Engineering Report, Minuteman Confidence Test Program - Antennas, LCC-1", Document D2-12070, The Boeing Company.

4. K. A. Norton, "The Propagation of Radio Waves Over the Earth in the Upper Atmosphere", Part I, Proceedings of the IRE, Volume 24, pp 1367-1387, October, 1936.

5. K. A. Norton, "The Propagation of Radio Waves Over the Surface of the Earth and in the Upper Atmosphere". Part II Proceedings of the IRE, Volume 25, pp 1203-1238, September, 1937.

6. K. A. Norton, "The Physicsl Reality of Space and Surface Waves in the Radiation Field of Radio Antennas", Proceedings of the IRE, Volume 25, pp 1192-1202, September, 1937.

7. J. R. Wait, "The Electromagnetic Fields of a Horizontal Dipole in the Presence of a Conducting Half-Space", Canadian Journal of Physics, Volume 39, 1961, pp 1017-1028.

8. J. A. Stratton, "Electromagnetic Theory", McGraw-Hill Book Co., 1941.

9. J. C. Jordan, "Electromagnetic Waves and Radiating Systems", Prentice-Hall, Inc., 1950.

10. R. C. Hansen, "Radiation and Reception With Buried and Submerged Antennas", Paper presented at the URSI Symposium on Electromagnetic Theory and Antennas, 25-30 June, 1962, Copenhagen, Denmark.

(X,Y,0) = AIR-EARTH INTERFACE

(X,Y,Z > 0) = AIR

(X,Y,Z < 0) = EARTH, THE CONDUCTIVE MEDIUM

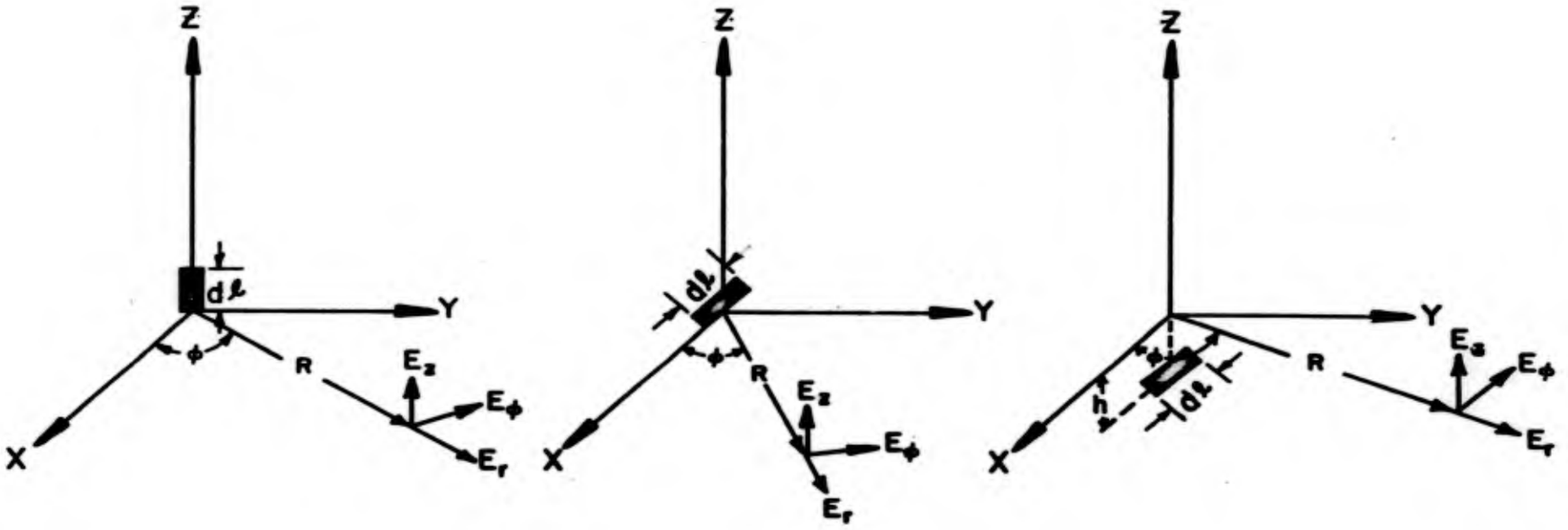

FIG. 1 VARIOUS ORIENTATION OF SMALL ELECTRIC DIPOLES

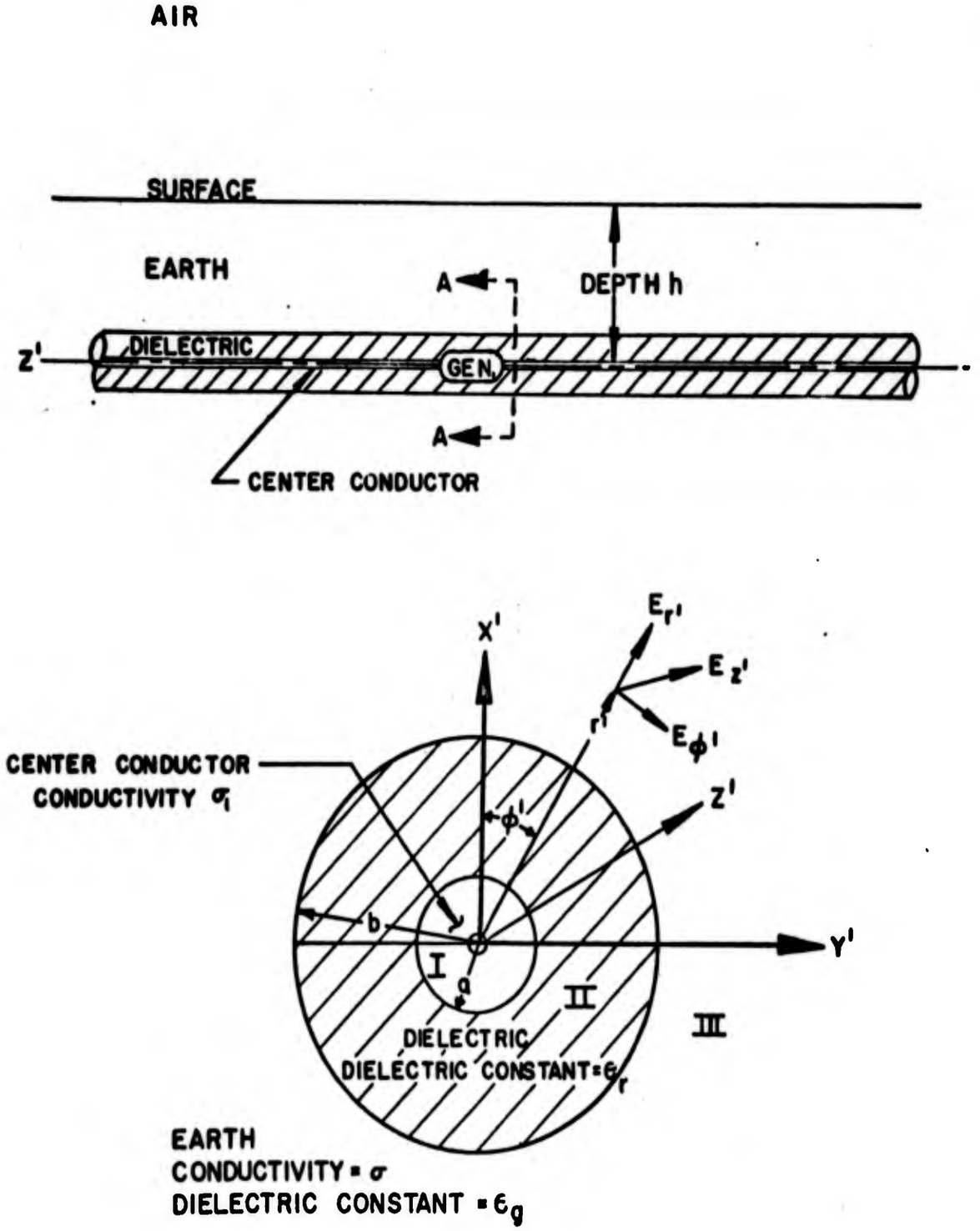

FIG. 2 THE BURIED INSULATED ANTENNA AND ITS COORDINATE SYSTEM FOR THE DERIVATION OF LOCAL FIELDS.

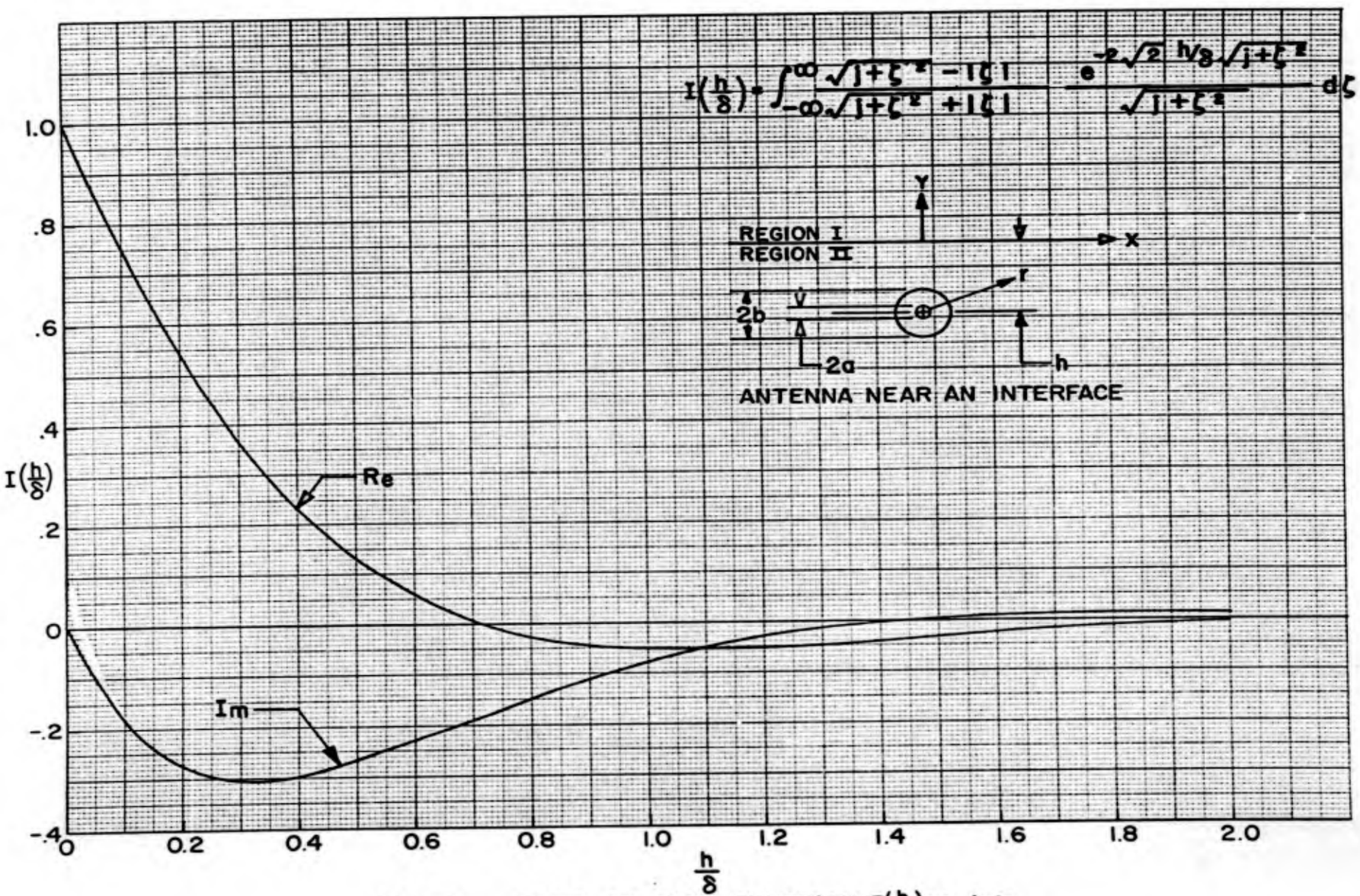

FIG. 3 PLOT OF THE FUNCTION $I\left(\frac{h}{\delta}\right)$ vs h/δ

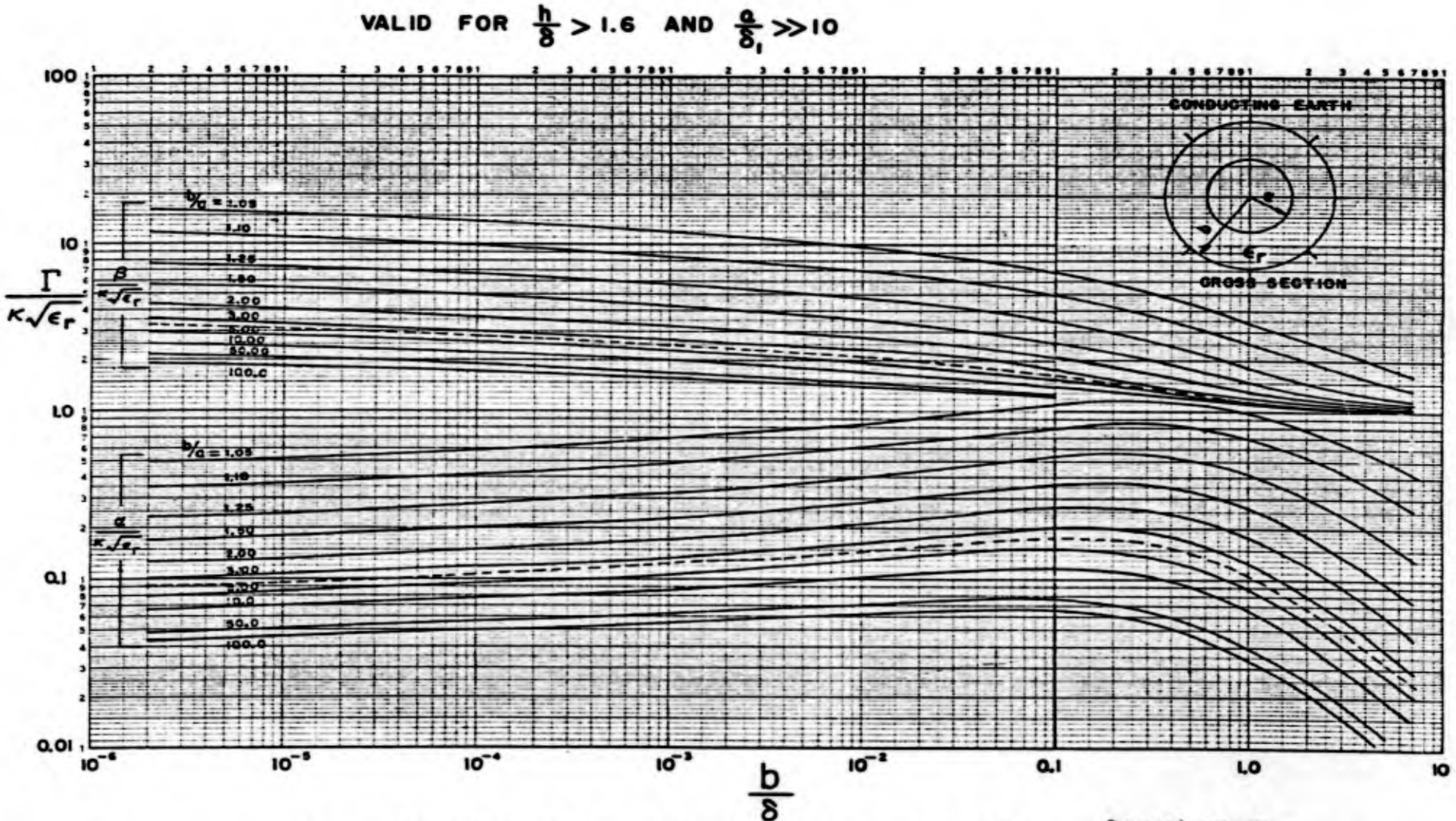

FIG. 4 PROPAGATION CONSTANT ($\Gamma = \alpha + j\beta$)

δ = SKIN DEPTH
ϵ = DIELECTRIC CONSTANT

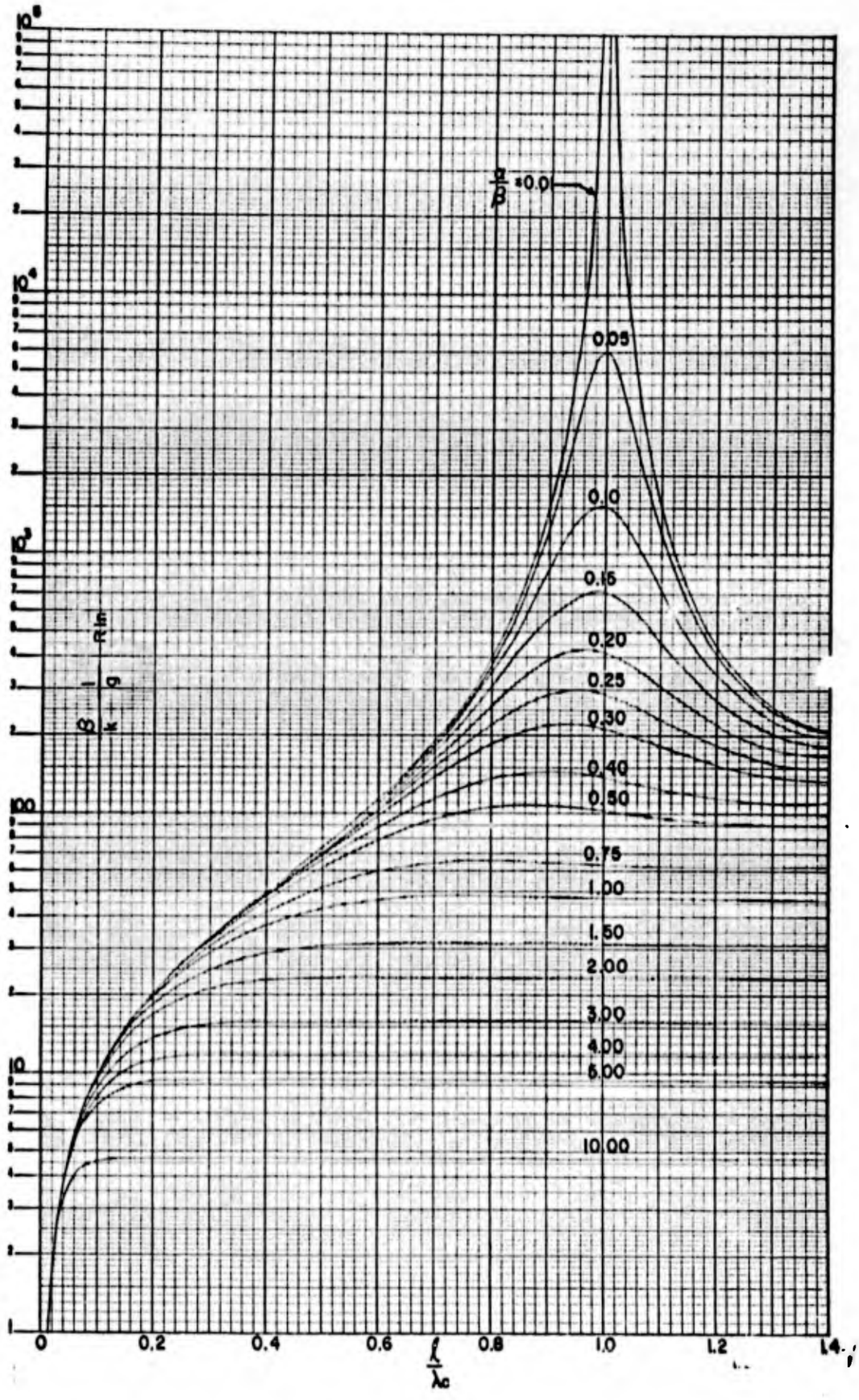

FIG. 5a RESISTANCE OF AN ANTENNA WITH OPEN ENDS

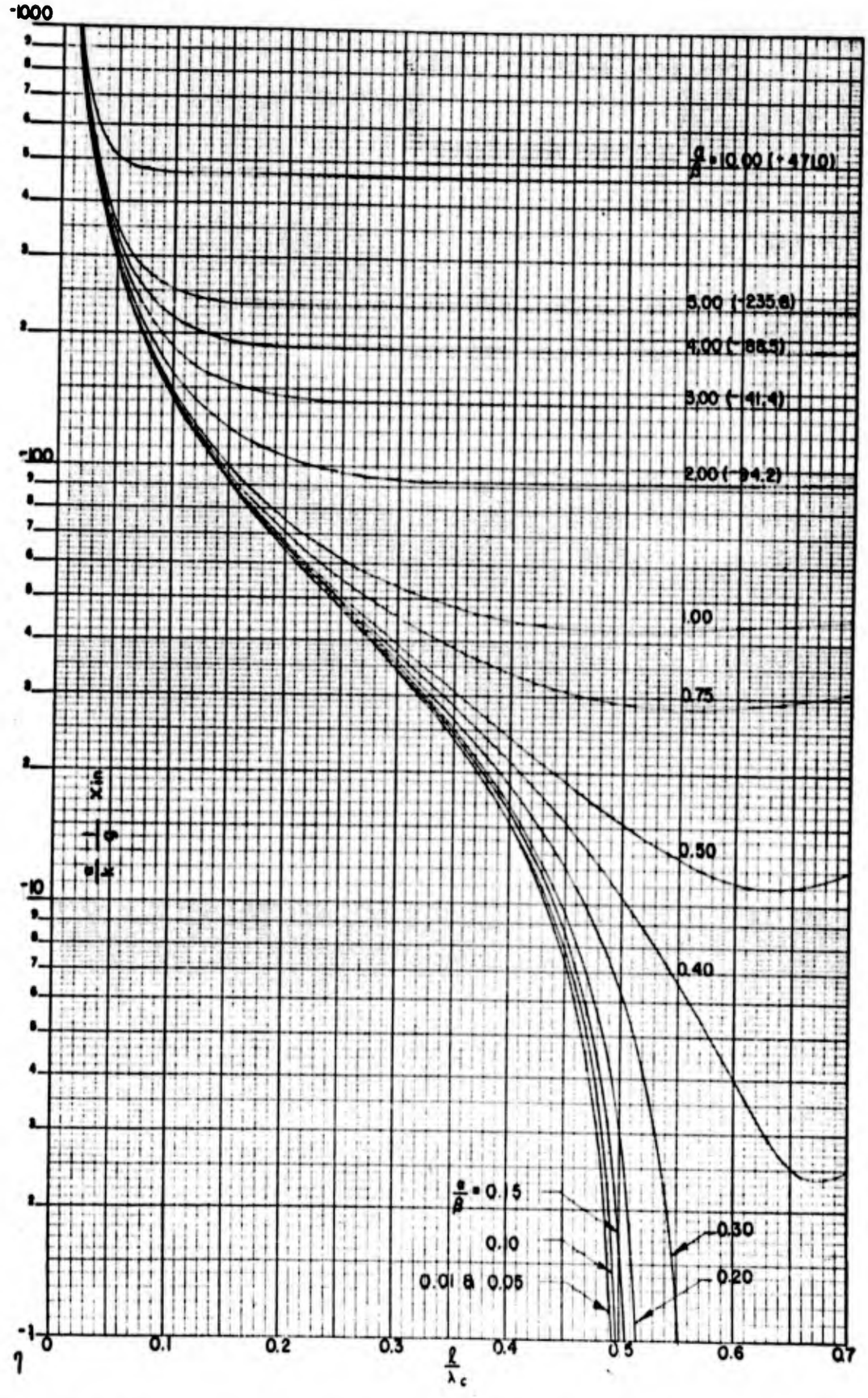

FIG. 5b REACTANCE OF AN ANTENNA WITH OPEN ENDS

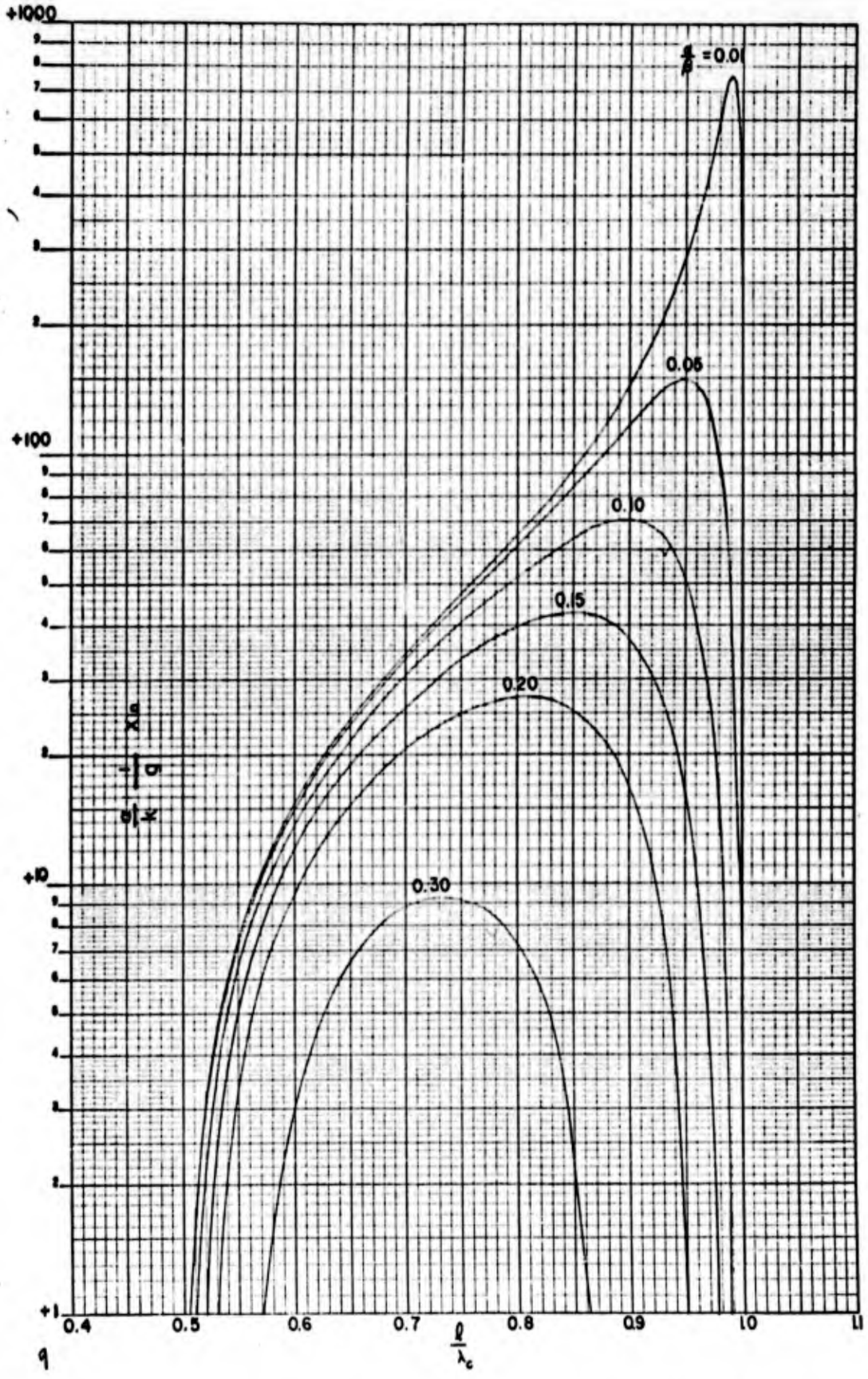

FIG. 5c REACTANCE OF AN ANTENNA WITH OPEN ENDS

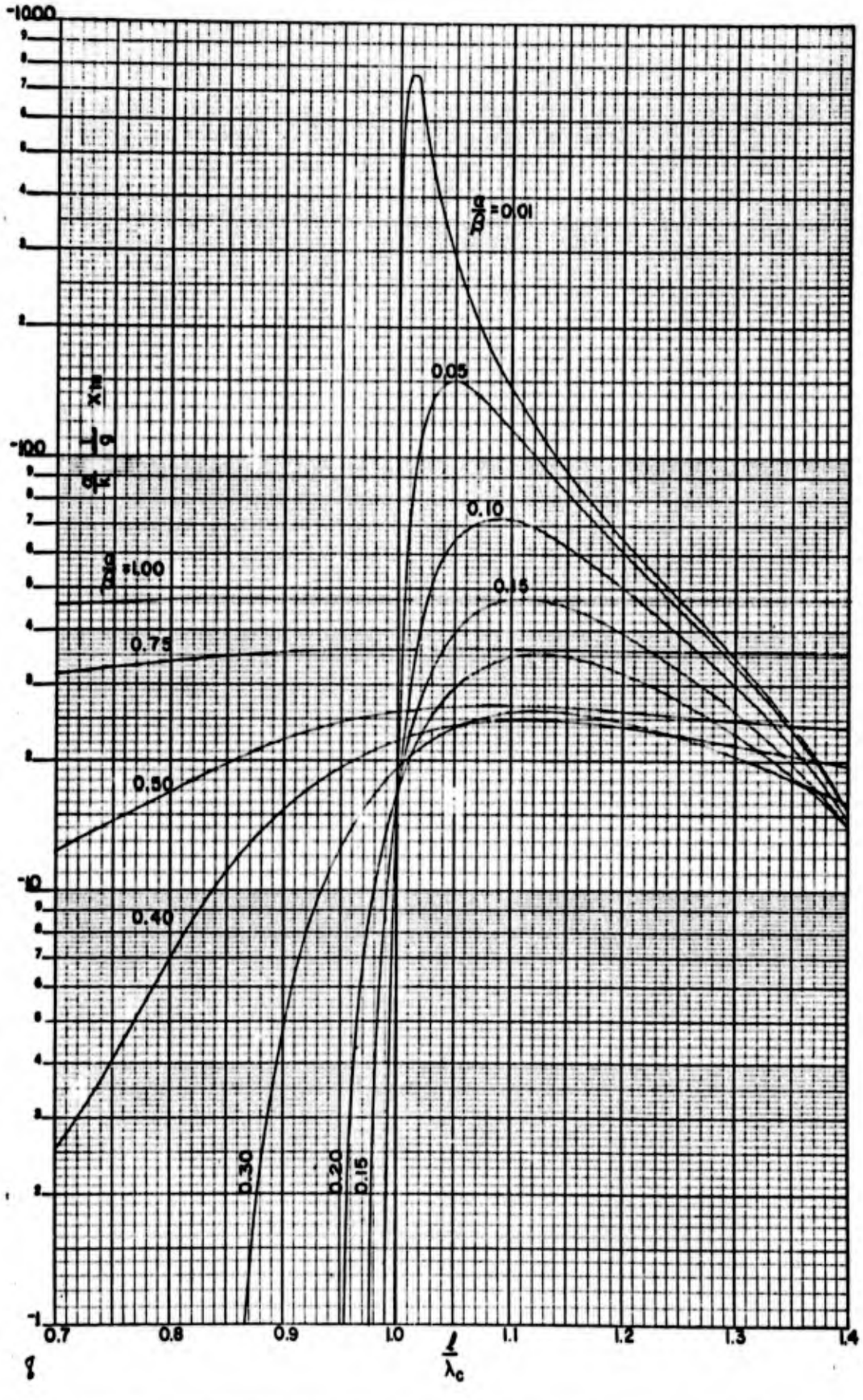

FIG. 5d REACTANCE OF AN ANTENNA WITH OPEN ENDS

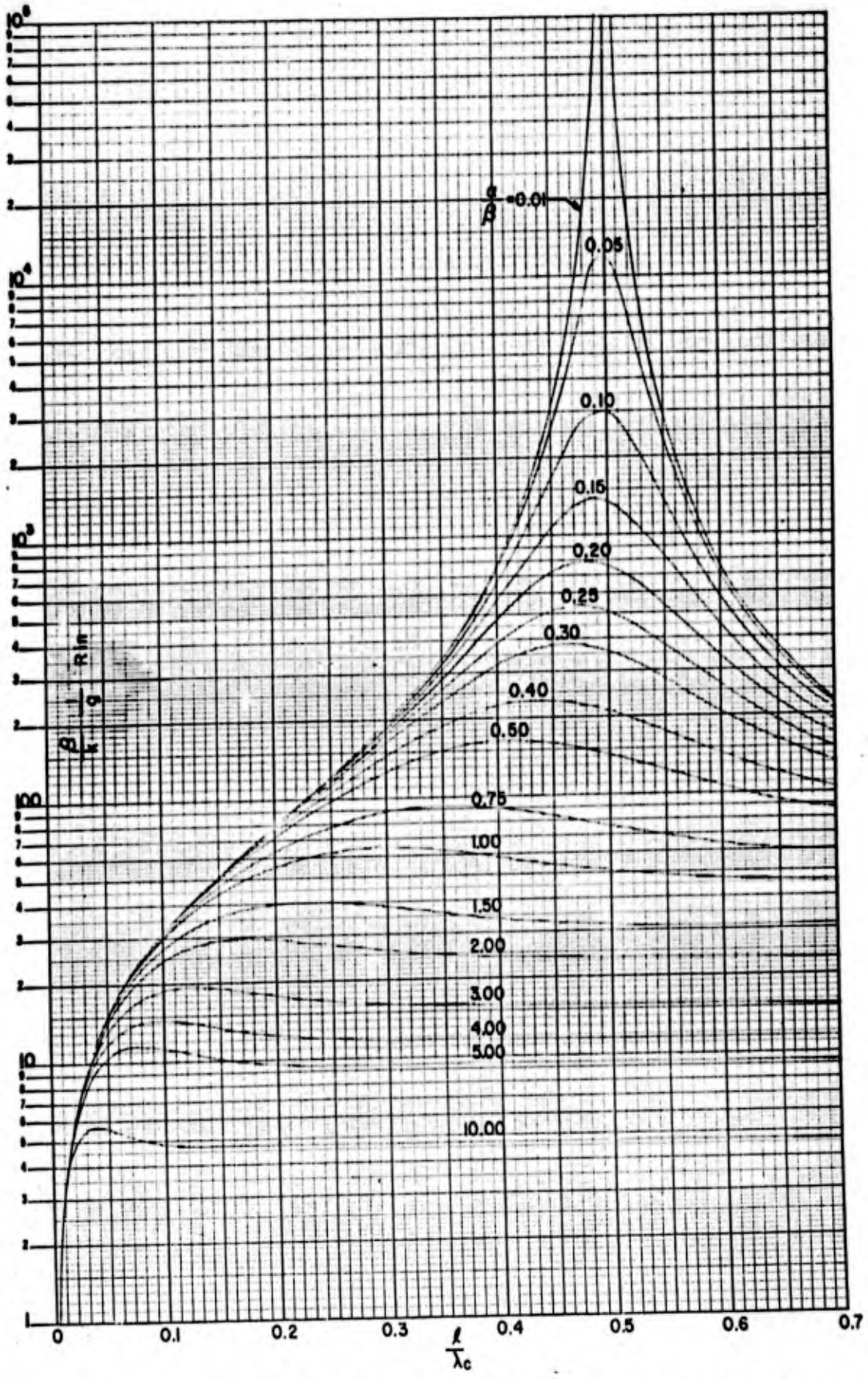

FIG. 6a RESISTANCE OF AN ANTENNA WITH SHORTED ENDS

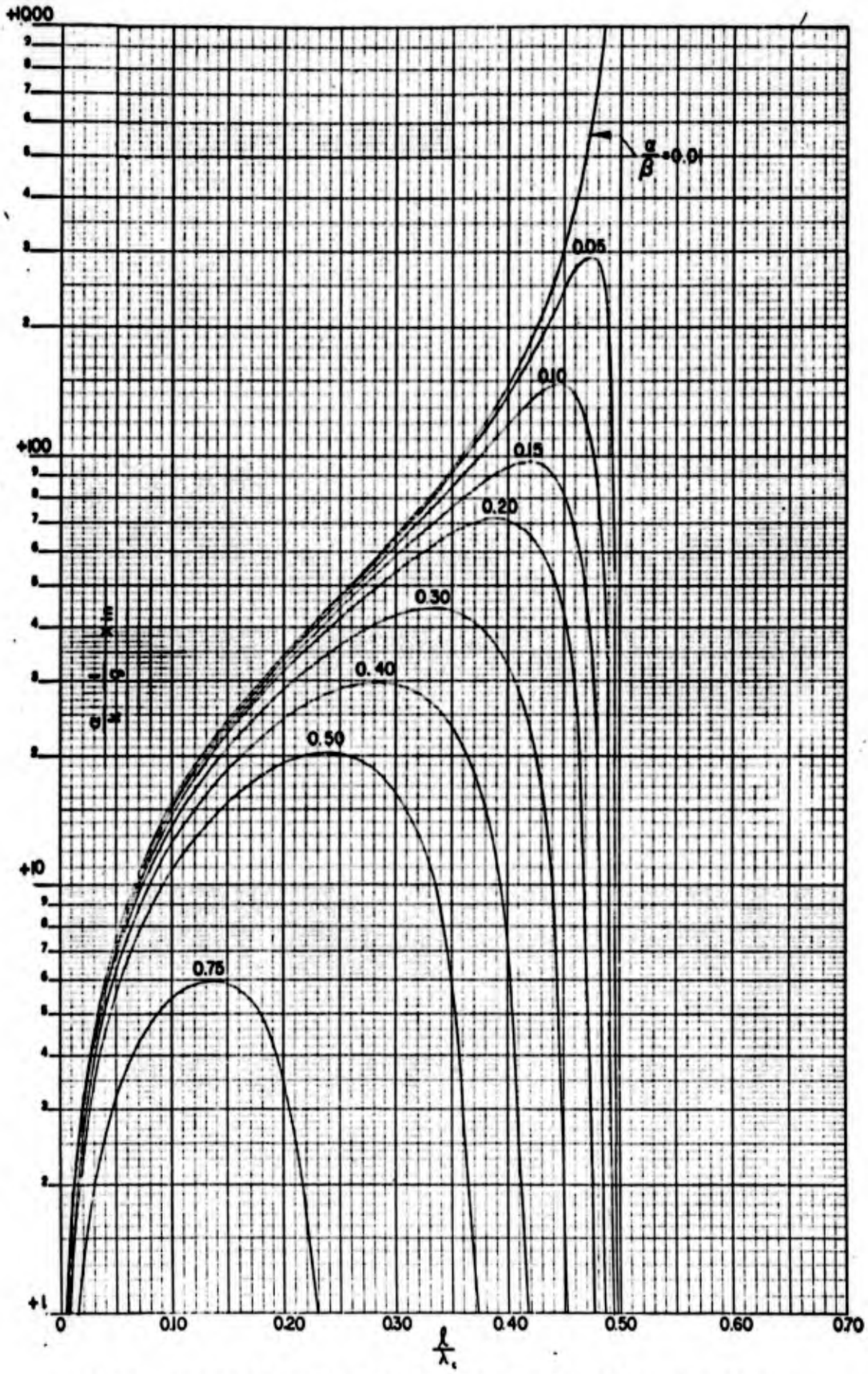

FIG. 6b REACTANCE OF AN ANTENNA WITH SHORTED ENDS

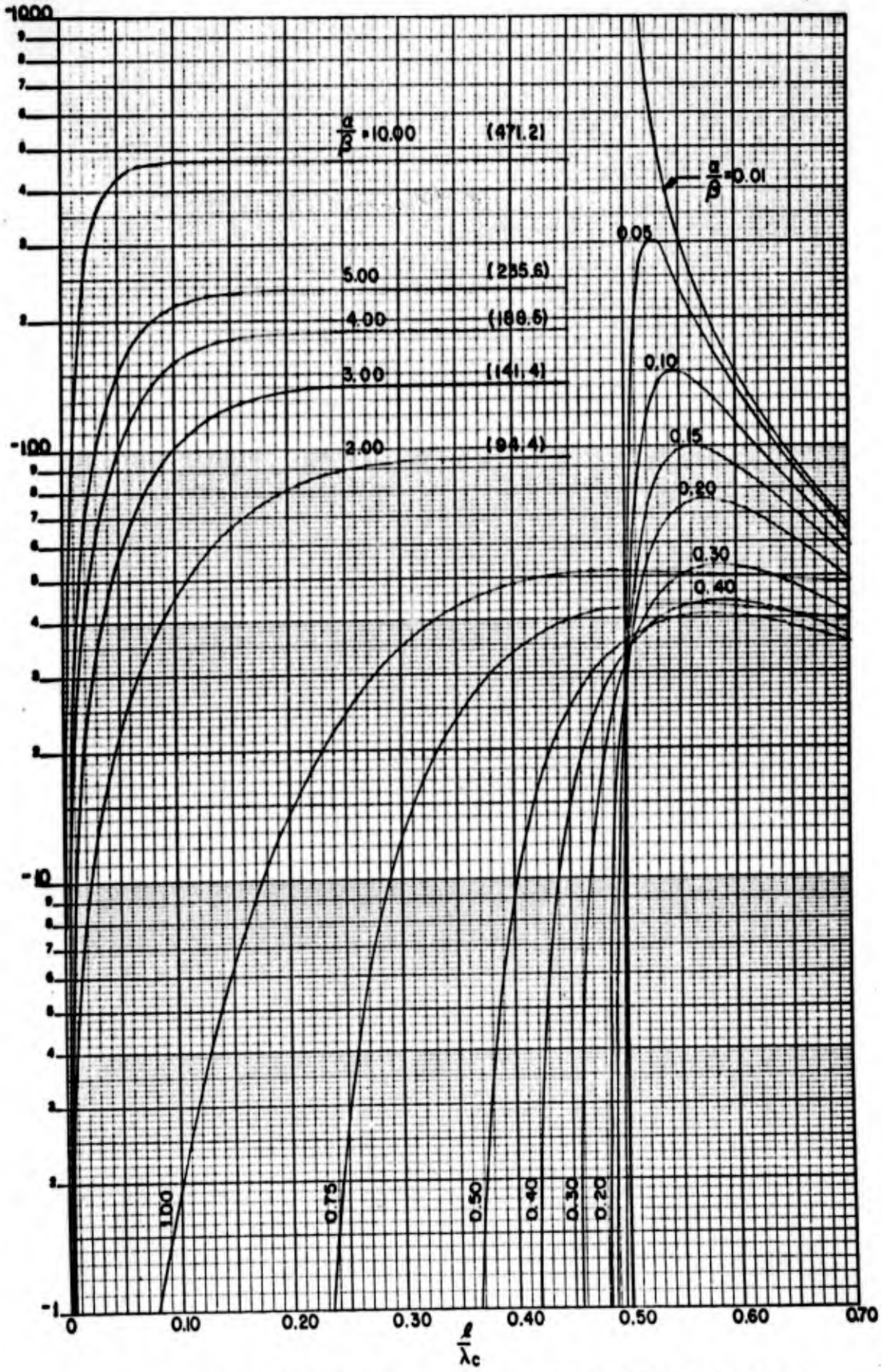

FIG. 6c REACTANCE OF AN ANTENNA WITH SHORTED ENDS

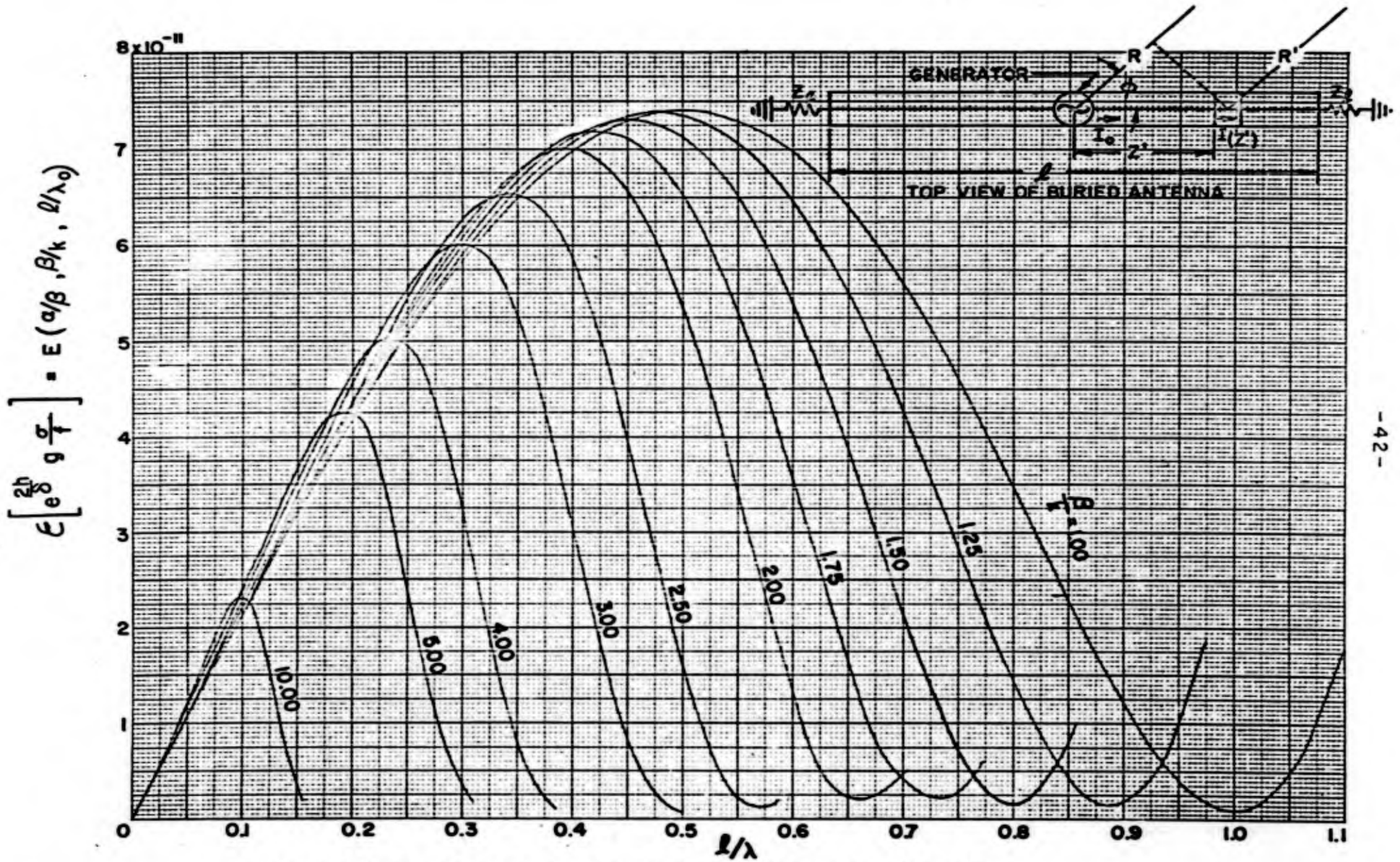

FIG. 7 ANTENNA WITH OPEN ENDS $\phi = 0°$; $\alpha/\beta = .05$

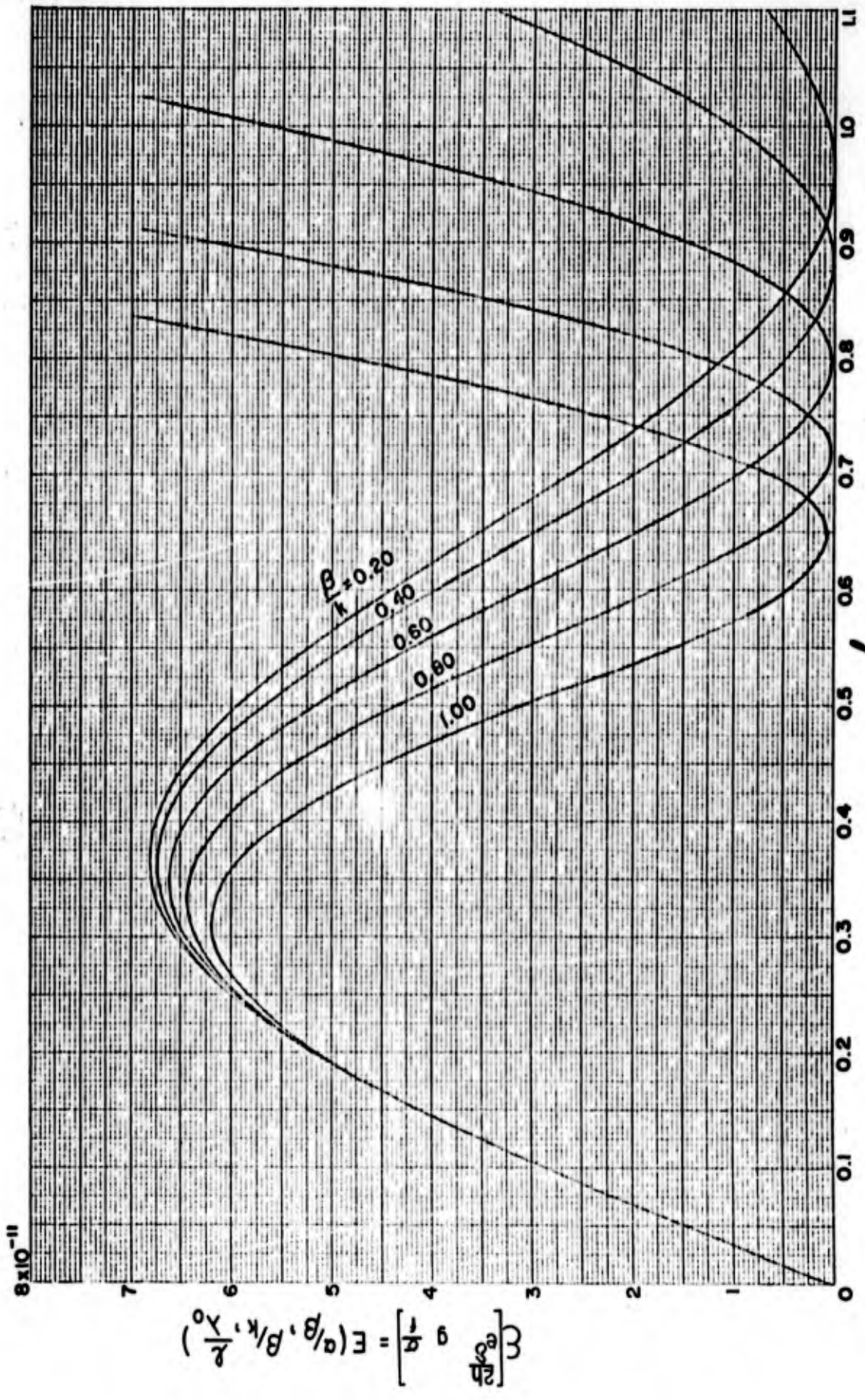

FIG. 8 ANTENNA WITH SHORTED ENDS $\phi = 0°$, $\frac{\alpha}{\beta} = .05$

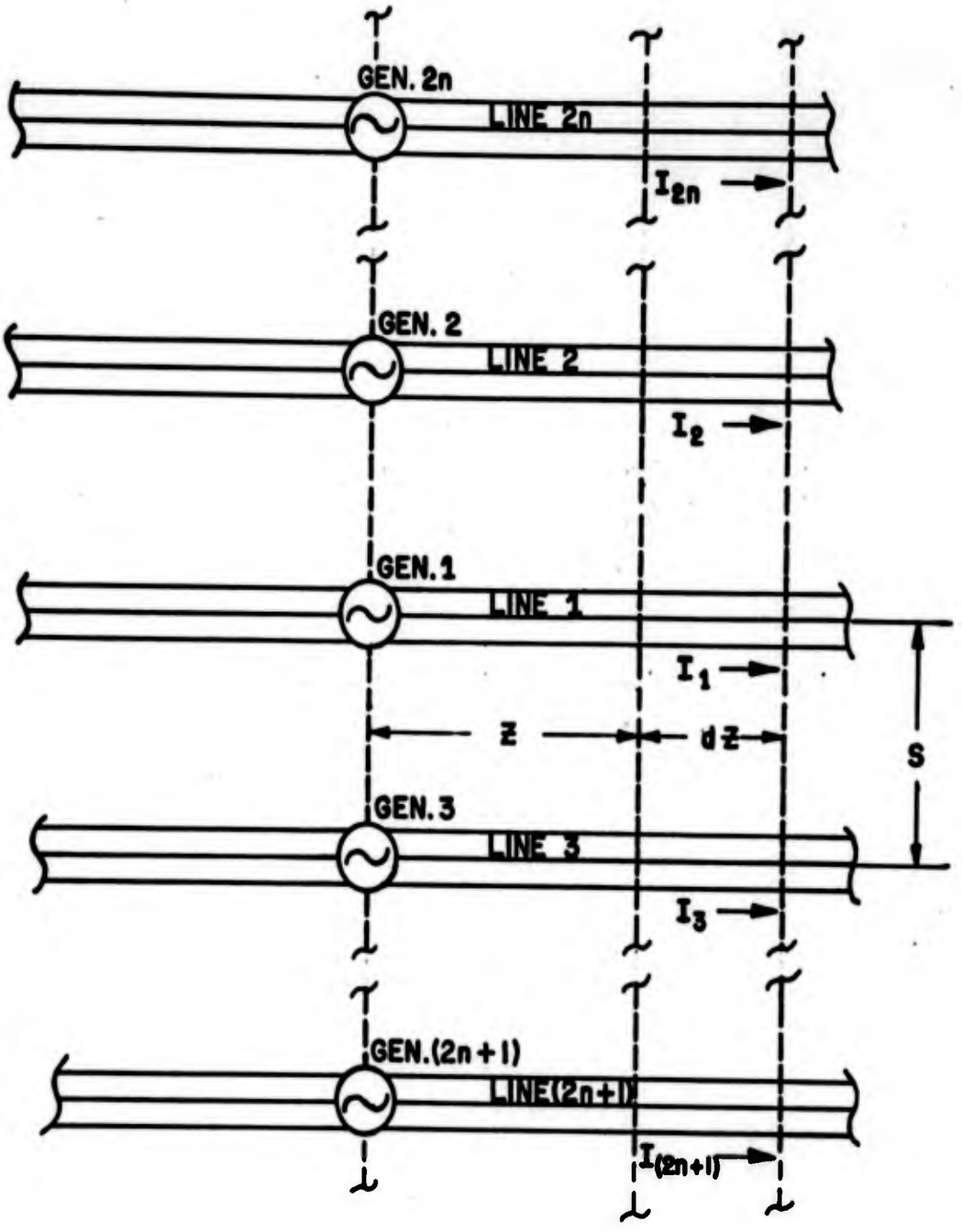

FIG. 9 MUTUAL COUPLING BETWEEN AN INFINITE ARRAY OF BURIED ANTENNAS

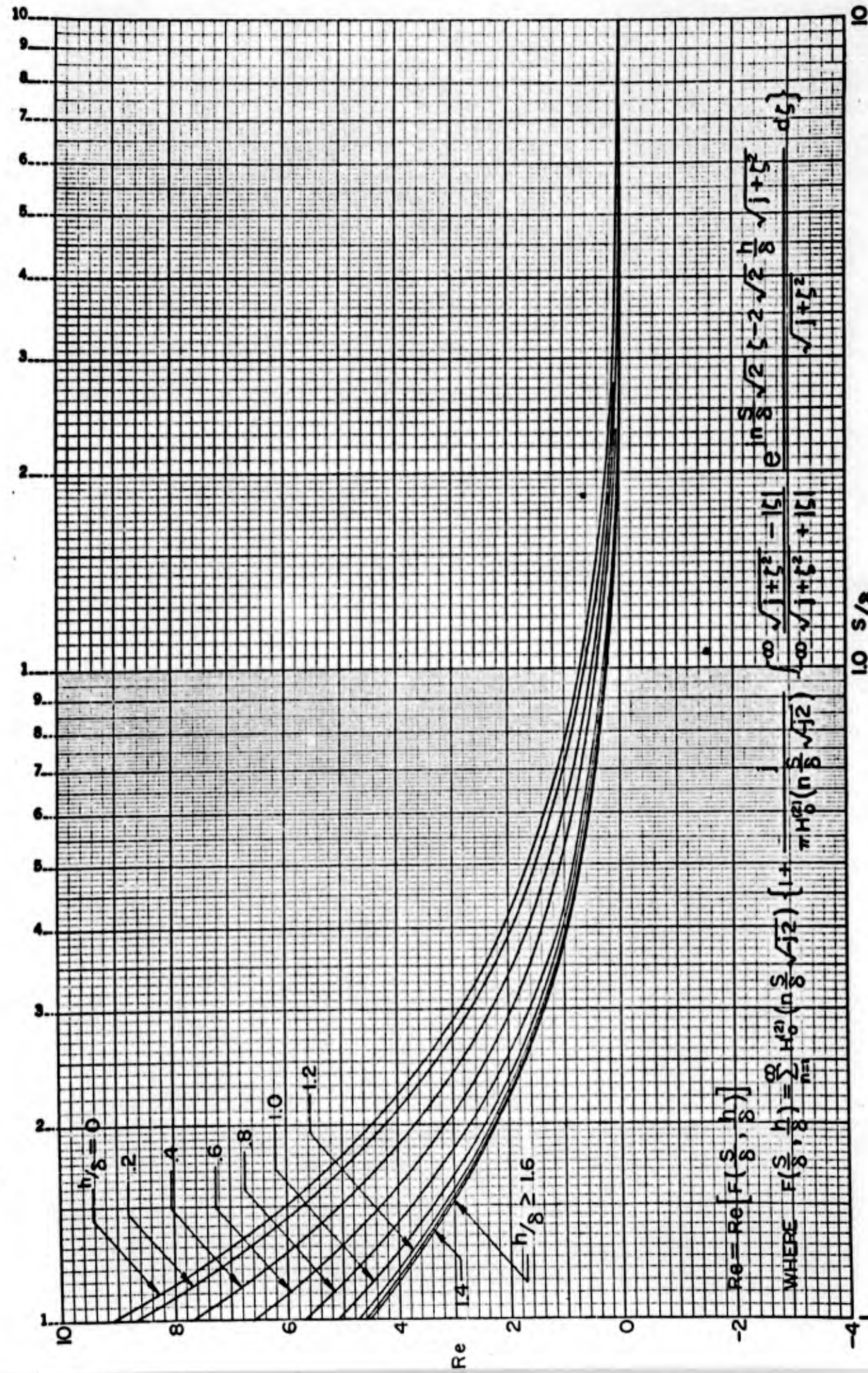

FIG. 10a Re $F(\frac{s}{\delta}, \frac{h}{\delta})$ vs. $\frac{s}{\delta}$

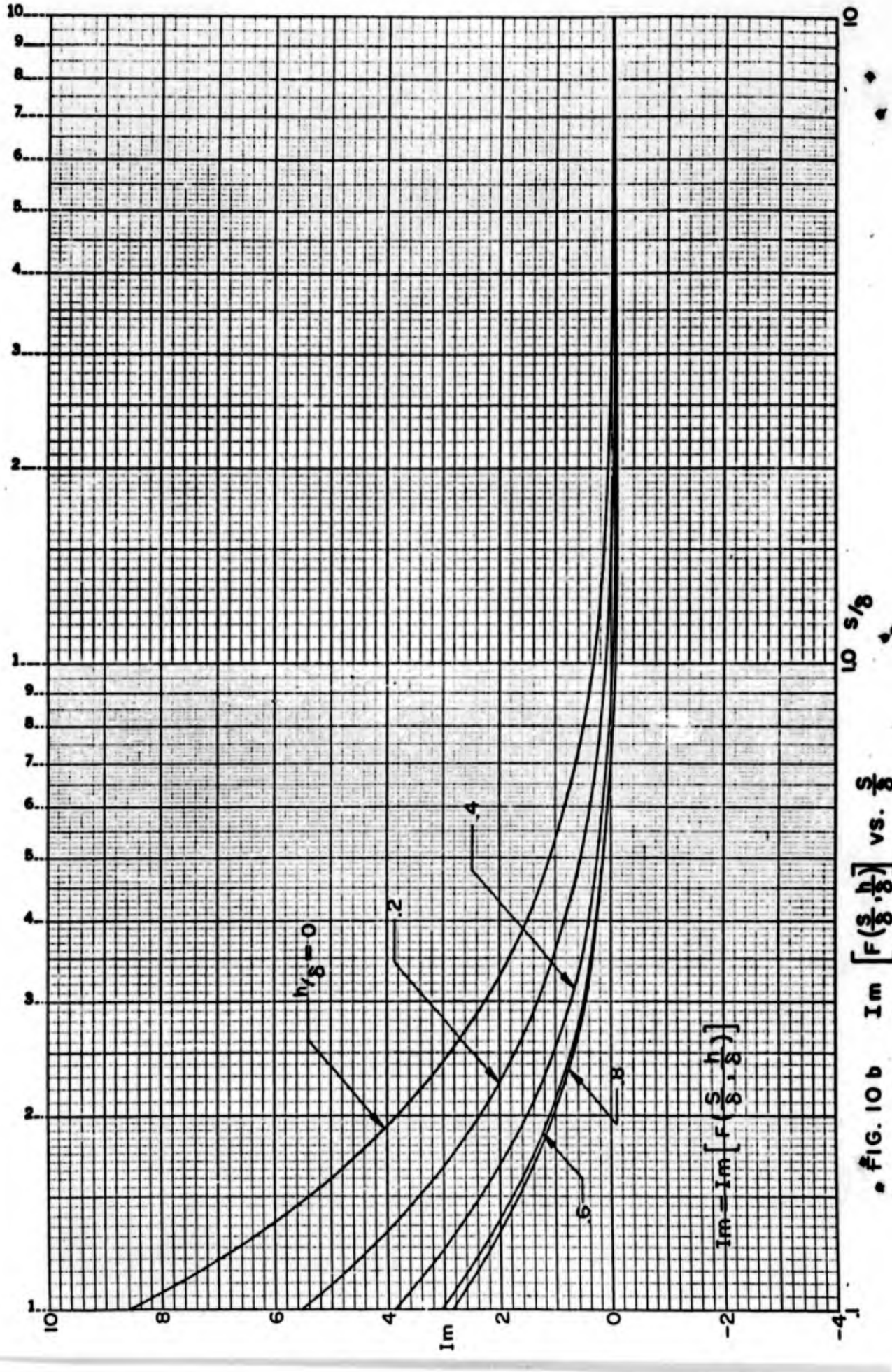

FIG. 10 b Im $\left[F\left(\frac{S}{\delta}, \frac{h}{\delta}\right)\right]$ vs. $\frac{S}{\delta}$

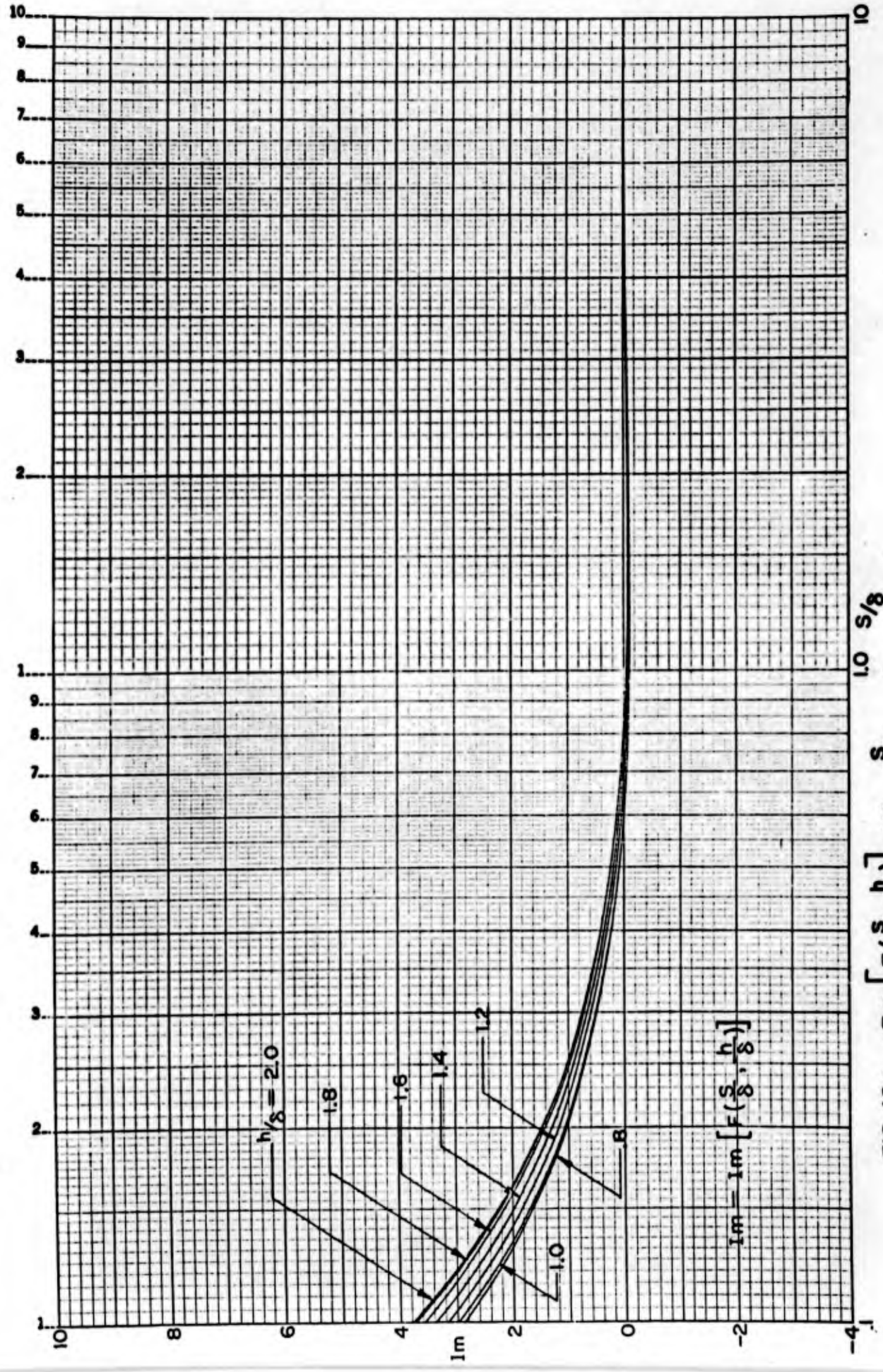

FIG. 10c $\mathrm{Im}\left[F\left(\frac{S}{\delta}, \frac{h}{\delta}\right)\right]$ vs. $\frac{S}{\delta}$

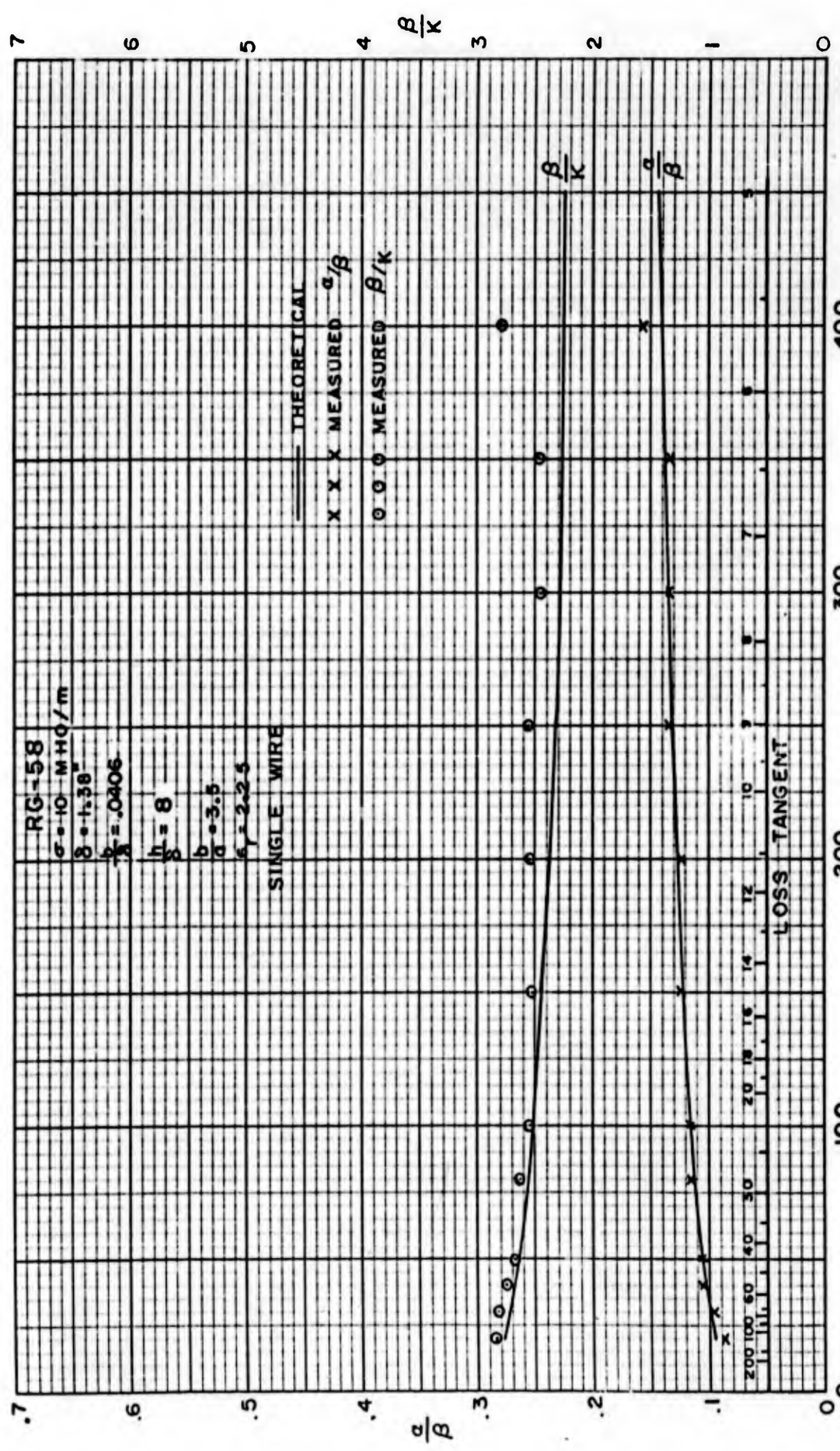

FIG. 11a. PROPAGATION CONSTANT VS. FREQUENCY FOR SINGLE WIRE AT LARGE DEPTH

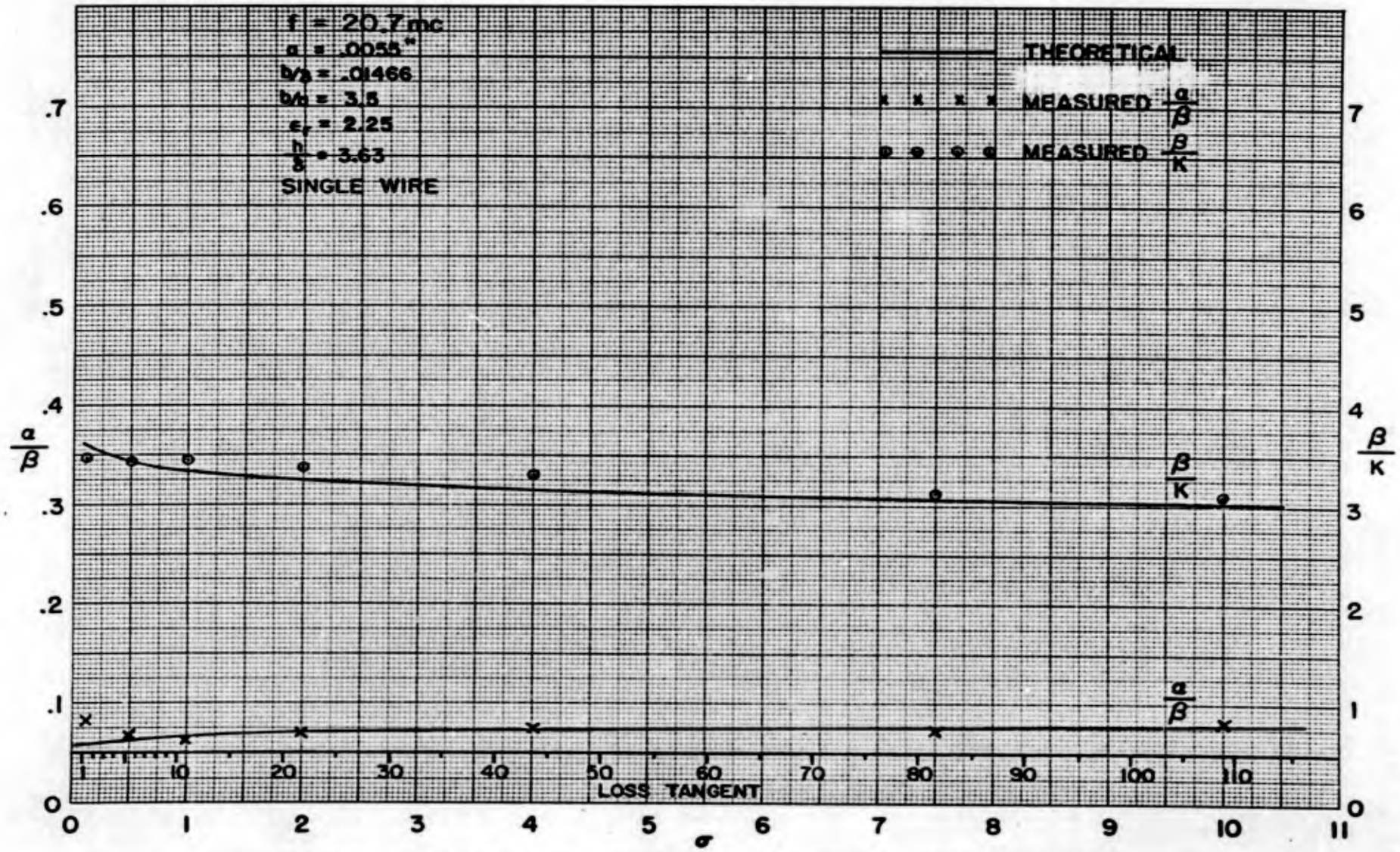

FIG. 11b PROPAGATION CONSTANT VS FREQUENCY FOR SINGLE WIRE AT LARGE DEPTH

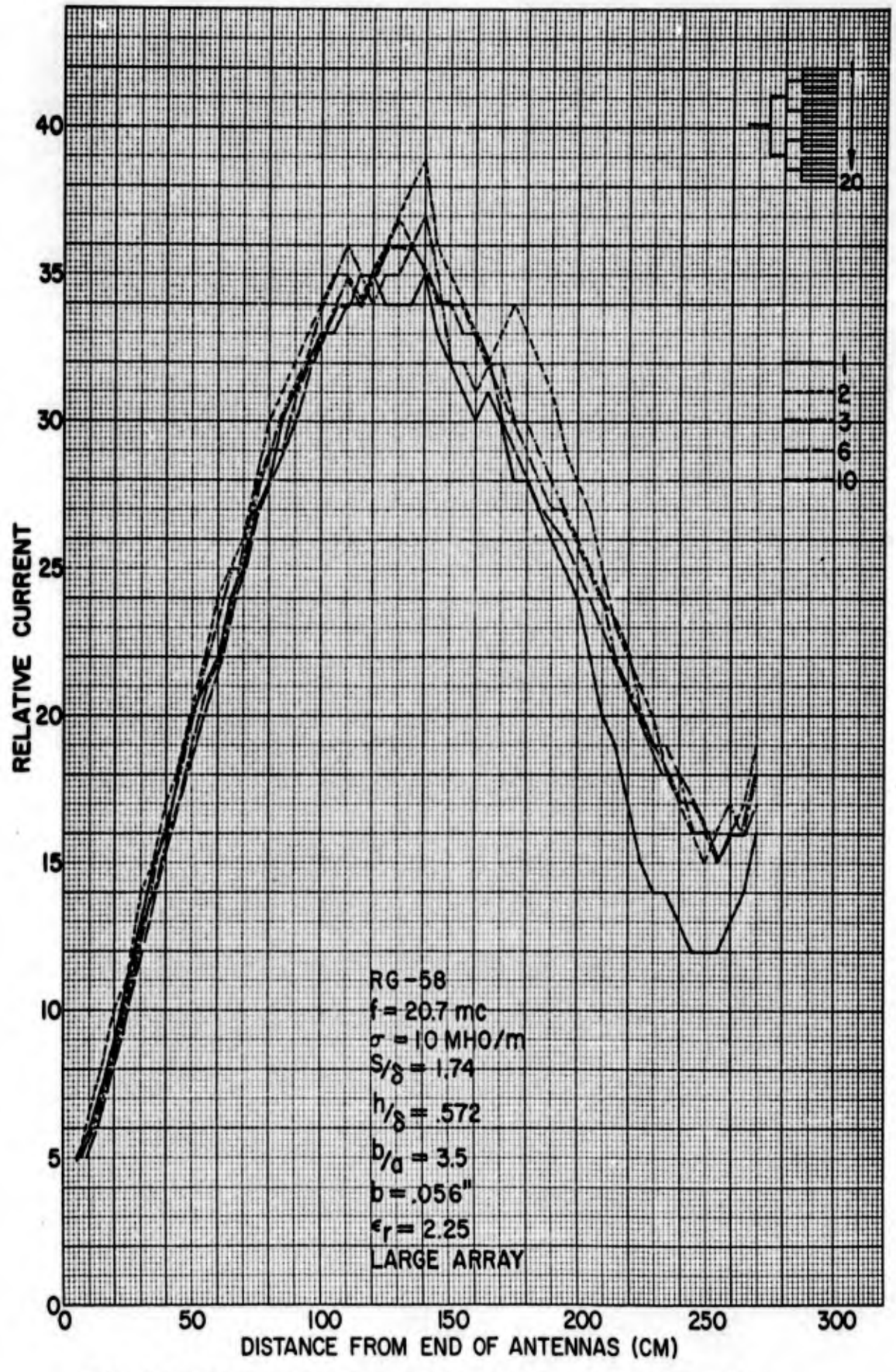

FIG. 12 CURRENT DISTRIBUTION ON ELEMENTS IN LARGE ARRAY

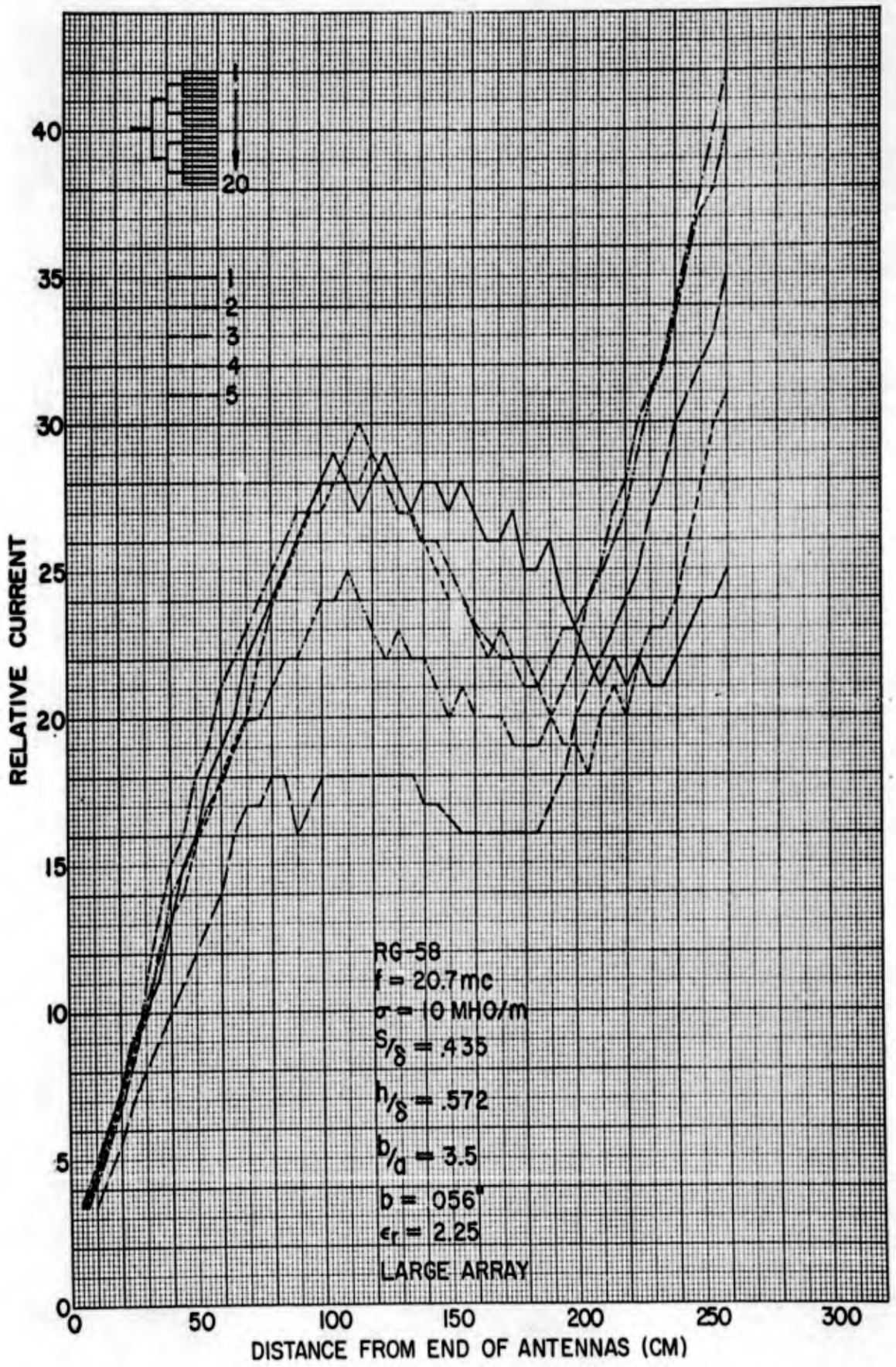

FIG. 13a CURRENT DISTRIBUTION ON ELEMENTS IN LARGE ARRAY

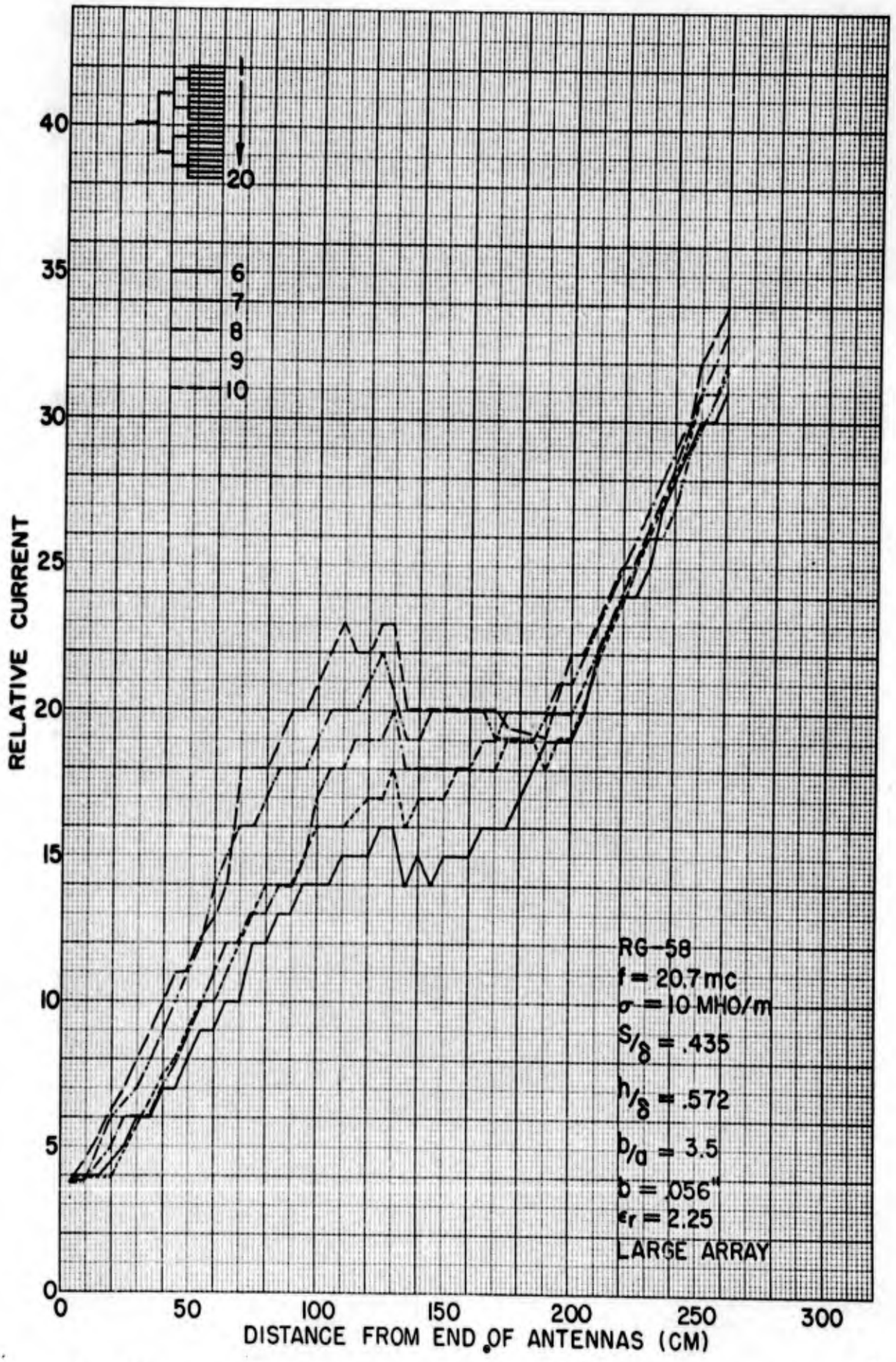

FIG. 13b CURRENT DISTRIBUTION OF ELEMENTS IN LARGE ARRAY

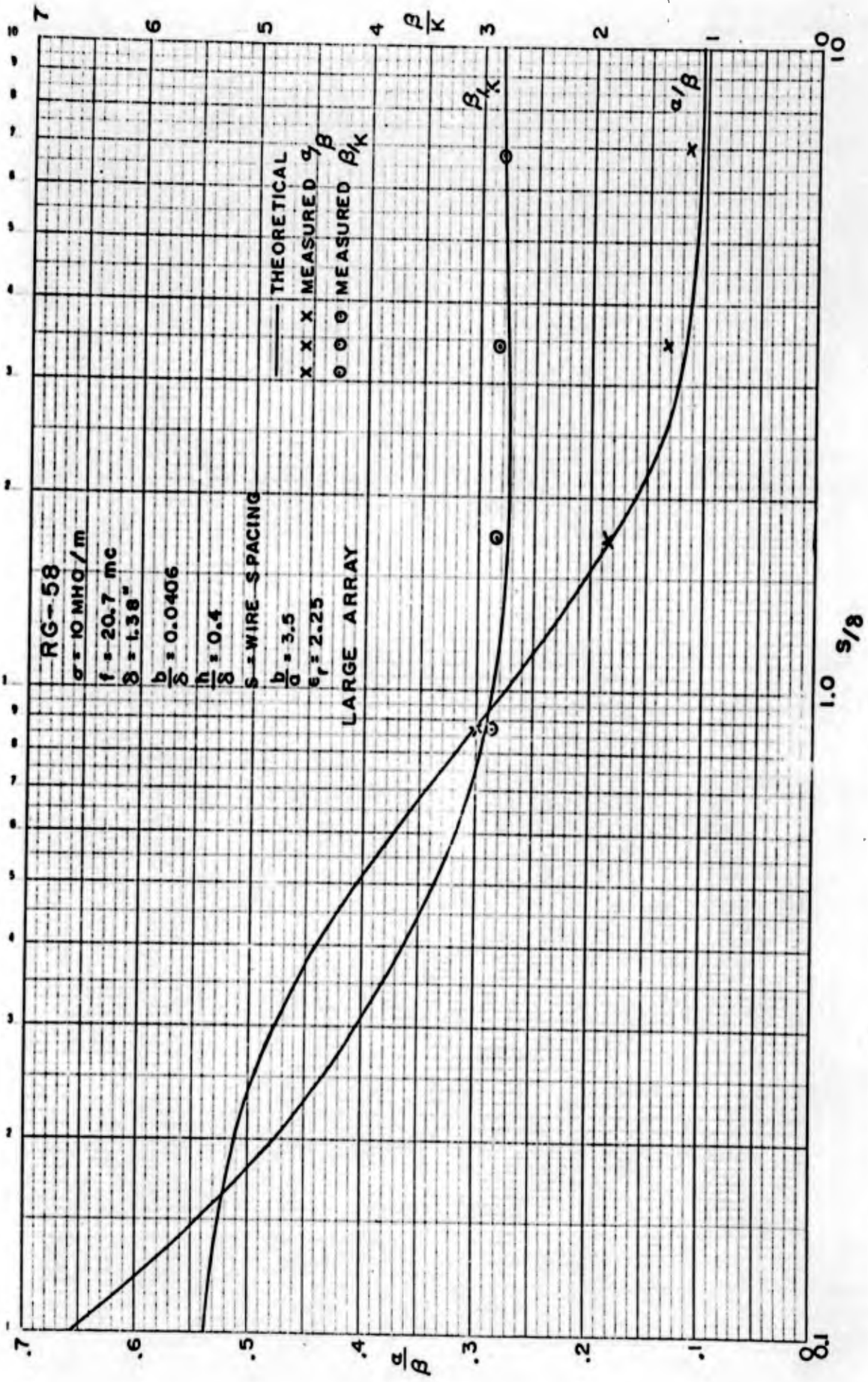

FIG. 14 PROPAGATION CONSTANT VS SPACING FOR LARGE ARRAY

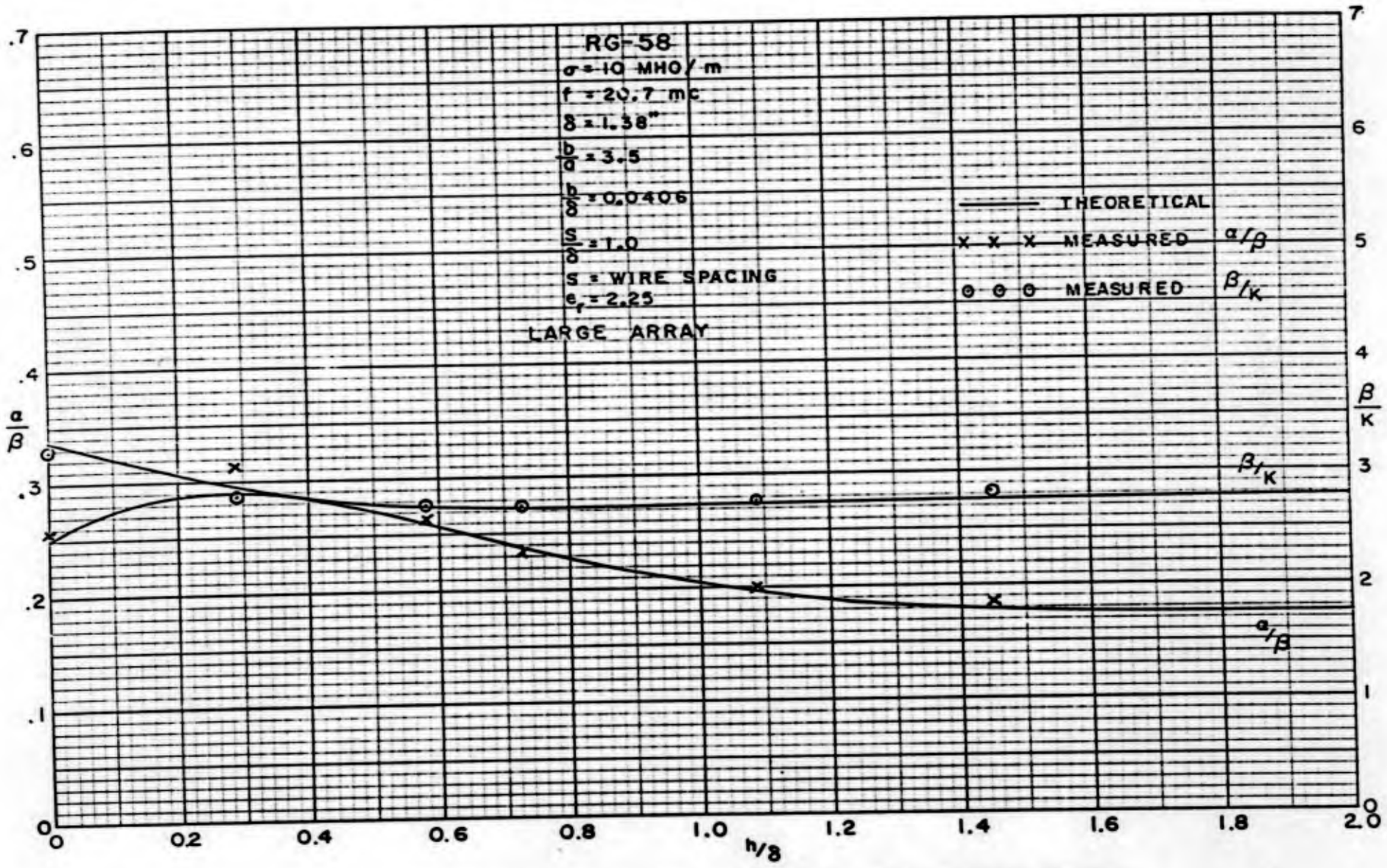

FIG. 15 PROPAGATION CONSTANT VS DEPTH FOR LARGE ARRAY

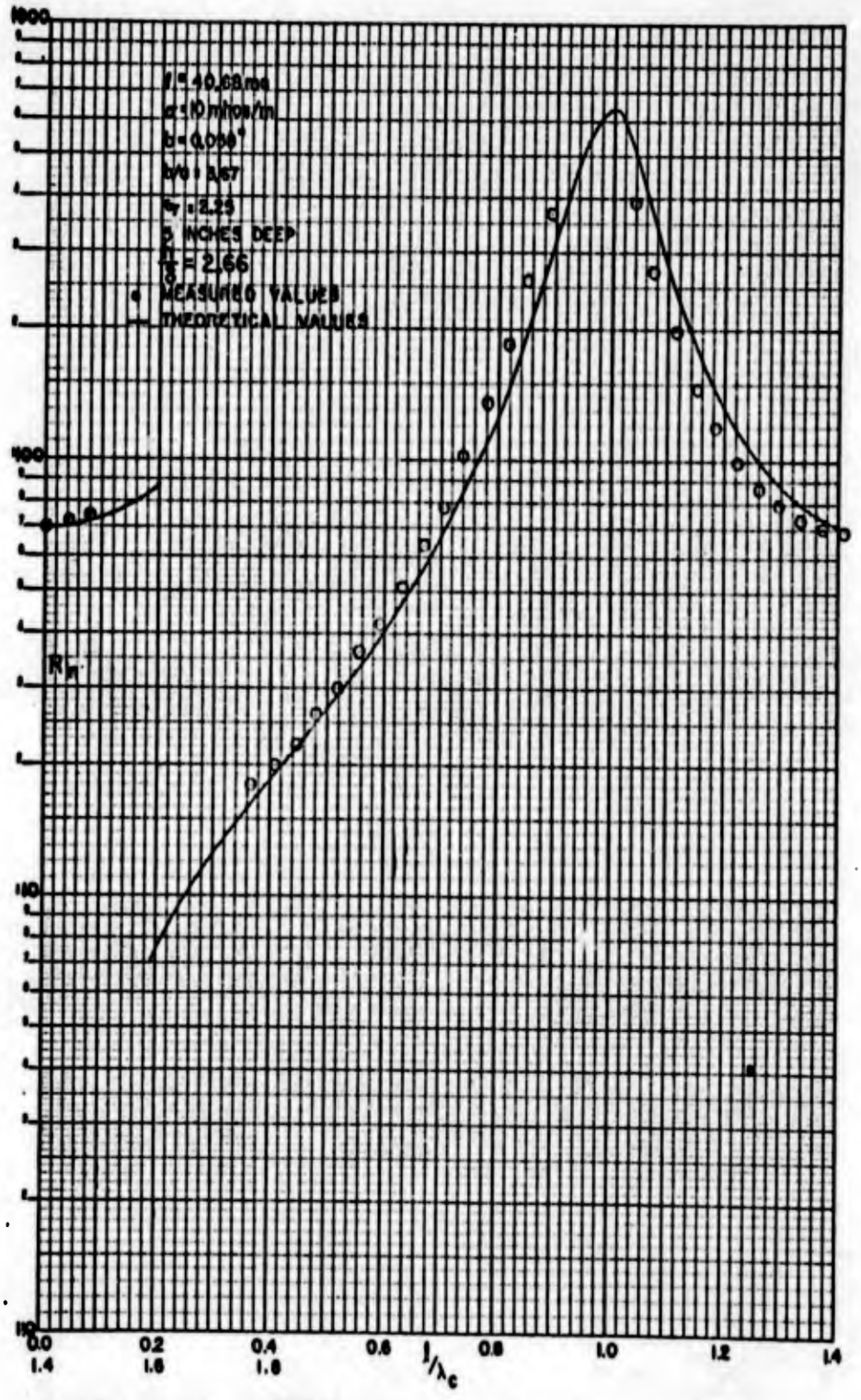

FIG.16a. INPUT RESISTANCE OF A BURIED ANTENNA WITH OPEN ENDS

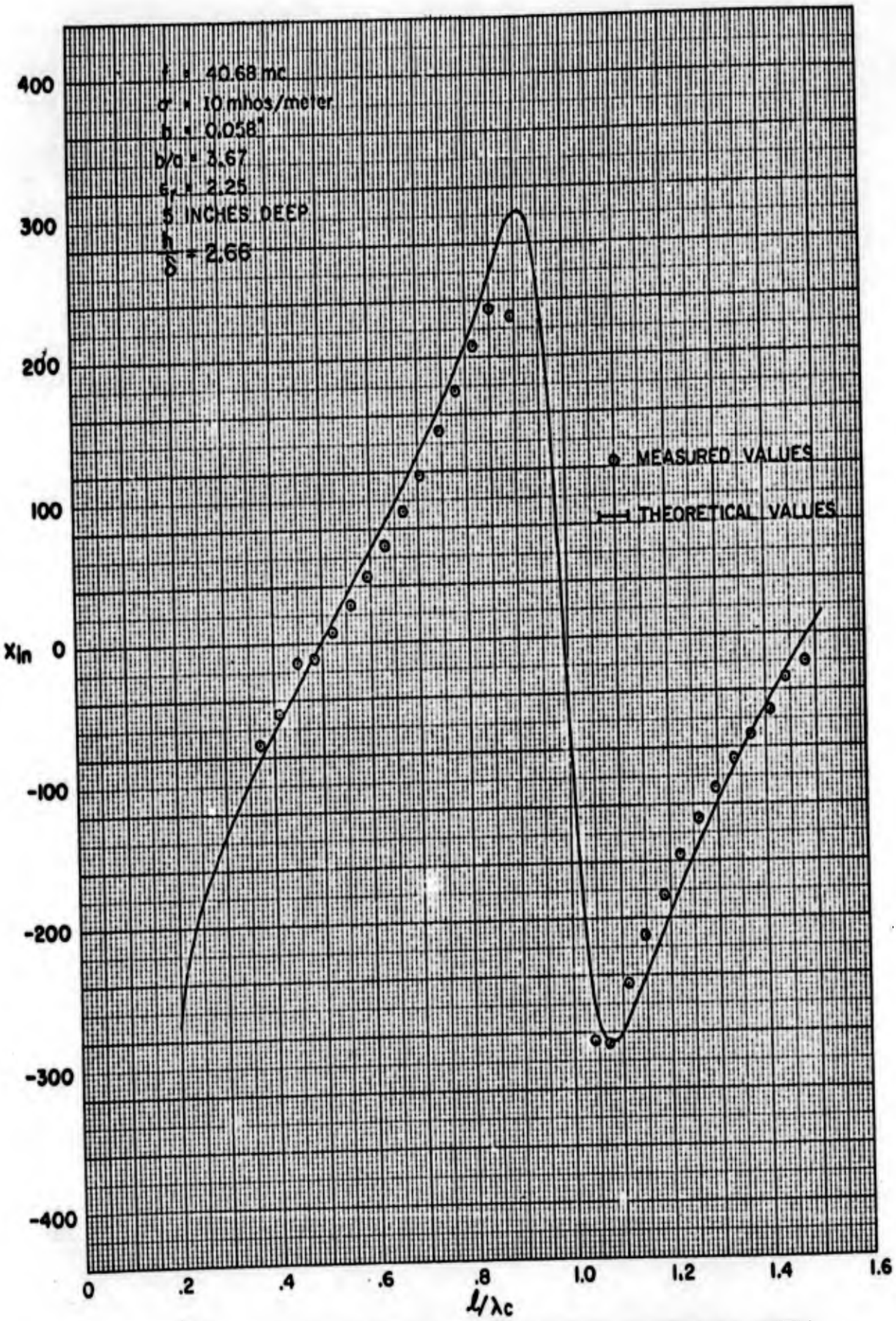

FIG. 16b INPUT REACTANCE OF BURIED ANTENNAS WITH OPEN ENDS

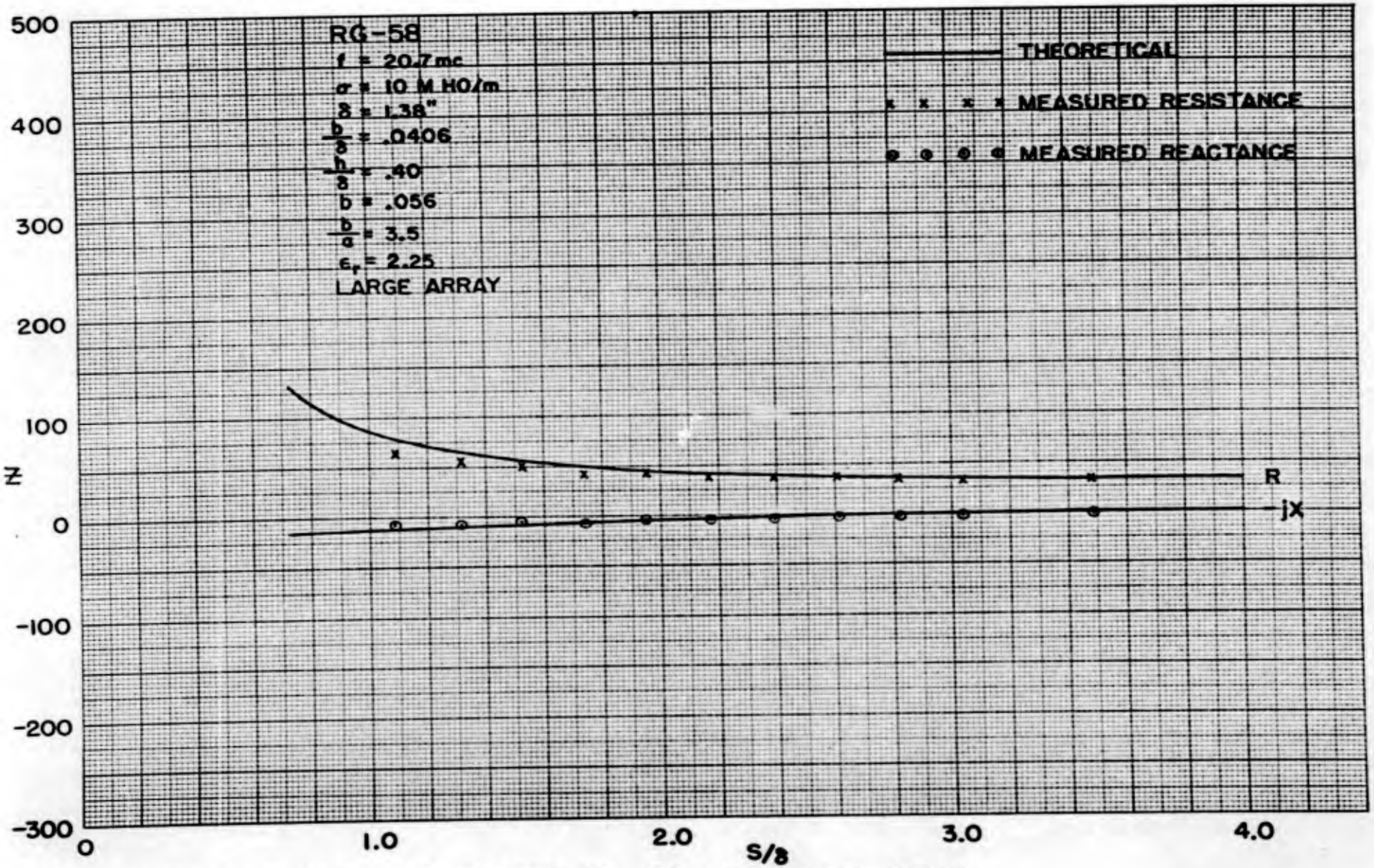

FIG. 17 INPUT Z PER ELEMENT VS S/δ FOR LARGE ARRAY

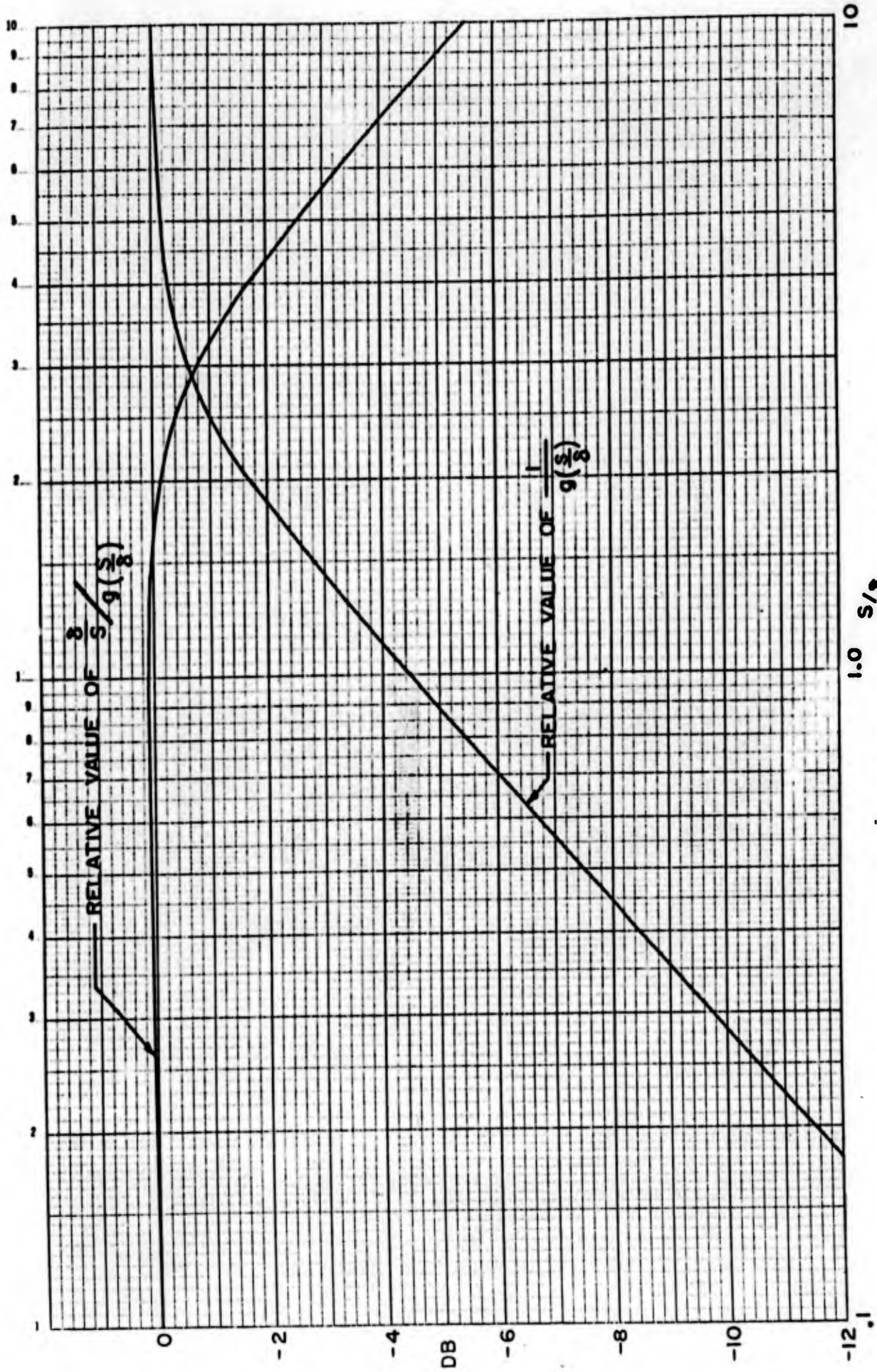

FIG. 18 RELATIVE VALUES OF $\frac{\delta}{S}/g(\frac{S}{\delta})$ AND $\frac{1}{g(\frac{S}{\delta})}$ VS. $\frac{S}{\delta}$

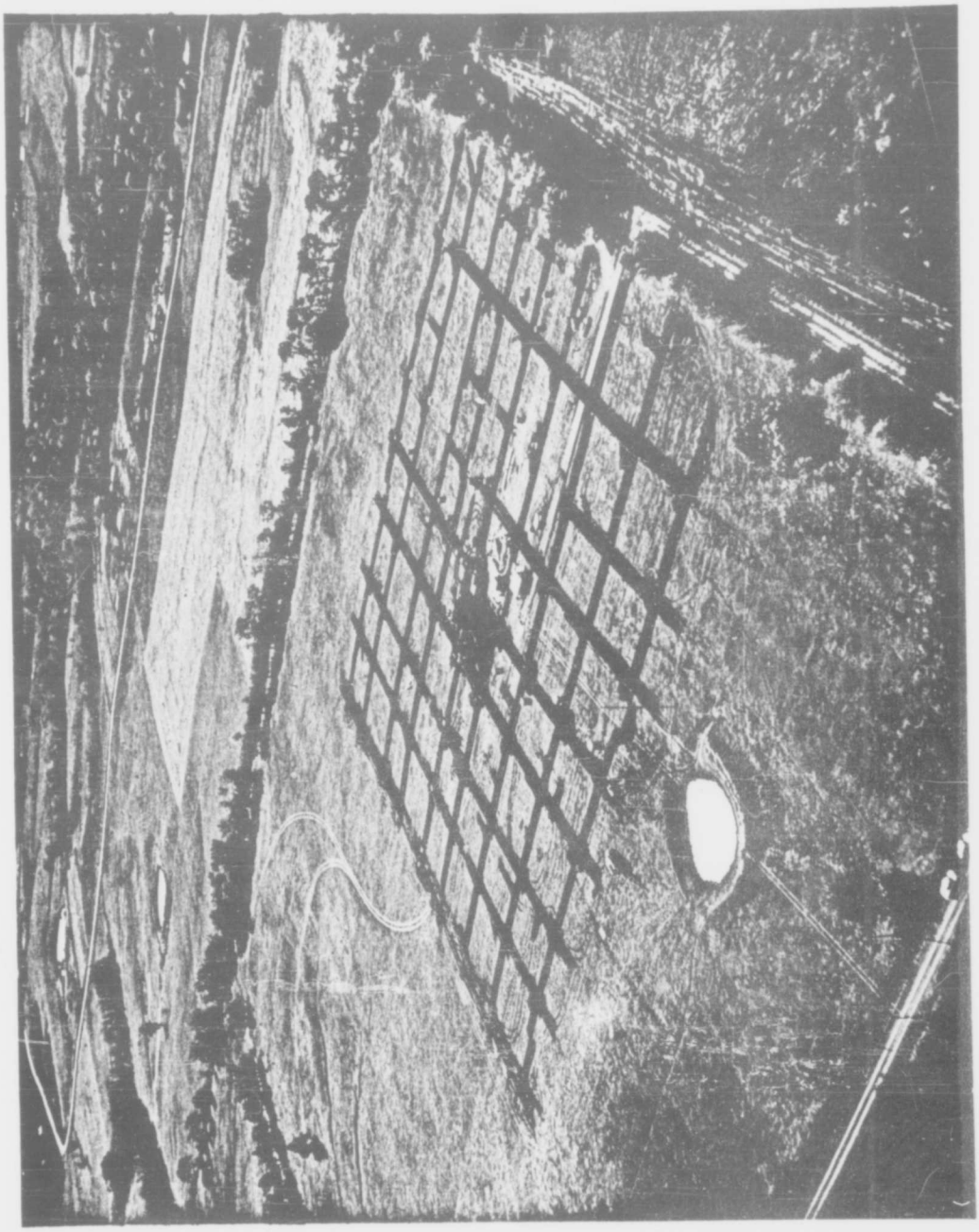

FIG. 19 CONSTRUCTION OF 8 x 8 ELEMENT OMNIDIRECTIONAL ANTENNA

RA51759

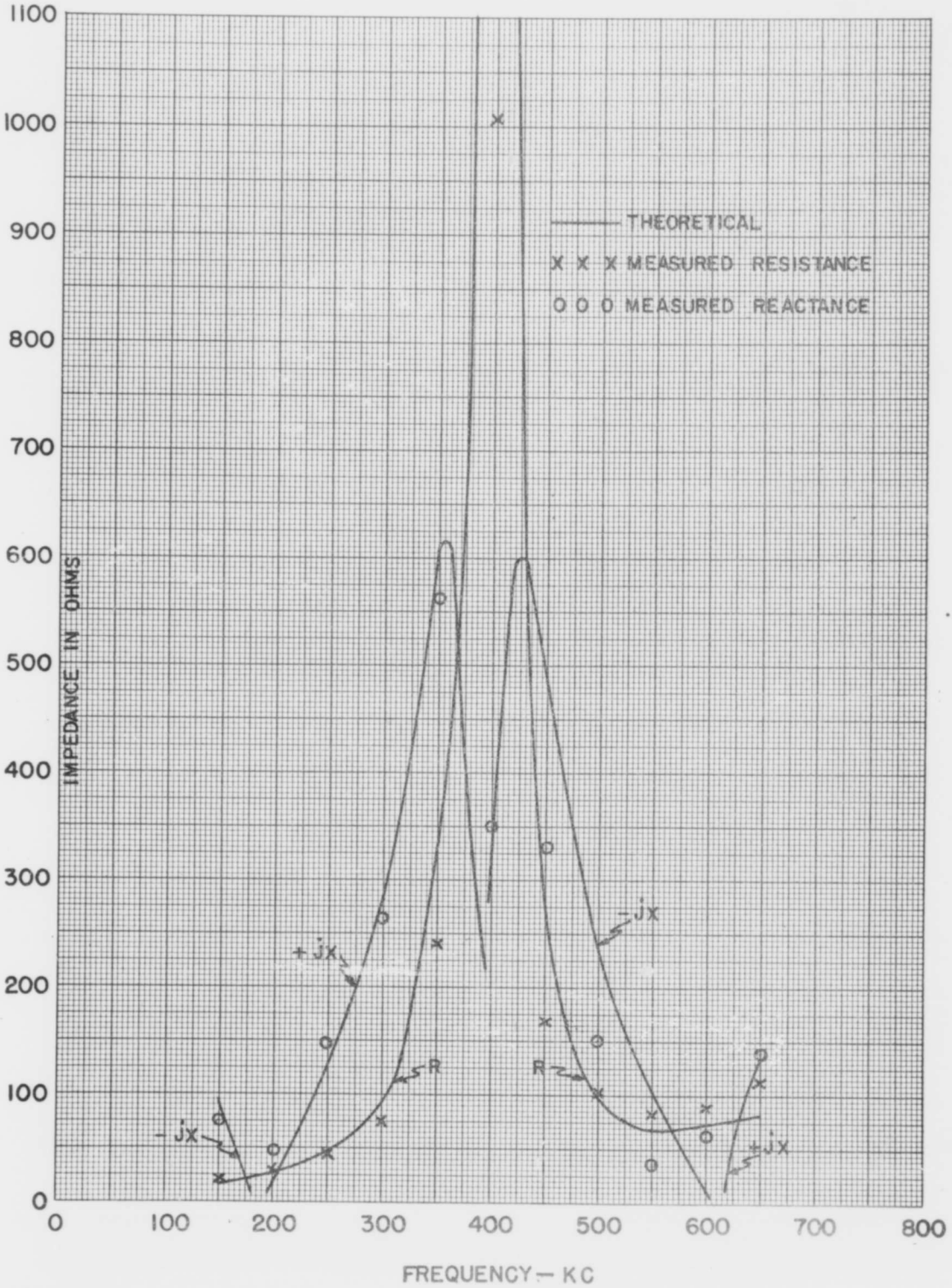

FIG. 20 $\not\equiv$ OF SINGLE ELEMENT IN FULL SCALE BURIED ANTENNA

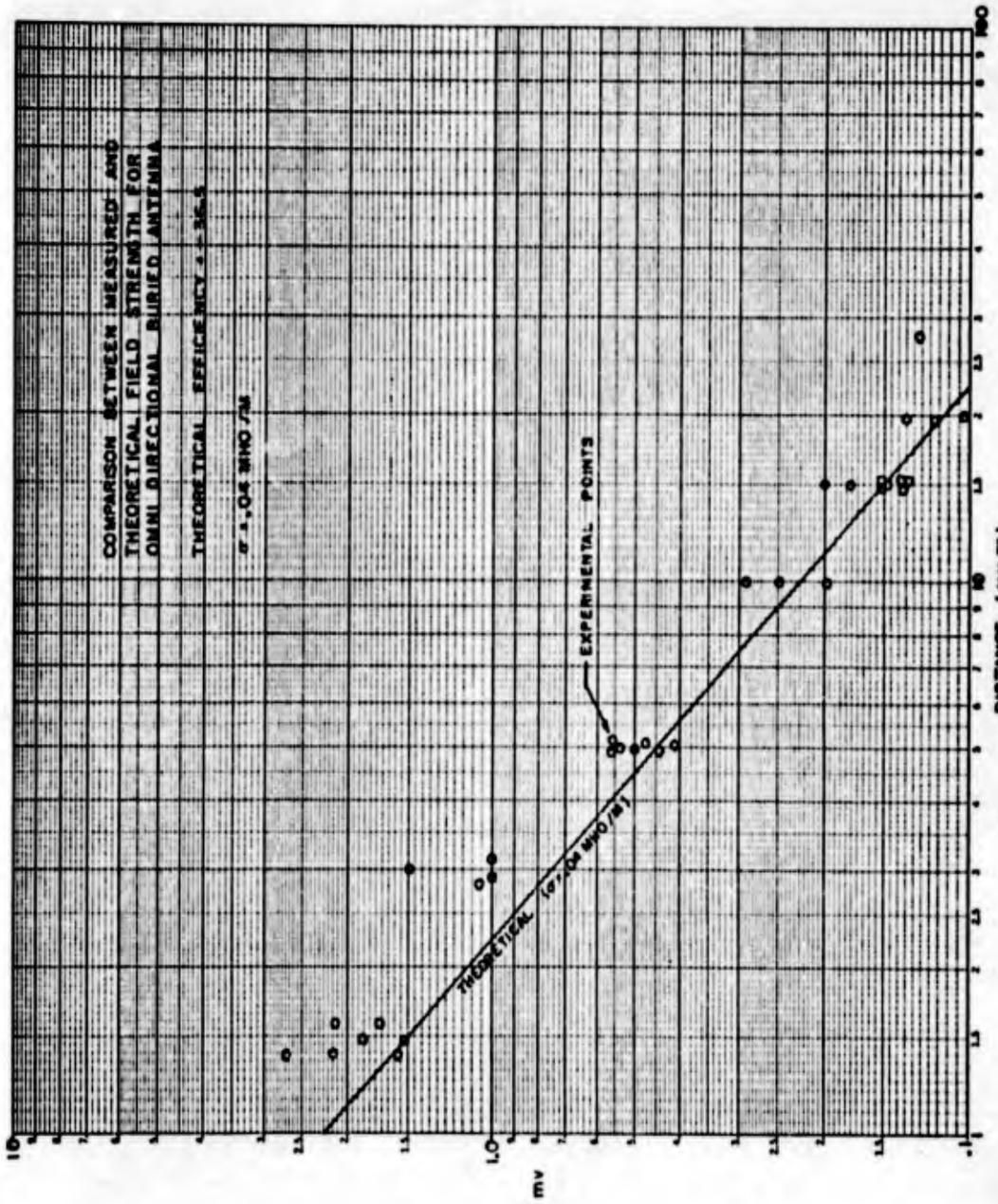

FIG, 21 MEASURED AND THEORETICAL FIELD STRENGTH

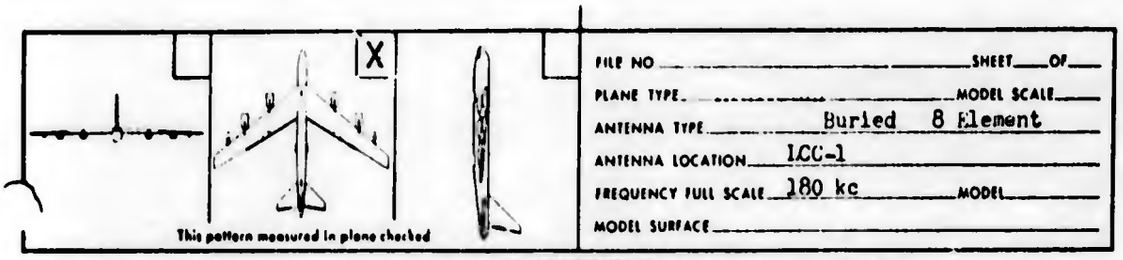

FIGURE 21

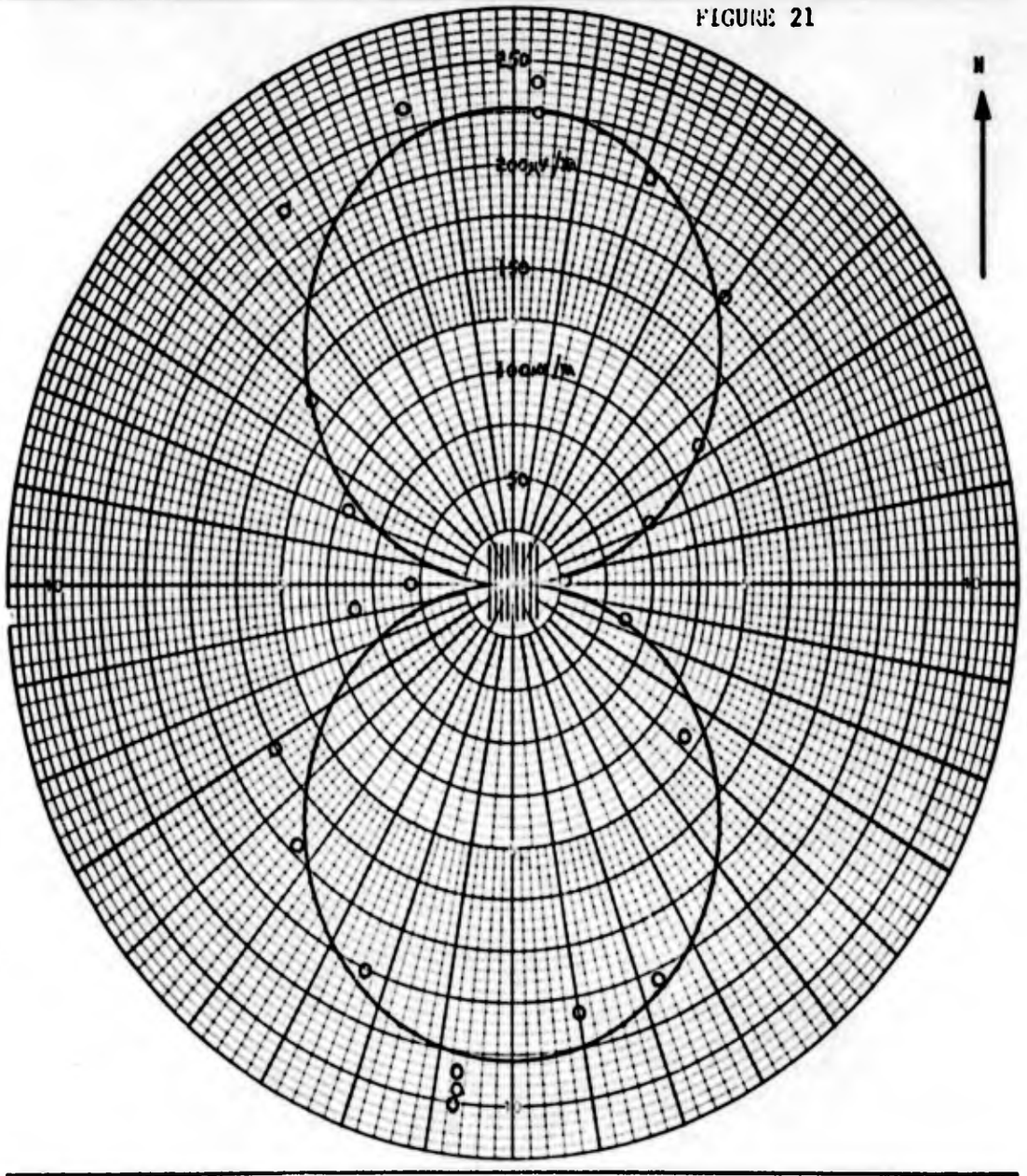

BOEING AIRPLANE COMPANY

REMARKS Airborne Measurements
10 mile radius 2,900' altitude
8 element N-S array
OPERATOR Light Plane DATE 12-13-6
APPROVED Whip Antenna DATE

VARIABLE ANGLE Φ (X), θ ( )
CONSTANT ANGLE Φ = ____ θ = ~0°
POLARIZATION E_Φ ( ), E_θ (X), ____
Φ = Horizontal angle θ = Vertical angle
CURVE PLOTTED IN VOLTAGE (X), POWER ( ), DECIBELS ( )

BAC 1866-R1 POLAR RECORDING CHART

FIG. 22 8 ELEMENT HORIZONTAL PATTERN

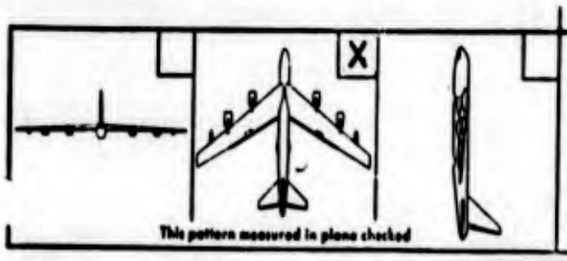

FILE NO. _____ SHEET ___ OF ___
PLANE TYPE _____ MODEL SCALE ___
ANTENNA TYPE Buried 8x8 array
ANTENNA LOCATION LCC-1
FREQUENCY FULL SCALE 180 kc MODEL ___
MODEL SURFACE _____

FIGURE 19

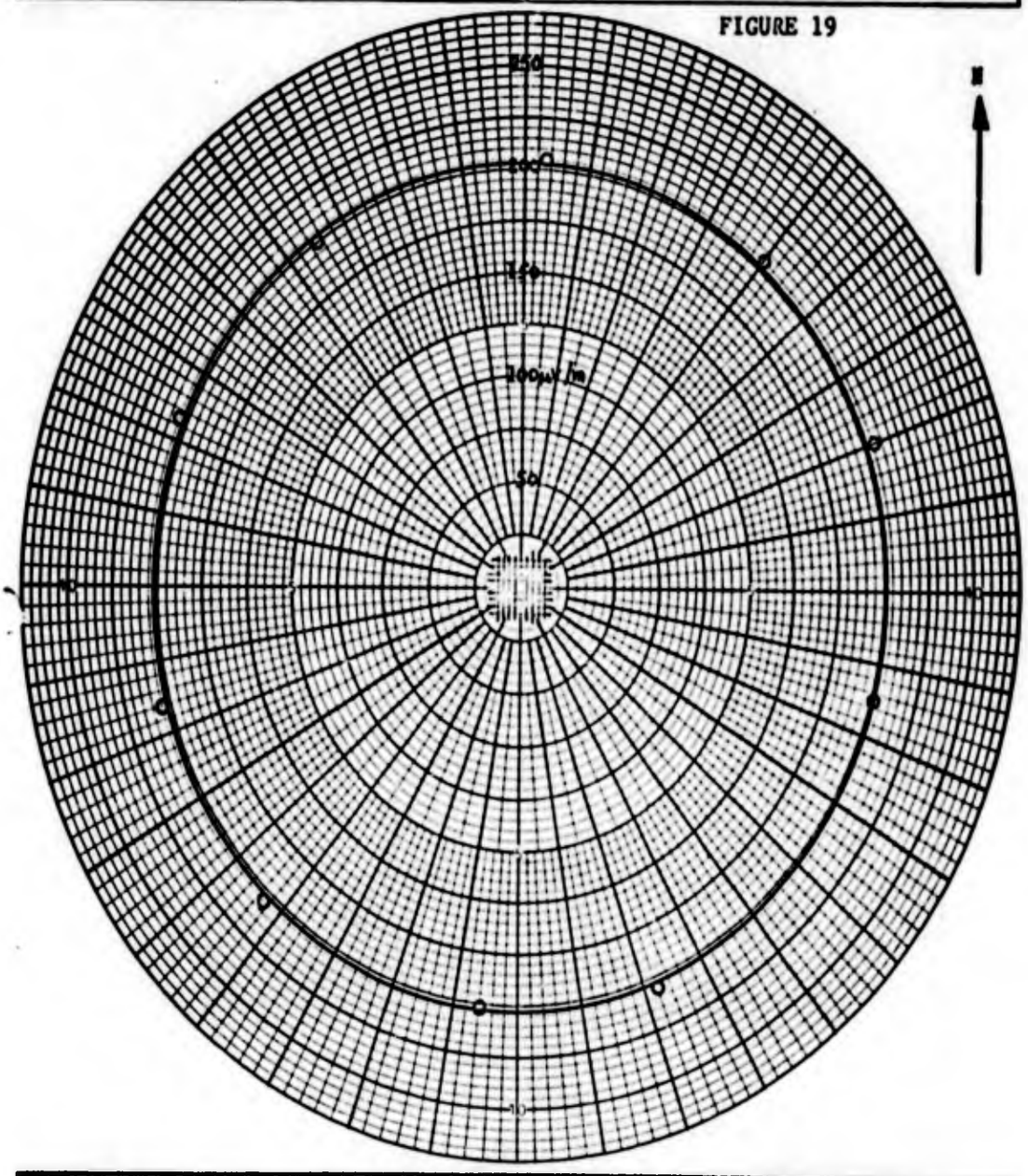

BOEING AIRPLANE COMPANY

REMARKS Airborne Measurements 8x8 Array
10 mile radius 2000' altitude
Light Plane Whip Antenna
OPERATOR _____ DATE 12-15-60
APPROVED _____ DATE _____

VARIABLE ANGLE Φ (X), θ ( )
CONSTANT ANGLE Φ = ____ θ = ~0°
POLARIZATION E_Φ ( ), E_θ (X), ____
Φ = Horizontal angle θ = Vertical angle
CURVE PLOTTED IN: VOLTAGE (X), POWER ( ), DECIBELS ( )

BAC 1866-R1 POLAR RECORDING CHART

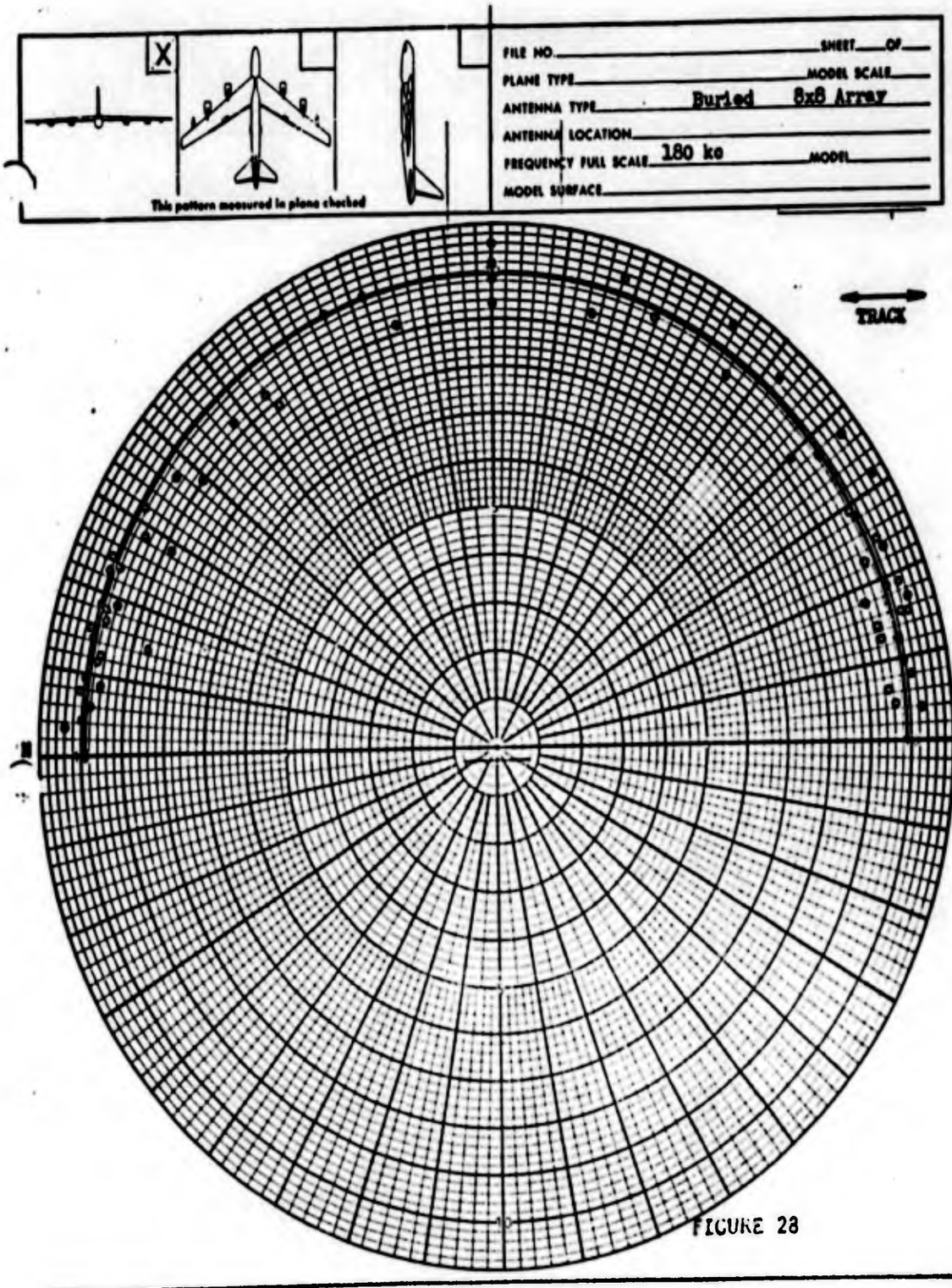

FIGURE 28

FIG. 24 8 X 8 ELEMENT ELEVATION PATTERN

EVALUATION OF RE-ENTRY VEHICLE ANTENNA WINDOWS: A TEST TECHNIQUE

Harry A. May

Electronic Systems & Products Division
Martin Company
Baltimore 3, Maryland

EVALUATION OF RE-ENTRY VEHICLE ANTENNA WINDOWS: A TEST TECHNIQUE

Harry A. May
Electronic Systems and Products Division
Martin Company
Baltimore 3, Maryland

INTRODUCTION

This paper describes a test technique developed to evaluate candidate antenna window materials for possible use on re-entry vehicles. Surface temperatures recorded for earth re-entry vehicles, particularly the lifting-body variety, extend far beyond existing material electrical properties data, and, in fact, appear to be beyond the limit of existing classical dielectric constant and loss tangent type of measurement in heated cavities. The test method described here records directly the RF signal transmission and reflection properties of an antenna-window combination during simulated re-entry heating of the window surface.

ANTENNA CONFIGURATIONS

We shall consider two types of antenna-window installations that are frequently required on re-entry vehicles (Fig. 1). Both are flush-mounted to form a smooth aerodynamic fairing, and two distinct frequency ranges are usually covered. The first is within the VHF-UHF range with wavelengths in the vicinity of one meter, and the second is within the C- or X-band with wavelengths less than 10 cm. The longer wavelength antennas are commonly in the form of rectangular slots, approximately 16 in. long and 4 in. wide. The shorter wavelength antennas are generally circular cavities approximately 2 or 3 in. in diameter.

Figure 2 shows the heat input profile for two types of re-entry vehicles. The first represents a ballistic re-entry vehicle, such as Pershing, and the second represents a lifting-body type, such as Apollo. The area under each of these curves gives the total heat input during re-entry.

DESIGN CRITERIA

The necessity for antenna windows is one of the most unpleasant facts facing the designer of re-entering hardware, whether he is concerned with structures or with antennas. The problem will be considered from each point of view (Fig. 3).

To the structural designer, antenna windows represent a discontinuity in the heat shield. All such discontinuities are possible failure areas demanding close attention to their boundaries if reliability is to be maintained. Secondly, the structure beneath the heat shield is interrupted by the antenna penetration, and provisions for carrying loads around this area are necessary. Also, the problem can seldom be alleviated by locating these windows in noncritical areas, because good pattern coverage requirements usually dictate the antenna locations within rather narrow limits. To further complicate the problem, the choice of materials is limited to the very few which meet both the electrical and structural requirements.

The antenna designer has a similar dilemma. The windows must be made of a low loss material to avoid excessive attenuation of the signal. If the window can be made electrically thin, its effect on antenna tuning will be small. Because the electrical thickness is proportional to the physical thickness and the dielectric constant, a low dielectric constant is advantageous. If the window can not be thin, changes in electrical thickness during ablation will affect the tuning of the antenna, so it must be kept at a minimum. The window material must be electrically isotropic and uniform.

It is evident that understanding compromises must be reached between the structural designer who wants the antenna windows to look just like the rest of the heat shield and the antenna designer who wants them to look like nothing at all.

Many advantages are gained if the ablation material used on the remainder of the vehicle can be used as the antenna window material. The window can be fabricated as an integral part of the heat shield, eliminating special antenna window fabrication and installation steps. The continuity of the heat shield increases its reliability, and attachment problems are avoided. The only problems are those of providing a radio frequency-transparent replacement for the metal structure, and of making sure that opaque adhesives and insulators are not used in the window area.

The feasibility of this approach is dependent on acceptable electrical properties of the ablation material. When it is recalled that several centimeters of ablation material may be used and that this thickness does change during re-entry, we realize that such windows cannot be considered for the short wavelength range.

Figure 4 shows the electrical properties of two commonly used ablative materials measured at 1 mc and room temperature. The dielectric constants are within acceptable limits and the dissipation factors, while higher than one would like to see, do not eliminate the materials from consideration. There is, however, a factor that would logically dash

our hopes for using these materials. They form a carbonaceous char during ablation that should effectively block all RF transmission, a supposition that is easily put to the test. A nylon phenolic window was fabricated and tested, after charring to two depths, and finally after removal of the char. Figure 5 shows the surprising results of this experiment. The presence of cold char is not a serious barrier to microwaves at the frequencies tested. A similar test with similar results has been run with asbestos-phenolic. We now have an antenna window for the long wavelengths which is easy to fabricate and which is reliable structurally and thermally. This window will function throughout a mission, up to re-entry heat pulse, and will function after the heat pulse. There remains only the electrical behavior during ablation to consider.

PROPOSED TEST CONFIGURATION

Figure 6 shows the proposed elevated temperature test configuration. A test specimen, consisting of an antenna-window combination, is installed as shown directly within the exhaust of a heat source. RF transmission and reflected properties of the test specimen are monitored, respectively, by a secondary pick-up antenna and a reflectometer, and are fed to a pen recorder. Surface temperatures of the window specimens are recorded with the use of an optical pyrometer and are used to control the output of the heat source. Detuning of the test specimen and/or pattern distortion caused by the proximity of the heat source are normalized from the test results by a straight-forward calibration process.

TEST RESULTS

Figures 7 and 8 show the VHF nylon-phenolic window specimen and the subsequent test in the 14-in. diameter hot gas generator.

During this test, the heat was applied in two pulses so that the recovery of transmission upon cooling could be observed. Figure 9 shows that signal attenuation increases rapidly with temperature, and that the signal returns, but not to its original level, as the window cools. Because of the sharp cutoff of the heat pulse, and because accurate surface temperature data is not available below approximately 1500° F, no conclusions can be reached at present except that antenna blackout does occur during ablation of nylon phenolic. More information is needed about the details of this blackout to determine whether it corresponds to the ion-sheath blackout that occurs in any case or whether it extends beyond that blackout. Figure 10 shows the loss characteristics of molded versus laminated nylon phenolic.

In the event that the phenolic windows fail to meet the criteria, the next candidate for VHF-UHF antenna windows is ceramic reinforced Teflon, which ablates without charring.

For the high frequency antenna windows the use of ceramic materials is feasible and perhaps mandatory. Their low loss characteristics and refractory qualities provide the electrical stability required for this frequency range. Disadvantages are the special attachment problems arising from their brittleness and low coefficients of expansion, their high dielectric constants, and their high thermal conductivities. The recent development of these materials in uniform foams helps greatly to solve some of these problems.

Because the ambient properties of the ceramics are well known, this paper will be confined to a description of our recent efforts to measure the properties of these materials at high temperatures.

Figures 11 and 12 show a C-band antenna-window specimen under test in the Radiant Heat and Oxyacetylene Torch Facilities. Surface temperatures of 2000° F have been achieved in the radiant heat facility and of 4000° F in the torch facility.

Typical RF attenuation characteristics are given for the C-band test specimens in Fig. 13. Multiform silica foam has a small increase in attenuation at approximately 3000° F surface temperature with recovery at both lower and higher temperatures. Aluminum foam has a more significant attenuation characteristic within this same temperature range; however, a major improvement in response is noted when these samples have been prefired for several minutes in an oven.

CONCLUSIONS

The test technique described in this paper has been used successfully to evaluate antenna window materials at extremely high surface temperatures. The test results do not permit direct extraction of the dielectric constant and dissipation factors as normally desired, but the transmission and reflection characteristics provide an equally sound means of performance appraisal for the particular antenna-window configuration under test.

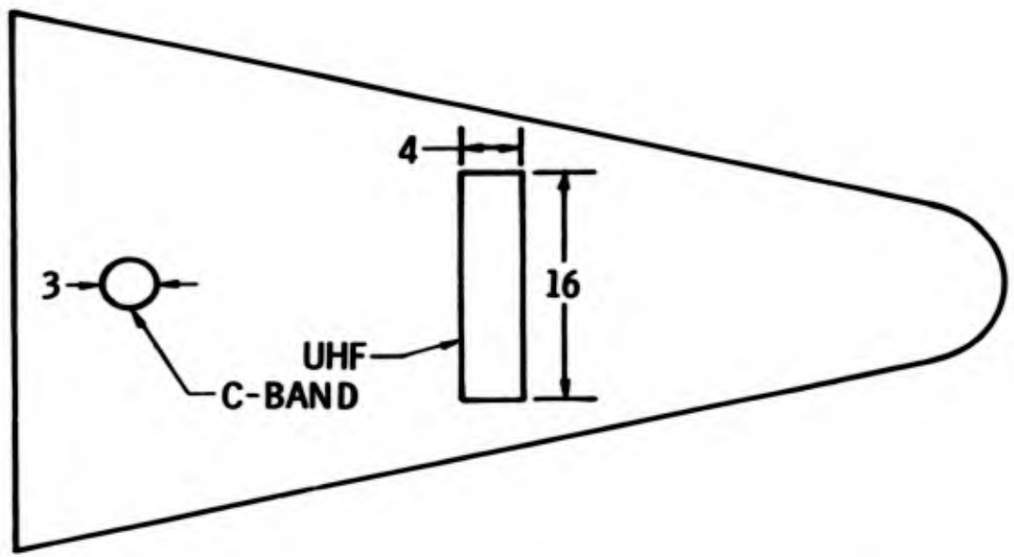

FIG. 1. TYPICAL RE-ENTRY ANTENNA CONFIGURATIONS

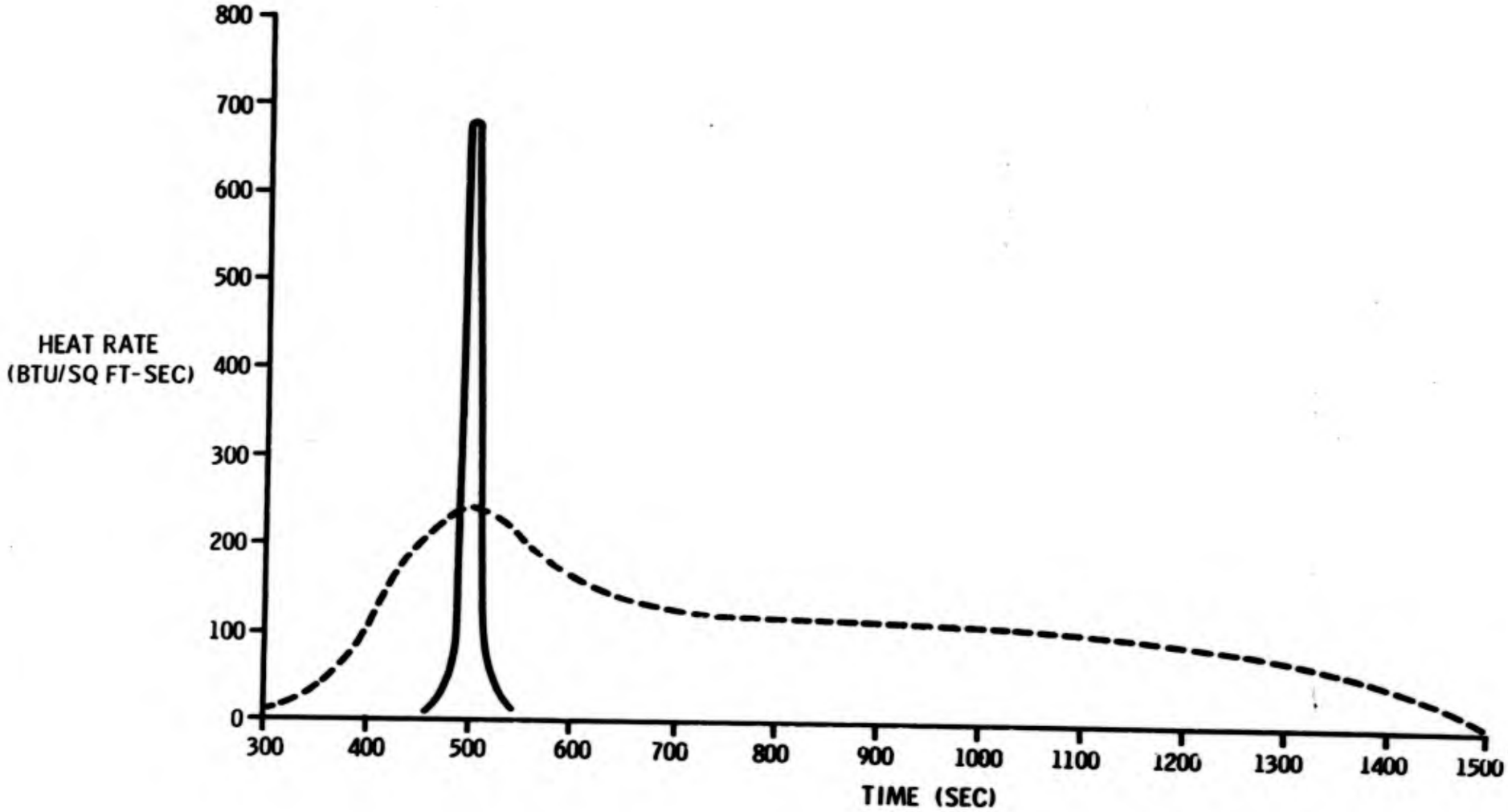

FIG. 2. TYPICAL HEAT PROFILES FOR BALLISTIC AND LIFTING-TYPE RE-ENTRY VEHICLES

Structural

Must not jeopardize heat shield

Must not jeopardize structure

Locate in noncritical area

Electrical

Low loss.

Electrically thin ($\sqrt{\varepsilon}t < \frac{\lambda}{16}$)

Minimum thickness change

Isotropic and uniform

Must protect antenna

FIG. 3. RE-ENTRY ANTENNA WINDOW CRITERIA

Material	Dielectric Constant	Dissipation Factor
Asbestos-phenolic	5.5 to 10.0	0.08 to 0.14
Nylon-phenolic	3.3 to 4.5	0.015 to 0.04

FIG. 4. ELECTRICAL PROPERTIES OF ABLATIVE MATERIALS (MEASURED AT 1 MEGACYCLE--73° F)

NYLON PHENOLIC

Change in Radiation Efficiency (db)				
Frequency (mc)	Before Char	1/16-In. Char Depth	3/16-In. Char Depth	Char Removed
250	0.25	0.25	0.40	0.20
420	0.60	0.60	0.85	0.30

FIG. 5. TRANSMISSION TEST RESULTS--COLD CHAR

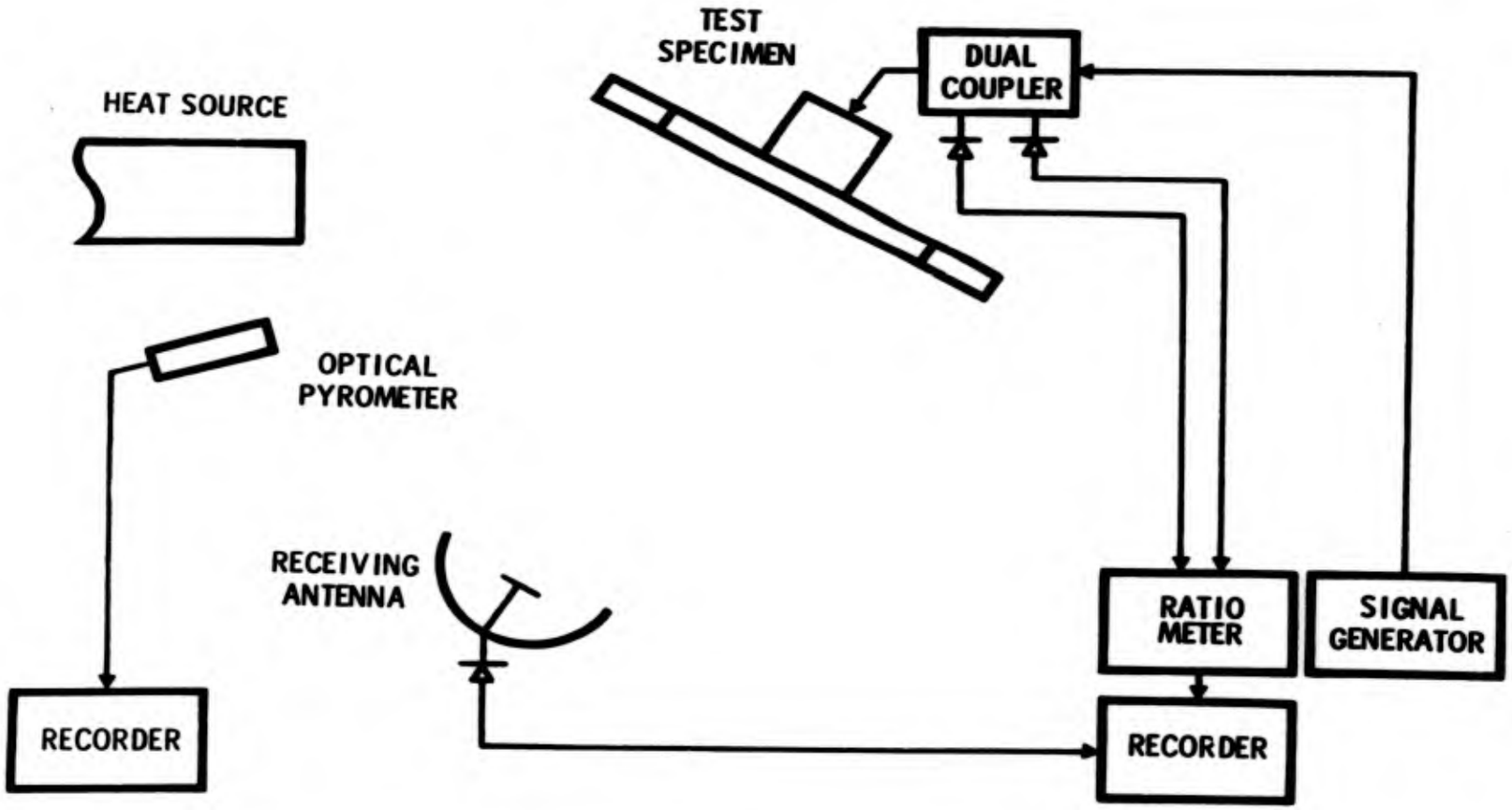

FIG. 6. PROPOSED ELEVATED TEMPERATURE TEST CONFIGURATION

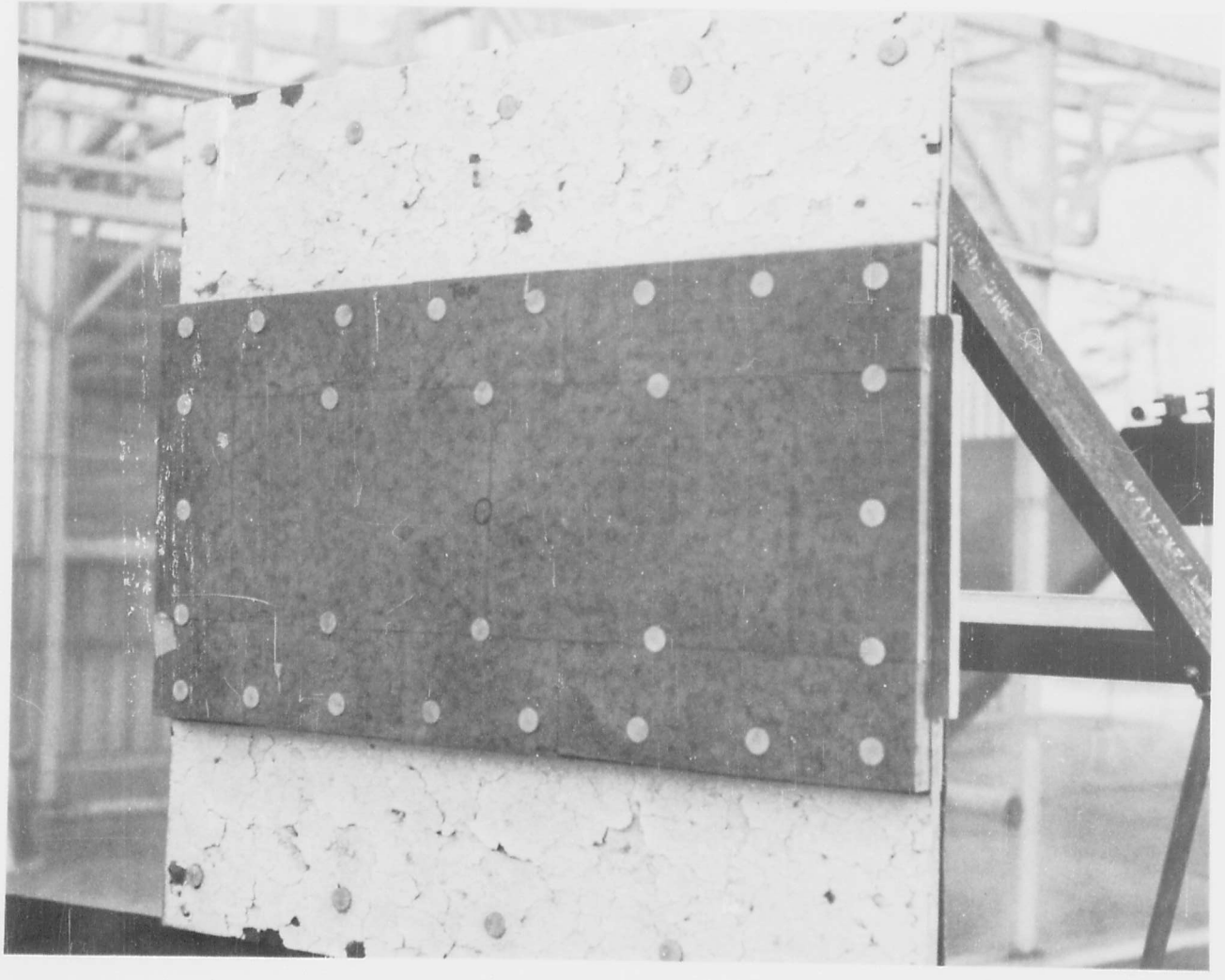

FIG. 7. MOLDED NYLON-PHENOLIC TEST ANTENNA WINDOW

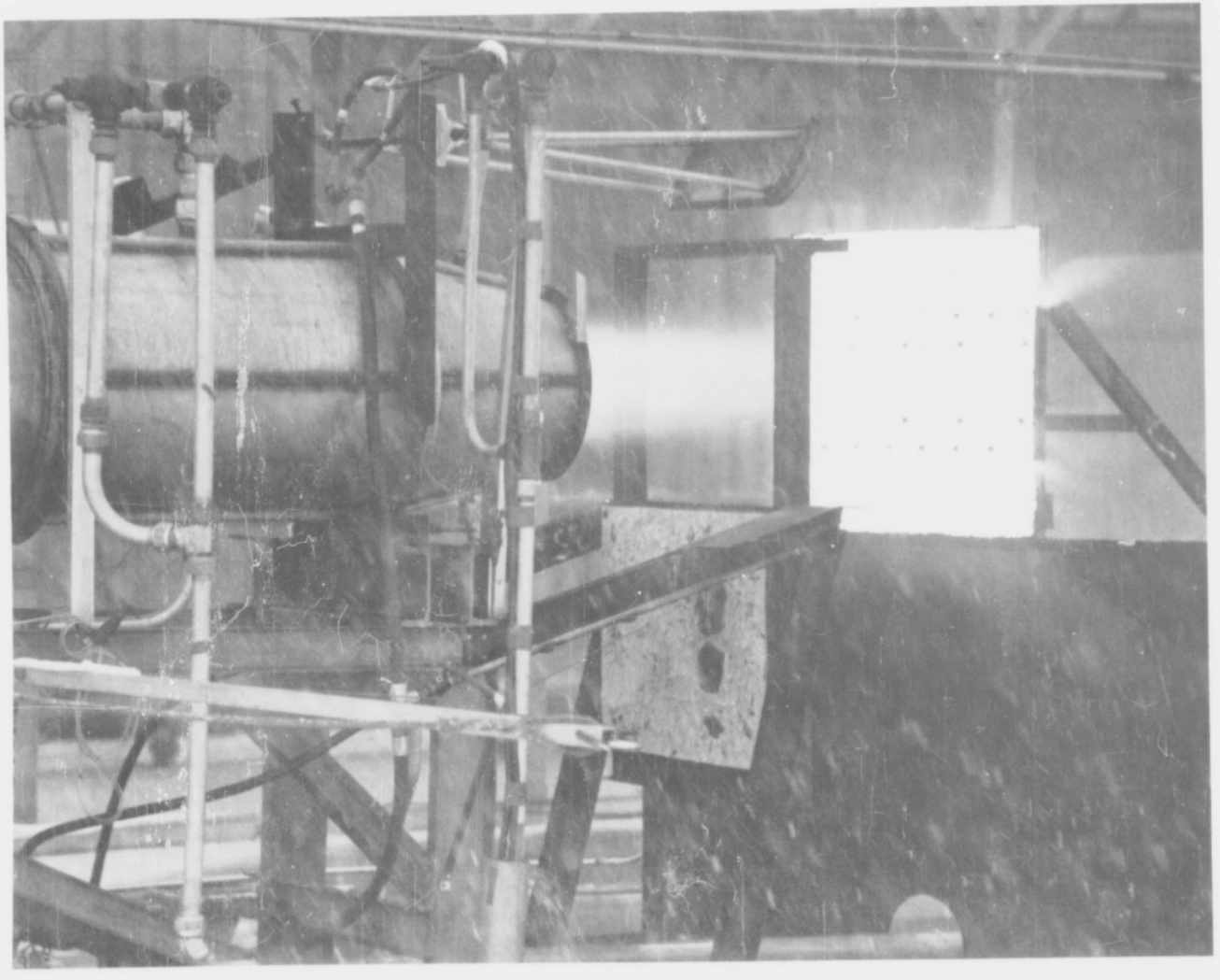

FIG. 8. HOT CHAR TRANSMISSION TEST--NYLON-PHENOLIC WINDOW

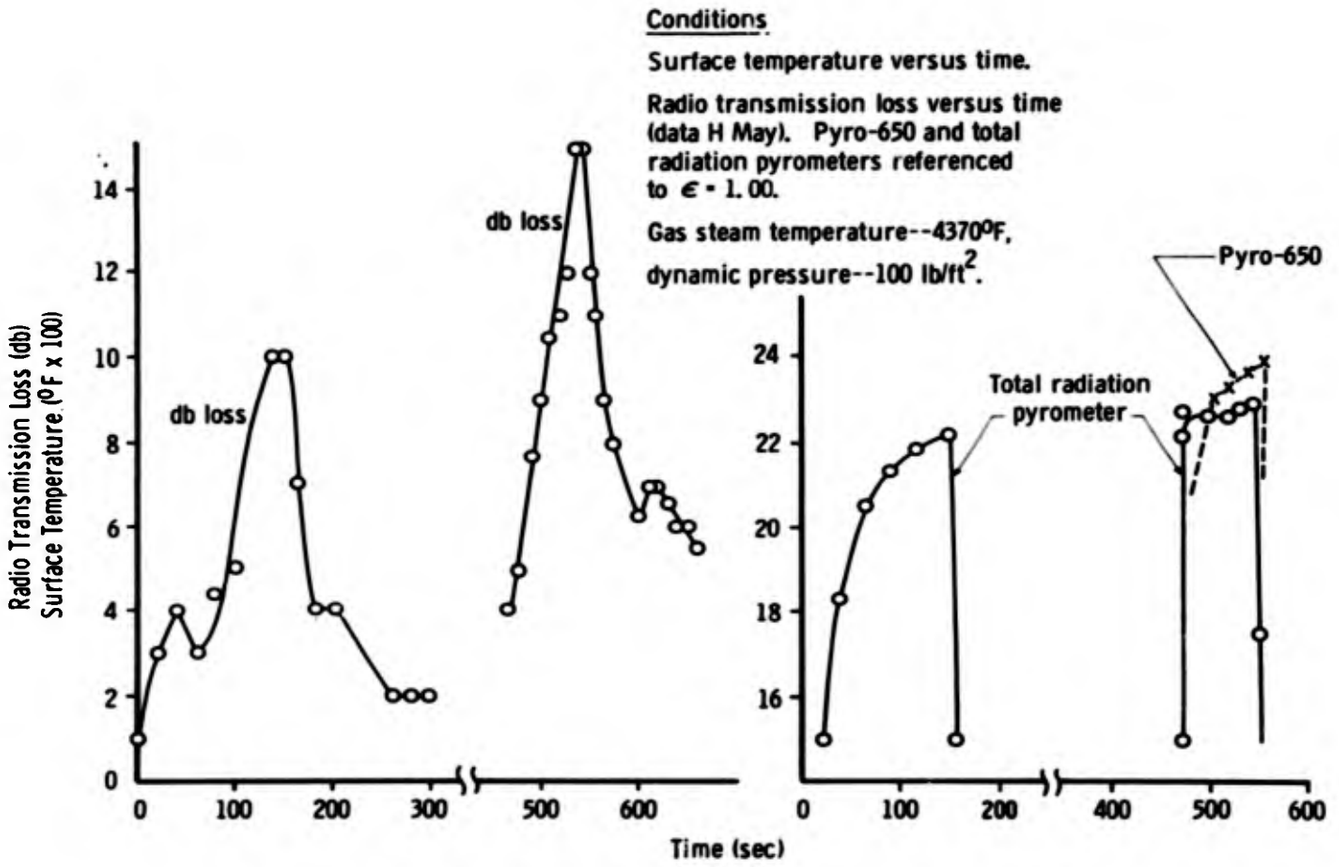

FIG. 9. ANTENNA WINDOW--HOT GAS TEST NO. 2

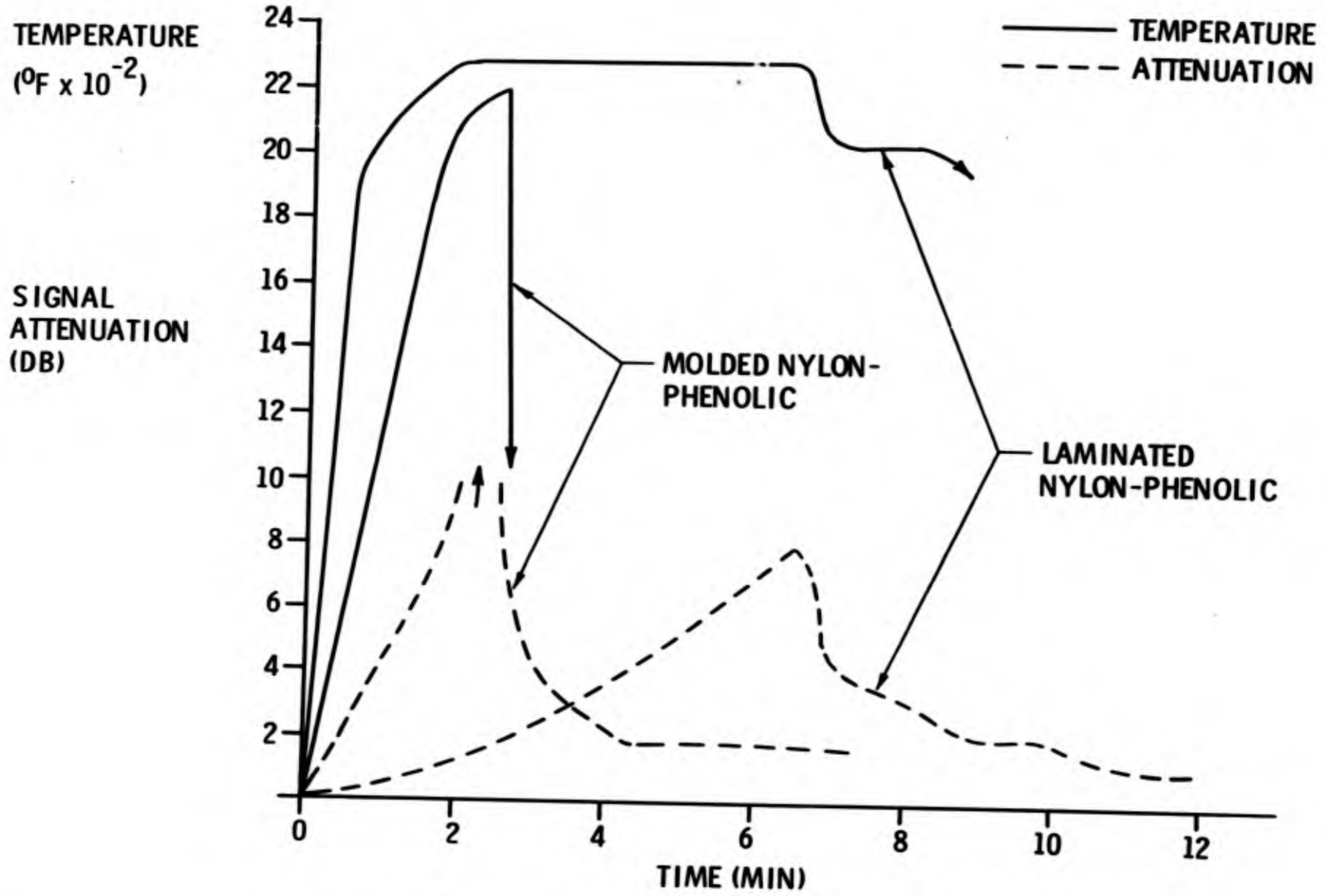

FIG. 10. VHF HOT GAS TESTS

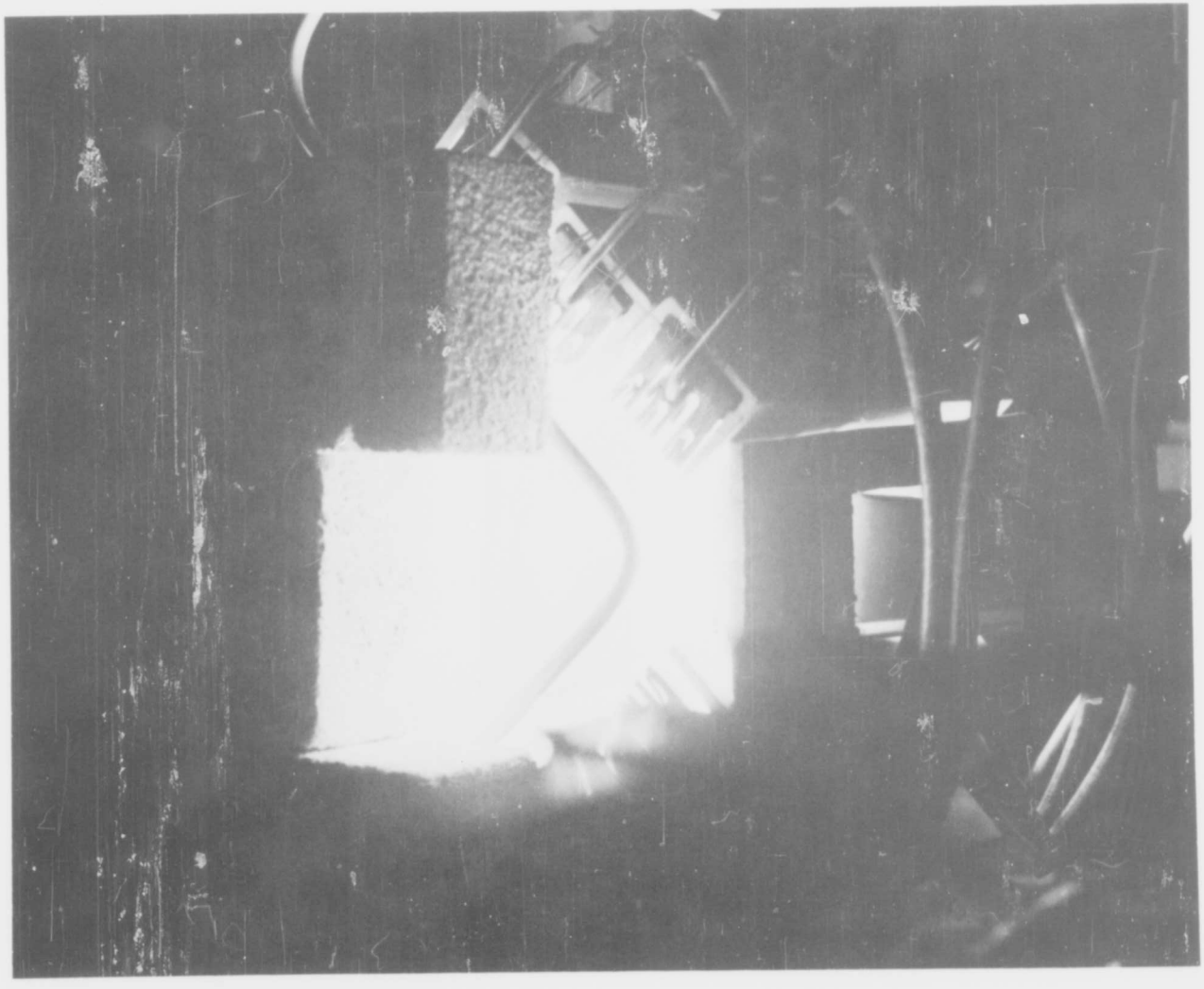

FIG. 11. ELEVATED TEMPERATURE TRANSMISSION TEST--
CERAMIC ANTENNA WINDOW

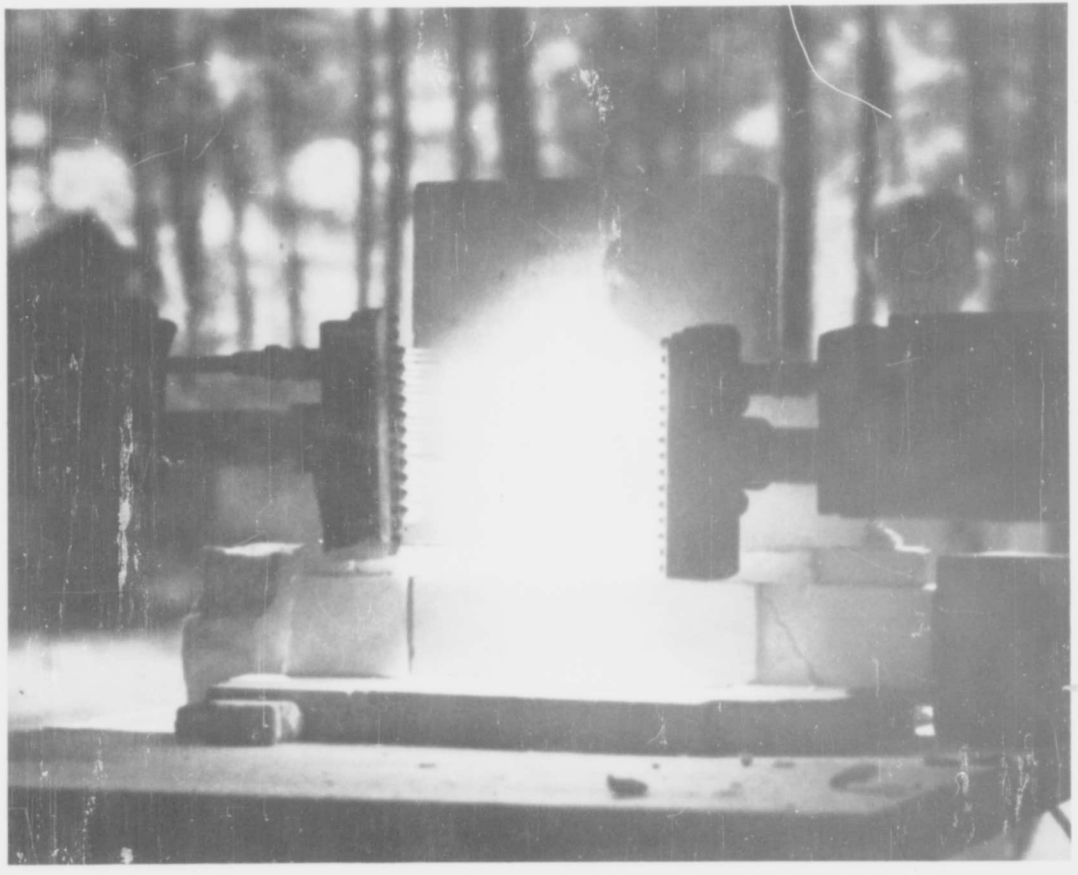

FIG. 12. ELEVATED TEMPERATURE TRANSMISSION TEST--
CERAMIC ANTENNA WINDOW

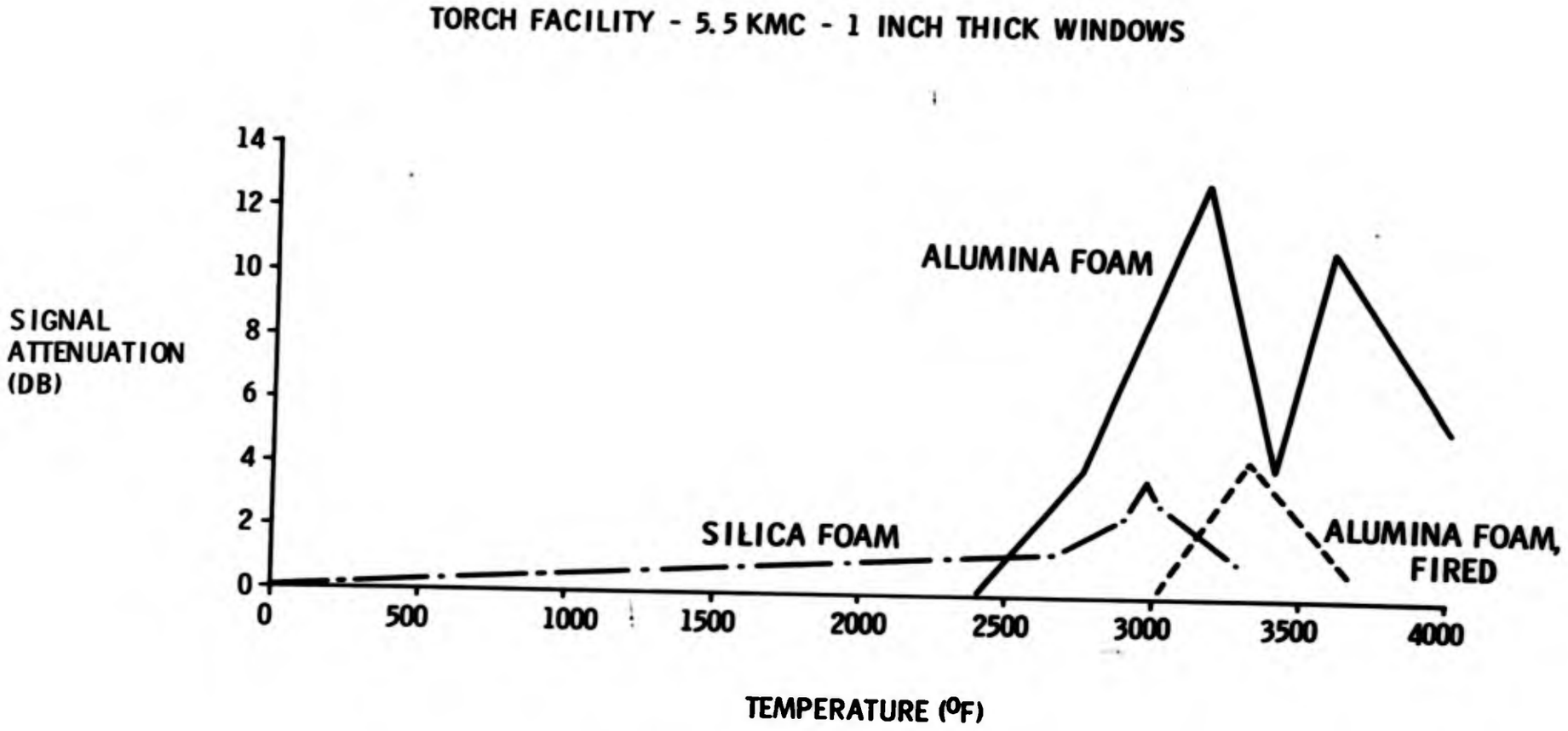

FIG. 13. ANTENNA WINDOW ATTENUATION

THE
REFLECTARRAY ANTENNA
SYSTEM

by

R. G. Malech

D. G. Berry

W. A. Kennedy

DORNE & MARGOLIN, Inc.
AEROSPACE Division
9730 Cozycroft Avenue
Chatsworth, California

THE REFLECTARRAY ANTENNA SYSTEM

R. G. Malech,* D. G. Berry,** and
W. A. Kennedy**

INTRODUCTION

Large aperture antennas fall into one of two general categories: reflectors based on geometrical optics, and arrays composed of a large number of radiating elements whose amplitude and phase can be individually controlled. Each of these systems possesses distinct advantages over the other, some of which are listed in Figure 1.

	REFLECTORS	ARRAYS
1	SHAPED SURFACE	FLAT OR CURVED SURFACE
2	LESS EXPENSIVE	MUCH MORE EXPENSIVE
3	ONLY ONE BEAM	MANY BEAMS
4	SCAN ONLY BY MECHANICAL MEANS	ELECTRONIC SCANNING
5	NO SIDE LOBE OR BEAM SHAPE CONTROL	HAS SIDE LOBE AND BEAM SHAPE CONTROL
6	CAN USE ONLY FEED RECEIVERS	CAN USE UP TO ONE RECEIVER PER ELEMENT
7	SUFFERS FROM APERTURE BLOCK	NO APERTURE BLOCK
8	IS WELL SUITED FOR VERY LARGE APERTURES	LINE LOSSES BECOME EXCESSIVE FOR VERY LARGE ARRAYS
9	USES STANDARD PERIPHERAL EQUIPMENT	PERIPHERAL EQUIPMENT MUST BE OF SPECIAL FORM FACTOR

Figure 1. Comparison of Advantages and Disadvantages of Reflectors and Arrays

The major advantage of reflector systems is simplicity. A single RF feed is utilized with the rest of the antenna being passive. Arrays are much more complex, having extensive corporate feed systems and the losses associated with them. Much more control of the radiation

*Dorne & Margolin, Inc., Special Devices Department, Westbury, N.Y.
**Dorne & Margolin, Inc., Aerospace Division, Chatsworth, California

pattern can be achieved, of course, using the array technique. The subject of this paper, the Reflectarray antenna, is a third class of aperture antennas combining the advantage of simplicity of the reflector with some of the control of the array.

The Reflectarray consists of an array of radiating elements illuminated by a primary feed. The elements may be any of a number of simple radiators such as dipoles, spirals or waveguides. In the transmission system of each element can be place a phase shifter and/or an attenuator as shown schematically in Figure 2. (Figure 4 is a photograph of an experimental model of the Reflectarray using waveguides as radiating elements.)

The energy radiated by the primary feed illuminates the array of elements and enters their transmission system, passes through any phase shifting and attenuating devices that may be placed in them, is reflected by a short circuit and re-radiated in the direction from which it came. The phase and amplitude of the re-radiated field with respect to the incident field depends, of course, on the path that it has traveled in

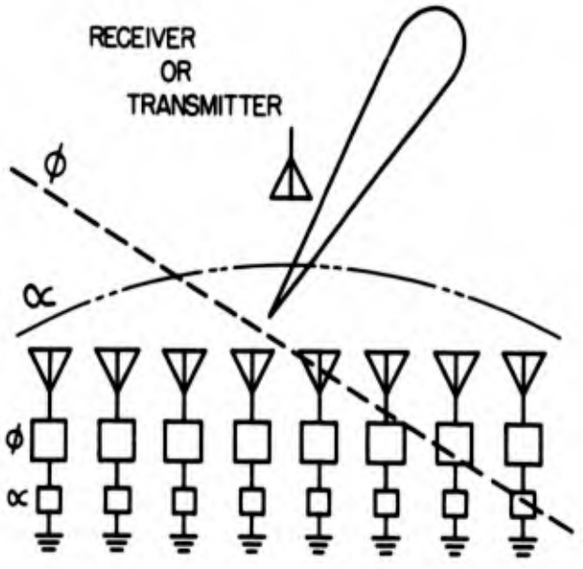

SYMBOL	MEANING
ϕ	ELECTRONICALLY CONTROLLED RF PHASE SHIFTER
∝	ELECTRONICALLY CONTROLLED RF AMPLITUDE ATTENUATOR
⏚	SHORTING (REFLECTING) PLATE

Figure 2. Schematic Representation of Reflectarray Principle

the transmission system and the nature of the devices that have been placed in this system.

The shape of the phase front emerging from the Reflectarray is determined by the electrical path length in each of the element transmission systems and can be chosen arbitrarily. Control of the side lobes can be achieved by attenuators in each of the elements, although their use is by no means necessary, and attenuators were not used to achieve the results of the experimental program that will be described later.

As an example, assume that the phase shifters are set to convert a plane phase front to a circular phase front. The primary feed is then placed at the focus and the system is now operating in the same manner as a parabolic reflector and feed. Several advantages are immediately apparent.

1. The phase shifters need only be set to within a few electrical degrees, thereby obviating the need for close tolerance control in the construction.
2. The amplitude attenuators, if used, can be set to minimize the beamwidth-side lobe product, or to produce any other desired beam shape.
3. The amplitude and phase fronts can be set to produce the desired beam shape in each plane independent of the other.
4. As the target moves, the phase front can be changed from parabolic (which focuses an infinite point at the feed) to an elliptical front (which will focus the target at the feed).
5. If electronic phase shifters and amplitude attenuators are used (ferrites, ferroelectrics, or diode switches) the phase front and beam shape can be continuously, rapidly, and accurately controlled.
6. The Reflectarray can be used to replace either a reflecting dish or an array. Also, time-share dish-array operation can be achieved. Figure 3 shows how two separate systems may simultaneously share the same Reflectarray; one using the reflected beam, one the direct beam.

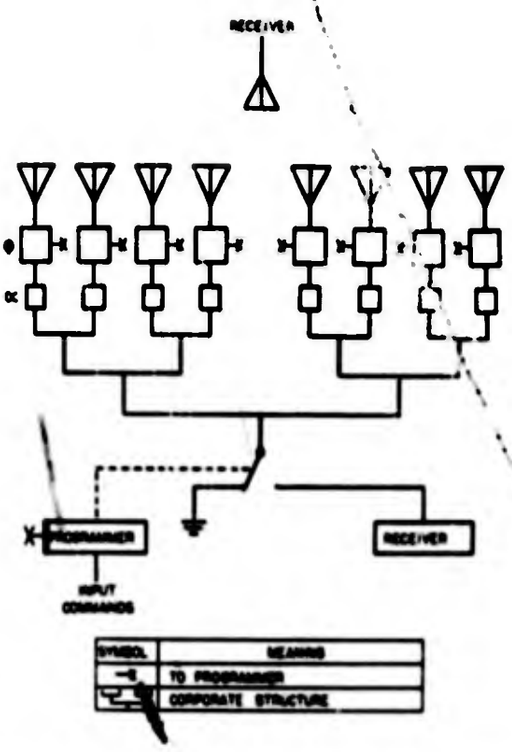

Figure 3. Reflectarray as both a Reflector and an Array on a Time Share Basis

The following sections give the results of an experimental program designed to verify the feasibility of the Reflectarray. Applications in which the Reflectarray would prove useful are also discussed.

EXPERIMENTAL INVESTIGATION

In order to verify the general Reflectarray principle and investigate its electrical properties,* the array illustrated in Figure 4 was constructed. The antenna consists of a 26 x 4 array of open-ended waveguides, each waveguide being approximately 0.6λ square at the operating frequency. The overall size of array is 27-1/2" x 4". An offset feed arrangement was employed to minimize aperture blocking from the primary feed. The feed was adjusted to give approximately a 10 db edge illumination taper for the array and the phase of the re-radiated signal from each element was established by the placement of shorting plates

*The electrical properties studies are beamwidth, bandwidth, aperture efficiencies, side lobe level and phase control technique.

Figure 4. Experimental Model of Reflectarray

in each element. A design frequency of 7080 Mcs was chosen to yield as large a scan angle as possible consistent with the requirement for the existence of the fundamental mode in the waveguide elements.

The resulting E- and H-plane patterns for the in-phase or maximum gain condition is shown in Figure 5. Also shown is a calculated H-plane pattern. The effect of interface reflections are not included in theoretical calculations and hence, the side lobe lavels are not directly comparable.* In general, though, the theoretical and measured patterns are in close agreement.

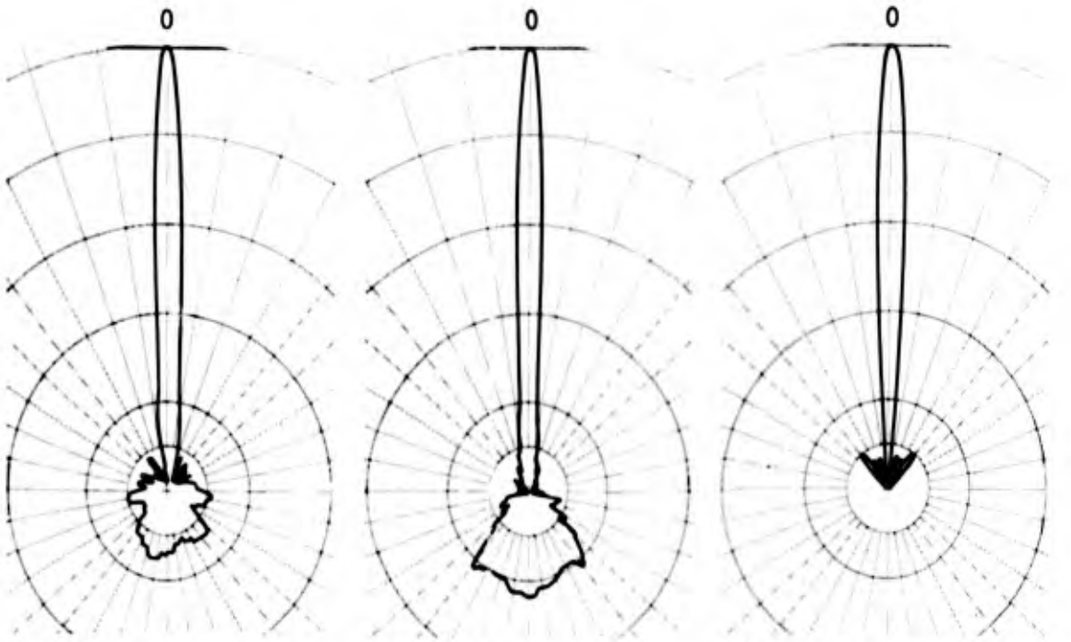

(a) As E-plane Array (b) As H-plane Array (c) Theoretical H-plane Array Pattern

Figure 5. Experimental Reflectarray Voltage Patterns, High-Gain Mode, (a) As E-plane Array, (b) As H-plane Array, and (c) Theoretical H-plane Array Patterns

The patterns shown in Figure 6 are representative of the scanning ability of the array. The increase in beamwidth with scan angle results from a decrease in the effective aperture of the array. Excluding scan

*The back lobes evident in the measured patterns, result from the restricted aperture in the vertical plane of the experimental model.

angles that approach end fire conditions, the effective aperture of the array varies approximately as the cosine of the scan angle.

Because the array spacing is 0.6λ the pattern at a scan angle of 45 degrees has a grating lobe. The maximum scan angle possible before grating lobes appear may be increased by reducing the array spacing. However, for a waveguide array, the minimum spacing is limited by the cut-off of the guide. If the waveguide element is loaded, a smaller spacing can be achieved, but the interface mismatch increases. Another solution to this problem is a staggered arrangement. This was accom-

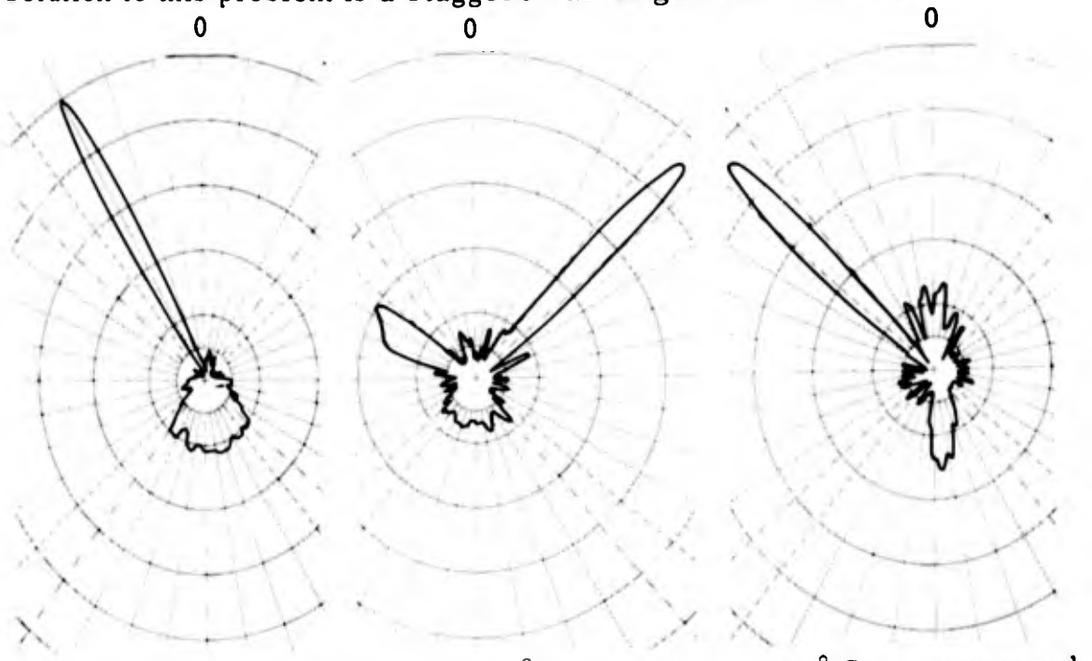

(a) 30° Scan (b) 45° Scan (c) 45° Scan, staggered element arrangement (0.75λ spacing)

Figure 6. Experimental Reflectarray Radiation Patterns for Scanning Modes as H-plane Array (0.6λ spacing), (a) 30° Scan, (b) 45° Scan, and (c) 45° Scan, staggered element arrangement (0.75λ spacing)

plished by shifting the elements in every other row of the array by one-half of their width in a brickwork pattern as shown in Figure 7. The apparent array spacing is 3/8λ while the actual spacing in each row is 3/4λ. Figure 6C illustrates the 45 degree scanned beam in the horizontal place from this array. The increased side lobes are due largely to the thick walls of the waveguides used in this array.

Reflections at the interface of the array result from the finite walls of the waveguide elements and any mismatch between the free space wave impedance and the guided wave impedance. The waveguide dimensions

determine the wave impedance match and, hence may be predicted by guide wave theory.

An indication of the reflection from the finite walls of the waveguide elements was obtained by comparing the pattern results from the array of Figure 4 with that of an array similar to Figure 7. Although the elements of the array in Figure 7 are shown to be staggered, for the purposes of this test, the elements were arranged in a non-staggered fashion. The thicker walls of this array represented 35 percent of the

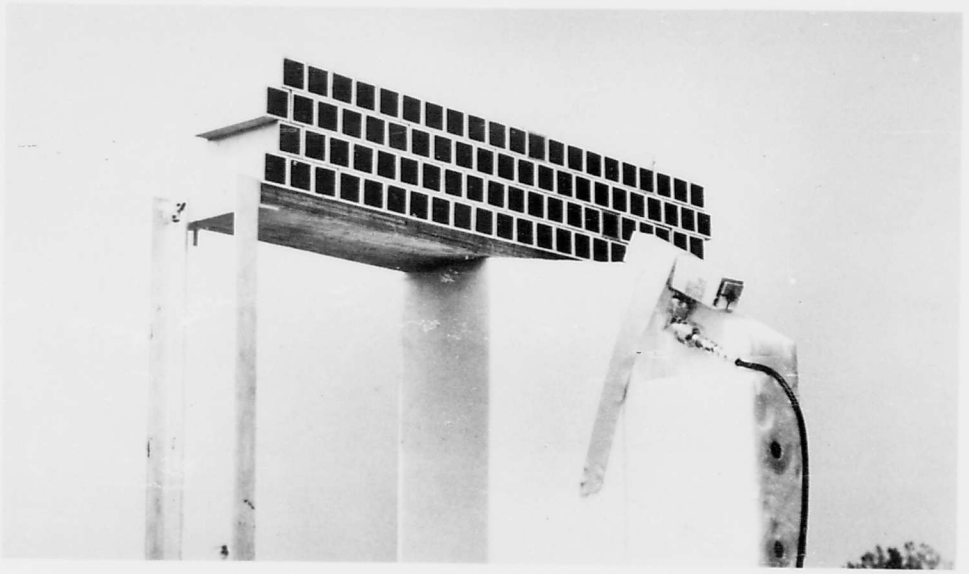

Figure 7. Experimental Reflectarray Model, 22 x 4 Array, 0.75λ element spacing

total aperture as compared to 6 percent for the array of Figure 4. Figure 8 illustrates the patterns and by comparing these results with that of Figure 5, it is noted that the side lobe level increased an appreciable amount.

The staggered element arrangement mentioned earlier also provides a means of reducing the side lobe level. Comparison of pattern measurements for the staggered and non-staggered conditions of Figure 8 indicates an additional improvement for staggered arrangement. The above measurements were made with the model shown in Figure 7.

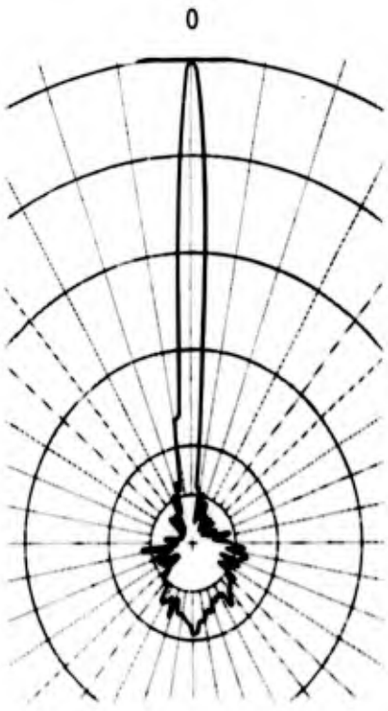

(a) As E-plane array non-staggered

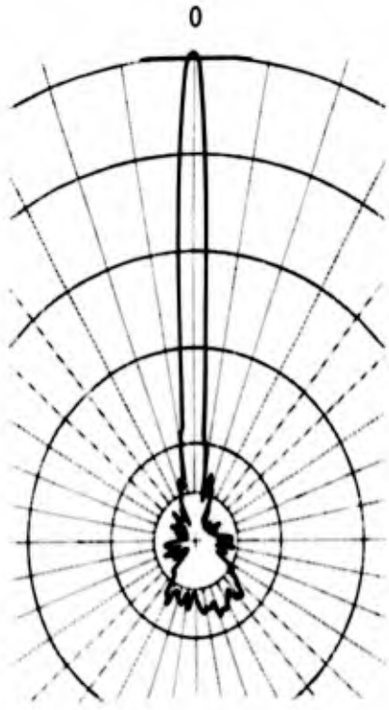

(b) As H-plane array non-staggered

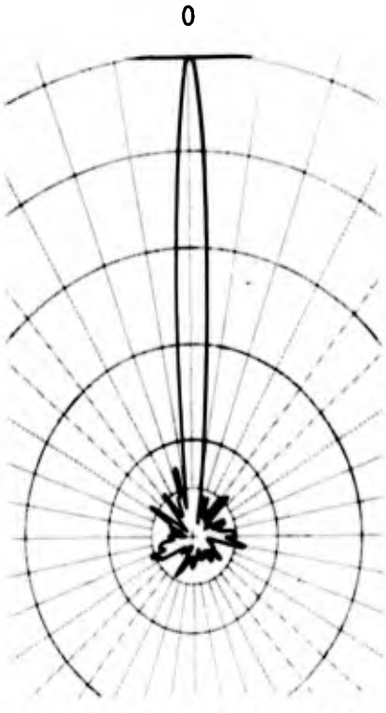

(c) As E-plane array staggered

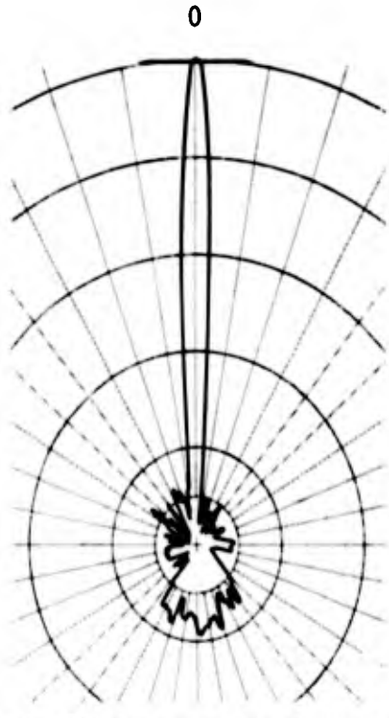

(d) As H-plane array staggered

Figure 8. Experimental Reflectarray Radiation Patterns for 0.75λ spacing for both non-staggered and staggered arrangements: (a) As E-plane array non-staggered, (b) As H-plane array non-staggered, (c) As E-plane array staggered, (d) As H-plane array staggered

Beam broadening is accomplished by adjusting the phase of the radiated signal from each element to correspond to the phase of a hypothetical antenna located at a particular point behind the array. This image feed antenna is placed such as to yield a 10 db edge illumination taper at the face of the array. The phase delay from such an image source, relative to the array center, will increase as the cosine of the subtended angle. A diagram of this arrangement is shown in Figure 9. When the phase of the re-radiated signal from each element is delayed as indicated above, the pattern characteristics of the Reflectarray resembles closely that assumed for the image feed antenna.

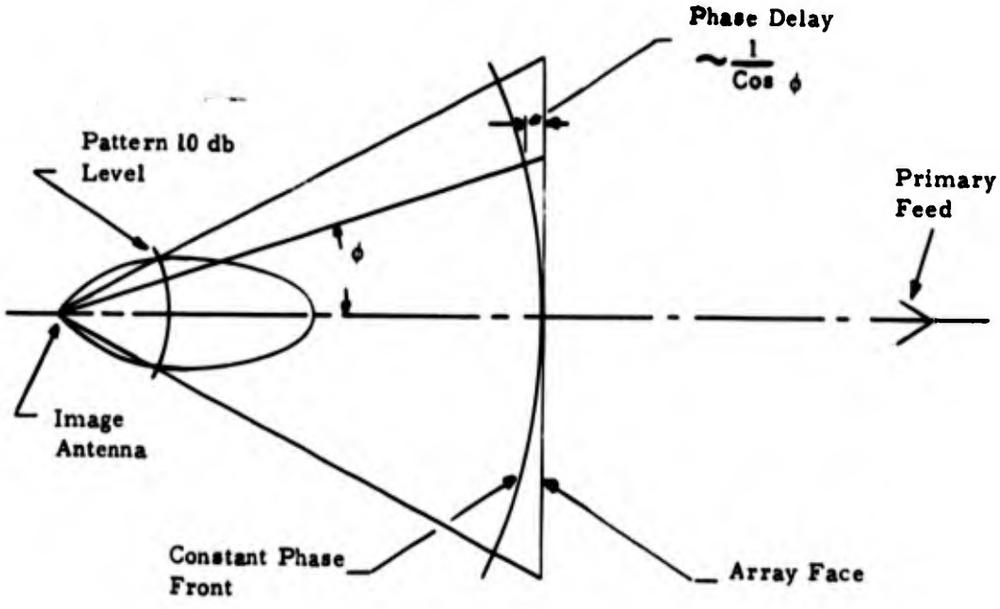

Figure 9. Phase Diagram for Broad Beam Mode Synthesis

Figure 10 illustrates the E- and H-plane array patterns synthesized from such an image antenna with a 23-degree half-power beamwidth. An H-plane calculated pattern is included for comparison. Both the theoretical and the measured pattern have greater directivity than the pattern from which the array was synthesized. This evidently is a result of diffraction from the individual apertures. The anomalies in the measured pattern for the medium gain condition result from reflections at the interface. A significant change in these anomalies (but not in the

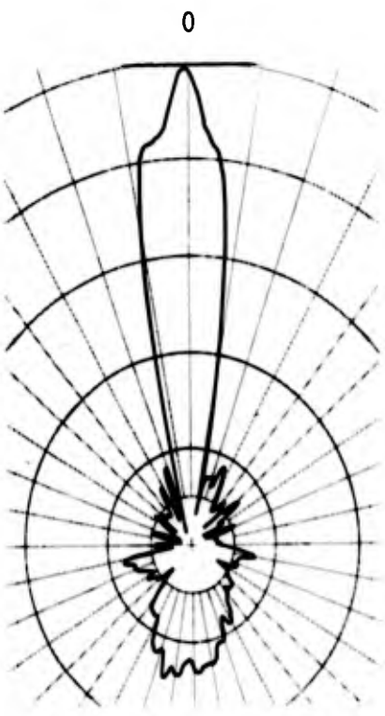

(a) As E-plane Array

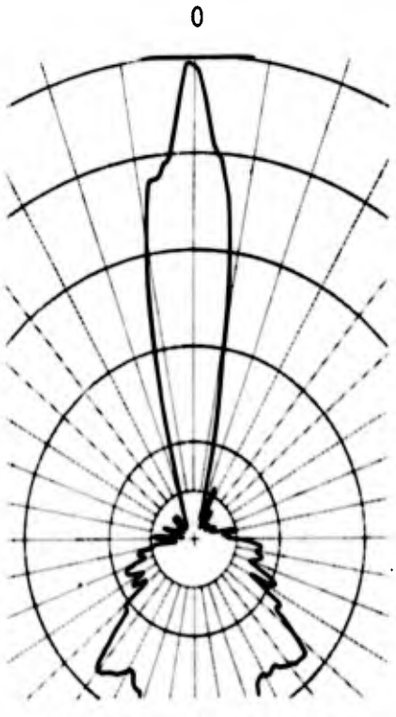

(b) As H-plane Array

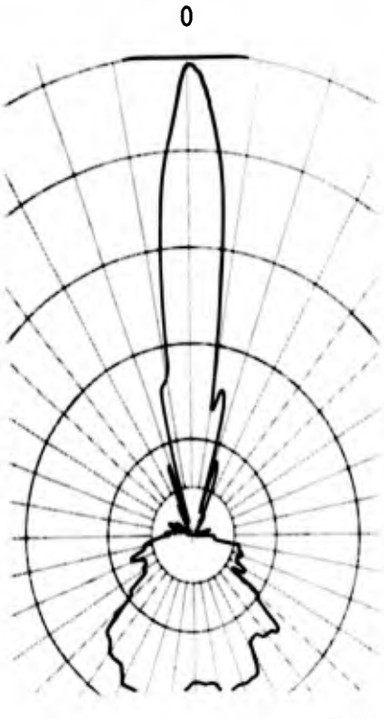

(c) As H-plane Array with Reflecting plane in elements shifted λ/4

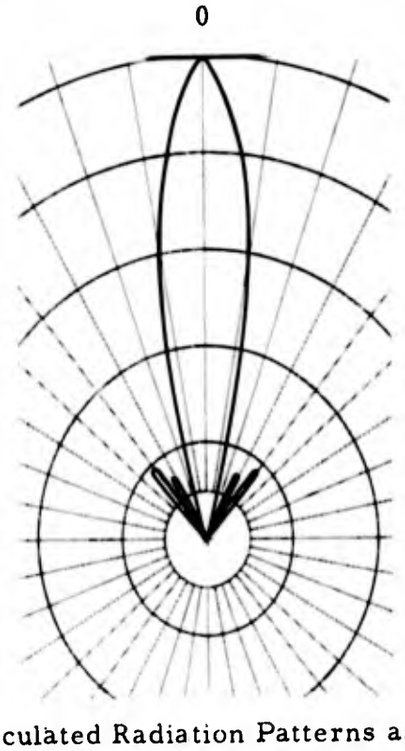

(d) Calculated Radiation Patterns as H-plane Array in Broad Beam Mode

Figure 10. Experimental Reflectarray Radiation Patterns for Broad Beam Mode, (a) As E-plane Array, (b) As H-plane Array, (c) As H-plane Array with Reflecting plane in elements shifted λ/4, and (d) Calculated Radiation Patterns as H-plane Array in Broad Beam Mode

general character of the pattern) was observed when the effective reflecting plane in the elements was shifted $\lambda/4$ with respect to the interface. This is illustrated by Figure 10C. This results because the phase of the reflected signal from the interface remains unchanged while the phase of the re-radiated signal depends on the position of the reflecting shorts. This shift of the reflecting shorts does not effect the formation of the beam since it depends on the relative phase between the waveguide elements. By proper choice then, of the reflecting surface with respect to the interface, it is possible to provide a component of the re-radiated signal out of phase with interface field to give cancellation.

The amount of the beam may be broadened without the side lobe level increasing beyond a reasonable value is dependent to some extent on the interface reflections. As may be noted, the beam was broadened approximately 4 beamwidths with good results. Further improvement in the side lobe level could be realized by a reduction of the interface reflection.* If one assumes a perfect interface (no reflection), the amount the beam may be broadened still has a practical limit. This results because a beam produced from a larger than necessary aperture requires storage of energy in the aperture much in the same way energy is stored in a supergained array.

In order to have a rapidly scannable beam, the method of phase change must be simple and practical. A metallic short, of course, provides a satisfactory reflection in the guide, but is difficult to re-position, particularly in a rapidly varying manner.

Considerable improvement in the speed of re-positioning the reflecting short of each element results if one uses microwave diodes as shorts. The diodes are placed at discreet intervals and the proper diode biased to give the required phase. The number of diodes employed determines the increment of phase change available. The patterns

*It should be noted that had the array been full size in the vertical plane, the increased gain would reduce the effect of interface reflections by approximately 8 db.

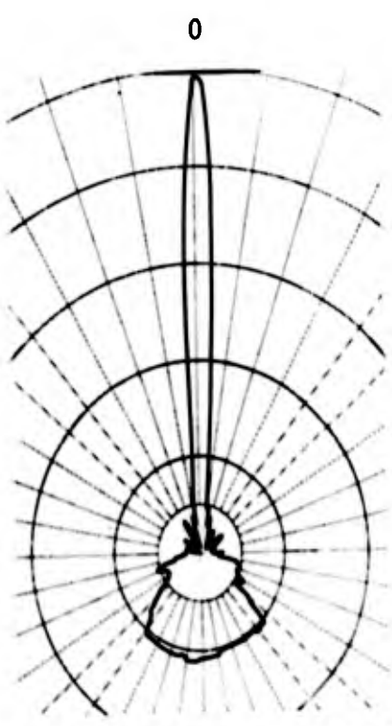

(a) Maximum Phase Error ±22.5°

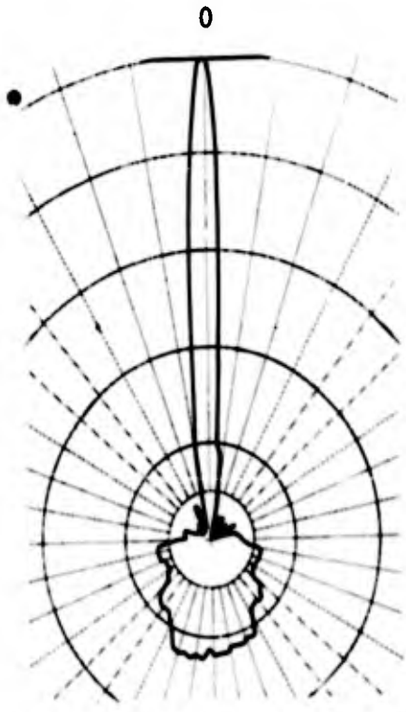

(b) Maximum Phase Error ±30°

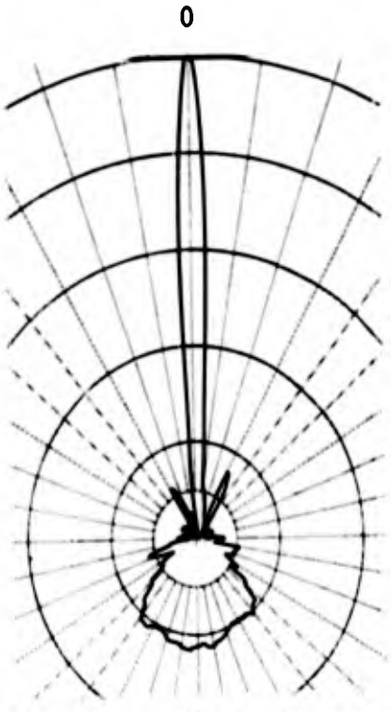

(c) Maximum Phase Error ±45°

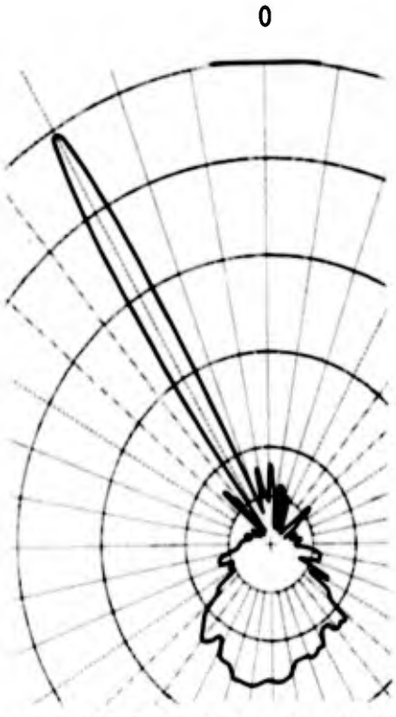

(d) In 30° Scan Mode for Maximum Phase Error of ±45°

Figure 11. Experimental Reflectarray Radiation Patterns for Discreet Phase Settings of Element Reflecting Shorts, (a) Maximum Phase Error ±22.5°, (b) Maximum Phase Error ±30°, (c) Maximum Phase Error ±45°, and (d) In 30° Scan Mode for Maximum Phase Error of ±45°

shown in Figure 11 illustrate how the directivity varies for phase increments of 22.5 degrees, 30 degrees, and 45 degrees. For the case of 45 degree phase increment the side lobe level has increased to a level of -16 db. Actually, for the 30 degree increment condition there is an improvement over the exact phase condition due to a cancelling effect with the interface reflection. In a full scale array it is expected that the degradation will be much less than that illustrated. Figure 11d shows a scanned beam at 30 degrees employing four short positions. Published data indicates that switching times of three nanoseconds are possible with microwave diodes. Preliminary study has also shown that the total RF system loss due to the diodes will be slightly over 1 db.*

The maximum operating bandwidth depends on the allowable degradation for a particular application. Measurements indicate that a 16 percent bandwidth will result in a gain reduction of approximately 1.5 db at the band edges. One requirement for securing maximum bandwidth is to zone the reflecting planes in the array. The above quoted bandwidth is that attainable without re-phasing of the array. When establishment of new phase condition is allowed, the bandwidth would be limited only by the bandwidth of the individual elements and the primary feed.

For certain system applications, such as monopulse work, it is necessary to have a well-defined phase center. The array's phase center properties were determined on a theoretical basis from the pattern calculation data. It was found that the phase center is well defined for all aperture phase properties that can be specified by some spherical wave front, and corresponds to the point behind the array assumed for the image antenna.

The aperture efficiency of the array was determined by measuring the gain of the array. Aperture efficiencies greater than 55 percent were realized after correction for the spillover in the vertical plane.

---

*Dorne & Margolin, Inc., Interim Engineering Report, Project 9008, August 1962.

In a full scale array this efficiency would correspond that normally realizable from the more conventional passive reflectors of the same aperture size.

Polarization properties of the Reflectarray are determined entirely by the primary feed. For orthogonal linear or circular polarization, symmetrical array elements must be employed as well as additional phasing circuitry.

USES

The Reflectarray concept lends itself to a variety of uses. Since it is an array and also a reflector it encompasses most applications where a microwave optical antenna is required. Rather than list these quasi-standard uses, some newer ideas employing the Reflectarray concept are given:

1. Conical scanning, lobe-on-receive-only, etc., can be accomplished with a Reflectarray by either using a standard feed tracker (as is used presently with reflectors) or by phasing the array properly. In some instances the feed and the array can be varied with time to produce many modes of operation.
2. The Reflectarray principle can be applied to Cassegrain optics by making the secondary mirror (the hyperbola) from Reflectarray elements. The primary parabolic surface may or may not be a Reflectarray. By electronically controlling the phase shift (and/or amplitude taper) over the hyperbolic Reflectarray, optimum phase and amplitude fronts can be achieved.
3. Reflectarray elements arranged in the form of a sphere can be used as a pseudo-omnidirectional echo enhancer. In such a device the short positions would be programmed in such a fashion as to always return a directional beam towards the transmitter. It would have the additional advantage of being easily "spoiled" for an unwanted signal.
4. The Reflectarray concept should be considered in all cases where the antenna must "hug" or wrap around an odd contour. A spaceborne Reflectarray could be wrapped partially around a

satellite with only the feed extending. A large ground installation for zenith coverage could be built directly over small hills and valleys. Appropriate settings of the phase shifters would compensate for the uneven contours.

5. The Reflectarray can be used for bi-directional high gain coverage on a time-sharing basis. The forward sector is covered using Reflectarray techniques as discussed in this paper. Rear coverage is achieved by removing all of the shorts. In this mode, the waveguide "egg-crate" array acts as a simple waveguide lens. Scanning can be performed in this mode also.
6. When the Reflectarray is used with certain continuous rather than discreet phase shifters, only half the amount required by a standard array need be used. This is so because the signal passes through each phase shifter twice.
7. The changeable beamwidth property of the Reflectarray can be utilized in tracking. The wide beam mode can be used for search and the narrow beam mode used after acquisition.

CONCLUSIONS

The performance of the arrays investigated indicate that it is possible to use the Reflectarray principle to produce rapidly scannable beams in a multiplicity of modes. Aperture efficiencies and side lobe levels follow closely that attainable from other passive reflector systems. The relative simplicity of the diode phasing systems proposed makes the Reflectarray adaptable to systems where weight must be kept to an absolute minimum. In many applications, the shape of the Reflectarray could be made to conform to the contour of its vehicle. This, for instance, is advantageous for satellite systems.

In the scanned beam modes, scan angles of ±45 degrees are easily realized. By establishing a phase condition corresponding to a predetermined spherical wave front, medium gain or broad-beam modes may be synthesized. Pattern measurements indicate that exact phase control is not necessary to produce a given pattern and, in fact, an improvement in side lobe levels was found when a random phase error was

introduced. Random phase errors up to 45 degrees do not seriously degrade the performance of the Reflectarray.

The basic advantage of the Reflectarray is that of simplicity. A large number of modes can be produced without alteration of the RF system. Corporate feed systems, in the usual sense, are unnecessary.

ANGULAR ERROR DUE TO NOISE

FOR A

SIMPLE VEHICLE TRACKING INTERFEROMETER

By

D. G. Henry and R. H. Duncan

August 1962

Physical Science Laboratory
New Mexico State University
Box 548
University Park, New Mexico

ANGULAR ERROR DUE TO NOISE FOR A SIMPLE VEHICLE TRACKING INTERFEROMETER

D. G. Henry and R. H. Duncan

ABSTRACT

The Physical Science Laboratory at New Mexico State University has conducted a feasibility study for the National Aeronautics and Space Administration on a high frequency precision satellite tracking system. As a part of this study an optimum frequency was chosen from a band of allowable frequencies and an analysis of the error due to noise on an interferometer was made.

The optimum frequency selection was a function of various atmospheric phenomena. These phenomena included cosmic, solar, and atmospheric noise. Refraction and loss also played an important part in this frequency selection. The presence of noise at all frequencies gave rise to the question of the effects of this noise on the accuracy of a simple interferometer.

The effect of the noise on the angular accuracy of an interferometer was determined by first assuming that the noise was purely random and uncorrelated between antennas. A single antenna was then taken and the effect of noise on the phase of the incoming signal was obtained. The phase uncertainty is then combined from the two antennas of the interferometer and a standard deviation of the angular measurement of the system is derived.

This standard deviation is a function of S/N ratio and interferometer spacing.

The end result of this analysis is to get a design tool from which the acceptable S/N ratio can be determined for a given spacing between the interferometer elements.

Curves of standard deviation as a function of S/N and interferometer spacing are given.

This work was done under Contract NAS 5-1032 - Task BVIII.

INTRODUCTION

The Physical Science Laboratory at New Mexico State University, University Park, New Mexico, has conducted a feasibility study for the National Aeronautics and Space Administration on a high frequency precision satellite tracking system. This study included optimum frequency selection in the 0.4 to 8.5 Gc/sec region and analysis of error due to noise.

The paper is presented in two parts. The first part deals with the frequency selection and the second part deals with the analysis of the error due to noise present in an interferometer system.

PART I - FREQUENCY SELECTION

1.0 FREQUENCY ALLOCATION

At the I. T. U. Conference in Geneva in September 1959 various bands of frequencies were set aside for use in space communications. The frequencies for tracking were space bands three through seven. These frequencies are 400 to 401 Mc, 1427 to 1435 Mc, 1700 to 1710 Mc, 2290 to 2300 Mc, and 8400 to 8500 Mc. It is from these frequencies that an optimum frequency must be selected for the proposed tracking system.

To determine the optimum frequency such factors as cosmic noise, solar noise, atmospheric noise, refraction, atmospheric absorption, free space loss, and Faraday rotation were studied in relation to the above frequencies.

2.0 COSMIC NOISE

The cosmic noise or sky noise varies with sky position and inversely with the frequency squared. The Galatic center has the highest value with discrete sources at other angular positions of almost this magnitude. These discrete sources are of very small angular extent and with antenna beamwidths of a few degrees do not contributed appreciably to the overall noise power. A more useful way to express cosmic noise is by the absolute temperature as shown in Fig. I-1. Using the absolute temperature and the following relationship the noise power for any bandwidth may be found.

$$N = KTB \qquad (1)$$

where N = noise power in watts, K = Boltzman's constant = 1.38×10^{-23} watts-sec/°K, B = bandwidth of the receiver in cycles per second, and T = temperature in degrees Kelvin.

The sky noise temperature is averaged over the antenna beamwidth. For very narrow beamwidths the noise temperature may be twice that given in Fig. II-1. However, for antenna beamwidths of one degree or larger the noise temperature is very nearly that given by Fig. I-1.

The maximum value of the noise temperature should be taken when determining the system sensitivity as the Galatic center cannot be avoided.

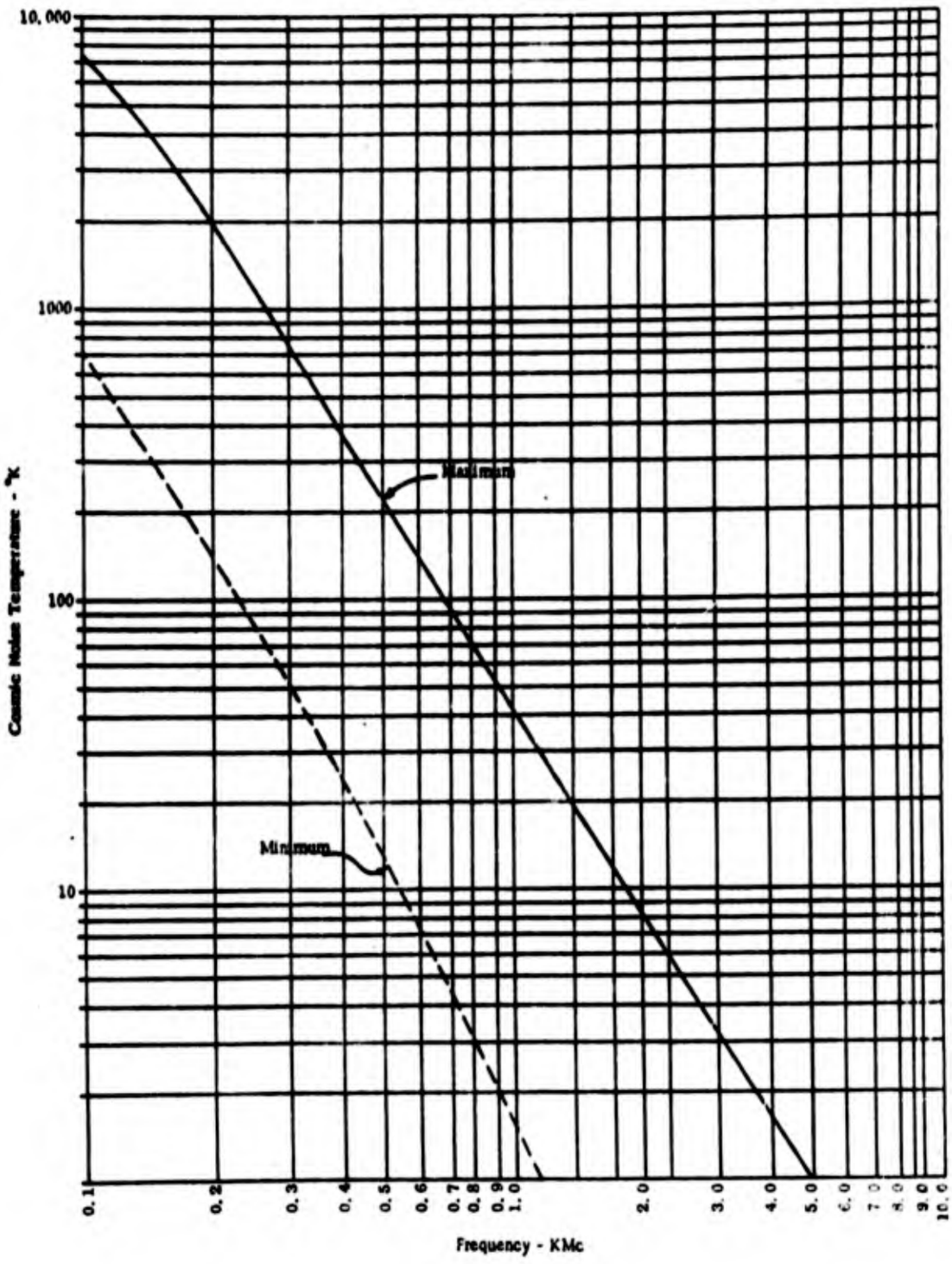

FIG. I-1 - COSMIC NOISE TEMPERATURE VERSUS FREQUENCY[3]

3.0 SOLAR NOISE

Solar noise temperature from a quiet sun may be approximated by

$$T_{sun} = \frac{195,750}{f} \qquad (2)$$

where f - frequency in K Mc, and T_{sun} - °K. This expression is valid from 400 to 10,000 Mc.

The angular extent of the sun at a radio emitter is approximately 0.5 degrees at the higher frequencies (400 to 10,000 Mc) and may approach 1.0 degree at the lower frequencies (60 - 100 Mc). If the antenna beamwidth is smaller than the angular extent of the sun the noise temperature will be that given by Eq. (2). If the beamwidth is larger than the sun the noise temperature is given by

$$T_a = T_{sun} \left(\frac{0.5}{\Phi}\right)^2 \qquad (3)$$

where $\Phi \geq 0.5°$ and is the antenna beamwidth. These values are for an antenna pointed directly at the sun. If the sun is not in the antenna beam it contributes very little noise.

The noise due to the sun cannot be avoided if the satellite passes between the sun and the tracking station. This is not serious for an antenna that tracks the satellite or one with a large beamwidth that is fixed in position. For space probes, if the trajectory goes too near the earth-sun line, the problem is more severe since the angular velocity of a space probe is much slower than that of a close-in satellite. The only method to minimize the effect of the sun is to choose trajectories removed from the sun as far as possible.

4.0 ATMOSPHERIC NOISE

Noise in the earth's atmosphere is due to absorption of radio waves by oxygen and water vapor. The total contribution to system noise depends upon the altitude of the receiving site, weather conditions, and the angle of the antenna beam to the horizon. This noise is also a function of frequency falling off rapidly below 1000 Mc and increasing rapidly above 10,000 Mc.

falling off rapidly below 1000 Mc and increasing rapidly above 10,000 Mc. (Fig. I-2). Between 5000 and 10,000 Mc the noise will vary considerably depending upon the local weather conditions. Representative values have been tabulated for 8.5 Gc for a sea level receiving site and a vertical beam path. (Table I) A heavy fog (100 foot visibility) could contribute approximately 10°K at 2000 Mc for a low angle beam path but effect of rain and oxygen absorption is negligible.

High altitude receiving sites reduce the amount of oxygen and water vapor content in the antenna beam path thus reducing the noise temperature. A 4 to 1 reduction in noise can be achieved for a vertical beam by locating the receiving site at an altitude of 14,000 feet.

5.0 ATMOSPHERIC REFRACTION

Radio waves passing through the atmosphere will undergo a refraction. This results in an error due to the angular difference between the apparent direction of arrival of radiation from the source and the true direction to the source. This refraction error can be broken into two parts, ionospheric and tropospheric.

5.1 Ionosphere

The index of refraction of the ionosphere varies inversely with the frequency squared and directly with the electron density. The resulting error is a function not only of the frequency and electron density but also the angle of the antenna beam to the horizon. This dependence is shown in Fig. I-3 for various angles and conditions. The electron density is a function of solar activity and time of day. From these variables it is seen that the ionospheric refraction error not only varies considerably but can also vary swiftly. Any correction made for ionospheric refraction will at best be only an approximation. The maximum error at 2300 Mc with no correction for the conditions given in Fig. I-3 will be approximately one second of arc for a satellite above 1000 kilometer altitude and at an angle of 25° above the horizon. Therefore with no correction the error could be on the order of magnitude of the desired accuracy and with a correction an order of magnitude less. With correction the ionospheric refraction will not mask the desired sensitivity of two to five seconds of arc.

5.2 Troposphere

The index of refraction of the troposphere is independent of frequency from 100 to 10,000 Mc, thus the refraction will be essentially a constant for a given altitude over the frequency range of interest. (Fig. I-4) Since this error is independent of frequency, this effect will not affect the frequency selection.

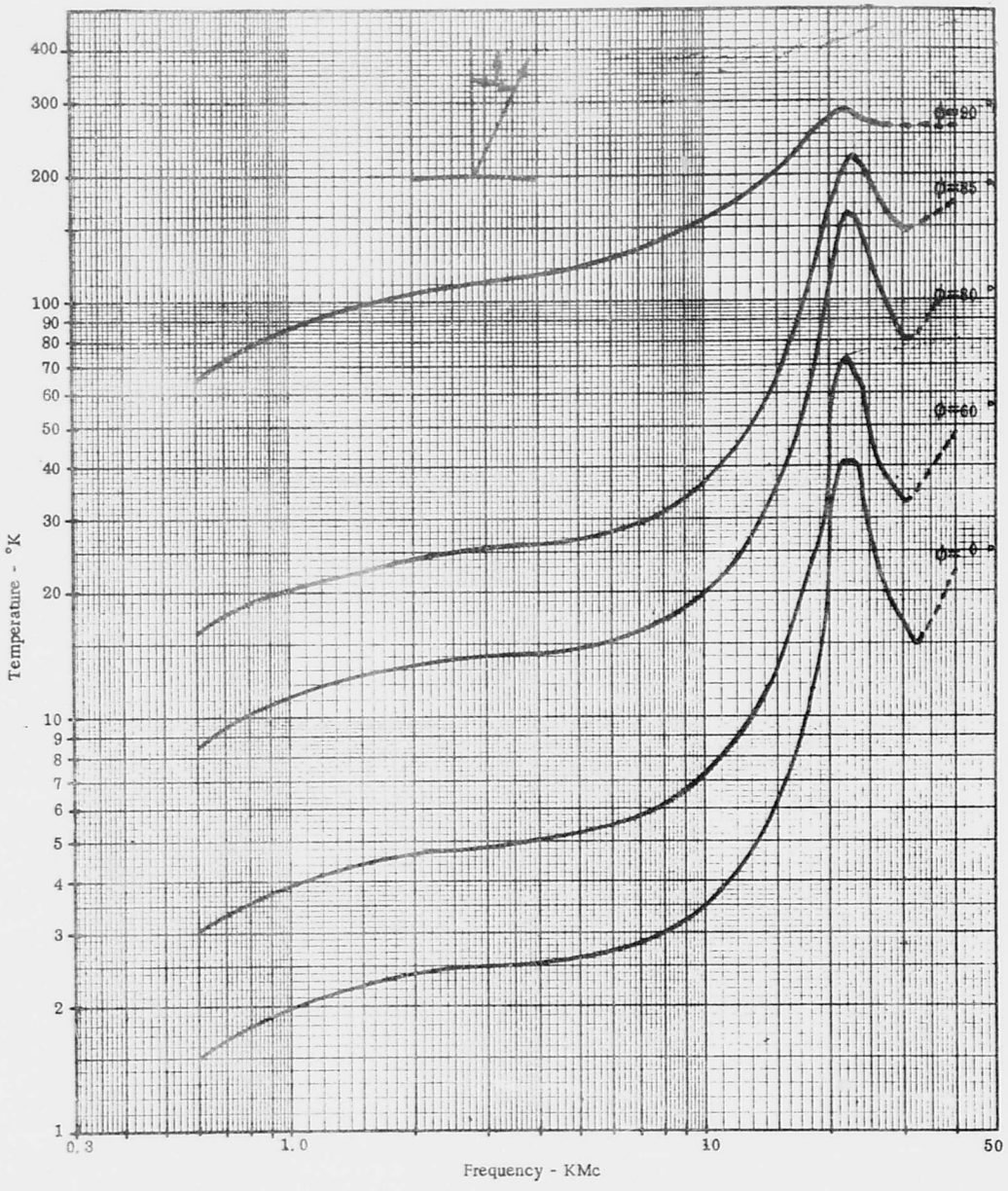

FIG. I-2 - ATMOSPHERIC NOISE TEMPERATURE VERSUS FREQUENCY[2]

TABLE I

Noise Temperature for Various Weather Conditions

Frequency	Weather Conditions	Noise Temperatures
8.5 K Mc	Heavy Rain (16 mm/hr)	80° K
	Moderate Rain (4 mm/hr)	15° K
	Light Rain (1 mm/hr)	4° K
	Fog (100 ft visibility, 2.3 gm/m^3)	30° K
	Fog (400 ft visibility, 0.32 gm/m^3)	5° K
	Saturated Troposphere	2° K

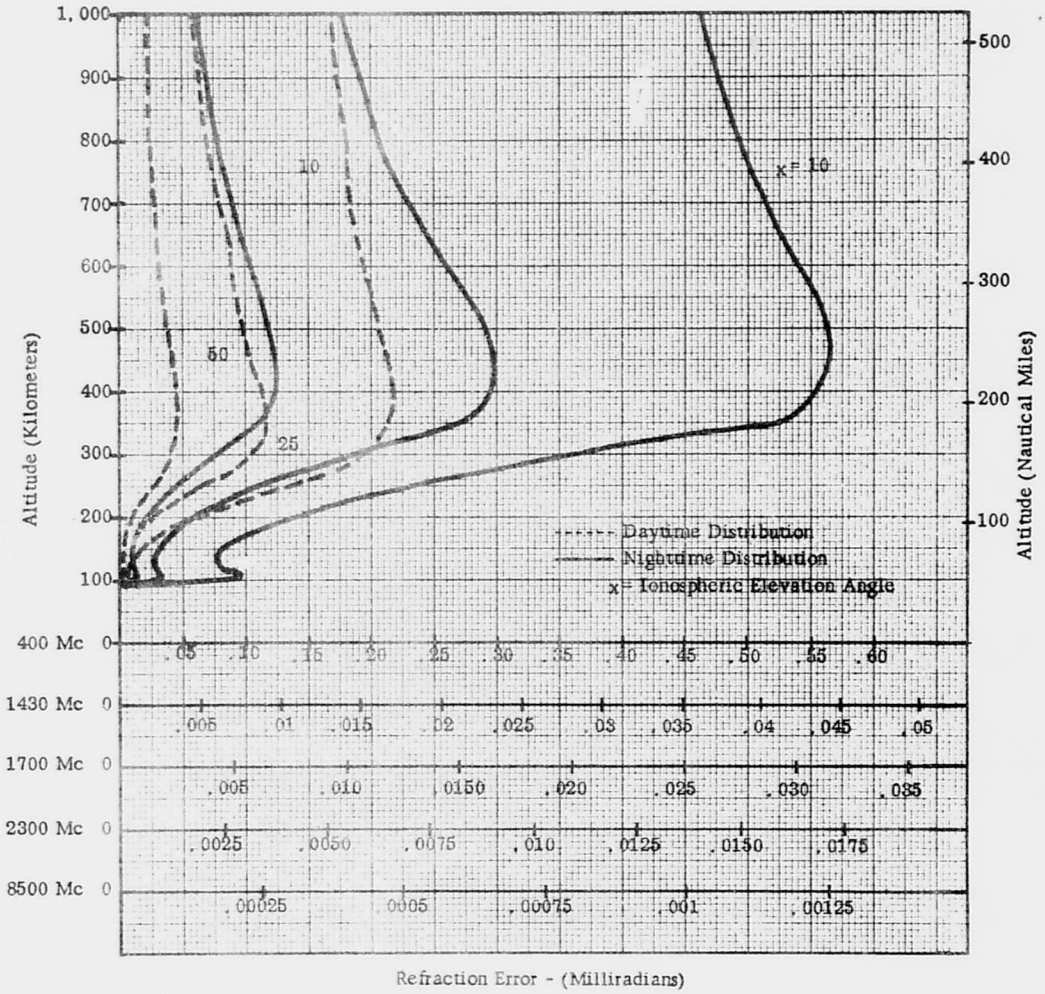

FIG. I-3 - IONOSPHERIC REFRACTION ERROR - DECAYING DISTRIBUTION OF ELECTRON DENSITY ABOVE F-LAYER MAXIMUM[5]

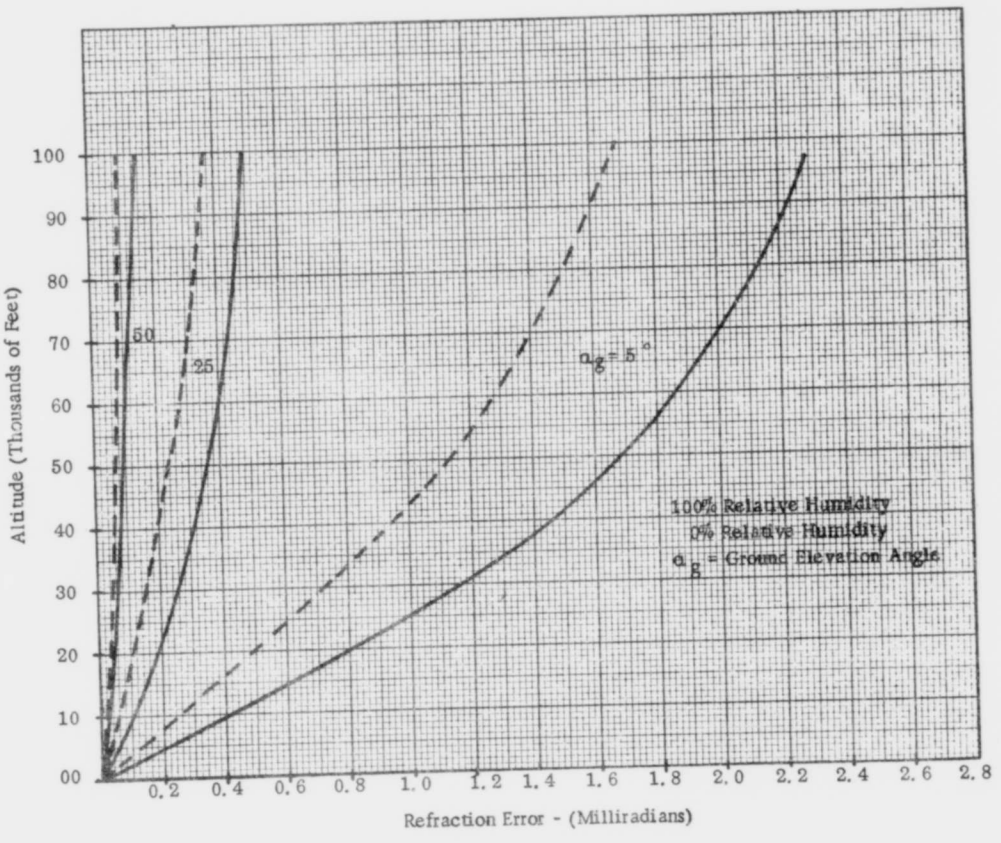

FIG. I-4 - TROPOSPHERIC REFRACTION ERRORS FOR A STANDARD ATMOSPHERE[5]

6.0 ABSORPTION

Atmospheric absorption or attenuation is a function of the oxygen and water vapor content. Since it is dependent on these two quantities absorption is also a function of local weather conditions and the angle of the antenna beam to the horizon. Curves for attenuation versus frequency for oxygen and water vapor are shown in Fig. I-5. These curves are for a sea level receiving site and saturated atmosphere.

If the receiving site is elevated the effect of the atmosphere can be reduced. Selection of a site where rainfall and humidity are very low can also reduce this atmospheric absorption.

7.0 FARADAY ROTATION

The plane of polarization of a radio wave is rotated by passing through the ionosphere. This effect varies inversely with the square of the frequency and directly with ionospheric electron density. It is also affected by the angle that the radio waves make with the earth's magnetic fields. (Fig. II-6 and Fig. I-7).

The Faraday effect causes fading when a linear receiving antenna is used, and for this reason circular polarization should be used on the satellite or on the ground. The use of circular polarization at either the receiver or the transmitter, and linear at the other, will cause a system loss of 3 db. The choice of the system frequency is not a function of the Faraday effect since the 3 db loss is the same for all frequencies.

8.0 FREE SPACE LOSS

The free space loss between a receiver and a transmitter is given by

$$\text{Space Loss} = \lambda^2/(4\pi R)^2 \qquad (4)$$

where λ is the wavelength and R is the range. The wavelength and the range must be in the same units. Figure II-8 gives curves for the space loss for the frequencies under consideration. The free space loss is added to atmospheric losses to obtain a total loss between the two antennas. This total loss then is used to determine power requirements and gain of the receiving and transmitting antennas.

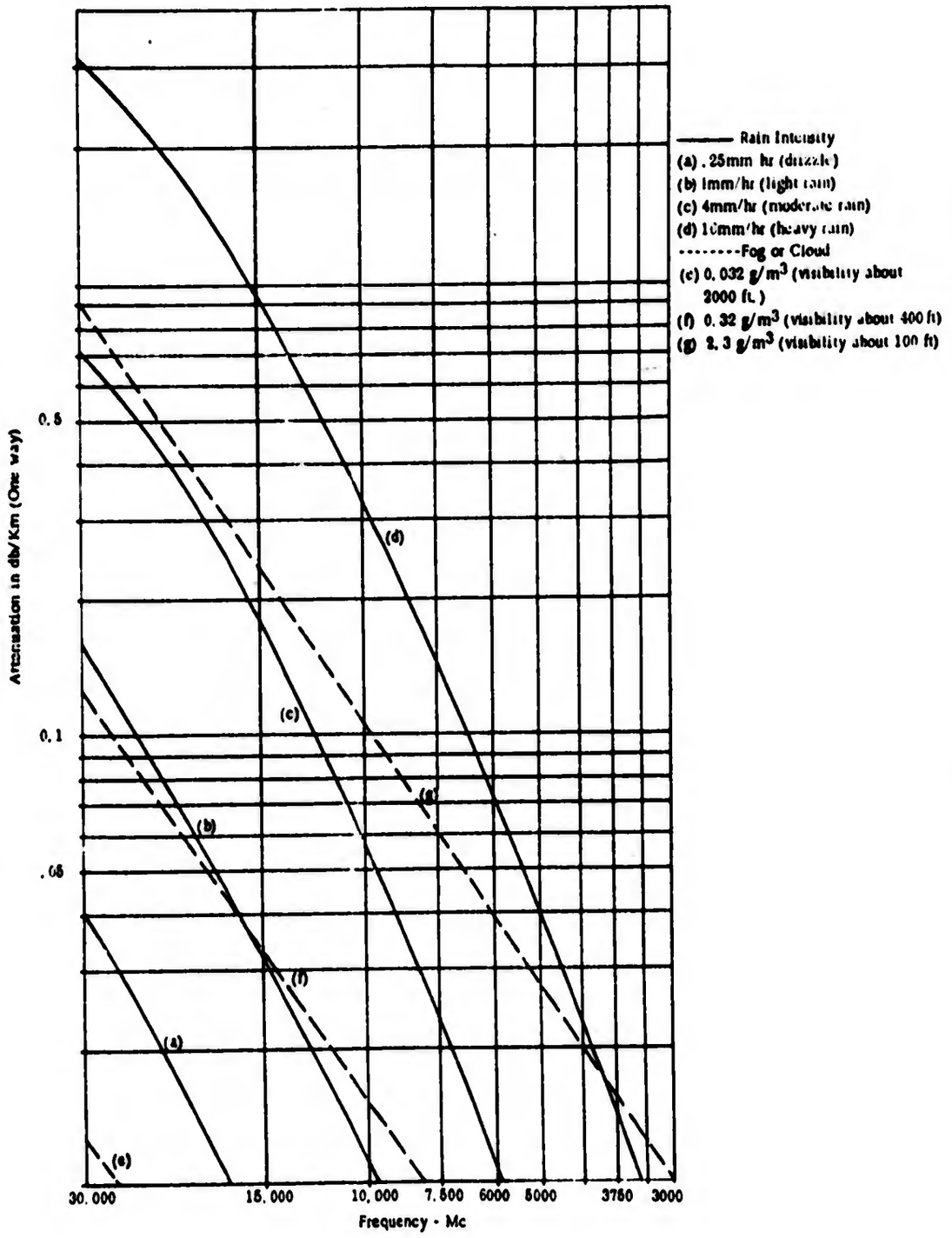

FIG. 1-5 - ATTENUATION DUE TO OXYGEN AND VAPOR VERSUS FREQUENCY[9]

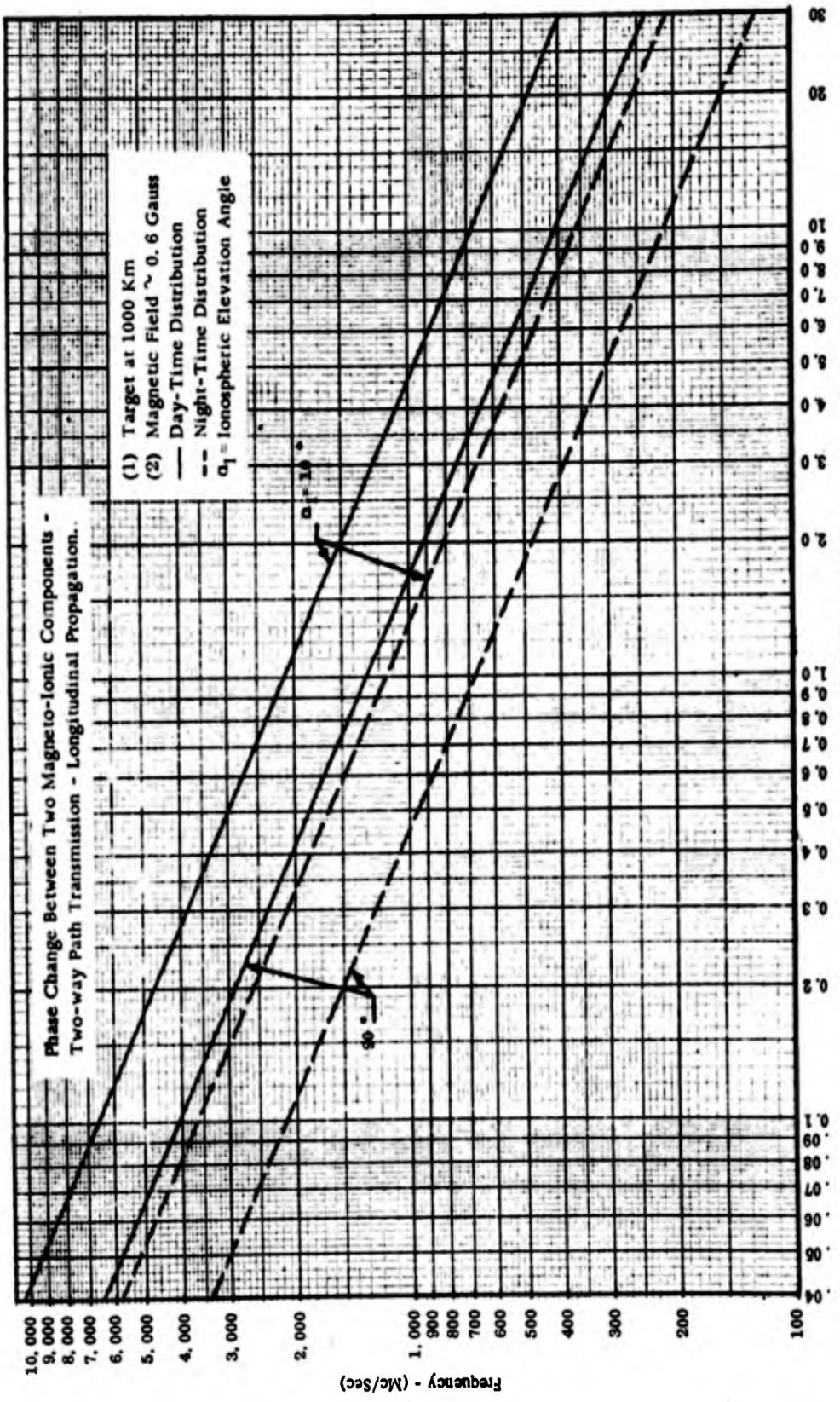

FIG. 1-6 - FARADAY ROTATION FOR RADIO WAVE PARALLEL TO EARTH MAGNETIC FIELD - TWO WAY PATH[5]

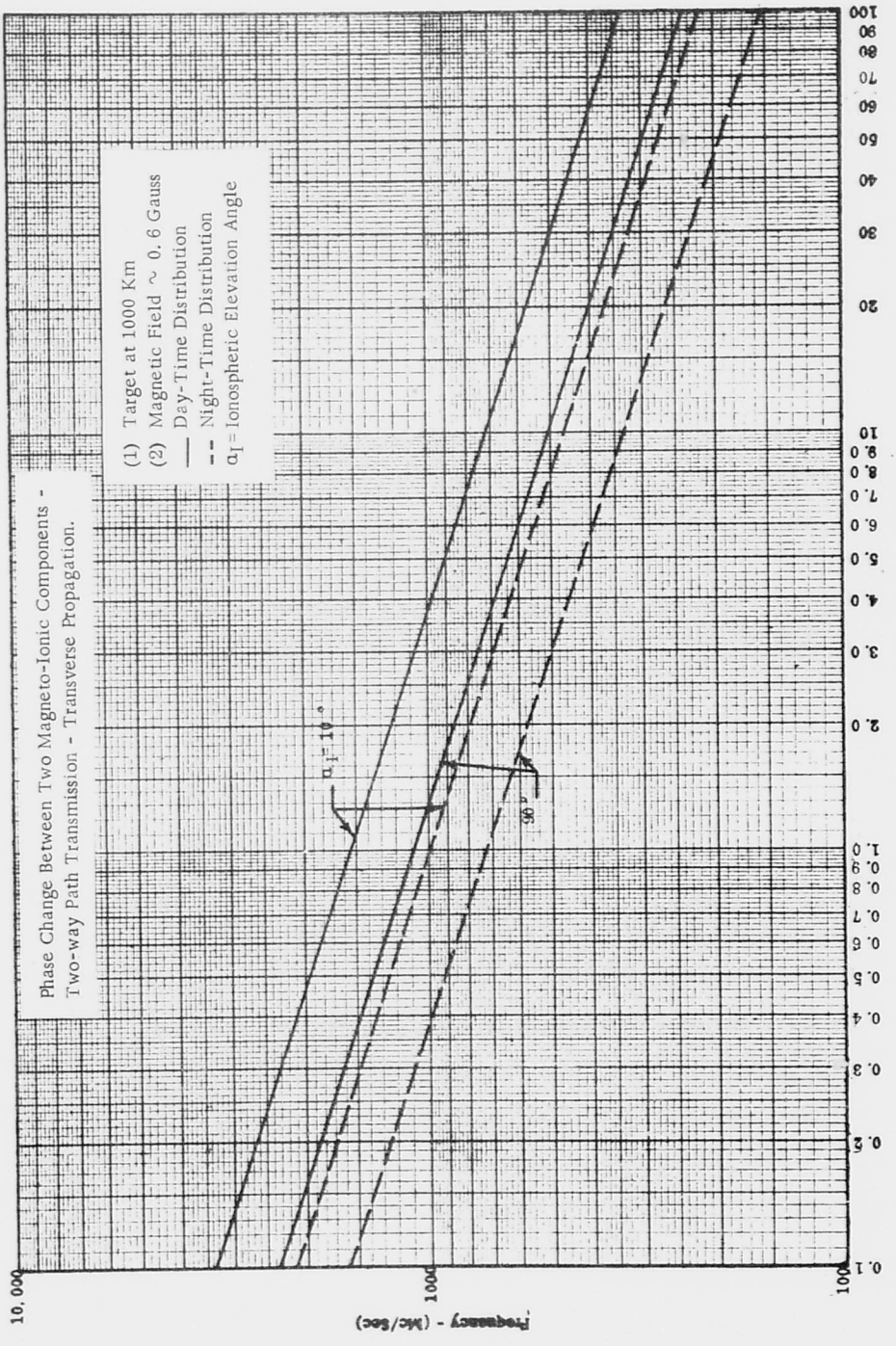

FIG. I-7 - FARADAY ROTATION FOR RADIO WAVE PERPENDICULAR TO EARTH MAGNETIC FIELD - TWO WAY PATH[5]

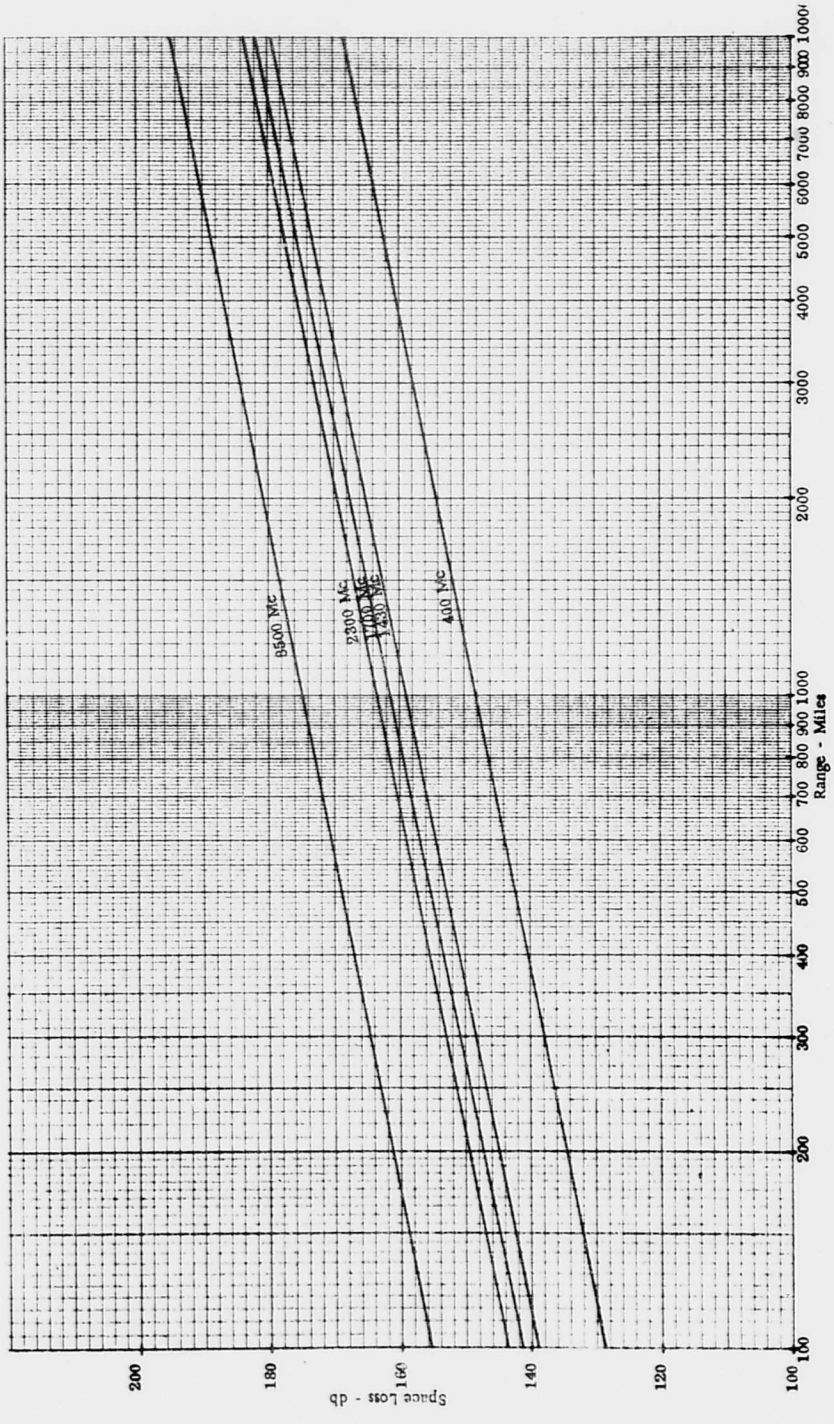

FIG. I-8 - FREE SPACE LOSS VERSUS RANGE

9.0 CONCLUSIONS

In attempting to choose the optimum frequency all the above factors were taken into account. Some of these factors are at best approximations and hence the frequency selection is to a degree arbitrary.

Table II gives the gain of the receiving antenna for a 1000 mile range, 0.1 watt transmitter power, 18 db signal to noise ratio and omnidirectional transmitting antenna. The limit of the receiver sensitivity is assumed to be the cosmic noise. No losses other than the free space loss are taken into account. As can be seen from Table II the required gain of the receiving antenna does not change with frequency to any great degree. However, when atmospheric noise is taken into account the maximum sensitivity of the receiver is degraded at the frequencies approaching X-band. At 8500 Mc a heavy rain will add approximately 20 db noise. The lower frequencies are not affected by this noise. The heavy rain will also introduce 3 db loss at 8500 Mc for a vertical antenna beam. Other atmospheric disturbances such as aurora have negligible effect above 400 Mc. The gain of the receiving antenna should also be increased 3 db at all frequencies due to the Faraday rotation of the radio waves. This will counteract the loss incurred by the difference in polarization between the receiving and transmitting antennas.

From the viewpoint taken (natural limitations only) the higher the frequency the less the effects due to the atmosphere. This is true up to a point, but as shown above 8500 Mc is adversely affected by weather conditions. The next highest frequency is 2300 Mc and atmospheric effects here are negligible (absorption, attenuation, noise, etc.). For this reason and the ones given above it seems obvious that 2290 to 2300 Mc is the best frequency range to be used for satellite tracking.

TABLE II

Receiving Antenna Gain for Each Frequency
for an
18 db Signal-to-Noise Ratio and Conditions as Shown

Frequency	Receiver Sensitivity	Power	Range	S/N	Receiver Gain
400 Mc	-116 dbm	100 mw	1000 mi	18 db	31 db
1427 Mc	-128 dbm				30 db
1700 Mc	-130 dbm				29 db
2300 Mc	-134 dbm				28 db
8400 Mc	-143 dbm				30 db

PART II - ANALYSIS OF ANGULAR ERROR DUE TO NOISE

1.0 INTERFEROMETER RESOLVING POWER

A phase comparison interferometer is a system which compares the phase of the received signal of two identical antennas spaced some distance apart. The relative phase between the two antennas gives the difference in path length from the source to each antenna. This difference in path length can then be used to find the direction cosine to the source. Two interferometers at right angles give two direction cosines and from these the third can be computed. The precision with which the angular position can be measured depends upon the spacing between the two antennas

$$\sin\theta = \frac{a}{D} \tag{1}$$

where θ is the space angle, D is the spacing between antennas in wavelengths and a is the number of wavelengths that the path lengths differ. The relative phase between the antennas gives a. In the absence of noise then the resolving power of an interferometer is given by

$$\Delta\theta = \frac{\theta_0}{360^\circ}\,\delta \tag{2}$$

where θ_0 is the space angle over which the relative phase will change 360° and is found from Eq. (1) by letting $a = 1$ then $\theta_0 = \arcsin 1/D$ and δ is the precision of the phase measuring instrument.

2.0 SIGNAL PLUS NOISE

In the presence of noise the phase of the incoming signal will have an uncertainty which will degrade the accuracy of the system to some degree dependent upon the signal-to-noise ratio. In order to obtain the accuracy of the system the phase deviation due to noise will be studied for a single antenna and then the effects of two such antennas will be combined.

First let the signal without noise be given by

$$s(t) = A\cos\omega t \tag{3}$$

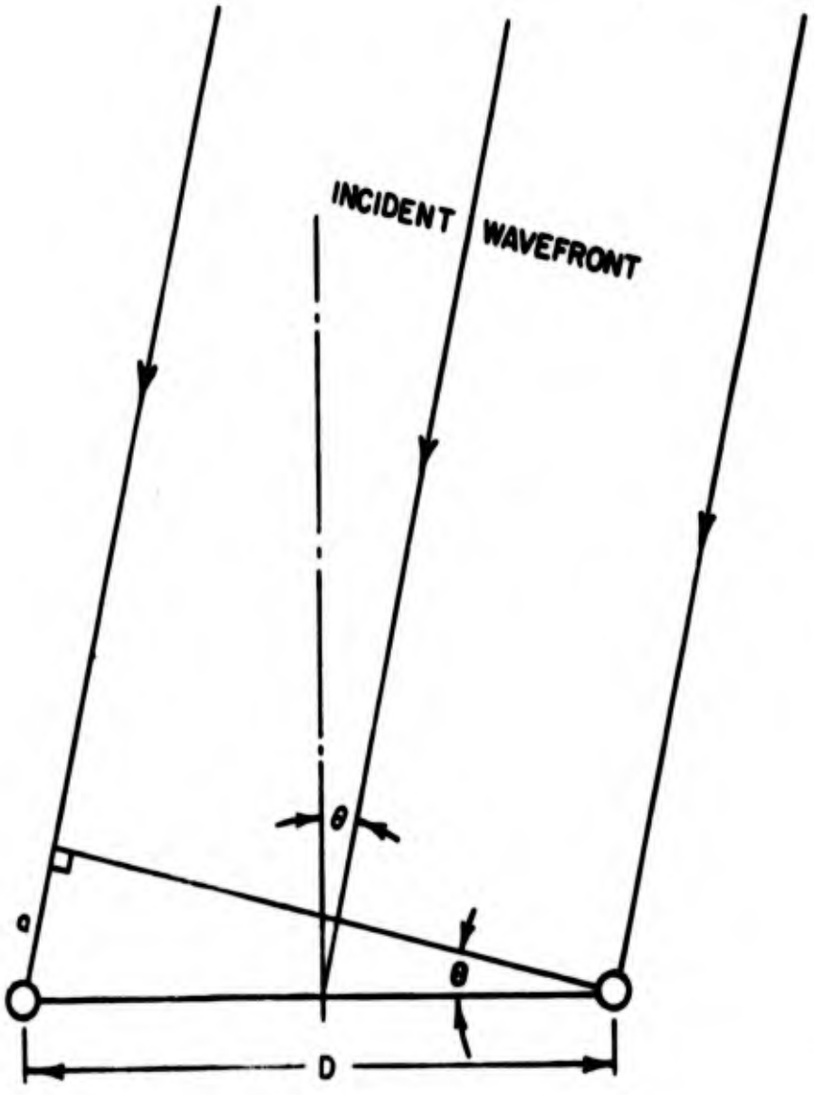

FIG. II-1 - TWO-DIMENSIONAL INTERFEROMETER

A noise signal will now be added to this signal. The narrow band expression for the noise will be used. This will not hinder the use of the theory since any practical system will indeed be narrow-banded. The narrow band expression for the noise is given by

$$n(t) = x_c(t) \cos \omega t - x_s(t) \sin \omega t \tag{4}$$

where x_c and x_s are random gaussian variables with zero mean. Addition of Eq. (3) and (4) and combining terms yields

$$Y(t) = s(t) + n(t) = [A + x_c(t)] \cos \omega t - x_s(t) \sin \omega t \tag{5a}$$

Letting

$$X_c = [A + x_c(t)] \quad \text{and} \quad X_s = x_s(t) \tag{5b}$$

and simplifying to a cosine wave plus a phase term yields

$$Y(t) = V \cos(\omega t + \phi) \tag{6}$$

where

$$V = [X_c^2 + X_s^2]^{\frac{1}{2}} \qquad \text{and} \qquad \phi = \arctan X_s/X_c$$

This shows that the incoming signal has some phase distortion due to the noise. The next step is to find the phase density distribution function so that the standard deviation of the phase can be found.

3.0 PHASE DENSITY DISTRIBUTION

Since the coefficients of the noise expression are random gaussian variables they have a distribution of the form

$$p(x_c, x_s)dx_c\,dx_s = \frac{1}{2\pi\sigma^2} e^{-(x_c^2+x_s^2)/2\sigma^2} dx_c\,dx_s \tag{7}$$

where σ^2 is the average noise power. To obtain the density function for ϕ and V two transformations of variables must be completed.

The first of these is to transform Eq. (7) into X_c and X_s. From Eq. (5b)

$$x_c(t) = X_c - A \qquad \text{and} \qquad x_s(t) = X_s \tag{8}$$

then

$$dx_c = dX_c \qquad \text{and} \qquad dx_s = dX_s \tag{9}$$

therefore the density function now becomes

$$p(X_c, X_s)dX_c\,dX_s = \frac{1}{2\pi\sigma^2}\, e^{-[(X_c-A)^2 + X_s^2]/2\sigma^2} dX_c dX_s . \tag{10}$$

Simplifying the exponent by use of Eq. (6) yields

$$p(X_c, X_s)dX_c dX_s = \frac{1}{2\pi\sigma^2}\, e^{-(V^2-2AX_c+A^2)/2\sigma^2} dX_c\,dX_s . \tag{11}$$

Again from Eq. (6)

$$X_c = V\cos\phi$$

then Eq. (11) becomes

$$p(X_s, X_c) = \frac{1}{2\pi\sigma^2}\, e^{-[(V-A\cos\phi)^2 + A^2\sin^2\phi]/2\sigma^2} dX_c dX_s . \tag{12}$$

Transforming Eq. (12) from $p(X_s, X_c)$ to $p(V, \phi)$ by the relationship $dX_c dX_s = V dV d\phi$ gives

$$p(V,\phi)dVd\phi = \frac{V}{2\pi\sigma^2}\, e^{-[(V-A\cos\phi)^2 + A^2\sin^2\phi]/2\sigma^2} \; dVd\phi . \tag{13}$$

This is the bivariate density function for the phase and amplitude of the signal plus noise. To obtain the phase density the amplitude

variable must be integrated out,

$$p(\phi)\,d\phi = \frac{1}{2\pi\sigma^2}\, e^{-A^2 \sin^2\phi/2\sigma^2}\, d\phi \int_0^\infty V e^{-(V-A\cos\phi)^2/2\sigma^2}\, dV \quad (14)$$

since $V \geq 0$ the lower limit has been changed from $-\infty$ to 0. To evaluate the integral let

$$\frac{V-A\cos\phi}{\sigma} = u \quad (15)$$

then

$$dV = \sigma du \quad . \quad (16)$$

Using Eq. (15) and (16) in Eq. (14) yields

$$p(\phi)d\phi = \frac{1}{2\pi\sigma^2}\, e^{-A^2\sin^2\phi/2\sigma^2}\, d\phi \int_{\frac{-A\cos\phi}{\sigma}}^\infty (\sigma u + A\cos\phi) e^{-u^2/2}\, du \quad (17)$$

Combining terms and simplifying Eq. (17) becomes

$$p(\phi) = \frac{1}{2\pi} e^{-A^2/2\sigma^2} + \frac{A\cos\phi}{2\pi\sigma} e^{\frac{-A^2\sin^2\phi}{2\sigma^2}} \int_{-\infty}^{\frac{A\cos\phi}{\sigma}} e^{-u^2/2}\, du \quad . \quad (18)$$

The limits on the integral can be reversed since the integrand is an even function. The integral is now of the form of an error function or a cumulative normal distribution and values have been tabulated for this function. Equation (18) is the form of the phase density function that was used in obtaining standard deviations for the phase and in turn the deviation in angular accuracy.

Curves showing the phase density for various signal to noise ratios are given in Fig. II-2. Using the integral

$$\sigma_\phi = \left[\int_{-\pi}^{+\pi} \phi^2 p(\phi) d\phi\right]^{\frac{1}{2}} \tag{19}$$

the standard deviation of the phase for various signal to noise ratios can be determined for a single antenna. (Fig. II-2)

4.0 STANDARD DEVIATION OF ANGULAR MEASUREMENT

As stated before, the foregoing analysis is for a single antenna. To obtain the standard deviation of the relative phase between the two antennas of the interferometer the phases of the two antennas must be compared as

$$\Phi = \phi_1 - \phi_2 \tag{20}$$

where Φ is the relative phase and ϕ_1, ϕ_2 are the phases of each of the antennas. The variance, σ_Φ^2, of the relative phase is the sum of the variances of the two antennas

$$\sigma_\Phi^2 = \sigma_{\phi_1}^2 + \sigma_{\phi_2}^2 \quad . \tag{21}$$

Since $\sigma_{\phi_1}^2 = \sigma_{\phi_2}^2 = \sigma_\phi^2$ the standard deviation of the relative phase is

$$\sigma_\Phi = \sqrt{2}\ \sigma_\phi \quad . \tag{22}$$

As seen by Eq. (1) the angular position of the source can be determined by knowing the path length difference. This angle can also be expressed by

$$\theta = \arcsin \frac{\Phi}{2\pi D} \tag{23}$$

where D is again the spacing in wavelengths and Φ is the relative phase. Equation (23) shows that as the phase varies from 0° to 360° or 0 to 2π radians the angular position can be measured very precisely. [Since the phase cycles from 0° to 360° there is no way of knowing if the path length differs by less than one wavelength or many wavelengths. There must be some way to resolve the ambiguities that result when the path length differs by many wavelengths. This is done by more closely spaced interferometers.]

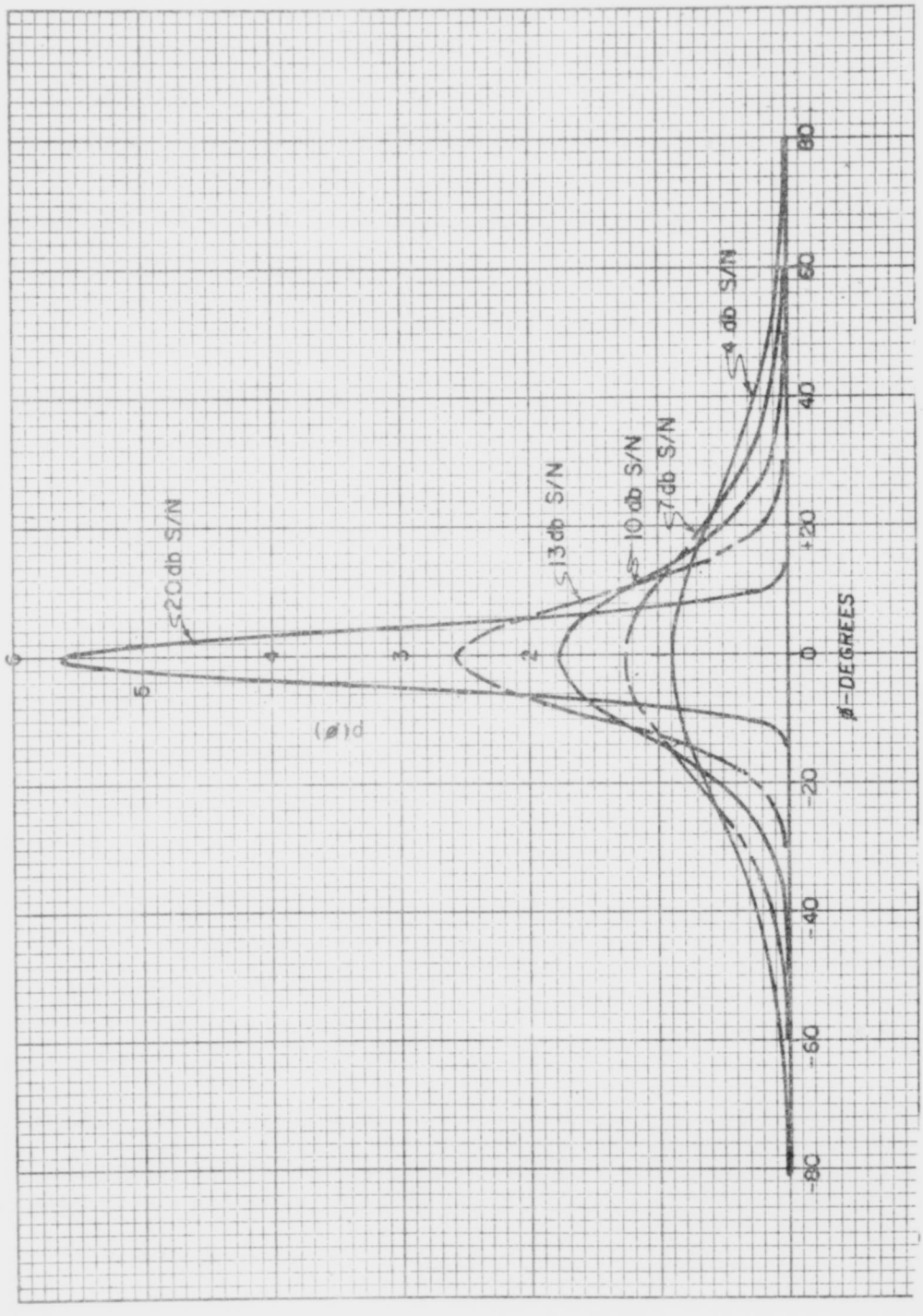

FIG. II-2 - PHASE DENSITY DISTRIBUTION OF A SINGLE ANTENNA FOR VARIOUS SIGNAL-TO-NOISE RATIOS

Expansion of Eq. (23) gives

$$\theta = \frac{1}{2\pi D}\,\phi + \frac{1}{6}\left(\frac{1}{2\pi D}\right)^2 \phi^2 + \ldots\ldots \tag{24}$$

but for any practical case $D \gg 1$ then $\frac{1}{D} \ll 1$ so that Eq. (24) becomes

$$\theta \approx \phi/2\pi D \quad . \tag{25}$$

Squaring both sides of Eq. (25)and taking the expectation value gives

$$E(\theta^2) = \left(\frac{1}{2\pi D}\right)^2 E(\phi^2) \tag{26}$$

but the expectation value of the variable squared is the variance, therefore Eq. (26) becomes

$$E(\theta^2) = \sigma_\theta^2 = \left(\frac{1}{2\pi D}\right)^2 \sigma_\phi^2 \quad . \tag{27}$$

Taking the square root of Eq. (27) will yield the standard deviation of the space angle. Thus

$$\sigma_\theta = \frac{1}{2\pi D}\,\sigma_\phi \tag{28}$$

but from Eq. (22) this becomes

$$\sigma_\theta = \frac{1}{\sqrt{2}\,\pi D}\,\sigma_\phi \tag{29}$$

where σ_ϕ can be found from Fig. II-3. The resolving power of an ideal interferometer is given by Eq. (2), but when $\sigma_\theta \gg \Delta\theta$ then σ_θ is the limiting case and conversely when $\Delta\theta \gg \sigma_\theta$ then $\Delta\theta$ is the limiting case. At intermediate points between these two extremes the deviation of the measured space angle is given by

$$\sigma_R = \left[(\Delta\theta)^2 + (\sigma_\theta)^2\right]^{\frac{1}{2}} \quad . \tag{30}$$

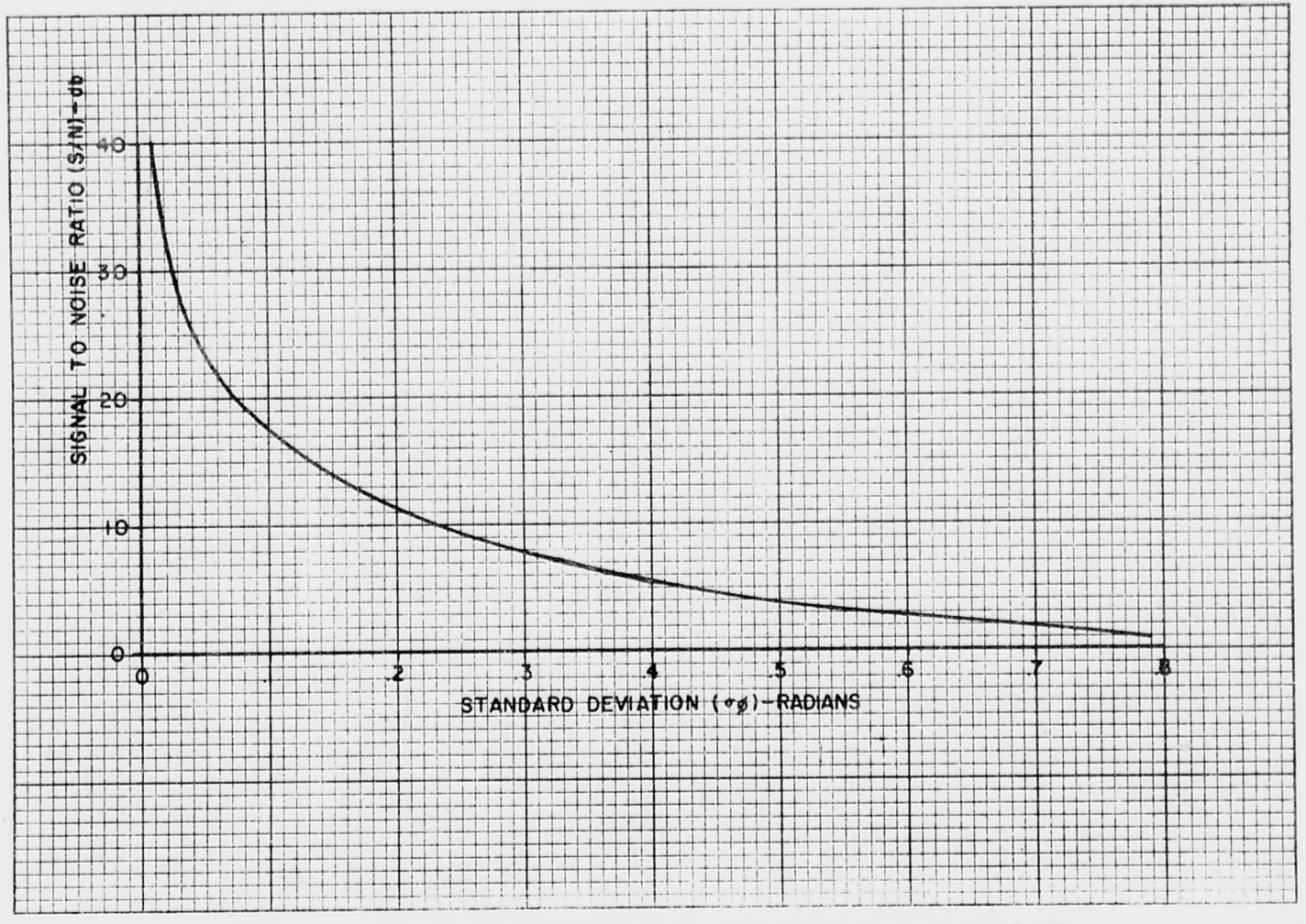

FIG. II-3 - STANDARD DEVIATION OF THE PHASE FOR A SINGLE ANTENNA VERSUS SIGNAL-TO- NOISE RATIO

A graph showing σ_R for various signal-to-noise ratios as a function of interferometer spacing, D, in wavelengths is shown in Fig. II-4.

5.0 LIMITATIONS AND CONCLUSIONS OF ANALYSIS

In making this analysis it was assumed that the noise at each antenna is uncorrelated. The correlation coefficient for the noise becomes small with increasing spacing and the assumption that there is no correlation is good for large spacings ($D >> \lambda$). In the case of a monopulse radar this is not so since the spacing is small (on the order of one wavelength). Therefore the results presented here give a good idea of the angular error for a widely spaced interferometer but gives a much worse error for a monopulse radar or similar system.

The effect of instrumentation was excluded except for narrowbanding and phase meter precision. Data smoothing by taking a succession of measurements at one site or data from many sites was also ignored. The degree to which each of these factors affect the final results are not known. However, the effect due to instrumentation will degrade the accuracy while data smoothing will make it better. From this point of view it seems that the final results (Fig. II-4) give a very good idea of the angular accuracy of an interferometer.

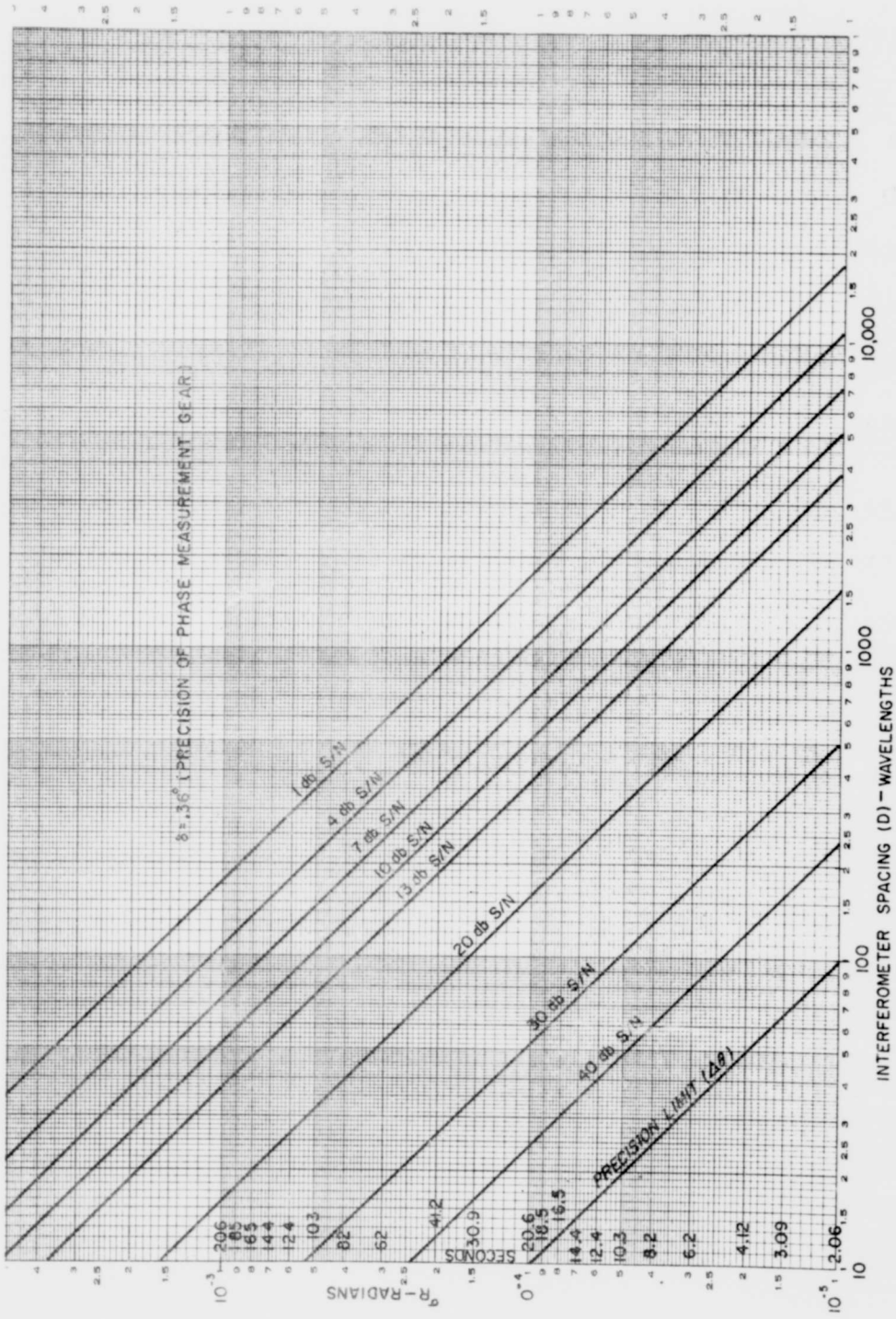

FIG. II-4 - STANDARD DEVIATION OF ANGULAR MEASUREMENT VERSUS INTERFEROMETER SPACING FOR VARIOUS SIGNAL-TO-NOISE RATIOS

GLOSSARY - Part I I

a	=	Path length difference in wavelengths.
D	=	Spacing between interferometer elements in wavelengths.
$\Delta\theta$	=	Resolving power of an interferometer.
s	=	Precision of phase measuring instrument.
σ_ϕ	=	Standard deviation of the phase for a single antenna.
σ_ψ	=	Standard deviation of phase difference between interferometer elements.
σ_θ	=	Standard deviation of measured space angle due to the noise.
σ_R	=	Resultant standard deviation (combination of σ_θ and $\Delta\theta$).

BIBLIOGRAPHY - Part I

1. Haydon, G. W., "Optimum Frequencies for Outer Space Communications," Journal of Research of the National Bureau of Standards - D, Radio Propagation, Vol. 64 D, Mar-Apr 1960.

2. Hogg, D. C., and Mumford, W. W., "The Effective Noise Temperature of the Sky," Microwave Journal, March 1960.

3. Kelley, L. C., Perlman, S., Russel, W. J., and Sturat, W. D., "Tentative Evaluation of Transmission Factors for Space Vehicle Communications," U. S. Army Signal Radio Propagation Agency Project NR. 664, September 1958.

4. Mayer, C. H., "Measurements of Planetary Radiation at Centimeter Wavelength," I. R. E. Proceedings, January 1958.

5. Millman, G. H., "Atmospheric Effects on VHF and UHF Propagation," I. R. E. Proceedings, August 1958.

6. McCoy, C. T., "Space Communications," Philco Corporation, Research Division, Philco Report 279, November 1958.

7. Rechtin, E., "Space Communications," Jet Propulsion Laboratory Technical Release No. 34-68, May 1960.

8. Smith, A. G., "Extraterrestrial Noise as a Factor in Space Communications," I. R. E. Proceedings, April 1960.

9. White, D. R. J., "Design and Evaluation of Space Communication Systems Using Computer Simulation Techniques," I. R. E. Proceedings, 1959 National Symposium on Space Electronics and Telemetry, September 1959.

BIBLIOGRAPHY - Part I I

Davenport and Root, Introduction to Random Signals and Noise, McGraw-Hill Book Co., Inc. (1958).

Mood, A. M., Introduction to the Theory of Statistics, McGraw-Hill Book Co., Inc. (1950).

Schwartz, M., Information Transmission, Modulation, and Noise, McGraw-Hill Book Co., Inc. (1959).

Unpublished notes by R. H. Duncan, New Mexico State University.

POWER INTERFERENCE LEVELS OF RECTANGULAR SLOT ANTENNAS IN A COMMON GROUND PLANE BY SIMPLIFIED ANALYSIS AND TESTS

D. K. Adams, R. B. Harris, Y. K. Kwon,
and J. A. M. Lyon

The University of Michigan
Ann Arbor, Michigan

ABSTRACT

This paper presents both simplified analysis and experimental data on the possible power interference levels present when a number of slot antennas operate in a common ground plane. By a series of simple tests using no more than three rectangular slots at any one time it is possible to predict the interference from one slot antenna to any other slot antenna when many slot antennas are mounted in the same common conducting ground plane.

Experiments and calculations appear to be valid in the extreme near field region as well as in the far field region. The prediction of power coupling by analysis is based upon simple formulas obtained from Huygens-Kirchoff principles. The correspondence of theoretical prediction and experimental values has been so close that experiments with arrangements of large numbers of slot antennas in a common ground plane have been eliminated.

The effect of higher modes is included in the analysis of the near field situation. A dynamic range of 60 db power coupling is

covered in the experimental and theoretical studies.

Although this paper describes the power coupling levels for rectangular resonant half-wave slots similar studies are being planned for other antennas including circularly polarized ones. It is believed that the methods described can be modified for additional types.

INTRODUCTION

Concern over the problem of coupling interference between two or more antennas can be traced back to the early days of radio communication. Often the only reasonable solution for this problem has been an empirical one. First, coupling measurements are made and then the antenna system is adjusted to eliminate, or otherwise compensate for each unwanted coupling. Since this is often an uncertain and expensive procedure, simple analytical methods for predicting antenna coupling are needed.

This paper presents both simplified analysis and experimental data on the power interference levels that can exist when a number of rectangular slot antennas operate in a common ground plane. Various approaches have been used for this problem over a considerable span of years. It may be claimed that some of these approaches are more exact than the one to be presented here. The emphasis in the work now to be described has been upon a simplified

approach with the objective of readily ascertaining the power interference levels prevailing for a given configuration of antennas mounted in a ground plane. Future work will consider other antenna elements besides the rectangular slots described here.

The coupling between two rectangular slots in a common ground plane was chosen for initial study because slot antennas are frequently found flush mounted in close proximity. Furthermore, the rectangular slot antenna has low directivity which accentuates the interference problem. The coupling present of such antennas mounted in a common ground plane can be due to the main lobe of the pattern and not just weak and stray radiation associated with defects in the pattern. The type of slot that will receive particular attention here is the open ended waveguide shown in Fig. 1.

The basic definition of coupling that will be employed is

$$C = \sqrt{\frac{W_r}{W_t}} \; e^{j\psi} \qquad (1)$$

where W_t is the total transmitted power, W_r is the received power, and ψ is the phase difference between the principal mode components in each aperture. Since only the principal mode is assumed to propagate, the transmitted and received power can be expressed in terms of the principal mode components.

In essence, each quantity in (1) can be calculated from a knowledge of the aperture fields, although the latter are rarely known exactly. The important attribute here, concerning aperture fields, is that the coupling factor, C, is stationary with respect to these fields (Ref. 1). Therefore, if C is calculated from approximate aperture field distributions, the resulting errors in C will tend to be smaller than the corresponding errors in field distribution. Hence, the approach of this analysis is twofold: (1) to calculate the coupling factor assuming the aperture fields, and (2) to establish methods of estimating, and then improving the estimate, of the aperture fields. One basic assumption will be introduced to simplify the latter step. It arises from the fact that slot couplings are relatively weak (less than 10 db in most cases), and therefore the effect of the receiver on the transmitter will be considered negligible.

SURVEY OF COUPLING INFLUENCES

The general coupling situation is illustrated in Fig. 2, where two waveguides are coupled on the free space side of a ground plane. The sequence of events associated with the coupling in Fig. 2 can be visualized as follows:

(a) A traveling wave with principal mode amplitude E^t_{10} is incident on the transmitting aperture, where it is partially reflected, partially radiated, and partially converted into higher order modes.

As a result, a tangential aperture electric field $E_A^t(x,y)$ is established. For purposes of illustration, E_A^t is assumed to be oriented in the x direction only. Of course E_A^t vanishes everywhere except on the transmitting slot.

(b) The power transmitted is

$$W_t = \frac{1}{2} |E_{10}^t|^2 \, Y_o^t (1 - |\rho_t|^2) = \frac{1}{2} \left| \frac{(E_A^t)_{10}}{1+\rho_t} \right|^2 Y_o^t (1 - |\rho_t|^2) \tag{2}$$

where ρ_t is the transmitter reflection coefficient. As shown in the appendix, the reflection coefficient must satisfy the relation:

$$\frac{Y_t}{Y_o^t} = \frac{1-\rho_t}{1+\rho_t} = \frac{1}{(E_A^t)_{10}^2} \int_{ap} E(x,y) \, E(\xi,\eta) \, G(x,y,\xi,\eta) \, dx \, dg \, d\xi \, d\eta \tag{3}$$

which is stationary with respect to variations in E_A^t. In (3), Y_t is the transmitter radiation admittance, while G is a composite waveguide and free space Green's function, also given in the Appendix. Now, W_t in (1) can be estimated by assuming a trial function for E_A^t, finding its principal mode component $(E_A^t)_{10}$, then solving (3) for ρ_t, and finally using the results in (2). An important observation that allows this procedure to be "simplified" is that rather crude estimates of E_A^t can yield satisfactory estimates of W_t, due to stationarity.

(c) The transmitted magnetic field can also be calculated from E_A^t, by the relation

$$H(x,y,z) = \int_{ap} E_A^t(\xi,\eta)\, G_{fs}(\xi,\eta,x,y,z)\, d\xi\, d\eta \qquad (4)$$

where G_{fs} is the free space Green's function listed in the Appendix. In particular, (4) yields the H field incident on the receiving slot

$$H_o = H(x,y,0) \qquad (5)$$

It must be understood that H_o is the ground plane magnetic field before the second slot is cut.

(d) When the second slot is cut, a displacement current is immediately set up which produces a receiving aperture field $E_A^r(x',y')$. However, E_A^r has no simple relationship to H_o, because it too is associated with transmitted, reflected, and energy storage components. The reflected field is now in the free space region, so it obeys a relation similar to (4). But when the reflected field is superimposed on H_o, the original ground plane fields and currents change. Therefore, E_A^r must be chosen so the corresponding H field is consistent both with H_o and with reflections in the receiving waveguide. In the Appendix it is shown that E_A^r must satisfy the relation

$$\frac{Y_r}{Y_o^r} = \frac{1-\rho_r}{1+\rho_r} = \frac{\int\int_{ap} E_A^r(x',y') E_A^r(\xi',\eta')\, G(x',y',\xi',\eta')\, dx'dy'd\xi'd\eta'}{(E_A^r)_{10}^2}$$

$$+ \left(\frac{2}{ab\,Y_o^r}\right) \frac{\int\int_{ap} H_o\, E_A^r(x'y')\, dx'dy'}{(E_A^r)_{10}^2} \qquad (6)$$

where Y_r can be identified as an effective load admittance. The received power is then:

$$W_r = \frac{1}{2}\left|\frac{(E_A^r)_{10}}{1+\rho_r}\right|^2 (1 - |\rho_r|^2) \qquad (7)$$

The receiving antenna reflection coefficient is deserving of further comment. Physically ρ_r would arise if matching were employed in the receiving waveguide, but (6) suggests that such matching will depend on the nature of H_o. Normally, antenna impedance is expected to be the same for both transmitting and receiving, but this is not always the case. To analyze a matched receiver exactly, one would have to search for the E_A^r that maximizes W_r, and the associated ρ_r would yield the proper matching admittance. However, to find the transmitting admittance, one must vary E_A^t in (3) until Y_t is minimized. There is no guarantee that these procedures will yield the same aperture fields or admittances, particularly since H_o in (6) is quite arbitrary.

However, in practice it is often observed that antennas matched for transmitting are pretty well matched for receiving, especially if the incident wave is a plane wave. This result is undoubtedly related to stationarity. In this case, ρ_r would be the conjugate of ρ_t (assuming the same waveguide sizes). Then if E_A^t has approximately the same spatial distribution as E_A^r, the first term of the

right of (6) will be the conjugate of Y_r. In this case for a matched receiving antenna:

$$\frac{\int\int H_o E_A^r \, dx'dy'}{ab(\dot{E}_A^r)_{10}^2} \cong -jB \qquad (8)$$

where B is the aperture susceptance. The importance of (8) is its relating of $(E_A^r)_{10}$ to H_o.

In general W_r is more difficult to calculate than W_t. However, for a given waveguide W_r depends ultimately on H_o. Therefore, if W_r is known for a simple case, such as a plane wave incident field, corrections for nonuniform H_o fields can be obtained from (8), or more exactly from (6). To illustrate, if the aperture field is entirely in the principal mode, then:

$$E_A^r(x,y) = (E_A^r)_{10} \cos \frac{\pi y}{b} \qquad (9)$$

and (8) becomes

$$\frac{(H_o)_{10}}{(E_A^r)_{10}} = -2jB \qquad (10)$$

where:

$$(H_o)_{10} = \frac{2}{ab} \int\int H_o \cos \frac{\pi y}{b} \, dy$$

Therefore if B is relatively insensitive to H_o, due to stationarity, it follows that $(E_A^r)_{10}$ must be proportional to the principal mode component

of the incident H field in the aperture. Therefore

$$W_r \propto |(H_o)_{10}|^2 \tag{11}$$

This result is clearly useful because W_r can be found quite simply in special cases. Other cases can then be treated by using (11) for scaling.

FAR FIELD COUPLING PREDICTIONS--A SPECIAL CASE

It has just been shown that different slot couplings can be related by simple scaling procedures. Therefore, to make coupling predictions, one reference coupling must be determined. From basic antenna theory, the far field coupling between matched antennas (where a plane wave is incident on the receiving antenna) can be expressed by

$$|C|^2 = \frac{g_t g_r \lambda^2}{(4\pi r)^2} \tag{12}$$

where g_t and g_r are the gains of the transmitting and receiving antennas, respectively; λ is the radiation wavelength; and r the mean antenna separation. By definition

$$g = \frac{P(4\pi r^2)}{W} \tag{13}$$

where P is the far field power density

$$P = \frac{1}{2} |H(x,y,z)|^2 / \eta \qquad (14)$$

where η is the free space intrinsic and W is the total power radiated impedance, as shown by:

$$W = \int_{\text{sphere}} P r^2 \sin\theta d\theta d\phi \qquad (15)$$

To use (12) for absolute coupling prediction, the antenna gains must be calculated, but this can be done using (4) to obtain the radiation fields. Again one must assume an aperture field, but taking advantage of stationarity one can compromise between choosing a mathematically simple field and one with proper physical basis. Hence we assume only a principal mode paerture field:

$$E_A^t(x,y) = E_{10} \cos\frac{\pi y}{b} \qquad \begin{matrix} |x| < a/2 \\ |y| < b/2 \end{matrix} \qquad (16)$$

in which case (4) reduces to:

$$H_x = \frac{j E_o}{2\pi\omega\mu} \int_{-a/2}^{a/2} d\xi \int_{-b/2}^{b/2} d\eta \cos\frac{\pi\eta}{b} \frac{\partial^2}{\partial x \partial y} \left(\frac{e^{-jk|r - R|}}{|r - R|} \right) \qquad (17a)$$

$$H_y = \frac{j E_o}{2\pi\omega\mu} \int_{a/2}^{a/2} d\xi \int_{-b/2}^{b/2} d\eta \cos\frac{\pi\eta}{b} \left(k^2 + \frac{\partial^2}{\partial y^2}\right) \left(\frac{e^{-jk|r-R|}}{|\bar{r} - R|} \right) \qquad (17b)$$

where:

$$|r - R| = \sqrt{(x - \xi)^2 + (y - \eta)^2 + z^2} \cong r - \frac{(x\xi + y\eta)}{r} \quad (18)$$

and

$$r = \sqrt{x^2 + y^2 + z^2}$$

The assumption above is good as long as any linear dimension of the slot is much smaller than $|r - R|$. The result of the integration of (17) after taking into account the assumptions in (18) is:

$$H_x = -2j\omega\epsilon E_o \frac{b}{\pi^2} \frac{e^{-jkr}}{kr} \left(\frac{\sin(\frac{ak}{2} \sin\theta \cos\phi)}{\sin\theta \cos\phi}\right)\left(\frac{\cos(\frac{kb}{2} \sin\theta \sin\phi)}{1-(\frac{kb}{\pi})^2 \sin^2\theta \sin^2\phi}\right) \quad (19a)$$

$$\times \sin^2\theta \sin\phi \cos\phi + 0\left(\frac{1}{r^2}\right)$$

$$H_y = +2j\omega\epsilon E_o \frac{b}{\pi^2} \frac{e^{-jkr}}{kr} \left(\frac{\sin(\frac{ak}{2} \sin\theta \cos\phi)}{\sin\theta \cos\phi}\right)\left(\frac{\cos(\frac{kb}{2} \sin\theta \sin\phi)}{1-(\frac{kb}{\pi})^2 \sin^2\theta \sin^2\phi}\right) \quad (19b)$$

$$\times (1 - \sin^2\theta \sin^2\phi) + 0\left(\frac{1}{r^2}\right)$$

The notation above is reviewed in Fig. 3. Also, the term $0(1/r^2)$ means of order $1/r^2$ and is therefore ignored.

Now, from (14), the radiated power density on the ground plane is:

$$P_z = \sqrt{\frac{\mu}{\epsilon}} \frac{2\omega^2 \epsilon^2 b^2 E_0^2}{\pi^4 k^2 r^2} \left[\sin\left(\frac{ak}{2}\cos\phi\right)\right]^2 \left(\frac{\cos\left(\frac{kb}{2}\sin\phi\right)}{1-\left(\frac{kb}{\pi}\right)^2 \sin^2\phi}\right)^2 \tag{20}$$

The power radiated W can now be found from (20) through (15), or by (3), or by integrating the average pointing vector in the aperture. In the latter case the result is:

$$W = \frac{16}{3\pi} \sqrt{\frac{\epsilon}{\mu}} \frac{(ab)^2}{\lambda^2} F \tag{21a}$$

where:

$$F = \left[1 - \frac{3}{15}(\pi^2 - 8)\frac{b^2}{\lambda^2} + \frac{1}{105}(3\pi^4 - 72\pi^2 + 432)\frac{b^4}{\lambda^4}\right.$$

$$- \frac{1}{105}(\pi^6 - 60\pi^4 + 1080\pi^2 - 5760)\frac{b^6}{\lambda^6}$$

$$- \frac{2\pi^2}{15}\frac{a^2}{\lambda^2}\left\{1 - \frac{1}{\eta}(\pi^2 - 8)\frac{b^2}{\lambda^2} + \frac{1}{28}(\pi^4 - 24\pi^2 + 144)\frac{b^4}{\lambda^4}\right\}$$

$$\left. + \frac{3\pi^4}{525}\frac{a^4}{\lambda^4} + \cdots\right] \tag{21b}$$

Therefore, by (13), the gain along the ground plane becomes:

$$g = \frac{3}{2}\frac{\lambda^2}{\pi^2 a^2} \frac{\left[\sin\left(\frac{ak}{2}\cos\phi\right)\right]^2 \left[\frac{\cos\left(\frac{kb}{2}\sin\phi\right)}{1-\left(\frac{kb}{\pi}\right)^2 \sin^2\phi}\right]^2}{F} \tag{22}$$

This formula will be useful for all orientations of the two antennas where far fields dominate in the coupling. When (22) is applied to the two antennas in Fig. 3, the coupling becomes:

$$|C|^2 = \frac{g(\phi_1)\, g(\phi_2)\, \lambda^2}{(4\pi r)^2} \qquad (23)$$

This formula has been used to predict the coupling in various ground plane configurations, as discussed in the next section.

EXPERIMENTAL WORK

Measurements have been made of the coupling between two matched, open-ended, X-band waveguides in representative orientations on a conducting ground plane. A standard RF bridge configuration was employed, with calibrated variable attenuators and phase shifters as reference elements. The configuration used in the measurements reported here is shown in Fig. 4. One feature of this bridge is the use of flexible cables to accommodate changes in slot position. In a later version of the bridge (Fig. 5), the cables were replaced by rotary joints to eliminate phase errors, and the phase shifter was replaced by a slotted line phase detector.

At the present time, the phase measurements are incomplete, but their precision is expected to be better than $\pm 5^{\circ}$. The procedure for phase measurement is to measure the overall phase shift from plane tt' to plane rr' (see Fig. 1), and then to correct for the

phase shift in the matching sections. In this way, all phase shifts are referred to the aperture.

Three purposes have been included in our experimental program: (a) to discover predominant coupling effects from which simplified theoretical models could be inferred; (b) to determine the consistency of alternate experimental techniques; and (c) to provide spot checks on theoretical prediction.

Under item (a) above it has been observed that the couplings were all quite weak and also they fell off essentially as $1/r^2$ in the broadside configurations (Fig. 6), and as $1/r^4$ in the end to end configuration (Fig. 7). This supports the dipole representations used in the previous section for theoretical prediction.

Several different experimental procedures have been carried out. In one, a ground plane was prepared with 10 slots at various spacings and angles. Couplings measurements were made between various pairs with each of the other slots being covered with foil. Some representative results are shown in Figs. 6, 7, and 8. Later tests in other ground planes showed no serious effects from the foil. Also, various pairs of slots were moved from the center of the ground plane toward one edge. The differences in coupling were within experimental error, so it is concluded that edge effects are negligible in the data reported.

When a third slot is introduced in the ground plane, small changes in coupling result. It is anticipated that the present method

of prediction can account for these effects. This step will be taken up in a later phase of our coupling prediction program.

DISCUSSION

It has been demonstrated that the simple far field gain formula (12) can accurately predict most of the couplings observed. The success of this formula in the present case arises because the slot dimensions are relatively large, such that really close center to center spacings are impossible. However, the main purpose of this work is to show how coupling can be estimated by simple means, and a method has been found to extend the usefulness of elementary formulas such as (12). The resulting procedure assumes a knowledge of the incident field (H_0) on the receiving antenna.

If H_0 is known, and if the absolute coupling is known for one special case (such as for slots spaced by several wavelengths), then other configurations can be treated according to the variation in H_0. The procedure uses scaling formulas such as (11), and is of course valid for near fields as well as far fields. The receiving antenna does not know one from the other. It only sees the incident H_0 field in the receiving slot.

The procedure of scaling based on variations in H_0 was used in making the near field predictions in Fig. 7. It is expected that this procedure can be used to explain the deviation between

experiment and theory for the closest slot spacing in Fig. 6. This deviation is due to nonuniformities in H_0, since the theoretical curve shown assumed uniform H_0 for a first estimate. The correction for nonuniform H_0 will be taken up in future calculations.

CONCLUSIONS

The low levels of coupling factors observed and calculated would be for many purposes negligible. However such levels are of considerable importance where the antenna elements involved represent different communication systems. If one of the antennas is a transmitting antenna and the other an antenna for a receiving system serious interference could be possible even at these apparently low levels of coupling. It has been with such possibilities in mind that the extremely low levels of coupling have been included in the measurements and analysis work of this paper. Oftentimes in earlier work such weak couplings were considered outside the range of interest.

ACKNOWLEDGEMENTS

The results presented here were obtained under Contract AF 33(657)-8178 issued by the Aeronautical Systems Division, Wright-Patterson AFB. The contributions and encouragement of Mr. E. M. Turner, Chief, and Mr. O. E. Horton, Project Engineer, both of the

Antenna-Radome Section, Electromagnetic Environment Branch of the Electromagnetic Warfare and Communications Laboratory of ASD are gratefully acknowledged. Likewise, Mr. A. I. Simanyi of the Cooley Electronics Laboratory and Mr. W. R. DeHart of the Countermeasures Laboratory of The University of Michigan have made valued contributions to the work.

APPENDIX

In the case of a general receiving antenna, as shown in Fig. 2, an aperture electric field (assuming no x' component) can be expressed by the following Fourier series of waveguide modes (Ref. 2)

$$E_A^r(x',y') = (E_A^r)_{10}(1+\rho_r)\cos\frac{\pi y'}{b} + j\omega u \sum_m \sum_n A_{mn}\cos\frac{m\pi y'}{b}\sin\frac{n\pi x'}{a} \tag{24}$$

Therefore, the tangential magnetic field just inside the aperture (which now has only an x' component) can be expressed by

$$H_A^r(x',y') = (E_A^r)_{10}\, Y_o^r\,(1-\rho_r)\cos\frac{\pi y'}{b} + j\omega u \sum_m \sum_n A_{mn}\, Y_{mn}\cos\frac{m\pi y'}{b}\sin\frac{n\pi x'}{a} \tag{25}$$

where Y_{mn} denotes the characteristic admittance of each higher order mode. Just outside the slot, the magnetic field has two parts: H_o and the scattered H field. Therefore

$$H_A^r(x',y') = H_o + \int\int E_A^r(\eta,\xi)\, G_{fs}(\eta,\xi,x',y')\, d\eta\, d\xi \tag{26}$$

where the free space Green's function, G_{fs}, has the components:

$$\begin{aligned} &\text{x' component} \quad \frac{j}{2\pi\omega u}\,\frac{\partial^2}{\partial x'\partial y'}\left(\frac{e^{-jK|r'-R'|}}{|r'-R'|}\right) \\ &\text{y' component} \quad \frac{j}{2\pi\omega u}\left(K^2+\frac{\partial^2}{\partial y'^2}\right)\left(\frac{e^{-jK|r'-R'|}}{|r'-R'|}\right) \end{aligned} \tag{27}$$

where r' and R' are as defined in Fig. 3. Only the x' component is needed in (26), but both are needed in obtaining (17). Now equating (25) and (26) yields (6), where

$$G = -\frac{\omega u a b}{2 Y_0^r}\left(\frac{\partial^2}{\partial y^2} + k^2\right)\left[\frac{1}{2\pi j\omega u}\left(\frac{e^{-jK|r-R|}}{|r-R|}\right) + \frac{4}{ab}\sum\sum Y_{mn}\cos\frac{m\pi y}{b}\sin\frac{n\pi x}{a}\cos\frac{m\pi\xi}{b}\sin\frac{n\pi\eta}{a}\right] \tag{28}$$

If H_0 is set to zero, then (3.) results.

REFERENCES

M. K. Hu and Y. Y. Hu, "Successive Variational Approximation of Impedance Parameters in a Coupled Antenna System," IRE Trans. on Antennas and Prop., October 1959, pp. 373-379.

L. Lewin, Advanced Theory of Wave Guide, ILIHHE and Sons, LTD: London, p. 123.

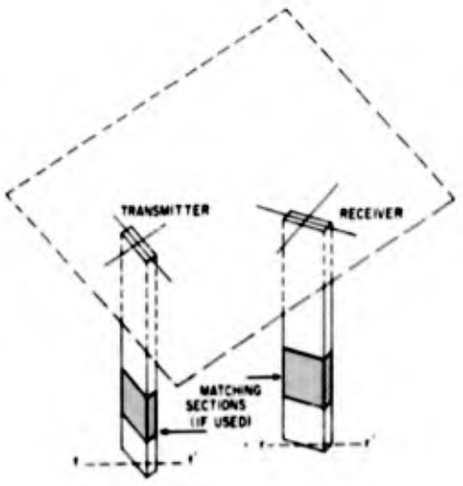

Fig. 1. Open ended waveguide antennas in a common ground plane.

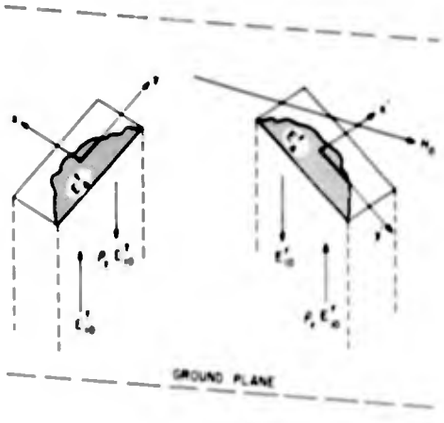

$E_A^t(x,y)$ = tangential electric field in transmitting aperture

$E_A^r(x',y')$ = tangential electric field in receiving aperture

$H_o(x,y)$ = ground plane magnetic field in absence of receiving slot

E_{10}^t, E_{10}^r = incident and emerging principal mode components in transmitting and receiving guides, respectively

$(E_A^t)_{10}$, $(E_A^r)_{10}$ = principal mode components of transmitting and receiving aperture fields, respectively

$(E_A^t)_{10} = E_{10}^t(1+\rho_t)$; $(E_A^r)_{10} = E_{10}^r(1+\rho_r)$

Y_o^t, Y_o^r = characteristic admittances of principal modes in transmitting and receiving waveguides

Fig. 2. Notation used in this discussion.

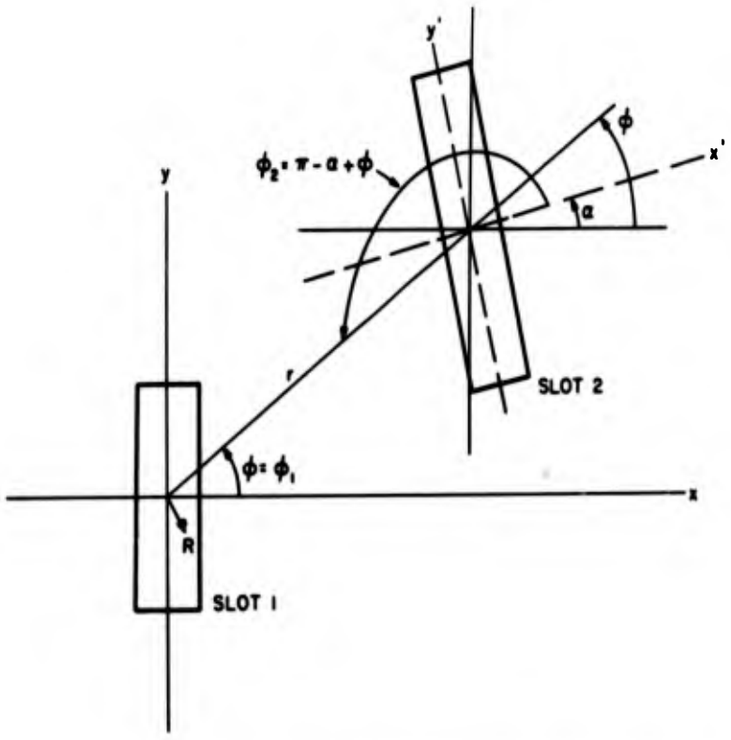

Fig. 3. Notation used in computing slot antenna gain and far field coupling.

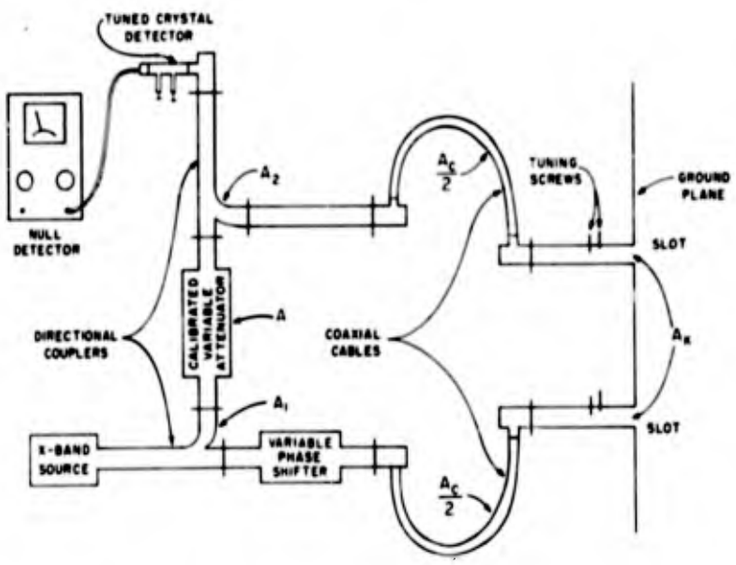

Fig. 4. RF bridge used in slot coupling measurement.

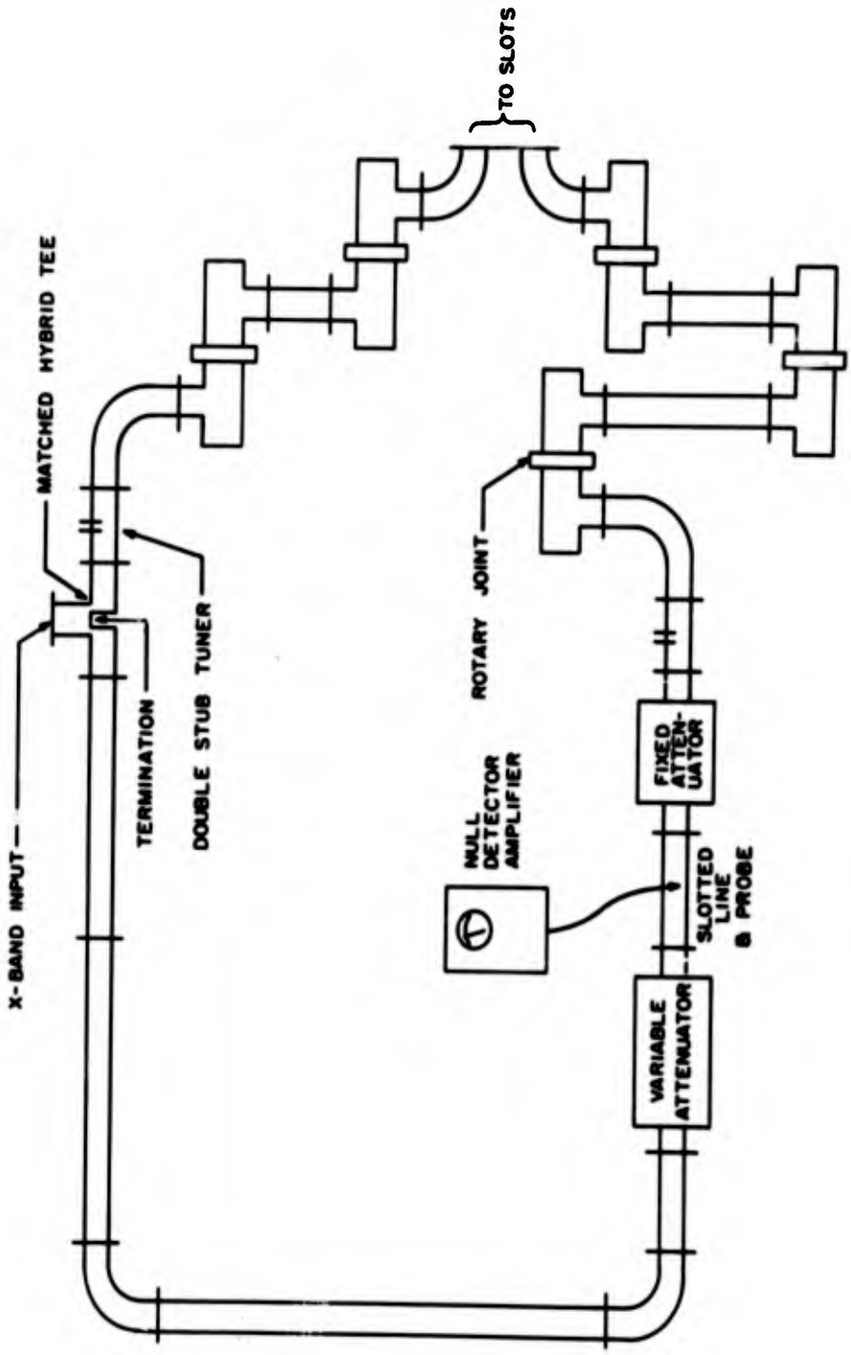

Fig. 5. Modified RF bridge.

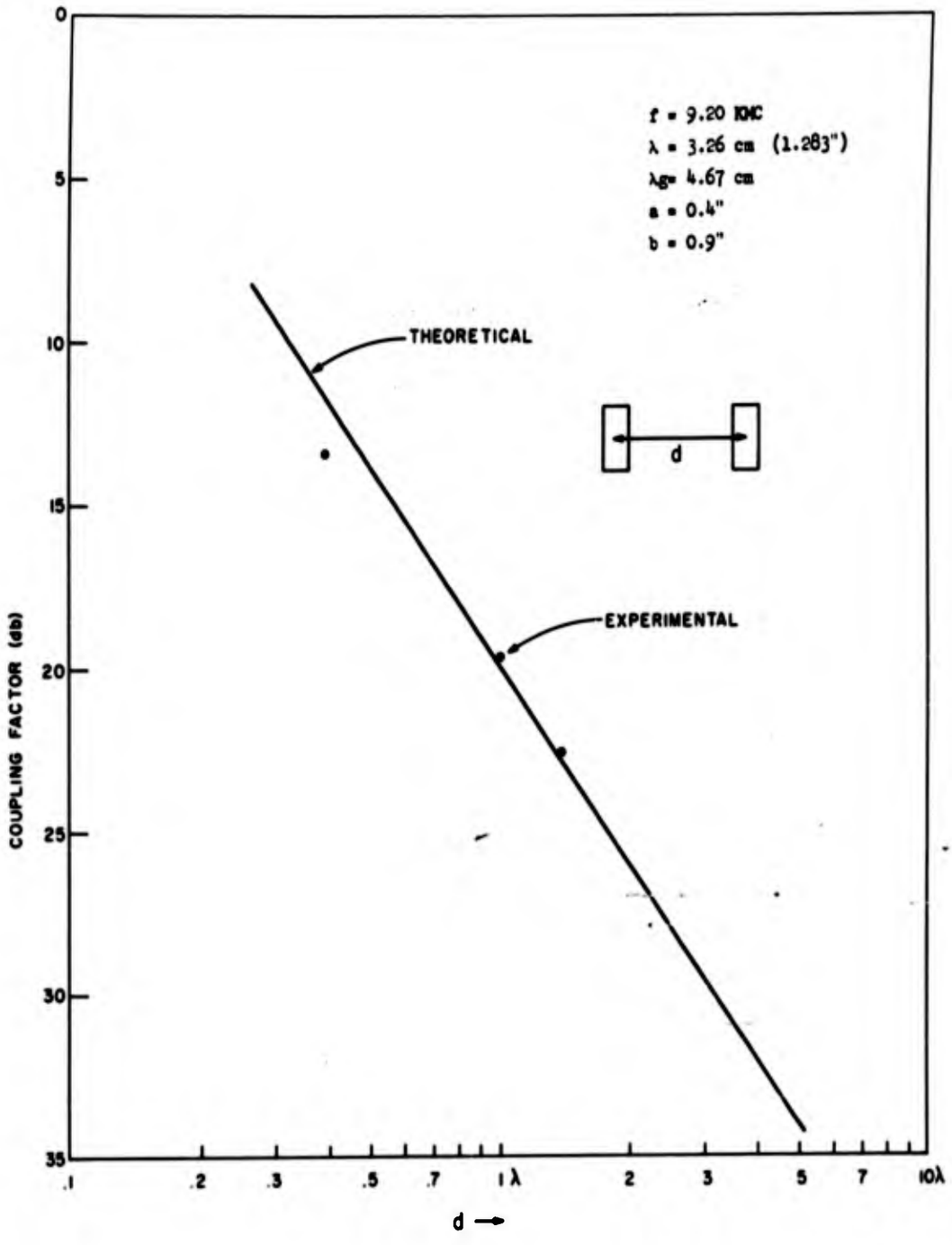

Fig. 6. Broadside to broadside coupling of closely spaced rectangular slots, showing a $1/r^2$ trend.

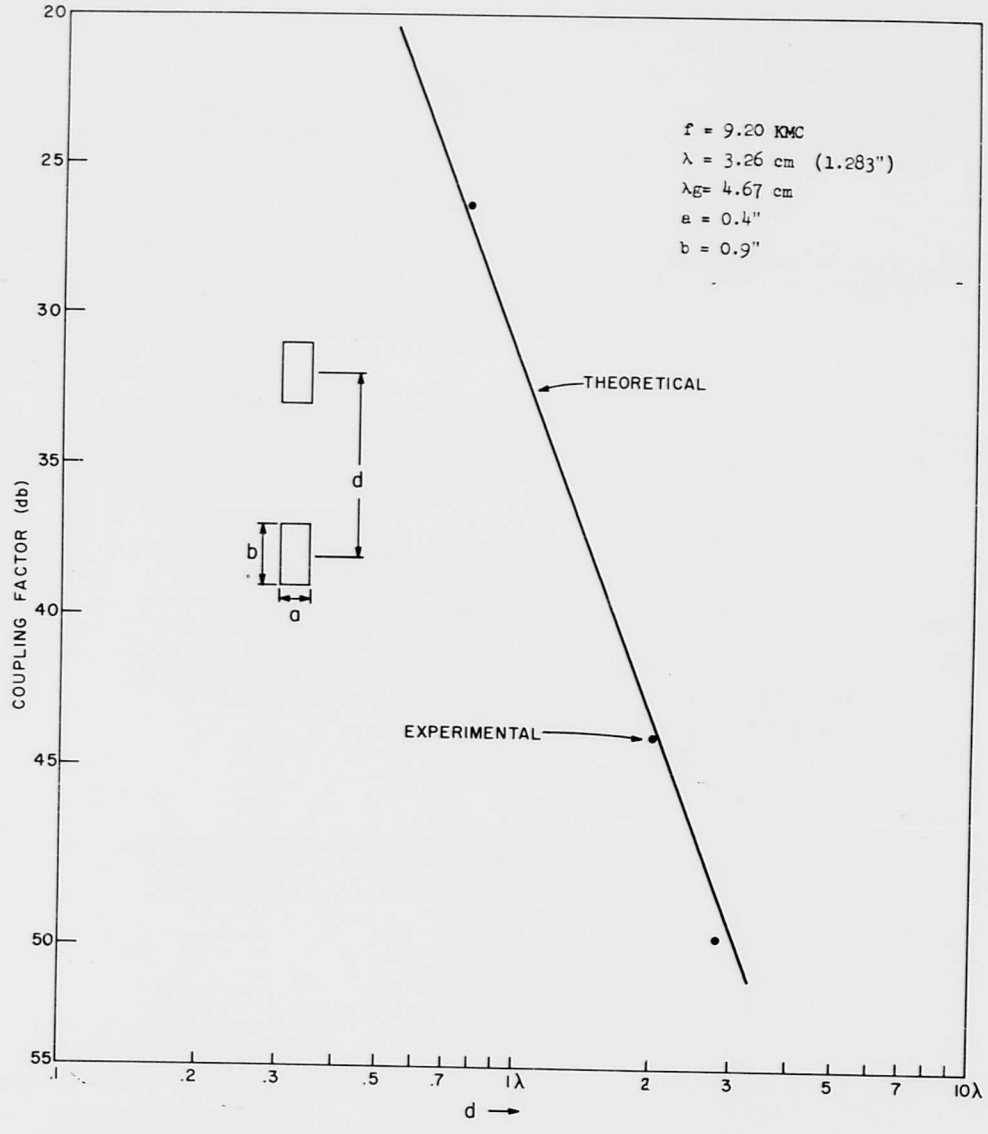

Fig. 7. End to end coupling of closely spaced rectangular slots, showing a $1/r^4$ trend.

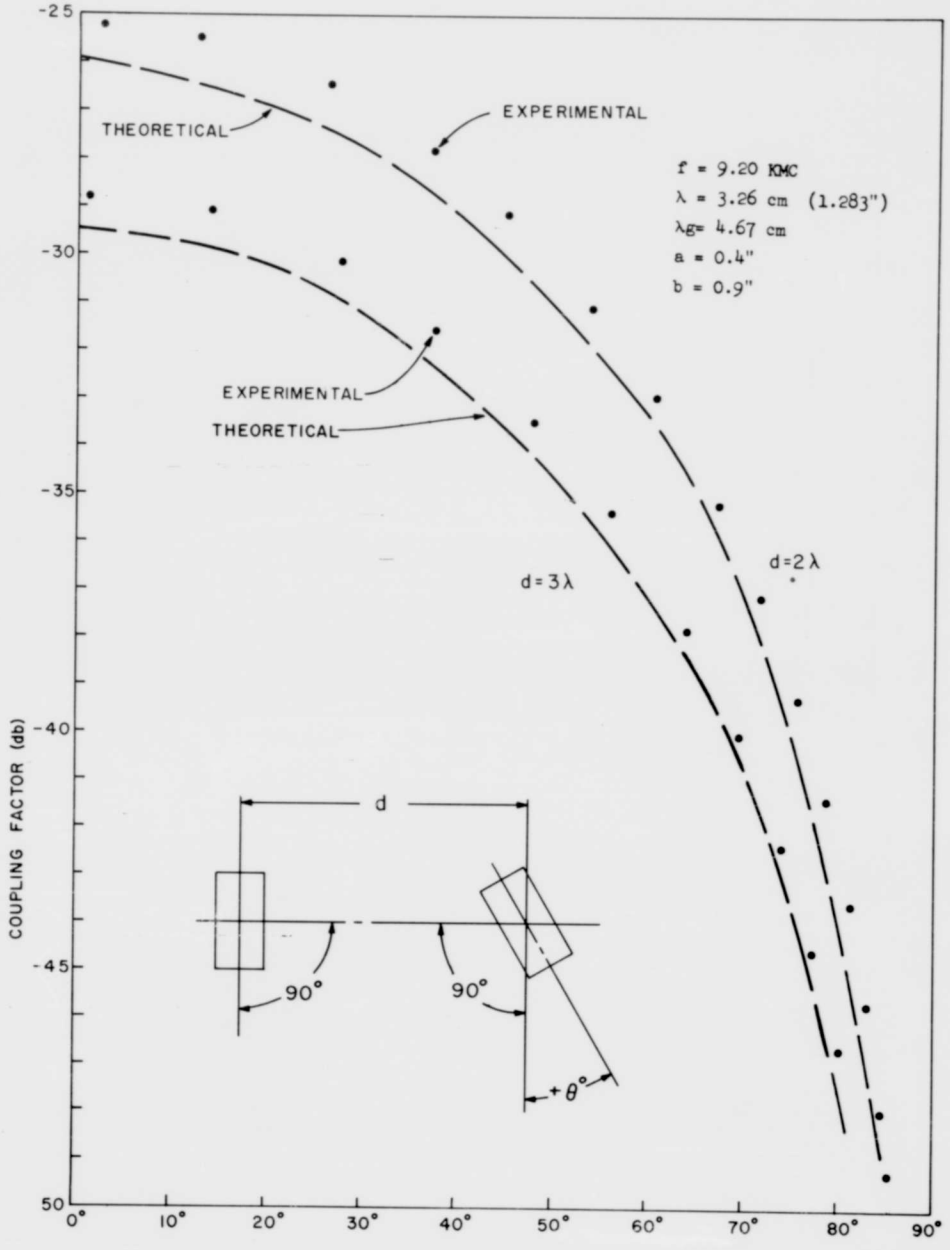

Fig. 8. Far field coupling for representative angles.

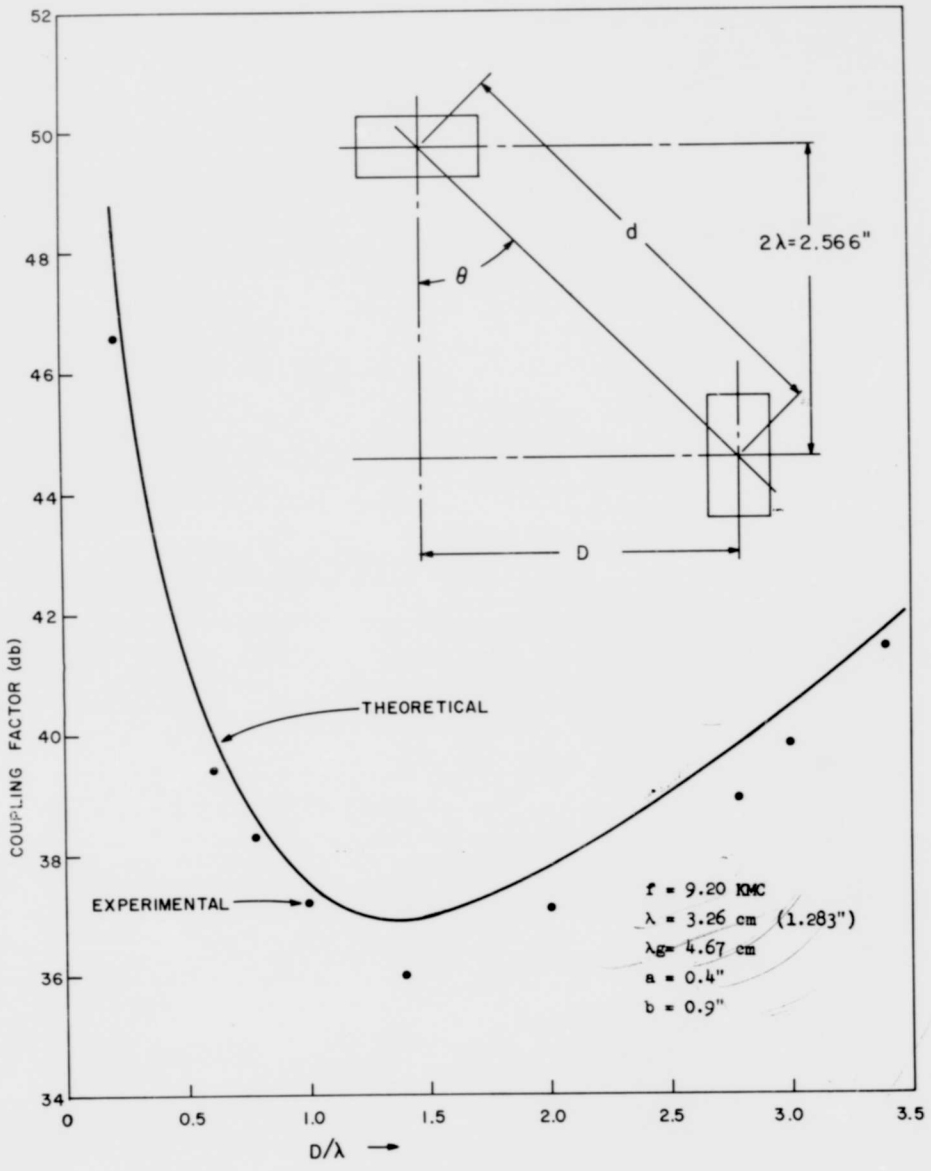

Fig. 9. Far field coupling for representative angles.

4 September 1962

A PORTABLE RADIO[illegible]METER FOR ANTENNA STUDIES

by

G. L. Johnson and F. P. St[illegible]rke, Jr.

PHILCO CORPORATION
A Subsidiary of Ford Motor Company
Western Development Laboratories
Palo Alto, California

A PORTABLE RADIOMETER FOR ANTENNA STUDIES*

By

G. L. Johnson and F. P. Storke, Jr.**

PHILCO CORPORATION
A subsidiary of Ford Motor Company

Western Development Laboratories

Palo Alto, California

Introduction

Historically radiometers have been used in radio astronomy. However, the techniques of radiometry are applicable to many other fields and often they are used to good advantage. Some examples of this are an iceberg detector[1], automatic noise figure meters[2], and power meters which balance the unknown radio frequency power[3]. This paper describes the application of radiometric techniques to antenna studies.

In the context of this paper, it is helpful to consider the radiometer receiver as a very sensitive, stable power meter rather than a device for detecting astronomical phenomena. With this concept many applications for the device become apparent. For antenna studies a maximum sensitivity of about 1° Kelvin appears to be adequate, based on the expected noise temperatures, their variations, and the usefulness of more accurate measurements on microwave components.

The radiometer is used to measure certain parameters of antenna system performance, including pattern, and losses in microwave components. It can be used for site surveys to measure background radiation, both natural and man-made. It can also be used for antenna position calibration with either coherent or noncoherent signal sources. The device is also useful for measuring the excess noise temperature of low noise receivers, especially those with

* This radiometer was developed under Air Force Space Systems Division Contracts AF04(647)-532 and -829

** Presently with Syntax, Inc., Emeryville, California

excess noise temperatures of less than 100° Kelvin.

WDL Radiometer

In radio astronomy the emphasis has been to obtain greater and greater sensitivity. In the device described, extremely high sensitivity (in the radio astronomy sense) is not required. Sensitivity equal to that of a very low noise instrument is obtained by using radiometer techniques with a relatively noisy receiver. A radiometer receiver with a sensitivity of about 1° Kelvin can be constructed simply and economically.

At WDL a radiometer has been constructed with the characteristics shown in Table 1. The unit is portable and may be operated with either a battery pack or a-c power. The radiometer is constructed of solid state subassemblies. Solid state units were selected primarily because of their efficiency, performance and voltage requirements, as well as for ruggedness and reliability. Small size was also a factor since a high degree of portability is mandatory. Portability is very important since measurements may be desired at many points in the antenna system. Figure 1 shows the complete radiometer.

Table 1. WDL Portable Radiometer Characteristics

Type of Radiometer	Dicke
Center Operating Frequency	2240 Mc
Minimum Detectable Signal	0.8° K
Maximum Input Signal	500° K
Bandwidth	6 Mc
Noise Figure	10 db
Integration Times	0.1, 0.3, 1, 3, 10, 30 seconds
Power	100 watts - either battery or a-c operated
Size	Radiometer 14" x 15" x 27" Battery Pack 8" x 8" x 12" Power Supply 6" x 15" x 16"
Weight	Radiometer 80 pounds Battery Pack 34 pounds Power Supply 40 pounds

Before describing the details of the radiometer, it is informative to review the basic theoretical considerations of a radiometer and see how they guide the design of the radiometer. The sensitivity of a receiver may be broken down into three basic factors: the sensitivity limit due to internal noise, that due to impedance modulation, and that due to gain fluctuation.

Generally, for a total sensitivity of about 1° K, the largest of the threshold sensitivities is the first, namely the one due to internal noise. This threshold is described by Equation 1.[4]

$$T_N = \frac{k\,T_R}{B\,\tau} \qquad (1)$$

In this equation T_N is the threshold differential temperature.

k is a constant relating the efficiency of switching, detection, filtering, and operator detectability.

T_R is the effective noise temperature of the receiver.

B is the predetection bandwidth.

τ is the output integration time constant.

From Equation 1, it can be seen that the threshold sensitivity can be lowered by lowering the receiver noise figure, by increasing the predetection bandwidth or by increasing the integration time. Radiometers have been built which emphasize each of these techniques. The maser radiometer at the University of Michigan is typical of those emphasizing low noise figure.[5] An Ewen Knight tuned radio frequency traveling wave tube radiometer has a 1000 mc bandwidth showing the possibilities in that direction.[6] Other radiometers have been constructed emphasizing gain stability which allow integration times of several minutes.

The threshold due to gain fluctuations is described by Equation 2.

$$T_G = T_{C1} - T_{C2} \qquad (2)$$

where

T_G = the threshold temperature determined by gain fluctuation.

T_{C1} , T_{C2} = temperatures of the comparison sources.

ℓ - 1 = gain variability factor defined by

$$\ell = 1 + \frac{\frac{G(t) - G_o}{G_o} \quad \frac{A(t) - A_o}{A_o}}{\text{rms}} \qquad (3)$$

G(t) = predetection power gain at time t.

G_o = average predetection power gain.

A(t) = postdetection voltage gain at time t.

A_o = average postdetection voltage gain.

With careful design ℓ - 1 can be made 0.001 or less. Using a thermal reference at 300° and looking into the cold sky, one obtains a threshold of approximately 0.3° K.

The sensitivity threshold due to impedance fluctuation is a result of mismatch between the receiver and the reference noise source or the antenna noise source. This effect can be taken into account in the calibration of the radiometer and this threshold can be eliminated if constant impedances can be maintained. However, in the case of a moving antenna, the characteristic impedance of the source may vary with antenna position and thus the match between the antenna and the source may vary with antenna position. For most antenna measurements this variation is not pertinent since one is interested in the antenna noise temperature rather than the source temperature.

These thresholds may be considered random in nature and the total sensitivity of the radiometer is the sum of the individual thresholds. As pointed out earlier, for the present case this is essentially the threshold due to internally generated noise.

It was determined that the required sensitivity could be attained with a receiver having a noise figure of 10 db and a predetection bandwidth of 6 mc. Six megacycles was selected as it approximates the bandwidth of many receivers. This would allow a 1° K sensitivity for an integration time of 20 seconds.

Figure 2 shows a plot of the sensitivity versus integration time.

Figure 3 is a block diagram of the [illegible] radiometer. It is a Dicke type radiometer with a conventional superheterodyne receiver. The operation of the device is as follows: the receiver measures the difference in average noise power between the two sources connected alternately to the receiver by the rf switch. One source, noise source number 2, provides the reference level, the other source consists of the antenna plus noise source number 1. Extra noise is added to the antenna noise to reduce the difference between the noise levels on either side of the switch. Minimizing the difference between the noise levels lowers the requirements upon receiver gain stability. Noise source 1, a gas discharge source, is also used to calibrate the system. Noise source 2 is resistive termination maintained at a constant temperature. The rf switch is a reversible ferrite circulator driven at approximately 80 cycles per second.

Since only a 10 db noise figure is required, a double channel crystal mixer centered near 2200 Mc, followed by a transistorized IF amplifier, is adequate. This technique eliminates the need for costly, complex, microwave amplification. The local oscillator signal derives from a crystal controlled oscillator via a harmonic generator chain. The IF amplifier operates at 30 Mc and has a bandwidth of 6 Mc.

A square-law detector determines the difference between the two inputs and converts the power difference to a voltage difference. This type of a detector can be shown to be superior to a linear detector for radiometer applications.

The audio amplifier raises the signal up to a suitable level for recording and a phase detector determines the proper sign of the noise difference. The information is integrated with a selected time constant and recorded. Integration times from 0.1 to 30 seconds are available.

Antenna Noise Measurements

The receiver described was constructed to measure the antenna noise temperature of a 60 foot parabolic antenna. The purpose of the

measurement was to determine the applicability of low noise receivers to such an antenna. Most of the design criteria for the radiometer was consequently dictated by the requirements of the antenna noise measurement. The antenna noise consists of noise received by the antenna from all directions. There are contributions from the main, side, and back lobes and losses in the reflector. The sources of the received noise are thermal noise from the ground and atmosphere, extra-terrestrial noise, and man-made noise. Thus, it can be seen that the total antenna temperature at a given frequency can vary greatly as a function of antenna pattern, antenna pointing direction, site location, and atmospheric conditions.

The antenna noise temperature represents the lower limit of the effective system noise temperature. It would be the system noise temperature if one had a noiseless receiving system. Therefore, it is very important to know this limit and consider it when choosing a receiving system. For example, a system with a receiver whose effective noise temperature is 10° K is not 10 db better than a system with a 100° receiver. If the two were used with a typical 60 foot parabolic reflector, the system with the 10° K receiver would at best be only about 5 db better.

Effective antenna noise temperature is measured by connecting the radiometer as close to the antenna feedhorn as possible and measuring the noise at that point. The measured noise must be reduced by the noise from losses in the interconnecting sections between the radiometer and the feedhorn in order to determine the actual antenna noise temperature. Generally the noise due to losses is inferred from short circuit impedance measurements.

Antenna Patterns

The radiometer can be used as a sensitive receiver to measure the pattern of an antenna. It may be used in conjunction with a coherent generator as has been standard practice. The radiometer was checked using a 10 foot parabolic antenna and found to be about 20 db more sensitive than the conventional receiver that was normally

used. The increased sensitivity makes it possible to consider the use of a convenient noncoherent signal source, the sun.

Extraterrestrial sources are desirable signal sources for two reasons. First, the measurement can be made with the elevation angle of the antenna sufficiently great to eliminate reflections from the ground. Secondly, and possibly more important, as antennas become larger and larger, it is more difficult to place a signal source in the far field. The commonly accepted far field distance, $2D^2/\lambda$, is so great that the curvature of the earth and other limitations make stationary signal sources very costly. Other techniques, such as signal sources aboard aircraft or balloons, are also expensive and seemingly operationally unreliable. Thus, extraterrestrial sources present an interesting possibility. They are definitely in the far field, very reliable, and very inexpensive to operate.

With a radiometer with a sensitivity limit of 1° K, the only practical extraterrestrial source is the sun. None of the other sources is powerful enough to be useful. At S-band the noise temperature of the sun is about 100,000° K, and thus side lobe levels down nearly 50 db can be measured. This is true for antennas with beamwidths less than the angular width of the sun. For antennas with a beamwidth greater than the sun's width, the measurable side lobe level would be less due to a decrease in the effective noise temperature of the sun. Since the sun subtends a finite angle, it will appear to broaden the antenna beamwidth. Techniques are available for eliminating this effect from the measured results.[7] This effect is smaller than one intuitively feels it would be. For example, the angular width of the sun is approximately 1/2°. When observed with an antenna whose beamwidth is 1/2°, the broadening factor is only 1.20.

Antenna Alignment

Antenna alignment, boresighting, consists of alignment of the radio frequency main beam axis with the antenna position readout devices. The radiometer is used as the receiver and either a coherent or

noncoherent source, whose position is known, is used as the boresighting target. The application using coherent sources is self evident. The possible use of weak noncoherent sources makes boresighting with radio stars very appealing. The advantages cited in the previous section concerning the sun apply to this case as well, plus the additional facts that the position of the stars is well known and the apparent movement of the stars makes it possible to calibrate the antenna over virtually the entire hemisphere rather than at just a few points, as is the case with a fixed boresighting tower.

The antenna may be pointed in a given direction and let the radio source drift through the beam, or if the source is sufficiently powerful, the beam can be swept across or locked on the source. The choice of technique is determined primarily be the integration time required to obtain a clear signal from the source. If the time is very long, the drift technique is required. The other techniques will probably allow quicker calibration.

Component Loss

The radiometer is useful for many other applications besides measurements directly involving the antenna proper. One of the most important is its use in measuring the loss in microwave components. In connection with antenna systems this would include such devices as waveguide and coaxial sections, filters, isolators, duplexers, etc. In low noise systems, loss in components is a very important consideration. Important generally because of the thermal noise added by the loss and not because of the signal loss. The following example helps illustrate this point.

Assume an antenna temperature of 35° K and a loss in the feedhorn and waveguide section connecting the antenna to the receiver of 0.4 db. If the waveguide section is uncooled, the noise added by the lossy section is 25° K. The total noise at the input to the receiver is 57° K or an increase of 63%. The signal loss is 9%, almost a negligible amount. The signal to the noise ratio at the receiver is 1.8 times poorer than at the input to the feedhorn.

The radiometer is used to measure the change in noise level and from this the loss can be calculated. The input and output noise of a lossy section is desribed by Equation 4.

$$T_{out} = \frac{T_{in}}{L} + \frac{T_L(L - 1)}{L} \qquad (4)$$

Solving for L

$$L = \frac{T_L - T_{in}}{T_L - T_{out}} \qquad (5)$$

L = loss of the component

T_L = temperature of the lossy element in degrees Kelvin

T_{in} is measured by placing the radiometer in front of the component. T_{out} is measured by connecting the radiometer to the output of the component.

The question arises "How accurate is this type of measurement?" From Equation (5) it can be seen that for a given accuracy in measuring T_{in} and T_{out} the accuracy of the loss measurement will depend upon the magnitude of T_{in}. Figure 4 shows a comparison of the accuracy available with this technique with that from a measurement of loss with a standing wave measurement. The standing wave curve is constructed, assuming a perfect short at the input of the component and that the standing wave ratio measured to an accuracy of 1%. The radiometer curves assume that T_{in} and T_{out} are measured to an accuracy of 1° K. Both sets of curves assume that the component is matched to the measuring device. The curves show that accuracy comparable to that obtained with standing wave measurements is possible.

There are two distinct advantages to loss measurement by measuring the added noise. The first is the fact that no short circuit is required. The second is that the loss of unilateral devices, such as isolators and circulators, can be measured. Loss in unilateral devices is generally determined with a simple insertion measurement. However, for small losses, this method provides limited accuracy. The noise measurement, on the other hand, works best for small losses.

Receiver Effective Noise Temperature Measurement

Another application of the radiometer is the measurement of the effective noise temperature of low noise amplifiers. The noise temperature is measured by the standard technique of determining a Y factor. The Y factor is determined by the amplifier output being supplied with two different noises T_1 and T_2. The receiver output noise T_{01} and T_{02} is described by the following

$$T_{01} = (T_1 + T_R) \; G_1 \; G_3 + T_3 \; G_3 \tag{6}$$

$$T_{02} = (T_2 + T_R) \; G_2 \; G_3 + T_3 \; G_3 \tag{7}$$

where T_R = amplifier effective noise temperature

G_1 = receiver gain when connected to source 1

G_2 = receiver gain when connected to source 2

G_3 = gain of units following the amplifier

T_3 = effective noise temperature of units following the amplifier

If the amplifier gain is high enough and $G_1 = G_2$, Equations 6 and 7 reduce to

$$\frac{T_{01}}{T_{02}} = \frac{T_1 + T_R}{T_2 + T_R} = Y \tag{8}$$

Solving for T_R

$$T_R = \frac{T_1 - YT_2}{Y - 1} \tag{9}$$

Equation 9 points out the fact that if T_R is small, then T_1 and T_2 should also be small to make Y sensitive to changes in T_R. This is where the radiometer is helpful. A good source of low noise is the cold sky, and the radiometer can be used to measure its noise temperature. The other noise source can then be obtained in several ways. A good way is to add thermal noise to the sky noise by inserting a precision attenuator in the line. A matched termination cooled by liquid nitrogen or dry ice, or, for certain cases, a room temperature load provides a stable reference noise source.

It would be desirable to be able to select the set of sources yielding the most accurate determination of T_R for a given accuracy of T_1 and T_2. Figure 5 shows several possible combinations. The best choice

is that which has the flattest slope in the region of the expected noise temperature. It can be shown that the best choice is for T_2 to be zero or as small as possible and T_1 to be equal to T_R.

In addition to measuring the noise temperature of the sources, the radiometer can be used to measure the Y factor. This can be done in the following way. Assume that the cold sky is selected for T_2, and T_1 is a matched termination cooled by liquid nitrogen. These are connected to the unknown and reference inputs of the radiometer and the low noise receiver inserted between the circulator and the mixer. The radiometer will then switch between the two sources and the Y factor can be measured at the output of the square-law detector.

Antenna Measurements

The radiometer described was used to measure the antenna noise temperature of a 60 foot parabolic antenna located at Vandenberg Air Force Base. Several drift patterns of the moon and Cassiopeia A were also taken to demonstrate the feasibility of boresighting large antennas using extraterrestrial sources as boresighting targets.

The radiometer was connected at the normal location of the preamplifier, approximately 60 feet from the reflector focus. The loss in the connecting waveguide and feedhorn was compensated for, allowing the actual antenna temperature to be recorded directly. The sky was mapped by pointing the antenna at a selected azimuth angle and moving the antenna through all declination angles very slowly. Declination angle information was recorded along with the antenna noise temperature. Data was taken at several azimuth angles. The antenna temperature was found to be nearly independent of azimuth angle. Figure 6 shows a plot of antenna noise temperature vs. elevation angle.

An interesting point was the noise temperature received when the antenna was pointing toward the ocean. As one would expect, the noise received was considerably less than that received from the ground. Another point of interest was the shape of the noise

temperature curve. The ground and high elevation angle noise was very close to the predicted values, but the noise at low elevation angles was lower than anticipated. This tends to indicate that the first side lobe level is lower than that for a typical parabolic reflector.

Drift patterns of the moon were taken by positioning the antenna visually and letting the moon drift through the beam. Drift patterns of Casseopeia A were also taken. Both the moon and Casseopeia A were easily detected with their peak levels very near the expected value.[8] The moon was very new when it was observed and probably near its coldest phase. Figures 7 and 8 show typical smoothed drift patterns. The noise level on the actual recordings was approximately 2° K.

Conclusions

This project has shown that a very sensitive power meter is an important piece of test equipment for work on low noise receiving systems. The radiometer technique described appears to be the simplest and most economical way to construct an instrument with the desired sensitivity. The instrument is useful for many types of antenna studies, calibration, and maintenance. It is also useful for measurement of loss in microwave components and effective noise temperature of low noise amplifiers.

Acknowledgement

The authors are indebted to J.D. Bowes for his work on the antenna measurements and to Dr. D.A. Linden for his helpful suggestions in the preparation of the manuscript.

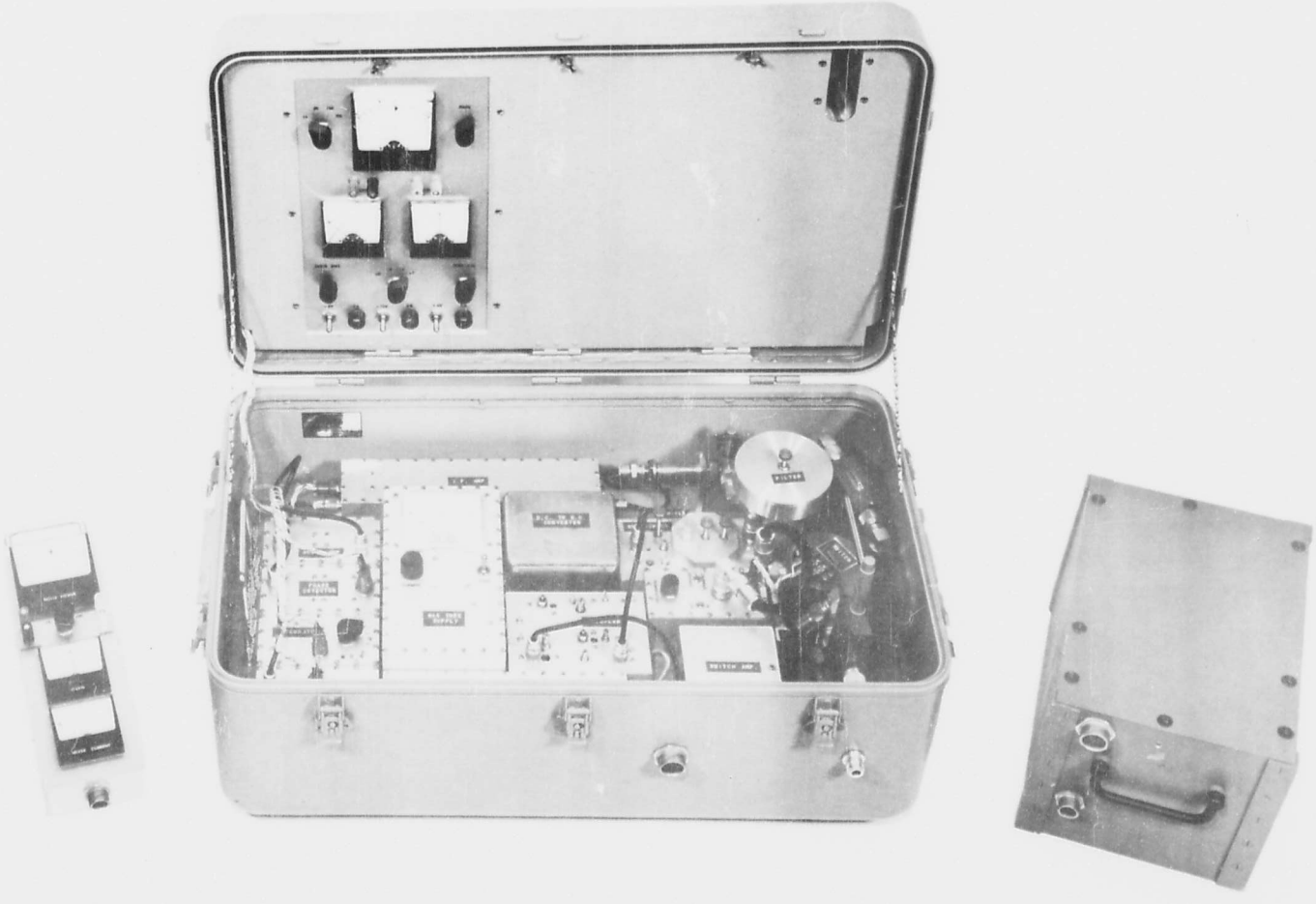

Figure 1 Complete Radiometer

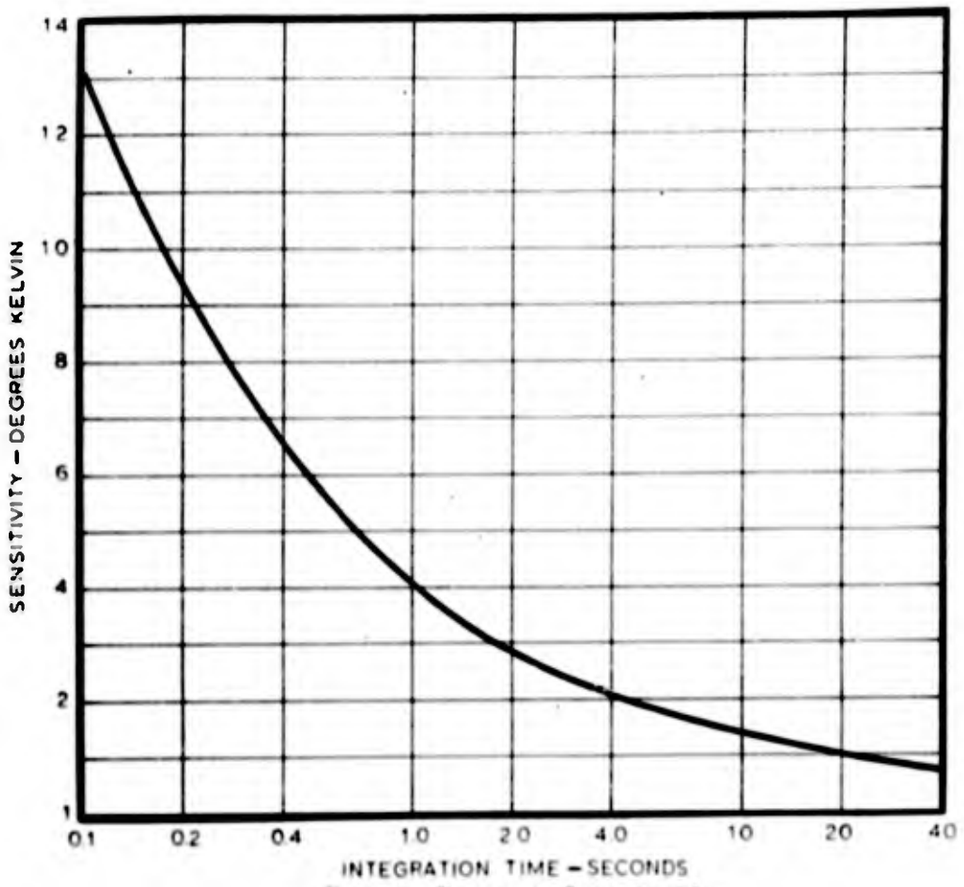

Fig. 2 Receiver Sensitivity

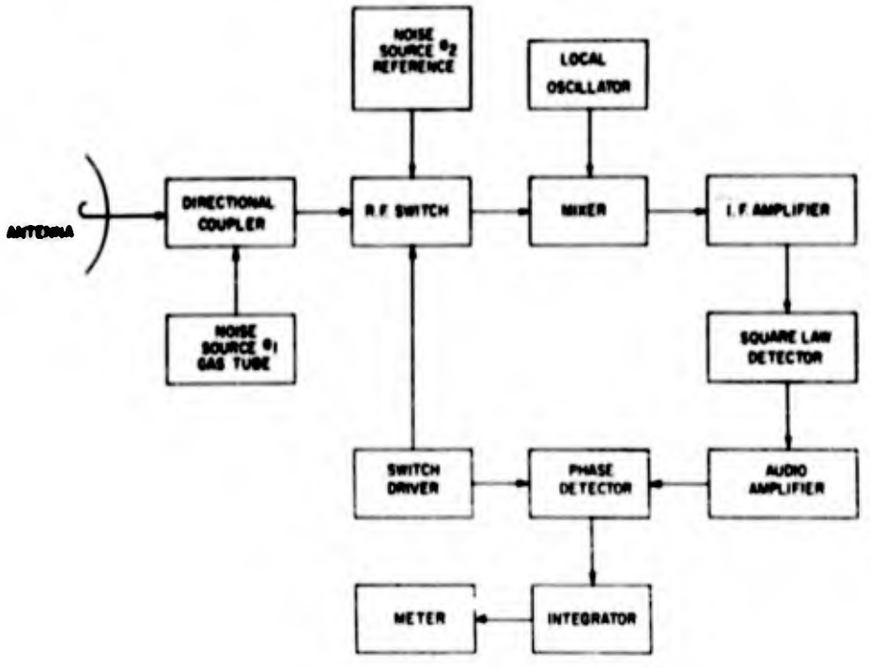

Fig. 3 PORTABLE RADIOMETER

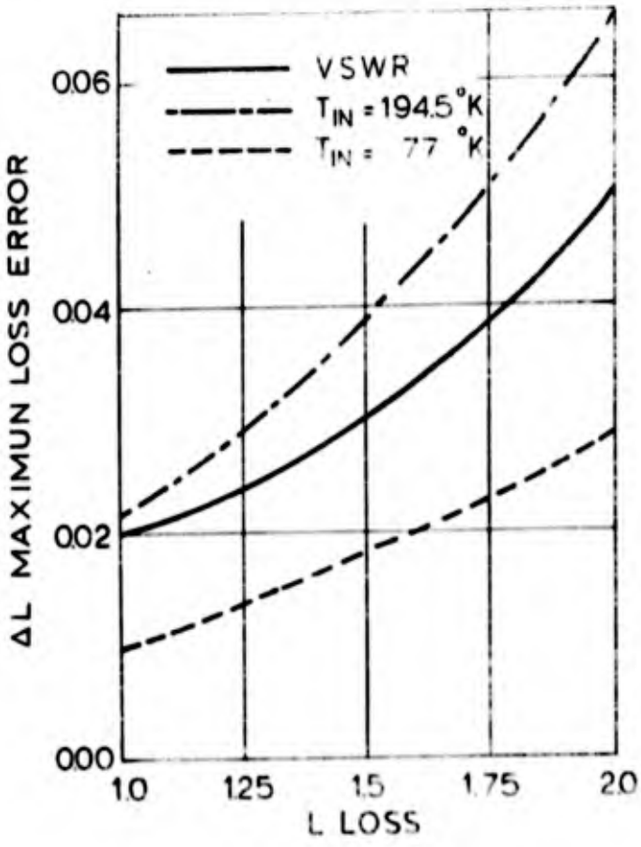

FIG 4 MEASUREMENT ACCURACY

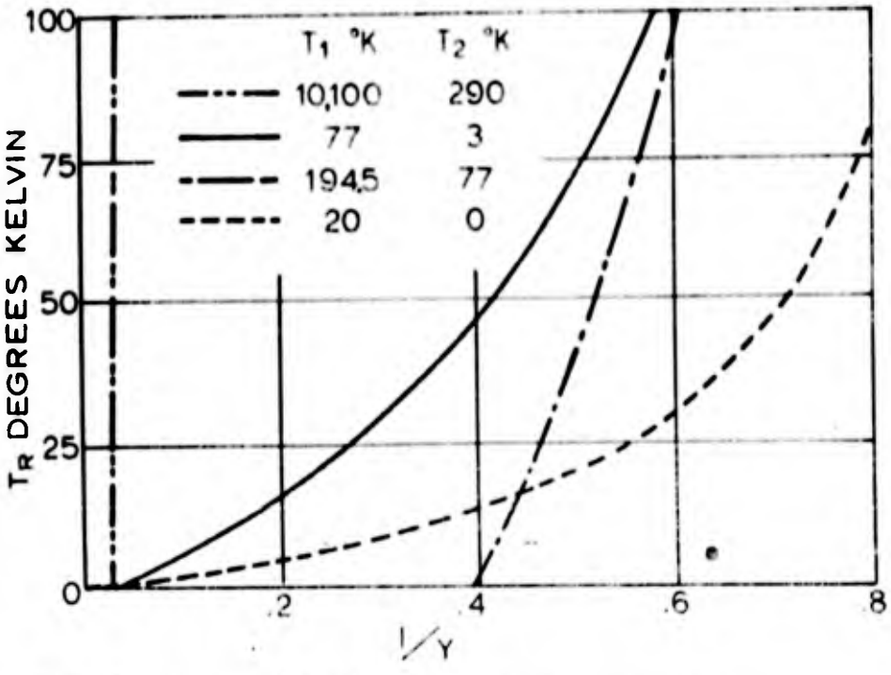

FIG. 5 SELECTION OF NOISE SOURCES

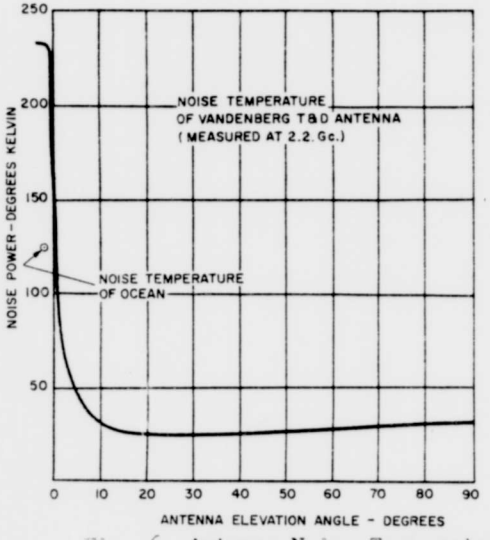

Fig. 6 Antenna Noise Temperature

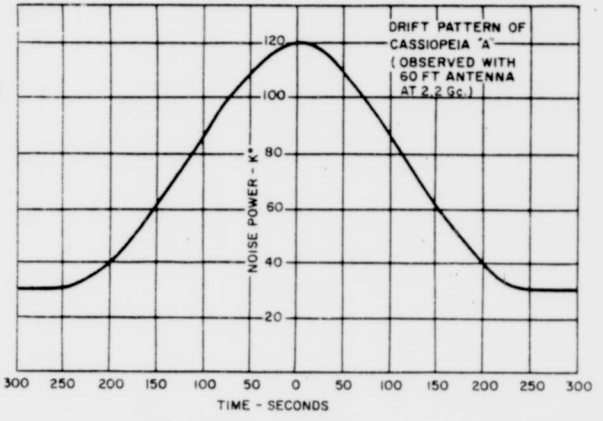

Fig. 7 Drift Pattern of Radio Star

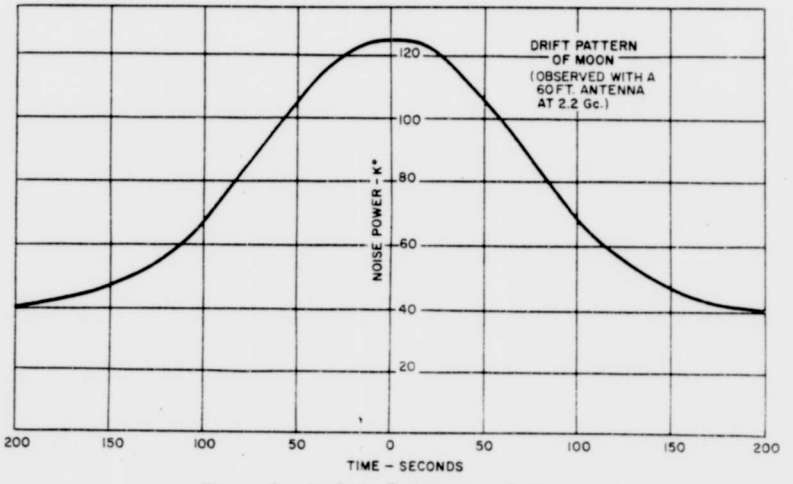

Fig. 8 Drfit Pattern of Moon

References

1. T.V. Seling, D.K. Nance, "Sensitive Microwave Radiometer Detects Small Icebergs", Electronics Vol. 34, No. 19, May 12, 1961, pp 72-75
2. Hewlett Packard Instruction Manual - Model 342A Automatic Noise Figure Meter, Section III Theory of Operation
3. E.L. Ginzton, Microwave Measurements, McGraw-Hill Book Company, New York, 1957, pp 175-177
4. Peter D. Strum, "Considerations in High-Sensitivity Microwave Radiometry", Proceedings of the IRE, Vol. 46, No. 1, Jan. 1958, pp 43-53
5. J.J. Cook, et al., "A Low-Noise X-band Radiometer Using Maser" Proceedings of the IRE, Vol. 49, No. 4, April 1961, pp 765-778
6. F.D. Drake and H.I. Ewen, "A Broad-Band Microwave Source Comparison Radiometer for Advanced Research in Radio Astronomy", Proceedings of the IRE, Vol. 46, No. 1, Jan. 1958, pp 54-60
7. S. Matt and J.D. Kraus, "TheEffect of Source Distribution on Antenna Patterns", Proceedings of the IRE, Vol. 43, No. 7, July 1955, pp 821-825
8. A.R. Giddis, "Limitations of Communication Systems by Antenna Noise", Philco Western Development Laboratories Report, WDL-TR1692, Section 3

APERTURE CHARACTERISTICS OF FLAT PLATE CONICAL SCAN ANTENNAS

John E. McSweeny
Electronic Engineer

GENERAL DYNAMICS/POMONA
POMONA, CALIFORNIA

30 August 1962

APERTURE CHARACTERISTICS OF FLAT PLATE CONICAL SCAN ANTENNAS

I. INTRODUCTION

The object of this paper is to compare the scanning characteristics of the $(1-r^2)^p$ family of distributions for circular apertures. The reason such a study was undertaken was the increased interest in conical scanners as tracking antennas and the space requirements often limiting these scanners to circular configurations.

To most efficiently use the circular aperture each quadrant is treated as a separate antenna. The phase shifter located in each arm are driven sinusoidally and in quadrature.

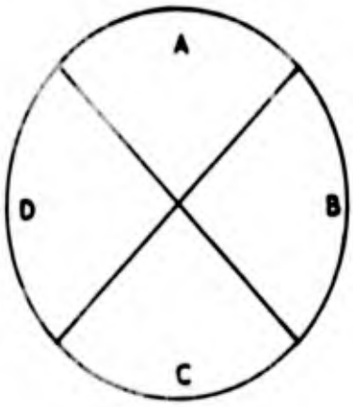

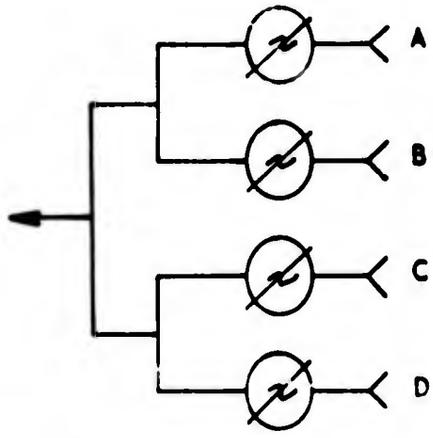

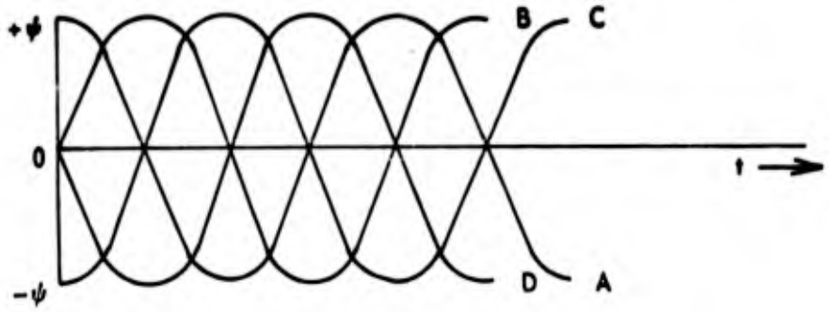

The output of the antenna when used as a receiving antenna is an amplitude modulated carrier. The tracking is based upon the magnitude of this AM and is a function of beam width, pattern symmetry, cross-over level, aperture characteristics as well as tracking error. These problems will be considered in this paper.

A number of difficulties are encountered in theoretically analyzing the operation of these antennas as well as problems inherent to the system. It is hoped that a solution to these problems is resolved in this paper and, although heuristic in nature, enough data presented to help synthesize these antennas for future applications.

II. PROBLEM

Previous to this study many of the antennas being designed for conical scanning used various forms of tapered distributions. In an effort to get a little deeper knowledge of the operation and predict the characteristics of these antennas several distributions of the form $(1-r^2)^p$ were investigated, where $p = 0, 1, 2$. It was hoped a knowledge of the uniform distribution ($p = 0$), parabolic ($p = 1$), and parabolic squared ($p = 2$) characteristics would reveal the limitation of tapered distributions over uniform. The gain and beam width characteristics of the uniform distribution offered an incentive but it was not known what would happen to the already high side lobes when the antenna was in the scanning mode. Tapered distributions have undesirable side-lobe characteristics when scanned. The low side lobes these distributions produce come up very rapidly when used on conical scan antennas. A solution suggested for these high side lobes is a passive center element which remains at zero phase. However, packaging requirements often make this solution impossible.

A number of attempts have been made to simplify the theoretical approach to the four element scanning array. They include arguments based on the existence of discrete phase centers and certain pattern assumptions in the cross-over region. Considering each quadrant as a separate element, a survey of the literature would indicate such an element does not have a phase center (References 1, 2, 3, 4). By a phase center, the author means that point in an antenna from which a spherical wave front can be considered to eminate. Further study of this subject has no place in this paper and will be left to the reader. Many of the pattern assumptions in the cross-over region provide interesting insights to the design parameters in the

cross-over region. Little if any work has been done to reveal side-lobe characteristics, however, which would of course include a more accurate knowledge in the cross-over region.

The direct application of a synthesis technique to this problem seems somewhat intangible as it is not known at the outset what phase shift is optimum for the optimum pattern and vice versa. To the best of the author's knowledge at this time, the synthesis techniques for aperture antennas assume constant phase distributions. Techniques have been suggested for synthesizing optimum difference patterns but there seems to be no reason to believe an antenna which operates in a mode which is neither sum nor difference will have optimum side-lobe characteristics. With this in mind, the class of $(1-r^2)^p$ aperture distributions was considered from scalar diffraction theory (References 5, 6).

III. THEORETICAL APPROACH

From Kirchoff Diffraction Theory, the disturbances at P' for an incident, uniform, cophasal, plane wave, subject to the assumption $\lambda \ll 2\pi r$, becomes:

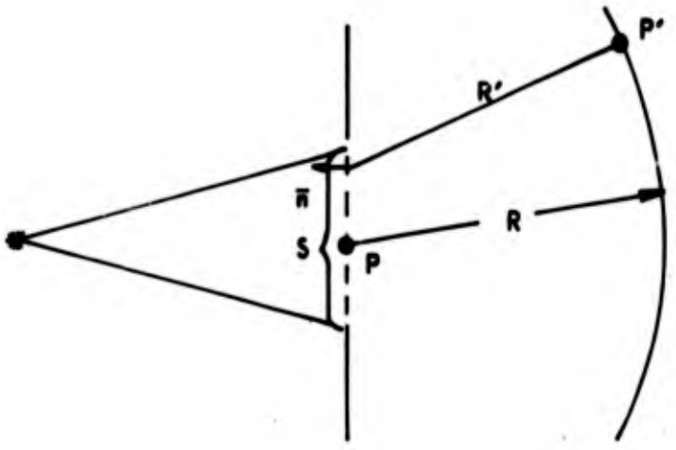

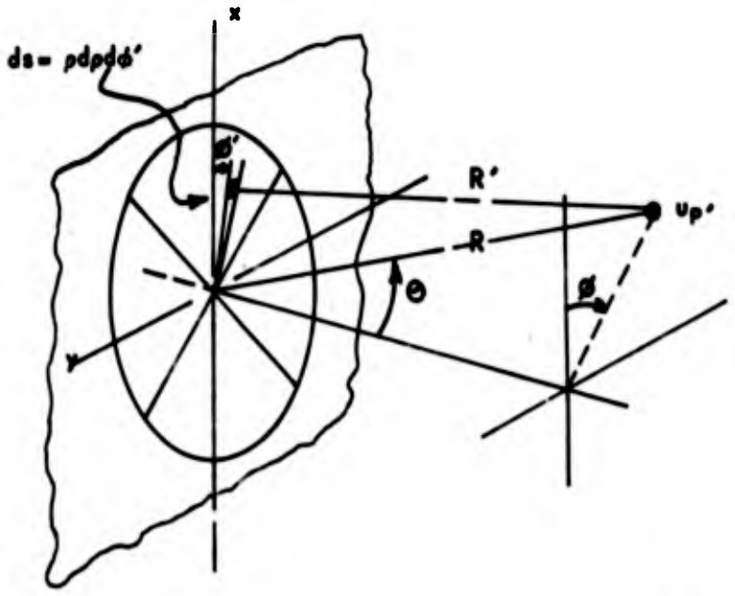

$$U_{P'} = \frac{1}{4\pi} \int_s \left[j \frac{\beta A e^{-j\beta R'}}{R'} + j \frac{\beta A e^{-j\beta R'}}{R'} \cos(\bar{n}, R') \right] dS$$

where $A = (a' - \rho')^P$ = aperture distribution, $(\bar{n}, R') \cong \theta$ in Fraunhofer region. If we assume P' is in the far zone, then:

$$R' \cong R - x \sin\theta \cos\phi - y \sin\theta \sin\phi$$

$$\begin{cases} x = \rho \cos\phi' \\ y = \rho \sin\phi' \end{cases}$$

or

$$R' \cong R - \rho \sin\theta \cos(\phi' - \phi)$$

Therefore,

$$U_{P'} = j \frac{\beta e^{-j\beta R}}{4\pi R} (1 + \cos\theta) \int_{\rho=0}^{a} \int_{\phi'=0}^{2\pi} A e^{j\beta\rho\cos(\phi' - \phi)} \sin\theta \, \rho d\rho d\phi'$$

Recall, this antenna is really a four element scanning array where each element is a quadrant driven separately and in phase quadrature. For this reason the above integral will be broken into four parts where each quadrant will be considered a separate aperture. In this way a phase term (ψ) can be assigned to each integral which is an independent variable and hence the total integral represents the circular aperture as a scanning array.

$$U_{p'} = j \frac{\beta e^{-j\beta R}}{4\pi R} (1 + \cos\theta) \; e^{j\psi_A} \int_{\rho=o}^{a} \int_{\phi'=-\pi/4}^{\pi/4} A e^{j\beta\rho \cos(\phi' - \phi) \sin\theta} \rho d\rho d\phi'$$

$$+ e^{j\psi_B} \int_{\rho=o}^{a} \int_{\pi/4}^{3\pi/4} A \ldots$$

$$+ e^{j\psi_C} \int_{\rho=o}^{a} \int_{3\pi/4}^{5\pi/4} A \ldots$$

$$+ e^{j\psi_D} \int_{\rho=o}^{a} \int_{5\pi/4}^{-\pi/4} A \ldots \qquad (1)$$

where

$\psi_A = \omega_1 t + \psi \sin(\omega_2 t)$

$\psi_B = \omega_1 t + \psi \sin(\omega_2 t + 90)$

$\psi_C = \omega_1 t + \psi \sin(\omega_2 t + 180)$

$\psi_D = \omega_1 t + \psi \sin(\omega_2 t + 270)$

ω_1 = carrier frequency

ω_2 = scan frequency

Consider quadrant A neglecting the phase term for now.

$$u_{p'_A} = j \frac{\beta e^{-j\beta R} (1 + \cos\theta)}{4\pi R} \int_o^a \int_{-\pi/4}^{\pi/4} (a^2 - \rho^2)^p \; e^{j\beta\rho \cos(\phi' - \phi) \sin\theta} \rho d\rho d\phi'$$

Let

$$r = \rho/a \ , \ u = \frac{2\pi a}{\lambda} \sin\theta = \frac{\pi D}{\lambda} \sin\theta$$

$$u_{P'_A} = j\frac{\beta e^{-j\beta R}}{4\pi R}(1+\cos\theta)\, a^2 \int_0^1 \int_{-\pi/4}^{\pi/4} (1-r^2)^P \, e^{jur\cos(\phi'-\phi)}\, r\,dr\,d\phi'$$

where the distribution function has been normalized to unity. It can be shown (Appendix I) that,

$$u_{P'_A} = j\frac{\beta e^{-j\beta R}(1+\cos\theta)}{4\pi R}\, a^2 \int_0^1 (1-r^2)^P \left\{ \sum_{-\infty}^{\infty} (j)^n \frac{J_n(ur)}{n} \left[2\sin\frac{n\pi}{4}\cos n\phi \right.\right.$$

$$\left.\left. + j2\sin\frac{n\pi}{4}\sin n\phi \right] \right\} r\,dr$$

$$u_{P'_A} = j\frac{\beta e^{-j\beta R}}{4\pi R}(1+\cos\theta)\, a^2 \int_0^1 (1-r^2)^P \left\{ \frac{\pi}{2} J_0(ur) \right.$$

$$+ 4\sum_{n=0}^{\infty} (-1)^{n+1} \frac{J_{2(2n+1)}(ur)}{2(2n+1)} \cos 2(2n+1)\phi$$

$$\left. + j4\sum_{n=0}^{\infty} (-1)^n \frac{J_{2(2n+1)}(ur)}{2n+1} \cos(2n+1)\phi \sin\frac{(2n+1)}{4}\pi \right\} r\,dr \qquad (2)$$

All but the first term are extremely difficult to integrate so it will be necessary to expand each Bessel function and integrate term by term for particular values of ϕ.

$$u_{p'_A} = j \frac{\beta e^{-j\beta R}(1+\cos\theta)}{4\pi R} a^2 \int_0^1 (1-r^2)^p \left\{ \frac{\pi}{2} J_0(ur) \right.$$

$$-4 \sum_{n=0}^{\infty} (-1)^n \frac{\cos 2(2n+1)\phi}{2(2n+1)} \sum_{m=0}^{\infty} \frac{(-1)^m (ur)^{2(2n+1)+2m}}{2^{2(2n+1)+2m} m!\ \Gamma(2n+m+2)}$$

$$\left. + j4 \sum_{n=0}^{\infty} (-1)^n \frac{\cos(2n+1)\phi \sin(2n+1)\pi/4}{2n+1} \sum_{m=0}^{\infty} \frac{(-1)^m (ur)^{2n+2m+1}}{2^{2m+2n+1} m!\,\Gamma(2n+m+2)} \right\} rdr \quad (3)$$

The integrated forms of U_p' for p = 0, 1, 2 will be found in Appendix II. It is easily shown that the expressions for $u_{p'_B}$, $u_{p'_C}$ and $u_{p'_D}$ are derived by a mere change of variable.

$$U_{p'_B} = U_{p'_A}(\phi - 90).$$

$$U_{p'_C} = U_{p'_A}(\phi - 180)$$

$$U_{p'_D} = U_{p'_A}(\phi - 270) \quad (4)$$

To get some understanding of the harmonic characteristics of this type of antenna, we may expand Eq. (1) replacing the integrals by $U_{p'_A}$, $U_{p'_B}$, etc.

$$U_{p'} = U_{p'_A} e^{j(\omega_1 t + \psi \sin \omega_1 t)} + U_{p'_B} e^{j[\omega_1 t + \psi \sin(\omega_1 t + 90)]}$$

$$+ U_{p'_C} e^{j[\omega_1 t + \psi \sin(\omega_1 t + 180)]} + U_{p'_D} e^{j[\omega_1 t + \psi \sin(\omega_1 t + 270)]} \quad (5)$$

$$U_{p'} = [U_{p'_A} \cos\psi \sin\omega_1 t + jU_{p'_A} \sin\psi \sin\omega_1 t$$

$$+ U_{p'_B} \cos\psi \sin(\omega_1 t + 90) + jU_{p'_B} \sin\psi \sin(\omega_1 t + 90)$$

$$+ U_{p'_C} \cos\psi \sin(\omega_1 t + 180) + jU_{p'_C} \sin\psi \sin(\omega_1 t + 180)$$

$$+ U_{p'_D} \cos\psi \sin(\omega_1 t + 270) + jU_{p'_D} \sin\psi \sin(\omega_1 t + 270)]\, e^{j\omega_1 t}$$

$$U_{P'} = \Big\{ U_{P'_A} \cos\psi \sin\omega_2 t + j\, U_{P'_A} \sin\psi \sin\omega_2 t$$
$$+ U_{P'_B} \cos\psi \cos\omega_2 t + j\, U_{P'_B} \sin\psi \cos\omega_2 t$$
$$+ U_{P'_C} \cos\psi \sin\omega_2 t - j\, U_{P'_C} \sin\psi \sin\omega_2 t$$
$$+ U_{P'_D} \cos\psi \cos\omega_2 t - j\, U_{P'_D} \sin\psi \cos\omega_2 t \Big\} e^{j\omega_1 t}$$

From Appendix II and Eq. (4), it can be shown,

$$\begin{cases} U_{P'_A} - U_{P'_C} = 2Re\, U_{P'_A} \\ U_{P'_B} - U_{P'_D} = 2Re\, U_{P'_B} \end{cases}$$

$$\begin{cases} U_{P'_A} + U_{P'_C} = j\,2Im\, U_{P'_A} \\ U_{P'_B} + U_{P'_D} = j\,2Im\, U_{P'_B} \end{cases}$$

assuming phase quadrature, $|U_{P'_A}| = |U_{P'_C}|$, and $|U_{P'_B}| = |U_{P'_D}|$.

Therefore,

$$U_{P'} = j2 \Big\{ Im\, U_{P'_A} \cos\psi \sin\omega_2 t$$
$$+ Im\, U_{P'_B} \cos\psi \cos\omega_2 t$$
$$+ Re\, U_{P'_A} \sin\psi \sin\omega_2 t$$
$$+ Re\, U_{P'_B} \sin\psi \cos\omega_2 t \Big\} e^{j\omega_1 t}$$

The multiplier in the brackets is the modulation term which can be put in a more convenient form to separate out the harmonics.

$$u_{P'} = j2 \Big\{ Imu_{P'_A} \Big[J_o(\psi) + 2 \sum_{k=1}^{\infty} J_{2k}(\psi) \cos 2k\omega_2 t \Big]$$
$$+ Imu_{P'_B} \Big[J_o(\psi) + 2 \sum_{k=1}^{\infty} (-1)^k J_{2k}(\psi) \cos 2k\omega_2 t \Big]$$

$$+ Re u_{P'_A}\left[2\sum_{k=1}^{\infty} J_{2k-1}(\psi)\sin(2k-1)\omega_2 t\right]$$

$$+ Re u_{P'_B}\left[2\sum_{k=1}^{\infty} (-1)^{k-1} J_{2k-1}(\psi)\cos(2k-1)\omega_2 t\right]\Bigg| e^{j\omega_1 t}$$

$$\begin{aligned} U_{P'} = j2 \Big| & (Im\, U_{P'_A} + Im\, U_{P'_B})\, J_0(\psi) \\ & + 2Re\, U_{P'_A}\, J_1(\psi)\cos\omega_2 t \\ & + 2Re\, U_{P'_B}\, J_1(\psi)\sin\omega_2 t \\ & + 2(Im\, U_{P'_A} - Im\, U_{P'_B})\, J_2(\psi)\cos 2\omega_2 t \\ & + \ldots \Big| e^{j\omega_1 t} \end{aligned}$$

This can be further simplified to

$$\begin{aligned} U_{P'} = j2 \Big| & (Im\, U_{P'_A} + Im\, U_{P'_B})\, J_0(\psi) \\ & + 2\sqrt{(Re\, U_{P'_A})^2 + (Re\, U_{P'_B})^2}\, J_1(\psi)\sin\left(\omega_2 t + \tan^{-1}\frac{Re\, U_{P'_A}}{Re\, U_{P'_B}}\right) \\ & + 2(Im\, U_{P'_A} - Im\, U_{P'_B})\, J_2(\psi)\cos 2\omega_2 t \\ & + \ldots \Big| e^{j\omega_1 t} \end{aligned} \quad (6)$$

Since the first harmonic is generally of prime interest, its modulation index would be:

$$m_1 = \frac{2\sqrt{(Re\, U_{P'_A})^2 + (Re\, U_{P'_B})^2}\, J_1(\psi)}{(Im\, U_{P'_A} + Im\, U_{P'_B})\, J_0(\psi)} \quad (7)$$

To evaluate equations such as those appearing in Appendix II by hand would be prohibitive. As a result, an IBM 7090 computer was used to calculate required parameters and a Stromberg-Carlson 4020 Plotter for necessary graphs. The computer program followed these general steps: (1) Determined the required phase shift (ψ) by a trial and error procedure for the specified modulation/degree from Eq. (7); (2) Determine the maximum look angle from a predetermined u_{max}; (3) Break the region of interest into 100 points and calculate $\ell_{F'_A}$, $\ell_{F'_B}$, $\ell_{F'_C}$ and $\ell_{F'_D}$ at each point for $\beta = 0$ and 45°; (4) Solve for the total $\ell_{F'}$ from Eq. (5) for $\beta = 0$ and 45°. The taped output was fed into the 4020 Plotter and curves such as those shown in Figures 1 and 2 recorded. Tabulated information tapped off the computer consisted of the real and imaginary parts of $\ell_{F'_A}$, $\ell_{F'_B}$, $\ell_{F'_C}$ and $\ell_{F'_D}$; the magnitude and complex form of total $\ell_{F'}$; and required peak phase shift. This information was tabulated to facilitate calculation of harmonic levels which might be needed at a later date. Although 10%/degree of modulation was chosen for this paper, the program is general in application. The only parameters that must be supplied to the computer are modulation/degree and aperture radius. The reason a u_{max} is necessary in Step #2 is because only a finite number of terms in the series are calculated and u_{max} guarantees convergence.

IV. CONCLUSIONS

Concerning the results themselves, a number of things should be pointed out. For antennas $< 5\lambda$ in radius there seems to be no side lobe advantages from tapered distributions (See Figures 3 and 4). This effect should be even more pronounced for higher modulation sensitivity. In these smaller antennas packaging may be a problem so that the higher phase shift requirements (Figure 5) of tapered distributions could be objectionable. Important cross-over gain (Figure 6) can be saved if the uniform distribution is used for antennas $< 5\lambda$ in radius. For antennas larger than this, phase shift is not an important parameter and therefore gain will be determined by side-lobe requirements or vice versa. As mentioned before, these effects will be more severe for increased modulation sensitivity. The curves, however, present useful and reliable design information for 10%/degree modulation sensitivity.

An antenna approximately 1.75 in radius has been built at General Dynamics/Pomona. Broadside and tilted (AM) patterns are compared with theory in Figures 7 and 8. The required phase shift of 75.4° determined by the computer agrees quite well to the 78° by experiment. These results seem to lend support to the reliable application of the design curves.

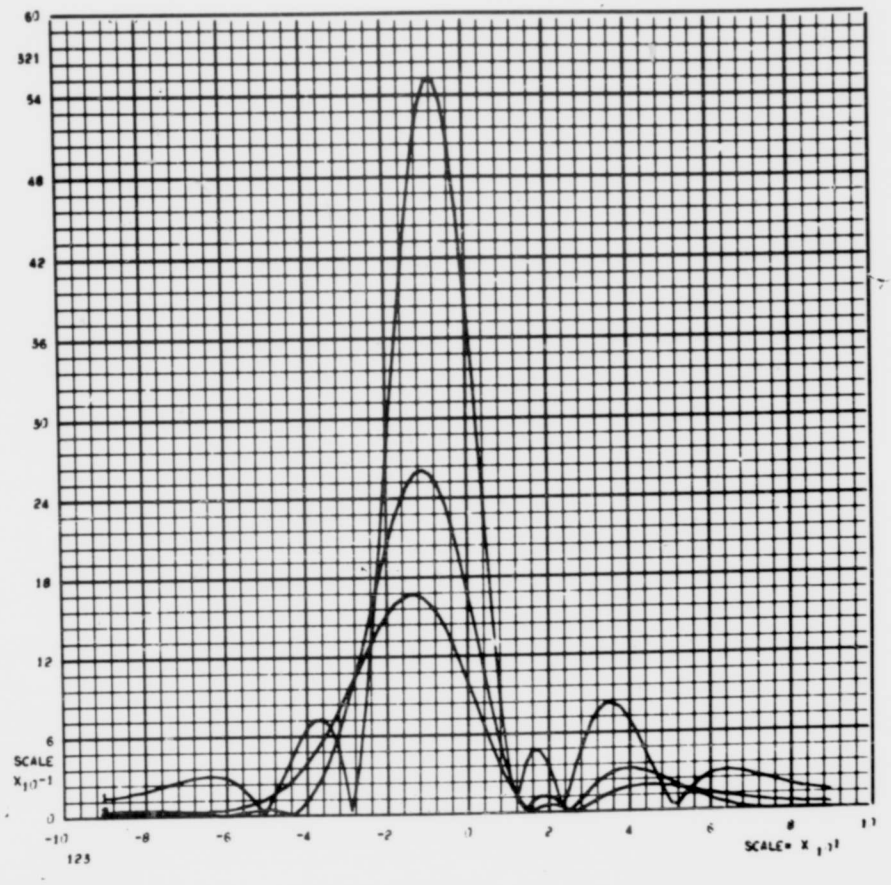
60
321
54
48
42
36
30
24
18
12
6
SCALE
X_{10}^{-1}
0
-10
-8
-6
-4
-2
0
2
4
6
8
10
123
SCALE= X_{10}^{1}
E VS THETA MOD/1.0=10 A=1.765 PHI=1 PLOT1,P=1 PLOT2,P=1 PLOT3,P=2

Figure 1.

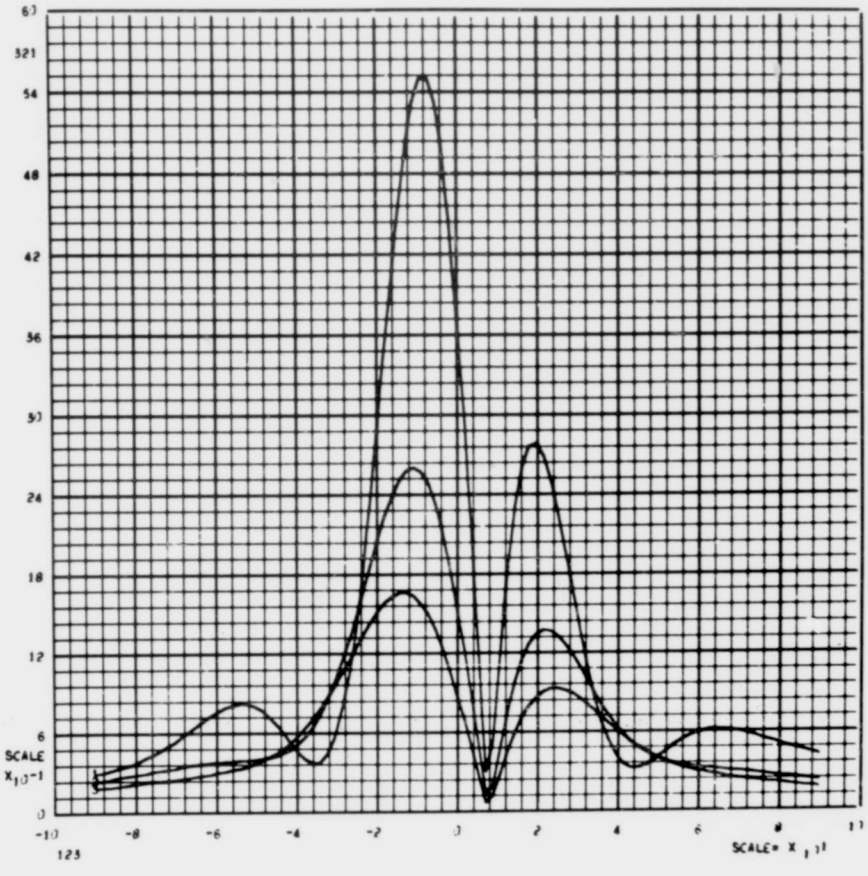

E VS THETA MOD/1.,0=10 A=1.765 PHI=45 PLOT1,P=1 PLOT2,P=1 PLOT3,P=2

Figure 2.

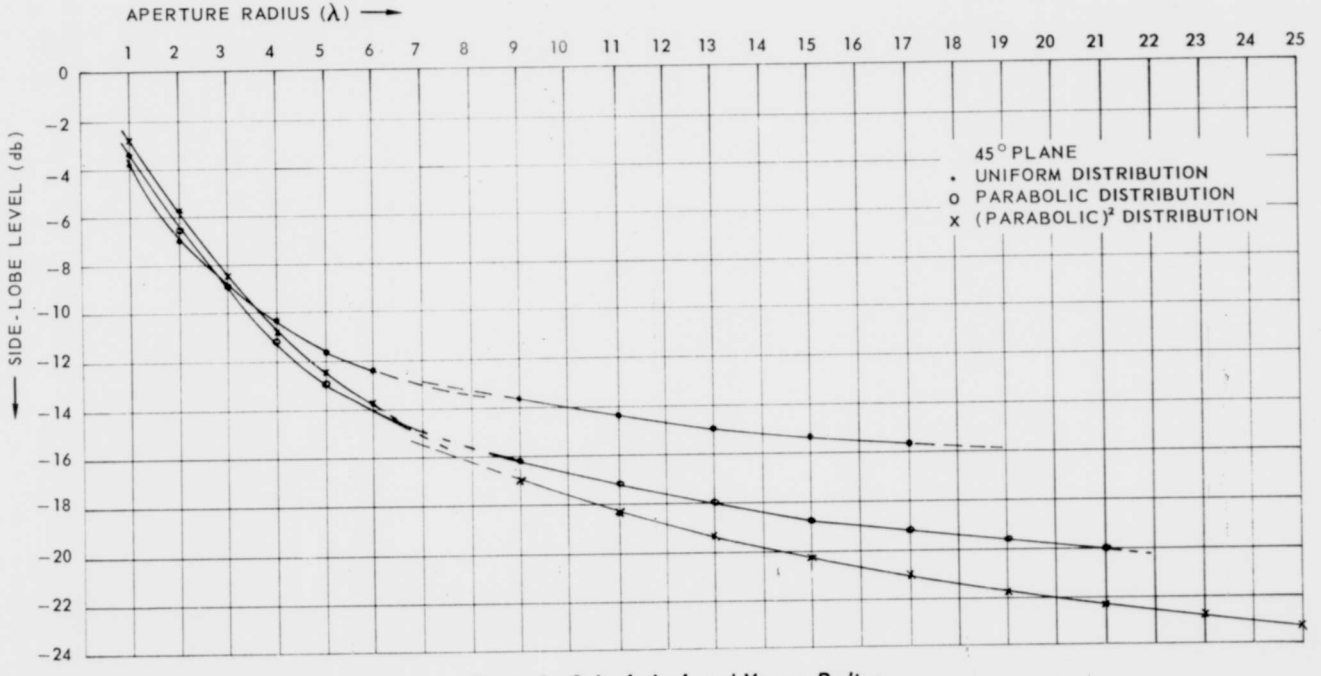

Figure 3. Side-Lobe Level Versus Radius.

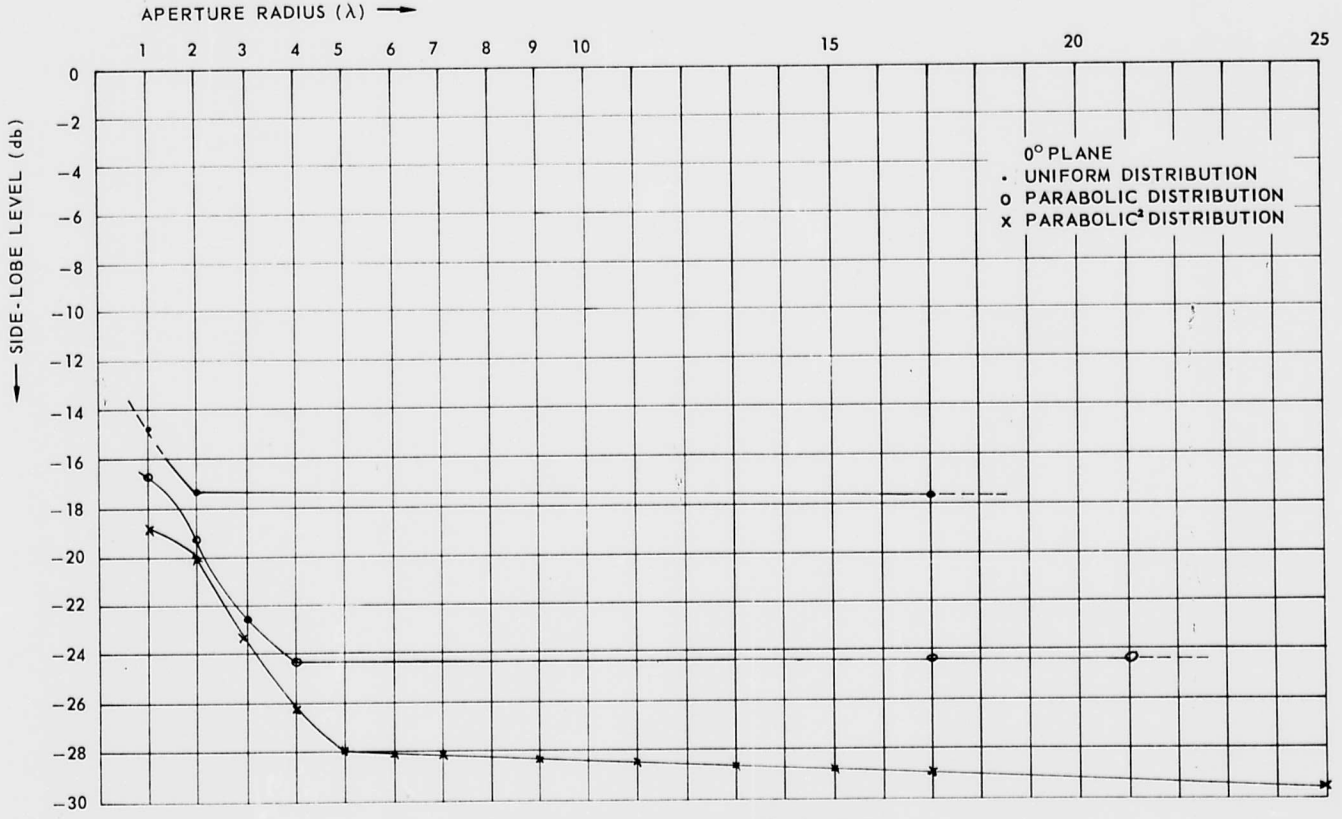

Figure 4. Side-Lobe Level Versus Radius.

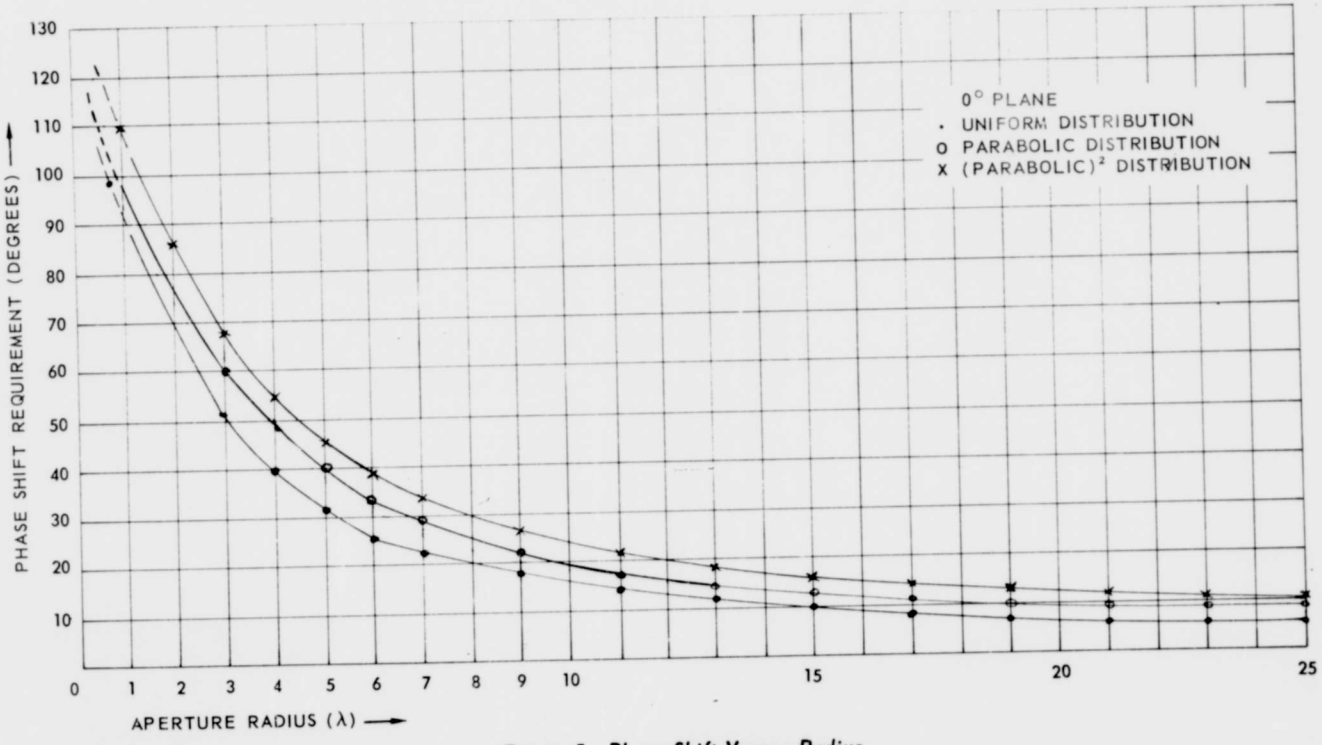

Figure 5. Phase Shift Versus Radius.

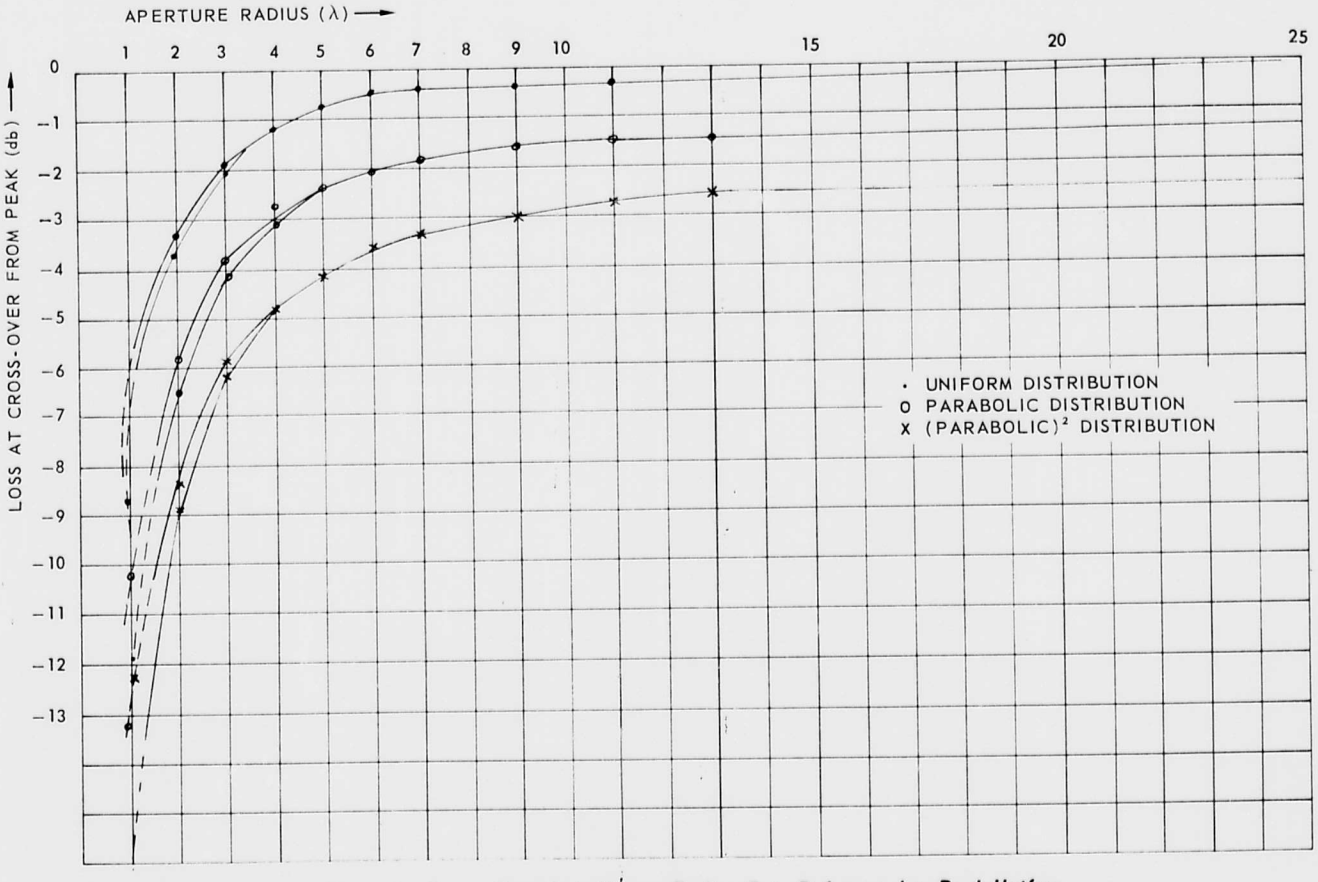

Figure 6. Cross-Over Gain Versus Radius Gain Referenced to Peak Uniform.

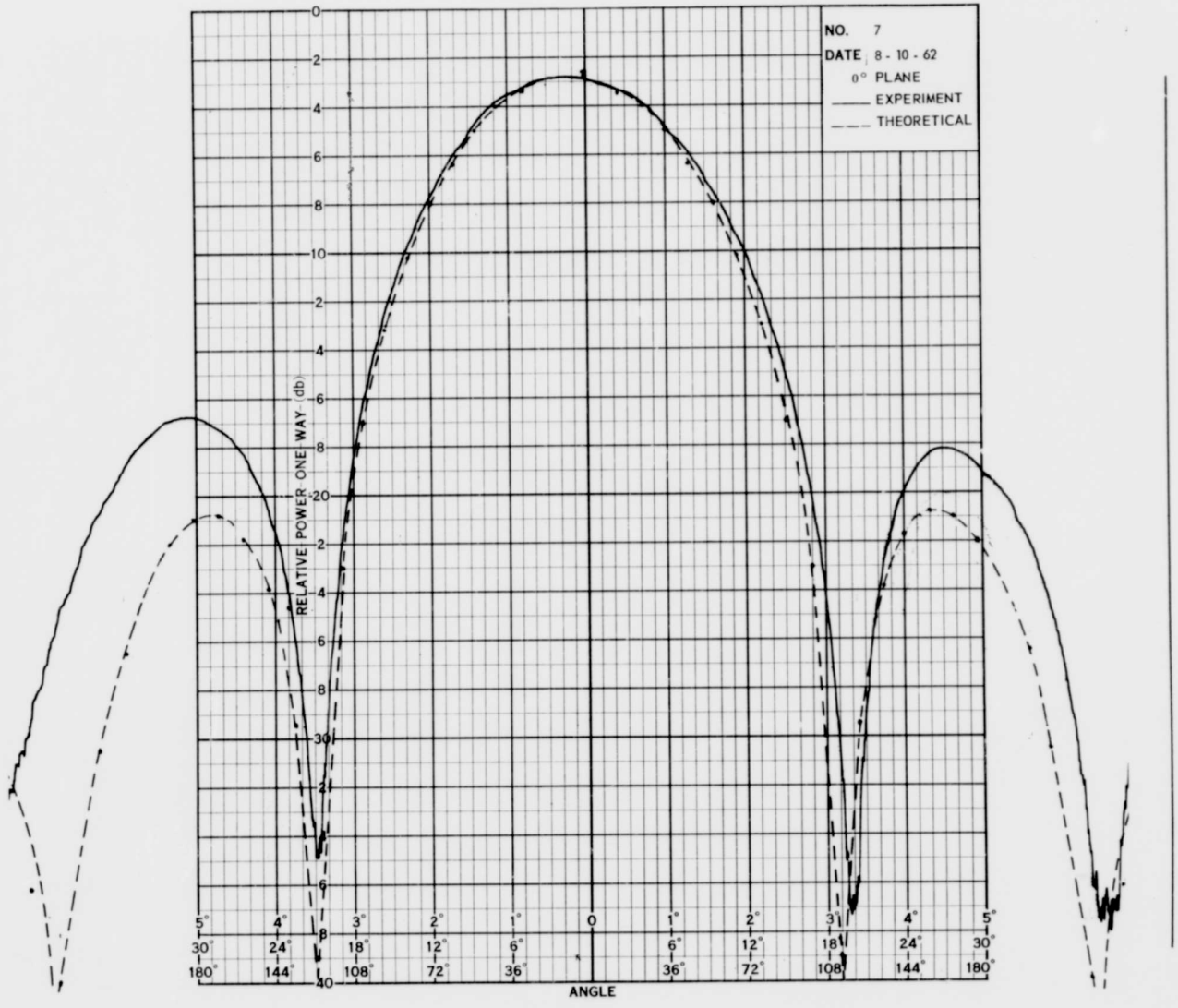
NO. 7
DATE 8 - 10 - 62
0° PLANE
EXPERIMENT
THEORETICAL
RELATIVE POWER ONE WAY (db)
ANGLE

Figure 7.

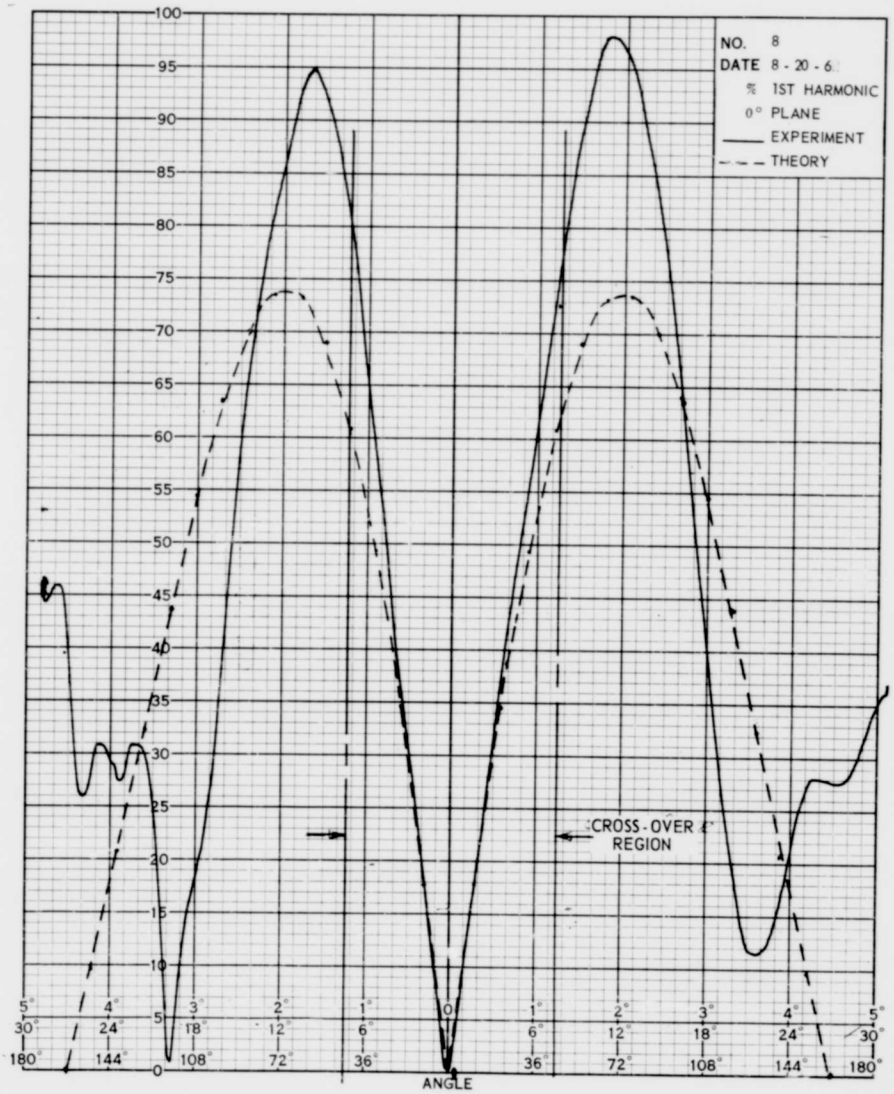
NO. 8
DATE 8 - 20 - 6
% 1ST HARMONIC
0° PLANE
EXPERIMENT
THEORY
CROSS-OVER REGION
ANGLE

Figure 8.

APPENDIX I

$$U_{P}' = j\frac{\beta e^{-j\beta R}}{4\pi R}(1+\cos\theta)\,a^{2}\int_{o}^{1}\int_{-\pi/4}^{\pi/4}(1-r^{2})^{P}\,e^{jur\cos(\phi'-\phi)}\,rdrd\phi'$$

Since,

$$e^{jur\cos(\phi'-\phi)} = \sum_{n=-\infty}^{\infty}(j)^{n}\,J_{n}(ur)\,e^{-jn(\phi'-\phi)}$$

$$U_{P_A}' = j\frac{\beta e^{-jR}\,a^{2}(1+\cos\theta)}{4\pi R}\int_{o}^{1}(1-r^{2})^{P}\int_{-\pi/4}^{\pi/4}\left[\sum_{n=-\infty}^{\infty}(j)^{n}\,J_{n}(ur)\,e^{-jn(\phi'-\phi)}\right]d\phi' rdr$$

Now,

$$\int_{-\pi/4}^{\pi/4}\sum_{n=-\infty}^{\infty}(j)^{n}\,J_{n}(ur)\,e^{-jn(\phi'-\phi)}\,d\phi' = \sum_{n=-\infty}^{\infty}(j)^{n}\,J_{n}(ur)\int_{-\pi/4}^{\pi/4}[\cos n(\phi'-\phi) - j\sin n(\phi'-\phi)]\,d\phi$$

$$= \sum_{n=-\infty}^{\infty}(j)^{n}\,J_{n}(ur)\int_{-\pi/4}^{\pi/4}[(\cos n\phi'\cos n\phi + \sin n\phi'\sin n\phi) - j(\sin n\phi'\cos n\phi - \cos n\phi'\sin n\phi)]\,d\phi'$$

$$= \sum_{n=-\infty}^{\infty}(j)^{n}\frac{J_{n}(ur)}{n}\Big|(\sin n\phi'\cos n\phi - \cos n\phi'\sin n\phi) + j(\cos n\phi'\cos n\phi + \sin n\phi'\sin n\phi)\Big|_{-\pi/4}^{\pi/4}$$

$$= \sum_{n=-\infty}^{\infty}(j)^{n}\frac{J_{n}(ur)}{n}\Big[(\sin\frac{n\pi}{4}\cos n\phi - \cos\frac{n\pi}{4}\sin n\phi + \sin\frac{n\pi}{4}\cos n\phi + \cos\frac{n\pi}{4}\sin n\phi) + j(\cos\frac{n\pi}{4}\cos n\phi + \sin\frac{n\pi}{4}\sin n\phi - \cos\frac{n\pi}{4}\cos n\phi + \sin\frac{n\pi}{4}\sin n\phi)\Big]$$

$$= \sum_{n=0}^{\infty} (j)^n \frac{J_n(ur)}{n} \left[2 \sin \frac{n\pi}{4} \cos n\phi + j\, 2 \sin \frac{n\pi}{4} \sin n\phi \right]$$

Therefore,

$$U_{P'_A} = j \frac{\beta e^{-j\beta R}(1 + \cos\theta)}{4\pi R} a^2 \int_0^1 (1 - r^2)^P \left\{ \sum_{n=0}^{\infty} (j)^n \frac{J_n(ur)}{n} \left[2 \sin \frac{n\pi}{4} \cos n\phi + j\, 2 \sin \frac{n\pi}{4} \sin n\phi \right] \right\} dr$$

This can be expanded and simplified,

$$= j \frac{\beta e^{-j\beta R}}{4\pi R}(1 + \cos\theta)\, a^2 \int_0^1 (1 - r^2)^P \left[\frac{\pi}{2} J_0(ur) \right.$$

$$- \frac{J_2(ur)}{2} 4 \cos 2\phi + j \frac{J_1(ur)}{1} 4 \cos\phi \sin \frac{\pi}{4}$$

$$+ 0 \qquad - j \frac{J_3(ur)}{3} 4 \cos 3\phi \sin \frac{3\pi}{4}$$

$$+ \frac{J_4(ur)}{6} 4 \cos 6\phi + j \frac{J_5(ur)}{5} 4 \cos 5\phi \sin \frac{5\pi}{4}$$

$$+ 0 \qquad - j \frac{J_7(ur)}{7} 4 \cos 7\phi \sin \frac{7\pi}{4}$$

$$\left. + \ldots \right|$$

or,

$$U_{P'_A} = j \frac{\beta e^{-j\beta R}}{4\pi R}(1 + \cos\theta) a^2 \int_0^1 (1 - r^2)^P \left\{ \frac{\pi}{2} J_0(ur) \right.$$

$$+ 4 \sum_{n=0}^{\infty} (-1)^{n+1} \frac{J_{2(2n+1)}(ur)}{2(2n+1)} \cos 2(2n+1)\phi$$

$$\left. + j4 \sum_{n=0}^{\infty} (-1)^n \frac{J_{2n+1}(ur)}{2n+1} \cos(2n+1)\phi \sin \frac{(2n+1)\pi}{4} \right\} r\, dr \quad (2)$$

APPENDIX II

@ $p = 0$

$$u_{p'_A} = j \frac{\beta e^{-j\beta R}(1+\cos\theta)a^2}{4\pi R}\left\{\frac{\pi}{4}\Lambda_1(u)\right.$$

$$-4\sum_{n=o}^{\infty}\frac{(-1)^n\cos 2(2n+1)}{2(2n+1)}\phi\sum_{m=o}^{\infty}\frac{(-1)^m\dfrac{u^{2(2n+1)+2m}}{2(2n+1)+2m+2}}{2^{2m+2(2n+1)}m!\Gamma(2(2n+1)+m+1)}$$

$$\left.+j4\sum_{n=o}^{\infty}\frac{(-1)^n\cos(2n+1)\phi\sin(2n+1)\pi/4}{2n+1}\cdot\sum_{m=o}^{\infty}\frac{(-1)^m\dfrac{u^{2n+2m+1}}{2n+1+2m+2}}{2^{2m+2n+1}m!\Gamma(2n+m+2)}\right\}$$

@ $p = 1$

$$u_{p'_A} = j \frac{\beta e^{-j\beta R}(1+\cos\theta)}{4\pi R}a^2\left\{\frac{\pi}{8}\Lambda_2(u)\right.$$

$$-4\sum_{n=o}^{\infty}\frac{(-1)^n\cos 2(2n+1)\phi}{2(2n+1)}\sum_{m=o}^{\infty}\frac{(-1)^m\left[\dfrac{1}{4n+2m+4}-\dfrac{1}{4n+2m+6}\right]u^{4n+2m+2}}{2^{2m+2(2n+1)}m!\Gamma(2(2n+1)+m+1)}$$

$$+j4\sum_{n=o}^{\infty}\frac{(-1)^m\cos(2n+1)\phi\sin(2n+1)\pi/4}{2n+1}\sum_{m=o}^{\infty}\frac{(-1)^m\left[\dfrac{1}{2n+2m+3}-\dfrac{1}{2n+2m+5}\right]u^{2n+2m+1}}{2^{2m+2n+1}m!\Gamma(2n+m+2)}$$

*$\Lambda(u)$ is a special form of the Bessel function. Confer, E. Jahnke and F. Emde, Tables of Functions, Dover.

@ p = 2

$$u_{P'_A} = j \frac{\beta e^{-j\beta R}(1+\cos\theta)a^2}{4\pi R} \left\{ \frac{\pi}{12} \Lambda_3(u) \right.$$

$$- 4 \sum_{n=o}^{\infty} \frac{(-1)^n \cos 2(2n+1)\phi}{2(2n+1)} \sum_{m=o}^{\infty} \frac{(-1)^m \left[\frac{1}{4n+2m+4} - \frac{2}{4n+2m+6} + \frac{1}{4n+2m+8} \right] u^{4n+2m+2}}{2^{4n+2m+2} m! \Gamma(4n+m+3)}$$

$$+ j4 \sum_{n=o}^{\infty} \frac{(-1)^n \cos(2n+1)\phi \sin(2n+1)\pi/4}{2n+1} \cdot$$

$$\left. \sum_{m=o}^{\infty} \frac{(-1)^m \left[\frac{1}{2n+2m+3} - \frac{2}{2n+2m+5} + \frac{1}{2n+2m+7} \right] u^{2n+2m+1}}{2^{2m+2n+1} m! \Gamma(2n+m+2)} \right.$$

NOTE: In using these equations, it must be remembered that the three aperture distributions considered have been normalized to 1. As a result, direct comparison of the cross-over levels, as shown in Figures 1 and 2, would lead to erroneous results. For practical antenna systems, equal power would be supplied to each antenna (p = 0, 1, 2) and hence the aperture distribution function would in fact be unnormalized. In compiling the data for Figure 6 this has been done.

UNCLASSIFIED